Self-Centering Steel Plate Shear Walls: Subassembly and Full-Scale Testing

Patricia M. Clayton

A dissertation
submitted in partial fulfillment of the
requirements for the degree of

Doctor of Philosophy

University of Washington

2013

Reading Committee:

Jeffrey Berman, Chair

Laura Lowes

Michael Motley

Program Authorized to Offer Degree:
Civil & Environmental Engineering

©Copyright 2013
Patricia M. Clayton

University of Washington

Abstract

Self-Centering Steel Plate Shear Walls:
Subassembly and Full-Scale Testing

Patricia M. Clayton

Chair of the Supervisory Committee:
Associate Professor Jeffrey Berman
Civil & Environmental Engineering

The self-centering steel plate shear wall (SC-SPSW) is a lateral force-resisting system that is capable of providing enhanced seismic performance, including recentering after an earthquake. The primary lateral strength of the SC-SPSW is provided by thin steel infill plates, referred to as web plates, that are connected to the beams and columns. During lateral sway, the web plate resists lateral load through the development of tension field action, and energy is dissipated through ductile yielding of the plate. Unlike conventional steel plate shear walls, the boundary frame in the SC-SPSW employs post-tensioned (PT) beam-to-column connections that are allowed to rock open during lateral sway. If properly designed, the PT connections eliminate damage in the boundary frame and provide restoring forces necessary to recentering the building during an earthquake, thus reducing post-earthquake downtime and repair costs.

This research builds upon previous analytical and numerical proof-of-concept studies on SC-SPSWs. Experimental testing was conducted to better understand SC-SPSW behavior and seismic performance. The experimental program consisted of (1) a series of large-scale subassembly cyclic tests to evaluate the impact of various design parameters on SC-SPSW behavior and component demands and (2) full-scale two-story pseudo-dynamic tests to evaluate system performance at three different seismic hazard levels. These tests also investigated possible performance-enhancing variations in SC-SPSW design that were not

considered in the previous proof-of-concept study. Post-tensioned column base connections were proposed to eliminate damage in the columns and provide additional recentering. SC-SPSWs with web plates that are only connected to the beams were proposed as a means of mitigating web plate tearing and reducing column demands. Methods for designing PT column base connections and SC-SPSWs with web plates connected to the beams only are presented.

Numerical investigations were conducted to evaluate different methods of modeling web plate behavior in SC-SPSWs, ranging from the relatively simple tension-only strip model to the more complex shell element model. When used in cyclic or dynamic analyses, the tension-only strip model was found to significantly underestimate the energy dissipation provided by the web plate, while the shell element model was too computationally demanding for wide-spread implementation. Based on numerical and experimental observations, a modified tension-compression strip model was proposed to conservatively approximate the web plate unloading resistance and the additional energy dissipation it provides.

Nonlinear response history analyses were conducted to asses seismic performance of several three- and nine-story SC-SPSW designs. These analyses compared SC-SPSWs with web plates connected to the beams and columns (fully-connected) and SC-SPSWs with web plates connected to the beams only (beam-connected). Results showed that SC-SPSWs using beam-connected web plates had smaller boundary frame members and larger drift demands than their fully-connected web plate counterparts; however, they were still able to meet proposed performance objectives. The numerical simulations also investigated the effects of considering the web plate unloading resistance in the model (e.g. the traditional tension-only model vs. the modified tension-compression model). These analyses showed that considering even small amounts of compression in the strip model significantly reduced drift demands.

TABLE OF CONTENTS

Page

List of Figures viii

List of Tables xxvii

Chapter 1: Introduction 1
1.1 Background and Motivation 1
1.2 SC-SPSW Mechanics 3
1.2.1 System Forces 3
1.2.2 Cyclic Response 8
1.3 Research Needs 11
1.4 Scope and Organization 12
1.4.1 Objectives and Scope of Research 12
1.4.2 Organization of Dissertation 13

Chapter 2: Literature Review 15
2.1 Introduction 15
2.2 Previous Steel PT Connection Research 15
2.2.1 PT beam-to-column connections with yielding elements 16
2.2.2 PT beam-to-column connections with friction devices 26
2.2.3 Effects of slab on PT beam-to-column connection 34
2.2.4 PT column base connection 39
2.3 Previous SPSW Research 43
2.3.1 Tromposch and Kulak (1987) 44
2.3.2 Caccese et al. (1993) 44
2.3.3 Schumacher et al. (1997) 45
2.3.4 Qu et al. (2008) 46
2.3.5 Vian et al. (2009) 47
2.3.6 Lin, Tsai, and Li (2010) 47
2.4 Previous SC-SPSW Research 50

2.4.1 Clayton (2010) . . . 51
2.4.2 Winkley (2011) . . . 59
2.4.3 Dowden (2012) . . . 60
2.5 Conclusions and Research Needs . . . 67

Chapter 3: Supplemental Mechanics for SC-SPSW Variations . . . 70
3.1 Introduction . . . 70
3.2 Web Plates Connected to HBEs Only . . . 70
3.2.1 Motivation . . . 70
3.2.2 General behavior . . . 72
3.2.3 HBE forces and moments . . . 77
3.2.4 VBE demands . . . 89
3.3 PT Column Base Connection . . . 91
3.3.1 Motivation and general behavior . . . 91
3.3.2 Column PT forces . . . 93
3.3.3 PT column base connection moment . . . 95
3.4 Summary . . . 96

Chapter 4: Subassembly Testing . . . 97
4.1 Introduction . . . 97
4.2 Test Set-up . . . 97
4.2.1 Specimen design . . . 97
4.2.2 Specimen descriptions . . . 101
4.2.3 Instrumentation . . . 105
4.2.4 Material properties . . . 114
4.2.5 Load protocol . . . 116
4.3 Experimental Observations and Results . . . 119
4.3.1 W18-6s75k . . . 119
4.3.2 W18-8s100k20Ga-2 . . . 120
4.3.3 W18-8s100k16Ga20Ga . . . 128
4.3.4 W18-8s100k20GaW . . . 134
4.3.5 W14-6s75k . . . 137
4.3.6 W14-8s100k16Ga . . . 139
4.3.7 W14-8s100k16GaHBE . . . 144
4.3.8 W14-8s100k20Ga . . . 147
4.3.9 W14-6s75k20Ga . . . 150

4.4 Data Corrections . . . 153
4.5 Summary of Subassembly Testing . . . 159

Chapter 5: Full-scale Testing . . . 162
5.1 Introduction . . . 162
5.2 Prototype Building . . . 162
5.3 Test Set-up . . . 165
5.3.1 Specimen description . . . 165
5.3.2 Instrumentation . . . 173
5.3.3 Material properties . . . 185
5.4 Loading . . . 186
5.4.1 Prototype design . . . 186
5.4.2 Prototype building numerical model . . . 191
5.4.3 Ground motion selection . . . 193
5.4.4 Response spectra . . . 199
5.4.5 Loading sequence . . . 203
5.4.6 Pseudo-dynamic loading algorithm . . . 204
5.5 Experimental Observations and Results . . . 206
5.5.1 Free Vibration Test . . . 206
5.5.2 Elastic test . . . 207
5.5.3 50/50 test . . . 209
5.5.4 10/50 test . . . 211
5.5.5 2/50 test . . . 220
5.5.6 Inelastic cyclic test . . . 227
5.6 Data Corrections . . . 235
5.7 Summary of Pseudo-dynamic testing . . . 236

Chapter 6: Data Analysis and Results . . . 239
6.1 Introduction . . . 239
6.2 Subassembly Test Data Analysis . . . 239
6.2.1 PT force and gap rotation . . . 239
6.2.2 PT losses . . . 244
6.2.3 HBE Axial force and moment demands . . . 246
6.2.4 Energy dissipation . . . 260
6.2.5 Initial and recentering stiffness . . . 262
6.2.6 Residual drift . . . 267

6.2.7 Web plate strains . . . 269
6.3 Comparison of Subassembly Responses . . . 272
6.3.1 Effects of load protocol . . . 272
6.3.2 Web plate thickness, t_w . . . 274
6.3.3 Number of PT strands, N_s, and initial force, T_o . . . 275
6.3.4 Effects of HBE depth . . . 276
6.3.5 Effects of web plate connection details . . . 277
6.3.6 Effect of web plate configuration . . . 279
6.3.7 Web plates connected to only HBEs . . . 281
6.4 Full-scale Test Data Analysis . . . 285
6.4.1 Fundamental period and damping . . . 285
6.4.2 PT force and gap rotation . . . 287
6.4.3 PT losses . . . 297
6.4.4 Strains near connections . . . 300
6.4.5 Axial force and moment demands . . . 303
6.4.6 Initial and recentering stiffnesses . . . 314
6.4.7 Residual drift . . . 317
6.4.8 Web plate strains . . . 320
6.5 Comparison with Conventional SPSW . . . 322
6.6 Summary of Data Analysis . . . 326
6.6.1 Summary of subassembly testing . . . 326
6.6.2 Summary of full-scale testing . . . 327

Chapter 7: Numerical Modeling . . . 329
7.1 Introduction . . . 329
7.2 OpenSees Model . . . 330
7.2.1 Description of model . . . 330
7.2.2 Web plate strip models . . . 332
7.2.3 Comparison of global response . . . 341
7.2.4 Comparison of boundary element demands . . . 354
7.2.5 Comparison of PT and connection responses . . . 363
7.2.6 Comparison of dynamic response histories . . . 369
7.3 ABAQUS Model . . . 374
7.3.1 Description of model and analysis . . . 374
7.3.2 Comparison with subassembly experimental results . . . 381

7.3.3 Comparison with full-scale experimental results . . . 391
7.4 Preliminary Results for Model WP . . . 404
7.4.1 Comparison with experimental results . . . 404
7.4.2 Comparison with ABAQUS model . . . 408
7.4.3 Comparison of energy dissipation with Model TC . . . 410
7.5 Summary of Numerical Models and Recommendations . . . 411
7.5.1 Summary of Numerical Models . . . 411
7.5.2 Modeling Recommendations . . . 415
7.5.3 Future improvements . . . 417

Chapter 8: Numerical Investigation of Building Response . . . 419
8.1 Introduction . . . 419
8.2 Prototype Building . . . 420
8.2.1 Building and site information . . . 420
8.2.2 SC-SPSW designs and member sizes . . . 421
8.2.3 Results of nonlinear response history analyses using tension-only strips 421
8.3 HBE-only Web Plate Connectivity Investigation . . . 425
8.3.1 Design process and assumptions . . . 425
8.3.2 HBE-only SC-SPSW designs . . . 432
8.3.3 Modeling validation . . . 434
8.4 Web Plate Residual Strength Investigation . . . 449
8.4.1 Modeling assumptions . . . 449
8.4.2 SC-SPSW buildings considered . . . 451
8.5 Nonlinear Response History Results . . . 452
8.5.1 Two-story models . . . 453
8.5.2 Three-story models . . . 456
8.5.3 Nine-story models . . . 472
8.6 Effects of Web Plate Connectivity on Design and Response . . . 497
8.6.1 Comparison of designs . . . 497
8.6.2 Comparison of response . . . 500
8.7 Effects of Web Plate Residual Strength . . . 502
8.7.1 Peak story drift demands . . . 502
8.7.2 Residual story drift demands . . . 503
8.7.3 HBE and VBE interaction values . . . 503
8.8 Summary of Numerical Study . . . 504

Chapter 9: Design Considerations and Recommendations . . . 507
9.1 Introduction . . . 507
9.2 PT Column Base Connection . . . 507
9.2.1 PT column base configurations . . . 508
9.2.2 Column PT design . . . 512
9.2.3 Limitations of PT column base connections implementation . . . 520
9.3 Web Plate Detailing . . . 526
9.3.1 Corner cutout . . . 526
9.3.2 Bolted vs. welded connection . . . 527
9.4 PT Connection Flange Detailing . . . 529
9.5 Diaphragm Connection Detailing . . . 530
9.5.1 Single-column loading configurations . . . 534
9.5.2 Two-column loading configurations . . . 536
9.5.3 Further research required . . . 537
9.6 Reduction in Column Sizes . . . 537
9.6.1 Benefits from reducing column sizes . . . 538
9.6.2 Possible approaches to reducing column sizes . . . 540
9.7 Updated Performance-based Seismic Design Procedure . . . 543
9.8 Summary of Design Recommendations . . . 547

Chapter 10: Summary and Conclusions . . . 549
10.1 Summary . . . 549
10.1.1 Subassembly testing . . . 549
10.1.2 Full-scale testing . . . 551
10.1.3 Numerical modeling approaches . . . 552
10.1.4 Numerical investigation of building response . . . 554
10.1.5 Design recommendations . . . 555
10.2 Conclusions . . . 556

References . . . 558

Appendix A: Additional Figures for Full-Scale Test Specimen and Instrumentation . 568
A.1 Fabrication Drawings . . . 568
A.2 Strain Gage Layout . . . 586

Appendix B: Additional Figures for Experimental Data Analysis of Subassembly Tests . . . 588
B.1 Gap Rotation and PT forces . . . 588
B.2 Axial and Moment Demands . . . 594
B.3 PT losses . . . 636
B.4 Web plate strains . . . 639

Appendix C: Additional Figures for OpenSees Models of Subassembly Tests . . . 647

Appendix D: Additional Figures for OpenSees Models of Full-scale Test . . . 667

Appendix E: Additional Figures for ABAQUS Models of Subassembly Tests . . . 674

Appendix F: Response parameters from tension-only SC-SPSW building numerical study . . . 688

LIST OF FIGURES

Figure Number Page

1.1 SC-SPSW elevation 4
1.2 Partial free-body diagram of deformed intermediate story of SC-SPSW 5
1.3 Free-body diagram of intermediate HBE 6
1.4 (a) Compression flange reaction component, (b) net vertical web plate component, (c) net horizontal web plate component, and (d) combined moment diagram of intermediate HBE 7
1.5 System force-displacement idealized responses 9

2.1 PT frame elevation [Garlock, 2002] 17
2.2 Kinematics of PT frame subassembly tests [Garlock, 2002] 18
2.3 Response of Specimen 20s-18-W. [Garlock, 2002] 19
2.4 Response of Specimen 20s-18-W without angles. [Garlock, 2002] 20
2.5 PT frame design objectives. [Garlock, 2002] 21
2.6 Experimental setup for PTED connection test [Christopoulos et al., 2002a] . 23
2.7 Hysteretic behavior of PTED connection [Christopoulos et al., 2002a] 24
2.8 Proposed PT beam-to-CFT column connection: (a) frame and (b) connection details [Chou et al., 2006] 25
2.9 Moment versus beam deflection response of (a) Specimen 1, (b) Specimen 2, and (c) Specimen 3 [Chou et al., 2006]. 26
2.10 Longitudinal stress distribution in FE model of Specimen 1 (a) after application of initial PT and (b) at 2% drift [Chou et al., 2006]. 27
2.11 Schematic of (a) PT frame and (b) post-tensioned friction damped connection detail [Rojas et al., 2005]. 28
2.12 (a) Schematic and (b) moment vs. relative rotation response of a PT connection with BFFD [Wolski et al., 2009]. 30
2.13 Schematic of PT connection with WBFD [Tsai et al., 2008]. 32
2.14 Schematic of (a) SC-MRF with WFD and (b) connection details [Lin et al., 2008]. 33
2.15 Schematic of (a) prototype building plan and (b) SC-MRF with PT-WFD test specimen [Lin et al., 2008]. 34
2.16 Frame expansion and collector beams [Garlock and Li, 2007] 35

2.17 Beam growth restraint at first floor HBE [Kim and Christopoulos, 2008] . . . 36
2.18 Detailing to eliminate slab restraint [Kim and Christopoulos, 2008] 36
2.19 Floor slab details for (a) partial bonded slab and (b) rigid bay slab systems presented by Chou and Chen [2011a]. 38
2.20 Two-bay PT frame test in Chou and Chen [2011a]. 40
2.21 Schematic of PT column base [Chi et al., 2008] 41
2.22 (a) Elevation of SC frame with post-tensioned base; (b) photo of PT column base [Chou and Chen, 2011b] 41
2.23 Schematic of PT column base spring model [Chou and Chen, 2011b] 42
2.24 Schematic of specimen tested by Tromposch and Kulak [1987] 44
2.25 Four narrow SPSW and R-SPSW test specimens [Tsai et al., 2010] 49
2.26 Narrow SPSW test set-up [Li et al., 2010] 50
2.27 Schematic elevation of intermediate story of SC-SPSW with web plates connected to HBEs and VBEs [Clayton, 2010] 52
2.28 Performance based design objectives of SC-SPSW 56
2.29 (a)Numerical model of 3-story SC-SPSW with (b) detail of numerical PT connection model 63
2.30 (a) Centerline rocking and (b) NewZ-BREAKSS PT HBE-to-VBE connections 63
2.31 Dimensions of UB specimens with (a) full web plates and (b) web plate strips. 64
2.32 Test set-up for quasi-static tests at UB. 65
2.33 Force vs. displacement response of quasi-static tests at UB. 66

3.1 Schematic elevation of intermediate story of SC-SPSW with web plates connected to HBEs only 74
3.2 Free-body diagram of intermediate story of SC-SPSW with web plates connected to HBEs only in deformed configuration 75
3.3 Portion of partial tension field acting on the beam as a function of panel aspect ratio 76
3.4 Free-body diagram of intermediate HBE for SC-SPSW with web plates connected to HBEs only 78
3.5 Illustration of flange compression component at intermediate HBE for SC-SPSW with web plates connected to HBEs only 79
3.6 Moment contribution from PT forces acting at rocking point 79
3.7 Illustration of vertical web plate component at intermediate HBE 80
3.8 Moment contribution from vertical distributed loads from plates 82
3.9 Illustration of horizontal web plate component at intermediate HBE 83
3.10 Axial contribution from horizontal distributed loads from plates 84

3.11 Moment contribution from horizontal distributed loads from plates 84
3.12 Axial force diagram for HBE with web plates connected to HBEs only 86
3.13 Moment diagram for HBE with web plates connected to HBEs only 87
3.14 VBE free-body diagrams for SPSWs with fully connected web plates [Berman and Bruneau, 2008] 90
3.15 (a) Left and (b) right VBE free-body diagrams for web plates not connected to VBEs 91
3.16 Schematic of PT column base connection 92

4.1 (a) Photo and (b) schematic drawing of SC-SPSW subassembly test setup. Further details and dimensions can be found in Winkley (2011). 99
4.2 PT connection detail. Further details and dimensions can be found in Winkley (2011). 100
4.3 (a) Welded and (b) bolted web plate-to-fish plate connection details 104
4.4 Schematic of W14-8s100k16GaHBE with web plates connected to only the HBEs. 105
4.5 Layout and naming of linear potentiometers, string potentiometers, and PT load cells. 107
4.6 Strain gage layout for W18-8s100k and W18-6s75k. 109
4.7 Strain gage layout for W18 SC-SPSW subassembly specimens 110
4.8 Strain gage layout for W14-6s75k, W14-8s100k16Ga, W14-8s100k16GaHBE. No strain gages were installed on the web plates in these specimens. 111
4.9 Strain gage layout for W14-8s100k20Ga. 112
4.10 Strain gage layout for W14-6s75k20Ga 113
4.11 Dimensions for web plate coupon specimens 114
4.12 Stress-strain curve for single web plate coupon test. 114
4.13 Displacement loading history for (a) LP1, (b) LP2, and (c) BF. 118
4.14 Photo of W18-6s75k before test 120
4.15 (a) Actuator force and (b) middle HBE PT force vs. drift responses of W18-6s75k 121
4.16 (a) Actuator force and (b) middle HBE PT force vs. drift response of W18-8s100k20Ga-2 122
4.17 (a) Tension field buckles and (b) residual deformation in web plate during 0.5% drift cycle (W18-8s100k20Ga-2) 123
4.18 Initial observation of slip in the bolted web plate-to-fish plate connection. . . 124
4.19 Typical SC-SPSW specimen in deformed configuration (shown here for W18-8s100k20Ga-2 at 1% drift). 125

4.20 Initial observation of web plate tearing at 3% drift (W18-8s100k20Ga-2). . . . 126
4.21 Schematic of progression of web plate tearing (W18-8s100k20Ga-2). 127
4.22 Web plate torn along the entire length of the bottom HBE at 4.4% drift (W18-8s100k20Ga-2). 128
4.23 Actuator force vs. drift response of W18-8s100k16Ga20Ga 129
4.24 Local kinking in interior of first story web plate at 1.5% drift 130
4.25 Schematic of progression of web plate tearing (W18-8s100k16Ga20Ga). 131
4.26 Slip in southwest corner of first story web plate of W18-8s100k16Ga20Ga at 4% drift. 132
4.27 Threaded spacer for PT strand squashed at 5% drift (W18-8s100k16Ga20Ga) 132
4.28 W18-8s100k16Ga20Ga at end of testing 133
4.29 Bolt hole elongation and deformation in the southwest corner of the first story web plate in W18-8s100k16Ga20Ga. 133
4.30 Actuator force vs. drift response of W18-8s100k20GaW 134
4.31 First observations of tearing in W18-8s100k20GaW at 0.75% drift. 135
4.32 Schematic of progression of web plate tearing (W18-8s100k20GaW). 136
4.33 Propagation of web plate tearing outside of the HAZ (W18-8s100k20GaW) . 137
4.34 Tearing along the VBEs after loading at 4.5% drift 137
4.35 (a) Actuator force and (b) middle HBE PT force vs. drift responses of W14-6s75k 138
4.36 Actuator force vs. drift response of W14-8s100k16Ga 139
4.37 Initial pullout of the first story web plate at the south end of the middle HBE (W14-8s100k16Ga) 141
4.38 Schematic of progression of web plate tearing (W14-8s100k16Ga). 142
4.39 Pullout of the first story web plate along the middle HBE at 4.5% drift (W14-8s100k16Ga) 143
4.40 Photo of W14-8s100k16GaHBE before test 144
4.41 Actuator force vs. drift response of W14-8s100k16GaHBE 144
4.42 Diagonal tension field at 0.75% drift in W14-8s100k16GaHBE 146
4.43 Schematic of progression of web plate tearing (W14-8s100k16GaHBE). 148
4.44 Actuator force vs. drift response of W14-8s100k20Ga 149
4.45 Shim plate welded to South VBE at top flange of middle HBE. 149
4.46 Schematic of progression of web plate tearing (W14-8s100k20Ga). 151
4.47 Photo of W14-6s75k20Ga before testing 152
4.48 Actuator force vs. drift response of W14-6s75k20Ga 152
4.49 Schematic of progression of web plate tearing (W14-6s75k20Ga). 154

4.50 (a) Axial and (b) moment demands calculated from strain gages of W18-6s75k after PT post-tensioning and before testing. . . . 158
4.51 Axial force demands calculated from strain gages of W14-8s100k16GaHBE after PT post-tensioning, during web plate installation, and before testing. . . 159
5.1 Plan and elevation of prototype building . . . 164
5.2 Elevation and details of Specimen FR . . . 168
5.3 Photo of Specimen FR setup . . . 169
5.4 Elevation and plan schematic drawings of lateral bracing and loading system. 170
5.5 Web plates being put into place in the horizontal plane . . . 172
5.6 String potentiometer attached to reference column . . . 174
5.7 Actuators and temposonic . . . 174
5.8 Displacement transducers to measure (a) BB double-angle and (b) TB PT connection rotations . . . 175
5.9 Displacement transducers to measure column PT connection gap opening . . 176
5.10 Diagonal displacement transducers to estimate web plate strain . . . 176
5.11 Displacement transducers to measure (a) shear bracket and (b) base pedestal slip . . . 177
5.12 Displacement transducer and string potentiometer layout and naming . . . 179
5.13 Strain gage layout . . . 180
5.14 Load cells for beam PT strands and column PT bars . . . 181
5.15 (a) Strain gage panel and (b) switch boxes used to collect instrument data signals . . . 182
5.16 Approximate camera locations and directions . . . 184
5.17 Photos of (a) camera column and (b) close-up of cameras at location MB-N . 184
5.18 Monotonic stress vs. strain response of LYS225 web plate material . . . 185
5.19 Virtual work method for approximating PT frame strength . . . 190
5.20 Schematic of OpenSees model of prototype SC-SPSW . . . 192
5.21 (a) Typical cyclic response of shear connection with composite slab and (b) proposed shear connection backbone model [Lui and Astaneh-Asl, 2004] . . . 194
5.22 Cyclic response of shear connection model used in OpenSees analyses . . . 195
5.23 Peak roof drift for each ground motion in preliminary prototype numerical model . . . 196
5.24 Ground excitations used in pseudo-dynamic tests . . . 198
5.25 Elastic strength demand response spectra for all Los Angeles SAC ground motions with median and 84^{th} percentiles shown [FEMA, 2000a] . . . 200

5.26 Median elastic strength demand spectra for Los Angeles SAC ground motion ensemble [FEMA, 2000a] . . . 201
5.27 Response and target spectra for excitations used in PSD tests . . . 202
5.28 Free vibration response . . . 207
5.29 Elastic cyclic response . . . 208
5.30 50/50 response . . . 210
5.31 10/50 response . . . 213
5.32 Specimen FR after the 10/50 PSD test. . . . 214
5.33 (a) East end of TB and (b) EC base PT connection gap openings at 10/50N1 214
5.34 Minor whitewash flaking in the column webs at the (a) column base and (b) just above the doubler plate in the panel zone during the 10/50 test. . . . 215
5.35 Yield lines in BB double angle connections . . . 216
5.36 Web plate tearing at end of 10/50 test. . . . 217
5.37 First web plate tearing (2 mm long) observed along first story of WC fish plate at 10/50R1 . . . 218
5.38 Longest web plate tear (13 cm long) at the end of 10/50 test . . . 219
5.39 Out-of-plane deformation of the web plate at the fish plate near the corner cutouts . . . 219
5.40 Force and drift vs. time for 10/50 test. (Notable times at zero force are marked with vertical dashed lines.) . . . 221
5.41 2/50 response . . . 222
5.42 Web plate tearing at end of 2/50 test. . . . 223
5.43 Tearing in top-east corner of first story web plate along (a) HBE and (b) VBE at 2/50P1 . . . 224
5.44 Out-of-plane buckling of web plate along fish plate . . . 224
5.45 Tearing in top-east corner of first story web plate along HBE at 2/50R1 . . . 225
5.46 Minor whitewash flaking in the column webs at the (a) column base and (b) just below the doubler plate in the panel zone during the 2/50 test. . . . 226
5.47 (a) Yield lines and (b) angle leg offset in double angles at BB connections. . . 226
5.48 EC exterior flange rounding at 2/50P1 . . . 227
5.49 Inelastic cyclic response . . . 228
5.50 Specimen FR after all tests. . . . 229
5.51 Web plate tearing at end of inelastic cyclic test (EOT). . . . 230
5.52 Diagonal yield lines at (a) east and (b) west column base . . . 231
5.53 Diagonal yield lines in east column web (a) above and (b) below the web doubler plate at the middle beam location . . . 232

5.54 Yielding in the double angle connections at the bottom beam at the end of testing . . . 233
5.55 Vertical yield lines on the (a) south and (b) north sides of the east end of the top beam web . . . 233
5.56 (a) North and (b) south side of the west column web at the middle beam connection (PT stands removed after testing) . . . 234
5.57 Typical flange reinforcing plate . . . 235

6.1 PT connection gap rotation response in middle HBE of W18-8s100k. (a) Gap rotation vs. drift, (b) total PT force vs. gap rotation . . . 240
6.2 PT connection gap rotation response in middle HBE of W18-8s100k16Ga. (a) Gap rotation vs. drift, (b) total PT force vs. gap rotation . . . 241
6.3 PT connection gap rotation response in middle HBE of W14-8s100k16Ga. (a) Gap rotation vs. drift, (b) total PT force vs. gap rotation . . . 243
6.4 Gap rotation vs. drift response in middle HBE of W14-8s100k16GaHBE. . . . 243
6.5 PT force loss vs. peak cycle drift for bottom, middle, and top HBEs of W18-8s100k20Ga-2 . . . 246
6.6 (a) Moment and (b) axial force demand vs. drift along middle HBE in W18-8s100k . . . 249
6.7 Moment demands along middle HBE in W18-8s100k at certain (a) positive and (b) negative drift demands . . . 250
6.8 (a) Moment and (b) axial force demand vs. drift along middle HBE in W18-8s100k20Ga-2 . . . 252
6.9 Moment demands along middle HBE in W18-8s100k20Ga-2 at certain (a) positive and (b) negative drift demands . . . 253
6.10 (a) Moment and (b) axial force demand vs. drift along bottom HBE in W18-8s100k20Ga-2 . . . 255
6.11 (a) Moment and (b) axial force demand vs. drift along top HBE in W18-8s100k20Ga-2 . . . 255
6.12 Influence of transfer of North VBE shear forces to pin at base of South VBE (PT and web plate forces not shown for clarity). . . . 256
6.13 (a) Moment and (b,c) axial force demand vs. drift along middle HBE in W18-8s100k16Ga20Ga . . . 259
6.14 Example of reduction in compression at HBE ends at large drift demands in W18-8s100k16Ga20Ga . . . 259
6.15 (a) Moment and (b) axial force demand vs. drift along middle HBE in W14-8s100k16GaHBE. . . . 261
6.16 Energy dissipated per cycle for specimens with displacement histories (a) BF, (b) LP1, and (c) LP2 . . . 263

6.17 Cumulative energy dissipated per cycle for specimens with displacement histories (a) BF, (b) LP1, and (c) LP2 . . . 264
6.18 Force vs. displacement plots showing $K_{i,exp}$ and data used to determine $K_{r,exp}$ for (a) W14-6s75k and (b) W14-8s100k16Ga . . . 267
6.19 Corner cutout strains in (a) W18-8s100k20GaW and (b) W18-8s100k20Ga-2 in 1st story web plate nearest the middle HBE. . . . 271
6.20 W14-8s100k20Ga: 1st story along middle HBE (a) principal strain and (b) angle of inclination at peak drifts . . . 273
6.21 Corner cutout strains in W14-6s75k20Ga in 1st story web plate nearest the middle HBE . . . 273
6.22 Comparison of specimens with different web plate thicknesses. . . . 275
6.23 Comparison of specimens with different number of PT strands and initial PT force. . . . 276
6.24 Comparison of specimens with different beam depth . . . 277
6.25 Comparison of total PT force in middle HBE for specimens with different beam depth . . . 278
6.26 Comparison of specimens with bolted (W18-8s100k20Ga-2) and welded (W18-8s100k20GaW) web plate-to-fish plate connection details . . . 280
6.27 Comparison of specimens with 20Ga web plates (W18-8s100k20Ga-2), 16Ga (W18-8s100k16Ga), and both (W18-8s100k16Ga20Ga) web plates . . . 281
6.28 Comparison of specimens with web plate connected along all edges (W14-8s100k16Ga) and along the HBEs only (W14-8s100k20GaHBE) . . . 283
6.29 Comparison of PT force in middle HBE of specimens with web plate connected along all edges (W14-8s100k16Ga) and along the HBEs only (W14-8s100k20GaHBE) . . . 284
6.30 Comparison of average measured axial force in specimens with web plate connected along all edges (W14-8s100k16Ga) and along the HBEs only (W14-8s100k20GaHBE) during 2% cycle . . . 284
6.31 Gap opening vs. drift during 10/50 PSD test . . . 288
6.32 Gap opening vs. PT force during 10/50 PSD test . . . 290
6.33 PT force vs. drift for 50/50 PSD test . . . 292
6.34 PT force vs. drift for 10/50 PSD test . . . 292
6.35 PT force vs. drift for 2/50 PSD test . . . 293
6.36 PT force vs. drift for Inelastic cyclic test . . . 293
6.37 Comparison of experimental and analytical column PT force demands. . . . 296
6.38 PT force loss vs. peak drift in Specimen FR . . . 298

6.39 Raw strain gage data vs. gap rotation for gages on the inside flange (IF) and outside flange (OF) near base of WC . . . 300
6.40 Corrected and averaged strain gage data vs. gap rotation for each flange near the base of the (a) WC and (b) EC . . . 301
6.41 Corrected and averaged strain gage data vs. gap rotation for each flange near the (a) west and (b) east ends of the MB . . . 302
6.42 Corrected and averaged strain gage data vs. gap rotation for each flange near the (a) west and (b) east ends of the TB . . . 302
6.43 (a) Axial force and (b) moment demands in the strain gage section in the BB 305
6.44 (a) Axial force and (b) moment demands vs. drift in the strain gage sections in the MB . . . 308
6.45 (a) Axial force and (b) moment demand distributions along the MB . . . 308
6.46 Axial force in MB due to web plate forces (i.e. $P_{HBE} - P_{PT}$) . . . 309
6.47 (a) Axial force and (b) moment demands in the strain gage sections in the TB311
6.48 (a) Axial force and (b) moment demand distributions along the TB . . . 311
6.49 Axial force in TB due to web plate and actuator loading forces (i.e. $P_{HBE}-P_{PT}$)312
6.50 (a) Axial force, (b) moment, and (c) axial force without PT contribution ($P_{VBE} - P_{PT}$) demands vs. drift for strain gage sections near bottom (B1) at top (T1) of WC first story . . . 315
6.51 (a) Axial force, (b) moment, and (c) axial force without PT contribution ($P_{VBE} - P_{PT}$) demands vs. drift for strain gage sections near bottom (B1) at top (T1) of EC first story . . . 316
6.52 Recentering stiffness calculations for (1)10/50, (b) 2/50, and (c) Inelastic tests318
6.53 Estimated strains in 1st story web plate from DTs on (a) south and (b) north side of the specimen . . . 321
6.54 Estimated strains in 2nd story web plate from DTs on (a) south and (b) north side of the specimen . . . 321
6.55 Specimen NC [Li et al., 2012] . . . 323
6.56 Specimen NC Web plate damage typical in corners at end of test [Lee, 2011] . 324
6.57 Comparison of conventional SPSW (Specimen NC) and SC-SPSW (Specimen FR) . . . 325
7.1 Schematic of numerical model of (a) subassembly specimen, (b) full-scale specimen, (c) strip rigid offset, and (d) PT connection . . . 333
7.2 Schematic of OpenSees numerical model of specimen with web plate connected to HBEs only. . . . 334
7.3 (a) Experimental and (b) tension-only strip model numerical response for SPSW specimen [Lubell et al., 2000] . . . 335

7.4 Residual strength (V_{res}) normalized by yield strength (V_y) from ABAQUS web plate models [Webster, 2013] . . . 336
7.5 Total web plate lateral strength as sum of tension and compression strip resistance . . . 337
7.6 Web plate tension-only (Model TO) and tension-compression (Model TC) strip material models fit to monotonic coupon test data . . . 338
7.7 SPSW web plate material model (Model WP) under monotonic and cyclic loading fit to coupon data . . . 339
7.8 Comparison of Models TO, TC, and WP strip response during repeated cycle of loading . . . 341
7.9 F_{TR}, F_{RES}, and F_{ST} in SPSW web plate uniaxial material (Model WP) hysteresis [Webster, 2013] . . . 342
7.10 Comparison of specimen W14-8s100k20Ga response with (a) tension-only (Model TO) and (b) tension-compression (Model TC) strip model responses . 343
7.11 Comparison of 10/50 test response with (a) tension-only (Model TO) and (b) tension-compression (Model TC) strip model responses during the (c) 2% cycle 344
7.12 Comparison of 10/50 test response with (a) tension-only (Model TO) and (b) tension-compression (Model TC) strip model responses during (c) free vibration . . . 345
7.13 Boundary frame models to estimate initial stiffness with non-idealized initial PT connection stiffness . . . 348
7.14 Typical gap rotation vs. drift response north end of bottom beam (shown for W18-8s100k16Ga). . . . 349
7.15 Comparison of specimen W14-8s100k16GaHBE response and numerical model with tension-compression (Model TC) strips . . . 355
7.16 Moment distribution at 2% drift for specimens (a) W18-8s100k20Ga-2 and (b) W14-8s100k20Ga . . . 357
7.17 Comparison of experimental (10/50) and numerical (Model TC) axial force vs. drift demands for certain locations in full-scale specimen beams . . . 359
7.18 Comparison of experimental (10/50) and numerical (Model TC) moment vs. drift demands for certain locations in full-scale specimen beams . . . 360
7.19 Comparison of experimental (10/50) and numerical (Model TC) axial force vs. drift demands for certain locations in full-scale specimen columns . . . 361
7.20 Comparison of experimental (10/50) and numerical (Model TC) moment vs. drift demands for certain locations in full-scale specimen columns . . . 362
7.21 Comparison of experimental and numerical PT connection response during 2% cycle . . . 364
7.22 Comparison of experimental and numerical PT force response during 2% cycle 365

7.23 Comparison of numerical (Model TC) and experimental (10/50 test) responses of beam PT connections for full-scale specimen 366
7.24 Comparison of numerical (Model TC) and experimental (10/50 test) responses of column base PT connections for full-scale specimen 367
7.25 Comparison of responses of different OpenSees models for 50/50 PSD test . . 371
7.26 Comparison of responses of different OpenSees models for 10/50 PSD test . . 372
7.27 Comparison of responses of different OpenSees models for 2/50 PSD test . . . 373
7.28 Schematic of ABAQUS model for (a) subassembly specimen and (b) full-scale specimen 377
7.29 Example of engineering stress vs. plastic strain yield surface from the monotonic coupon test and the true stress vs. logarithmic plastic strain yield surface used in ABAQUS web plate material model (shown here for second story of subassembly specimen W18-8s100k20Ga) 380
7.30 W18-8s100k20Ga-2 web plate deformation in experiment and ABAQUS model 383
7.31 W14-8s100k16Ga web plate deformation in experiment and ABAQUS model 384
7.32 W14-8s100k16GaHBE web plate deformation in experiment and ABAQUS model 385
7.33 Comparison of experimental and finite element model force vs. drift responses for specimens (a) W18-8s100k20Ga, (b) W18-8s100k20Ga-2, (c) W14-8s100k20Ga, and (d) W14-8s100k16GaHBE 387
7.34 Preliminary results of W14-8s100k20Ga ABAQUS model with lower web plate elastic modulus 389
7.35 Comparison of ABAQUS, OpenSees, and experimental middle HBE moment distributions at approx. 2% drift for (a) W18-8s100k20Ga-2 and (b) W14-8s1000k20Ga 390
7.36 (a) PT force and (b) gap rotation vs. drift response for middle HBE in W18-8s100k20Ga 391
7.37 Full-scale specimen web plate deformation at (a) the peak negative drift, at (b) the peak positive drift, and at (c) the end of the 10/50 displacement history 392
7.38 (a) Drift and (b) force time histories of ABAQUS and experimental results for 10/50 PSD 394
7.39 Force vs. drift response of ABAQUS and experimental results for 10/50 PSD highlighting the (a) peak cycle and (b) free vibration responses 394
7.40 Comparison of ABAQUS model and experimental (10/50 test) axial force vs. drift demands for certain locations in full-scale specimen beams 396
7.41 Comparison of ABAQUS model and experimental (10/50 test) moment vs. drift demands for certain locations in full-scale specimen beams 397

7.42 Comparison of ABAQUS model and experimental (10/50 test) axial force vs. drift demands for certain locations in full-scale specimen columns 398
7.43 Comparison of ABAQUS model and experimental (10/50 test) moment vs. drift demands for certain locations in full-scale specimen columns 399
7.44 Comparison of ABAQUS model and experimental (10/50 test) responses of beam PT connections for full-scale specimen 401
7.45 Comparison of ABAQUS model and experimental (10/50 test) responses of column base PT connections for full-scale specimen 402
7.46 PEEQ and corresponding tearing in upper-west corner of 1st story web plate at 1050N1 405
7.47 PEEQ and corresponding tearing in lower-east corner of 1st story web plate at 1050N1 406
7.48 Comparison of specimen (a) W18-6s75k20Ga, (b) W14-6s75k20Ga, and (c) W14-8s100k20Ga response with SPSW web plate (Model WP) strip model responses 407
7.49 Comparison of experimental, Model WP, and ABAQUS force vs. drift response 409
7.50 Comparison of Model TC and Model WP strip response 412

8.1 β_{web} vs. web plate aspect ratio 427
8.2 Plastic collapse mechanics for single-story SPSW with in-span hinge [Purba and Bruneau, 2010] 428
8.3 Design force diagrams for left VBE from 3-1050-6HBE (HBE-only) and 3-1050-6 (fully-conn.) at 5% drift 433
8.4 Design force diagrams for right VBE from 3-1050-6HBE (HBE-only) and 3-1050-6 (fully-conn.) at 5% drift 433
8.5 Comparison of OpenSees, ABAQUS, and experimental moment distributions for middle HBE at approx. +2% drift 438
8.6 Comparison of (a) cyclic and (b) monotonic OpenSees and ABAQUS models with different web plate connectivities and thicknesses 440
8.7 Middle HBE (a) moment distributions and (b) axial force at 2% drift for models with different web plate connectivities and thicknesses 442
8.8 Von Mises stress contours and vectors for HBE-only web plate 444
8.9 (a) Assumed constant web plate demands, (b) actual nonlinear web plate demands, and (c) approximate HBE axial distributions for HBE-only web plate 445
8.10 Left VBE (a) moment distributions and (b) axial force at 2% drift for models with different web plate connectivities and thicknesses 447
8.11 Right VBE (a) moment distributions and (b) axial force at 2% drift for models with different web plate connectivities and thicknesses 448

8.12 Normalized $\mu_{1/2}$ and 84^{th} percentile (a) peak story drifts and (b) residual story drifts at each hazard level for two-story SC-SPSW 455
8.13 Normalized $\mu_{1/2}$ and 84^{th} percentile (a) HBE and (b) VBE interaction values, D_{HBE} and D_{VBE}, at each hazard level for two-story SC-SPSW 455
8.14 Peak story drift response for SC-SPSWs with fully-connected and HBE-only web plates (Models TO) 461
8.15 Residual story drift response for SC-SPSWs with fully-connected and HBE-only web plates (Models TO) 461
8.16 HBE damage value for SC-SPSWs with fully-connected and HBE-only web plates (Models TO) 462
8.17 VBE damage value for SC-SPSWs with fully-connected and HBE-only web plates (Models TO) 462
8.18 Peak story drift response for SC-SPSWs with fully-connected and HBE-only web plates (Models TC25) 463
8.19 Residual story drift response for SC-SPSWs with fully-connected and HBE-only web plates (Models TC25) 463
8.20 HBE damage value for SC-SPSWs with fully-connected and HBE-only web plates (Models TC25) 464
8.21 VBE damage value for SC-SPSWs with fully-connected and HBE-only web plates (Models TC25) 464
8.22 Peak story drift response for SC-SPSWs with fully-connected web plates (Models TO and TC) 466
8.23 Residual story drift response for SC-SPSWs with fully-connected web plates (Models TO and TC) 466
8.24 HBE damage value for SC-SPSWs with fully-connected web plates (Models TO and TC) 467
8.25 VBE damage value for SC-SPSWs with fully-connected web plates (Models TO and TC) 467
8.26 Peak story drift response for SC-SPSWs with web plates connected to HBEs only (Models TO and TC) 468
8.27 Residual story drift response for SC-SPSWs with web plates connected to HBEs only (Models TO and TC) 469
8.28 HBE damage value for SC-SPSWs with web plates connected to HBEs only (Models TO and TC) 470
8.29 VBE damage value for SC-SPSWs with web plates connected to HBEs only (Models TO and TC) 471
8.30 Representative 50/50 (LA43) responses for 9-1050-6-TC25 and 9-1050-6HBE-TC25 478

8.31 Representative 50/50 (LA43) responses for 9-1050-8-TC25 and 9-1050-8HBE-TC25 . . . 479
8.32 Representative 50/50 (LA43) responses for 9-1050-10-TC25 and 9-1050-10HBE-TC25 . . . 480
8.33 Representative 10/50 (LA11) responses for 9-1050-6-TC25 and 9-1050-6HBE-TC25 . . . 481
8.34 Representative 10/50 (LA11) responses for 9-1050-8-TC25 and 9-1050-8HBE-TC25 . . . 482
8.35 Representative 10/50 (LA11) responses for 9-1050-10-TC25 and 9-1050-10HBE-TC25 . . . 483
8.36 Representative 2/50 (LA24) responses for 9-1050-6-TC25 and 9-1050-6HBE-TC25 . . . 484
8.37 Representative 2/50 (LA24) responses for 9-1050-8-TC25 and 9-1050-8HBE-TC25 . . . 485
8.38 Representative 2/50 (LA24) responses for 9-1050-10-TC25 and 9-1050-10HBE-TC25 . . . 486
8.39 Representative 50/50 (LA43) responses for 9-1050-6-TC25 and 9-1050-6-TC25 488
8.40 Representative 50/50 (LA43) responses for 9-1050-8-TC25 and 9-1050-8-TC25 489
8.41 Representative 50/50 (LA43) responses for 9-1050-10-TC25 and 9-1050-10-TC25 . . . 490
8.42 Representative 10/50 (LA11) responses for 9-1050-6-TC25 and 9-1050-6-TC25 491
8.43 Representative 10/50 (LA11) responses for 9-1050-8-TC25 and 9-1050-8-TC25 492
8.44 Representative 10/50 (LA11) responses for 9-1050-10-TC25 and 9-1050-10-TC25 . . . 493
8.45 Representative 2/50 (LA24) responses for 9-1050-6-TC25 and 9-1050-6-TC25 494
8.46 Representative 2/50 (LA24) responses for 9-1050-8-TC25 and 9-1050-8-TC25 495
8.47 Representative 2/50 (LA24) responses for 9-1050-10-TC25 and 9-1050-10-TC25 496

9.1 Possible column base PT connection configurations . . . 509
9.2 Estimation of column base forces due to wind loading . . . 514
9.3 Example of unequal column base shear forces for configurations where (a) the first story web plate forces are transfered to the columns and where (b) the web plate is anchored to the foundation. (Only horizontal forces at the base are shown for simplicity.) . . . 519
9.4 Examples of PT anchorage that is free to rotate (left) and is fixed (right). (Deformations are exaggerated) . . . 521
9.5 Examples of convex (left) and concave (right) domed PT anchorage bearings 521
9.6 Simplified free-body diagram for estimating maximum column uplift forces . 524

9.7 Approximate limits for employing PT column base connections 525
9.8 Schematic showing the location of the maximum tensile strains at the web plate corner cutouts 527
9.9 Schematic of diaphragm connection (one-column configurations) 532
9.10 Schematic of diaphragm connection (two-column configurations) 533
9.11 Stiff column effect 539

A.1 Strain gage layout with naming 587

B.1 W18-8s100k: PT connection gap opening and PT force response 588
B.2 W18-8s100k20Ga: PT connection gap opening and PT force response (Note: potentiometer pgs2t (south end of HBE) was sticking due to a sticky substance on the shaft of the moving plunger. The problem was most evident at small drifts less than 2% drift.) . 589
B.3 W18-6s75k20Ga: PT connection gap opening and PT force response 589
B.4 W18-6s75k16Ga: PT connection gap opening and PT force response 589
B.5 W18-8s100k16Ga: PT connection gap opening and PT force response 590
B.6 W18-6s75k: PT connection gap opening and PT force response 590
B.7 W18-8s100k20Ga-2: PT connection gap opening and PT force response . . . 590
B.8 W18-8s100k16Ga20Ga: PT connection gap opening and PT force response . 591
B.9 W18-8s100k20GaW: PT connection gap opening and PT force response (Note: potentiometers pgs2t and pgn2b (south and north ends of HBE) were not adequately secured to the specimen. The adhesive used to connect these potentiometers to the specimen slipped throughout the entire test resulting in faulty θ_r measurements.) 591
B.10 W14-6s75k: PT connection gap opening and PT force response 592
B.11 W14-8s100k16Ga: PT connection gap opening and PT force response 592
B.12 W14-8s100k16GaHBE: PT connection gap opening and PT force response . . 592
B.13 W14-8s100k20Ga: PT connection gap opening and PT force response 593
B.14 W14-6s75k20Ga: PT connection gap opening and PT force response 593
B.15 W18-8s100k: Bottom HBE 594
B.16 W18-8s100k: Middle HBE 595
B.17 W18-8s100k: Top HBE 596
B.18 W18-8s100k20Ga: Bottom HBE 597
B.19 W18-8s100k20Ga: Middle HBE 598
B.20 W18-8s100k20Ga: Top HBE 599
B.21 W18-6s75k20Ga: Bottom HBE 600
B.22 W18-6s75k20Ga: Middle HBE 601
B.23 W18-6s75k20Ga: Top HBE 602

B.24 W18-6s75k16Ga: Bottom HBE . . . 603
B.25 W18-6s75k16Ga: Middle HBE . . . 604
B.26 W18-6s75k16Ga: Top HBE . . . 605
B.27 W18-8s100k16Ga: Bottom HBE . . . 606
B.28 W18-8s100k16Ga: Middle HBE . . . 607
B.29 W18-8s100k16Ga: Top HBE . . . 608
B.30 W18-6s75k: Bottom HBE . . . 609
B.31 W18-6s75k: Middle HBE . . . 610
B.32 W18-6s75k: Top HBE . . . 611
B.33 W18-8s100k20Ga-2: Bottom HBE . . . 612
B.34 W18-8s100k20Ga-2: Middle HBE . . . 613
B.35 W18-8s100k20Ga-2: Top HBE . . . 614
B.36 W18-8s100k16Ga20Ga: Bottom HBE . . . 615
B.37 W18-8s100k16Ga20Ga: Middle HBE . . . 616
B.38 W18-8s100k16Ga20Ga: Top HBE . . . 617
B.39 W18-8s100k20GaW: Bottom HBE . . . 618
B.40 W18-8s100k20GaW: Middle HBE . . . 619
B.41 W18-8s100k20GaW: Top HBE . . . 620
B.42 W14-6s75k: Bottom HBE . . . 621
B.43 W14-6s75k: Middle HBE . . . 622
B.44 W14-6s75k: Top HBE . . . 623
B.45 W14-8s100k16Ga: Bottom HBE . . . 624
B.46 W14-8s100k16Ga: Middle HBE . . . 625
B.47 W14-8s100k16Ga: Top HBE . . . 626
B.48 W14-8s100k16GaHBE: Bottom HBE . . . 627
B.49 W14-8s100k16GaHBE: Middle HBE . . . 628
B.50 W14-8s100k16GaHBE: Top HBE . . . 629
B.51 W14-8s100k20Ga: Bottom HBE . . . 630
B.52 W14-8s100k20Ga: Middle HBE . . . 631
B.53 W14-8s100k20Ga: Top HBE . . . 632
B.54 W14-6s75k20Ga: Bottom HBE . . . 633
B.55 W14-6s75k20Ga: Middle HBE . . . 634
B.56 W14-6s75k20Ga: Top HBE . . . 635
B.57 W18-8s100k: PT losses . . . 636
B.58 W18-8s100k20Ga: PT losses . . . 636

B.59 W18-6s75k20Ga: PT losses . . . 636
B.60 W18-6s75k16Ga: PT losses . . . 636
B.61 W18-8s100k16Ga: PT losses . . . 637
B.62 W18-6s75k: PT losses . . . 637
B.63 W18-8s100k20Ga-2: PT losses . . . 637
B.64 W18-8s100k16Ga20Ga: PT losses . . . 637
B.65 W18-8s100k20GaW: PT losses . . . 637
B.66 W14-6s75k: PT losses . . . 637
B.67 W14-8s100k16Ga: PT losses . . . 638
B.68 W14-8s100k16GaHBE: PT losses . . . 638
B.69 W14-8s100k20Ga: PT losses . . . 638
B.70 W14-6s75k20Ga: PT losses . . . 638
B.71 W18-8s100k20Ga-2: web plate strains . . . 640
B.72 W18-8s100k16Ga20Ga: web plate strains . . . 641
B.73 W18-8s100k20GaW: web plate strains . . . 642
B.74 W14-8s100k20Ga: 1st story along middle HBE, principal strains and directions 644
B.75 W14-8s100k20Ga: 2nd story along middle HBE, principal strains and directions 645
B.76 W14-6s75k20Ga: 1st story along middle HBE, principal strains and directions 646

C.1 Comparison of OpenSees model and experimental global force vs. drift responses (cont.) . . . 652
C.2 W18-8s100k: Comparison of OpenSees model and experimental component responses during 2% cycle . . . 653
C.3 W18-8s100k20Ga: Comparison of OpenSees model and experimental component responses during 2% cycle . . . 654
C.4 W18-6s75k20Ga: Comparison of OpenSees model and experimental component responses during 2% cycle . . . 655
C.5 W18-6s75k16Ga: Comparison of OpenSees model and experimental component responses during 2% cycle . . . 656
C.6 W18-8s100k16Ga: Comparison of OpenSees model and experimental component responses during 2% cycle . . . 657
C.7 W18-6s75k: Comparison of OpenSees model and experimental component responses during 2% cycle . . . 658
C.8 W18-8s100k20Ga-2: Comparison of OpenSees model and experimental component responses during 2% cycle . . . 659
C.9 W18-8s100k16Ga20Ga: Comparison of OpenSees model and experimental component responses during 2% cycle . . . 660

C.10 W18-8s100k20GaW: Comparison of OpenSees model and experimental component responses during 2% cycle 661
C.11 W14-6s75k: Comparison of OpenSees model and experimental component responses during 2% cycle 662
C.12 W14-8s100k16Ga: Comparison of OpenSees model and experimental component responses during 2% cycle 663
C.13 W14-8s100k16GaHBE: Comparison of OpenSees model and experimental component responses during 2% cycle 664
C.14 W14-8s100k20Ga: Comparison of OpenSees model and experimental component responses during 2% cycle 665
C.15 W14-6s75k20Ga: Comparison of OpenSees model and experimental component responses during 2% cycle 666

D.1 Comparison of experimental (10/50) and numerical (Model TO) axial force vs. drift demands for certain locations in full-scale specimen beams 668
D.2 Comparison of experimental (10/50) and numerical (Model TO) moment vs. drift demands for certain locations in full-scale specimen beams 669
D.3 Comparison of experimental (10/50) and numerical (Model TO) axial force vs. drift demands for certain locations in full-scale specimen columns 670
D.4 Comparison of experimental (10/50) and numerical (Model TO) moment vs. drift demands for certain locations in full-scale specimen columns 671
D.5 Comparison of numerical (Model TO) and experimental (10/50 test) responses of beam PT connections for full-scale specimen 672
D.6 Comparison of numerical (Model TO) and experimental (10/50 test) responses of column base PT connections for full-scale specimen 673

E.1 Comparison of OpenSees model and experimental global force vs. drift responses (cont.) 676
E.2 W18-8s100k20Ga: Comparison of ABAQUS model and experimental component responses during 2% cycle 677
E.3 W18-6s75k20Ga: Comparison of ABAQUS model and experimental component responses during 2% cycle 678
E.4 W18-6s75k16Ga: Comparison of ABAQUS model and experimental component responses during 2% cycle 679
E.5 W18-8s100k16Ga: Comparison of ABAQUS model and experimental component responses during 2% cycle 680
E.6 W18-8s100k20Ga-2: Comparison of ABAQUS model and experimental component responses during 2% cycle 681

E.7 W18-8s100k16Ga20Ga: Comparison of ABAQUS model and experimental component responses during 2% cycle 682
E.8 W18-8s100k20GaW: Comparison of ABAQUS model and experimental component responses during 2% cycle (Note: The experimental axial force measurements derived from strain gage readings in middle HBE were drifting to lower magnitudes over the course of the test (Fig. B.40); however, PT forces did not have a similar reduction throughout the test (Fig. B.9(b)). This reduction in experimental axial force magnitude (also used to extimate connection moments) is beleived to be an artificial result of faulty strain gage readings; however, similar trends in response can be observed.) 683
E.9 W14-8s100k16Ga: Comparison of ABAQUS model and experimental component responses during 2% cycle 684
E.10 W14-8s100k16GaHBE: Comparison of ABAQUS model and experimental component responses during 2% cycle 685
E.11 W14-8s100k20Ga: Comparison of ABAQUS model and experimental component responses during 2% cycle 686
E.12 W14-6s75k20Ga: Comparison of ABAQUS model and experimental component responses during 2% cycle 687

F.1 Peak story drift median ($\mu_{1/2}$) and 84th percentile response [Clayton, 2010] . 690
F.2 Residual story drift median ($\mu_{1/2}$) and 84th percentile response [Clayton, 2010] 691
F.3 HBE damage value median ($\mu_{1/2}$) and 84th percentile response [Clayton, 2010] 692
F.4 VBE damage value median ($\mu_{1/2}$) and 84th percentile response [Clayton, 2010] 693

LIST OF TABLES

Table Number Page

4.1 SC-SPSW subassembly specimen descriptions . . . 103
4.2 Web plate material properties . . . 115
4.3 Subassembly test damage observations . . . 155

5.1 Target Spectral Accelerations for Los Angeles location for Soil Type S_D for 5% Damping Level (from Somerville et al. [1997]) . . . 163
5.2 Summary of ground motions used for pseudo-dynamic tests . . . 198
5.3 Pseudo-dynamic tests . . . 203
5.4 Quasi-static tests . . . 203
5.5 Observations during pseudo-dynamic testing . . . 212

6.1 Initial PT force and PT losses for SC-SPSW subassembly specimens . . . 245
6.2 PT anchorage seating for SC-SPSW subassembly specimens . . . 247
6.3 Initial and recentering stiffnesses of SC-SPSW subassembly specimens . . . 266
6.4 Residual drifts of SC-SPSW subassembly specimens . . . 268
6.5 Fundamental period during free vibration of PSD tests . . . 285
6.6 Calculated equivalent viscous damping ratio during free vibration of PSD tests 286
6.7 Initial PT force and PT losses for Specimen FR . . . 298
6.8 PT anchorage seating for Specimen FR . . . 299
6.9 Initial and recentering stiffnesses of Specimen FR . . . 317
6.10 Residual drifts determined from different methods for each PSD test . . . 320
6.11 Comparison of frame and web plate properties for Specimen NC [Li et al., 2012] and Specimen FR . . . 324

7.1 Initial and recentering stiffnesses of OpenSees models (Model TO)‡ of specimens compared with experimental results . . . 346
7.2 Initial stiffnesses of OpenSees models (Model TO) of specimens assuming non-idealized initial PT connection response compared with experimental results . . . 350
7.3 Peak (min. and max.) drift demands in PSD tests and dynamic analyses . . . 370

8.1 Response Spectra Values for Los Angeles site (from Somerville et al. 1997) . . . 421

8.2 Design parameters for 3-story prototype designs [Clayton, 2010] 422
8.3 Design parameters for 9-story prototype designs [Clayton, 2010] 423
8.4 Design parameters for 3-story HBE-only web plate designs 434
8.5 Design parameters for 9-story HBE-only web plate designs 435
8.6 Strip compression strength considered in tension-variable compression (TCv) models 451
8.7 Summarized response parameters for 3-story SC-SPSWs with web plates connected to the HBEs only 457
8.8 Summarized response parameters for 3-story SC-SPSWs with fully-connected web plates and with tension-compression web plate models 458
8.9 Ground motions selected for 9-story analyses 472
8.10 Response parameters for 9-1050-6 SC-SPSWs with fully-connected web plates (TO and TC25) and HBE-only web plates (HBE-TC25) 474
8.11 Response parameters for 9-1050-8 SC-SPSWs with fully-connected web plates (TO and TC25) and HBE-only web plates (HBE-TC25) 475
8.12 Response parameters for 9-1050-10 SC-SPSWs with fully-connected web plates (TO and TC25) and HBE-only web plates (HBE-TC25) 476
8.13 Approximate weight savings for HBE-only web plate designs compared with fully-connected web plate designs 499

F.1 Summarized response parameters from nonlinear analyses [Clayton, 2010] . . 689

ACKNOWLEDGMENTS

I would like to express my sincere gratitude to my advisors Dr. Jeffrey Berman and Dr. Laura Lowes for their time and guidance throughout my research and their continued support in my academic career. I would also like to thank Dr. Michael Motley for serving on my reading committee and Kate Simonen for serving as my graduate school representative. A special thanks also goes to Dr. John Stanton whose support and encouragement has greatly impacted my academic career and aspirations. Thanks also to Dr. Keh-Chyuan Tsai of National Taiwan University (NTU) for serving as an advisor during my time at NCREE.

I would like to thank the Valle Scholarship Program for funding in my first year of graduate school, without which I would not have had the opportunity to study at the University of Washington. The financial support provided by the National Science Foundation under the George E. Brown, Jr. Network for Earthquake Engineering Simulation Research program (Award number CMMI-0830294), the Graduate Research Fellowship Program (Award number DGE-0718124), and the East Asia and Pacific Summer Research Institute program (Award number OISE-1209569) is also appreciated. Thanks also to the American Institute of Steel Construction for donation of material used in the experimental programs.

Much of the experimental work would not have been possible without the kind help of many students and staff: Tyler Winkley, Ryan Ganey, Vince Chaijaroen, and Yiming Liu of UW; Chao-Hsien Li, Dr. K.-J. Wang, and Chih-Hsiung Chou of NCREE; and Jonathan Su, Huang Tung, Ching-Yi Tsai, and the KC512 research group of NTU. I would also like to acknowledge the additional support of my office mates at UW throughout the years including Jonathan Weigand, Bo-Shiuan Wang, Mohammad Malakoutian, Olafur Haraldsson, and Anna Birely.

Many of the numerical analyses presented in this dissertation were done using resources

provided by the Holland Computing Center of the University of Nebraska and by the Open Science Grid (OSG), which is supported by the National Science Foundation and the U.S. Department of Energy's Office of Science. I would particularly like to thank Marko Slyz and Gabriele Garzoglio of the OSG User Support Team for their assistance in running OpenSees on OSG.

A special thanks also goes to my colleagues and collaborators on this project: Daniel Dowden and Dr. Michel Bruneau of the University at Buffalo and David Webster and Tyler Winkley of UW. It was a pleasure working with each of you.

Finally, I would like to thank my friends and family for their support during all of my endeavors. I am lucky to have met such inspirational people during my time in Seattle, and I would not be where I am today without having my family as role models in my life. Thank you.

Chapter 1

INTRODUCTION

1.1 Background and Motivation

The steel plate shear wall (SPSW) has for decades been used as a primary lateral load resisting system in areas of high seismicity such as the U.S., Canada, Japan, and Taiwan. These systems comprise a steel frame consisting of beams, referred to as horizontal boundary elements (HBE), columns, referred to as vertical boundary elements (VBE), and a steel infill plate, referred to as the web plate. The terms beams and columns and HBEs and VBEs, respectively, may be used interchangably. Earlier implementations of the SPSW in Japan used thick, stiffened web plates to resist the lateral load through shear yielding. More recently, beginning with research in the early 1980s, the use of thin, unstiffened web plates were found to provide ductile performance while reducing the demands imposed on surrounding boundary elements. The thin plate design intentionally allows the web plates to buckle in shear and develop lateral load resistance through the development of diagonal tension field action, which results in more efficient designs by reducing the demands imposed on the boundary elements without drastically decreasing the lateral load capacity of the system [Sabelli and Bruneau, 2007]. The SPSW system offers benefits such as: more architectural flexibility than comparable concrete shear walls, due to its thin profile; high initial stiffness and ultimate strength; distributed yielding over multiple stories; ease of construction and post-earthquake replacement of web plates; and stable ductile performance where the web plate has significant deformation capacity following initial onset of tearing in the plate. In recent decades, the SPSW has been implemented successfully as the primary lateral load resisting system in several buildings [Robinson and Ames, 2000; Seilie and Hooper, 2005; Monnier and Harasimowicz, 2007; Kristeva, 2010]. However, yielding in the

boundary elements of a conventional SPSW can result in significant residual deformations following a seismic event, making for long and costly post-event repair and loss of building functionality.

To reduce post-earthquake structural repair and thereby decrease economic and functionality losses, self-centering systems have been developed to return a structural system back to a fully functional state following a seismic event. These systems typically rely on elastic post-tensioned elements to provide the restoring forces required to bring a building back to its original configuration. This concept was originally implemented in unbonded post-tensioned precast concrete walls and frames in the early 1990s [Stanton et al., 1997; Stanton and Nakaki, 2002; Priestly, 1991] and later extended to post-tensioned steel moment resisting frames in the early 2000s [Garlock, 2002]. The post-tensioned (PT) steel moment resisting frames (MRF) typically consist of high strength steel bars or strands placed within the depth of the beam and anchored to the columns. Although these PT connections do provide recentering capabilities for the structure, they remain elastic during a seismic event, thus providing no energy dissipation on their own; therefore, they need to be paired with energy dissipation elements to dissipate energy input from the ground motion and reduce accelerations. Examples of energy dissipation elements in previous PT steel MRF studies include yielding top and seat angles [Garlock, 2002], yielding energy dissipation bars [Christopoulos et al., 2002a], and flange friction devices [Rojas et al., 2005].

The PT connection develops its strength from the forces in the PT elements, as will be described in more detail in later chapters; therefore, these systems require substantial PT forces in order to develop adequate system strength comparable to conventional steel MRFs. If a PT frame were designed to have the same strength as a MRF, the PT strength and stiffness would have to be proportioned such that the connection capacity would be equivalent to the plastic moment capacity of the beam of the comparable moment resisting connection. Additionally, for the PT connection to retain its recentering capabilities, it would have to reach this capacity before the onset of PT yielding and before the beam reaches its plastic moment, reduced for the additional axial loads imposed by the PT elements. Therefore, if a PT connection is designed to have the same strength as a fully welded connection, a larger beam section and significant PT forces are required; however, if the PT connection

is paired with a system that resists lateral loads primarily through a mechanism other than connection moment strength, these PT forces can be greatly reduced.

In this research, a self-centering SPSW (SC-SPSW) system is proposed that combines the lateral load resisting benefits of the SPSW with the self-centering capabilities of the post-tensioned connection by replacing the typical moment-resisting connections of a conventional SPSW with PT HBE-to-VBE connections as shown in Figure 1.1. This system resists the lateral load and dissipates energy through tension field action and subsequent yielding of the web plate, while the PT HBE-to-VBE connections reduce the potential for damage in the HBEs and provide system recentering. The SPSW is ideal for being paired with self-centering mechanisms as the tension-only behavior (to be discussed later) provides near-zero resistance to recentering; therefore, unlike other self-centering systems with yielding elements that exhibit full hysteretic behavior (e.g. energy dissipating bars and angles), the SC-SPSW system can use smaller beams or fewer PT strands to overcome the resistance of the energy dissipating component during unloading. Additionally, the SPSW web plates provide a large initial stiffnesses and very ductile yielding. In the event that yielded or damaged web plates require repair or replacement following an earthquake, the building will be recentered while the relatively quick and easy repair of the plates takes place, greatly reducing the downtime associated with costly VBE and HBE repairs.

1.2 SC-SPSW Mechanics

1.2.1 System Forces

To determine the design demands on boundary elements and understand SC-SPSW behavior the partial free-body diagram of an intermediate story of a SC-SPSW in its deformed configuration, as shown in Fig. 1.2, can be used. There ω is the distributed web plate forces acting on the boundary elements in the direction, α, of the tension field, V_i is the lateral load applied at level i, T_{PT} is the total force in the PT elements at each connection, L is the centerline VBE dimension, θ_r is the gap rotation, θ_s is the column drift, and Δ_{gap} is the amount of frame expansion due to the HBEs rocking about their flanges [Garlock et al., 2007]. Clayton [2010] has detailed formulations for HBE demands. Note that in Fig. 1.2,

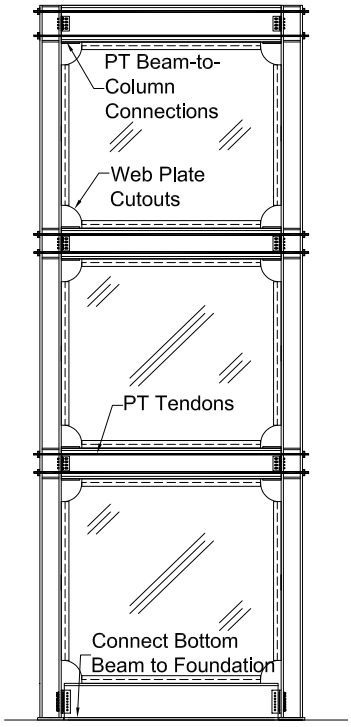

(a)

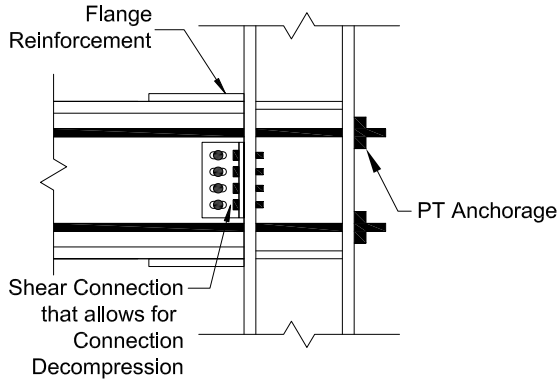

(b)

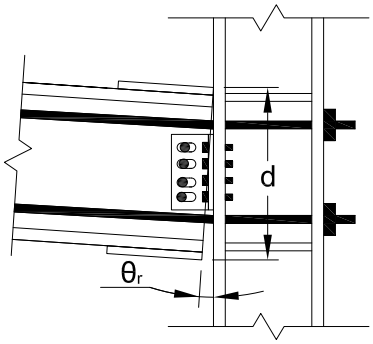

(c)

Figure 1.1: (a)Typical SC-SPSW elevation; PT HBE-to-VBE connection detail in the (b) undeformed and (c) deformed configurations.

the PT elements and shear connections are not shown for clarity.

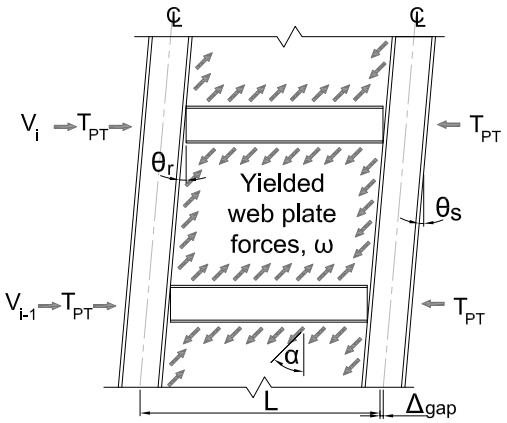

Figure 1.2: Partial free-body diagram of deformed intermediate story of SC-SPSW

1.2.1.1 HBE demands

The HBE is a key component in the SC-SPSW system. Understanding the mechanics of the HBE and the interaction of the web plate and PT connection forces acting on the HBE is important in understanding the behavior of the system and SC-SPSW design concepts.

Fig. 1.3 shows a free-body diagram of an intermediate HBE after connection decompression, where $\omega_{b(i)}$ and $\omega_{b(i+1)}$ are the distributed forces from the yielded web plate below and above the HBE acting in the direction of the diagonal tension field, T_{PT} is the total force of the PT strands acting on opposite flanges at the ends of the HBE, referred to as the connection rocking points, $P_{HBE(VBE)}$ is the compressive force acting at the HBE rocking points that is due to the distributed web plate forces pulling in the VBEs, $P_{HBE(web)}$ is the reaction force at the ends of the HBE due to the net axial distributed load acting on the HBE when the web plates above and below the HBE are of different strength or thickness, and V_L and V_R are the shear reactions at the left and right ends of the HBE, respectively. Expressions for $P_{HBE(VBE)}$ and $P_{HBE(web)}$ can be found in Sabelli and Bruneau [2007], and expressions for the shear forces and total PT force, including losses due to HBE shortening, can be found in Clayton [2010]. Although in construction, radial corner cutouts (as shown

in Fig. 1.1) would be necessary to prevent localized damage to the web plate during connection decompression, for the purpose of simplicity in this introduction, the corner cutouts are ignored, and the web plate is assumed to extend over the entire length of the HBE, L_{cf}. A discussion of the corner cutout's affect on HBE demands can be found in Clayton [2010].

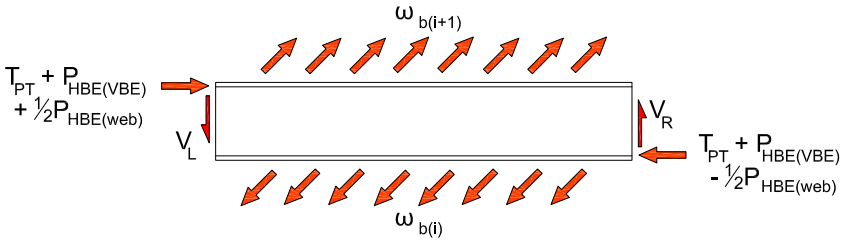

Figure 1.3: Free-body diagram of intermediate HBE

For design of the HBE, a moment diagram must be developed from the free-body diagram in Fig. 1.3 to better understand the interaction between the PT and web plate forces acting on the HBE. As shown in Fig. 1.4, the HBE moment diagram can be separated into components. Fig. 1.4(a) shows the linear moment diagram component due to the compressive forces from the total PT and VBE pull-in forces acting at the rocking points. The magnitude of the moment at the end of the HBE due to this component is the compressive reaction force from these components, $T_{PT} + P_{HBE(VBE)}$, times the lever arm of $d/2$, where d is the depth of the HBE. Fig. 1.4(b) shows the parabolic moment diagram component due to the vertical components of the net distributed web plate force acting on the HBE, ω_{yb}. Fig. 1.4(c) shows the constant moment diagram component due to the net horizontal distributed web plate forces acting on the HBE. The magnitude of this component is the end reaction due to the net horizontal web plate loading, $\frac{1}{2}P_{HBE(web)}$, times the lever arm of $d/2$. Each of these components can be superimposed onto one another to determine the total moment diagram shown in Fig. 1.4(d). More details on the moment, shear, and axial force diagrams of an intermediate HBE in a SC-SPSW can be found in Clayton [2010].

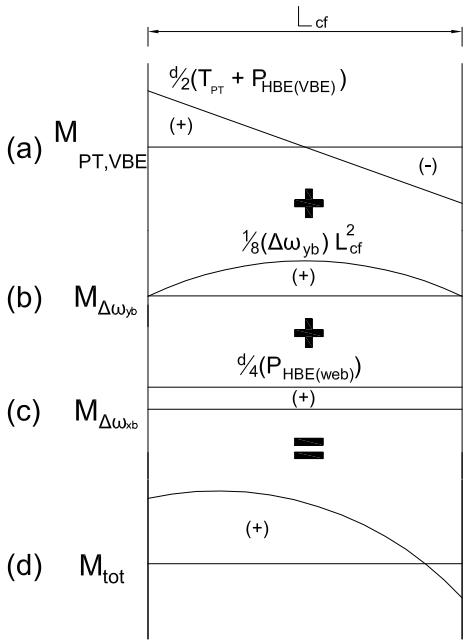

Figure 1.4: (a) Compression flange reaction component, (b) net vertical web plate component, (c) net horizontal web plate component, and (d) combined moment diagram of intermediate HBE

1.2.2 Cyclic Response

The behavior of the SC-SPSW system can be separated into contributions from the two components of the system, the PT frame and the SPSW web plates. The behavior of the individual components and the combined SC-SPSW system are presented below.

1.2.2.1 SPSW Behavior

The behavior of a conventional SPSW is primarily governed by the development of post-buckling tension field action in its web plates. The response of an idealized single-story SPSW with simple beam-to-column connections (Fig. 1.5(a)) shows a large initial stiffness upon development of the tension field, with a plateau at the point of full plate yielding. Web plate yielding results in distributed loading of the HBEs and VBEs. In Fig. 1.5(a) it has been assumed that the entire plate yields instantaneously, which is only true for the case of infinitely stiff boundary elements. As the HBE becomes more flexible, the backbone of the SPSW hysteresis becomes rounded as yielding occurs progressively over the web plate due to flexural deformation of the boundary elements, as shown in more detail in Dowden et al. [2012]. When fully unloaded after an inelastic excursion, the web plates are left with accumulated plastic strain; due to the slenderness of the web plates and the near-zero stiffness of the idealized web plate after unloading, relatively little force is required to return the SPSW to zero-displacement. Additional background on SPSW behavior can be found in Sabelli and Bruneau [2007]. It should also be noted that actual web plate behavior is more complex than this idealization, as will be discussed in later chapters; however, this idealization provides an introduction to the general web pate behavior necessary for understanding SC-SPSW behavior.

1.2.2.2 PT Connection Behavior

The self-centering portion of the SC-SPSW behavior is achieved with the use of post-tensioned (PT) HBE-to-VBE connections in the boundary frame. The connection consists of PT tendons spanning the length of the HBE and anchored at the outer flanges of the VBEs. Shear may be transferred from the HBE to VBE through any shear transfer mechanism that

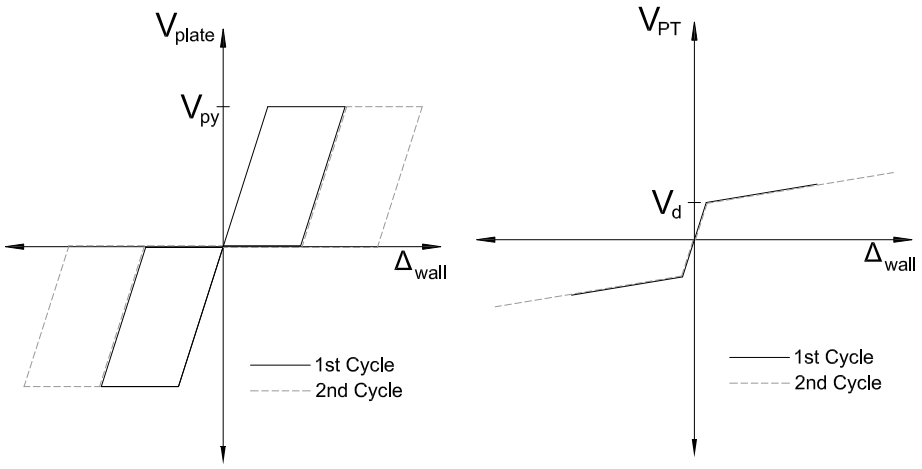

(a) SPSW response

(b) PT response

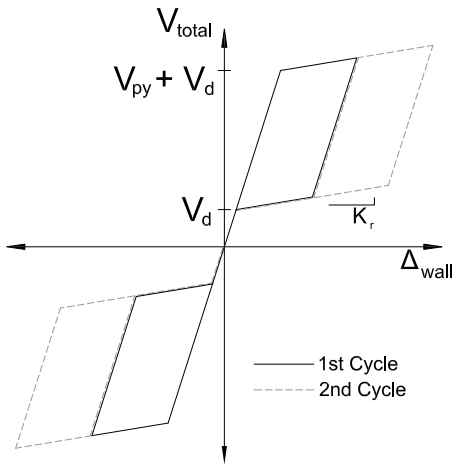

(c) SC-SPSW response

Figure 1.5: System force-displacement idealized responses

allows for rotation in the connection (Fig. 1.1(b)) Garlock et al. [2007]; Christopoulos et al. [2002a]. Figs. 1.5(b) and 1.1(c) show the nonlinear elastic behavior of the PT HBE-to-VBE connection.

Under zero lateral load, the connection is compressed by the initial PT force, T_o, applied by the tendons. As moment develops in the HBE from lateral load, the compression increases in one HBE flange and decreases in the other. At the decompression moment, M_d, one HBE flange unloads completely, and the connection rocks open, forming a gap between the VBE face and the unloaded HBE flange. As the gap opens at an angle of θ_r, the PT tendons elongate elastically, and the system develops the restoring, or self-centering, forces. After decompression, the connection moment is the total compressive load in the HBE times the distance from the HBE centroid to the outer tip of the flange, assuming a symmetric layout of PT tendons. The initial stiffness of the PT frame (shown in Fig. 1.5(b)) is equivalent to that of a frame with fully welded moment resisting connections, and the post-decompression stiffness reflects the reduced connection stiffness as the HBE rocks about its flanges. Post-tensioned column base details, as will be discussed in later chapters, have a similar bilinear elastic behavior.

1.2.2.3 Combined System Behavior

The conceptual SC-SPSW is shown in Fig. 1.1(a), and the idealized response of the combined system is shown in Fig. 1.5(c). The combined system retains the high initial stiffness and strength of the SPSW. Assuming the plates yield in an elastic-perfectly plastic manner, the stiffness of the system after plate yielding and connection decompression is equal to the post-decompression stiffness of the rocking connections. Upon unloading, the PT provides a restoring force and "recentering" stiffness, K_r, that closes the HBE-to-VBE joint gap, recenters the system, and is equal to the post-decompression stiffness of the PT connections. Using this approximate behavior, in subsequent cycles, the system retains the strength and stiffness contributions of the PT connections until the plates reach their previous peak plastic strain where they again contribute significant strength and stiffness to the system. When compared with more traditional seismic load resisting systems, this particular feature

of the assumed SC-SPSW behavior does limit the system's energy dissipation capabilities in cycles following significant web plate yielding; however, web plate behavior in reality is more complex, and web plates are capable of providing energy dissipation following significant yielding [Choi and Park, 2010]. Further discussion of SC-SPSW system and component behavior can be found in Clayton [2010].

1.3 Research Needs

For implementation of the new SC-SPSW system, research must be done to further demonstrate the viability of the system. Although approximations can be made to generalize the system's response, complexities of the component behaviors and interaction of these components that were not accounted for in the previously described idealizations must be better understood. To gain a deeper understanding of SC-SPSW performance and response, physical experiments and detailed finite element analyses can be used to validate and quantify certain aspects of system behavior and component and localized demands. The information gathered from such experimental and numerical studies must be distilled into tools for designers to employ the SC-SPSW as an advanced lateral load resisting system that can reduce the economic impact of earthquakes.

To fully realize the viability and implementation of the SC-SPSW system, the following research objectives should be addressed:

- Experimental and numerical verification of system response, accounting for complexities in behavior that are neglected in the idealized generalizations.

- Experimental and numerical verification of component demands, as these are integral parts of SC-SPSW design.

- Design procedures and recommendations that provide enhanced seismic performance while balancing structural efficiency and economy.

- Detailing recommendations that mitigate structural damage and aid in construction of the system.

- Understanding impacts of design parameters on system response, including but not limited to recentering, extent of web plate damage, and non-structural and gravity framing system impacts.

- Performance-based design tools for engineers to design a SC-SPSW to meet code- and performance-based requirements.

- Efficient modeling methods that are easily accessible to designers and practitioners.

This document will discuss the experimental and numerical research that has been done to better understand SC-SPSW seismic behavior and to bring the SC-SPSW system closer to implementation in practice.

1.4 Scope and Organization

1.4.1 Objectives and Scope of Research

The objectives of this research are outlined below:

- Experimental investigation into the interaction between SPSW web plates and PT HBE-to-VBE connections

- Validation of numerical and analytical models with experimental results

- Characterization of the effects of various design parameters on SC-SPSW behavior

- Improvement of the understanding of complex web plate behavior

- Investigation of of PT VBE base connection and how it affects SC-SPSW behavior

- Verification of SC-SPSW performance at the full-scale, system level

- Development of simple numerical models to predict SC-SPSW behavior

- Comparison of detailed finite element models to simpler numerical models and experimental results

- Development of recommendations for SC-SPSW design and modeling

1.4.2 Organization of Dissertation

The remaining chapters of this dissertation are organized as follows:

- *Chapter 2* contains an overview of previous related research on SPSWs, post-tensioned connections in steel frames, and SC-SPSW development.

- *Chapter 3* contains an overview of the mechanics associated with variations in SC-SPSWs that were not considered in the previous SC-SPSW development study. The mechanics presented here are meant to supplement the basic mechanics presented in previous SC-SPSW research and summarized in Chapter 2.

- *Chapter 4* contains an overview of the SC-SPSW subassembly experimental program conducted at the University of Washington. The specimen descriptions, overall specimen response, and observations for each specimen are presented.

- *Chapter 5* contains an overview of the pseudo-dynamic testing of a full-scale SC-SPSW specimen conducted at the National Center for Research on Earthquake Engineering in Taiwan. The test setup, loading, overall specimen response, and observations are presented.

- *Chapter 6* contains an overview of the data analysis from both of the experimental programs presented above. Data analysis includes, but is not limited to, investigation of HBE, PT, and connection component demands, recentering stiffness, energy dissipation, and residual drifts.

- *Chapter 7* contains an overview of the different numerical modeling methods that can be used to simulate SC-SPSW behavior. Each of the models are presented and compared with experimental results.

- *Chapter 8* contains and overview of the numerical study investigating the seismic response of SC-SPSW building systems. These numerical simulations investigate the impact of different web plate connectivity configurations and web plate residual strength.

- *Chapter 9* contains an overview of design recommendations and considerations that came out out of this body of research. These design recommendations are intended to serve as an addendum to the design methodologies presented in Clayton [2010] and provide recommendations for further research and improvement of the system.

- *Chapter 10* provides a summary of the key findings from this research.

Chapter 2

LITERATURE REVIEW

2.1 Introduction

The concept of the SC-SPSW system incorporates previous reserch from the fields of self-centering steel systems and SPSWs. This dissertation focuses primarily on experimental investigation of the SC-SPSW system. For this reason, the scope of the literature review is limited to experimental research in these two fields. For further discussion of previous numerical and analytical research in these fields, please refer to Clayton [2010].

2.2 Previous Steel PT Connection Research

The concept of using post-tensioned connections to reduce seismic component damage and provide recntering capabilities was first introduced in the early 1990s in the field of precast concrete construction with the Precast Seismic Structural Systems (PRESSS) project [Priestly, 1991; Stanton et al., 1997; Nakaki et al., 1999]. This research included post-tentioned precast beam-to-column connections and precast wall systems that could lift off and rock about their base. The post-tensioned concept was extended to steel construction in the early 2000s with post-tentioned beam-to-colum connections by Ricles et al. [2001] and Christolpulos et al. [2002a]. Other steel lateral load resisting systems and components incorporating post-tensioned self-centering capabilities were also developed, including self-centering braced frames allowed to uplift and rock about their base [Eatherton et al., 2008], self-centering braced frames with post-tensioned braces [Christopoulos et al., 2008], post-tensioned column base moment-resisting connections [Chi et al., 2008], and a myriad of post-tensioned beam-to-column connections integrating different means of energy dissipation (discussed below). Due to the extensive research on self-centering systems, this literature review will focus on post-tensioned moment-resisting beam-to-column connections and column base connections as these are the self-centering components utilized in

this research.

2.2.1 PT beam-to-column connections with yielding elements

2.2.1.1 Garlock (2002)

Garlock [2002] performed analytical and experimental investigations of a beam-to-column connection that used top and seat angles and high-strength steel post-tensioning strand extending over multiple bays of a PT moment resisting frame (Figure 2.1), where the top and seat angles acted as the primary energy dissipation mechanism of the system. A primary outcome of this study was a performance-based design approach to meet the objectives of Immediate Occupancy (IO) performance under a design basis earthquake (DBE) and Collapse Prevention (CP) under a maximum considered earthquake (MCE).

A series of PT connection subassembly tests were conducted to evaluate the PT connection performance on full-scale connections with top and seat angles. The experiments investigated the load-displacement hysteretic response, moment-beam relative rotation hysteretic response, maximum connection moment, initial and post-decompression stiffnesses, beam decompression moment, energy dissipation, post-tensioned strand behavior, and the behavior of the angles. The experiments consisted of a cruciform specimen (Figure 2.2) with a W36x150 beam and W14x398 (Grade 50) column, representing a full-scale model of an interior joint from the 3rd floor of a welded prototype frame, cyclicly loaded to drifts up to 4%. The member sizes were the same as those used in a previous test of welded moment frame connections to provide direct comparison between the PT and welded connection performance. The connections had varying number of PT strands and initial PT force per strand, ranging from 16 to 36 strands and 18 to 45 kips per strand, respectively.

The typical system and connection response is shown in Figure 2.3. The connection response is presented in terms of connection moment versus the gap rotation, θ_r. Initially, the system response is equivalent to that of a welded moment frame until the point of connection decompression, which is characterized by a reduction of system stiffness, as seen in Figure 2.3(a), and an increase in gap rotation, as seen in Figure 2.3(b). The moment at which the system decompresses is known as the decompression moment, M_d. The energy

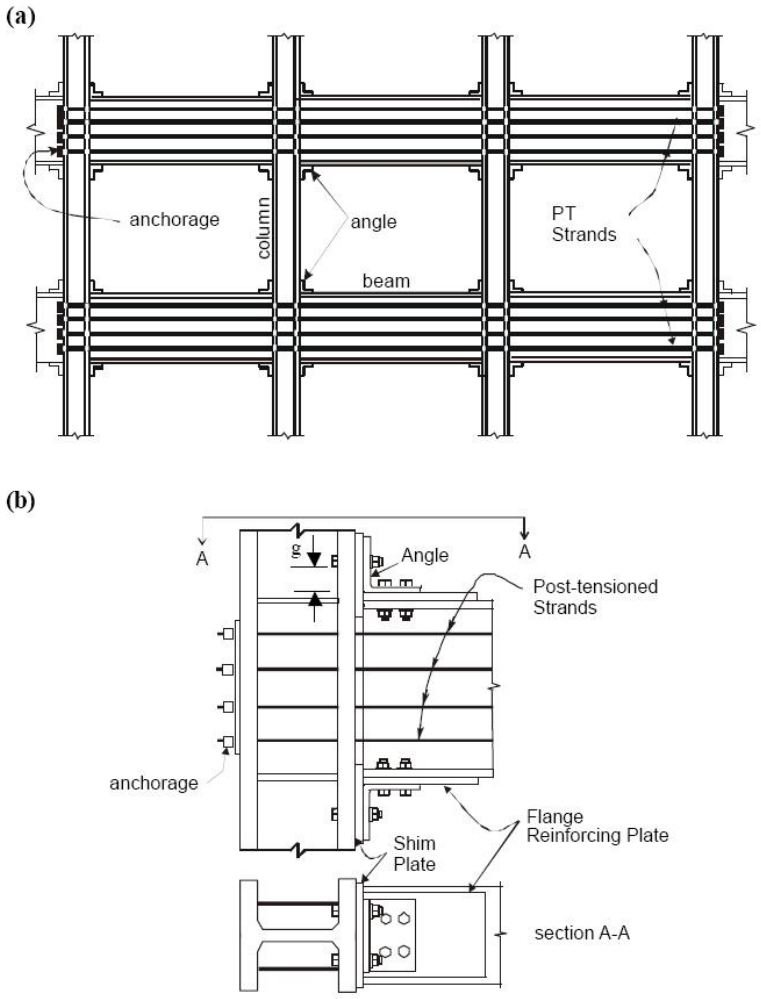

Figure 2.1: (a) Schematic elevation of a PT steel frame, and (b) details of a steel PT connection. [Garlock, 2002]

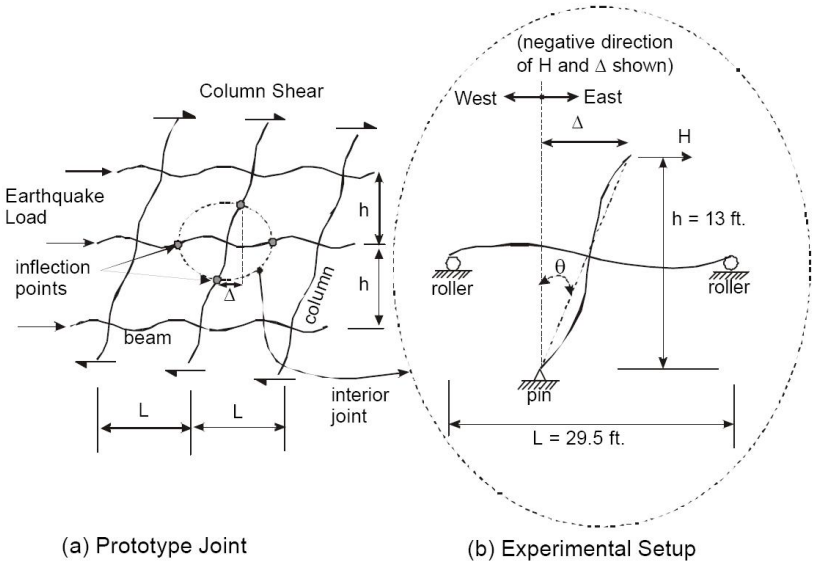

Figure 2.2: Kinematics of (a) prototype structure in connection region, and (b)experimental setup. [Garlock, 2002]

dissipation seen in Figure 2.3 is provided by the yielding of the top and seat angles. For comparison, the specimen was subjected to one cycle of loading without the presence of the angles, and the hysteretic response of the resulting system, as shown in Figure 2.4, shows a nonlinear elastic response with a reduction in stiffness following decompression and effectively no energy dissipation in the system.

The results of these experiments showed that connections with larger numbers of strands achieved larger connection moments due to the increased connection stiffness after decompression and angle yielding. However, these higher forces resulted in cases of beam web and flange local buckling, as well as horizontal shear yielding in the beam web. Any inelastic deformations of the beam resulted in a loss of self-centering capabilities. Connections with more strands were also fount to be more ductile as there were fewer cases of PT wire fracture since the initial force per strand was lower.

From the experimental results, a performance-based design procedure was developed with the limit states shown in Figure 2.5 used as key indicators of achieving IO and CP performance. Key components of the design procedure included: designing the angles to

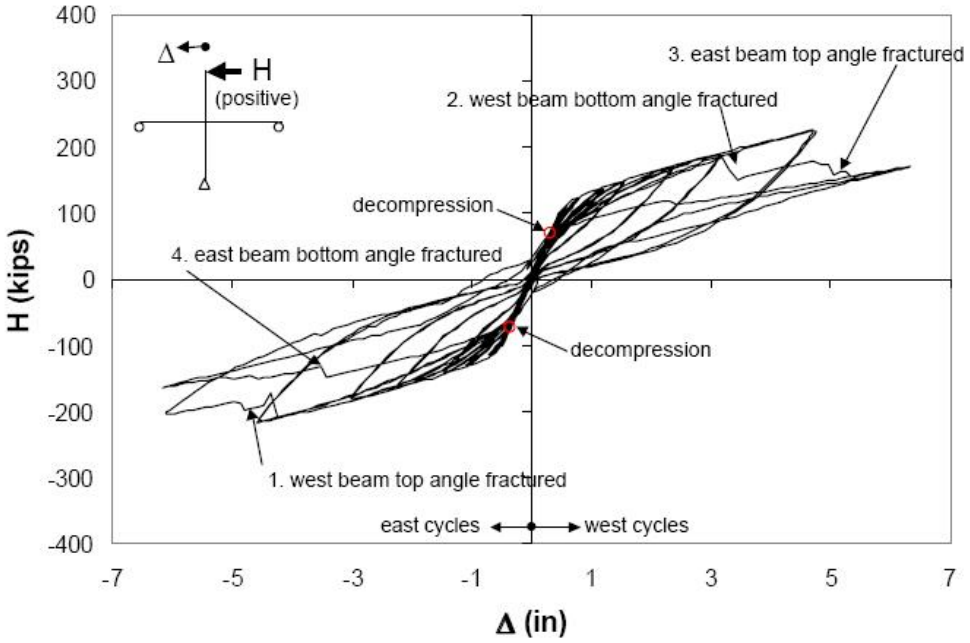

(a)

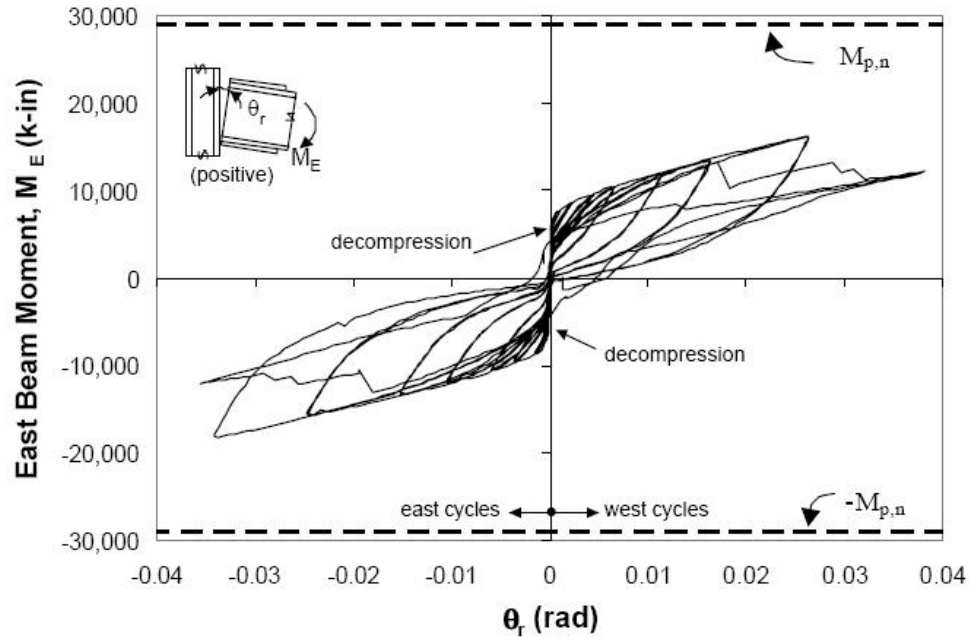

(b)

Figure 2.3: (a) Force–displacement and (b) connection moment–relative rotation response of Specimen 20s-18-W. [Garlock, 2002]

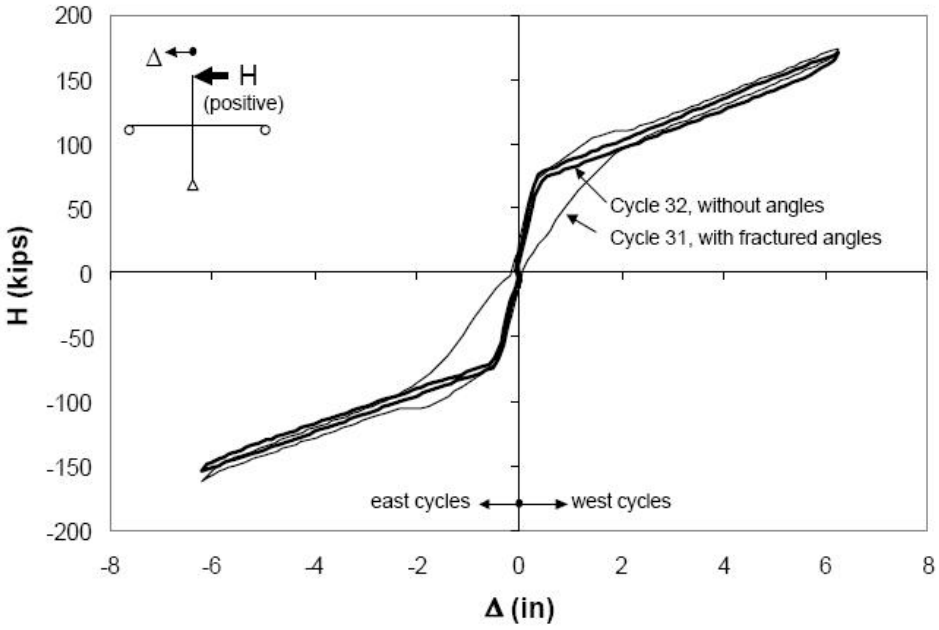

Figure 2.4: Force–displacement response of Specimen 20s-18-W without angles. [Garlock, 2002]

yield at 95% of the beam design moment, defined as the moment at the column face obtained from a linear elastic analysis in an equivalent lateral force procedure using code-based design loads; designing the connection strength, calculated from the expected gap rotations, θ_r, and system overstrength, Ω, at the DBE and MCE level to be approximately 1.5 and 1.8 times the beam design moment, respectively; and designing the "second-mode" stories in the upper stories of the building to have higher angle and connection strengths due to higher mode effects neglected in the code-based design.

Garlock [2002] also developed an analytical model for the PT frame which consisted of nonlinear truss elements to model the force-deformation behavior of the yielding angles, fiber elements with compression only material in the beam flanges close to the column face to model the beam and rocking behavior, and truss elements to model the PT strands. This connection model was validated with experimental data and then incorporated into a model of the prototype PT frame building and subjected to an ensemble of ground motions (one artificial and two real) scaled to represent DBE and MCE ground motions. Among

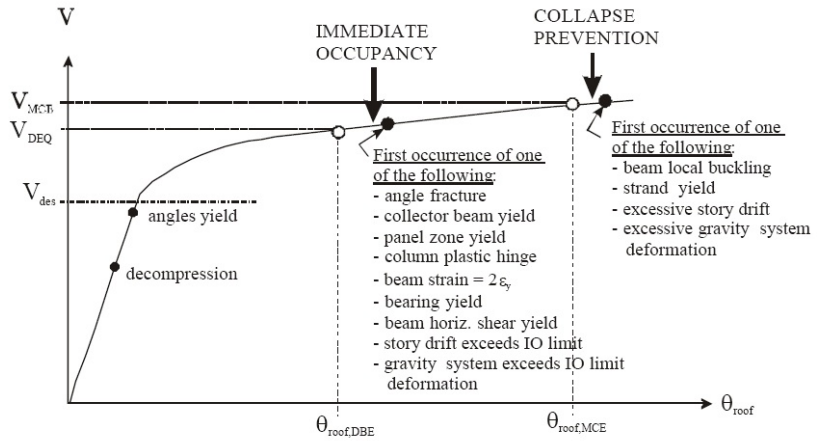

Figure 2.5: PT frame design objectives. [Garlock, 2002]

other outcomes, the results of the nonlinear time history analyses showed: maximum story drifts of the PT frame under DBE and MCE ground motions ranged from 0.027 to 0.042 radians and 0.034 to 0.057 radians, respectively; little to no residual displacements after DBE ground motions and small residual displacements following MCE ground motions; no PT strand yielding; and yielding in the first story columns at the fixed base at the ground level.

2.2.1.2 Christopoulos (2002)

Christopoulos et al. [2002a; 2002b] developed a PT rocking beam-to-column connection, known as the posttensioned energy dissipating (PTED) steel connection, that relied on yielding elements similar to the Garlock [2002] connection to dissipate energy. This connection consisted of buckling restrained energy dissipating (ED) bars welded to the inside of the beam flanges and the continuity plates in the columns that are designed to yield in tension and compression as the connection rocks open (Figure 2.6). The post-tensioning of the connection is provided by PT bars, as opposed to strands, located at the centroid of the beam. This research consisted of an experimental study of the proposed connection [Christopoulos et al., 2002a], as well as an analytical study of the seismic response of general self-centering systems with flag-shaped hysteresis [Christopoulos et al., 2002b].

The experimental program consisted of initial testing of the energy dissipating bars to determine the cyclic response of the components and to assess the effectiveness of the connection details in achieving tension and compression yielding. The ED bars were Dywidag System International (DSI) threaded bars that were threaded into couplers that were welded to steel plate representing the beam flanges. The tests showed the ED bars to have stable hysteretic response with good energy dissipating characteristics; however, upon cycles of plastic deformation, the bars did experience slip when transitioning from tension to compression loading due to the permanent deformation accumulated in the threaded portion of the bar.

The connection subassembly test modeled an exterior PTED beam-to-column connection and consisted of a W24x76 and W14x211 (A992) beam and column, respectively, with two 46 mm diameter DSI high strength bars positioned at middepth of the beam to provide the initial post tensioning, and four 22 mm diameter (No. 7) DSI threaded bars with an unbonded length of 550 mm for the ED bars (Figure 2.6). The specimen was loaded cyclicly up to drifts of 4%. The results of the test showed full recentering capabilities at the maximum drift of 4% with good energy dissipation characteristics and no damage to the beam and column members.

The experimental tests also served as validation for a simplified analytical model developed by Christopoulos et al. [2002a]. A simplified model was sought due to the considerable analytical and computational effort required by fiber models, making them impractical for use in design. The simplified model consisted of two rotation springs in parallel to model the connection behavior. One spring modeled the nonlinear elastic behavior of the PT, while the other modeled the bilinear hysteretic behavior of the ED bars, as demonstrated in Figure 2.7. The spring models were developed using a beam sectional approach by solving for the location of the connection neutral axis at a given gap rotation by integrating the normal stresses in the beam and PT and ED bars, then checking for horizontal equilibrium. The connection behavior using this simplified analytical method matched well with the results from the experimental test.

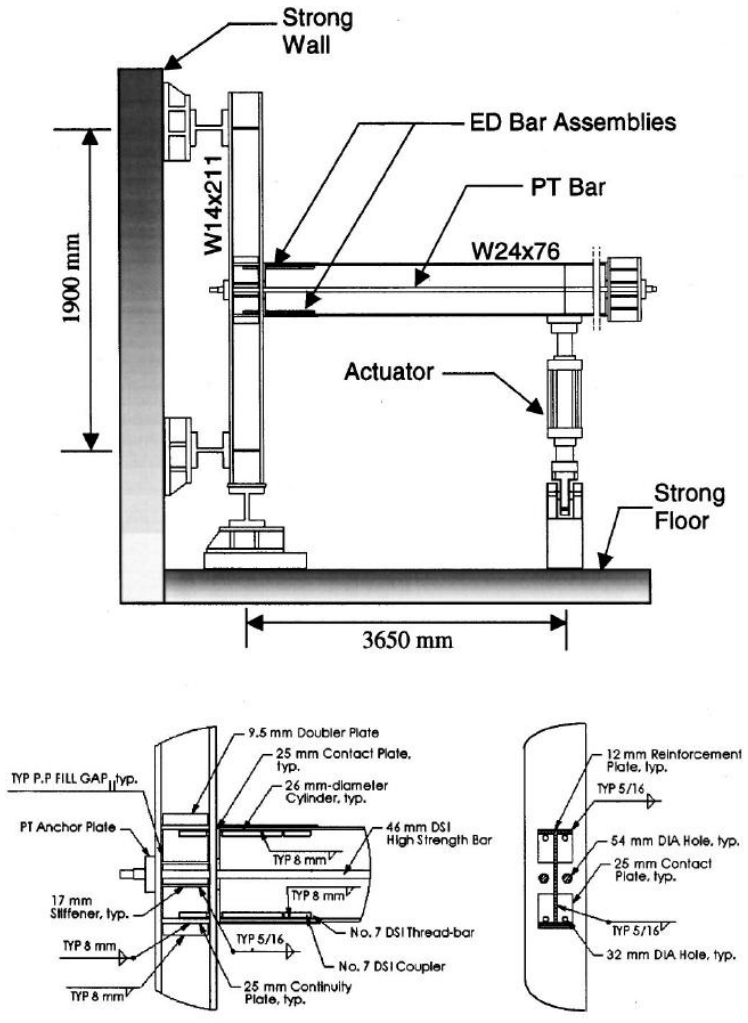

Figure 2.6: Experimental setup for PTED connection test [Christopoulos et al., 2002a]

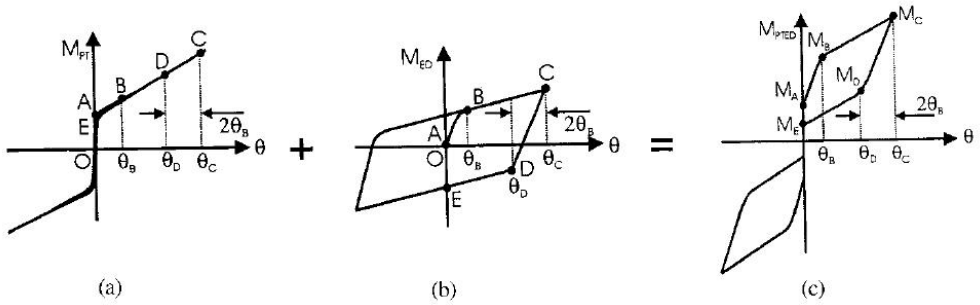

Figure 2.7: Idealized hysteretic behavior of PTED beam-to-column connection: (a) contribution of PT bars; (b) contribution of energy-dissipating bars; and (c) moment-rotation relationship of PTED connection [Christopoulos et al., 2002a]

2.2.1.3 Chou et al. (2006)

Chou et al. [2006] conducted experimental and analytical studies on moment resiting frames utilizing PT beam-to-column connections with reduced flange plates (RFPs) and concrete-filled tube (CFT) columns (Fig. 2.8). Here, the buckling-restrained RFPs are welded to the column and bolted to the beam such that they provide energy dissipation in tension and compression during PT connection gap opening.

Three full-scale, cruciform subassemblage specimens were experimentally tested under static cyclic loading. Specimen 1 investigated the PT connection only, without the presence of RFPs. Specimen 2 and 3 investigated the effects of the RFP with 5mm and 8mm thick RFPs, respectively. Specimen 3 also had the addition of a 10mm thick cover plate to prevent buckling of the RFP and accommodate stable RFP yielding in compression.

The connection moment versus displacement responses of the the three specimens are shown in Fig. 2.9. The accumulated energy dissipation, E_h, for Specimen 3 was 3.2 times larger than that of Specimen 2, although the RFP thickness ratio was only 1.6, indicating that the buckling-restrained RFP in Specimen 3 develops significantly larger energy dissipation than that without buckling restraint. Yielding was first observed in Specimens 2 and 3 at 3% drift, with significant beam flange and web bluckling during the third cycle at 4% drift, which resulted in a decrease in the PT strand force. No damage was observed in the

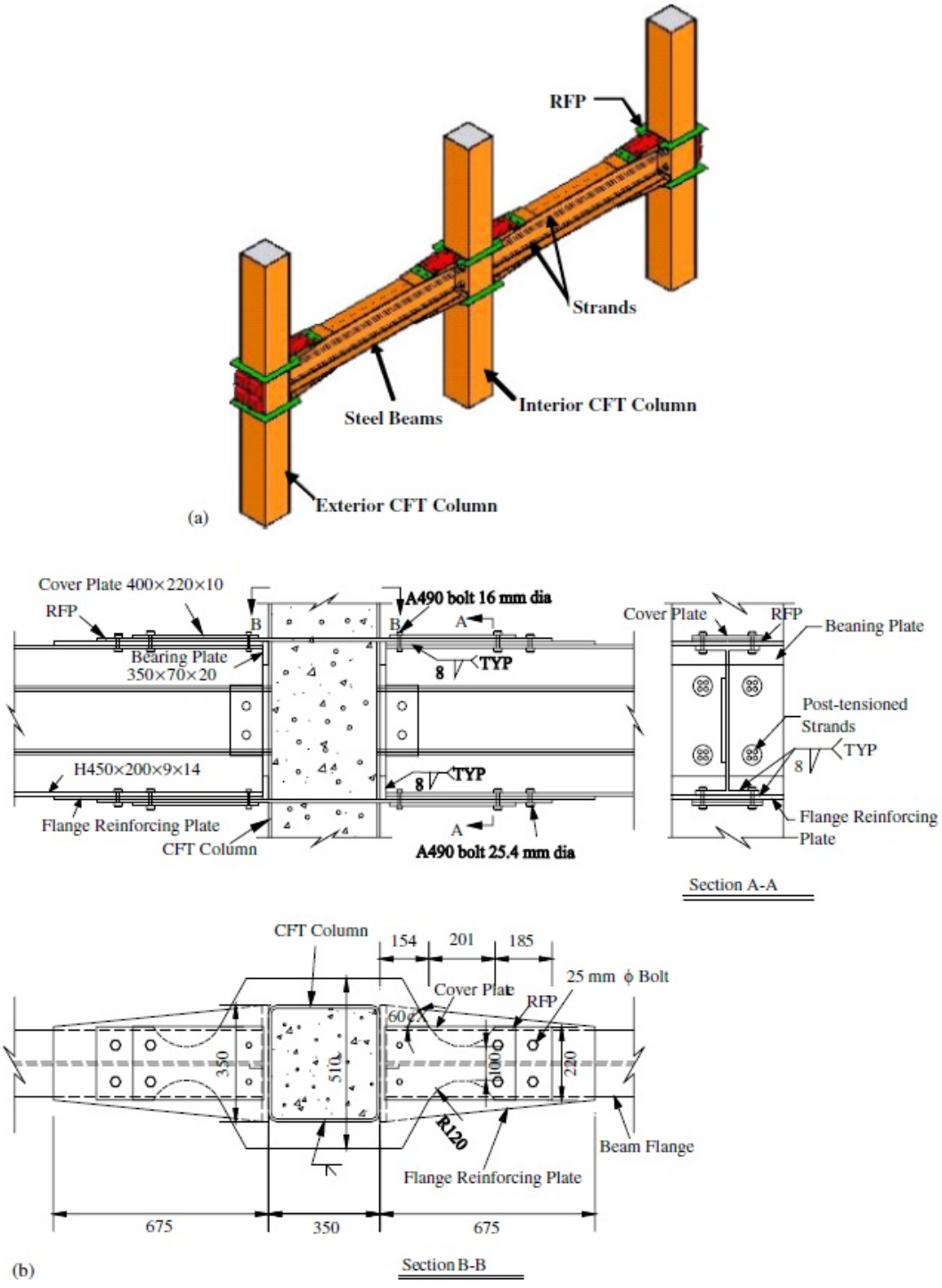

Figure 2.8: Proposed PT beam-to-CFT column connection: (a) frame and (b) connection details [Chou et al., 2006]

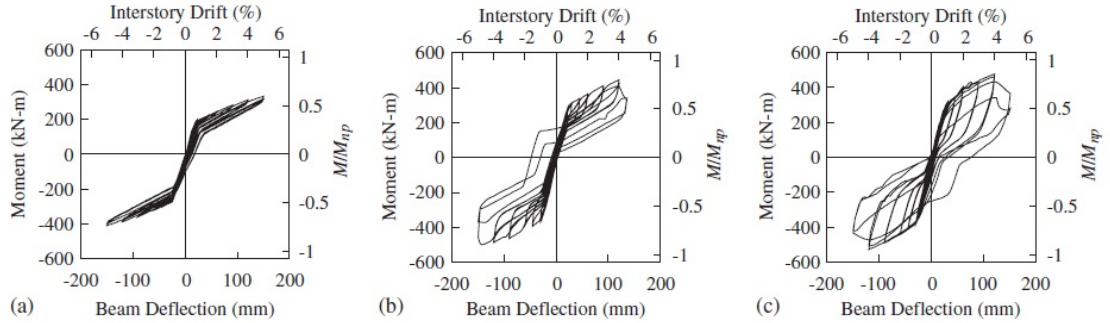

Figure 2.9: Moment versus beam deflection response of (a) Specimen 1, (b) Specimen 2, and (c) Specimen 3 [Chou et al., 2006].

CFT columns.

Chou et al. [2006] conducted nonlinear finite element (FE) analyses of Specimen 1 in ABAQUS to study the beam and PT connection behavior. The steel beams and flange reinforcing plates were modeled using shell, S4R, elements, while solid, C3D8R, elements were used to model the CFT steel tube and concrete infill, as well as the bearing plates and PT strands. Hard and rough contact behavior was modeled at the bearing plate and steel tube interface. The pushover response of the model matched well with the backbone of the Specimen 1 moment versus displacement response. The stress distribution in the FE analyses (Fig. 2.10) also showed that the region of nonuniform stress distributions due to concentrated loads at the beam bearing plates extends over a length approximately equal to the beam depth. The stresses predicted by the FE model also matched well with those experimentally determined through strain gage data.

2.2.2 PT beam-to-column connections with friction devices

2.2.2.1 Rojas et al. (2005)

Rojas et al. [2005] developed a post-tensioned friction damped connection (PFDC) for moment-resting steel frames. Similar to the post-tensioned connections presented by Garlock [2002] and Christopoulos et al. [2002a], post-tensioning runs parallel to the beam; however, energy dissipation is not provided by yielding elements. Instead, energy is dissi-

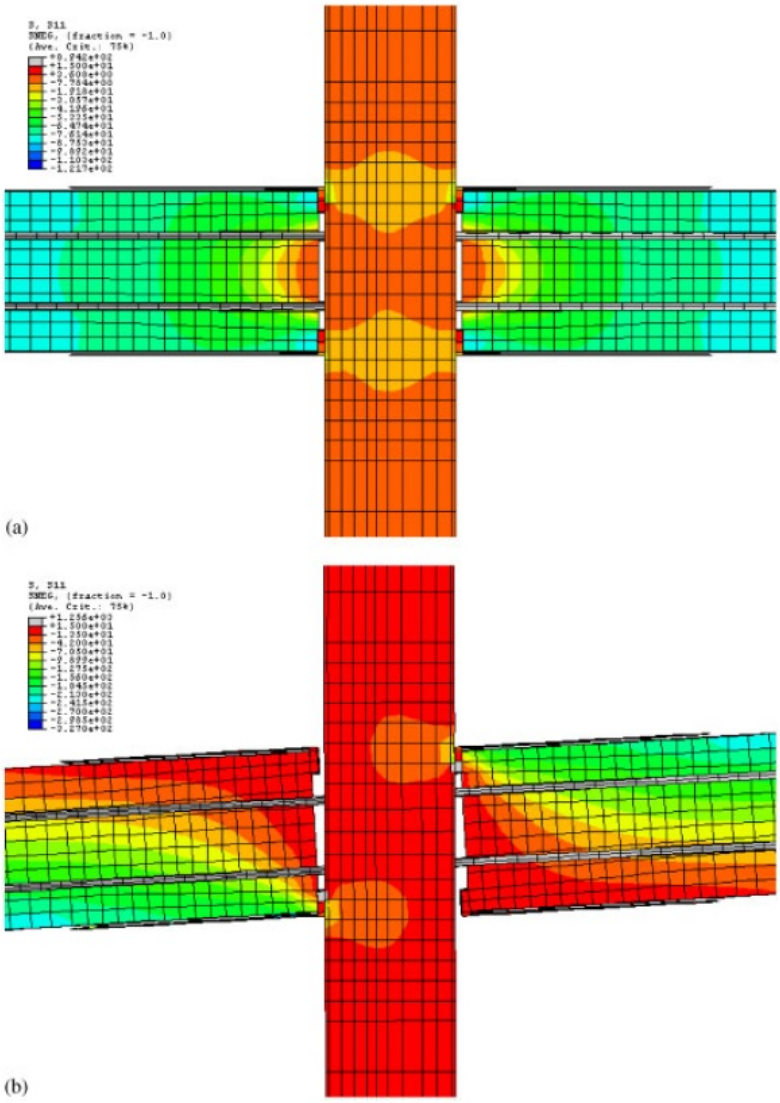

Figure 2.10: Longitudinal stress distribution in FE model of Specimen 1 (a) after application of initial PT and (b) at 2% drift [Chou et al., 2006].

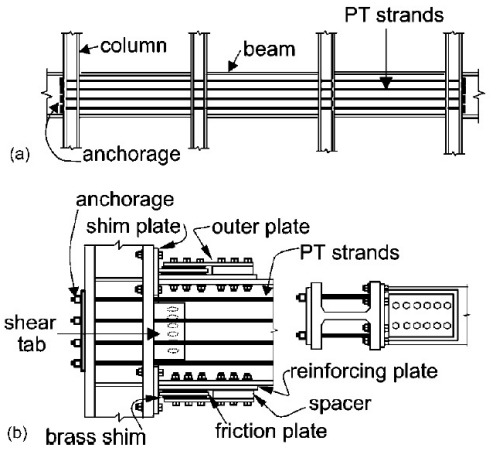

Figure 2.11: Schematic of (a) PT frame and (b) post-tensioned friction damped connection detail [Rojas et al., 2005].

pated through friction devices located at the beam flanges (Fig. 2.11) that are engaged as a gap forms in the connection. The friction device consist of a steel tee-shapes bolted to the column flange in which the tee stem, which serves as the friction plate, is sandwiched between two brass shim plates to produce the friction forces. Gravity shear forces in the beam are transfered to the column via a horizontal slotted hole shear tab to allow for connection rotation, while sway-induced shear forces are transfered via friction at the beam-column interface.

A performance-based design approach was proposed for the PFDC-MRF with the performance objectives of: (1) IO following a DBE, approximated by a 10% in 50 year earthquake and (2) CP following a MCE, approximated by a 2% in 50 year earthquake. The structural demands used in PFDC-MRF design were based on amplified code-based demands, where the amplification factors were determined based on nonlinear dynamic analyses performed by Rojas [2003].

To assess the seismic performance of the system, a six-story building in the Los Angeles, California area was designed using PFDC-MRFs, and another building was designed using conventional welded MRFs (termed FR-MRF) for comparison. Models of the FR-MRF and PFDC-MRF frames were constructed using the DRAIN-2DX [Prakash et al., 1993]

structural analysis software and were subjected to an ensemble of eight ground motions scaled to DBE and MCE levels.

The mean plus one standard deviation, $m + \sigma$, of the maximum story drifts observed at the DBE level were similar for the PFDC-MRF and FR-MRF and ranged from approximately 0.025 to 0.029 radians, while at the MCE level $m + \sigma$ story drift values for the PFDC-MRF (approximately 0.04 radians on average) were larger than those for the FR-MRF (approximately 0.035 radians on average). The $m + \sigma$ of the maximum residual story drifts for the PFDC-MRF were 0.11% and 0.26% for the DBE and MCE, respectively, and were 0.52% and 1.27% for the FR-MRF at the DBE and MCE levels, respectively. The largest residual story drifts always occured at the first story due to yielding at the base of the columns. A sensitivity analysis also showed that variability in the friction force in the connection does not have a significant effect on the PFDC-MRF sesimic response as the friction forces contribute, on average, only 20% of the connection moment resistance.

2.2.2.2 Iyama et al. (2009) and Wolski et al. (2009)

As part of the SC-MRF research program at Lehigh University [Garlock, 2002; Rojas et al., 2005; Lin et al., 2008], a PT connection with a bottom flange friction device (BFFD) was also developed. This connection was developed to avoid interference with the floor slab in the PDFC connection developed by Rojas et al. [2005]. The BFFD (Fig. 2.12(a)) consists of brass plates sandwiched between steel plates welded to the beam bottom flange and steel angles welded to the column flange [Wolski et al., 2009; Iyama et al., 2009]. Do to the friction device only being provided at the bottom flange, the connection response is asymmetric as shown in Fig. 2.12(b).

Wolski et al. [2009] conducted seven 0.6-scale subassembly tests on a single BFFD connection subassembly. The test parameters that were varied in the experimental program included friction force, F_f, in the BFFD, the effects of friction bolt bearing in the slotted bolt holes in the BFFD, the BFFD-to-beam bottom flange weld detail, and the loading history (e.g. symmetric cyclic loading vs. earthquake loading). The beam, column, and PT strands were designed to remain elastic throughout all of the tests. The experimental

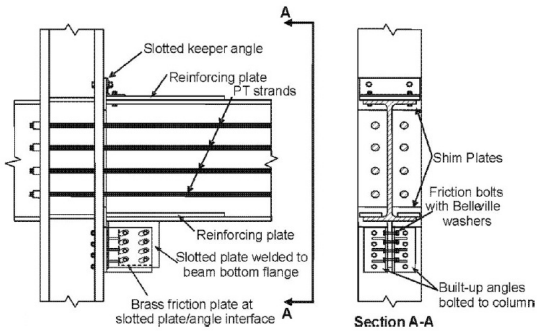

(a)

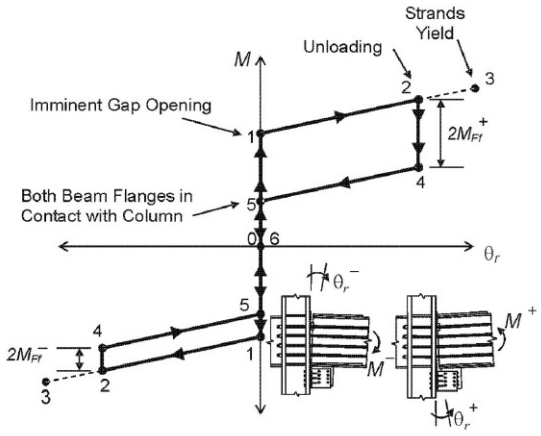

(b)

Figure 2.12: (a) Schematic and (b) moment vs. relative rotation response of a PT connection with BFFD [Wolski et al., 2009].

results showed that the BFFD connection provided consistent strength and energy dissipation independent of loading history or loading rate and can remain damage free if the PT strands are designed to remain elastic and the friction bolts in the BFFD are designed to fail in shear due to bearing at the ends of the slotted holes. Tests also showed that the BFFD-to-beam bottom flange connection should be a complete joint penetration (CJP) weld, as a fillet weld detail failed in low-cycle fatigue.

Iyama et al. [2009] outlines BFFD connection design methodologies, as well as, an analytical approach for modeling the changing direction of the friction force in the BFFD as the connection opens and closes. The BFFD analytical model was validated using experimental results from Wolski et al. [2009]. She conducted static pushover analyses and dynamic time-history analyses of the BFFD SC-MRF and compared these results to those of a PFDC SC-MRF [Rojas et al., 2005]. The dynamic time-history analyses showed BFFD and PFDC SC-MRFs to have similar responses with maximum story drifts of approximately 3% and 4.5% at the DBE and MCE levels.

2.2.2.3 Tsai et al. (2008)

Tsai et al. [2008] developed a bolted web friction device (BWFD) to provide energy dissipation beam-to-column connections of SC-MRFs. The BWFD connection consists of brass plates inserted between steel friction plates welded to the column on both sides of the beam web as shown in Fig. 2.13. Cyclic experimental tests were conducted on four PT beam-column subassemblages incorporating the BWFD to understand connection behavior. The design parameters varied during the test program were initial PT force, washer type, and number and size of bolts used to connect the friction device and the beam web. The PT connections were designed for and tested up to 5% drift.

The results of the experimental tests showed good agreement with analytically derived models. Oversized bolt holes were used in the beam web to accommodate rotation of the connection; however, it was determined that design of the oversized bolt hole should account for construction tolerance in that the bolt may not be centered in the hole during construction. The tests also showed that properly designed PT connections with BWFDs

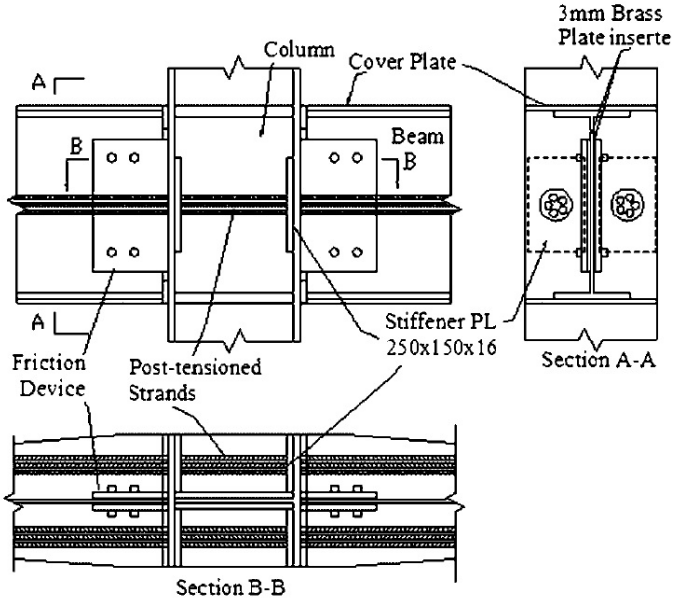

Figure 2.13: Schematic of PT connection with WBFD [Tsai et al., 2008].

can produce stable and repeatable recentering properties and decompression moments even after large cyclic deformation and that friction forces tend to be more stable and constant after the friction surface has been worn or when Belleville washers, as opposed to flat washers, are used.

2.2.2.4 Lin et al. (2008)

Lin et al. [2008] investigated self-centering moment resisting frames (SC-MRF) that incorporate beam web friction devices (WFDs) (Fig. 2.14(a)) to provide energy dissipation similar to the previously described BWFD connection tested by Tsai et al. [2008]. The post-tensioned WFD (PT-WFD) connections (Fig. 2.14(b)) consist of two channel sections welded to the column. These friction channels are bolted to the beam web with brass cartridge plates sandwiched between the web and the channel to provide friction. The bolt holes in the beam web are horizontally slotted to allow the connection to rock open. A performance-based design procedure was proposed with performance objectives of IO under a DBE and CP under a MCE. The design procedure and structural demand amplification

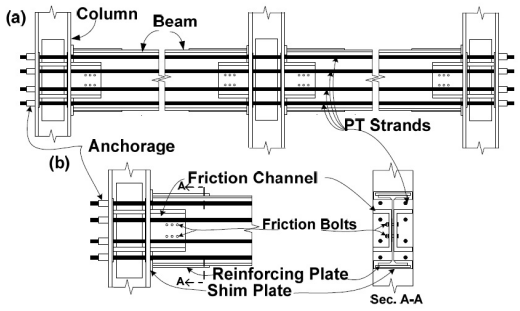

Figure 2.14: Schematic of (a) SC-MRF with WFD and (b) connection details [Lin et al., 2008].

factors are similar to those developed in previous SC-MRF research conducted at Lehigh University [Garlock, 2002; Rojas et al., 2005; Iyama et al., 2009].

Experimental testing was conducted on a 0.6-scale four-story two-bay SC-MRF with PT-WFD connection. The prototype building for the test specimen was located in the Los Angeles area and was the same as that used in the SC-MRF research by Rojas et al. [2005] and Garlock [2002]. The design story drift demands at the DBE and MCE levels were 0.039 and 0.059 radians, respectively. The specimen was loaded at the four floor levels via a load transfer beam connected to the middle of the beam in the north bay. The test matrix consisted of two static tests to obtain the stiffness matrix and cyclic response of the specimen, respectively, and nine pseudo-dynamic hybrid simulation tests under frequently occurring earthquake (FOE), DBE, MCE, and aftershock levels [Lin et al., 2008].

The hybrid pseudo-dynamic test consisted of the two-bay experimental substructure and an analytical substructure comprising a P-Delta column with building gravity loads, building mass, and numerical damping [Lin, 2012]. At the time of this writing, results for only the first DBE test (DBE-1) were available, with results from other tests in press; therefore, only these results will be discussed. The DBE-1 excitation was intended to simulate a low-level DBE with roof drift, story drift, and connection rotations expected to be approximately one-half of the design demands. During this test the maximum story drift and connection relative rotation observed were 1.9% and 1.7%, respectively. The test frame did recenter with a maximum residual stroy drift less than 0.2%.

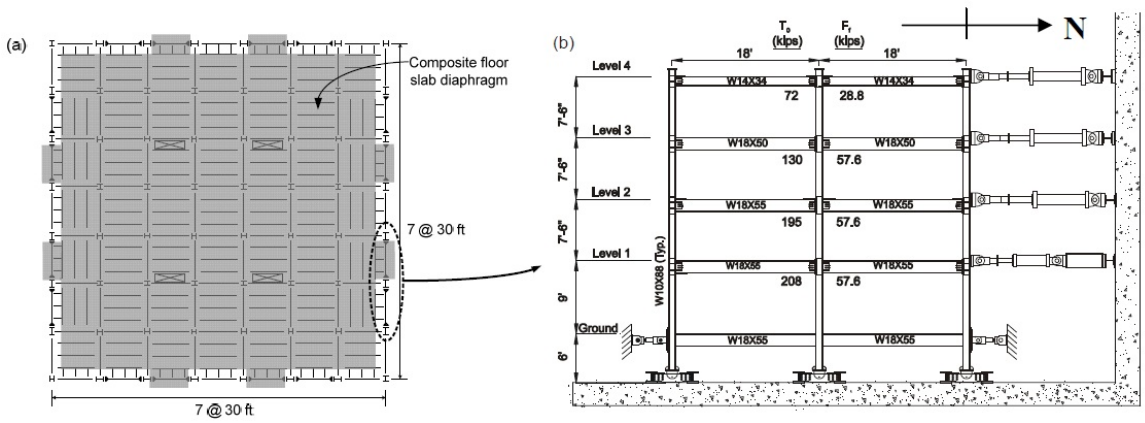

Figure 2.15: Schematic of (a) prototype building plan and (b) SC-MRF with PT-WFD test specimen [Lin et al., 2008].

2.2.3 Effects of slab on PT beam-to-column connection

2.2.3.1 Garlock and Li (2007)

Research conducted by Garlock and Li [2007] addressed the issue of frame expansion that occurs in PT frames as the connections decompress, as shown in Figure 2.16. This research specifically studied applications where collector beams act as the floor diaphragm, transmitting lateral loads to the PT frame. As connection decompression occurs and the PT frame expands, these collector beams deform to accommodate this expansion. This research looked at different collector beam strengths and stiffnesses and compared performance of frames designed with 3 and 15 collector beams as shown in Figure 2.16. Garlock and Li [2007] also provided closed-form equations to describe the influence of the floor diaphragm on the axial load in the beams and the connection moment. Several practical design considerations were also presented, including post-tensioning beams before pouring the floor slab, providing clearance between the slab and the columns of the PT frame, and providing slide bearings between the collector and PT beams and the metal floor decking.

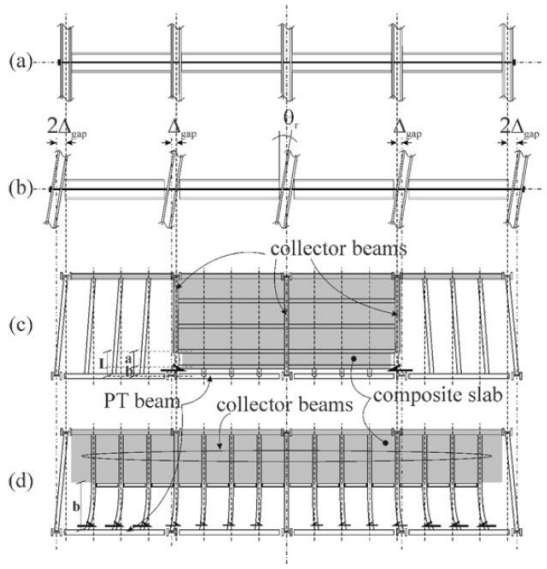

Figure 2.16: (a) Elevation of unloaded PT frame, (b) Expansion of PT frame as gap opens, (c) 3 collector beam and (d) 15 collector beam in deformed configuration [Garlock and Li, 2007]

2.2.3.2 Kim and Christopoulos (2008)

Kim and Christopoulos [2008] presented a comprehensive step-by-step design procedure for self-centering PT frames that incorporate friction dissipating devices placed symmetrically at the top and bottom beam flanges at the PT connection (SCFR frame) and also discussed the effects of column and slab restraint on PT frame design. An expression was developed to describe the increase in axial loads in the beams due to the column stiffness, particularly at the first floor beam where the column is fixed at its base, as demonstrated in Figure 2.17. A detail was also proposed that would eliminate the restraint provided by the slab as the frame expands following decompression. This detail, shown in Figure 2.18, restrains 2 of the 4 sides of the floor slab with shear connectors connected to the beams, while the other sides of the slab are allowed to slide along the beams that are supporting it as the frame expands. Teflon pads and flexible filler material are provided at all sliding and expanding interfaces at the joints.

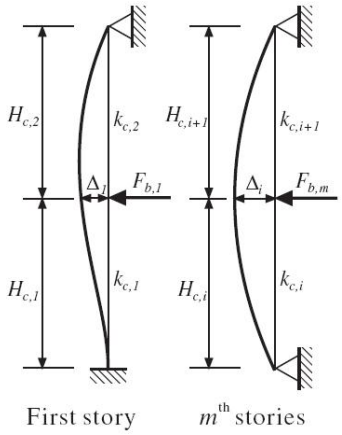

Figure 2.17: Beam growth restraint at first floor HBE due to VBE connection to foundation [Kim and Christopoulos, 2008]

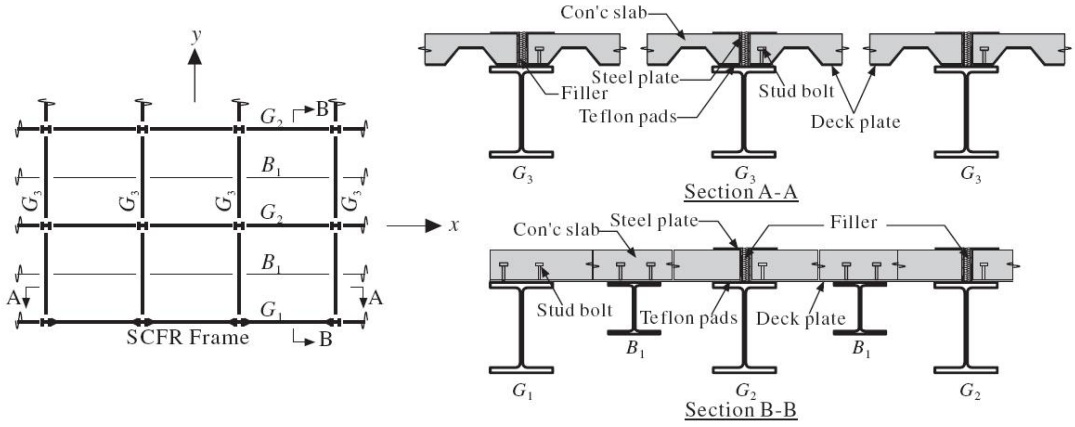

Figure 2.18: Detailing between concrete slab and PT frame to eliminate the restraining effect of slabs. [Kim and Christopoulos, 2008]

2.2.3.3 Chou and Chen (2011)

Chou and Chen [2011a] conducted experimental investigation of PT frames with two different floor slab connection configurations: (1) one that is similar to floor slabs in conventional MRFs in which the slab is connected to the PT frame beams with shear connectors; however, the metal decking is discontinuous and the longitudinal bars in the slab are debonded near the PT connections (Partial bonded slab system in Fig. 2.19(a)); and (2) one in which one bay of the PT frame is is rigidly connected to the slab via a truss force-transfer mechanism, and the other bays in the PT frame have sliding interfaces between them and the transverse gravity framing to accommodate differential movement between them (Rigid bay slab system in Fig. 2.19(b)). In this test program, the PT beam-to-column connections were similar to those presented in Chou et al. [2006] with CFT or reinforced concrete (RC) columns and RFP at the top and bottom beam flanges to provide energy dissipation.

Four cruciform specimens were tested cyclically to investigate the how the slab connection details affect connection response. Two specimens utilized the partial bonded slab connection details where the longitudinal reinforcing bars in the concrete slab in both specimens were debonded over a length of 2 m in the connection region; however, one specimen (Specimen 2) had continuous metal decking while the other specimen (Specimen 4) had separation of the metal decking along the column centerline. Also due to the composite action of the PT beam and floor slab connected with shear studs in this connection detail, the positive and negative moment capacities of the connection are different; therefore, the specimen with the discontinuous metal decking (Specimen 4) was also modified to have a thinner RFP on the top flange of the PT beam in order to produce a more symmetric response. Two specimens representing the rigid bay slab connection details were tested. Due to the noncomposite action of PT beams in this detail, no slabs were included in the cruciform test. One specimen had a CFT column (Specimen 1), while the other had a RC column (Specimen 3).

The results of the cruciform connection tests showed that partially bonded slab connection details did produce asymmetric connection response due to the slab reinforcement providing additional tension resistance at the top flange; however, this can be accounted for

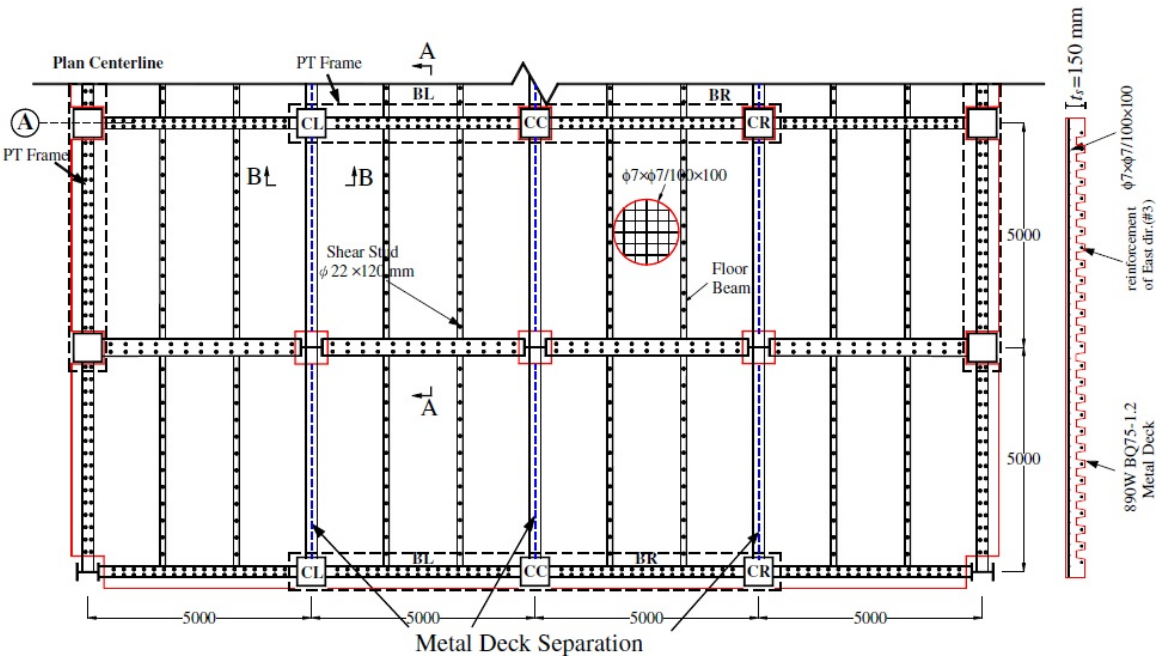

(a)

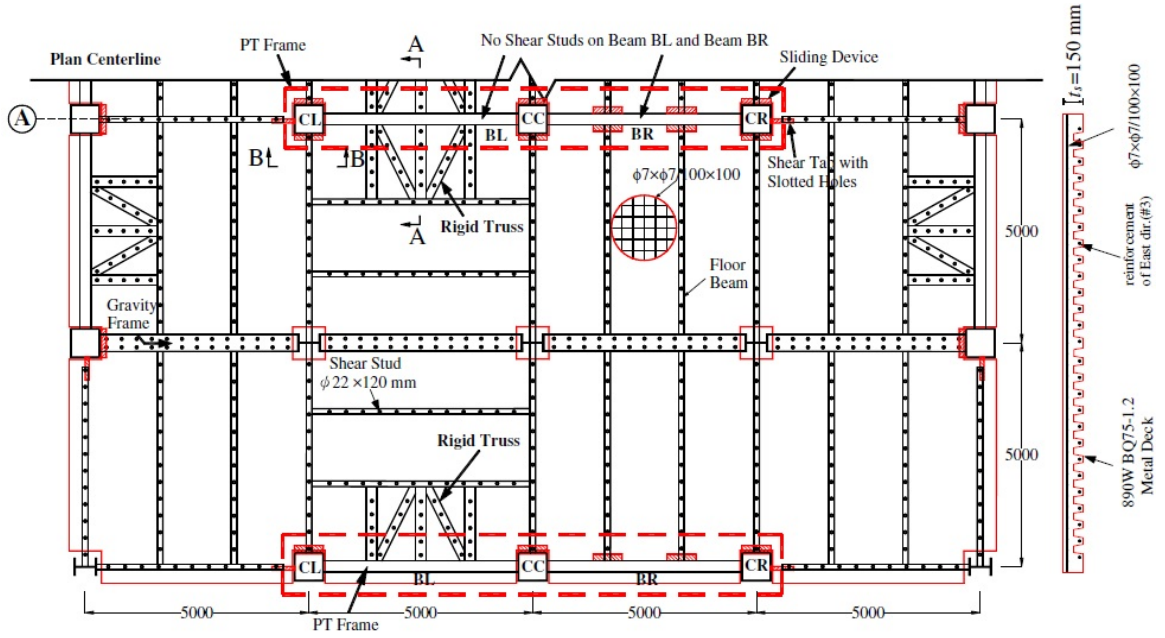

(b)

Figure 2.19: Floor slab details for (a) partial bonded slab and (b) rigid bay slab systems presented by Chou and Chen [2011a].

in design by reducing the RFP area on the top flange. Also, large residual drift were observed in the specimen with continuous metal decking in the composite floor slab (Specimen 2) after unloading from negative displacement; however, this residual drift was greatly reduced by introducing a separation in the metal decking at the column centerline (Specimen 4). Beam buckling was also observed at large drift demands near 4%, which also resulted in singnificant residual drifts; however, the slab was able to prevent buckling of the top flange when present, thus reducing the PT loss due to permanent beam shortening.

Chou and Chen [2011a] also tested a one-story two-bay PT frame (Fig. 2.20) in which the load was applied via a truss force transfer mechanism in one bay, similar to the load transfer in the rigid bay slab details in Fig. 2.19(b) . Two cyclic tests were conducted on the PT frame: one in which the actuators between the columns (Actuators 3 and 4) were allowed to deform freely with zero force, and one where these actuators were not allowed to deform, thus preventing frame expansion at the column tops. In both tests, no energy dissipating elements were provided in the PT connection such that the response was simply the bilinear elastic response of the PT frame only. These tests showed that restraining the column tops increased the post-decompression stiffness of the frame. The results of these tests were used to develop expressions for the forces in the beams due to column restraint and lateral loading.

2.2.4 PT column base connection

2.2.4.1 Chi (2009)

Previous research on PT MRFs noted that although PT connections could virtually eliminate beam damage and residual interstory drifts during an earthquake, many studies did report plastic hinges forming at the base of the columns, which is not easily repairable. The research by Chi [2009] proposes a rocking PT column base detail intended to eliminate damage at the columns bases. The detail, shown in Figure 2.21, incorporates PT bars, yielding steel plates for energy dissipation, flange reinforcing plates, and keeper plates for shear resistance. The PT bars would be anchored along the first story column and below the grade beam in the basement level, allowing the column to rock at the interface with the

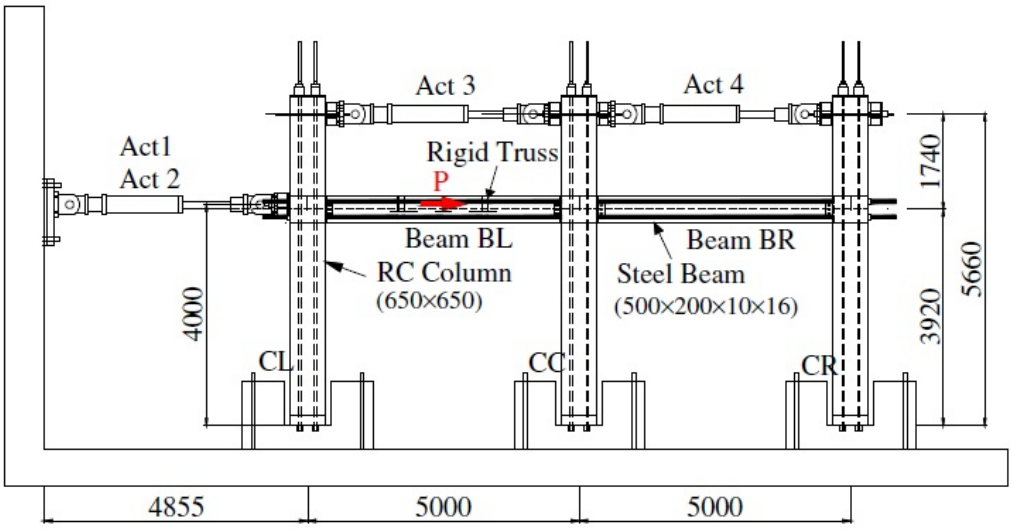

Figure 2.20: Two-bay PT frame test in Chou and Chen [2011a].

grade beam.

Quasi-static subassemblage tests were conducted on the PT column base connections with variations in design parameters such as initial PT force, column size, and load history. A detailed finite element model of the connection was constructed in ABAQUS. A parametric study of the finite element model of the connection detail showed that a properly proportioned PT column base is capable of recentering and remaining elastic at a target rotation of 0.04 radians [Chi et al., 2008]. This detailed model was used to validate a simplified analytical PT column base connection model developed in DRAIN-2DX.

This simplified PT column base connection model was incorporated into the six-story SC-MRF model also used by Garlock [2002]. The models were subjected to a suite of ground motions scaled to the DBE and MCE hazard levels. The average maximum story drifts for these two hazard levels were 0.023 radians and 0.032 radians, respectively, with residual drifts less than 0.2% following the DBE.

2.2.4.2 Chou and Chen (2011)

Chou and Chen [2011c] conducted scaled-shake table tests of a two-bay SC-MRF using the

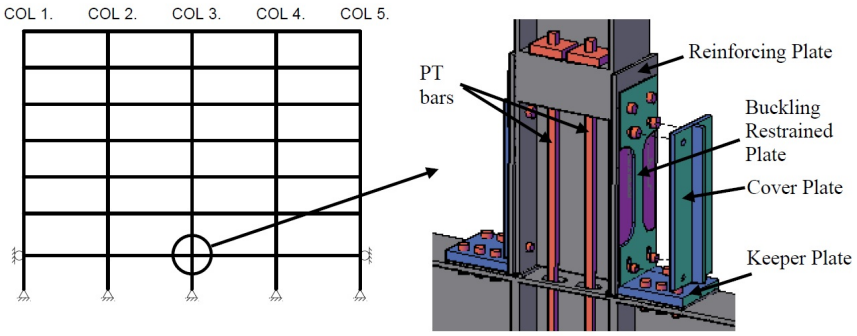

Figure 2.21: Schematic of PT column base [Chi et al., 2008]

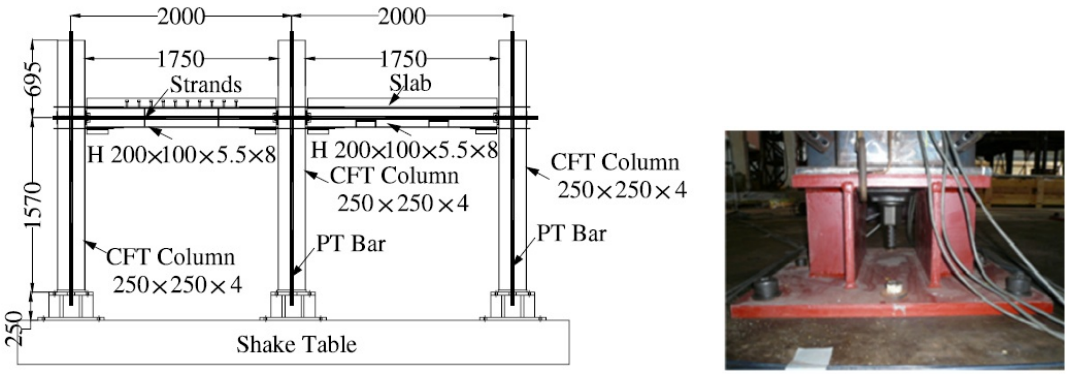

Figure 2.22: (a) Elevation of SC frame with post-tensioned base; (b) photo of PT column base [Chou and Chen, 2011b]

PT beam-to-column connections introduced previously in Chou et al. [2006] with RFPs to provide energy dissipation in the PT beam-to-column connections. This self-centering frame incorporated post-tensioned column base (PB) details (Fig. 2.22). The PB connection detail consisted of a single, debonded PT bar running vertically up the height of the CFT column, anchored at the top of the column and at the column base pedestal shown in Fig. 2.22(b). No additional energy dissipation was provided at the PB connection. Inertial forces were transfered from the slab to the self-centering PB (SCPB) frame via shear studs along the interior of the beam in only one bay of the frame (i.e. using the rigid bay slab configuration presented previously in Chou and Chen [2011a]).

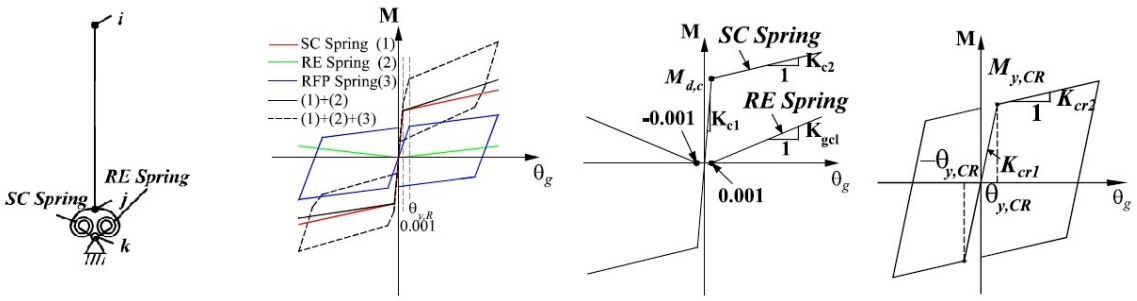

Figure 2.23: Schematic of PT column base spring model [Chou and Chen, 2011b]

The SCPB frame performed well under shake table testing, with residual drifts less than 0.01%. The tests were conducted mostly to assess the performance of the rigid bay slab configuration with the SC frame and RFP energy dissipation devices; therefore, few conclusions were made about the performance of the PB connection, indicating that it performed as intended. The primary conclusions of the shake table tests were verification that the sliding interface between the gravity beams and the SC fame allowed for the PT frame to expand without restraint. Similarly, discontinuous slab details at the columns, as presented previously in Chou and Chen [2011a], reduced the presence of cracks in the slab, greatly enhancing servacibility. Also, the axial forces in the beam with the slab-to-SC fame force transfer mechanism were larger than those of the non-composite bay; however, the distribution of shear forces at the base of the columns was symmetric with approximately half of the force going to the center column and the remaining force equally divided between the two exterior columns.

Chou and Chen [2011b] developed an analytical model for the SCPB frame used in the previously described shake table tests. The PT beam-to-column and column base connections were modeled using nonlinear rotational springs in parallel (Fig. 2.23): a SC spring that provides the bilinear elastic response of the rocking PT connection, a linear elastic RE spring that increases or decreases the connection stiffness due to the columns restraint to frame expansion, and an optional hysteretic RFP spring to model the energy dissipation of RFPs if used in the PT connection. The model was validated and showed good agreement with the shake table experimental results.

This modeling approach was used to model three-story self-centering (SC) buildings. The effect of the PT column base (PB) was evaluated by modifying aspects of the PB connection detail. One SC frame was modeled without energy dissipation at the column base, as investigated in the shake table test (SCPB), one incorporated RFP energy dissipation at the column base connection (SCRB), one was a SC frame with fixed column bases (SCFB), and one was a frame with conventional moment resisting connections at all beam-to-column and column base joints (MRF). Each model was subjected to a suite of fifteen ground motions, scaled to the DBE and MCE levels. The models showed that the column base connection dissipated approximately 30% and 12% of the input energy in the SCRB and SCFB frames, respectively. The story drifts for the MRF were smaller than the frames with PT column base details; however, the frames with PT column bases had virtually no residual drift. With the exception of the first floor of the SCPB frame, the mean plus one standard deviation ($m + \sigma$) story drifts for all of the frames were less than approximately 2% and 3% for the DBE and MCE levels.

2.3 Previous SPSW Research

The concept of utilizing thin, unstiffened steel web plates to resist lateral load through the development of a diagonal tension field was first introduced in the ealry 1980s [Thorburn et al., 1983; Timler and Kulak, 1983]. Since then, SPSWs have been successfully utilized in many high seismic applications [Robinson and Ames, 2000; Seilie and Hooper, 2005; Monnier and Harasimowicz, 2007; Kristeva, 2010] and have been included in U.S. and Canadian codes [AISC, 2005a; Canadian Standards Association , 2001]. Due to the vast extent of research on SPSWs [Sabelli and Bruneau, 2007; Clayton, 2010], the scope of this literature review is limited to research on SPSWs with different HBE-to-VBE connection types with an emphasis on experimental research, as this is the most applicable to the experimental research on SC-SPSWs with PT HBE-to-VBE connections being presented in this dissertation.

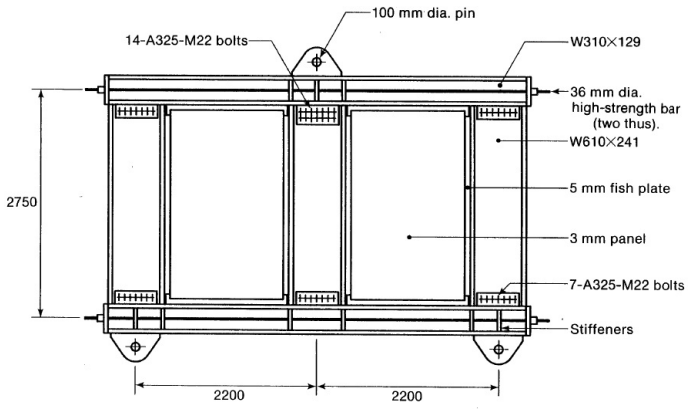

Figure 2.24: Schematic of specimen tested by Tromposch and Kulak [1987]

2.3.1 Tromposch and Kulak (1987)

Tromposch and Kulak [1987] conducted experimental tests on a single full-scale SPSW with comparisons to analytical SPSW models. The specimen consisted of two web plates with a boundary frame using simple shear bolted beam-to-column connections (Fig. 2.24). The specimen was loaded at the middle beam. This research developed an analytical strip model, based on the methods established by Thorburn et al. [1983] and Timler and Kulak [1983], that was able to reasonably predict experimentally obtained SPSW response; however, the bolted beam-to-column connections should be modeled as fixed at low load levels before bolt slip in the connections, after which a pinned beam-to-column connections can be used. This strip model was employed to predict the behavior of other SPSWs with different configurations, member sizes, and connection types. The results of this study showed that the effect of changing the connection from simple to moment resisting resulted in a less pinched hysteretic loop and a 150% increase in the energy dissipation due to the increase in frame stiffness.

2.3.2 Caccese et al. (1993)

Caccese et al. [1993] conducted an experimental program to investigate the effects of panel slenderness ratio and beam-to-column connection type on SPSW hysteretic behavior. The

test specimen consisted of one-fourth scale models of a three-story SPSW with web plate thicknesses of 0.03 in., 0.075 in., and 0.105 in. in the frame with moment-resisting connections and 0.03 in. and 0.075 in. in the frame with simple shear connections. For each of the tests, the plate thickness and connection type were the same at all stories, and the web plates were continuously welded to the boundary elements. The frame was loaded laterally at the top story only, and the columns were not preloaded to simulate the effects of gravity. The frame was loaded cyclically up to 2% drift.

The results of the test program showed that SPSWs with thicker web plates had failure modes governed by column instability and, therefore, did not provide significant increase in capacity compared to walls with more slender plates. The results also showed negligible difference between behavior of SPSWs with moment resisting connections and simple shear connections. This was attributed to the continuously welded panel to boundary element detail that essentially created a moment resting connection at the beam-to-column joint. Caccese's conclusions were later disputed by Kulak et al. [1994], who cited work by Tromposch and Kulak [1987] described later.

2.3.3 Schumacher et al. (1997)

Schumacher et al. [1997] investigated the effects of different web plate-to-boundary frame connection details, including welding directly to the boundary frame, welding to a fish plate connected to the boundary frame, and a combination of both. A modification of the fish plate connection detail in which a small 60mm-by-60mm corner cutout was provided in the web plate was proposed to reduced stress concentrations in the corners, as this is where web plate tearing typically initiated.

The test specimen consisted of a beam and column stub with a web plate connected to the beam and column along two edges using the various web plate-to-boundary frame connection details. An actuator loaded the web plate diagonally in tension simulating the tension field action, while actuators loaded the beam and column stubs simulating joint opening and closing. The tests found that the detail with the web plate welded directly to the boundary frame had minimal tearing, although this connection detail is difficult to

execute in the field due to construction tolerances. Tearing in the web plate-to-fish plate details was primarily due to out-of-plane bending of the web plate in the region of the less ductile heat affected zones where the web plate was welded to the edge of the fish plate. The presence of tears in the web plate did not have a significant impact on the web plate behavior or load carrying capacity.

2.3.4 Qu et al. (2008)

Qu et al. [2008] conducted experimental and analytical research on SPSWs with reduced beam section (RBS) connections. The RBS connections in the HBEs are used toensure system ductility and stable development of tension field action by ensuring that hinging occurs at the ends of the HBE, as opposed to the VBEs or within the HBE span.

The research conducted by Qu et al. [2008] consisted of a two-phase experimental program at the National Center for Research on Earthquake Engineering (NCREE) in Taiwan, where a full-scale two-story SPSW specimen with RBS connections and composite floors. The specimen was pseudodynamically tested, subjected to three ground motions of progressively decreasing intensity (Phase I), after which the buckled web plates were replaced and the specimen was tested pseudodynamically and cyclically to failure (Phase II). The specimen was also modeled using the tension strip method and a 3-D finite element model consisting of shell elements for all structural subassemblanges. The results of the tests showed that a SPSW repaired by replacing buckled web plates is capable of surviving subsequent earthquakes without significant boundary frame damage or strength degradation. During testing, the RBS connections in the anchor (top and foundation) beams performed as intended; however, fractures in the HBE flanges at the VBE face did lead to unexpected failure of the intermediate HBEs. The RBS flange region in these HBEs did not develop any fractures. Both the tension strip model and 3-D finite element model were shown to accurately predict the nonlinear behavior of the SPSW specimen when compared to the experimental performance with savings in the amount of steel required.

Qu and Bruneau [2009] also developed a design methodology that accounts for the strength of the moment resisting boundary frame when designing SPSWs. As implied by

code [AISC, 2005a], the web plates should be designed to resist the entire lateral design load. In the method proposed by Qu and Bruneau [2009], for a given aspect ratio, a designer can select a portion of the lateral load to be resisted by the web plate, κ, such that a MRF designed to resist the demands imposed by the yielding web plate will provide the remaining portion of the required lateral load resistance. For maximum efficiency, the ratio of the plastic strength of the resulting SPSW and the design loads should be one, thus called a balanced design. Qu and Bruneau [2009] presents a case study of SPSWs designed using the balanced design approach. Nonlinear analyses of these compared with conventionally designed SPSWs showed similar results.

2.3.5 Vian et al. (2009)

Vian et al. [2009a,b] conducted experimental and analytical investigation of special perforated SPSWs with RBS anchor beams. The perforations in the SPSW were intended to reduce the overstrength typically associated with SPSWs designed using minimum available plate thicknesses and to allow for utilities to pass through the plane of the wall. The RBS connections in the anchor beams were introduced to prevent hinging in the VBEs and within the HBE span. Three specimen were tested: one with multiple perforations within the panel (P), one with reinforced corner cutouts (CR), and one with a solid panel (S2). The test specimens were approximately half-scale single SPSW panels. All specimens were loaded cyclically up to at least 3% drift. Flange local buckling was observed in the P specimen at 3% drift, while fracture occurred in the RBS connection of the CR and S2 specimens at 3% drift, resulting in significantly reduced panel strengths. Monotonic and cyclic pushover analyses of finite element and strip models of the specimens showed good agreement with the overall behavior of the test specimens.

2.3.6 Lin, Tsai, and Li (2010)

2.3.6.1 Pseudo-dynamic testing of restrained and unrestrained SPSWs

Lin et al. [2010] conducted pseudo-dynamic testing of a full-scale two-story SPSW at NCREE. The specimen was loaded by actuators at each floor level. The load from the

actuators was transfered to the specimen via transfer beams along the edge of a concrete slab located at the top and middle beams. The specimen was restrained from out-of-plane movement by actuators attached to the concrete floor slabs orthogonal to the direction of loading. Gravity loads were simulated in the columns with vertical post-tensioned rods. The 1999 Chi-Chi Earthquake was used as the ground excitation for the pseudo-dynamic test and was scaled to represent the 2%, 10%, and 50% in 50 year hazard levels. The specimen was tested in two phases. In Phase I of testing, horizontal tube restrainers were provided in both stories to reduce out-of-plane deformation of the web plates and to reduce the sound of the web plate as it buckles. In Phase II of testing, the web plates from Phase I were removed and replaced, and the specimen was tested without the presence of the horizontal restrainers.

For the pseudo-dynamic test, a three-dimensional model of the two-story prototype building was constructed in the PISA3D software. The two-story SPSW was considered as a two degree-of-freedom stick model that represented the test specimen substructure. The restoring forces measured in the test specimen were then used by the PISA3D model to solve for the displacements to be imposed on the subsequent loading step.

The results of the pseudo-dynamic tests showed that the restrainers were effective in reducing the noise of the buckling web plate and reducing the out-of-plane web plate deformation from 250 mm to 50 mm. The overall response of the specimen with and without restrainers but with the same boundary frame were similar. Dynamic analyses in PISA3D of SPSW models using the equivalent brace and strip methods to model the web plate were able to capture trends in the story displacements and base shear time-histories observed in the pseudo-dynamic experiments. The web plates resisted approximately 50% of the total base shear at higher drifts.

2.3.6.2 Cyclic testing of narrow SPSWs

In a related SPSW test program at NCREE, Li et al. [2010] conducted quasi-static cyclic tests of four two-story narrow SPSW specimens (Fig. 2.25) with an aspect ratio (L/h) of approximately 0.6. The test set-up and overall specimen dimensions are shown in Fig. 2.26

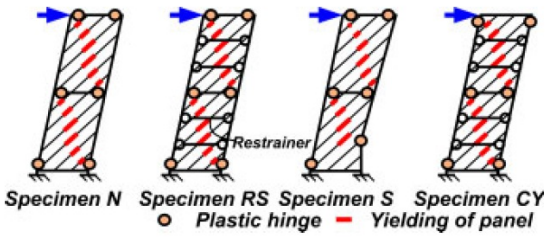

Figure 2.25: Four narrow SPSW and R-SPSW test specimens [Tsai et al., 2010]

with the specimens being loaded at the top beam only (Note that this test set-up served as the basis for the SC-SPSW tests conducted by the author at NCREE). RBS beam-to-column connections were used to ensure flexural hinging away from the welded connection. Two specimens also included horizontal stiffeners similar to those used in Lin et al. [2010], called restrainers, sandwiched on either side of the web plate to reduce out-of-plane deformation of the web plate and reduce the demands on the boundary frame due to web plate tension field action. The test program also investigated the effects of hinging in the columns at locations other that the column base. For this purpose, a conventional SPSW with hinging in the lower half of the first story and a restrained SPSW (R-SPSW) with hinging at the tops of the columns were considered (Specimens S and CY in Fig. 2.25, respectively). The design methodology and finite element analyses of narrow SPSWs and R-SPSWs was provided by Tsai et al. [2010].

Key results of the tests were that the restrainers successfully reduced the axial loads in the beams and flexural loads in the columns. Due to the reduced boundary frame demands with the introduction of restrainers, the R-SPSW (Specimen RS) was approximately 80% of the weight of the conventional SPSW (Specimen N), both of which exhibited hinging at the beam ends and column base as intended by the design procedure, indicating that R-SPSWs may have some cost savings benifits; however, it should also be noted that due to the larger boundary frame members, Specimen N did have approximately 15% more lateral load resistance than Specimen RS. The tests also confirmed that the column capacity design procedure proposed by Tsai et al. [2010] was effective in ensuring the formation of plastic hinges at the base of the first floor column.

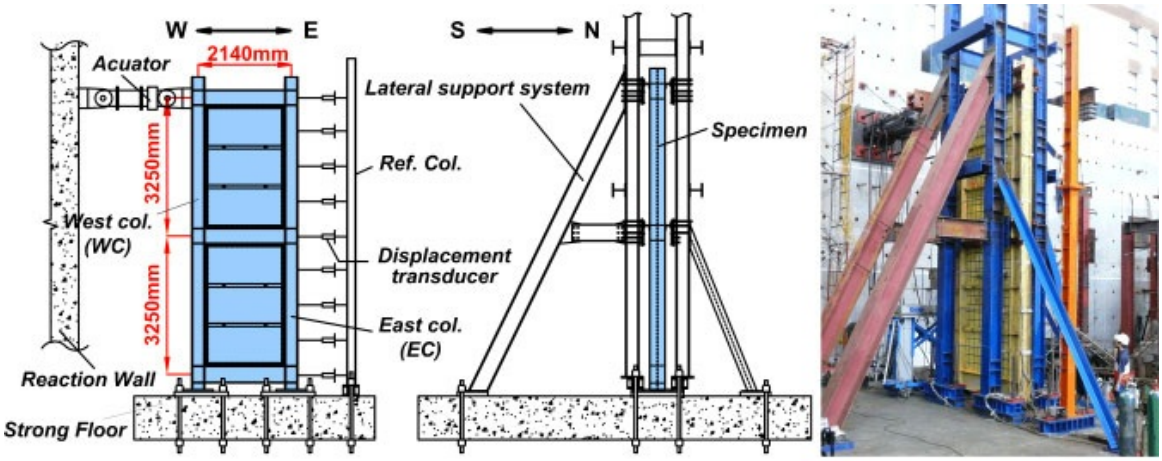

Figure 2.26: Narrow SPSW test set-up [Li et al., 2010]

2.4 Previous SC-SPSW Research

The SC-SPSW was first developed as part of a George E. Brown, Jr. Network for Earthquake Engineering Simulation (NEES)-funded research project entitled "Smart and Resilient Steel Walls for Reducing Earthquake Impacts." This project was a collaboration between researchers at University of Washington (UW), University of Illinois (UI), University at Buffalo (UB), and the National Center for Research on Earthquake Engineering (NCREE) in Taiwan. The key goals of this project were to fill in critical knowledge gaps in conventional SPSW behavior, to develop performance-based design tools (e.g. fragility curves) for conventional SPSWs, to test and develop design recommendations for coupled SPSWs, and to develop the new resilient SC-SPSW system. The latter topic is the focus of the author's research and is presented below.

As part of a NEES research project, information on participating researchers, testing, publications, and research outcomes can be found on the NEEShub Project Warehouse (https://nees.org/warehouse/project/631). Detailed information on equipment, instrumentation, data, and results from each of the tests conducted in this project (from all participating institutions) is accessible to the public through this data repository.

2.4.1 Clayton (2010)

This work was part of the author's Master's thesis and was part of the first investigation into the feasibility of the new SC-SPSW system. This work included understanding the system mechanics and analytical derivation of generalized SC-SPSW behavior, a brief overview of which was presented in Sec. 1.2. A schematic of an intermediate SC-SPSW story is shown in Fig. 2.27 to show key dimensions that are used in some of the following equations. Further details of the SC-SPSW mechanics and other components of this research are presented below.

2.4.1.1 Mechanics

Sec. 1.2 presented a brief overview of how the SC-SPSW system works. Fig. 1.2 showed a simple free-body diagram of a single SC-SPSW intermediate story. Figs. 1.3 and 1.4 also showed the forces acting on an intermediate HBE and a superposition method for estimating the HBE moment distribution, respectively, both of which were discussed in more detail in Clayton [2010]. Clayton [2010] also provided the following equations to estimate the HBE moment, axial, and shear distributions, PT forces, and system and connection stiffnesses. Some particular equations are shown below as they are most relevant to the research presented in this dissertation.

Clayton [2010] provided expressions for determining the horizontal and vertical components of the web plate forces acting on the HBEs and VBEs (ω_{xb}, ω_{yb}, ω_{xc}, and ω_{yc}, respectively). These distributed force components are based on the web plate thickness, t_w, web plate yield strength, ω_{yw}, and the tension field angle of inclination, α, which can be calculated as [Sabelli and Bruneau, 2007]:

$$\alpha = \arctan \sqrt[4]{\frac{1 + \frac{t_w L}{2A_c}}{1 + t_w h\left(\frac{1}{A_b} + \frac{h^3}{360 I_c L}\right)}} \tag{2.1}$$

where, h is the story height, L is the bay width, I_c is the moment of inertia for the VBEs, A_c is the cross-sectional area of the VBEs, and A_b is the cross-sectional area of the HBEs. The nominal lateral strength of the web plate, V_n, can be taken as [Sabelli and Bruneau,

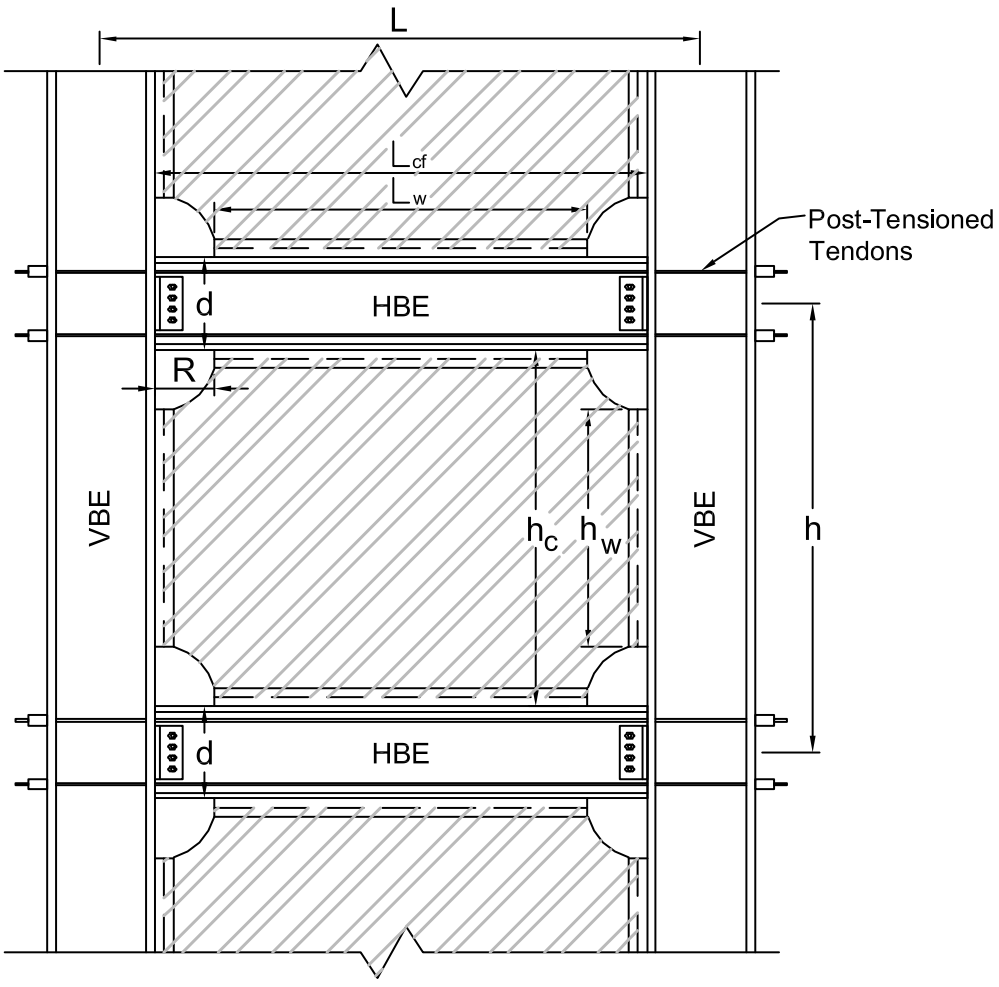

Figure 2.27: Schematic elevation of intermediate story of SC-SPSW with web plates connected to HBEs and VBEs [Clayton, 2010]

2007]:

$$V_n = 0.42 F_y t_w L_{cf} \sin(2\alpha) \tag{2.2}$$

where, F_y in this equation is the web plate yield strength and all other variables are previously defined.

In the SC-SPSW, the PT elements provide restoring forces as the PT connections rock open, causing the PT to elongate. The axial force in the PT elements can be determined by:

$$T_{PT} = T_o + \frac{k_{PT}}{k_{PT} + k_{HBE}} \left(k_{HBE} \theta_r d - P_{HBE(VBE)} \right) \tag{2.3}$$

where, T_o is the initial PT force for a given HBE, θ_r is the gap rotation, and k_{PT} and k_{HBE} are the axial stiffnesses (EA/L) of all the PT elements at a given HBE or the HBE, respectively. The gap rotation, θ_r, can typically be approximated as the same as the column drift [Clayton, 2010]. Actual gap rotation response will be presented later in the experimental data.

The HBE was shown to be a critical component in the SC-SPSW system. The demands on the HBE are influenced by the PT forces, the rocking connection transferring forces through only one flange, and the distributed forces from the yielded web plates. Expressions for the complex HBE axial, shear, and moment demand distributions were provided for use in HBE design. The equation for the moment along the length of the HBE can be written as (Eqn. 3.22 in Clayton [2010]):

$$M(x) = \begin{cases} \left(T_{PT} + P_{HBE(VBE)}\right)\left(\frac{d}{2} - \frac{d}{L_{cf}}x\right) + \frac{1}{2}\Delta\omega_{yb} L_w x \\ \qquad + \frac{d}{2}\left(\frac{1}{2}P_{HBE(web)} - \frac{\sum \omega_{yb} L_w}{L_{cf}}x\right) & \text{for } 0 \le x \le R \\ \left(T_{PT} + P_{HBE(VBE)}\right)\left(\frac{d}{2} - \frac{d}{L_{cf}}x\right) + \frac{1}{2}\Delta\omega_{yb}\left(R + (x-R)L_w - (x-R)^2\right) \\ \qquad + \frac{d}{2}\left(\frac{1}{2}P_{HBE(web)} + \sum \omega_{yb}\left(\frac{2R}{L_{cf}}x - R\right)\right) & \text{for } R < x \le L_w + R \\ \left(T_{PT} + P_{HBE(VBE)}\right)\left(\frac{d}{2} - \frac{d}{L_{cf}}x\right) + \frac{1}{2}\Delta\omega_{yb} L_w \left(L_{cf} - x\right) \\ \qquad + \frac{d}{2}\left(\frac{1}{2}P_{HBE(web)} + \sum \omega_{yb} L_w - \sum \omega_{yb}\frac{L_w}{L_{cf}}x\right) & \text{for } L_w + R < x \le L_{cf} \end{cases} \tag{2.4}$$

where, T_{PT} is the PT force shown above, $P_{HBE(VBE)}$ is the HBE axial load due to pull-in of the VBEs [Sabelli and Bruneau, 2007], d is the HBE rocking depth, L_{cf} is the VBE clear distance, L_w is the length of the web plate connected to the HBE, R is the length of the web plate radial corner cutout, and ω_{yb} and ω_{xb} are the y- and x-components of the diagonal web plate forces acting on the HBE [Clayton, 2010; Berman and Bruneau, 2008].

The axial force distribution along the HBE can also be determined by (Eqn. 3.31 in Clayton [2010]):

$$P(x) = \begin{cases} T_{PT} + P_{HBE(VBE)} + \frac{1}{2}P_{HBE(web)} & \text{for } 0 \le x \le R \\ T_{PT} + P_{HBE(VBE)} + \frac{1}{2}P_{HBE(web)} - \frac{P_{HBE(web)}}{L_w}(x - R) & \text{for } R < x \le L_w + R \\ T_{PT} + P_{HBE(VBE)} - \frac{1}{2}P_{HBE(web)} & \text{for } L_w + R < x \le L_{cf} \end{cases} \tag{2.5}$$

where all terms are as previously defined. All of these formulations assume that the distributed web plate forces are constant along its length and that the web plate has an elastic-perfectly plastic response.

As presented in Sec. 1.2, the recentering stiffness, K_r, is the SC-SPSW stiffness during unloading, after the web plates are fully unloaded and before the connection decompresses. Assuming that the web plate has negligible stiffness after unloading, the recentering stiffness at a particular story accounting for gravity load P-Delta effects can be estimated as (Eqn. 4.2 in Clayton [2010]):

$$K_r = \frac{\Sigma k_d^\theta}{h^2} - \frac{P}{h} \ge 0 \tag{2.6}$$

where, h is the story height, P is the portion of the p-delta load that must be resisted by the SC-SPSW at a particular story, and Σk_d^θ is the sum of the post-decompression rotational stiffnesses of the connections at a particular story and may be calculated using as:

$$k_d^\theta = \frac{d^2}{2}\left(\frac{k_{PT}k_{HBE}}{k_{PT} + k_{HBE}}\right) \tag{2.7}$$

where all terms have been previously defined.

2.4.1.2 Performance-based design procedure

A performance-based seismic design (PBSD) procedure was developed for the SC-SPSW system. The seismic hazard levels considered in the PBSD procedure are earthquakes with a 50%, 10%, and 2% probability of exceedance in 50 years. The following performance objectives (PO), shown schamatically in Fig. 2.28, were proposed:

1. *No connection decompression under wind or gravity loading.*

2. *System recenters and no repair of the system is required following an earthquake representing the 50% in 50 (50/50) year hazard level.* In evaluating whether a system has achieved recentering, a residual drift limit of less than 0.2% is imposed, as this corresponds to out-of-plumb limits in construction [ATC, 2009]. In this study, buildings requiring no repair should have peak story drifts less than 0.5%, the median story drift found by Baldvins et al. [2010] to require plate repair.

3. *System recenters and only web plate repair is required following an earthquake representing the 10% in 50 (10/50) year hazard level.* Significant yielding may occur in the web plates, requiring repair; however, the boundary elements and PT connection elements should remain elastic. Repair of the web plates consists of replacing the damaged plates, a procedure that is relatively quick and easy compared with repair of other lateral framing systems [Qu et al., 2008]. Story drifts should also be less than the 2% code-based drift limit [ASCE, 2005].

4. *Damage limited to prevent collapse during an earthquake representing the 2% in 50 (2/50) year hazard level.* Both residual drift and frame yielding may occur; however, to prevent sudden loss of stiffness and strength due to loss of connection capacity or a soft story collapse mechanism, the PT elements, HBEs, and VBEs should remain essentially elastic. A target drift limit for this PO was established as 4%, based on engineering judgment and the drift at which conventional SPSW test data show significant structural damage and strength loss [Baldvins et al., 2010].

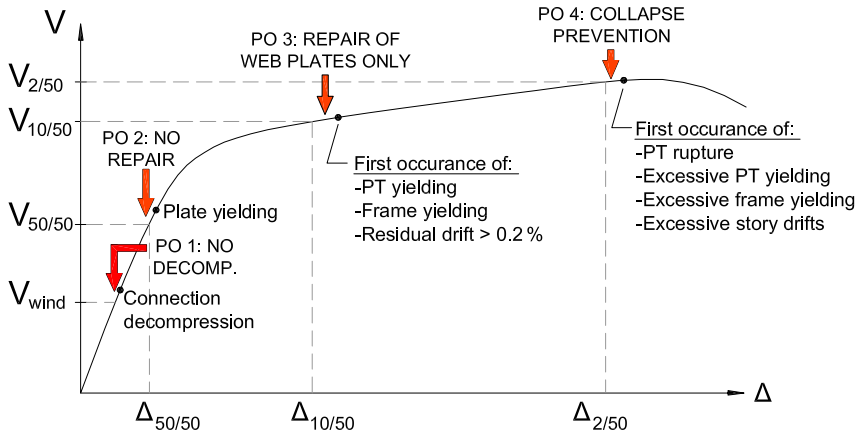

Figure 2.28: Performance based design objectives of SC-SPSW

The no repair performance objective, PO 2, was considered to be optional. In locations such as Los Angeles, where 50/50 forces can be significant, designing a building to remain essentially elastic at this hazard level may result in uneconomical or infeasible designs; therefore, it is up to the designers and stakeholders to determine the level of performance desired.

A step-by-step design procedure incorporating these performance objectives was also presented. The design steps can be summarized as:

1. Determine the seismic loads and lateral load distribution. The load distribution should account for high-mode effects per Chao et al. [2007].

2. Design the web plates for either the code-based design forces (i.e. design-level forces reduced by a response modification factor, R) or for the 50/50 forces, depending on the use of the optional PO 2.

3. Design the PT connection to have sufficient stiffness to ensure a positive recentering stiffness, K_r, under the influence of P-Delta effects.

4. Capacity design the PT and HBE to remain elastic and prevent in-span hinging up to 4% drift.

5. Capacity design the VBEs to remain elastic up to 5% drift [Berman and Bruneau, 2008].

6. Check design feasibility and iterate.

2.4.1.3 Numerical model

A numerical model (Fig. 2.29) was developed for the SC-SPSW in OpenSees [Mazzoni et al., 2009]. The web plate was modeled with tension-only truss elements oriented in the directions of the tension field as described by Sabelli and Bruneau [2007]. The strip elements were rigidly offset from the frame members by half of the member depth. The boundary frame was modeled using force-based nonlinear beam-column elements with fiber cross-sections to allow for distributed yielding along the members.

The PT connections (Fig. 7.1(d)) were modeled using: (1) stiff horizontal compression-only springs located at the HBE flanges to allow for decompression and gap opening, (2) diagonal compression-only springs at near-vertical inclinations to transfer shear forces while allowing for gap opening and vertical displacement of the HBE centroid as it displaces radially about the compression flange, and (3) a rigid beam element connecting the end of the HBE to the connection springs to ensure that the end of the HBE in contact with the VBE remains planar and is orthogonal to the HBE's longitudinal axis at that point. The tension-only truss elements used for the PT tendons were given an initial stress and also had a yield strength of $0.9F_u$ of ASTM grade 270 seven-wire strand, 1689 MPa.

Two P-Delta columns were placed symmetrically on both sides of the SC-SPSW to simulate the gravity loads of the building. Seismic mass was lumped at the HBE-to-VBE connections, and 2% Rayleigh damping was assumed [Clayton, 2010].

2.4.1.4 Evaluation of seismic performance

To evaluate the proposed PBSD procedure, a series of three- and nine-story SC-SPSW buildings were designed for the Los Angeles area and were modeled in OpenSees using the methods described above. A total of seven SC-SPSWs were designed, two of which incorporated the optional 50/50 no repair performance objective (PO 2). These models were subjected to a suite of 60 ground motions developed for the SAC project [FEMA, 2000a] for Los Angeles and represented the three seismic hazard levels considered in the design procedure. The seismic performance of the models was evaluated by a series of response parameters, including the peak story drift, $\theta_{s,max}$; the maximum residual story drift, $\theta_{resid,max}$; peak PT strain, $\epsilon_{PT,max}$, to evaluate the occurrence of PT yielding; and a measure of maximum frame element damage in the building, referred to as the damage value for VBEs and HBEs, D_{VBE} and D_{HBE}, respectively as evaluated by the interaction equation per Eqn. H1-1 [AISC, 2005b].

The results of the dynamic analyses showed that for all of the prototype buildings, the median responses, and in many cases the 84th percentile responses, show that the POs are achieved. The buildings that were designed for the enhanced performance level of no repair following a 50% in 50 year event (PO 2) showed the best response overall, but resulted in larger, more conservatively designed members. Buildings that were not designed to meet this enhanced performance objective showed adequate response at all hazard levels, meeting the proposed performance objectives at at least the median level. Although the proposed design procedure resulted in SC-SPSWs capable of meeting the intended performance objectives, a couple of modifications were suggested to further improve performance: accounting for the additional beam growth restraint at the base of the VBE when designing the first floor HBE, providing a period-dependent web plate force amplification factor to improve performance of low-rise structures, and increasing the 4% drift limit used in the PT design to better represent drifts observed at the 2% in 50 year hazard level and to ensure elastic boundary frame repsonse at this hazard level. Further discussion of this drift limit and balancing damage reduction and ecnomy in the PBSD procedure will be discussed as part of my future work.

2.4.2 Winkley (2011)

Winkley [2011] conducted the first phase of experimental SC-SPSW subassembly testing at the University of Washington (UW). During this phase of experimental investigation, the test set-up, which was used in the second phase of testing conducted by the author and described in this document, was constructed and five specimens were tested. The test matrix included one bare PT frame specimen (8s100k), and four SC-SPSW specimens with variations in number of PT strands and web plate thickness (8s100k20Ga, 6s75k20Ga, 6s75k16Ga, and 8s100k16Ga). All HBEs were W18x106. The results of these tests are compared with those from the second phase of testing conducted by the author, and this document gives further details of the test set-up, instrumentation, and loading in Sec. 4.2; therefore, those details will not be given here.

Some key findings from this study were:

- The bolted web plate-to-fish plate connection used in the subassembly tests adequately transfered web plate forces to the boundary elements.

- The residual strength of the web plates, which was not accounted for in the idealized tension-only web plate behavior originally assumed, had an impact on the residual drift (i.e. drift at zero force) of the specimen. The residual web plate strength was proportional to the web plate thickness; therefore, specimens with thicker plates had larger residual drifts.

- Specimens with more PT strands, and thus larger initial PT forces, had lower residual drifts. PT force losses due to anchorage seating during loading were significant, between 12% to 15%.

- Pushover curves from a SAP2000 [SAP] numerical model of the specimens showed good agreement with the backbone of the experimental cyclic response.

2.4.3 Dowden (2012)

Researchers at the University at Buffalo (UB) working on the same NEES-supported project as the author are also investigating the new SC-SPSW system. Their work includes developing capacity design procedures for the HBE component, development of new PT HBE-to-VBE connections that prevent frame expansion, and cyclic and shake table testing of several third-scale, three-story SC-SPSW specimens.

2.4.3.1 HBE capacity design

Dowden et al. [2012] gave mathematical expressions for the axial, shear, and moment demands along an HBE in a SC-SPSW. These analytically derived expressions compared well with the HBE demands in a numerical SAP2000 [SAP] model.

A capacity design procedure for a self-centering connection with a beam that rocks about both flanges was proposed. The procedure is as follows:

1. Select initial boundary frame sizes and web plate thicknesses.

2. Determine the lowest PT force that would be required to ensure that the maximum moment occurs at the HBE ends at a certain target drift (2% target drift was used for the design example provided in Dowden et al. [2012]).

3. Select post-tension to ensure the PT elements remain elastic up to 4% drift.

4. Select the initial PT force to provide an adequate decompression moment to resist gravity and wind loads.

5. Select the least cross-sectional area of PT to satisfy the previous conditions.

6. Assess the adequacy of the HBE considering the effect of the reduced flexural capacity due to large axial forces and the effect of PT losses due to HBE axial shortening.

7. Iterate to reduce the HBE size while satisfying the above requirements.

Dowden et al. [2012] included design curve and design space examples that could be used as graphical design aids.

2.4.3.2 Alternate PT HBE-to-VBE connections

Part of the research at UB included development of new PT connections that can eliminate frame expansion, a phenomenon that is typical of conventional PT frames and was discussed previously in work done by Garlock and Li [2007]. Two such connections were developed for this purpose: (1) one that rocks about a pin at the HBE centerline with PT strands above and below the rocking point (Fig. 2.30(a)) and (2) one that rocks about the top flange of the HBE only with PT strands located below the point of rocking (Fig. 2.30(b)), which has been named the New Zealand-inspired– Buffalo Resilient Earthquake-resistant Auto-centering while Keeping Slab Sound (NewZ-BREAKSS) rocking connection [Dowden and Bruneau, 2011].

Note that PT connections can only develop a restoring force when the PT elements elongate, and in conventional PT connections where the PT extends from column to column, this PT elongation is provided by frame expansion; however, in these proposed connections that eliminate frame expansion, the PT elements must be terminated along the length of the HBE to develop those restoring forces. Also note that in both of these connections it is possible for the PT elements to shorten where the existing gap (above or below the pin of the centerline rocking connection or below the top flange of the NewZ-BREAKSS connection) is closing during lateral sway. In this case, it is also possible for the PT elements to go completely slack. Also unlike the PT connections that rock about both flanges, these connections are initially decompressed, responding with the decreased post-decompression rotational stiffness upon initial loading (i.e. the decompression moment, M_d is zero). The resulting response of these alternative PT connections is linear, unlike the bilinear elastic response of the PT connection rocking about both flanges. It should be noted that the PT connection rotational stiffness can further decrease after the PT strands go slack as the force in these elements, which contributes to the PT connection resistance, no longer change as the connection rotation increases. The impact of this reduced rotational stiffness due

to PT strand detensioning and the compounding effects of P-Delta stiffness reduction have not been investigated.

Dowden and Bruneau [2011] provided a free-body diagram and the hysteretic behavior of a SC-SPSW utilizing the NewZ-BREAKSS connection. Here, a nonlinear dynamic analysis was conducted in SAP2000 [SAP] to show that the SC-SPSW system with NewZ-BREAKSS connections was able to recenter following a 10% in 50 year earthquake with a peak drift near 3.4%; however, it should be noted that this model assumed tension-only web plate behavior, and as noted previously the residual strength of the web plate during unloading can be significant and can have a negative impact on recentering capabilities [Winkley, 2011]. Both the centerline rocking and NewZ-BREAKSS connections are more sucseptable to the negative impacts of the residual web plate strength on recentering since they are initially "decompressed" and thus do not have a decompression strength (V_d in Fig. 1.5(c)) and have a reduced initial stiffness [Dowden and Bruneau, 2011].

2.4.3.3 Scaled system tests

Tests of one-third scaled, single-bay, three-story SC-SPSW specimens have also been conducted at UB. The test specimen, shown in Fig. 2.31(a), consists of W8x18, W8x15, W8x18 (Grade A572) HBEs at levels 3, 2, 1, respectively, and W6x25 VBEs. Web plate thicknesses are 26 GA (0.46 mm), 24 GA (0.61 mm), 22 GA (0.76 mm) (ASTM A1008) at levels 3, 2, 1, respectively, welded to steel fish plates along the boundary frame. Connection to the strong floor is provided by steel clevis and pin connections at the base of the VBEs to allow free rotation of the VBEs. A W6x20 HBE anchor beam is bolted to the foundation plate. PT monostrands with 13 mm diameter and a yield strength of 1860 MPa strands are provided at mid-depth of the HBE, one each side of the HBE web with an initial PT force of approximately 20% of the yield strength of the PT strands. The HBE clear span is 2134 mm while the level 1,2, and 3 floor-to-floor heights are 1191 mm , 1289 mm, and 1289 mm, respectively. [Clayton et al., 2012a]

A series of specimens were tested to investigate different web plate configurations and PT HBE-to-VBE connections. Three different boundary frames were constructed utilizing

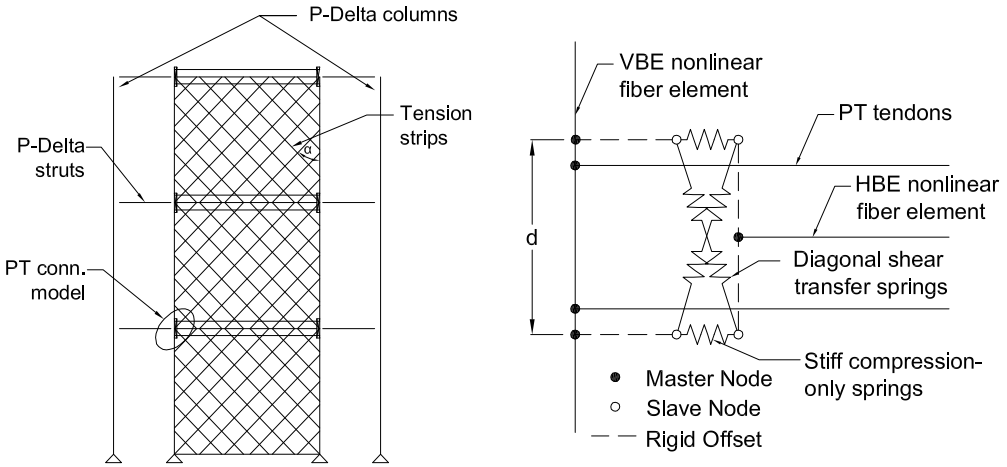

Figure 2.29: (a)Numerical model of 3-story SC-SPSW with (b) detail of numerical PT connection model

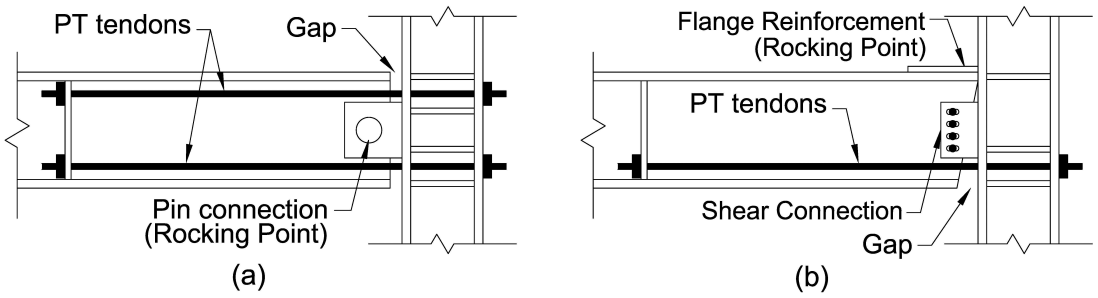

Figure 2.30: (a) Centerline rocking and (b) NewZ-BREAKSS PT HBE-to-VBE connections

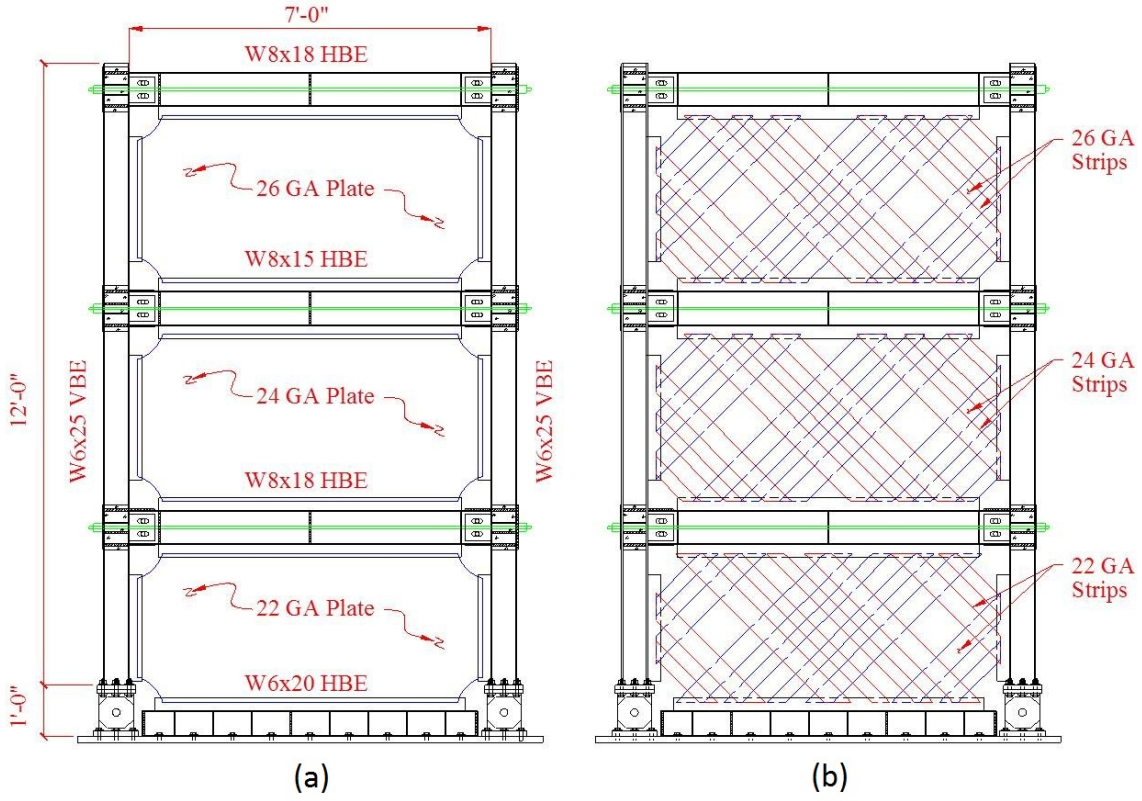

Figure 2.31: Dimensions of UB specimens with (a) full web plates and (b) web plate strips.

the three PT HBE-to-VBE connection types: (1) rocking about both flanges, (2) rocking about the HBE centerline, and (3) NewZ-BREAKSS connections. Each frame was then tested quasi-statically with three different web plate configurations: (1) bare PT frame without web plates, (2) full infill web plates (Fig. 2.31(a)), and (3) web plate strips oriented in the approximate direction of the tension field (Fig. 2.31(b)). The web plate strips were intended to simulate the idealized tension-only behavior assumed by the web plate strip model, thus removing some of the unknown complexities of web plate behavior including web plate residual strength and distribution of stresses along the boundary elements. Each of these specimens was tested under quasi-static loading with actuators loading at three levels, as shown in Fig. 2.32.

The preliminary results of the quasi-static tests are shown in Fig. 2.33. These plots

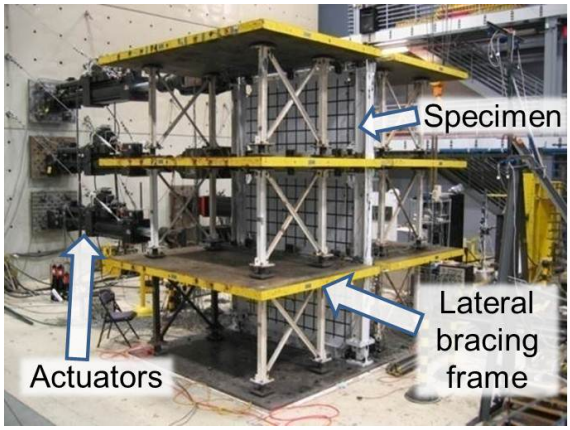

Figure 2.32: Test set-up for quasi-static tests at UB.

also include the single-cycle response of a numerical strip model constructed in SAP2000 [SAP], where the strips included some compression resistance as an attempt at capturing the web plate residual strength that was observed in previous tests by Winkley [2011] and Webster [2012]. The amount of compressive resistance is given as a percentage of the tensile yield strength. Note that in the flange rocking specimen, the negative stiffness in the force versus displacement response is caused by actuator interaction due to the displacement shape imposed on the specimen in the displacement-controlled loading procedure. The NewZ-BREAKSS and centerline rocking specimens were later tested using a revised force-controlled loading procedure wherein the roof-level actuator was displacement-controlled and the force of the other actuators were slaved to that of the roof actuator. This loading method corrected the problem of the artificial negative stiffness.

The flange rocking and NewZ-BREAKSS frames, each with the three web plate configurations, are currently being tested on a shake table to assess the dynamic response of the SC-SPSW system. Each specimen will be subjected to a synthetic ground motion developed to match the Los Angeles design spectrum. The ground motion will be linearly scaled to observe behavior under different earthquake intensities. Results from these tests are not yet available.

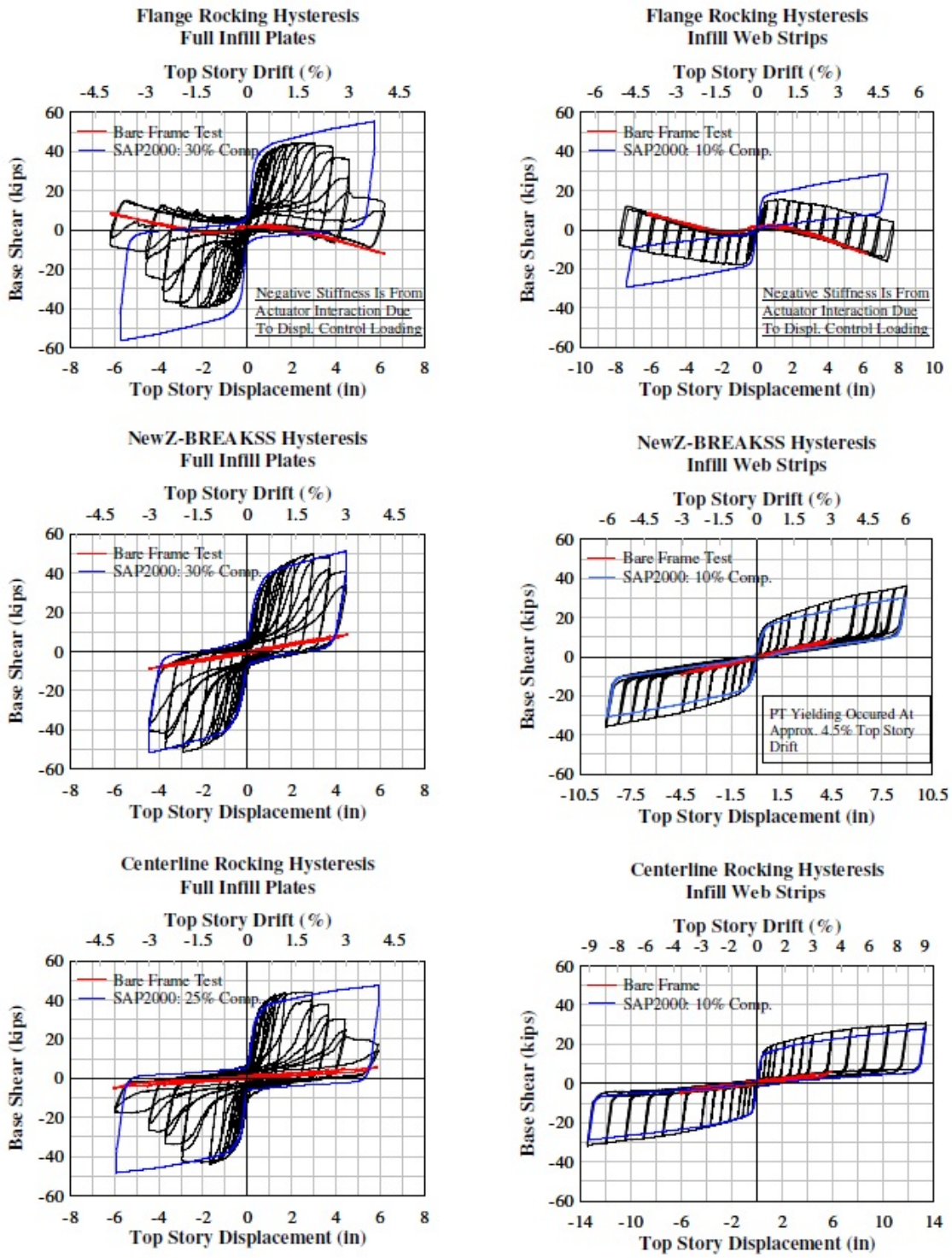

Figure 2.33: Force vs. displacement response of quasi-static tests at UB.

2.5 Conclusions and Research Needs

The broad research that has been conducted on PT connections and conventional SPSWs provided a foundation for the development of the SC-SPSW. The research presented in this chapter has addressed the following topics:

- Design methodologies and experimental testing of self-centering systems utilizing post-tensioned beam-to-column connections with various energy dissipation mechanisms including friction devices, yielding top and seat angles, yielding bars, and web plates.

- Proposed methods for accommodating frame expansion in typical self-centering systems including deformable collector beam elements and allowing the slab to slide freely on all but one bay of the self-centering frame. Although some numerical [Garlock and Li, 2007; Kim and Christopoulos, 2008] and experimental [Chou and Chen, 2011a] studies have been conducted to address the impact of the slab and transfer of inertial forces on the self-centering frame, more research is needed to verify the constructibility and three-dimensional performance of these proposed details.

- Numerical and experimental studies of PT column base details at the subassembly- and system-level, demonstrating its recentering capabilities and ability to reduce inelastic hinging at the column base.

- Large-scale quasi-static and pseudo-dynamic testing and recommendations for more efficient design of conventional SPSWs to encourage their implementation as a lateral force resisting system.

- Proof-of-concept numerical investigation and verification of the SC-SPSW concept using simplified approximations of PT connection and web plate behavior.

- Subassembly testing of SC-SPSWs to investigate impacts of web plate thickness and PT design on behavior.

- Scaled quasi-static and shake table (currently underway) testing of the SC-SPSW system with pinned column bases.

- Proposed PT connections to eliminate frame expansion in SC-SPSWs, thus eliminating the need for extensive diaphragm detailing as previously described [Garlock and Li, 2007; Kim and Christopoulos, 2008; Chou and Chen, 2011a].

Some key research issues that are necessary for addressing the objectives presented in Sec. 1.3 that have not yet been addressed by the previous SC-SPSW research include:

1. Detailed finite element modeling and further experimental validation to have a better understanding of the complex web plate and PT connection behavior. This complex behavior should be incorporated into the numerical modeling techniques used in the initial proof-of-concept study [Clayton, 2010] to ensure the system's viability considering non-idealized component behaviors.

2. Full-scale experimental verification of system performance. To do so, the issue of the column base connection should be addressed. Previous system-level SC-SPSW experimental and analytical research has only considered perfect pinned column base connections, which can be infeasible or impractical in actual construction. Extending the previously described PT column base connection to SC-SPSWs should be considered as a more economical alternative to provide base fixity while also providing recentering and damage reduction capabilities.

3. Design recommendations to improve structural efficiency while still meeting the proposed design objectives. Boundary frame sizes in the previous subassembly tests and SC-SPSWs designed using the design procedure proposed by Clayton [2010] were conservatively designed to ensure elastic frame performance, resulting in large and uneconomical member sizes. For wide-spread implementation of the SC-SPSW system, research must be done to reduce the required frame member size, while still achieving adequate performance. The results of this research should include easily accessible tools for designers wishing to implement the SC-SPSW system.

4. Conducting life-cycle cost analyses to assess the benefits of using the SC-SPSW system compared to a conventional SPSW or SC-MRF system. To adequately do so, the full building system must be considered, including probabilistic costs of constructing and repairing gravity framing systems, non-structural systems, and special diaphragm detailing.

Chapter 3

SUPPLEMENTAL MECHANICS FOR SC-SPSW VARIATIONS

3.1 Introduction

Much of the mechanics of the SC-SPSW system were presented in Clayton [2010] and summarized previously in Secs. 1.2 and 2.4.1.1. The previously presented mechanics include idealized system and PT connection cyclic behavior, HBE free-body diagrams, and HBE moment, axial, and shear force distributions. All of the previously presented material focused on post-tensioned HBE-to-VBE connections and SC-SPSWs with the web plate connected to the HBEs and VBEs (i.e. connected to the boundary frame on four sides of the plate).

This dissertation presents variations on the SC-SPSW system that were not presented in Clayton [2010], thus requiring discussion of the mechanics associated with these variations. The SC-SPSW variations that were introduced in this portion of SC-SPSW research include (1) web plates that are connected only to the HBEs and (2) post-tensioned (PT) column base connections. Both of these variations are optional and may be incorporated into the basic SC-SPSW system that was first introduced in Clayton [2010].

The following sections will present the motivation for introducing this SC-SPSW variation, a discussion of mechanics and behavior, and necessary design equations for determining component demands. The information presented in this chapter is intended to be supplemental to the SC-SPSW mechanics presented in Clayton [2010].

3.2 Web Plates Connected to HBEs Only

3.2.1 Motivation

Traditional SPSW systems comprise web plates connected on all four sides to the VBEs and HBEs. Here, lateral load resistance relies on the development of full tension field action in the web plate. Alternatively, web plates can be connected to the HBEs only, resulting in

development of a partial tension field (discussed later in Sec. 3.2.2). A very limited number of experimental studies have been conducted on SPSWs with web plates connected only to the HBEs [Guo et al., 2011; Vatansever and Yardimci, 2011]. Possible benefits that have been proposed for HBE-only web plate connectivity include reduction in column flexural demands and providing access to pass utilities through the frame [Guo et al., 2011]. The proposed benefits of HBE-only web plate connectivity are further amplified for SC-SPSW applications compared to those of conventional SPSWs due to certain aspects of SC-SPSW behavior. These potential benefits, discussed individually in the following sections, include potential reduction of VBE member sizes and potential mitigation of web plate damage.

Potential reduction of VBE member size The performance-based seismic design procedure presented in Clayton [2010] proposed capacity design of the VBEs such that HBE or PT yielding would occur prior to VBE yielding. The drift limit suggested for VBE design was 5%, which was larger than the 4% target drift used in the HBE and PT capacity designs. This conservative capacity design approach resulted in column sizes for 3- and 9-story buidlings that were very large, even requiring the use of built-up sections in some cases. This research suggested the need for methods of reducing VBE member sizes to improve structural econmy and design feasibility.

Connecting the web plate to the HBEs only removes the distributed web plate loads acting on the VBEs. Eliminating the in-span lateral load on the VBEs has the potential to reduce VBE flexural demands, with the added benefit of simplifying the VBE moment distribution for design. Removing the restraint along the vertical edges of the web plate does reduce the area of the tension field (discussed later), which does reduce its lateral load resisting capacity; therefore, the HBE-only web plates must be thicker or made of higher strength steel to have similar lateral load capacities as fully connected web plates. The increase in web plate demands on the HBEs due to the stronger web plates may result in an increase in the magnitude of forces transferred from the HBEs to the VBEs; therefore, research (presented in Chapter 8) must be done to assess the potential for VBE size reduction.

Potential mitigation of web plate damage Phase I of the SC-SPSW subassembly testing conducted by Winkley [2011] showed that much of the web plate damage was concentrated along the clamping bars in the bolted web plate-to-fish plate connection. Most specifically, tearing typically initiated due to cyclic folding of the web plate near the corner cutouts and was typically most sever along the bottom HBE where the frame expansion was largest (due to the roller restraint at the bottom of one of the columns). Similar trends in web plate tearing were observed in Phase II of the SC-SPSW subassembly testing and will be discussed in further detail in Chapter 4.

This web plate damage suggested two key mechanisms that promoted or accelerated web plate tearing:

- Increased tensile demands in the corners due to gap opening, which resulted in increased out-of-plane bending (i.e. folding) of the plastically stretched web plate upon gap closing.

- Increased horizontal strain demands throughout the web plate due to frame expansion.

Releasing the web plate from the columns eliminates the additional web plate strain demands due to gap opening and frame expansion. The SC-SPSW system was proposed as a means to mitigate structural damage and relies on web plate strength to primarily resist lateral loads; therefore, methods for delaying web plate damage can provide even further improvement of SC-SPSW performance. The experimental investigation of HBE-only web plate connectivity presented in Chapter 4 will evaluate mitigation of web plate damage, and a numerical study presented in Chapter 8 will evaluate the seismic performance of SC-SPSWs designed with this type of web plate connectivity.

3.2.2 General behavior

Fig. 3.1 shows a schematic of the SC-SPSW system with web plates connected to the HBEs only. This schematic can be compared to the intermediate story elevation presented in Fig. 2.27 [Clayton, 2010] for SC-SPSWs with web plates fully connected to the boundary frame along all four edges. In addition to the obvious difference of the web plates no longer

being connected to the VBEs, the HBE-only web plate configuration also allows the web plate to be extended over a longer length, L_w, of the HBE since corner cutouts are no longer required to accommodate the increased tensile strains associated with gap opening. The web plate can extend almost to the ends of the HBE but should be terminated far enough away from the HBE end such that the fish plate will not bear on the column flange under the expected range of connection gap rotation.

When the frame undergoes lateral sway, the web plate develops partial tension field action as shown for rightward sway in the partial free-body diagram of an intermediate story in Fig. 3.2. Again, this free-body diagram can be compared to the full tension field action of fully connected SC-SPSW web plates shown previously in Fig. 1.2. The partial tension field extends over the portion of the web plate in which diagonal tensile forces can develop between the HBEs above and below. The remainder of the web plate outside of the partial tension field is not contributing to the plate's lateral force resistance.

The concept of partial tension field action for SPSWs with infinitely flexible columns was discussed in Thorburn et al. [1983] and was based on previous research on tension field development in plate girders [Basler, 1961]. Although this previous research was focused on development of partial tension fields in thin plates with insufficient flexural restraint along two sides, the concepts of partial tension field action can be extended to the HBE-only web plate connectivity configuration where the columns provide no restraint on the web plates.

The partial tension field develops at an angle, θ, from the vertical direction which can be calculated from the equation: [Basler, 1961; Thorburn et al., 1983]

$$\tan 2\theta = \frac{L_w}{h_c} \tag{3.1}$$

where, L_w is the horizontal length of the web plate and h_c is the clear height of the web plate. This equation for partial tension field inclination was derived based on the concept that the partial tension field will orient itself in such a way that it can resist the maximum shear force. If the web plate is assumed to have negligible compressive resistance and a constant post-yield tension stress, an increase in shear load in the web plate must be accompanied by a change in the tension field orientation. Optimizing the shear resistance equation with

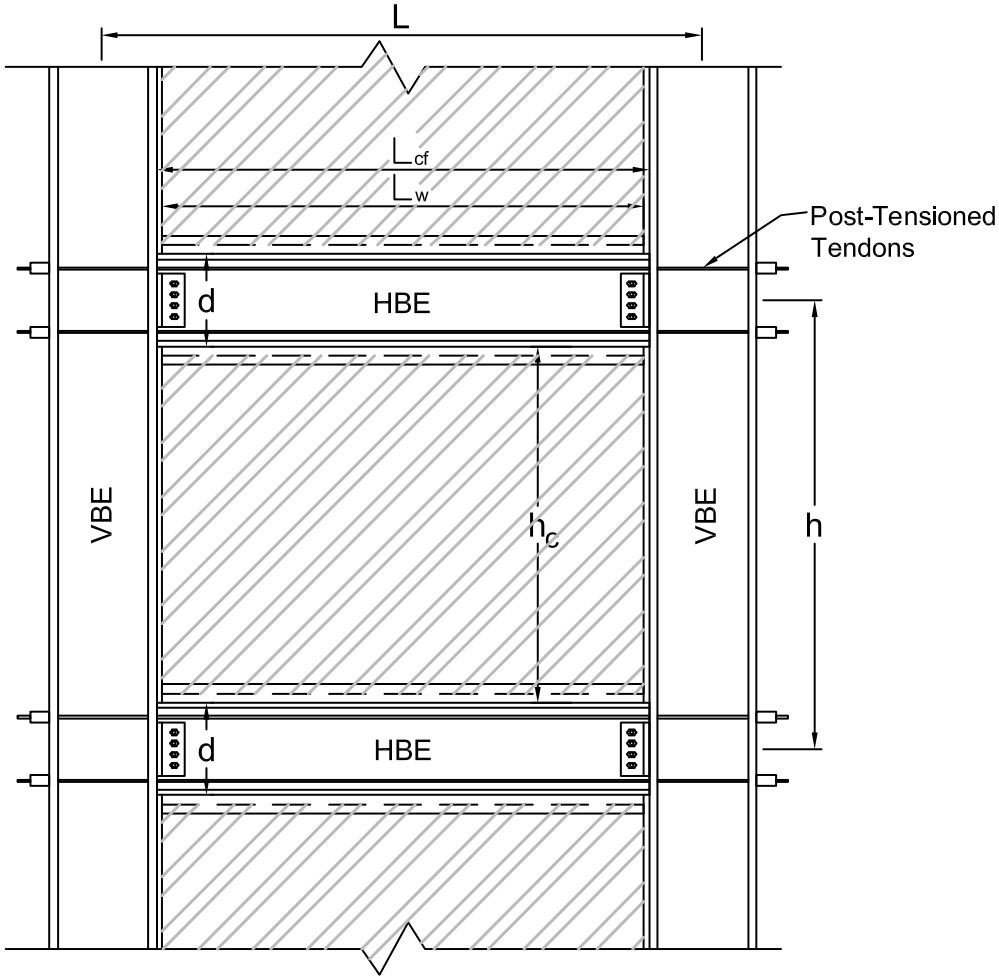

Figure 3.1: Schematic elevation of intermediate story of SC-SPSW with web plates connected to HBEs only

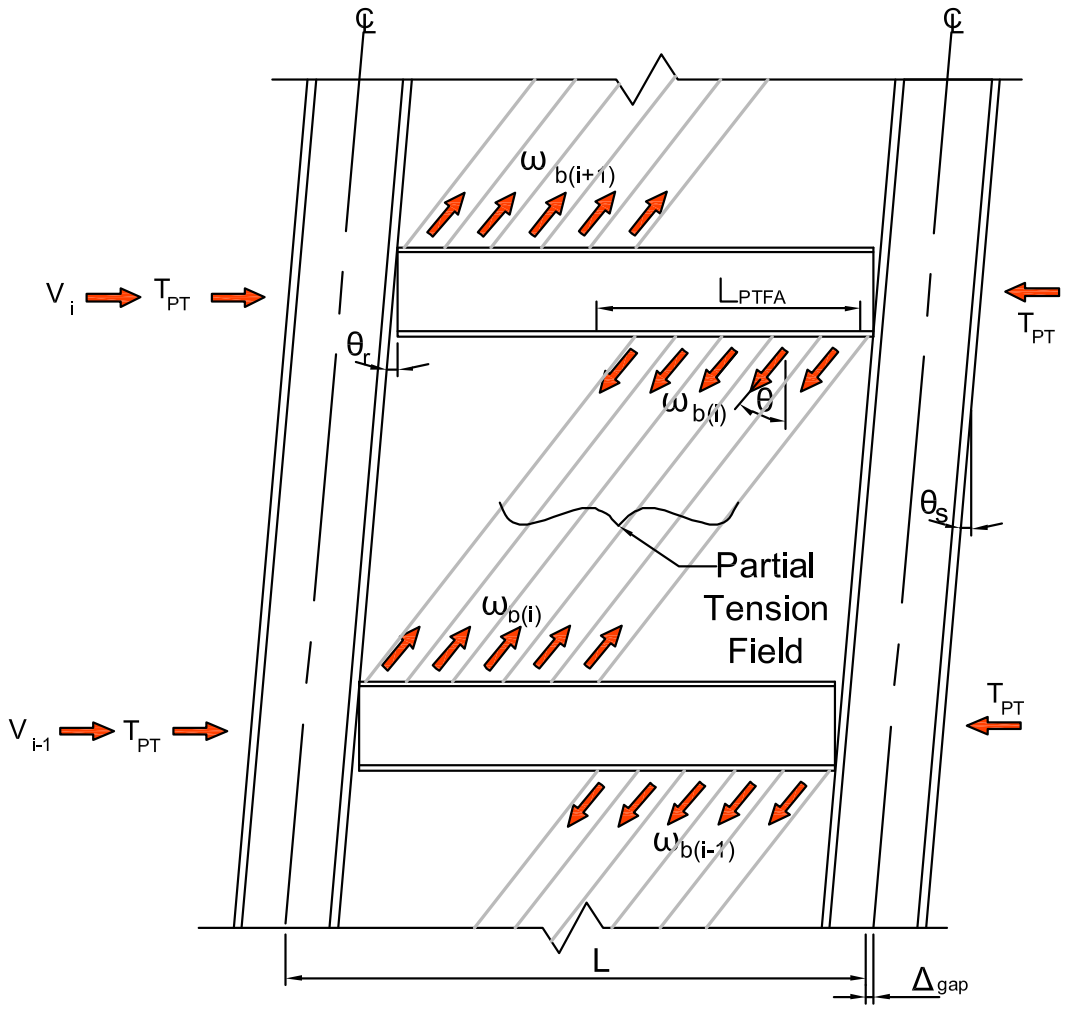

Figure 3.2: Free-body diagram of intermediate story of SC-SPSW with web plates connected to HBEs only in deformed configuration (PT and shear connections not shown for clarity)

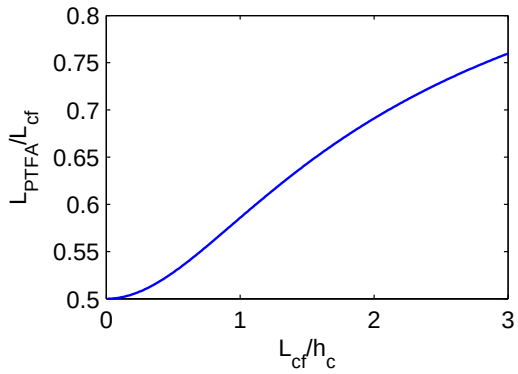

Figure 3.3: Portion of partial tension field acting on the beam as a function of panel aspect ratio

respect to the partial tension field angle results in that shown in Eqn. (3.1) [Basler, 1961]. Unlike the equation for full tension field angle of inclination, α, in Eqn. (2.1) that relies on parameters associated with web plate thickness and boundary frame axial and flexural stiffnesses, the partial tension field angle of inclination, θ, relies only on web plate geometry. More specifically, θ depends only on the web plate aspect ratio, L_w/h_c.

The partial tension field extends over a length, L_{PTFA}, along the HBE. The partial tension field horizontal length can be calculated as:

$$L_{PTFA} = L_w - h_c \tan\theta \tag{3.2}$$

When combined with the equation for θ (Eqn. (3.1)) the partial tension field length is a function of the panel aspect ratio, L_{cf}/h_c. The portion of the HBE over which the partial tension field acts, L_{PTFA}/L_{cf}, is shown as a function of the aspect ratio is Fig. 3.3. This figure shows that the partial tension field approaches approximately half the HBE length for very tall web plates (i.e. small L_{cf}/h_c) and increases to values of approximately 70% of the HBE length for panel aspect ratios around 2. This figure shows that for all practical panel aspect ratios[1], there will be some portion in the middle of the HBE where the partial tension fields above and below the HBE are simultaneously applying forces to the HBE.

[1]Note that the *AISC Seismic Provisions* [AISC, 2005a] limit SPSWs to apsect ratios of 0.8 to 2.5.

The x- and y-components of the distributed diagonal web plate forces acting on the HBE at story i , ω_{xbi} (Eqn. (3.3)) and ω_{ybi} (Eqn. (3.4)) respectively, can be determined using the same equations presented in Clayton [2010]; however, the θ associated with partial tension field inclination should replace the α associated with full tension field action.

$$\omega_{xbi} = \frac{1}{2} R_y F_y t_{wi} \sin(2\theta) \tag{3.3}$$

$$\omega_{ybi} = R_y F_y t_{wi} \cos^2 \theta \tag{3.4}$$

where, $R_y F_y$ is the expected yield strength of the web plate and t_w is the web plate thickness.

The lateral load resistance of the web plate connected only to the HBEs at any story i can be derived from that of fully connected web plates [Sabelli and Bruneau, 2007] by replacing the angle of inclination, α, with θ, and the clear web plate length, L_{cf}, with the partial tension field length, L_{PTFA}.

$$V_i = \frac{1}{2} F_y t_{wi} L_{PTFA(i)} \sin(2\theta) \tag{3.5}$$

where F_y is the web plate yield strength and all other variables are previously defined. For design, the nominal web plate lateral strength should be taken as

$$V_{ni} = 0.42 F_y t_{wi} L_{PTFA(i)} \sin(2\theta) \tag{3.6}$$

per the recommendations in Sabelli and Bruneau [2007] where the 0.50 ratio becomes 0.42 when divided by an overstrength factor of 1.2.

3.2.3 HBE forces and moments

Derivation of the HBE demand distributions can be done using similar superposition methods as those presented for fully connected web plates in Clayton [2010] (and summarized in Secs. 1.2.1.1 and 2.4.1.1). Unlike the fully connected web plates, the partial tension field web plate forces from the story above and below act over different portions of the HBE which introduces some additional complexity into the demand distributions. Fig. 3.4 shows

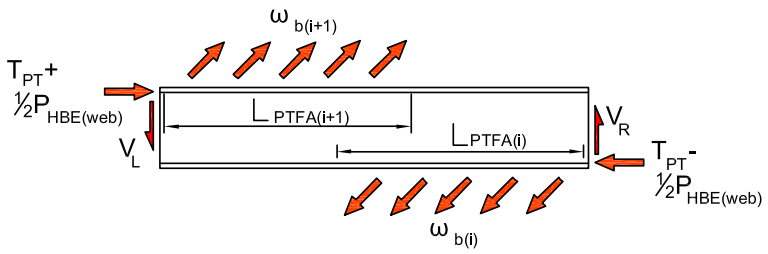

Figure 3.4: Free-body diagram of intermediate HBE for SC-SPSW with web plates connected to HBEs only

a free-body diagram of an intermediate HBE in a SC-SPSW with web plates connected to the HBEs only, shown here under sway in the rightward direction. This HBE free-body diagram can be compared to that of an HBE with fully connected web plates shown previously in Fig. 1.3.

In Fig. 3.4, $\omega_{b(i)}$ is the distributed web plate force acting over a length $L_{PTFA(i)}$ for story i, T_{PT} is the total PT force, $P_{HBE(web)}$ is the axial reaction at the ends of the HBE due to the net horizontal web plate force, and V_L and V_R are the shear forces at the left and right ends of the HBE, respectively. Note that unlike the HBE with fully connected web plates, the axial forces acting at the rocking points at the ends of the beam do not include a $P_{HBE(VBE)}$ component, as the web plates are not connected to the VBEs and therefore do not contribute to column pull-in forces.

To understand the complex demands on the HBE, the demands will be separated into its components: the axial forces acting at the rocking points, the vertical distributed web plate forces, and the horizontal distributed web plate forces.

3.2.3.1 Contribution from PT forces acting at the rocking points

Fig. 3.5 shows a partial free-body diagram of an intermediate HBE with the compressive forces due to the PT elements, T_{PT} (Eqn. (2.3)), acting at the rocking points at the HBE ends. The shear forces that develop at the ends of the HBE to resist the moment caused

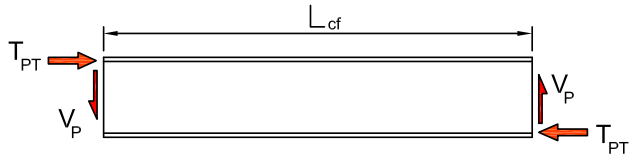

Figure 3.5: Illustration of flange compression component at intermediate HBE for SC-SPSW with web plates connected to HBEs only

by the eccentric flange compression forces is V_P:

$$V_P = \frac{d}{L_{cf}} \left(T_{PT}\right) \tag{3.7}$$

The moment distribution due to the PT forces acting at the rocking points can be taken as

$$M_{PT}\left(x\right) = \left(T_{PT}\right) \left(\frac{d}{2} - \frac{d}{L_{cf}} x\right) \tag{3.8}$$

where, x is the distance along the length of the HBE and L_{cf} is the clear distance between the columns. The moment distribution due to this component is linearly distributed as shown in Fig. 3.6 with positive and negative moments of equal magnitude at each end of the HBE.

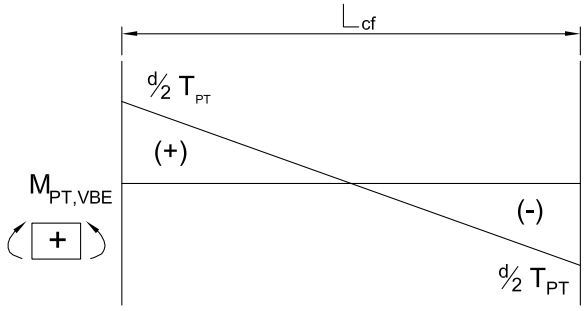

Figure 3.6: Moment contribution from PT forces acting at rocking point

3.2.3.2 Contribution from vertical distributed web plate forces

Fig. 3.7 shows the partial free-body diagram of an intermediate HBE with the vertical component of the distributed web plate forces. Unlike the fully connected web plate configuration where the web plate forces act over the same lengths above and below the HBE, the partial tension field of the HBE-only configuration results in unbalanced distributed forces. Therefore, the vertical distributed forces result in a piecewise moment distribution, even if the web plates above and below the HBE are the same strength.

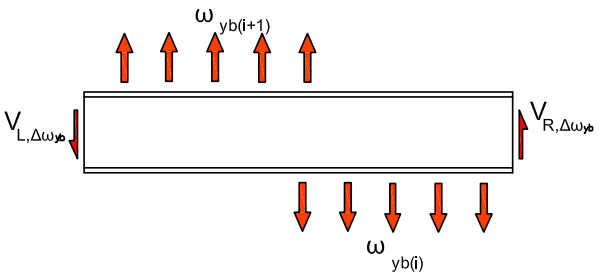

Figure 3.7: Illustration of vertical web plate component at intermediate HBE

From equilibrium of the partial free-body diagram, the shear forces at the left and right ends of the HBE due to the distributed vertical forces, $V_{L,\Delta\omega_{yb}}$ and $V_{R,\Delta\omega_{yb}}$, respectively, can be taken as:

$$V_{L,\Delta\omega_{yb}} = \omega_{yb(i+1)}\left(L_{PTFA(i+1)} - \frac{L^2_{PTFA(i+1)}}{2L_{cf}}\right) - \omega_{yb(i)}\frac{L^2_{PTFA(i)}}{2L_{cf}} \tag{3.9}$$

$$V_{R,\Delta\omega_{yb}} = \omega_{yb(i)}\left(L_{PTFA(i)} - \frac{L^2_{PTFA(i)}}{2L_{cf}}\right) - \omega_{yb(i+1)}\frac{L^2_{PTFA(i+1)}}{2L_{cf}} \tag{3.10}$$

Note that the partial tension field length acting on the HBE from the web plates above and below (stories $i+1$ and i, respectively) may be different based on web plate aspect ratios at each story. For regular story heights and similar HBE depths at each story, L_{PTFA} for adjacent stories will be roughly equal.

For simplification the web plate is assumed to extend over the entire HBE length, L_{cf}. The moment distribution due to the vertical distributed loads can be separated into three

piecewise functions. The three distinct zones along the HBE are:

Zone 1: $0 \leq x \leq L_{cf} - L_{PTFA(i)}$

The portion of the HBE where only the partial tension field *above* the HBE is engaged

Zone 2: $L_{cf} - L_{PTFA(i)} < x \leq L_{PTFA(i+1)}$

The portion in the middle of the HBE where the partial tension fields *above and below* the HBE are engaged

Zone 3: $L_{PTFA(i+1)} < x \leq L_{cf}$

The portion of the HBE where only the partial tension field *below* the HBE is engaged

For the top HBE, sometimes referred to as the anchor HBE, no web plate is present above; therefore, Zone 2 does not exist and Zone 3 extends for $L_{cf} - L_{PTFA(i)} < x \leq L_{cf}$.

The moment distribution in these three zones can be calculated as:

$$M_{\omega_{by}}(x) = \begin{cases} -V_{L,\Delta\omega_{yb}} x + \frac{1}{2}\omega_{yb(i+1)} x^2 & \text{for } 0 \leq x \leq L_{cf} - L_{PTFA(i)} \\ \frac{1}{2}\omega_{yb(i)}\left(L_{cf}^2 - 2L_{PTFA(i)}L_{cf} + L_{PTFA}^2\right) & \\ \quad + \left(-V_{L,\Delta\omega_{yb}} + \omega_{yb(i)}(L_{cf} - L_{PTFA(i)})\right) x & \\ \quad + \frac{1}{2}\left(\omega_{yb(i+1)} - \omega_{yb(i)}\right) x^2 & \text{for } L_{cf} - L_{PTFA(i)} < x \leq L_{PTFA(i+1)} \\ \frac{-1}{2}\omega_{yb(i)}(L_{cf} - L_{PTFA(i)})^2 - \frac{1}{2}\omega_{yb(i+1)} L_{PTFA(i+1)}^2 & \\ \quad + \left(-V_{R,\Delta\omega_{yb}} + \omega_{yb(i)} L_{cf}\right) x & \\ \quad - \frac{1}{2}\omega_{yb(i)} x^2 & \text{for } L_{PTFA(i+1)} < x \leq L_{cf} \end{cases} \tag{3.11}$$

Although complex, some key observations can be made from these equations and are demonstrated in Fig. 3.8. For the assumed lateral loading in the rightwards direction, the upwards web plate forces above the HBE produces a negative, concave up parabolic moment distribution in Zone 1 and the downwards web plate forces below the HBE produce positive, concave down parabolic moment distribution in Zone 3. When the web plate demands are equal above and below the HBE ($\omega_{yb(i)} = \omega_{yb(i+1)}$), this produces a symmetric moment distribution in double-curvature as shown in Fig. 3.8. In this case when the L_{PTFA} above and

below the HBE are equal, the moment distribution is linear in Zone 2 and passes through zero in the middle of the HBE. It should also be noted in this case that the signs of the moments on the left and right ends of the HBE are opposite from the moment signs caused by the PT forces as shown in Fig. 3.6.

As the web plate forces below the HBE increase ($\omega_{yb(i)} > \omega_{yb(i+1)}$), as would be the case for increasing web plate thicknesses in lower stories, the magnitude of the positive moment in Zone 3 increases. When the web plate force above the HBE equals zero ($\omega_{yb(i+1)} = 0$), as is the case at the top HBE, the moment distribution is linear with a positive slope in Zone 1 and concave down in Zone 3. Also note that in each of these cases, the vertical components of the web plate forces contribute no moment at the ends of the HBE.

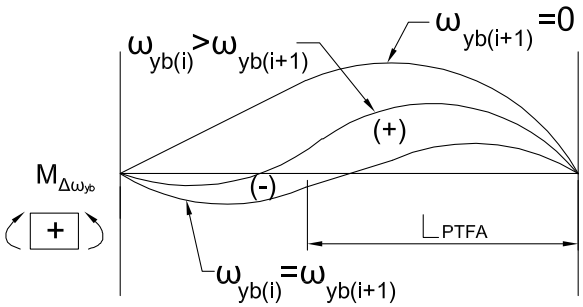

Figure 3.8: Moment contribution from vertical distributed loads from plates

3.2.3.3 Contribution from horizontal distributed web plate forces

Fig. 3.9 shows the partial free-body diagram of an intermediate HBE with the horizontal component of the distributed web plate forces. The axial member end reaction force due to the distributed loads is shown as $P_{HBE(web)}$ and can be calculated as the net horizontal force due to the difference in web plate demands above and below the HBE.

$$P_{HBE(web)} = \omega_{xb(i)} L_{PTFA(i)} - \omega_{xb(i+1)} L_{PTFA(i+1)} \tag{3.12}$$

Fig. 3.9 shows that the axial reaction force due to the distributed horizontal loads, $P_{HBE(web)}$, is distributed one-half to each end of the HBE, creating a compressive force on the left end and a tensile force (or reduction in net compressive force) on the right end for the assumed direction of loading. This distribution of $P_{HBE(web)}$ is a simplifying assumption based on symmetric transfer of inertial forces to both columns. If the SC-SPSW lateral loads are not applied equally to both columns, then the portion of $P_{HBE(web)}$ attributed to each end of the member may change. In this case, the axial force distribution would still remain the same but would shift up or down based on the distribution of the member end forces.

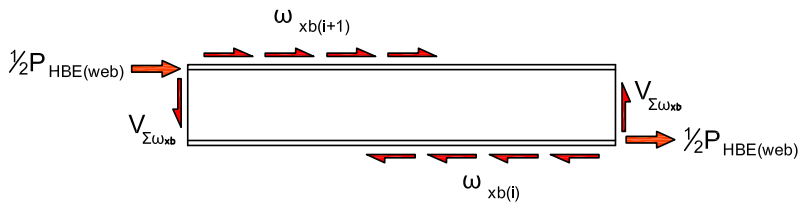

Figure 3.9: Illustration of horizontal web plate component at intermediate HBE

The axial force contribution, $P_{\omega_{bx}}(x)$, is piecewise linear with slopes based on the magnitude of the net horizontal distributed forces in each zone as illustrated in Fig. 3.10.

$$P_{\omega_{bx}}(x) = \begin{cases} -\frac{1}{2}P_{HBE(web)} - \omega_{xb(i+1)}x & \text{for } 0 \le x \le L_{cf} - L_{PTFA(i)} \\ -\frac{1}{2}P_{HBE(web)} - \omega_{xb(i)}\left(L_{cf} - L_{PTFA(i)}\right) + \left(\omega_{xb(i)} - \omega_{xb(i+1)}\right)x & \\ \qquad \text{for } L_{cf} - L_{PTFA(i)} < x \le L_{PTFA(i+1)} & \\ -\frac{1}{2}P_{HBE(web)} - \omega_{xb(i+1)}L_{PTFA(i+1)} - \omega_{xb(i)}\left(L_{cf} - L_{PTFA(i)}\right) + \omega_{xb(i)}x & \\ \qquad \text{for } L_{PTFA(i+1)} < x \le L_{cf} & \end{cases} \tag{3.13}$$

These equations result in a negative slope (i.e. increasing compression) in Zone 1 due to the rightward web plate forces from story $(i+1)$, a zero or slightly positive slope (i.e. decreasing compression) in Zone 2 based on the net difference between web plate horizontal forces, and a positive slope in Zone 3 due to the leftward web plate forces from story i. At the roof

level, the slope in Zone 1 is zero as there is no web plate above.

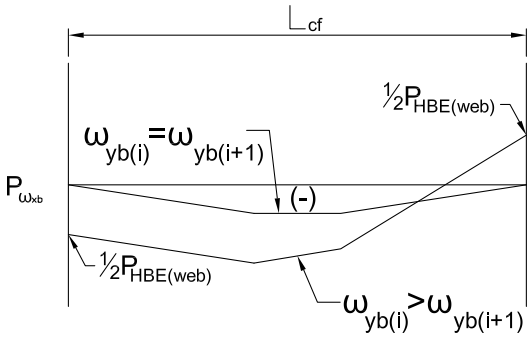

Figure 3.10: Axial contribution from horizontal distributed loads from plates

The horizontal forces acting eccentrically at the HBE flanges produces a moment in the HBE. This moment is resisted by shear forces at the HBE ends, $V_{\sum \omega_{xb}}$, acting in opposite directions as shown in Fig. 3.9. The magnitude of the member end shear force can be calculated as:

$$V_{\sum \omega_{xb}} = \frac{d}{2L_{cf}} \left(\omega_{xb(i)} L_{PTFA(i)} + \omega_{xb(i+1)} L_{PTFA(i+1)} \right) \tag{3.14}$$

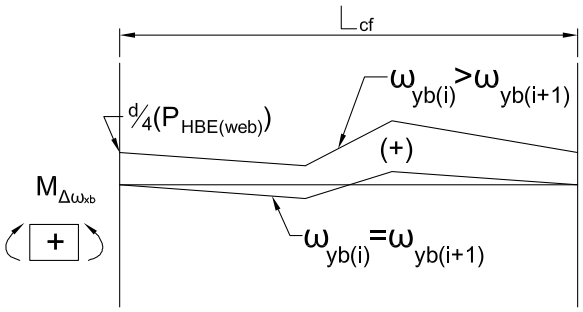

Figure 3.11: Moment contribution from horizontal distributed loads from plates

The moment distribution due to the eccentric horizontal loads is also piecewise linear

based on the net horizontal distributed load in each zone as illustrated in Fig. 3.11.

$$M_{\omega_{bx}}(x) = \begin{cases} \frac{d}{4}P_{HBE(web)} + \left(-V_{\sum\omega_{xb}} + \frac{d}{2}\omega_{xb(i+1)}\right)x & \text{for } 0 \le x \le L_{cf} - L_{PTFA(i)} \\ \frac{d}{4}P_{HBE(web)} - \frac{d}{2}\omega_{xb(i)}\left(L_{cf} - L_{PTFA(i)}\right) + \left(-V_{\sum\omega_{xb}} + \frac{d}{2}(\omega_{xb(i+1)} + \omega_{xb(i)})\right)x & \\ & \text{for } L_{cf} - L_{PTFA(i)} < x \le L_{PTFA(i+1)} \\ \frac{d}{4}P_{HBE(web)} + \frac{d}{2}\left(\omega_{xb(i+1)}L_{PTFA(i+1)} - \omega_{xb(i)}(L_{cf} - L_{PTFA(i)})\right) & \\ \quad + \left(-V_{\sum\omega_{xb}} + \frac{d}{2}\omega_{xb(i)}\right)x & \text{for } L_{PTFA(i+1)} < x \le L_{cf} \end{cases} \tag{3.15}$$

These equations result in positive moments of $\frac{d}{4}P_{HBE(web)}$ on each end of the HBE. The slope is negative in Zone 1 and is proportional to the horizontal web plate distributed force in story $(i+1)$; the slope is positive in Zone 2 and is proportional to the sum of the magnitudes of the horizontal distributed forces in stories i and $(i+1)$; and the slope is negative in Zone 3 and is proportional to the horizontal web plate distributed force in story i.

3.2.3.4 Combined HBE forces

Axial distribution To maintain contact between the HBE and VBE at the connection, the HBE must always be in compression; however, due to the horizontal component of the plate forces, the compression in the HBE varies along its length. For the HBE in Figure 3.4, the axial force distribution (shown schematically in Fig. 3.12) can be calculated as:

$$P(x) = \begin{cases} -T_{PT} - \frac{1}{2}P_{HBE(web)} - \omega_{xb(i+1)}x & \text{for } 0 \le x \le L_{cf} - L_{PTFA(i)} \\ -T_{PT} - \frac{1}{2}P_{HBE(web)} - \omega_{xb(i)}\left(L_{cf} - L_{PTFA(i)}\right) + \left(\omega_{xb(i)} - \omega_{xb(i+1)}\right)x & \\ & \text{for } L_{cf} - L_{PTFA(i)} < x \le L_{PTFA(i+1)} \\ -T_{PT} - \frac{1}{2}P_{HBE(web)} - \omega_{xb(i+1)}L_{PTFA(i+1)} - \omega_{xb(i)}\left(L_{cf} - L_{PTFA(i)}\right) + \omega_{xb(i)}x & \\ & \text{for } L_{PTFA(i+1)} < x \le L_{cf} \end{cases} \tag{3.16}$$

Fig 3.12 demonstrates that the maximum compressive force (for feasible SC-SPSW designs where the web plate strength is increasing or constant in successively lower stories)

can be taken as the axial force between Zones 1 and 2 at $x = L_{cf} - L_{PTFA(i)}$.

$$P_{max}\Big|_{x=L_{cf}-L_{PTFA(i)}} = -T_{PT} - \frac{1}{2}P_{HBE(web)} - \omega_{xb(i+1)}\left(L_{cf} - L_{PTFA(i)}\right) \tag{3.17}$$

where the negative signs denote compressive force. In the case for the top anchor HBE with no plate above, the maximum compressive axial force force is in Zone 1, where the axial demands are constant.

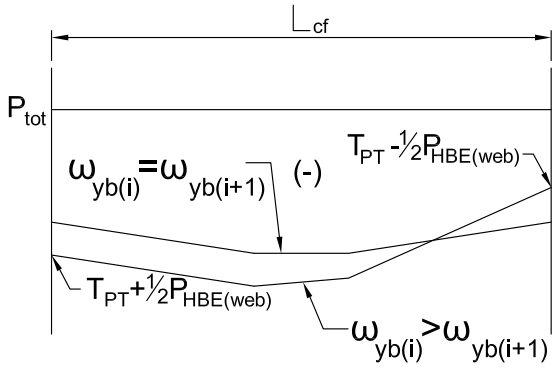

Figure 3.12: Axial force diagram for HBE with web plates connected to HBEs only

Shear end forces The shear forces in the HBE can also be found by superimposing the individual components described previously. The shear forces at the left and right ends of the HBE, V_L and V_R, as shown in Figure 3.4 are

$$V_L = V_P + V_{L,\Delta\omega_{yb}} + V_{\sum\omega_{xb}} \tag{3.18}$$

$$V_R = V_P + V_{R,\Delta\omega_{yb}} + V_{\sum\omega_{xb}} \tag{3.19}$$

where, V_P, $V_{L,\Delta\omega_{yb}}$,$V_{R,\Delta\omega_{yb}}$, and $V_{\sum\omega_{xb}}$ can be found in Eqns. (3.7), (3.9), (3.10), and (3.14), respectively. The shear force distribution along the HBE is linear piecewise based on the net vertical distributed web plate loading in each zone.

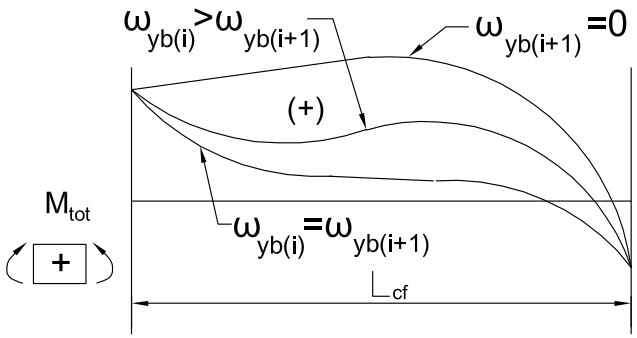

Figure 3.13: Moment diagram for HBE with web plates connected to HBEs only

Moment distribution The separate components of the moment diagram can be superimposed onto one another to form the complete moment diagram for a HBE in a SC-SPSW with web plates connected to the HBEs only, as shown in Fig. 3.13.

The equation for the moment along the length of the HBE can be written as:

$$M(x) = M_{PT}(x) + M_{\omega_{by}}(x) + M_{\omega_{bx}}(x)$$

$$= \begin{cases} T_{PT}\left(\frac{d}{2} - \frac{d}{L_{cf}}x\right) + -V_{L,\Delta\omega_{yb}}x + \frac{1}{2}\omega_{yb(i+1)}x^2 \\ \quad + \frac{d}{4}P_{HBE(web)} + \left(-V_{\sum\omega_{xb}} + \frac{d}{2}\omega_{xb(i+1)}\right)x \\ \qquad\qquad \text{for } 0 \le x \le L_{cf} - L_{PTFA(i)} \\ T_{PT}\left(\frac{d}{2} - \frac{d}{L_{cf}}x\right) + \frac{1}{2}\omega_{yb(i)}\left(L_{cf}^2 - 2L_{PTFA(i)}L_{cf} + L_{PTFA}^2\right) \\ \quad + \left(-V_{L,\Delta\omega_{yb}} + \omega_{yb(i)}(L_{cf} - L_{PTFA(i)})\right)x + \frac{1}{2}\left(\omega_{yb(i+1)} - \omega_{yb(i)}\right)x^2 \\ \quad + \frac{d}{4}P_{HBE(web)} - \frac{d}{2}\omega_{xb(i)}\left(L_{cf} - L_{PTFA(i)}\right) + \left(-V_{\sum\omega_{xb}} + \frac{d}{2}(\omega_{xb(i+1)} + \omega_{xb(i)})\right)x \\ \qquad\qquad \text{for } L_{cf} - L_{PTFA(i)} < x \le L_{PTFA(i+1)} \\ T_{PT}\left(\frac{d}{2} - \frac{d}{L_{cf}}x\right) + \left(\frac{-1}{2}\omega_{yb(i)}(L_{cf} - L_{PTFA(i)})^2 - \frac{1}{2}\omega_{yb(i+1)}L_{PTFA(i+1)}^2\right) \\ \quad + \left(-V_{R,\Delta\omega_{yb}} + \omega_{yb(i)}L_{cf}\right)x - \frac{1}{2}\omega_{yb(i)}x^2 + \frac{d}{4}P_{HBE(web)} \\ \quad + \frac{d}{2}\left(\omega_{xb(i+1)}L_{PTFA(i+1)} - \omega_{xb(i)}(L_{cf} - L_{PTFA(i)})\right) + \left(-V_{\sum\omega_{xb}} + \frac{d}{2}\omega_{xb(i)}\right)x \\ \qquad\qquad \text{for } L_{PTFA(i+1)} < x \le L_{cf} \end{cases} \tag{3.20}$$

Due to the parabolic moment distributions caused by the vertical distributed web plate forces from the partial tension field, it is possible for the maximum moment to occur within the length of the HBE (i.e. not at its ends), as is demonstrated in Fig. 3.13. The maximum moment can occur within the length of the HBE if the change in web plate strength between stories is large enough or, although less likely, if the web plate strengths at adjacent stories are equal but the moment due to web plate vertical forces outweighs the moment due to the PT forces.

For all practical SC-SPSW applications with constant or increasing strength web plates going down the height of the building, the maximum moment is likely to occur at the HBE ends or in Zone 3. The moment at the connections can be calculated as the axial force at

the HBE ends times half the rocking depth:

$$M_{conn} = \frac{d}{2}\left(T_{PT} \pm \frac{1}{2}P_{HBE(web)}\right) \tag{3.21}$$

where the plus/minus represents the different moments in the left and right ends of the HBE due to the net horizontal distributed web plate loading. The connection moment is the same as that of an HBE with fully-connected web plates, but without web plate column pull-in term, $P_{HBE(VBE)}$.

To determine the location of the maximum moment within the length of Zone 3, the derivative of the moment can be taken as:

$$\frac{dM}{dx}(x)\bigg|_{Zone3} = -\frac{d}{L_{cf}}T_{PT} - V_{R,\Delta\omega_{yb}} + \omega_{yb(i)}L_{cf} - \omega_{yb(i)}x - V_{\sum\omega_{xb}} + \frac{d}{2}\omega_{xb(i)} \tag{3.22}$$

When setting $\frac{dM}{dx} = 0$, the location of the potential local maximum moment within Zone 3 is found to be:

$$x_{max} = \frac{1}{\omega_{yb(i)}}\left(-\frac{d}{L_{cf}}T_{PT} - V_{R,\Delta\omega_{yb}} + \omega_{yb(i)}L_{cf} - V_{\sum\omega_{xb}} + \frac{d}{2}\omega_{xb(i)}\right) \tag{3.23}$$

for $L_{PTFA(i+1)} \leq x_{max} \leq L_{cf}$[2]. The maximum moment to be used for HBE design should be taken as the maximum of the moments at the connections and the possible local maximum at x_{max} in Zone 3.

3.2.4 VBE demands

Berman and Bruneau [2008] presented methods for determining VBE moment, shear, and axial force distributions for VBEs with fully connected web plates. The free-body diagrams used for this derivation are shown in Fig. 3.14. For direct comparison, Fig. 3.15, shows the same free-body diagrams for VBEs without web plates connected to them. The only difference between the two diagrams is the removal of the distributed web plate forces on the columns. This free-body diagram can be used to determine VBE design forces according to

[2] $L_{cf} - L_{PTFA(i)} \leq x_{max} \leq L_{cf}$ for the top anchor HBE with no web plate above.

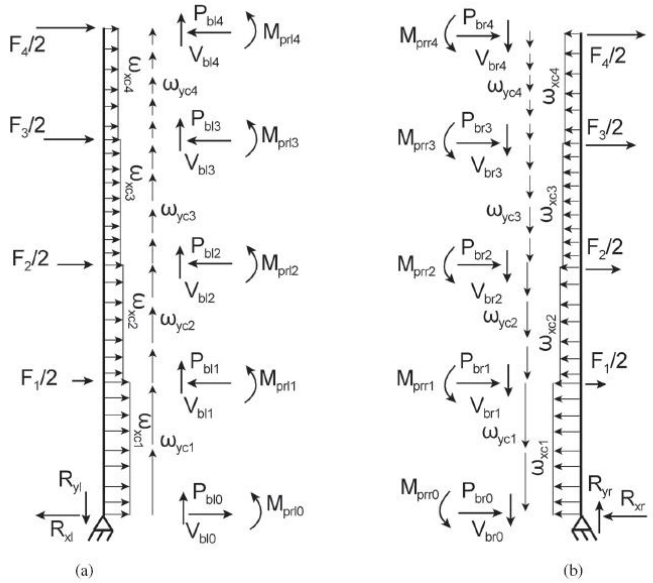

Figure 3.14: VBE free-body diagrams for SPSWs with fully connected web plates [Berman and Bruneau, 2008]

the same procedure presented in Berman and Bruneau [2008], where the x- and y-component of the column distributed, ω_{xc} and ω_{yc} respectively, can be set equal to zero.

It should be noted that in order to resist the same lateral load, the strength or thickness for HBE-only connected web plates must be larger than that of conventional fully-connected web plates. This increase in web plate resistance and unbalanced partial tension field on each end of the HBE may result in larger beam shear end reactions (V_{bl} and V_{br} in Figs. 3.14 and 3.15) as calculated per Eqns. (3.18) and (3.19). However, the moment at the connections (M_{pr} in Fig. 3.14 and M_{conn} in Fig. 3.15 and calculated in Eqn. (3.21)) and the beam axial end reaction (P_{bl} and P_{br} in Figs. 3.14 and 3.15 and calculated per Eqn. (3.16)) will be relatively unchanged with the exception of the removal of the $P_{HBE(VBE)}$ compressive force and the moment associated with it. The other connection moment and axial force terms depend primarily on the PT force, which is largely controlled by initial PT force and connection rotational stiffness, and the net horizontal web plate force due to change in plate strength at adjacent stories, which will be roughly equal for the HBE-only and fully connected web plate configurations as the net horizontal web plate force is intended to be

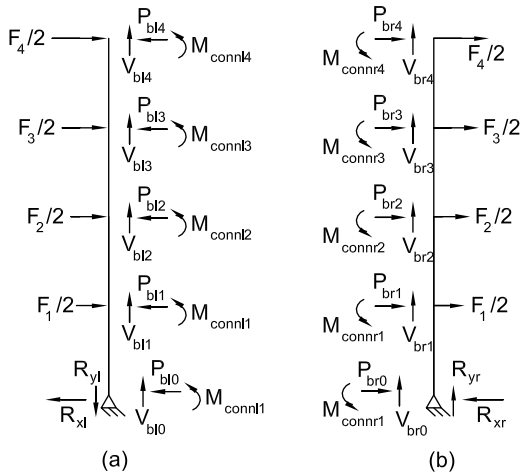

Figure 3.15: (a) Left and (b) right VBE free-body diagrams for web plates not connected to VBEs

equal to the applied lateral force at that story (F_i in Figs. 3.14 and 3.15). Therefore, even though the HBE-only web plate connectivity does remove the distributed axial and lateral demands on the VBEs, it is not readily apparent if the HBE-only configuration will result in reduced column demands. This effect will be investigated later in Chapter 8 when the SC-SPSW design methodology is applied to SC-SPSWs with web plates connected to the HBEs only.

3.3 PT Column Base Connection

3.3.1 Motivation and general behavior

Two of the key objectives of the SC-SPSW system are (1) to eliminate or significantly reduce damage to the boundary frame while concentrating the damage to easily replaceable energy dissipating elements (e.g. web plates), and (2) to provide a seismic force-resisting system that can recenter following an earthquake. The previous introductory SC-SPSW research [Clayton, 2010] focused on providing recentering and eliminating frame damage through the incorporation of PT beam-to-column connections. In this previous research, the design procedure and numerical study assumed columns with pinned bases. Due to

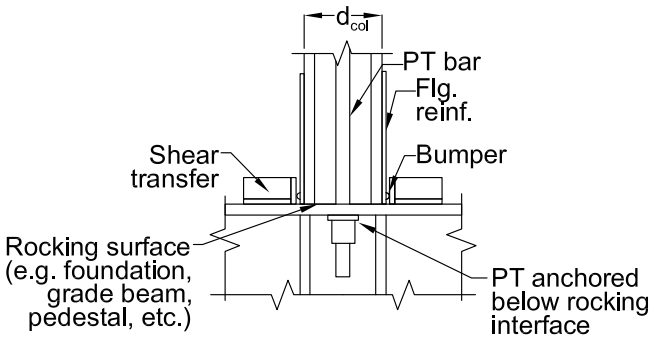

Figure 3.16: Schematic of PT column base connection

the large column demands, designing and detailing actual pinned column bases for mid-rise buildings can be impractical.

In this research program, experimental testing (introduced in Chapter 5) was done to investigate the use of PT column base connections. The PT column base connection, shown schematically in Fig. 3.16, behaves very similarly to the PT beam-to-column connection presented in Fig. 1.1(b). The column is allowed to rock about its flanges during lateral sway causing a gap, $\theta_{r,col}$, to form at the rocking interface at the base of the column. As with the beam-to-column PT connections, allowing the gap to form in the connection eliminates the plastic deformation that typically occurs at the base of SPSW columns [Li et al., 2012] and causes the vertical PT bars to elongate, which provides additional restoring forces for recentering.

The shear forces are transferred out of the columns through some sort of shear transfer mechanism that allows the connection to rock (shown as shear brackets in Fig. 3.16, but could be a concrete "moat" [Chou and Chen, 2011a] or keeper plates [Chi et al., 2008]). The compressive forces in the column flanges are transferred through bearing. The column base bears directly on the foundation, on a grade beam, or on some sort of intermediary pedestal to transfer forces to the foundation. The vertical PT elements, placed symmetrically about the center of the column, must be anchored somewhere along the height of the column and below the rocking interface at the column base. Details for the implementation of the PT column base in experimental testing is presented in Sec. 5.3.1, and further discussion of

possible PT column base configurations and detailing considerations are discussed later in Sec. 9.2.

3.3.2 Column PT forces

Unlike the PT beam-to-columns connection which rock at both ends of the beam, the rocking column only has one rocking interface at the base of the column; therefore, the column PT elongation is half of that of the horizontal PT elongation associated with a beam having an equal depth as the column. The column PT elongation due to this gap opening is

$$\Delta_{PT,col} = \frac{d_{col}}{2}\theta_{r,col} \tag{3.24}$$

where $\theta_{r,col}$ is the rotation at the base of the column and can be approximated to be the same as the column drift, θ_s in Fig. 1.2, for low-rise buildings, and d_{col} is the depth of the column. This equation assumes the PT bars are located at the centerline of the column. In the case where the PT bars are not placed along the centerline, this equation represents the average PT elongation (assuming the centroid of the PT element group is along the column centerline) and can be used for determining the total PT force. For checking the elongation of an individual PT bar not located at the column centerline, the $\frac{d_{col}}{2}$ term in Eqn. (3.24) can be replaced with the distance from the rocking point to that particular bar.

The total force in the vertical column PT elements for any given connection rotation can be expressed as

$$T_{PT,col} = T_{o,col} + k_{PT,col}\left(\Delta_{PT,col} - \delta_{col}\right) \tag{3.25}$$

where $T_{o,col}$ is the initial PT force for a particular column, $k_{PT,col}$ is the axial stiffness of all the PT elements in that column, and δ_{col} is the axial shortening of the column along the length of the PT element (i.e. between the column PT anchorage points).

The axial shortening in the column is due to two main mechanisms: (i) the increase in compression due to the increase in the PT force upon gap opening, and (ii) the deformation of the column due to the web plate, or overturning, forces. The PT elongation will always cause an increase in compression in the column (assuming at least one column flange is

still in contact with the supporting surface), while the web plates may either reduce or increase the compression in the column depending on the direction of loading. The critical case for column PT design (i.e. when the column PT forces are expected to be largest) is when the column is acting as the uplift column (i.e. the web plate forces are pulling the column upward). For the compression column, the downwards web plate forces provide some restraint to column base connection gap opening; therefore, the gap rotations at the base of the compression column will naturally be less than at the base of the uplift column.

When the web plate is pulling up on the uplift column, the web plate forces do not cause an increase in column compressive forces. Here, the increase in upwards web plate forces do not contribute to additional column shortening; however, they do not necessarily cause column elongation because tensile forces cannot develop at the column base as it is not physically attached to the foundation. Therefore, the column shortening can be approximated based only on the increase in compression due to PT elongation caused by gap opening as described in the equation:

$$\delta_{col} = \frac{k_{PT,col}\Delta_{PT,col}}{k_{PT,col}+k_{col}}\frac{d_{col}}{2}\theta_{r,col} \tag{3.26}$$

where k_{col} is the axial stiffness (EA/L) for the length of the column below the PT anchorage (i.e. L=the distance from the column base to the PT anchorage in the column), and all other terms are as previously defined.

By combining Eqns. (3.25) and (3.26), the column PT force can can be approximated for a given gap rotation as

$$T_{PT,col} = T_{o,col} + \frac{k_{PT,col}k_{col}}{k_{PT,col}+k_{col}}\frac{d_{col}}{2}\theta_{r,col} \tag{3.27}$$

It should be noted that the axial stiffness of the column k_{col} is much greater than the axial stiffness of the column PT, $k_{PT,col}$, for most SC-SPSW applications. This equation provides a reasonable approximation of peak column PT forces for the uplift column and conservatively overestimates the PT forces in the compression column where the downwards web plate forces result in smaller gap openings and more column shortening.

3.3.3 PT column base connection moment

The moment at the base of the decompressed column can be taken as the axial force in the column times the distance from the centroid of the column to the rocking point, typically taken as one-half the column depth, $d_{col}/2$. The axial force in the column has contributions from the column PT as well as the vertical component of the web plate forces. Methods for determining the column axial demands due to the yielded web plate forces were discussed in Clayton [2010] and also presented in Berman and Bruneau [2008]. Here, we will call the axial force at the base of the column due to web plate and HBE-to-VBE connection demands $P_{col,web}$, where a positive value represents a net upward force acting on the column, and a negative value represents a downward force acting on the column (creating additional compression at the column base). The axial force due to the web plates and HBE-to-VBE connections, $P_{col,web}$, can be determined from the methods presented in Berman and Bruneau [2008] and shown as R_{yl} and R_{yr} in the VBE free-body diagrams presented in Figs. 3.14 and 3.15.

The moment at the column base after web plate yielding, after column base connection decompression, and assuming that one flange of the column is still in contact with the foundation (i.e. there is still a net compressive fore in the column) can be estimated as

$$M_{conn,col} = \frac{d_{col}}{2}\left(T_{PT,col} - P_{col,web}\right) \tag{3.28}$$

Assuming that the web plate forces remain relatively constant after yield and that the column shortening is negligible, Eqns. (3.24), (3.25), and (3.28) can be combined to estimate the post-decompression and pre-uplift rotational stiffness, $k^{\theta}_{d,col}$, of the connection as

$$k^{\theta}_{d,col} = \frac{d^2_{col}}{4} k_{PT,col} \tag{3.29}$$

Note that this equation is essentially the same as k^{θ}_{d} for a beam-to-column PT connection as shown in Eqn. (2.7), except the 1/2 coefficient in Eqn. (2.7) is replaced with a 1/4 coefficient in this equation. The coefficient is reduced by half for the column PT connection due to the reduction in the number of rocking interfaces as described previously with regards

to the column PT elongation in Eqn. (3.24).

3.4 Summary

This chapter presented supplemental information on SC-SPSW mechanics that varied from those presented in Clayton [2010] and summarized in Sec. 2.4.1.1. The previous SC-SPSW mechanics presented in Clayton [2010] focused on SC-SPSWs with pinned column bases and with web plates that were connected fully to the HBEs and VBEs. Two variations in SC-SPSW designs were introduced in the experimental research presented in this dissertation. These variations included (1) connecting the web plates only to the HBEs to potentially reduce column demands and mitigate web plate damage, and (2) employing post-tensioned rocking column base connections to prevent axial-flexural hinging at the column base and to improve constructibility compared to the alternative of detailing pinned base connections for large column sections.

The mechanics that were presented for the HBE-only web plate connectivity include expressions for the partial tension field length and angle of inclination and methods for determining moment, shear, and axial force demands on HBEs and VBEs to be used in design. The mechanics presented for the PT column base connection include expressions for determining PT elongation and axial force, as well as connection moments and rotational stiffnesses.

Chapter 4

SUBASSEMBLY TESTING

4.1 Introduction

Subassembly tests of the SC-SPSW system were conducted at the University of Washington (UW) Structural Engineering Laboratory (SEL). The test setup was designed to simulate the loading and boundary conditions of an intermediate beam, mid-height in a SC-SPSW. The SC-SPSW test setup at UW was designed and constructed as part of a previous phase of SC-SPSW research [Winkley, 2011]. An overview of important details related to this phase of SC-SPSW subassembly testing will be described here; however, further detail on the subassembly test apparatus (e.g. reaction blocks, equipment, specimen design) can be found in Winkley [2011]. This phase of subassembly testing investigated additional design and test parameters including beam depth, web plate-to-fish plate connection details, web plate-to-boundary frame connectivity, and load history, while also providing more extensive data to be used in numerical model validation and quantification of complex component behaviors and demands. Specimens were selected to understand the implications variations in design parameters (e.g. stronger web plates paired with weaker PT connections and vice versa); to investigate how the performance of welded web plate connections, used more commonly in the field, compared to bolted web plate connections developed to facilitate web plate replacement between tests; or to investigate the potentials for web plates connected to the beams only for reducing column demands and mitigating web plate damage.

4.2 Test Set-up

4.2.1 Specimen design

In this phase of testing, a large number of specimens were tested. This section highlights features that were common to all of the specimens. Further details of the subassembly test set-up and shop drawings of specimen components can be found in Winkley [2011]. This

document [Winkley, 2011] and additional documentation of the test set-up, instrumentation, observations, and data can be found on the NEEShub Project Warehouse (https://nees.org/warehouse/project/631).

A photo and schematic of the test setup are shown in Figs. 4.1(a) and 4.1(b), respectively. The two-story configuration of the setup was designed to simulate the boundary conditions for an intermediate HBE (middle HBE in Fig. 4.1), where the web plates above and below the HBE apply axial and flexural demands on the boundary elements. The SC-SPSW subassembly measured 3235 mm wide (centerline VBE dimension), with story heights (HBE centerline dimensions) of 1724 mm. The actuator loaded the specimen at a height of 4178 mm above the center of the pinned base. The test setup was designed to accommodate the largest variation in design parameters while still satisfying laboratory constraints. Since these subassembly tests are intended to better understand SC-SPSW behavior and mechanics, the specimens were not based on scaled prototype buildings, although several normalized values of key parameters are the same as the prototypes described in Clayton et al. [2012b].

The South VBE was pinned at its base to allow for column rotation. However, due to the HBEs rocking about their flanges, as a gap forms in the connections, the VBEs spread apart [Garlock et al., 2007]. This frame expansion was accommodated in the physical model with a roller under the North VBE, allowing the frame to expand in the north-south direction without imposing additional compressive forces on the middle HBE due to VBE restraint at its base. While this pin-and-roller column base detail most importantly alleviates the column restraint to frame expansion, it also introduces some asymmetry in the system and load path, which does have a minor influence on demands on the north and south sides of the specimen as discussed in Clayton et al. [2012c]. For similar purposes, the top and bottom anchor HBEs also have PT HBE-to-VBE connections, such that the gap opening, and thus the frame expansion, at these levels are similar to the middle HBE. While fixities at the VBE base and certain diaphragm connection detailing may restrain frame expansion in actual buildings, these initial tests were focused on investigating characteristics of SC-SPSW behavior only; therefore, the specimens were designed to be free of these additional constraints.

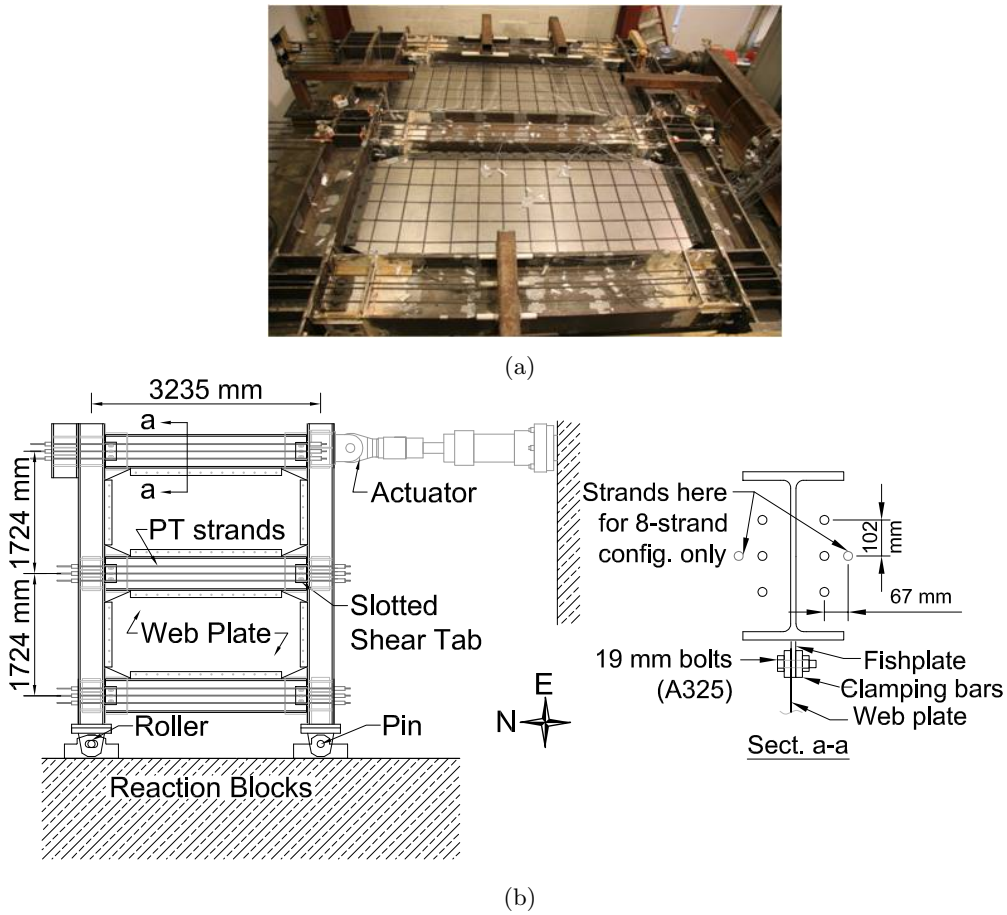

Figure 4.1: (a) Photo and (b) schematic drawing of SC-SPSW subassembly test setup. Further details and dimensions can be found in Winkley (2011).

The PT strands were 13 mm diameter Grade 270 seven-wire strand with reusable 3-wedge barrel anchors at each end. The PT strands were all placed symmetrically about the centerline of the HBE within the depth of its flanges as shown in Fig. 4.1(b) and were also designed to remain elastic during testing in order to be reused in multiple tests. The PT strands were typically anchored at the outside flanges of the VBEs, with the exception of the top HBE, where the actuator connection to the South VBE prevented this. At this location, the PT strands were anchored to the inside flange of the South VBE and an additional VBE stub was used to extend their length on the North VBE so that the PT strands at the top HBE would have the same length, stiffness, and yield deformation as the PT strands at the

other HBEs.

Shear forces at the PT HBE-to-VBE connections were transferred through slotted shear tab connections with snug-tight bolts as shown in Fig. 4.2. Long slotted bolt holes in the shear tabs allowed for connection rotation. The HBE flanges at the connections were also reinforced to protect against local damage due to the large compressive forces acting on the flanges after decompression. Similarly, horizontal stiffeners were provided in the VBEs due to the large compressive forces transferred through the HBE flanges. Flange stiffeners were also included in the HBEs at the ends of the flange reinforcing plates to prevent any local buckling in the unreinforced flange at this location. Slotted holes were provided in the flange stiffeners to allow the PT to pass through. Shim plates (12.7 mm thick) were tack welded to the VBEs to ensure that the HBEs bear only at their flanges to prevent HBE web yielding due to bearing stresses [Rojas et al., 2005]. Due to an uneven bearing surface on the south end of the middle HBE, caused by fabrication tolerances, an additional 1.6 mm thick shim plate was provided at the top flange on the south end of this HBE to ensure equal bearing on both flanges during PT tensioning.

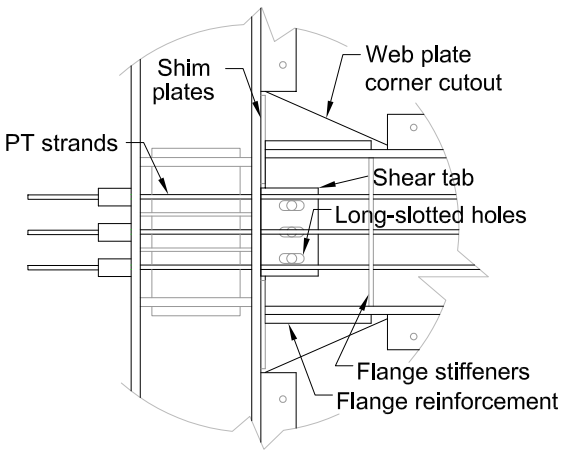

Figure 4.2: PT connection detail. Further details and dimensions can be found in Winkley (2011).

The web plates were ASTM A1008 steel. In all but one specimen, to be described in further detail later, the web plates were connected to the boundary elements via a slip-

critical bolted fish plate connection as shown in Fig. 4.1(b). Clamping bars, as shown in Fig. 4.3, were provided on either side of the web plate and fish plate to clamp the web plate into place. The bolted web plate-to-fish plate connection is used in the test to allow for the yielded web plates to be easily removed and replaced following each test so that multiple tests could be done using the same boundary frame members; this detail is not necessarily suggested for actual building design. Diagonal cutouts, as shown in Fig. 4.2, were provided in the corners of the web plates to prevent localized damage in the plate as a gap forms at the connection. Diagonal cutouts were employed here due to the shape of the cutout area, making radial cutouts more difficult to fabricate. The use of radial corner cutouts to further protect the web plate-to-fish plate connection near the PT connection region is discussed in Sec. 5.3. For all but one specimen, which will be described in further detail later, the web plates above and below the middle HBE had the same thickness.

The boundary frame members were A992 steel and were designed to remain elastic so that they could be reused for multiple tests. The HBEs in these tests were W18x106 or W14x90 shapes, depending on the specimen, and the VBEs were W14x132 shapes. Although the boundary elements were expected to remain elastic during testing, the W18x106 beams were whitewashed in the connection region to indicate the occurrence of potential yielding or localized damage. Lateral bracing was provided at top and bottom HBEs and the North and South VBE to prevent out-of-plane displacement of the boundary elements. The lateral bracing-to-specimen interface consisted of one surface of lubricated stainless steel and one surface of Polytetrafluoroethylene (PTFE) to reduce frictional forces. No gravity loading was applied to the specimens as they were intended to investigate fundamental component behavior.

4.2.2 Specimen descriptions

Table 4.1 shows a summary of all of the SC-SPSW subassembly tests conducted at UW, including those conducted by Winkley [2011], as indicated by an asterisk. The naming convention for the test specimens is the beam size (e.g. "W18"), followed by the number of PT strands per HBE (e.g. "8s"), followed by the initial total PT force at each HBE in units

of kips (e.g. "100k"), followed by the web plate gage thickness (e.g. "16Ga"), if applicable. The test program included variations in the following parameters: web plate thicknesses, t_w; initial PT force at each HBE, T_o; number of PT strands in each connection, N_s; HBE rocking depth that includes the thickness of the flange reinforcing plates, d; displacement history (BF, LP1, and LP2 in Table 4.1), different web plate thicknesses above and below the middle HBE; and web plate-to-boundary frame connection details and configurations. The range of parameters was selected based on limitations in the laboratory set-up and based on normalized values of design parameters (e.g. T_o/Ty) corresponding to those in the three- and nine-story SC-SPSWs presented in Clayton [2010]. Tests were also done without any web plates to ensure that the bare PT frame exhibited the desired nonlinear, elastic response. Below, specimens with considerably different characteristics (e.g. welded web plates, web plates connected to the HBEs only) are discussed.

4.2.2.1 Welded web plate connection

In specimen W18-8s100k20GaW, the web plate was welded to the boundary elements via a welded web plate-to-fish plate connection detail as shown in Fig. 4.3(a). The purpose of this specimen was to compare the characteristics, prorogation, and extent of damage in the web plates with respect to the web plate connection detail. The bolted web plate connection detail used in the other specimens (Fig. 4.3(b)) was developed to transfer the forces of the the yielded web plates to the boundary frame via friction between the clamping bars, fish plate, and web plate [Winkley, 2011]. A bolted connection was used primarily in this extensive test program to allow for rapid removal and installation of web plates between tests while still using the same boundary frame members. Although the tests showed that the bolted connection was able to adequately transfer web plate forces, a specimen with welded web plate connection details was also investigated, as welded web plate connection details are more typically used in practice.

Because the web plates used in the subassembly tests are much thinner than those commonly used in actual buildings, special care was taken to ensure adequate weld quality and strength. To prevent burning through the thin web plate material, the weld material

Table 4.1: SC-SPSW subassembly specimen descriptions

Specimen Name^{+}	t_w (mm)	N_s	T_o (kN)	d (mm)	Loading	Web plate conn.
W18-8s100k*	—	8	445	526	BF	—
W18-8s100k20Ga*	0.92	8	445	526	LP1	Bolted
W18-6s75k20Ga*	0.92	6	334	526	LP1	Bolted
W18-6s75k16Ga*	1.52	6	334	526	LP1	Bolted
W18-8s100k16Ga*	1.52	8	445	526	LP1	Bolted
W18-6s75k	—	6	334	526	BF	—
W18-8s100k20Ga-2	0.92	8	445	526	LP2	
W18-8s100k16Ga20Ga	1.52(1st) 0.92(2nd)	8	445	526	LP2	Bolted
W18-8s100k20GaW	0.92	8	445	526	LP2	Welded
W14-6s75k	—	6	334	381	BF	—
W14-6s75k16Ga	1.52	6	334	381	LP2	Bolted
W14-6s75k16GaHBE	1.52	6	334	381	LP2	Bolted (HBEs only)
W14-8s100k20Ga	0.92	8	445	381	LP2	Bolted
W14-6s75k20Ga	0.92	6	334	381	LP2	Bolted

$^{+}$ General naming convention: beam size (e.g. "W18"), number of PT strands (e.g. "6s"), initial PT force in kips (e.g. "75k"), web plate gage thickness (e.g. "20Ga"), and additional qualifiers if necessary

* Tests conducted by Winkley [2011]

was deposited on the fish plate along the edge of the web plate such that the weld bead rolled over the edge of the web plate. In full-scale building construction the web plates are thicker, and conventional fillet welding techniques can be used. A 0.030" (0.08 mm) diameter, 70 ksi solid wire (ER70S-6) electrode was used with a 75%/25% Argon/CO_2 shielding gas in the MIG welding process. This specimen was the last one to use the W18x106 HBEs, so that the weld material on the HBE fishplates did not have to be ground off. Because the VBEs were reused for the remaining specimens, the web plate and weld material was ground off of the VBE fish plates for the following specimens.

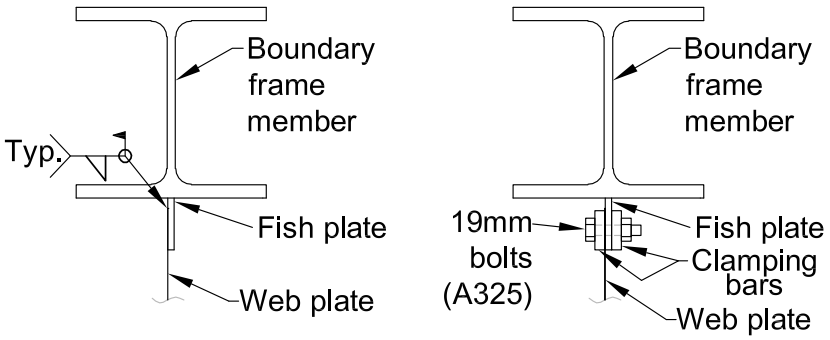

(a) (b)

Figure 4.3: (a) Welded and (b) bolted web plate-to-fish plate connection details

4.2.2.2 HBE-only web plate configuration

Specimen W14-8s100k16GaHBE had web plates that were connected to the HBEs only as shown in Fig. 4.4. The purpose of this test was to investigate how this web plate configuration affects the demands on the middle HBE and how it impacts the initiation and progression of damage in the web plate. By having the web plates connected to the HBEs only, the additional compression in the HBE due to web plate pull-in of the VBEs, $P_{HBE,VBE}$, is eliminated, which will affect the cyclic HBE axial force and moment response. Also, by disconnecting the web plate from the VBEs, the local strains near the corner cutouts due to the PT connection gap opening are reduced. Disconnecting the web plate from the VBEs also releases the out-of-plane displacement restraint along those two edges of the web plate, which could reduce some of the curvature demands associated with the out-of-plane restraint on both ends of the corner cutout. Both of these results were hypothesized to reduce damage in the web plate.

4.2.2.3 Specimen construction process

Boundary elements and PT strands were reused for multiple tests. PT strands were replaced after four to five tests when significant notching or fracture was observed near the anchor points. The construction sequence for each specimen began with the PT strands detensioned

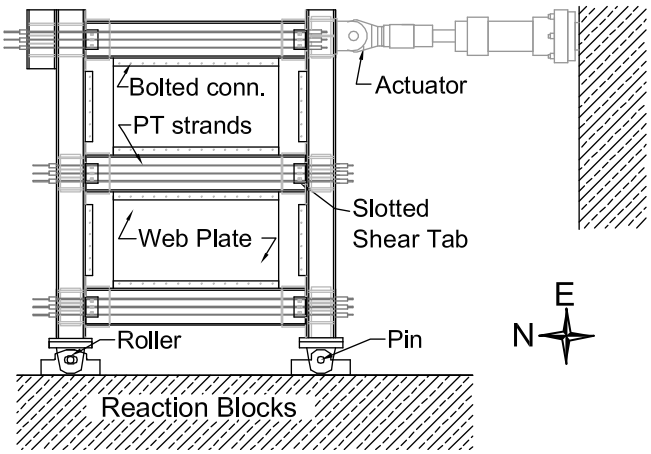

Figure 4.4: Schematic of W14-8s100k16GaHBE with web plates connected to only the HBEs.

and the HBE ends resting flush against the shim plates on the VBEs. The PT strands were then stressed to the appropriate values with the strands being stressed symmetrically to avoid eccentricity. Then the web plates and clamping bars were put into place, and all of the bolts in the web plate-to-fish plate connection were tensioned using the "turn of the nut" method, with the exception of the specimens without web plates and specimen W18-8s100k20GaW, in which case the web plates were welded to the fish plates at this time. In specimens where only six strands were used, the two strands farthest away from the HBE web, as shown in Fig. 4.1, were removed.

4.2.3 Instrumentation

Instrumentation was installed to measure global response of the specimen as well as the local connection, HBE, and web plate responses. The applied load was determined directly from the actuator load cell. String potentiometers were placed at the centerline height of every HBE on the North and South VBEs and at the center of the roller pin at the base of the North VBE to determine column and roller displacements, respectively. Linear potentiometers were also placed at the interface between the pin and roller clevises and the reaction blocks and at the interface between the VBE base plates and the pin and roller

clevises to measure slip at those locations. Similarly, linear potentiometers were placed at the base of the actuator and reaction blocks to measure any slip relative to the strong floor (Fig. 4.5). Load cells were used to measure the force in each individual PT strand. The PT load cell naming convention is shown in Fig. 4.5.

Linear potentiometers were placed on the inside face of each HBE flange at the VBEs to measure the amount of gap opening at each connection. For two specimens, W14-8s100k20Ga and W14-6s75k20Ga, linear potentiometers were also placed at the ends of the middle HBE to measure vertical displacements of the beam perpendicular to the direction of the slotted shear tab holes (pgv2n and pgv2s in Fig. 4.5). Due to the gap opening, the vertical potentiometers had to be located far enough away form the HBE end such that it would remain in contact with the HBE flange at the largest gap opening; therefore, a standoff was provided to locate the tip of the potentiometer 54 mm and 57 mm from the exterior face of the North and South VBE, respectively. A strip of PTFE was also attached to the top HBE flange to allow the tip of the potentiometer to slide along the surface as the gap opened.

Numerous strain gages were placed along the HBEs and VBEs to determine the axial forces and moments in the frame elements at different sections along the length of each member. The strain gages were placed parallel to the longitudinal axis of the member, and at least three strain gages were placed colinearly at each section along the frame member. These strain gages were typically placed on the webs, in the case of HBE sections, or on the web and inside faces of opposite flanges, in the case of VBE sections. These sections were placed far enough away from the connection areas to avoid local strain effects. Strain gages were also placed on the inside and outside faces of the HBE flanges near the VBEs to measure local strains in the flanges of the rocking connections.

The response of the web plate was evaluated qualitatively; grids drawn directly onto the web plate were used to facilitate the evaluation. Similarly, lines were drawn on the web plate along the edge of the clamping bars before testing to observe slip of the web plate in the bolted web plate-to fish plate connection during testing. In some specimens strain in the web plates were quantitatively measured in the middle of the panel and along the middle HBE either with uniaxial strain gages oriented in the approximate direction of the

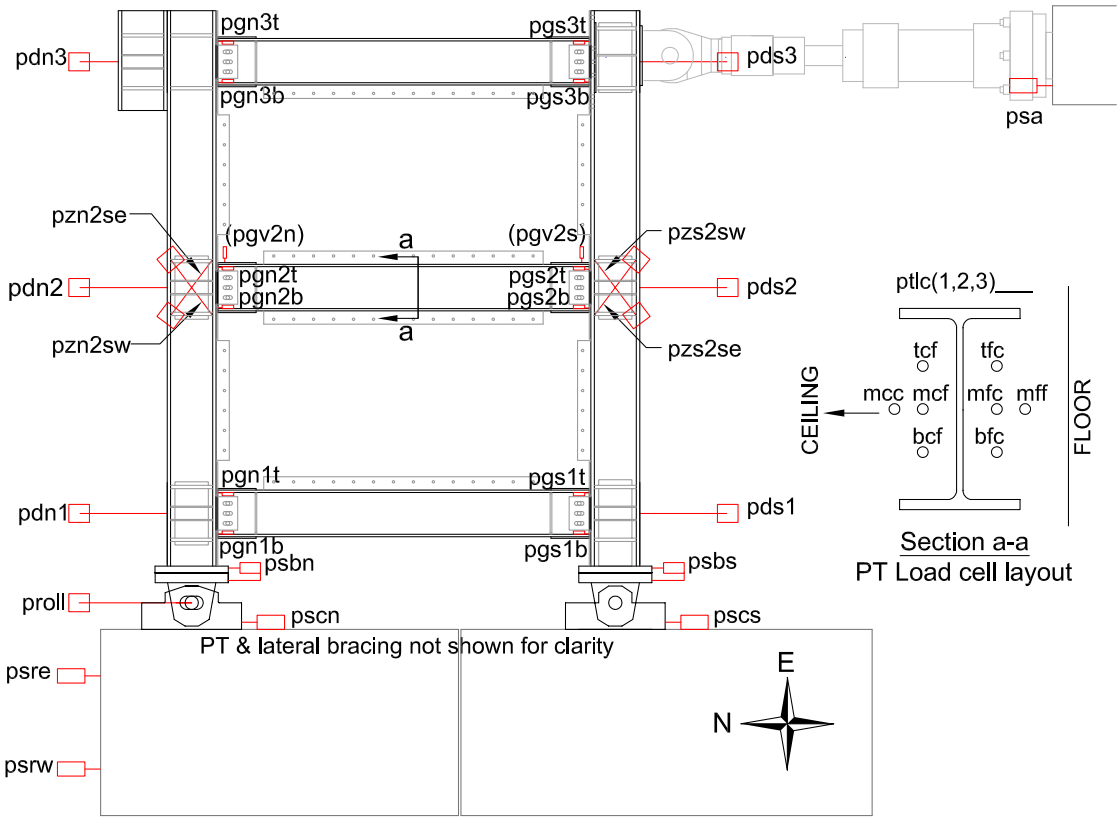

Figure 4.5: Layout and naming of linear potentiometers, string potentiometers, and PT load cells.

tension field (45° from horizontal) or with strain gage rosettes. In some specimens strain gages were also placed at the corner cutouts in the web plate to measure local strains in the plate due to connection gap opening. The various strain gage layouts for each specimen are shown in Figs. 4.6 through 4.10. In some locations strain gages were place on both sides, top and bottom, of the web plate at the same location in order to determine the average mid-thickness web plate strains. In the following figures, these locations are indicated by strain gage names ending in "c" to indicate the gage on the ceiling (i.e. top) side of the web plate and "f" to indicate the gage on the floor (i.e. bottom) side of the web plate.

All strain gages were manufactured by Tokyo Sokko Kenkyuojo Co., Ltd. The uniaxial strain gages used in the VBEs, W18x106 HBEs, and web plates were two-wire, high elongation, 5mm gage length (YFLA-5-5L) gages. The strain gages used in the W14x90 HBEs were two-wire, general use, 3mm gage length (FLA-3-11) gages. The strain gage rosettes used in the web plates were two-wire, high elongation, 5mm gage length YEFRA-5 45°/90° three-element rosettes. The linear and string potentiometers were classified as BEI 9600 Duncan Linear Conductive Potentiometers and Unimeasure Model 510 String Potentiometers, respectively. The LabVIEW version 7.1 software was used for data acquisition.

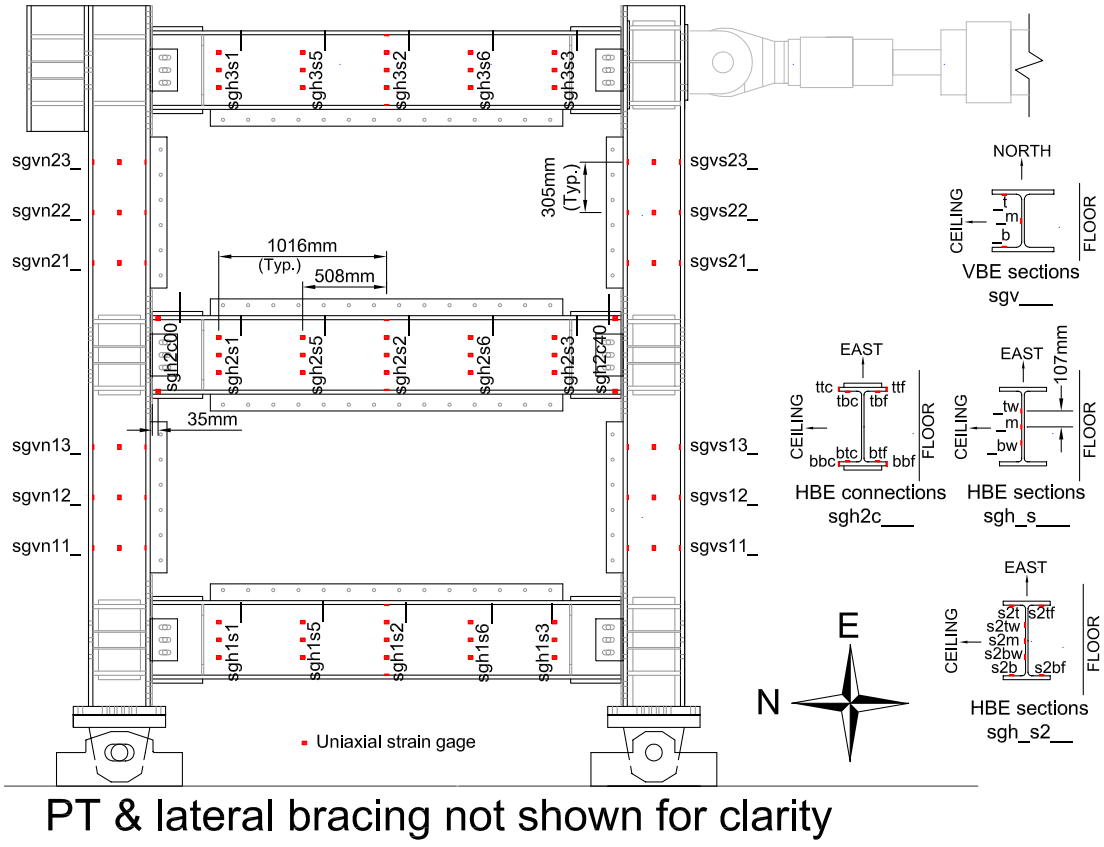

Figure 4.6: Strain gage layout for W18-8s100k and W18-6s75k.

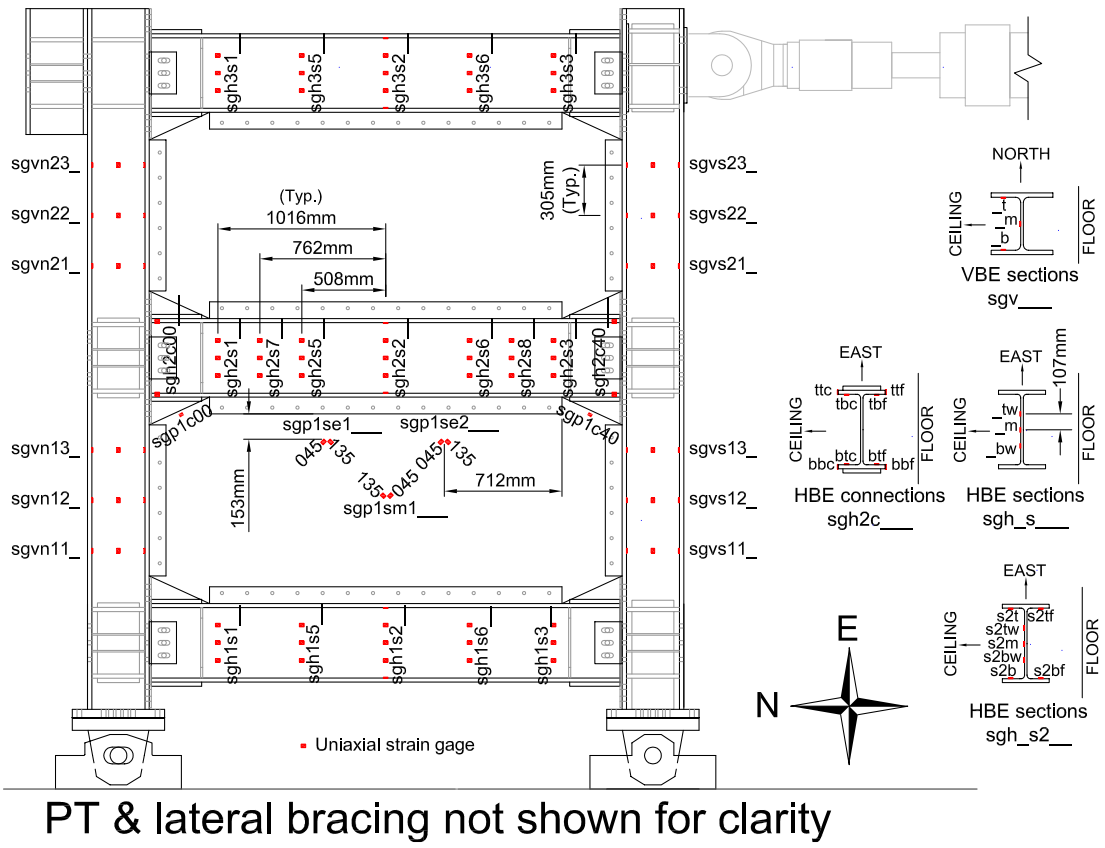

Figure 4.7: Strain gage layout for W18-8s100k20Ga, W18-6s100k16Ga, W18-6s75k20Ga, W18-8s100k16Ga, W18-8s100k20Ga-2, W18-8s100k16Ga20Ga, and W18-8s100k20GaW.

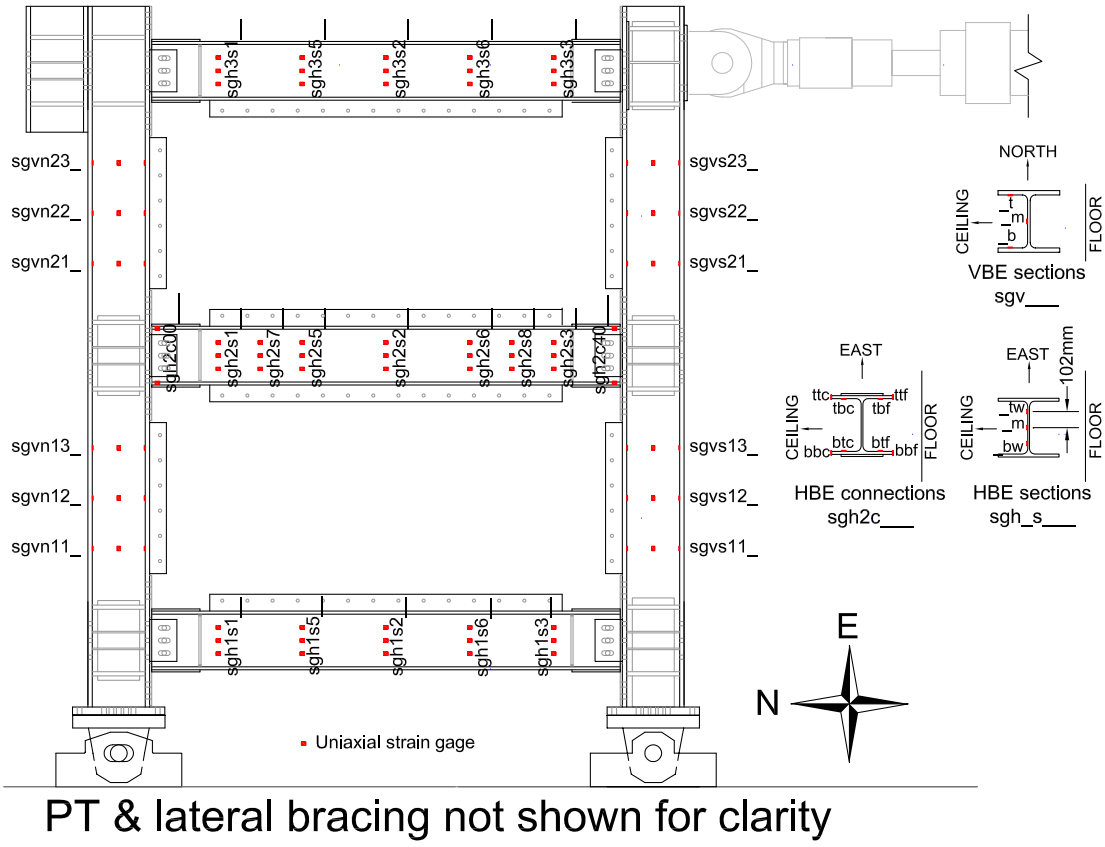

Figure 4.8: Strain gage layout for W14-6s75k, W14-8s100k16Ga, W14-8s100k16GaHBE. No strain gages were installed on the web plates in these specimens.

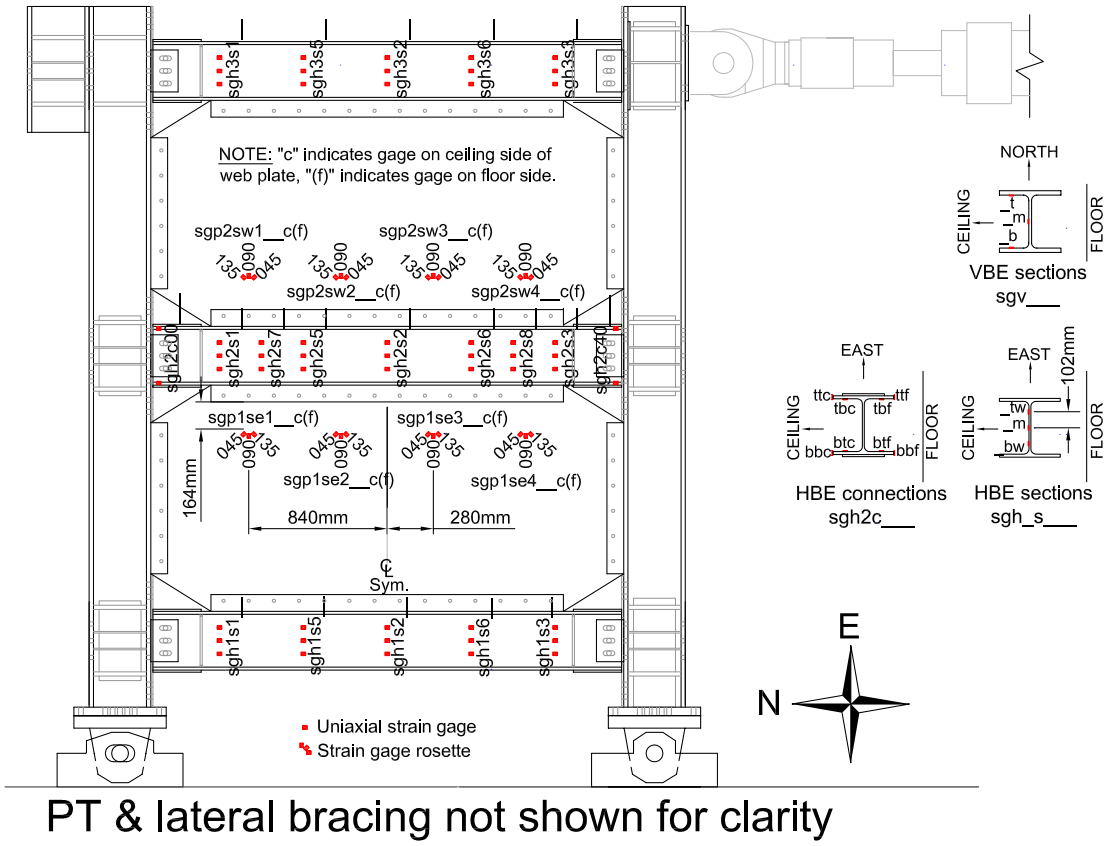

Figure 4.9: Strain gage layout for W14-8s100k20Ga.

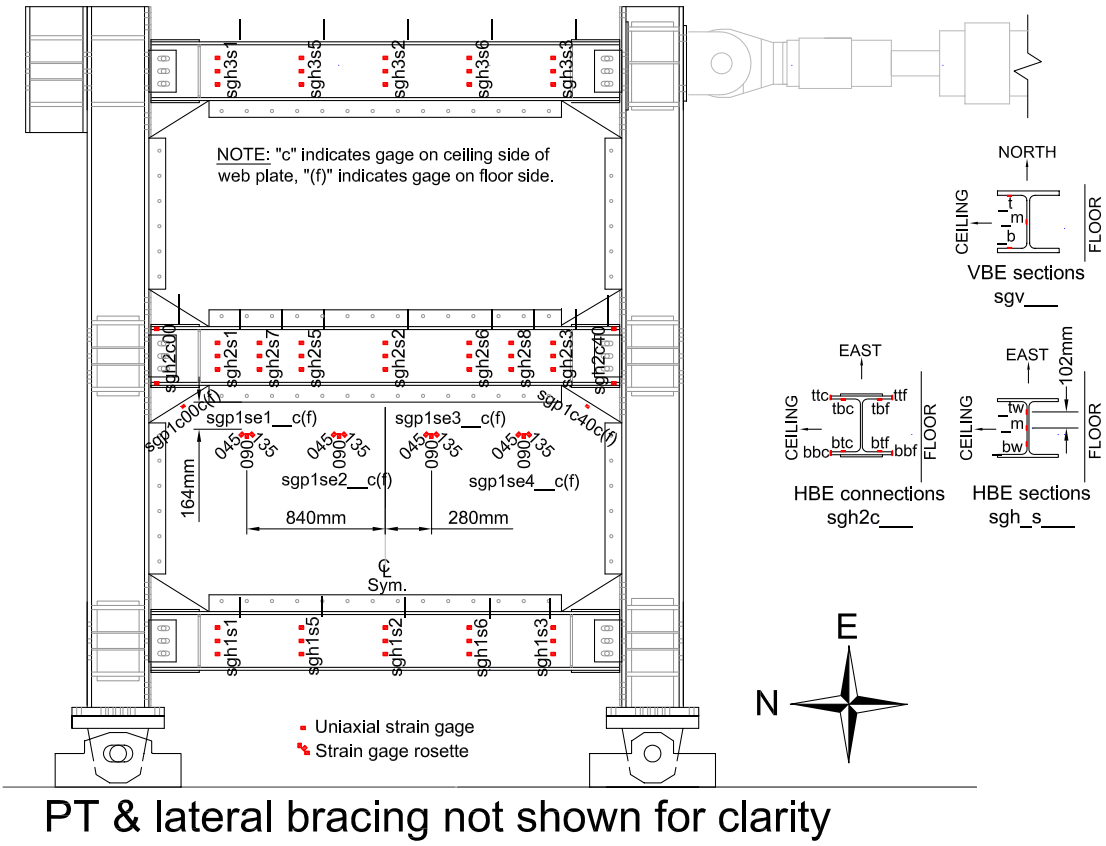

Figure 4.10: Strain gage layout for W14-6s75k20Ga

4.2.4 Material properties

Coupon tests were conducted on the web plate material (ASTM A1008) to determine its monotonic uniaxial material behavior. The coupons (Fig. 4.11) were in accordance with the ASTM A370 standard for tensile tests of sheet-type specimens less than $\frac{1}{2}$ inch thick. A total of six (6) specimens were taken from the excess steel material used for each web plate; three (3) were cut in the longitudinal direction, and three (3) in the transverse direction of the web plate. The resulting stress-strain curves did not exhibit distinct yield plateaus as seen in Fig. 4.12(a); therefore, a 0.02% offset was used to determine the yield stress, σ_{yw} as shown in Fig. 4.12(b). The web plate material properties (Table 4.2) were taken as the averages from all the coupon tests for each web plate, where t_w is the web plate thickness, E_w is the initial modulus of elasticity, and σ_{uw} is the ultimate stress.

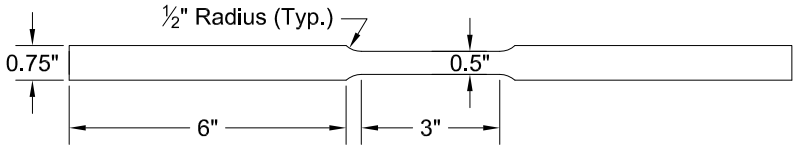

Figure 4.11: Dimensions for web plate coupon specimens

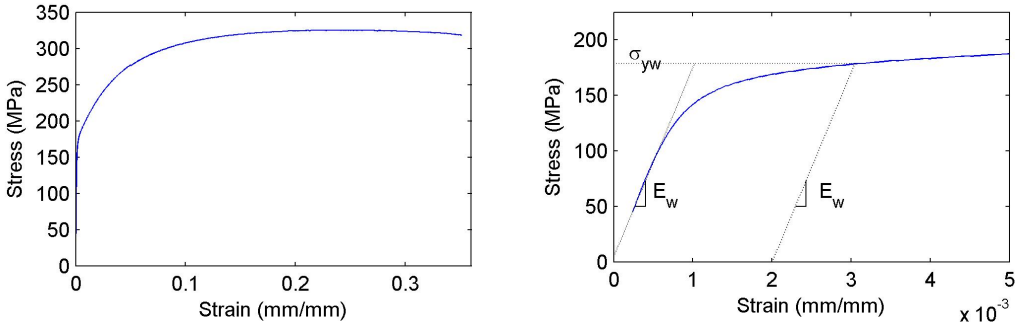

(a) Full monotonic response

(b) Response at small strains

Figure 4.12: Stress-strain curve for single web plate coupon test.

Table 4.2: Web plate material properties

Specimen Name	Story	t_w (mm)	σ_{yw} (Mpa)	σ_{uw} (MPa)	E_w (GPa)
W18-8s100k20Ga	1	0.92	190	339	161
	2	0.92	183	328	175
W18-6s75k20Ga	1	0.92	179	314	125
	2	0.92	179	321	168
W18-6s75k16Ga	1	1.52	244	346	174
	2	1.52	205	339	172
W18-8s100k16Ga	1	1.52	240	335	170
	2	1.52	237	341	188
W18-8s100k20Ga-2	1	0.92	196	340	208
	2	0.92	196	352	204
W18-8s100k16Ga20Ga	1	1.52	251	356	180
	2	0.92	184	335	201
W18-8s100k20GaW	1	0.92	202	347	212
	2	0.92	206	349	224
W14-8s100k16Ga	1	1.52	182	321	176
	2	1.52	178	311	166
W14-8s100k16GaHBE	1	1.52	235	326	213
	2	1.52	181	308	210
W14-8s100k20Ga	1	0.92	178	311	197
	2	0.92	176	305	210
W14-6s75k20Ga	1	0.92	165	292	161
	2	0.92	166	292	168

Since the boundary elements and PT strands were designed to remain elastic, tests were not conducted on these materials; however, as previously stated, the materials were specified to be ASTM A992 and ASTM seven-wire Grade 270 prestressing strand, respectively. For analysis, the elastic moduli were taken to be 200 GPa for the boundary elements and 196.5 GPa for the PT strand.

4.2.5 Load protocol

A total of three different displacement histories were used to load the specimens as mentioned above. These three loading protocols are discussed below. In the Phase I of testing conducted by Winkley [2011], the MTS 442 controller was used to conduct the displacement controlled cyclic loading. All of the specimens Phase II of testing were loaded using the MTS FlexTest 60 controller. The actuator was a RexRoth 350 kip actuator with a ±10 inch stroke.

4.2.5.1 LP1

The target cyclic displacement history for the first phase of testing, referred to as LP1 (Fig. 4.13(a)), is a modification of ATC-24 [ATC, 1992] and is similar to the displacement history used in previous SPSW experiments by Vian et al. [2009a]. It comprised three cycles each to peak displacement demands of 0.25, 0.5, 0.75, and 1.0 of the estimated displacement at web plate yielding, δ_y (0.35% drift). After this, the peak displacements were increased in multiples of δ_y up to approximately 2% drift. Finally, the peak displacements were increased in increments of 0.5% drift up to 4.5%. Three cycles were done at each peak displacement level up to approximately 1% drift, and only two cycles were done at each subsequent drift level. Displacement was measured at the centerline of the actuator load and drift was taken as this value divided by the height from the actuator centerline to the center of the pin at the base.

4.2.5.2 LP2

In Phase II of testing another load protocol, referred to as LP2 (Fig. 4.13(b)), was used. LP2 was based on the displacement histories used in other SPSW experiments by Li et al. [2010]. It comprised two cycles at 0.08%, a drift less than the expected connection decompression drift, followed by two cycles at target peak drifts of 0.1%, 0.25%, 0.5%, 1%, 1.5%, 2%, 2.5%, 3%, 4%, 4.5%, and up to 5% in specimens where the web plate damage was minimal at larger drifts.

As will be discussed later, it was determined that the progression of web plate damage (e.g. drifts associated with initial tearing and complete tearing along the entire web plate-to-fish plate connection) were not significantly different in specimens using LP1 and LP2. Since the time to execute LP2 was shorter due to the fewer cycles at small drifts, LP2 was used for all tests in the second phase of testing.

4.2.5.3 BF

Since the specimens without web plates were expected to remain elastic during the entire test, an abbreviated displacement history was used, referred to as BF (Fig. 4.13(c)). For this test, two cycles were done at 0.06%, a drift less than the expected connection decompression drift; this was followed by two cycles each at target peak drifts of 0.5%, 1%, and 2% and one cycle at 3% drift.

4.2.5.4 Displacement Controllers

As indicated previously, all tests were conducted under displacement control to the targeted drift demands in the specified load protocol. All tests in Phase I were conducted using an MTS 442 controller where the target displacements were prescribed by turning a "set point" knob. In these tests, the actual peak displacement often times was less than the target drift displacement due to inherent inaccuracies in determining and setting the "set point". Specimen W18-8s100k20Ga from Phase I of testing is most significantly affected by the "undershooting" of the target displacement. As this was one of the first SC-SPSW subassembly tests conducted in this setup, the scale factor for determining the "set point"

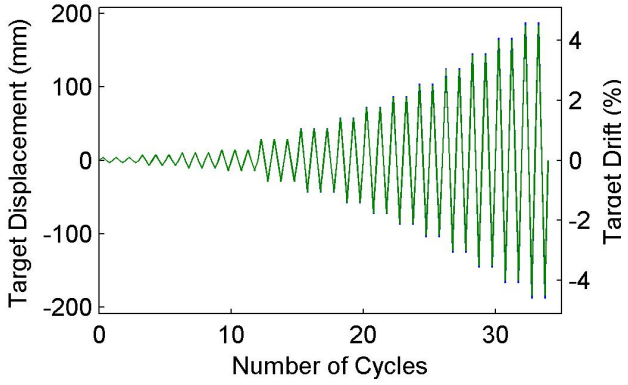

(a)

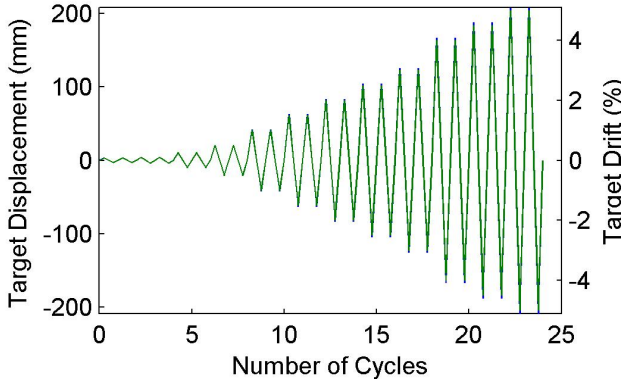

(b)

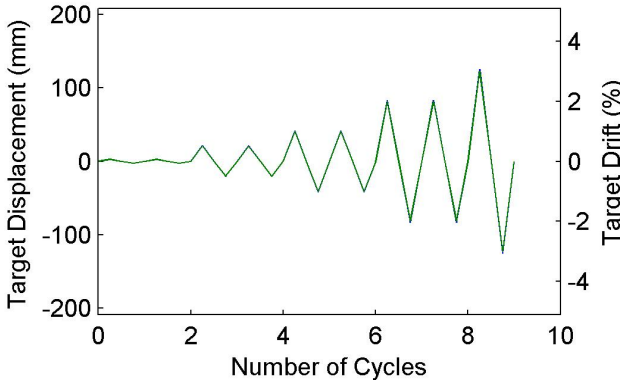

(c)

Figure 4.13: Displacement loading history for (a) LP1, (b) LP2, and (c) BF.

from a target displacement was underestimated. In later tests with the MTS 442 controller, a more appropriate scale factor was used, and peak displacements were closer to those targeted. In Phase II of testing, an MTS FlexTest 60 controller was used to impose displacements based on the LVDT in the actuator. Using the MTS FlexTest controller resulted in peak displacements that more closely matched the target displacements than Phase I tests.

4.3 Experimental Observations and Results

This section describes the visual observations made during each test conducted during Phase II of testing, including the initiation and progression of web plate damage, as well as, PT strand and rocking connection behavior. A similar discussion of Phase I tests can be found in Winkley [2011]. Qualitative response of the specimens will be presented for each test. Interpretation and analysis of response data will be discussed in Chapter 6. For ease of comparison and interpretation of the results, the displacement measured at the top beam has been converted to a drift (%) by normalizing with the height from the center of the pin at the base to the center of the top beam (4178 mm). Displacements towards the north are considered to be positive. The PT force response is presented as the sum of the force in the PT strands in the the middle HBE.

The progression of web plate damage is shown for each specimen. The initial observation of tearing in a certain location is marked in blue progressing to dark red to represent the tear propagating completely through an entire edge of the web plate. Each observation is labeled with the direction of loading ('+' represents the actuator pushing towards the north, and '-' represents the actuator pulling towards the south), the peak drift magnitude, and the cycle number at that drift level. For example, '+4(2)' represents tearing observed as the specimen is pushed towards the north during the second cycle of loading at 4% drift.

4.3.1 W18-6s75k

Specimen W18-6s75k (shown in Fig. 4.14) remained completely elastic during testing as intended. The cyclic force versus drift response (Fig. 4.15(a)) was bilinear elastic as expected

of a PT frame without any energy dissipating devices. The slight hysteresis in Fig. 4.15(a) can be attributed to friction inherent in the system and test setup.

Similarly, the middle HBE PT force versus drift response (Fig. 4.15(b)) was also elastic, showing that the PT strands elongated elastically as the PT connection decompressed during loading in both directions. In theory, the PT strands will not elongate until the connection had decompressed and a gap forms in the connection. The V-shape of Fig. 4.15(b) suggests that the PT connection decompresses at very low drift levels. The slight decrease of the PT force at zero drift is due to prestress losses associated with PT anchorage seating and will be discussed in further detail later.

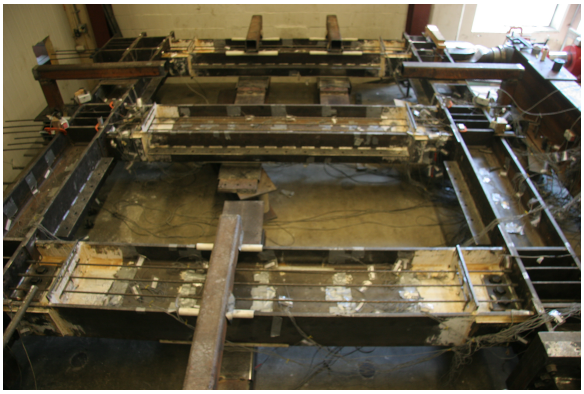

Figure 4.14: Photo of W18-6s75k before test

4.3.2 W18-8s100k20Ga-2

Specimen W18-8s100k20Ga-2 had the same design parameters as a specimen tested during the Phase I of SC-SPSW subassembly testing (W18-8s100k20Ga); however, the load protocol used in this test had fewer cycles at small drift than that used in Phase I of testing. This load protocol, LP2 (Fig. 4.13(b)), was also used for all subsequent tests. The resulting cyclic force versus drift response is shown in Fig. 4.16(a).The middle HBE PT force versus drift response is also shown in Fig. 4.16(b) for comparison to that of the bare PT frame (Fig. 4.15(b)). The PT response from this test is typical of all SC-SPSW specimen. Just as in the bare PT frame, the PT response is linear, indicating that the PT force is related to

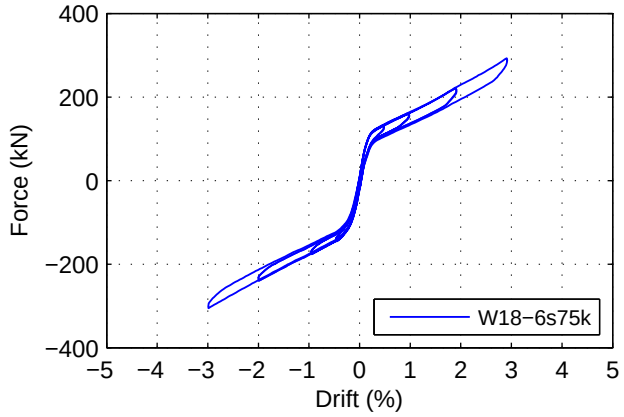

(a)

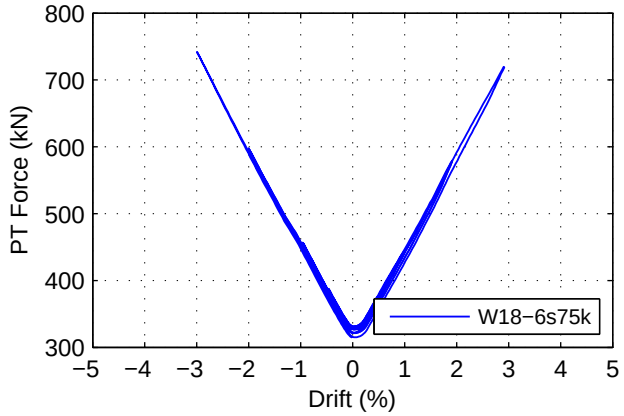

(b)

Figure 4.15: (a) Actuator force and (b) middle HBE PT force vs. drift responses of W18-6s75k

the drift demands and is not significantly impacted by the presence of web plates.

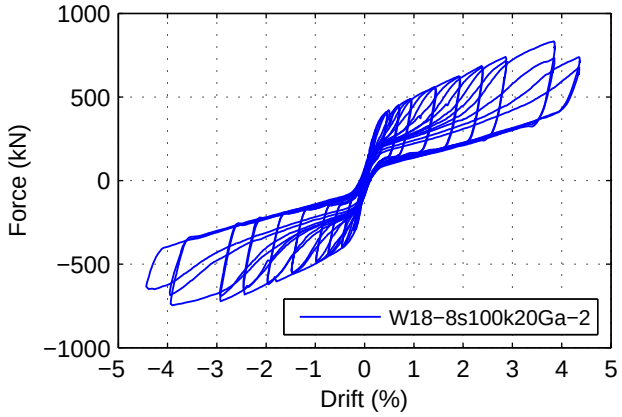

(a)

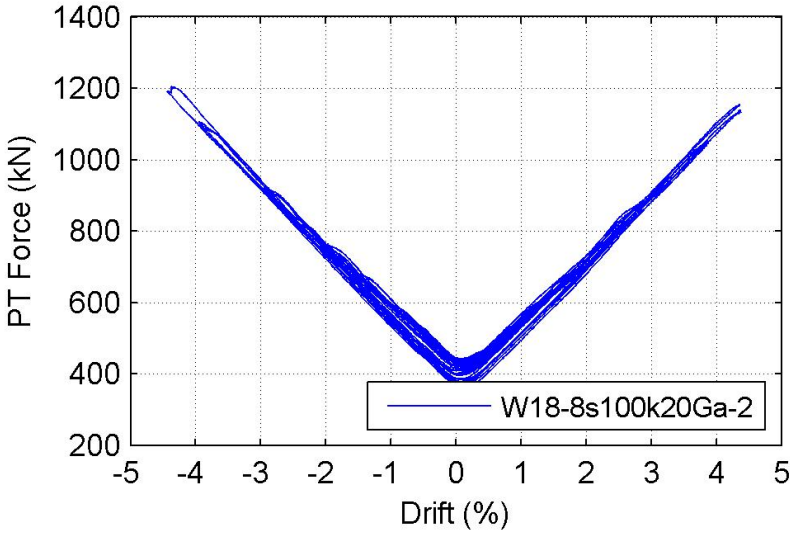

(b)

Figure 4.16: (a) Actuator force and (b) middle HBE PT force vs. drift response of W18-8s100k20Ga-2

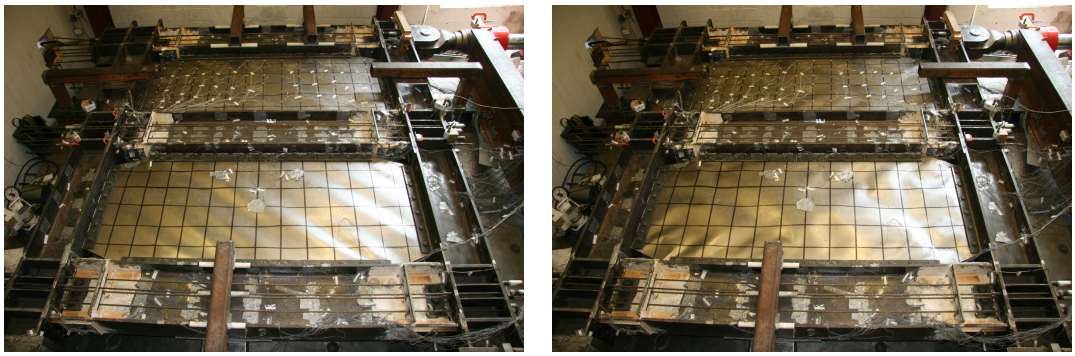

(a) (b)

Figure 4.17: (a) Tension field buckles and (b) residual deformation in web plate during 0.5% drift cycle (W18-8s100k20Ga-2)

During the initial cycles (0.08% drift), no PT connection decompression was visible, as is also suggested by the linear force versus displacement response at this drift level (Fig. 4.16(a)). Elastic buckling of the web plate was observed visually with approximately three low amplitude buckles and low frequency noises coming from the web plate as the buckles formed.

At 0.25% drift PT connection decompression was barely visible. Creaking sounds were heard near the PT connections and were believed to be due to the connection gap opening and rotation of the HBE flange bearing surfaces. Connection decompression was most visible at the bottom HBE and the amount of gap opening decreased at the middle and top HBEs. At this drift level, approximately five daigonal buckles we observed in each web plate with an approximate height (from peak to trough of buckle) of 15 mm.

At 0.5% drift, approximately six buckles were visible in the web plates (Fig. 4.17(a)). The hysteresis in the force vs. drift plot (Fig. 4.16(a)) at this drift level and the residual deformation of the web plate when unloaded to its original location (Fig. 4.17(b)) suggest that the web plate was fully yielded. No tearing or slip in the bolted web plate-to-fishplate connection was visible.

Just before reaching 0.75% drift, there was a lound “bang” noise that eminated from the specimen. The cause of the noise is unclear; however, it was associated with an approx-

Figure 4.18: Initial observation of slip in the bolted web plate-to-fish plate connection.

imately 100 kN drop in actuator load before quickly reagining strength along its previous trajectory. These bangs and associated short-term drops in actuator load were observed in prior and subseuent tests. They appear to coincide with formation of new buckles in the web plate. Slip was first observed in the bolted web plate-to-fish plate connection of a magnitude of approximately 3 mm over a length of approximately 75 mm, from the first bolt to the end of both the HBE and VBE clamping bars where the clamping forces are not as large (Fig. 4.18).

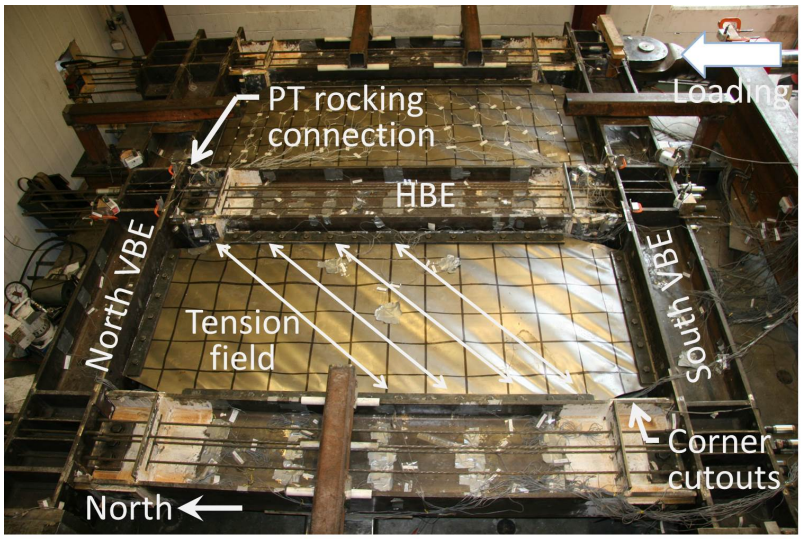

Figure 4.19: Typical SC-SPSW specimen in deformed configuration (shown here for W18-8s100k20Ga-2 at 1% drift).

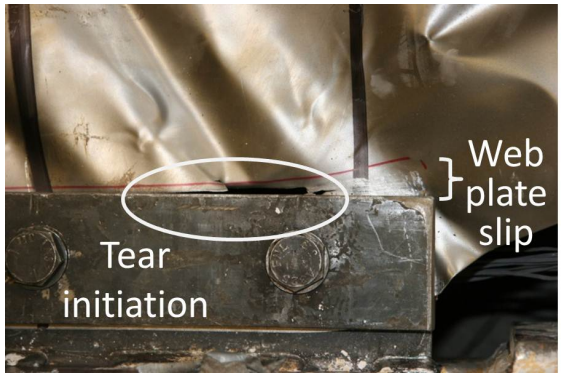

Figure 4.20: Initial observation of web plate tearing at 3% drift (W18-8s100k20Ga-2).

At 1% drift (Fig. 4.19), approximately nine diagonal buckles were visible in the web plate with an approximate height of 25 mm. The out-of-plane amplitude of the web plate buckle in the unrestrained corner cutouts closest to the HBE flanges in compression was larger than the diagonal tension field buckles. Slip of the web plate was visible along the ends of the clamping bars as previously described. The magnitude of the slip was similar to the magnitude of HBE gap opening and, just as observed in the HBE gap opening, was smaller near the top HBE than the bottom HBE. After unloading, the web plate had significant residual deformation including some kinks or folds in the web plate near the corners.

The general observations of web plate slip and diagonal tension field buckles were similar at increasing drift amplitudes. Web plate tearing was first observed in the first cycle at 3% drift (Fig. 4.20). A tear of approximatley 125 mm was first visible along the bottom HBE in the southwest corner of the 1st story web plate between the first and second bolt from the south end of the HBE. The tear was in the portion of the web plate that was between the clamping bars and was already of significant length when first observed; therefore, it is possible that the tear formed prior to observation as it was hidden underneath the clamping bars.

The progression of web plate tearing is shown schematically in Fig. 4.21. In general, most of the tearing was along the edge of the clamping bars along the HBEs, and in particular, the bottom HBE. Tearing was first observed along the VBE clamping bars at 4% drift. The

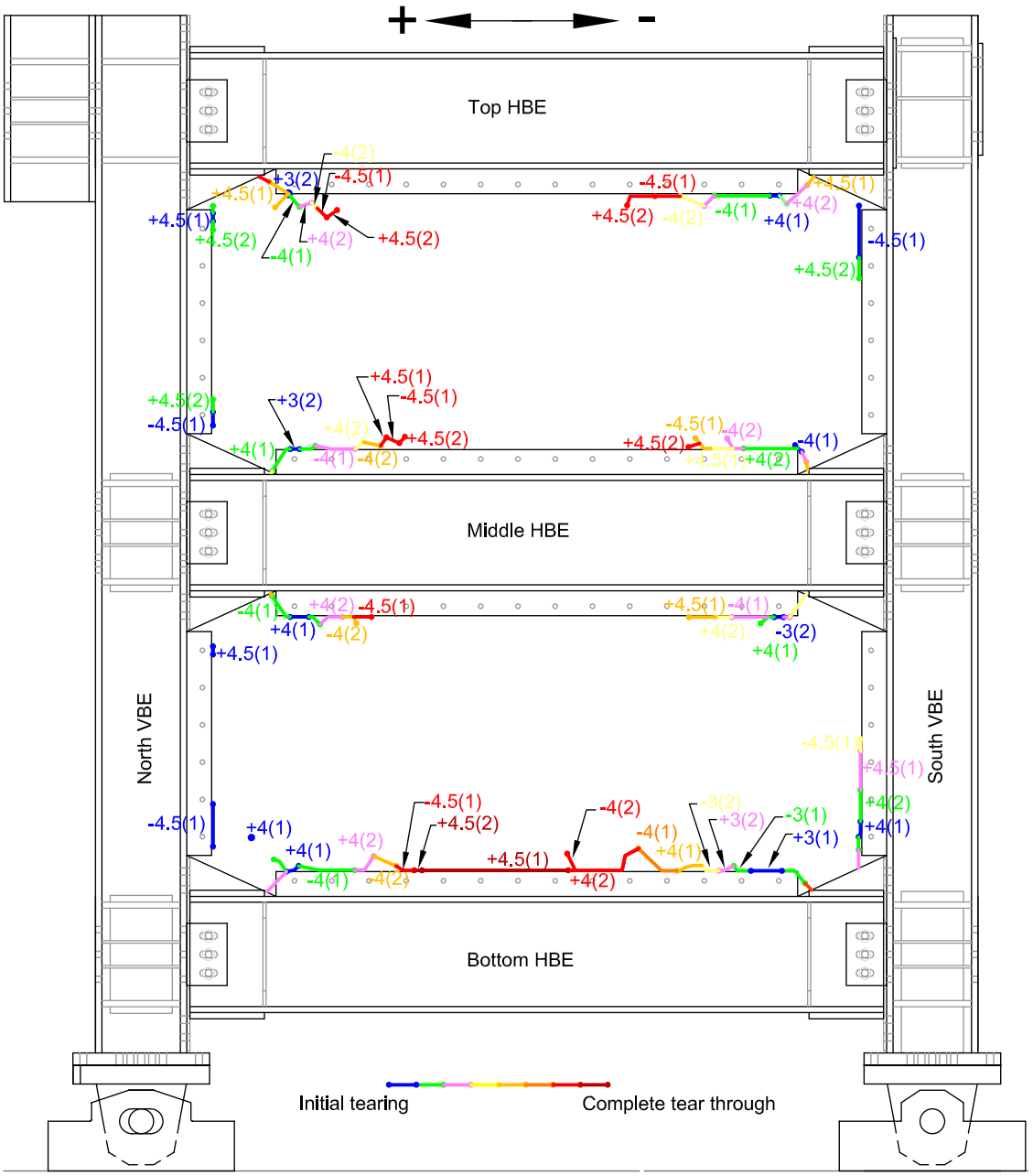

Figure 4.21: Schematic of progression of web plate tearing (W18-8s100k20Ga-2).

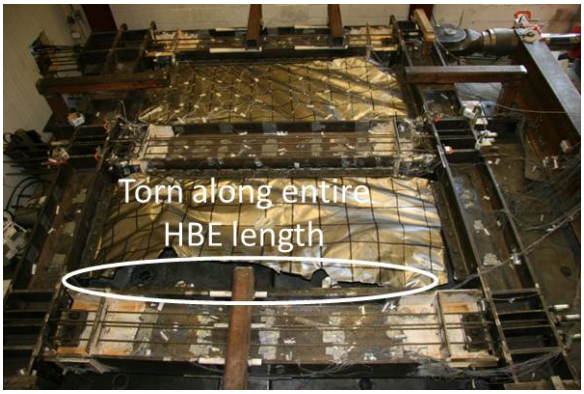

Figure 4.22: Web plate torn along the entire length of the bottom HBE at 4.4% drift (W18-8s100k20Ga-2).

propagation of web plate tearing resulted in loss of lateral load resisting capacity after peak load at the first cycle of loading at 4% drift. The lateral load resisting capacity reduced to 89% and 81% of the peak positive load during the first and second cycles at 4.4% drift, respectively. The test was ended after the web plate tore completely through its entire edge along the bottom HBE during the second cycle of positive loading at 4.4% drift (Fig. 4.22).

4.3.3 W18-8s100k16Ga20Ga

Specimen W18-8s100k16Ga20Ga consisted of different web plate thicknesses above and below the middle HBE, with the thicker web plate being below the middle HBE. The resulting cyclic force versus drift response is shown in Fig. 4.23.

Elastic buckling of the web plate was very visible at 0.25% drift, with two larger amplitude buckles in the first story web plate and approximately three lower amplitude buckles in the second. This trend of fewer buckles in the thicker first story web plate is consistent throughout the entire test.

Significant web plate yielding was first observed at 0.5% drift, as indicated by the residual deformation in the web plate after unloading. Connection decompression was first observed in the bottom and middle HBE at 0.5% drift and in the top HBE at 0.75% drift. Very minor slip of the web plate near the ends of the web plate clamping bars was first observed

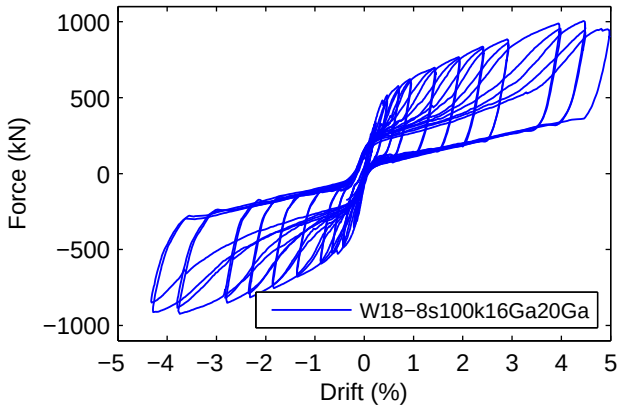

Figure 4.23: Actuator force vs. drift response of W18-8s100k16Ga20Ga

at 0.75% drift for the second story web plate and 1.0% drift for the first story web plate. Similar to the previous test, the magnitude of web plate slip in the region just beyond the outer-most bolt of the web plate clamping bars was similar to the magnidue to gap opening.

Some kinking and localized folding of the web plate was first observed at 1.5% drift (Fig. 4.24); however, web plate tearing was first observed along the top of the middle HBE at zero load after two full cycles of loading at 2.5% drift. The tears started near the outer-most bolts of the clamping bar and were approximately 75 mm and 40 mm long on the south and north ends, respectively, of the clamping bar. The progression of web plate tearing is shown in Fig. 4.25. Tearing was first observed along the VBE in the second story web plate at 4% drift.

Minor tearing (approximately 10 mm in length) in the first story web plate was first observed along the south end of the middle HBE at 4% drift. The tearing in the first story web plate tended to be at the corners of the clamping bars instead of along the edge of the clamping bar and was less severe than tearing in the thinner second story web plate. Slip at the ends of the clamping bars in the first story web plate also increased at large drifts without the presence of significant tearing as shown in Fig. 4.26.

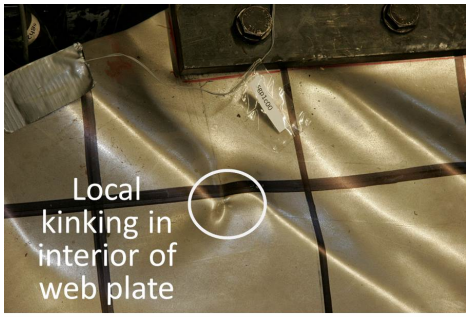

Figure 4.24: Local kinking in interior of first story web plate at 1.5% drift (W18-8s100k16Ga20Ga)

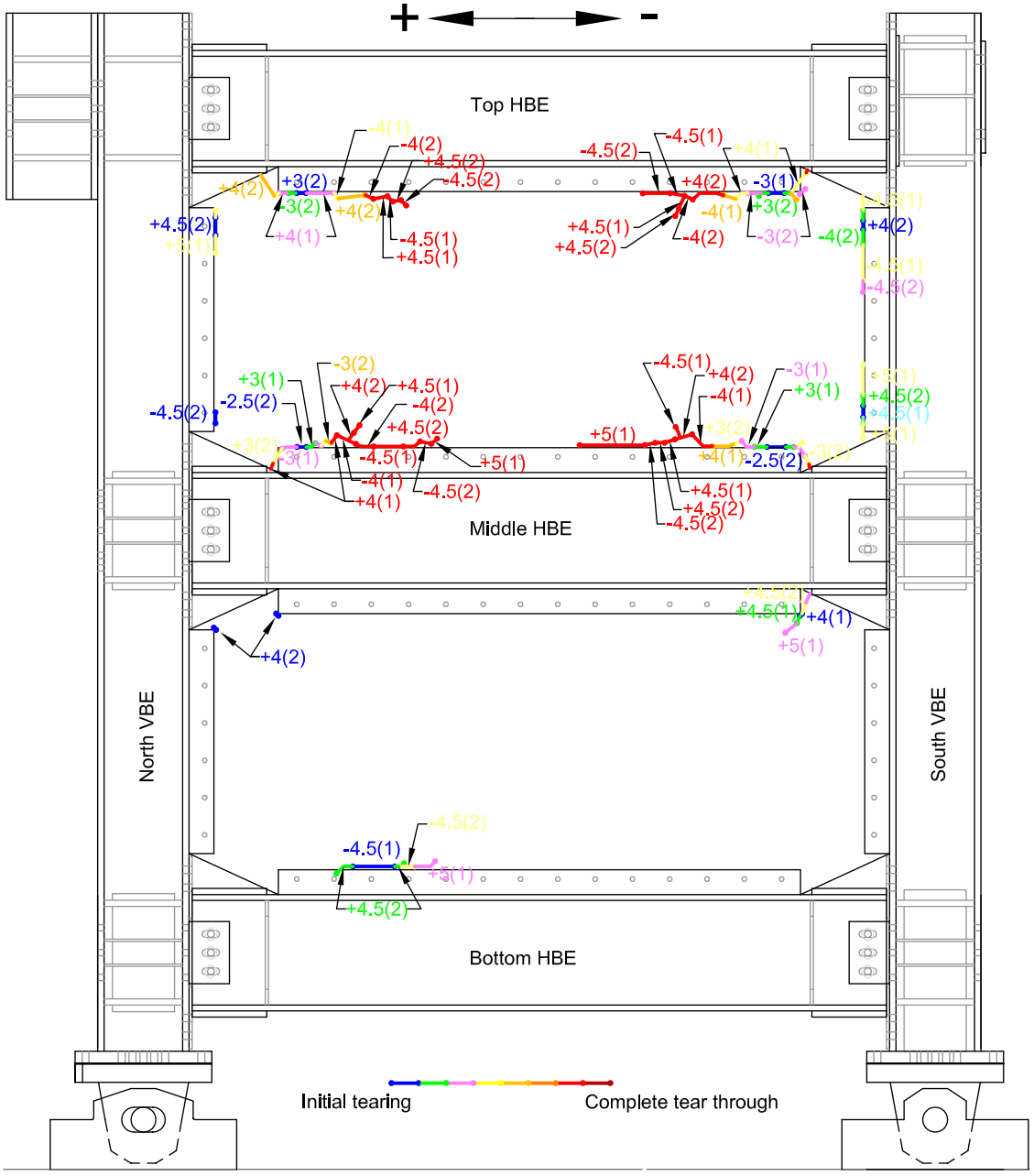

Figure 4.25: Schematic of progression of web plate tearing (W18-8s100k16Ga20Ga).

Figure 4.26: Slip in southwest corner of first story web plate of W18-8s100k16Ga20Ga at 4% drift.

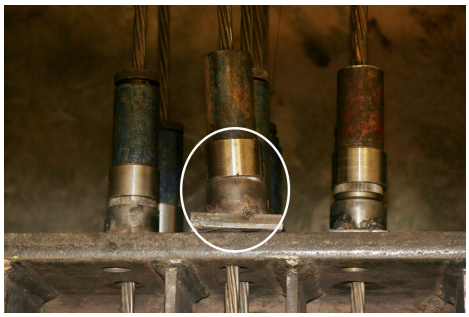

Figure 4.27: Threaded spacer for PT strand squashed at 5% drift (W18-8s100k16Ga20Ga)

The test was ended after half of a cycle at 5% drift due to squashing of one of the threaded spacers used to adjust the initial PT force in the strands located at the bottom HBE and shown in Fig. 4.27. Squashing of the threaded spacers was also observed in tests conducted by Winkley [2011] due to buckling of the outer threaded cyclider under lage compressive loads. At the end of testing (Fig. 4.28), tearing in the first story web plate was minimal; however, significant slip and bolt hole elongation was observed near the ends of the clamping bars in the first story as shown in Fig. 4.29.

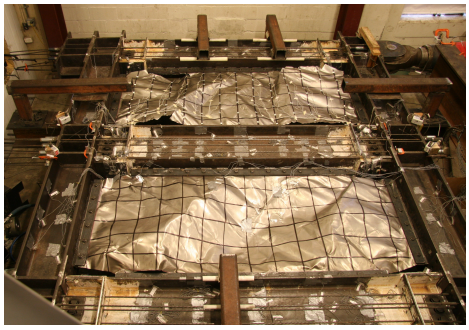

Figure 4.28: W18-8s100k16Ga20Ga at end of testing

Figure 4.29: Bolt hole elongation and deformation in the southwest corner of the first story web plate in W18-8s100k16Ga20Ga.

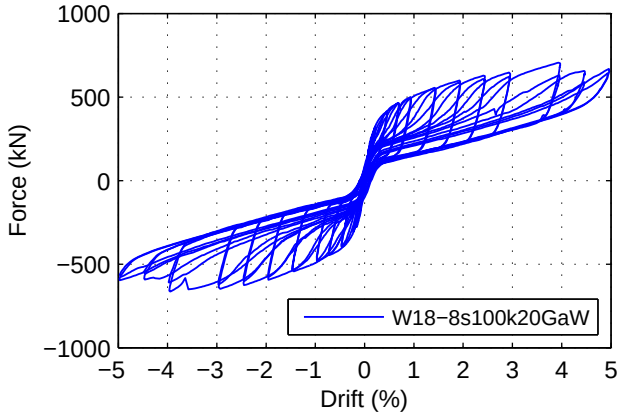

Figure 4.30: Actuator force vs. drift response of W18-8s100k20GaW

4.3.4 W18-8s100k20GaW

Specimen W18-8s100k20GaW investigated a welded web plate-to-fish plate connection detail (Fig. 4.3(a)), as opposed to the bolted connection detail (Fig. 4.3(b)) used in other specimens. The resulting cyclic force versus drift response is shown in Fig. 4.30

Elastic buckling was observed at 0.25% drift. It should be noted that prior to testing, there were some very minor localized out-of-plane deformation of the web plate along the edges due to the welding process. The web plate was welded to the fish plate initially with tack welds spaced every 10 to 15 cm, then the edges between the tacks were wlded with a single bead. The uneven heating and cooling between each bead resulted in localized deformations in the web plate in its initial configuration. Significant residual deformation was visible in the web plate after loading at 0.5% drift.

Initial tearing in the welded web plate-to-fish plate connection detail (i.e. weld crack initiation) was first observed at 0.75% drift (Fig. 4.31). This drift at first observed web palte tearing was much lower than initial observations of web plate tearing in the bolted web plate connection detail, which was typicaly around 2.5 to 3% drift. The tears propagated slowly, as shown in Fig. 4.32, in a zig-zag pattern as the specimen was loaded in the positive and negative directions of loading. While tearing initiated at the toe of the weld, the propagation of tearing was outside of the heat affected zone (HAZ) as shown for a tear along the south

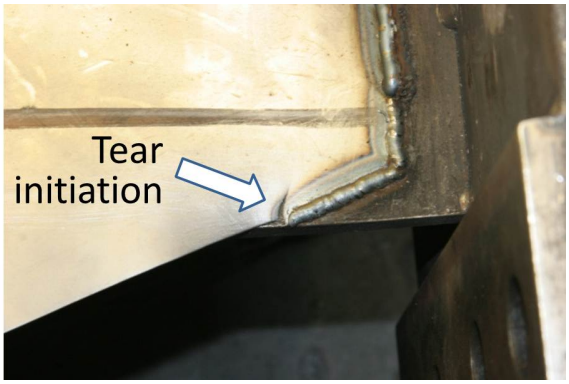

Figure 4.31: First observations of tearing in W18-8s100k20GaW at 0.75% drift.

end of the bottom HBE at 2.5% in Fig. 4.33. The north edge of the second story web plate (along the VBE) tore completely through during the second cycle at 4% drift, with the remaining VBE edges tearing through during the 4.5% cycles, as shown in Fig. 4.34 and as indicated by the significant reduction in strength at this drift level (Fig. 4.30). The test ended after two cycles of loading at 5%. The specimen strength during the 5% drift cycles was slightly greater than 90% of the peak strength. The area of the tension field was greatly reduced due to the extent of web plate tearing, as seen by the single diagonal buckle in the middle of the web plates in Fig. 4.34

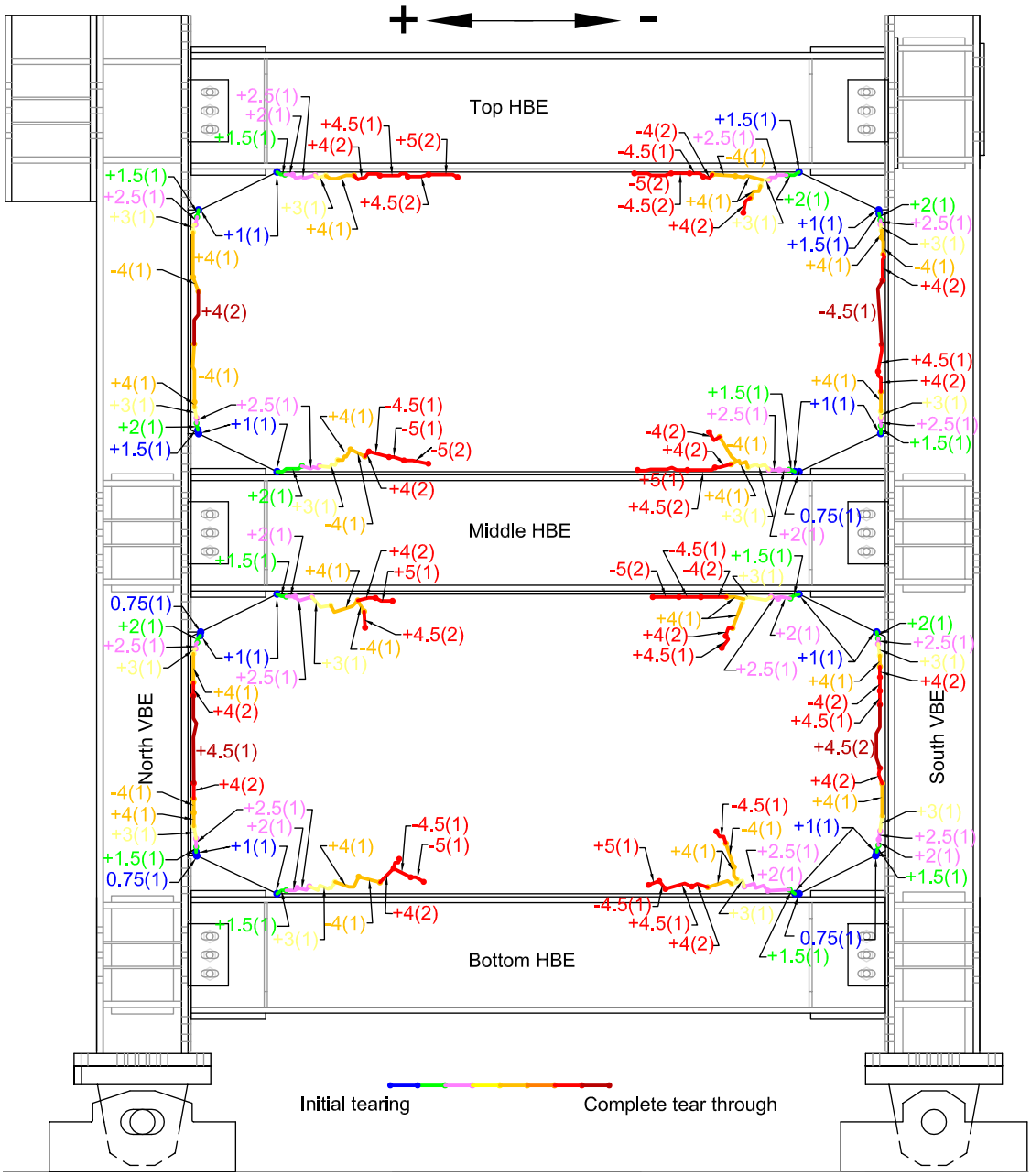

Figure 4.32: Schematic of progression of web plate tearing (W18-8s100k20GaW).

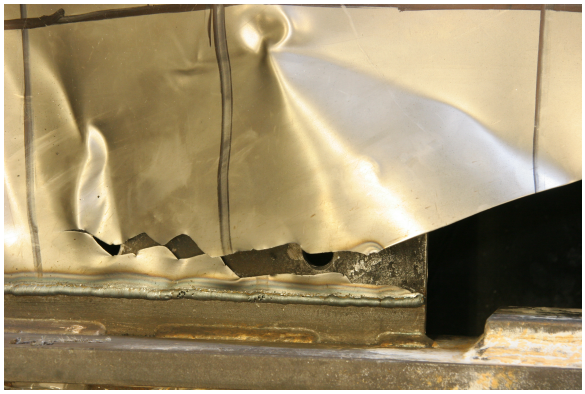

Figure 4.33: Propagation of web plate tearing outside of the HAZ (W18-8s100k20GaW)

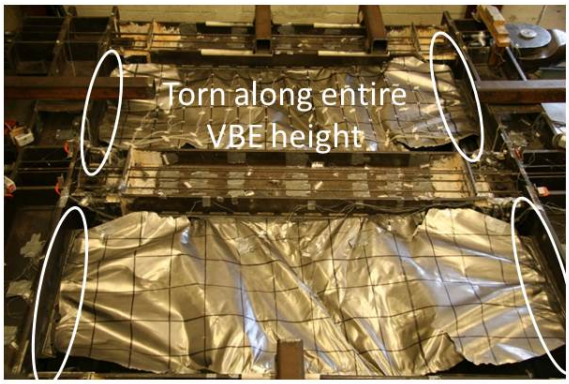

Figure 4.34: Tearing along the VBEs after loading at 4.5% drift

4.3.5 W14-6s75k

Since this specimen was a bare PT frame, where the PT and boundary frame components remained elastic, there were no observations of damage. The cyclic force versus drift and middle HBE PT force versus drift responses (Figs. 4.35(a) and 4.35(b), respectively) were bilinear elastic as expected. The slight hysteresis in the force versus drift response can be attributed to friction inherent in the system and test setup.

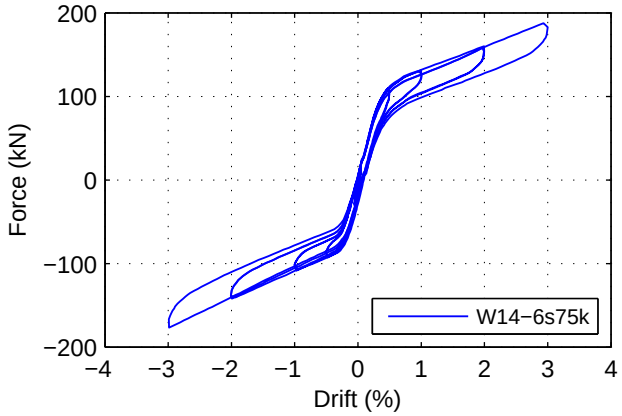

(a)

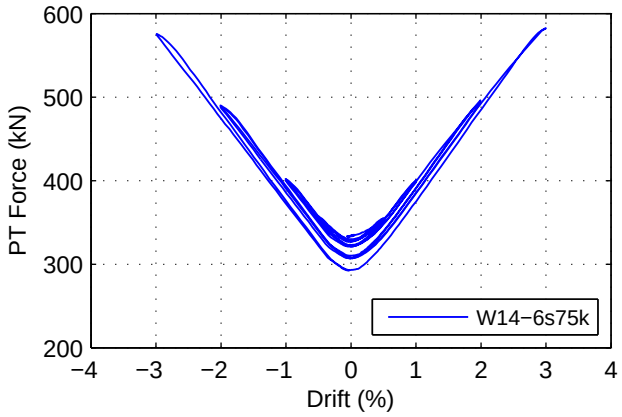

(b)

Figure 4.35: (a) Actuator force and (b) middle HBE PT force vs. drift responses of W14-6s75k

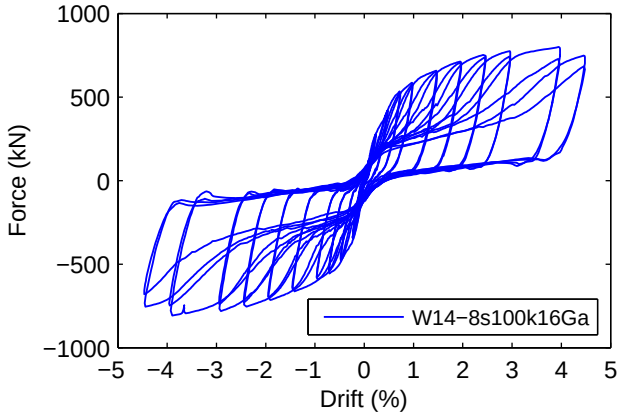

Figure 4.36: Actuator force vs. drift response of W14-8s100k16Ga

4.3.6 W14-8s100k16Ga

Specimen W14-8s100k16Ga was the first specimen with W14x90 HBEs to be tested. The resulting cyclic force versus drift response is shown in Figs. 4.36

Elastic buckling was first observed in the web plate at 0.1% drift with residual web plate deformation first being observed following the cycles at 0.5% drift. Connection decompression was first observed in the top HBE at +0.5% drift, and it was visible at the bottom and top HBE at +0.75%; however, the middle HBE did not appear to have visual signs of connection decompression at this point. At +1% drift, connection decompression was visible at the north end of the middle HBE but was not visible at the south end; at -1% drift, decompression was visible at both ends of the middle HBE. It should be noted that the 1.6 mm thick shim plate that was added to the top flange bearing surface of the south end of the middle VBE that was present during the tests with W18x106 HBEs was removed when the HBEs were switched to W14x90. The asymmetry of the middle HBE gap openings on the north and south ends and during positive and negative loading implies that the uneven bearing surface previously thought to be attributed to the W18x106 middle HBE cut surface, may actually be attributed to the VBE bearing plates or flanges at this location; however, this was not aparent during the time of testing.

At 3% drift, it was bserved that the first story web plate had pulled out of the clamping

bars approximately 2.5 cm over a length of approximately 25 cm along the south end of the middle HBE fish plate as shown in Fig. 4.37; whereas at other locations, the web plate pull out was appriximately 1.5 cm, which was typical compared to pullout during previous tests at similar PT connection gap opening demands. At the first excursion to -3% drift, the hole in the web plate from the southern-most bolt at this location had pulled out beyong the clamping bars such that it became visible as indicated in Fig. 4.38. Other than the exposed bolt hole, no web plate tearing was observed at this point.

After the 4% drift cycles, a total of eight of the fourteen bolt holes along the east edge of the first story web plate were exposed. At a few locations tears were observed to be eminating from the exposed bolt holes. Small tears also formed in the interior of the web plate at locations where cyclic folding of the plate created highly concentrated plastic strains that resulted in what appeared to look like puncture holes at those points (as shown in Fig. 4.38). The bolt hole tearout continued to lengthen with each cycle, until the test is ended after two cycles at 4.5% drift, at which point the east edge of the first story web plate has very little contact with the middle HBE as can be seen in Fig. 4.39.

At the end of the test the second story web plate had minimal tearing along the edge of the clamping bar, and the majority of the damage in the first story web plate was due to the web plate pulling out of the HBE clamping bar connection. This damage mechanism was unexpected based on the typical web plate tearing damage observed along the clamping bars in other tests. In previous tests, web plate pullout was only observed in the localized slip at the ends of the clamping bar; no web plate pullout had previously been observed along the entire length of the clamping bars.

The pullout of the east edge of the first story web plate was believed to be due to metal debris that was produced during the in-place drilling of the bolt holes. The excessive debris along the bottom of the middle HBE may be due to use of a dull drill bit and improper removal of the drilling debris at this location. The accumulation of debris between the clamping bars and the web plate prevented the clamping bars from maintaining contact with the web plate, thus greatly reducing the surface area over which frictional forces, necessary for transferring the web plate forces to the HBE, could act. However, it should be noted that despite the human error in fabricating the bolted web plate-to-fish plate detail at

Figure 4.37: Initial pullout of the first story web plate at the south end of the middle HBE (W14-8s100k16Ga)

this location, the specimen still had significant strength and energy dissipation (Fig. 4.36), indicating the inherent redundancy in the web plate of the SC-SPSW system.

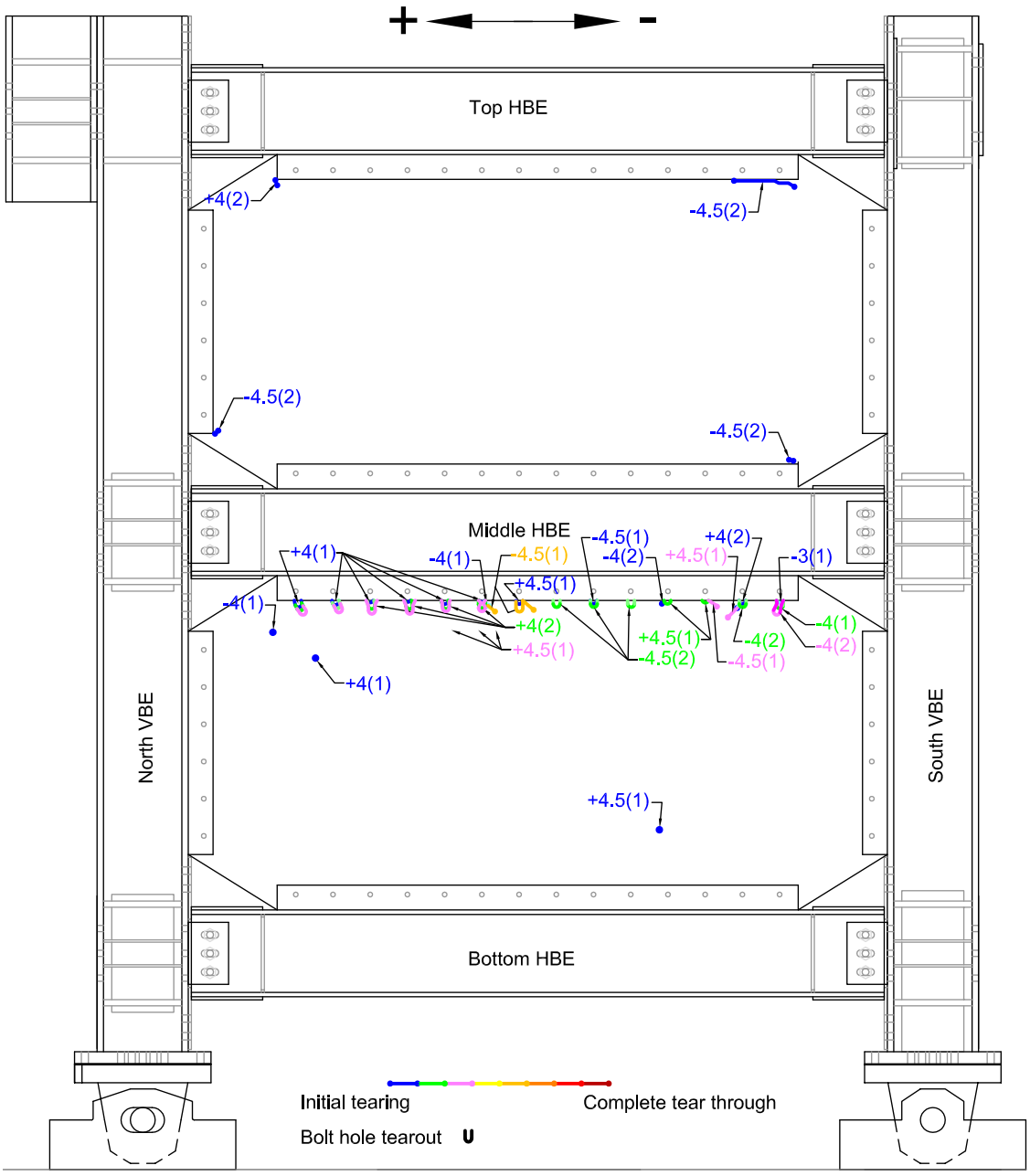

Figure 4.38: Schematic of progression of web plate tearing (W14-8s100k16Ga).

Figure 4.39: Pullout of the first story web plate along the middle HBE at 4.5% drift (W14-8s100k16Ga)

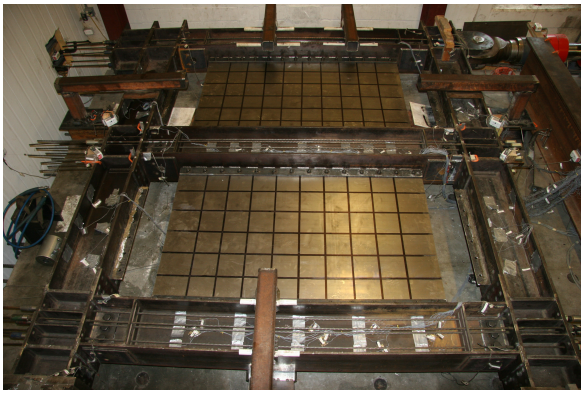

Figure 4.40: Photo of W14-8s100k16GaHBE before test

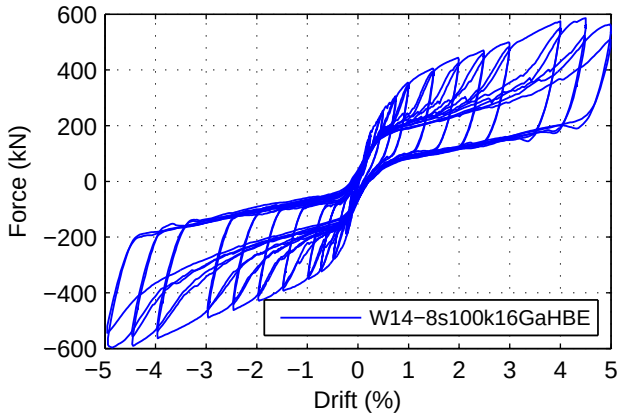

Figure 4.41: Actuator force vs. drift response of W14-8s100k16GaHBE

4.3.7 W14-8s100k16GaHBE

Specimen W14-8s100k16GaHBE (shown before testing in Fig. 4.40) had web plates connected to the HBEs only. The resulting cyclic force versus drift response is shown in Fig. 4.41

Due to the self-weight of the web plate supported only along two edges, the initial out-of-plane sag of the web plate was approximately 12 mm along the south free edge of the first story web plate. Out-of-plane deformation was measured along the free edge of the web plate in this specimen, unlike the fully-connected web plates in the other tests, where

out-of-plane web plate deformations could not be measured directly as the reference plane was more difficult to identify. Elastic buckling was first observed during the initial cycles of loading at 0.08% drift with a single, small amplitude, long wavelength buckle. At 0.25% drift the number of buckles in the web plate increased to two and some residual deformation was observed after unloading as indicate by a maximum out-of-plane defromation of approximately 30 mm along the free edge of the web plate.

At 0.25% drift, the specimen emitted loud creaking and popping sounds during loading; although no decompression was visbile, the HBEs did appear to move vertically in the plane of the frame during the loud popping sounds. In previous specimens, loud "bang" sounds were typically observed during reorientation of the tension field; however, in this specimen, similar noises occurred prior to significant web plate buckling. It is thought that these loud popping sounds, which were also observed at larger drift levels, are associated with the HBE shifting to transfer the shear forces in the HBE through bolt bearing in the horizontally slotted holes in the shear tab as the shear force changes direction. Although much of the shear force can be transfered through friction at the HBE and VBE flange interface [Christopoulos et al., 2002a], the shear forces produced by the web plate, especially at the top and bottom anchor HBE, may be greater than the frictional resistance. This is especially true prior to connection decompression when the compression force at the friction interface increases and when the bearing surface through which frictional forces are transmitted is uneven (as was the case for the south end of the middle HBE). When the shear force is unable to tranfer soley through friction, the bolted shear tab connections must transfer the remaining shear force through bolt bearing.

Observations of vertical HBE movement during previous tests had not been specifically observed; however, when the sounds occurred, attention was typically focused on the web plate tension field reorientation that was also taking place. It is possible that the HBE was also shifting in previous specimens, and that this shifting also was also associated with tension field reorientation, both of which would produce popping or banging sounds. It is difficult to determine if one event (HBE shifting or tension field reorientation) was a cause or effect of the other or from where each specific noise was emanating. Shifting of the HBE may have been particularly evident in this specimen as the uneven bearing surface at the south

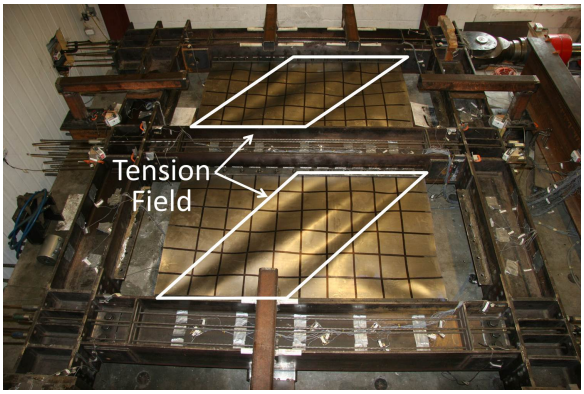

Figure 4.42: Diagonal tension field at 0.75% drift in W14-8s100k16GaHBE

end of the middle HBE may not have been able to transfer shear forces through friction, resulting in HBE slipping (to resist shear through bolt bearing) earlier in the loading history compared to the previous W18 specimens.

Connection decompression was first observed at the south end of the bottom HBE and north end of the top HBE at +0.5% drift. Decompression was first observed in the middle HBE at -0.75%, although it was not visible at +0.75% drift. This discrepency between the amount of gap opening in the middle HBE under positive and negative loading indicates an uneven bearing surface at the south end of the HBE as similarly noted in the previous specimen (W14-8s100k16Ga). After testing of this specimen, a 1.6 mm shim similar to the one used in the specimens with W18x106 HBEs was added to the top flange bearing surface at the south end of the middle HBE to correct this problem in future tests. Note that decompression could have occured earlier at -0.5% drift; however, visual observations were not made at this point.

At 0.75% drift, the web plate tension field consisted of two to three buckles spanning the diagonal region bounded by an HBE above and below as shown in Fig. 4.42. Some slip of the web plate at the ends of the clamping bars was also oberved similar to previous tests.

Tearing was first observed in the web plate at 4.5% drift as shown in Fig. 4.43, which was much later than the first observation of plate tearing in other specimens with bolted web plate connections along the HBEs and VBEs. The extent of tearing at the end of the test,

after two cycles at 5% drift, were minimal. No tearing was observed along the bottom HBE, the location at which full web plate tear through was typically observed in other specimens. This delay of tearing indicates that connecting the web plate to the HBEs only may be a means of mitigating damage to the web plate. This reduction of tearing when releasing the web plate from the VBEs may be due to several reasons: alleviating the concentrated tensile strains in the corner cutout due to gap opening; reducing the overall horizontal web plate strain associated with frame expansion and VBE spreading; or reducing the large curvature and, thus, plastic strain accumulation along the clamping bars by allowing two edges of the web plate to deform freely out-of-plane.

4.3.8 W14-8s100k20Ga

The cyclic force versus drift response for specimen W14-8s100k20Ga is shown in Fig. 4.44. In this test, a 1.6 mm shim plate was tack welded to the south VBE at the middle HBE top flange bearing location (Fig. 4.45) to mitigate the problem observed with asymmetric gap opening and uneven bearing surfaces as described in the previous tests with W14x90 HBEs.

Elastic web plate buckling was observed in the initial cycles at 0.08% drift with two to three buckles per plate. Some slight residual web plate deformation was observed after loading at 0.25% drift, indicating web plate yielding. The number of buckles in the web plate increased from approximatley three at 0.25% drift to seven at 1% drift. Very minor localized slip of the web plate at the ends of the clamping bars was first observed at 0.5% drift, but was noticable at all connection locations at 1.5% drift.

Connection decompression was first observed in the south end of the bottom HBE and the north end of the top HBE at -0.5% drift, but was observed at all connections at 0.75% drift. The connection gap openings tended to be larger at the bottom HBE and progressivly smaller in the middle and top HBEs. Similarly, the gap openings at peak negative loading appeared to be slightly larger than those at peak positive loading.

Tearing was first observed along the HBEs in the first story web plate at 3% drift as indicated in Fig. 4.46. Although initial tearing along the second story of the south VBE

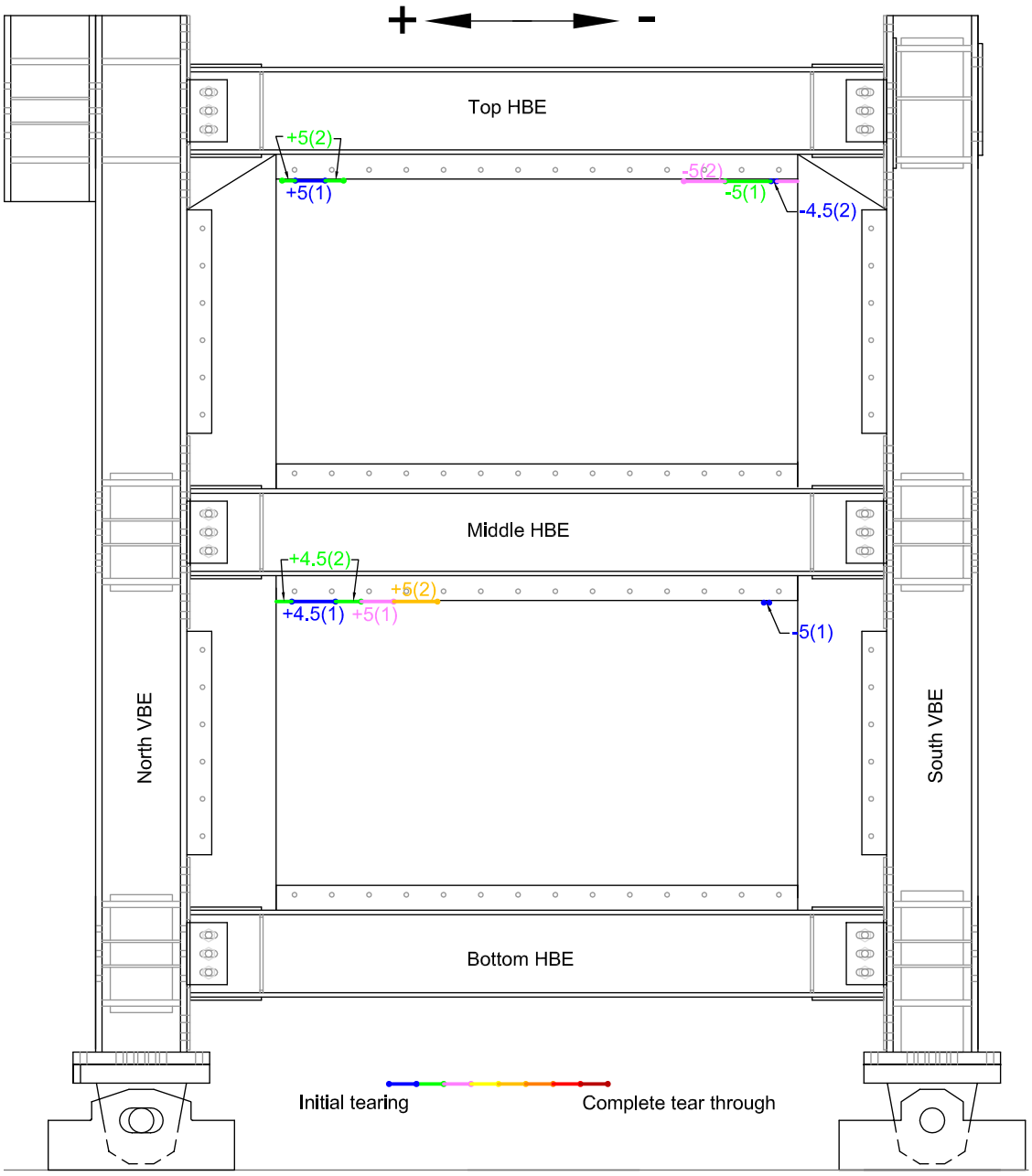

Figure 4.43: Schematic of progression of web plate tearing (W14-8s100k16GaHBE).

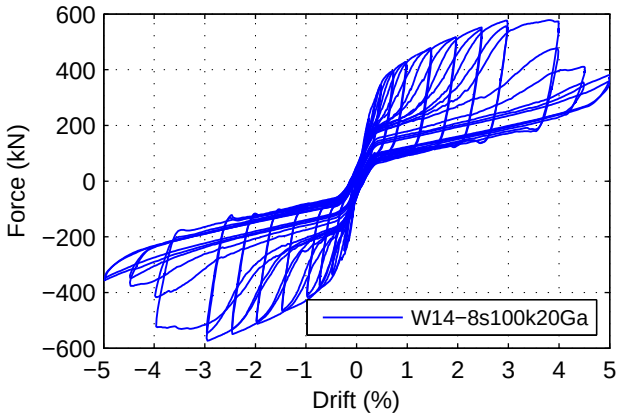

Figure 4.44: Actuator force vs. drift response of W14-8s100k20Ga

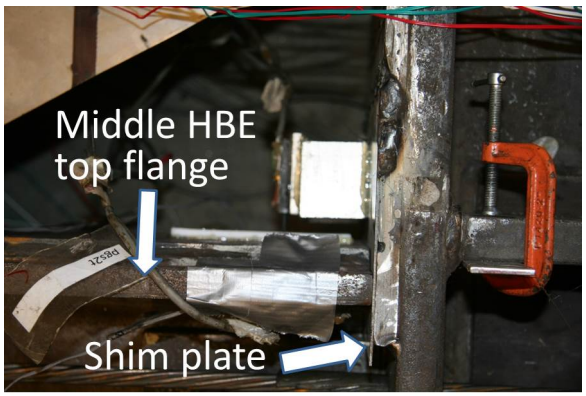

Figure 4.45: Shim plate welded to South VBE at top flange of middle HBE.

was first observed at -3% drift, tearing along all of the VBEs grew substantially during cycles of loading at 4% drift. All web plate edges along the VBEs were torn completely through by the end of the 4.5% cycles, resulting in a 17% and 29% drop in peak strength during the second cycle at +4% and the first cycle at +4.5% drift, respectively. Tearing along the HBEs did not propagate as quickly following the complete tear through along the VBEs; therefore, there was not significant loss of load carrying capacity following the cycles at 4.5% drift. After two cycles of loading at 5% drift the bottom of the second story web plate along the middle HBE was torn almost completely through with only approximately 30 mm of web plate still transferring load to the HBE as shown in Fig. 4.46.

4.3.9 W14-6s75k20Ga

Specimen W14-6s75k20Ga is shown before testing in Fig. 4.47. Two small amplitude elastic buckles were present in the pre-test photo due to a minor initial lateral displacement that was imposed on the specimen the day prior to the test. The accidental displacement occurred as the hydraulics that power the actuator were turned on; a short circuit in the FlexTest controller hydraulic service manifold (HSM) connection caused the actuator to jump, pushing the specimen approximately 1.5 mm before the internal safety emergency stop was triggered. The test was started from this initial position, and the subsequent actuator force readings were offset to account for the initial actuator force imposed during this short circuit event. The resulting cyclic force versus drift response is shown in Figs. 4.48

Elastic buckling was observed in the initial cycles of loading at 0.08% drift. Some minor residual deformation was observed in the web plate following the cycles of loading at 0.25% indicating some web plate yielding; however, more significant residual deformation was observed over the entire web plate after loading at 0.5% drift.

Connection decompression was first observed in the bottom and top HBE at +0.5% drift and was visible at all connections at -0.5% drift. Minor slip of the web plates near the ends of the clamping bar, as described in previous teasts, was first noticeable at 0.75% drift but became more apparent at all web plate corners at 1% drift.

Web plate tearing was first observed during the first cycle of loading at -3% drift as

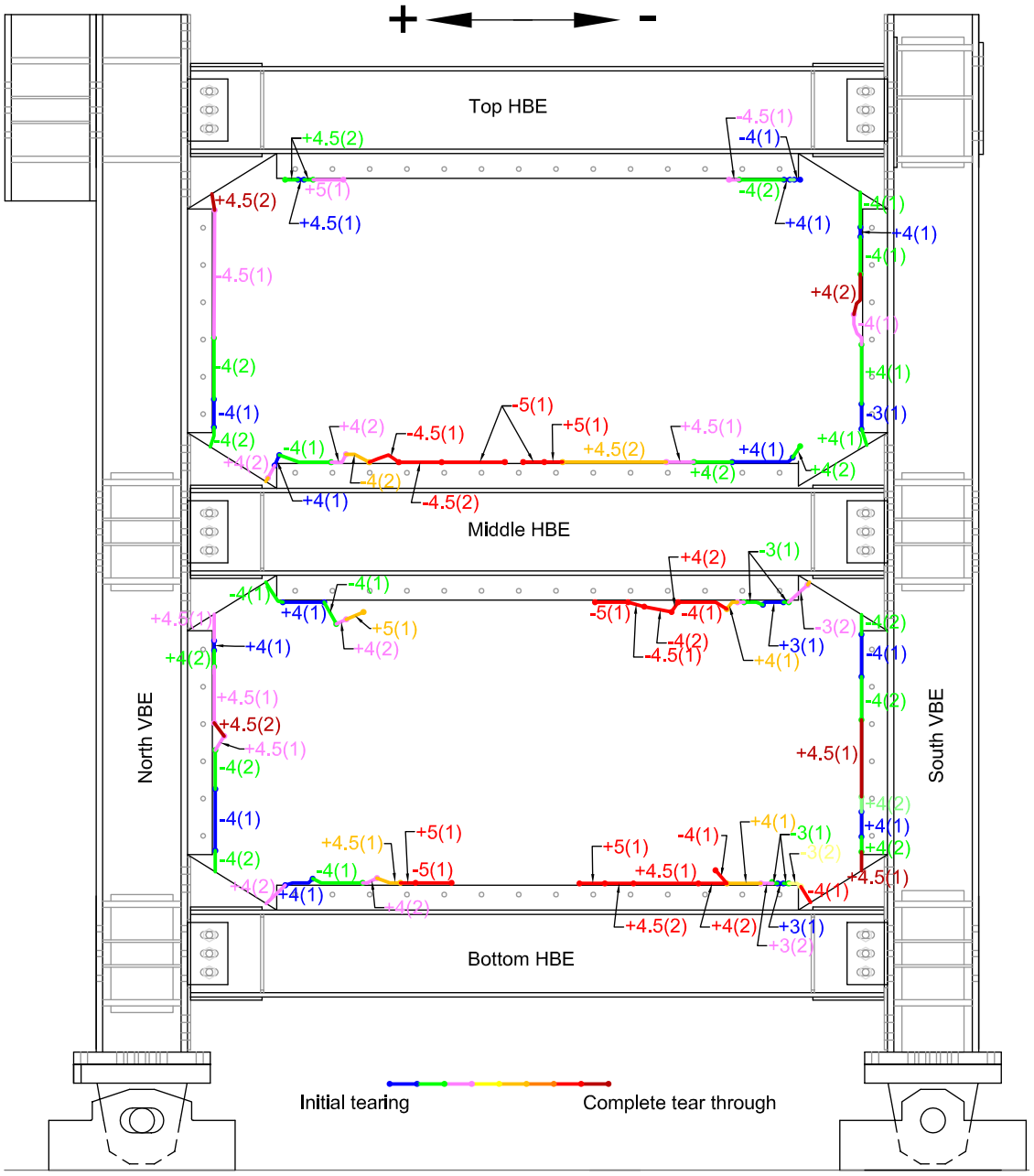

Figure 4.46: Schematic of progression of web plate tearing (W14-8s100k20Ga).

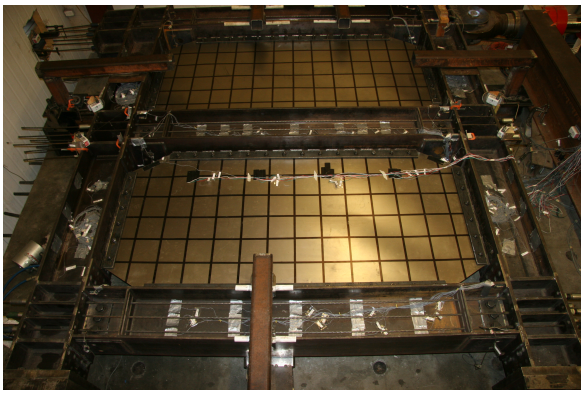

Figure 4.47: Photo of W14-6s75k20Ga before testing

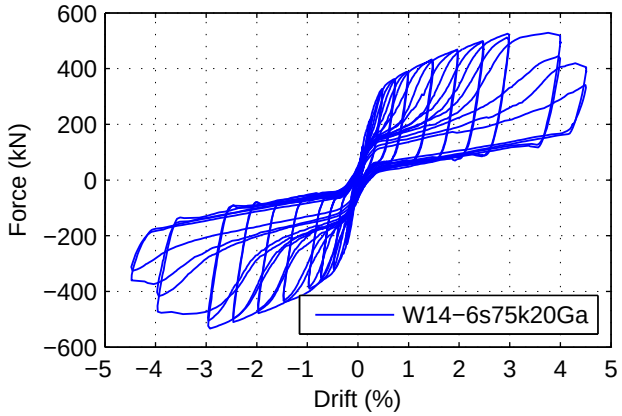

Figure 4.48: Actuator force vs. drift response of W14-6s75k20Ga

shown in Fig. 4.49, with one tear forming along the north end of the bottom HBE clamping bar and another diagonal tear forming in the northeast corner of the first story web plate. The diagonal tear was initiated by a kink or fold (similar to Fig. 4.24) forming in the web plate at that location. The tears formed and propagated most rapidly along the top and bottom HBEs with some minor tearing along the middle HBE and VBEs. The test was ended after two cycles of loading at 4.5% drift, at which point the entire web plate was torn through along the top HBE. The specimen strength was reduced to 83% and 63% of the peak strength during the second cycles of loading at +4% and +4.5% drift, respectively, due to web plate tearing.

4.3.9.1 Summary of observations

For comparison, Table 4.3 provides several performance parameters described in the previous section. These parameters include: the drift at which certain damage states are first observed, the peak strength and associated drift, and the specimen strength (normalized by the peak strength) and maximum drift during the last cycle of loading. The key damage states documented here include first observance of web plate tearing, $DS_{tear,i}$ (corresponding to DS9 in Baldvins et al. [2010]) and first observance of a tear propagating along an entire HBE or VBE edge, $DS_{tear,u}$. Note that in none of the tests was any boundary frame or PT yielding observed. Also note that the test of W18-8s100k16Ga was terminated prior to the observance of web plate tearing due to PT wire fracture. The wire fracture was due to reuse of the PT strands for numerous tests as described in Clayton et al. [2012c] and is not believed to be of concern in actual SC-SPSW applications.

4.4 Data Corrections

All of the raw data from each experiment was first cleaned by removing data points when the load protocol was paused and by removing data where the instrument either had a faulty signal or had fallen off. Before testing all potentiometer, LVDT, and actuator load cell readings were reset to zero. When a potentiometer fell off or was moved during testing, the faulty data was removed, and the new potentiometer readings after re-placement of the instrument were corrected to account for the new initial offset of the device.

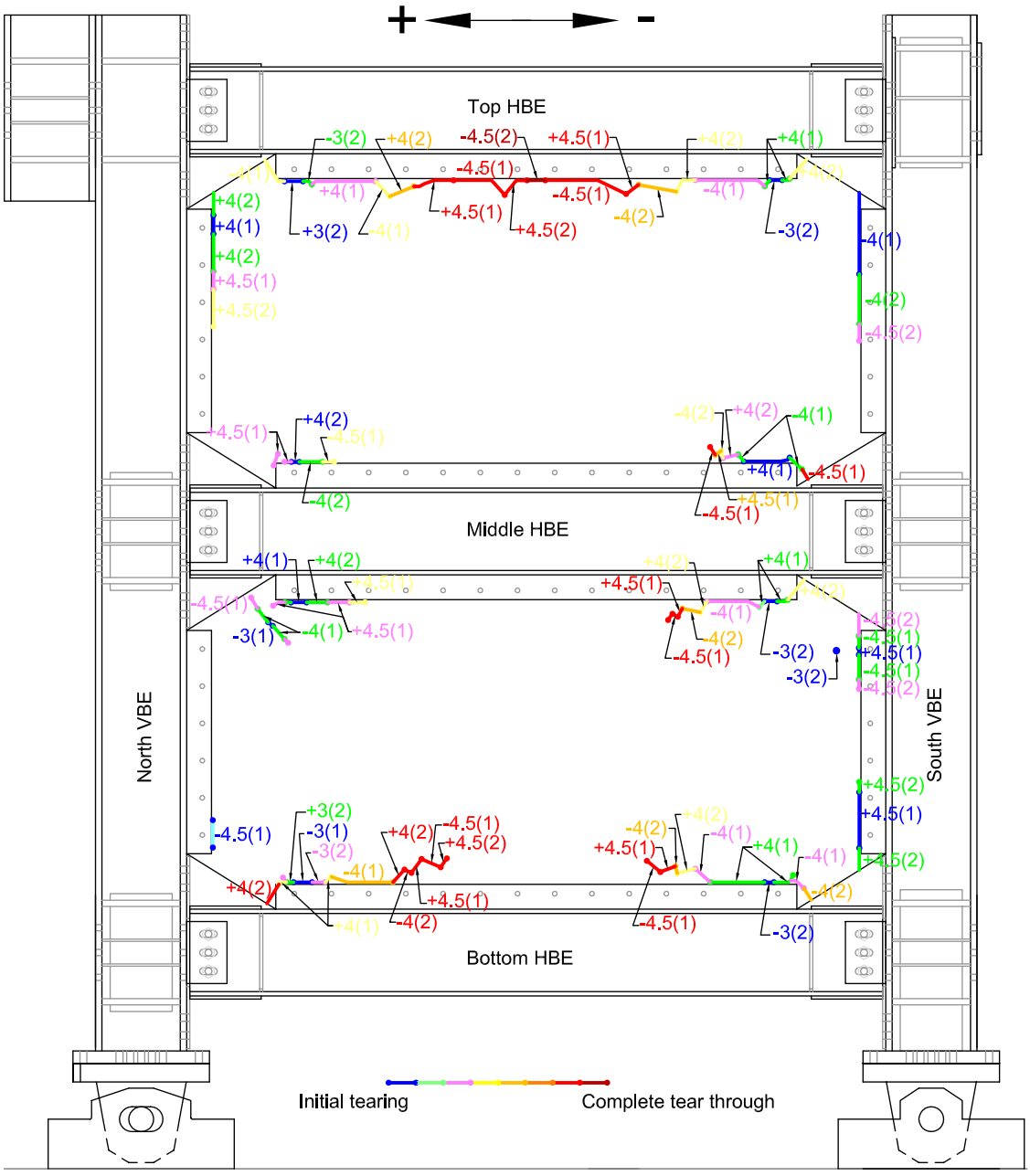

Figure 4.49: Schematic of progression of web plate tearing (W14-6s75k20Ga).

Table 4.3: Subassembly test damage observations

Specimen Name	Drift (%) $DS_{tear,i}$	Drift (%) $DS_{tear,u}$	V_{max} (kN)	Drift at V_{max} (%)	V_{end}/V_{max}	Max. Drift (%)
W18-8s100k20Ga	2.8	3.6	810	2.8	0.81	3.7^{+}
W18-6s75k20Ga	2.6	—	706	3.1	0.87	4.2
W18-6s75k16Ga	3.6	4.2	1102	3.7	0.73	4.7
W18-8s100k16Ga*	—*	—*	1064*	2.5*	1.0*	2.5*
W18-8s100k20Ga-2	2.9	4.4	833	3.8	0.81	4.4
W18-8s100k16Ga20Ga	2.4	—	1004	4.5	0.95	5.0
W18-8s100k20GaW	0.7	4.0	706	3.9	0.91	5.0
W14-8s100k16Ga	3.0	4.5	800	3.9	0.86	4.5
W14-8s100k16GaHBE	4.5	—	586	4.5	0.87	5.0
W14-8s100k20Ga	3.0	4.0	576	3.7	0.62	5.0
W14-6s75k20Ga	3.0	4.5	528	3.8	0.65	4.5

$^{+}$ Target drift was 4.5%. Actual drifts were less than target drifts due to controller scaling, which was corrected in later tests.
* Test was ended prematurely due to PT wire fracture [Winkley, 2011].

In some cases the actuator hydraulics had already been turned on prior to initiation of the DAQ system, resulting in a small load being applied to the specimen at the time of the zero reset. In these cases, the actuator load cell data was corrected with an initial offset. The initial offset was determined based on voltage readings taken from the actuator load cell when actuator hydraulics were turned on. In cases where accurate voltage readings were not available, the actuator load cell data was offset such that the envelope of the force response was symmetric for drift values of opposite signs.

The strain gage and PT load cell readings were set to zero before post-tensioning of the PT strands. Post-tensioning often occurred several days prior to testing. During the time between post-tensioning and testing, the strain gage readings often had some drift or periodic fluctuation associated with daily temperature cycles[1]. In several cases, there were

[1]All strain gages placed on the boundary frame and web plates were two-wire gages in a quarter-bridge circuit as previously described. Although the strain gage backing material is designed to compensate for thermal expansion of the specimen, temperature-induced resistance changes in the lead wires can result in fluctuation of voltage, and thus, strain readings. Three-wire strain gages compensate for this thermal resistance fluctuation and provide an increased measurement sensitivity compared to two-wire gages [Mic,

also some sudden jumps or offsets in the strain gage data that might have been caused by movement of the strain gage lead wires where they connected to the data acquisition (DAQ) system. These jumps most often occurred during specimen fabrication and were not prevalent during the actual test. Because the thermal drifts were not the same for each gage[2] and because the gages showed phantom jumps in the readings due to sudden lead wire movement, the initial readings just prior to testing may not have been representative of the actual strain state.

Figs. 4.50 and 4.51 show examples of strain gage reading fluctuation over time. Fig. 4.50 shows the axial and moment demands calculated from each strain gage section (calculation methods to be discussed later in Sec. 6.2.3) in the middle HBE of specimen W18-6s75k after the PT strands were post-tensioned and before testing took place. The location of each section from the North end of the HBE is indicated in the legend. These readings were taken over the weekend when there was no work being done on the specimen. In this figure, the cyclic 24-hour periodic fluctuation of the readings are due to temperature fluctuation. The range of fluctuation in calculated axial force can be upwards of 50% of the initial PT force and is not the same for each strain gage section. Also, the strain gage section at x=2045mm is an example of a phantom jump in strain gage reading causing a jump in calculated axial and moment demand between hours 36 to 42. The cause of this jump is unknown but is related to electrical circuitry and not an physical change in HBE demands.

Similarly, Fig. 4.51 shows another example of the axial demands calculated from the strain gage readings for the middle HBE in specimen W14-8s100k16GaHBE for a week-long period after PT strand post-tensioning, during installation of the web plates (approximately during hours 48 through 79), and over a weekend (approximately during hours 79 through

---

2010]; however, three-wire gages were not used in these test due to limitations in number of DAQ channels and availability. Since temperature fluctuation during the duration of the test was not substantial, the temperature-induced strain measurement fluctuation was ignored.

[2]In a two-wire strain gage the resistance in the lead wires can change as much as 22% for a 100°F temperature change [Mic, 2010]. When placed in a 120-ohm quarter-bridge circuit, as was used during testing, a 10°F change in temperature in the lead wires can create a 156 microstrain change in strain reading due to changes in lead wire resistance (i.e. the change in strain gage reading is not due to any thermal expansion of the specimen). This change in strain due to resistance fluctuation in the lead wires can result in a phantom 7.7 ksi (0.03 GPa) change in stress in steel [Mic, 2010]. With longer lead wires, as were used in testing, the lead wires are more prone to temperature change and change in lead wire resistance.

140) prior to testing. Again, this figure shows the 24-hour periodic fluctuation in calculated axial forces while the specimen is sitting at rest without significant disturbance from people walking around the specimen (most notably during hours 0 through 48 and 79 through the end). The phantom jumps in readings, most notably in the section located at x=2045mm between hours 48 through 79, are most likely due to disturbance of the lead wires as the web plates were being installed. These phantom jumps due to wire disturbance can be very large and not representative of any real loading. However, during testing disturbance of the wires was minimal, and phantom jumps of this magnitude were not be present during testing.

Figs. 4.50 and 4.51 are typical of all specimens and HBEs prior to testing and also represent strain gages on specimens with both W18 and W14 HBEs. The W18 and W14 HBEs used different strain gages, and the strain gages were connected to different channels in the DAQ system. The fact that readings in both HBEs had similar fluctuations and phantom jumps indicate that these variations are due to inherent uncertainty in the 2-wire quarter-bridge circuit used in the DAQ system and not a problem with particular strain gages or data channels. The uncertainty in strain gage readings due to these fluctuations should be considered when analyzing results derived from strain gage readings in later sections.

To account for the presence of these artificial changes in strain readings prior to testing, the strain gage data was often analyzed as a change in strain from the beginning of the test. More details will be given in how the strain gage data was used to determine axial force and moment demands below.

The PT load cells were fabricated at UW SEL using three-wire strain gages and did not exhibit the temperature-induced fluctuations as observed in the two-wire strain gage readings. However, there were a few instances where a load cell reading would jump to an impossibly large load reading or the signal would become completely saturated. This problem was believed to be due to poor electrical connection between the PT load cells and the DAQ system. The few cases of PT load cell malfunction tended to occur later in the testing program. The deterioration in the PT load cell-to-DAQ connection quality was due to wear-and-tear from having been used in numerous SC-SPSW tests and other test

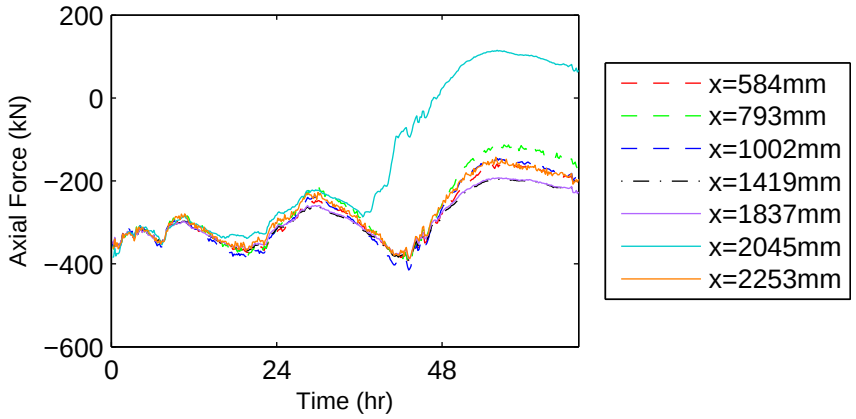

(a)

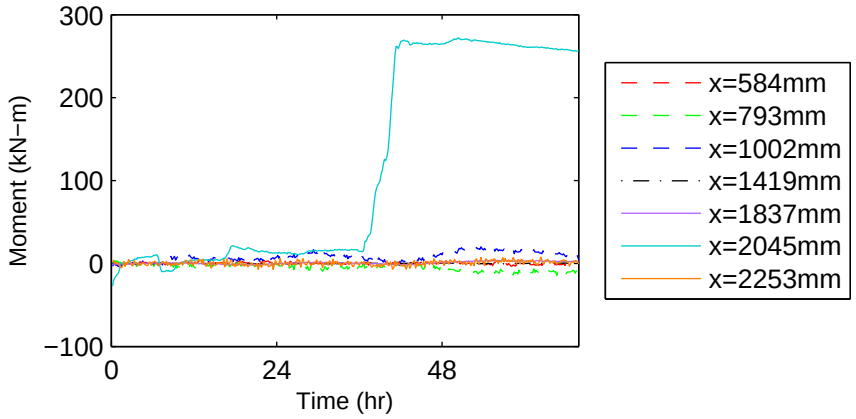

(b)

Figure 4.50: (a) Axial and (b) moment demands calculated from strain gages of W18-6s75k after PT post-tensioning and before testing.

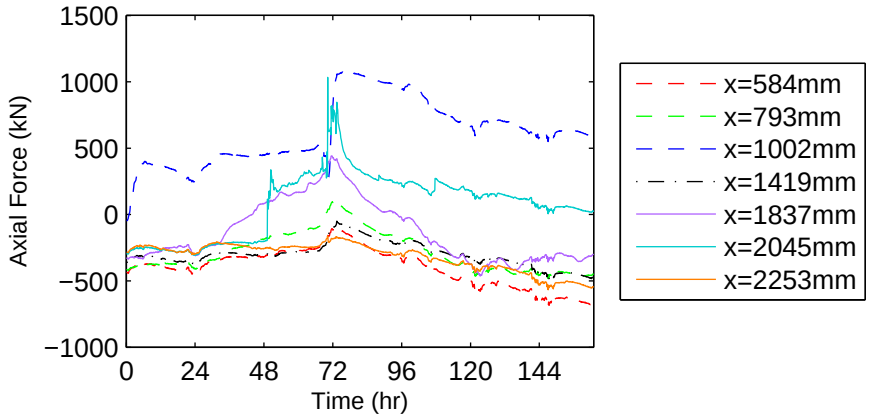

Figure 4.51: Axial force demands calculated from strain gages of W14-8s100k16GaHBE after PT post-tensioning, during web plate installation, and before testing.

programs in the laboratory.

Because of the symmetric nature of the PT layout, all PT strands are theoretically supposed to have the same force if the gap rotation at both ends of the HBE are equal. This was generally true throughout the tests; therefore, when a PT load cell malfunctioned, the faulty data was replaced with the median PT value from all other load cells at that particular HBE. The total PT force at that HBE was approximated as the sum of all functioning load cells and the replacement median PT force data for the faulty load cell. Using this method to determine total PT forces did not have any apparent affect on PT force responses.

4.5 Summary of Subassembly Testing

A two-story SC-SPSW subassembly was tested under quasi-static cyclic loading to investigate SC-SPSW response and intermediate HBE and PT demands. Multiple tests were conducted to investigate the effects of various parameters including: web plate thickness, t_w; number of PT strands, N_s; initial PT force, T_o; HBE depth, d; load protocol; bolted and welded web plate-to-fish plate connection details; and web plate-to-boundary frame connection configurations. The results of these tests include:

- The force vs. drift response of the specimens matched well with the assumed idealized SC-SPSW and PT frame behavior, including high initial stiffness, energy dissipation provided by the web plates, and unloading along a bilinear path to minimize displacements at zero force. The experimental response differed from the idealized response in two distinct ways: (1) the web plate was able to resist load prior to reaching the peak plastic strain of the previous cycles, and (2) unlike the assumed tension-only web plate behavior, the web plate did provide some resistance during unloading, termed web plate residual strength. Both of these observations result in more energy dissipation in the web plate than assumed in the idealization; however, the web plate residual strength may impact SC-SPSW recentering capabilities and should be investigated further.

- Most specimens were subjected to drifts of at least 4% before the web plate tearing propogated along an entire edge. Even after significant web plate tearing the specimens retained a large percentage of their peak strength (often more than 80% of peak strength) up to drifts of 4.5 and 5%. The large strength after extensive web plate tearing is partly due to the distributed load path and redundant nature of the web plate and partly due to the increasing strength of the elastic PT boundary frame.

- The bolted web plate-to-fish plate connection detail was able to transfer web plate forces to the boundary fame as intended. Initial web plate tearing was typically first observed in the specimens with the bolted web plate connection detail around 2.5 to 3% drift, while the specimen with the welded web plate connection detail had initial tearing at 0.75% drift. However, the peak strength of specimens with both connection details were similar up to approximately 2% drift, within the expected design-level drift demands.

- Web plate tearing in the bolted web plate connection detail typically occurred along the edge of the clamping bars and was believed to be due to out-of-plane bending of the web plate as the buckles formed in both directions of loading. There was some slip of the web plate at the ends of the clamping bars where the web plate strains

were highest, due to the PT connection gap opening; however, the extent of the slip was typically outside of the outermost bolt in the slip-critical connection, and was not believed to result in significant strength reduction.

- The PT connection decompression was affected by the presence of uneven bearing surfaces in the boundary frame due to fabrication tolerances. The use of sheet steel shims welded to the VBE were able to reduce the presence of the initial gap between the HBE flange and VBE bearing surface. Care should be taken in SC-SPSW construction to ensure all HBE flanges are bearing equally on the VBEs in the initial configuration to ensure that the connection behaves with the expected bilinear response and high initial stiffness.

- Connecting the web plates to the HBEs only delayed the initiation of and significantly reduced the extent of tearing in the web plate. Releasing the web plate from the VBEs eliminates the localized strains in the web plate near the corner cutouts and the horizontal strains in the web plate associated with PT connection gap opening and frame expansion. It also eliminates the additional HBE axial force due to web plate pull-in of the VBEs, $P_{HBE(VBE)}$. The lateral strength provided by the web plate connected only to the HBEs was reduced (compared to a web plate connected to HBEs and VBEs) due to the development of partial tension field action [Thorburn et al., 1983].

Chapter 5

FULL-SCALE TESTING

5.1 Introduction

A full-scale, two-story SC-SPSW was tested at the National Center for Research on Earthquake Engineering (NCREE) in Taipei, Taiwan. This test was conducted as part of a two-specimen SC-SPSW test program at NCREE. The two specimens were (1) a specimen with PT HBE-to-VBE connections that rock about both flanges as described in previous sections of this document, which is the focus of the author's research, and (2) a specimen with PT HBE-to-VBE connections that rock about the top flange only [Dowden and Bruneau, 2011], which is the focus of a collaborative Ph.D. researcher at the University at Buffalo (UB) and will therefore not be discussed in this document. The specimens were loaded pseudo-dynamically to investigate the SC-SPSW system performance at three different seismic hazard levels. These specimens also investigated application of the PT column based connection detail in SC-SPSW construction. An overview of the prototype building, test set-up, specimen description, and experimental observations will be presented here.

5.2 Prototype Building

For comparison with previous analytical "proof-of-concept" studies on SC-SPSWs done as part of the author's Master's thesis [Clayton, 2010; Clayton et al., 2012b], the prototype building for the full-scale test at NCREE was selected to be based on the three-story SAC building [Gupta and Krawinkler, 1999] located in Los Angeles, California. Due to space limitations and existing test set-up and lateral bracing apparatus at NCREE, the height of the full-scale specimen was limited to two stories; therefore, the prototype building was taken to be the bottom two stories of the three-story building considered in the previous study by Clayton [2010].

The two-story prototype building had uniform story heights of 3.96 m. The building

plan dimensions were 36.6m-by-54.9m with bays of 9.1m-by 9.1m [Gupta and Krawinkler, 1999] (Fig. 5.1). The seismic mass of each floor was taken as 9.56x10^5 kg (based on the floor-level mass in Gupta and Krawinkler [1999]), for a total building seismic weight of 18,560 kN. An importance factor, I, of 1 was assumed. A seismic force reduction factor, R, and overstrength factor, Ω_o, of 7 and 2, respectively, were assumed corresponding to that of conventional SPSWs [ASCE, 2005]. Previous numerical analyses [Clayton, 2010] have shown these values to result in adequate SC-SPSW performance; however, they have not been investigated using modern procedures such as those in FEMA [2009]. The target spectral accelerations for the Los Angeles location [Somerville et al., 1997] are shown in Table 5.1. As suggested by Somerville et al. [1997], the 10% and 2% in 50 year hazard levels were assumed to approximate the design basis and maximum considered earthquakes (DBE and MCE, respectively) for this site. These target spectral values are based on United States Geological Society (USGS) mapped values at the time of the Somerville et al. [1997] report.

Table 5.1: Target Spectral Accelerations for Los Angeles location for Soil Type S_D for 5% Damping Level (from Somerville et al. [1997])

	Period (sec)			
Hazard Level	0.3	1.0	2.0	4.0
50/50	0.514	0.288	0.149	0.069
10/50	1.070	0.680	0.330	0.123
2/50	1.610	1.190	0.540	0.190

The design spectral response acceleration parameters, taken as those for the 10% in 50 year hazard level as previously described, were 1.07 and 0.68 for the short (0.3 sec) period, S_{DS}, and 1 sec period, S_{D1}, respectively. The seimic base shear for the prototype building, $V_{protoype}$, was calculated to be 2,870 kN per ASCE [2005].

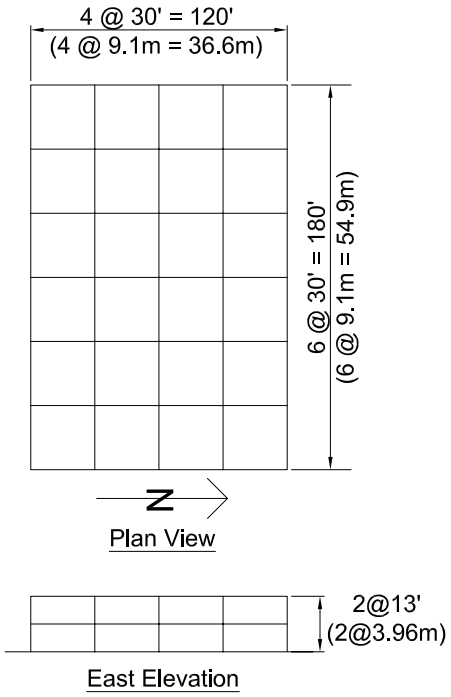

Figure 5.1: Plan and elevation of prototype building

5.3 Test Set-up

5.3.1 Specimen description

The specimen was a roughly full-scale, two-story SC-SPSW as shown in Fig. 5.2. The specimen dimensions and loading were similar to previous SPSW tests [Li et al., 2010] at NCREE such that the same lateral bracing frame could be used without significant modifications. Similar to those described in the previous subassembly tests, the PT HBE-to-VBE connections rock about both flanges; thus, the specimen was termed Specimen FR for "Flange Rocking". The middle beam (MB) and top beam (TB) both utilized the PT HBE-to-VBE connection shown in Fig. 5.2 (Detail 1/FR) to provide system recentering. More detailed drawings of the specimen can be found in Appendix A.1. Two seven-strand bundles of 15 mm (0.6") diameter, Grade 270 PT strands were extended from outer flanges of the west column (WC) to the east column (EC). The target initial PT force for the PT elements in both the MB and TB PT was 30% of yield (approximately 990 kN total initial force in each beam). Shear forces were transfered from the HBEs to the VBEs via horizontal slotted hole shear tabs, similar to the connections described in Sec. 4.2.

To prevent plastic hinges from forming at the base of the column [Li et al., 2010], which can be costly to repair and can cause permanent residual deformations in the building, and to provide additional recentering forces, a PT flange rocking column base detail (shown in Fig. 5.2) was utilized. Similar to the HBE-to-VBE connections, the PT column base is allowed to rock about both flanges. The shear forces at the column base are transfered to the foundation via built-up and stiffened angles, termed shear brackets, connected to the base pedestal via slip-critical bolts. A semi-circular steel bumper was welded to the VBE flanges to provide a contact surface to transfer these shear forces while still allowing the VBE to rotate and uplift freely. VBE uplift and recentering forces are transfered via two 69 mm diameter high-strength threaded bars placed on either side of the web of each VBE. The target initial PT force in each bar was 25% of yield (or approximately 1300 kN per threaded bar). The PT bars were anchored at the base pedestal (Fig. 5.2 Detail 2/FR) and 720 mm above the centerline of the MB (Fig. 5.2 Detail 3/FR). The length of the PT bars was determined based on limitations of the load cells used to measure forces in the PT bars.

To keep the PT bar forces under the 200-ton load cell capacity at large drifts, the PT length was increased to reduce its axial stiffness, thus the PT bar forces were expected to remain well below yielding. In a real building, the vertical PT can be shorter and could also be extended into the basement level of the building, allowing the vertical PT anchorage in the VBE to be placed farther away from the congested PT HBE-to-VBE connection regions, which would further simplify detailing of the column post-tensioning anchorage.

Due to the shear brackets restraining frame expansion at the column base, a PT HBE-to-VBE connection was not desirable at the bottom beam (BB) since this would introduce significant axial loads in the HBE and would reduce the recentering contribution as the PT connection gap opening would be restrained. Instead, the BB was connected to the columns via bolted-bolted double-angle connections intended to allow the connection to rotate without development of significant connection moments. The bolted angles were also intended to be easily replaceable in the case of angle yielding due to large connection rotations during a severe earthquake.

Specimen FR was loaded by two 1000 kN servo-hydraulic actuators connected to the west column (WC) at the location of the TB as shown in Fig. 5.3. The force from the two actuators was trasferred to the WC via a load transfer beam (orange beam in Figs. 5.3 and 5.4). Due to the single-point actuator loading at the TB-level, web plates in both the first and second stories were the same thickness of 2.7 mm. The web plate steel was a low yield strength (LYS) steel with a yield strength of approximately 208 MPa (LYS225 classification). The web plate was connected to the boundary frame via a welded web plate-to-fish plate connection with a single fillet weld along the edge of the web plate. Radial cutouts with a radius of approximately 400 mm were provided in the corners of the web plates to reduce the tensile strain in the web plate corners as the PT connection gap opens. A radial cutout, as opposed to the diagonal cutouts used in the previously described subassembly tests (Sec. 4.2), was also employed to mitigate initiation of web plate tearing by reducing the tensile strains at the end of the weld.

The LYS web plate material was provided by China Steel Corporation. The W-shapes used in the boundary frame were donated from the American Institute of Steel Construction (AISC). The W-shapes were manufactured in the US and shipped to Taiwan via container

ship. The shipping company used to ship the steel was World Cargo International, based out of Tukwila, WA. All other steel plates, bolts, PT strands and bars were provided by suppliers in Taiwan.

It should be noted that because the boundary frame members were being shipped from the US to Taiwan and because the availability of LYS plate being donated from China Steel was dependent on current stock at the time of the order, the boundary frame member design was finalized prior to knowing the exact thickness and strength of the web plate. For this reason, the boundary frame was capacity designed (according to the procedures detailed in Clayton [2010]) for a web plate yield strength of approximately 220 MPa and a thickness of 3.2 mm (approximately 20% greater than the thickness of the web plates used in the test) to provide an upper bound for the expected web plate demands. Therefore, the boundary frame and associated connections (e.g. design shear forces at the PT connections) are conservative for the actual web plates used in the test.

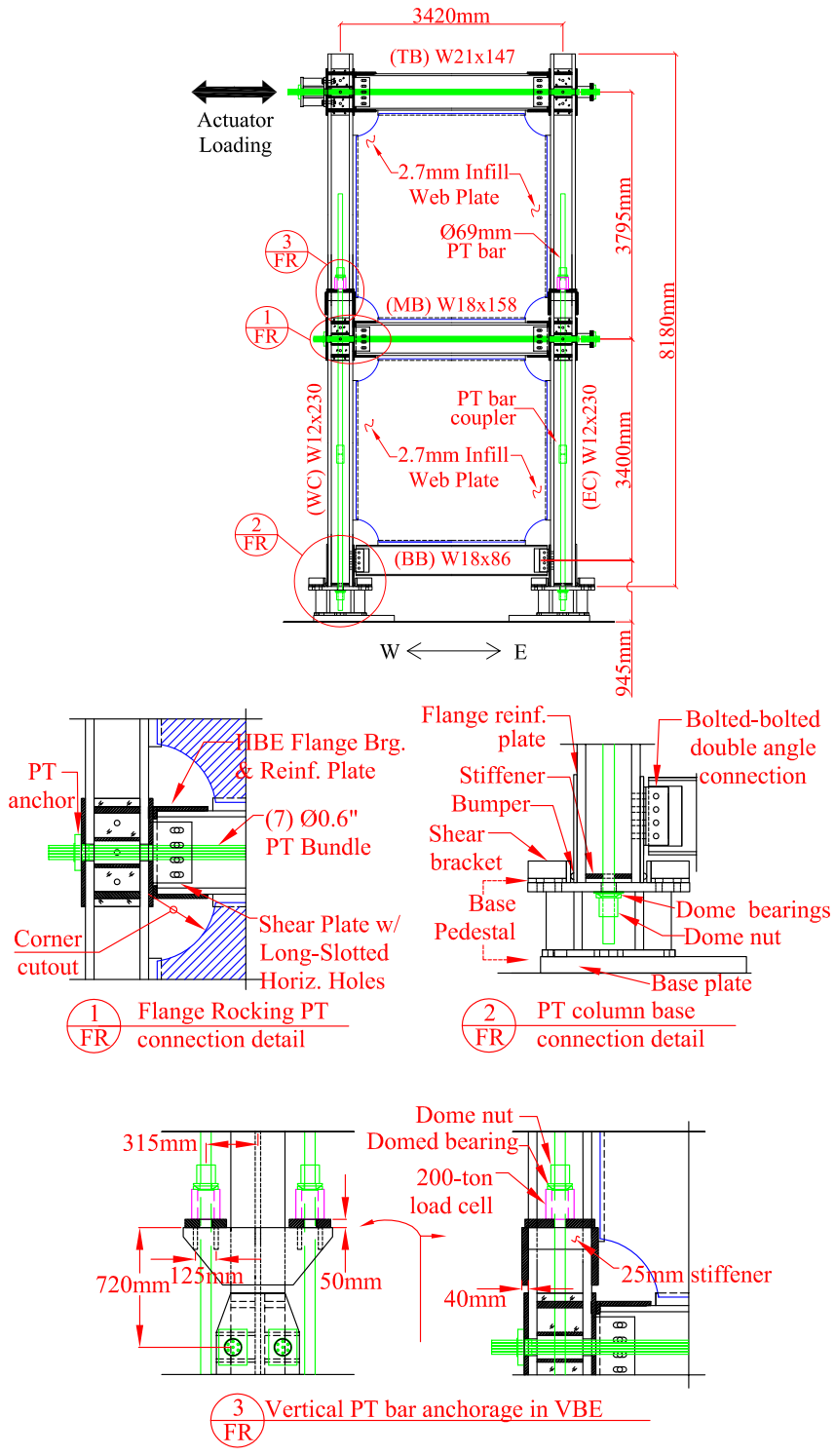

Figure 5.2: Elevation and details of Specimen FR

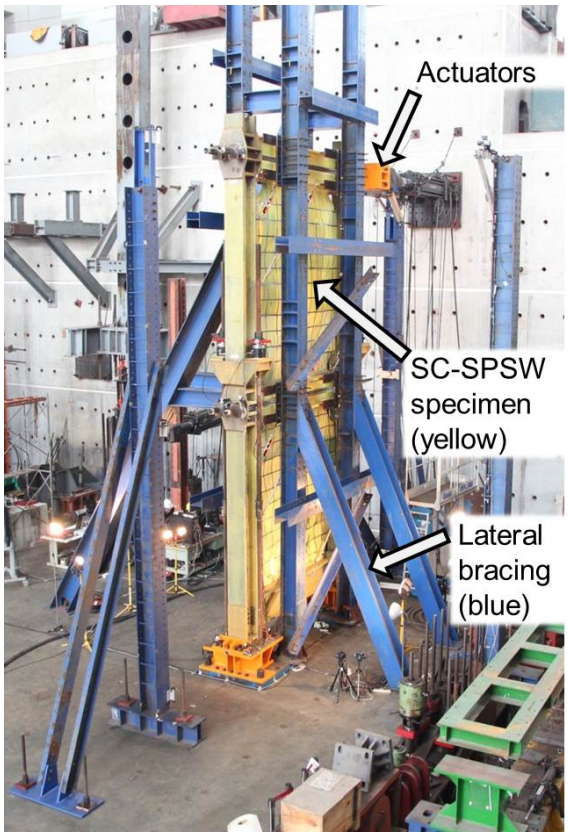

Figure 5.3: Photo of Specimen FR setup

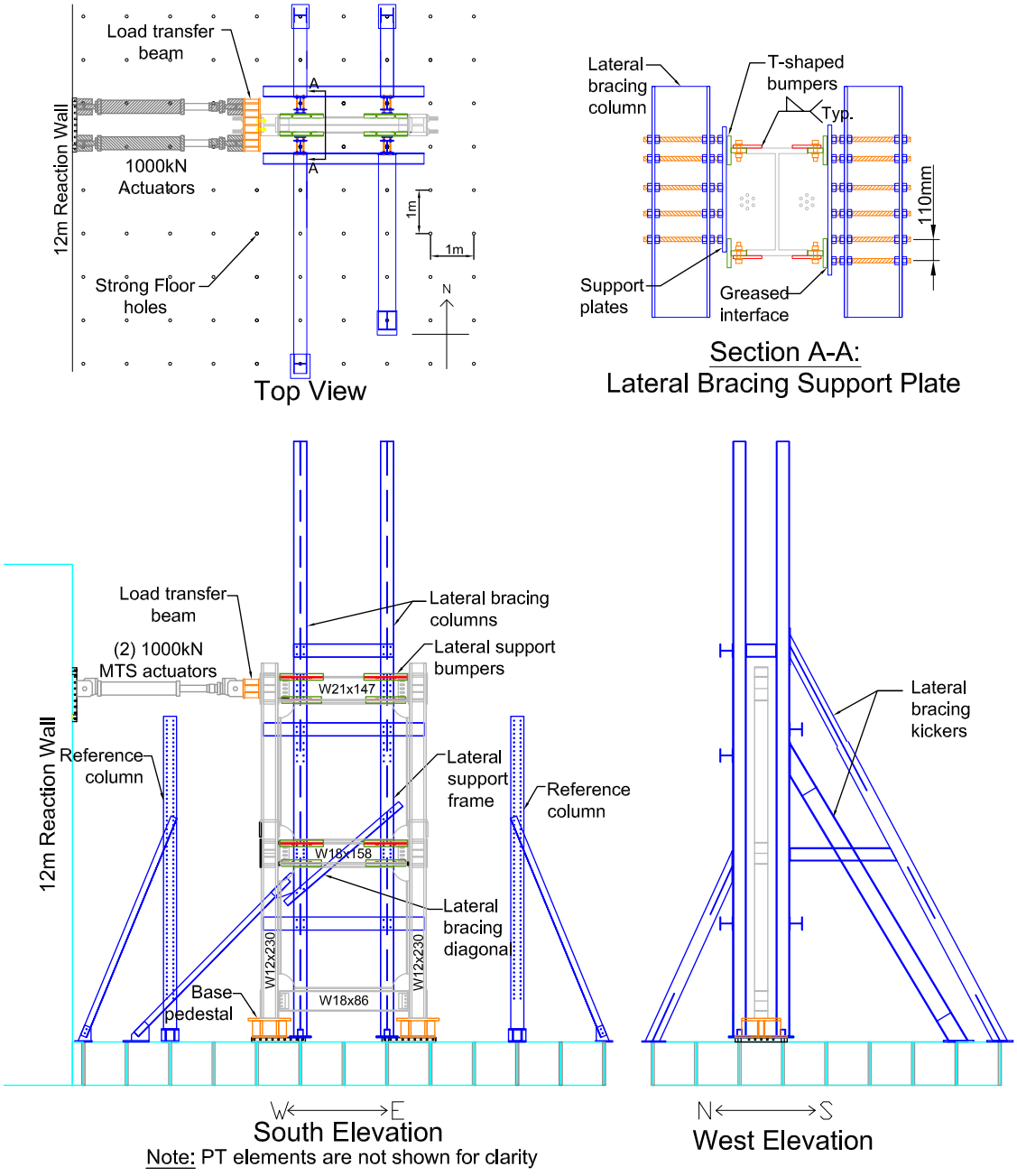

Figure 5.4: Elevation and plan schematic drawings of lateral bracing and loading system.

5.3.1.1 Lateral bracing

A lateral bracing frame, shown in Fig. 5.3, was constructed on the North and South side of the specimen to prevent out-of-plane motion. Greased steel plates were mounted to the columns of the lateral bracing frame. These sliding plates were in contact with T-shaped bumpers that were bolted to the edged of the MB and TB flanges approximately 470 mm from the HBE ends. The outer surface of the bumpers were greased to minimize friction in the bumper-to-sliding plate interface as the specimen was loaded. The T-shaped bumpers and sliding plates can also be seen in Figs. 5.8(b) and 5.14 in the following section of this document.

5.3.1.2 Construction sequence

The specimen was constructed on the ground in the horizontal plane (i.e. in the plane of the floor). The beams and columns were first laid out in the correct locations, with the beam and column centerline and story diagonal dimensions being measured to match those specified in the construction drawings. Threaded rods with a diameter of 39 mm were installed in the location of the beam PT strand holes, and a small pre-tensioning was applied to the rods to ensure that the beam ends were in contact with the columns before installation of the web plates.

Because the available web plate material did not come in sizes large enough to fill the entire clear story, three pieces of web plate material were butt-welded together, termed a seam weld, to form one continuous web plate. The seam welds ran from beam to beam in the vertical direction and were located at approximately one-third of the entire web plate width. The radial corner cutouts were cut out of the web plates prior to installation. In order to lift the web plates in the horizontal plane (parallel to the plane of the floor) with the crane and to prevent web plate sagging due to self-weight, steel stiffeners were tack welded to the web plate, running from column-to-column as shown in Fig. 5.5. The web plates were then put into place, laying on top of the fish plates. The web plates were welded to the fish plate, and the tack welded stiffeners were removed. Then the 39 mm threaded rods were removed.

Figure 5.5: Web plates being put into place in the horizontal plane

After the web plates were welded to the boundary frame, the strain gages were installed on the specimen. The PT strands, load cells, and anchors were installed in the middle and top beam. Technicians from Dywidag-Systems International (DSI) used monostrand hydraulic jacks to stress each PT strand individually. Because the load cells could only record the force of each seven-strand PT bundle, the stressing was done in stages to prevent overshooting of the target load. Each strand was stressed up to the same hydraulic jack pressure. The strands were stressed in a symmetric pattern, alternating strands on the north and south side of the beam web and alternating the location of the strand within the bundle. The target hydraulic pressure for the second round of stressing was based on the pressure and related PT bundle force from the previous round. Each strand was stressed again to the target hydraulic pressure, then small stresses were applied symmetrically to individual strands until the target initial PT force was met.

After beam PT stressing, the bolts in the slotted shear tabs were tightened to snug tight conditions. Painter's tape was applied to the web plates to form the 25 cm-by-25 cm grid spacing, and the web plates, middle beam, and top beam were whitewashed. The T-shaped bumpers were bolted to the middle and top beams. The specimen was then lifted into the vertical plane with a crane and was put into place on top of the base pedestals. The vertical PT bars and lateral bracing frames were then put into place, but the sliding plates on the lateral bracing frame were not put in full contact with the specimen. The shear brackets at

the base of the columns were tightened using a pneumatic torque wrench.

The domed bearings, load cells, and anchorage nuts were installed on the vertical PT bars. The PT bars were tensioned simultaneously using four hydraulic rams connected to the same hydraulic pump. The PT bars were each tensioned to the target initial PT force. After this, the sliding plates on the lateral bracing frame were tightened to be in contact with the T-shaped bumpers connected to the specimen. Then the columns and bottom beam were whitewashed, and the remaining instruments (to be discussed later) were attached to the specimen.

5.3.2 Instrumentation

Displacement transducers and string potentiometers were used to measure global and local deformations of the specimen and its components (Fig. 5.12). String potentiometers (SP) (shown in Fig. 5.6) measured the displacements of the WC and EC at the location of the MB and TB centerlines with the exception of the WC at the TB. Here, a temposonic sensor (Tempo) was used to measure the WC displacement at 120 mm below the TB and actuator centerlines (7475 mm above the VBE base) as shown in Fig. 5.7. The high accuracy and high resolution temposonic sensor (manufactured by MTS) was used at this location as it was used to control the displacement-controlled loading of the specimen (to be discussed later). SPs were also located at the top of the base pedestals to measure deformation and slip in the base pedestal and to serve as a reference for the location of the "foundation"-level. All SPs were manufactured by Intertechnology, Inc.

Displacement transducers (DT) were placed on the insides of the HBE flanges at both ends of the HBE to measure double-angle connection rotations at the ends of the BB as shown in Fig. 5.8(a). DTs were also placed on the outside of the HBE flanges at the MB and TB to measure PT connection gap rotation at these locations (Fig. 5.8(b)). Similarly, DTs were placed on the south side of the VBE flanges to measure the column base PT connection rotations as shown in Fig. 5.9. DTs were installed diagonally from VBE flange to HBE flange at four locations in both diagonal directions of each story (Fig. 5.10). These DTs were oriented at approximately 45° to obtain an approximate measure of the strain

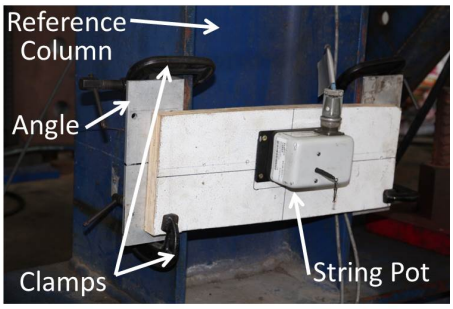

Figure 5.6: String potentiometer attached to reference column

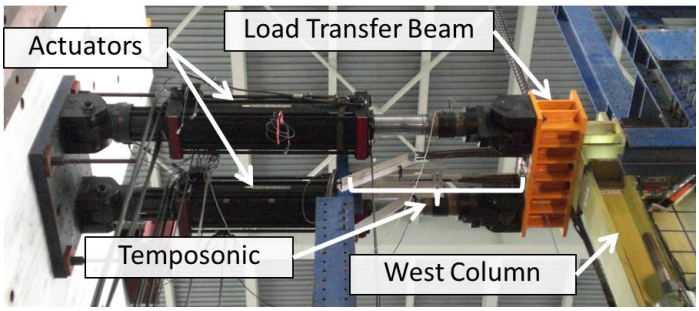

Figure 5.7: Actuators and temposonic

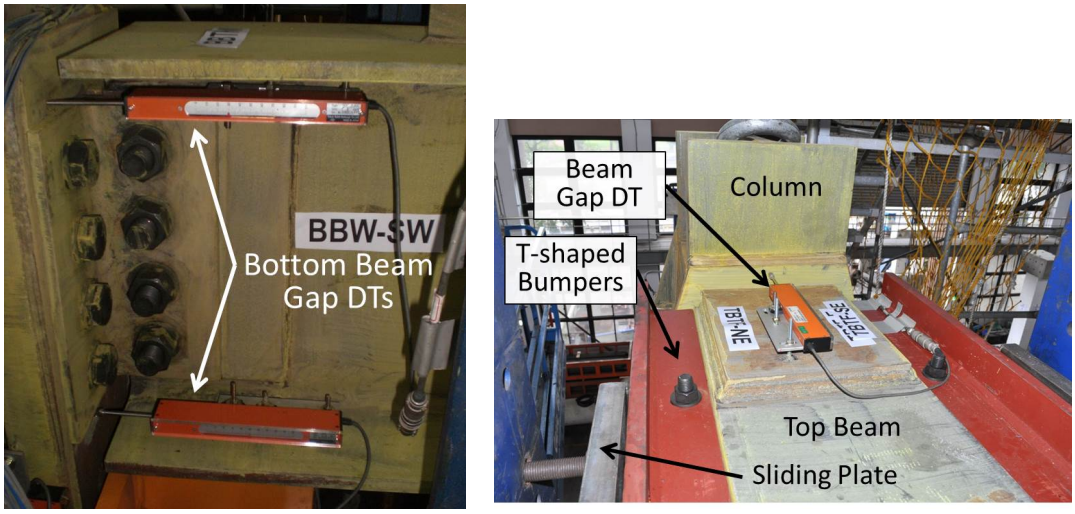

(a) (b)

Figure 5.8: Displacement transducers to measure (a) BB double-angle and (b) TB PT connection rotations

in the web plate at these locations. DTs were also located at critical interfaces such as the shear bracket-to-base pedestal (Fig. 5.11(a)), load transfer beam-to-WC, and the base pedestal-to-base plate (Fig. 5.11(b)) interfaces to measure potential slip. All DTs were manufactured by Tokyo Sokko Kenkyuojo Co., Ltd.

Strain gages were used to measure the demands in the boundary frame elements. At certain locations along the frame elements, termed strain gage sections, four strain gages were located on the inside of the flanges on either side of the web. Fig. 5.13 shows the locations of these strain gages and provides labels for key strain gage sections that will be discussed in further detail in later chapters. Five strain gage sections were located along the MB and TB with three being located within the extent of the web plate along the HBE, and two were placed in the PT HBE-to-VBE connection region where the web plate corner cutout was provided. A strain gage section was located at the middle of the BB, the location expected to have the largest demands. Three strain gage sections were also located in the WC and EC with two being placed at one-third and two-thirds of the clear story height and the other being located near the bottom of the VBE in the PT base connection region. As the boundary frame was expected to remain elastic, the strain gages sections

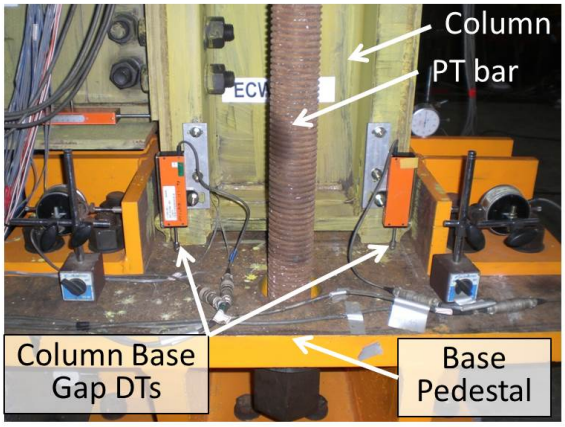

Figure 5.9: Displacement transducers to measure column PT connection gap opening

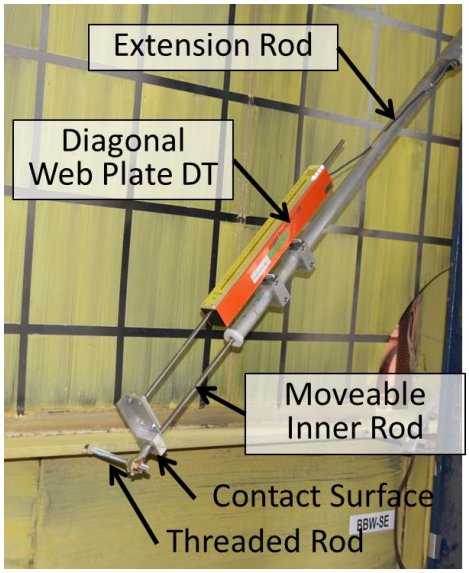

Figure 5.10: Diagonal displacement transducers to estimate web plate strain

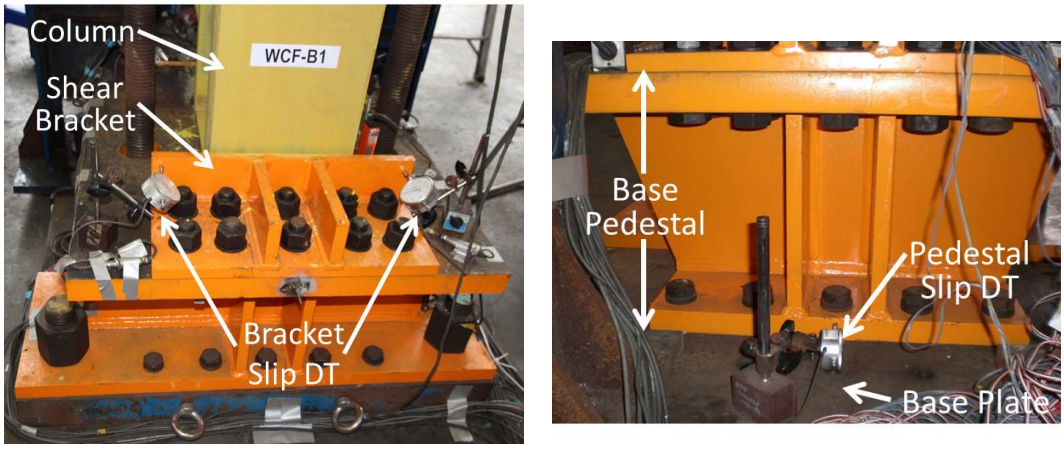

(a) (b)

Figure 5.11: Displacement transducers to measure (a) shear bracket and (b) base pedestal slip

were intended to determine axial force and moment demands in the members. All strain gages were three-wire YFLA-5-3LT uniaxial strain gages manufactured by Tokyo Sokko Kenkyuojo Co., Ltd.

Hollow-core load cells were used to directly measure the axial force in the PT threaded bars in the VBEs (shown in Fig. 5.14). Similarly, hollow-core load cells were used to measure the total axial load in each of the two PT bundles in the MB and TB (also shown in Fig. 5.14); here, the force in each individual strand was not measured, only the sum of all seven strands in the bundle. All load cells used to measure PT forces were 200-ton capacity. Each MTS actuator also housed load cells to measure the force being applied on the specimen.

The web plate and boundary frame were also painted with a "whitewash" to qualitatively indicate the presence of yielding in the steel. The whitewash was tinted with a yellow dye for the purposes of photographing the specimen. A 25 cm-by-25 cm grid of unpainted steel was also left on the web plates to aid in the visual observation of the diagonal buckles in the web plate.

All strain gage wires were connected to a strain gage panel (Fig. 5.15(a)) located on the floor beneath the specimen. The purpose of the strain gage panel was to combine

strain gage wires into fewer cords. The cords from the strain gage panel and from all SP, DT, and LC instruments were connected to a switch box (Fig. 5.15(b)) located near the data acquisition (DAQ) system. The switch boxes were connected to a Tokyo Sokko Kenkyuojo Co., Ltd. High-speed Data Logger THS-1100, which was then connected to the MTS FlexTest GT. The MTS Flextest GT output data from all instruments for each load step, as well as the displacement, velocity, and acceleration values used in each step of the pseudo-dynamic loading algorithm (described later). The MTS FlexTest also controlled the stationary camera system (described later) to take photographs at every fifth loading step. The Temposonic signal was input directly into the MTS FlexTest GT, as it was not compatible with the THS-1100 Data Logger.

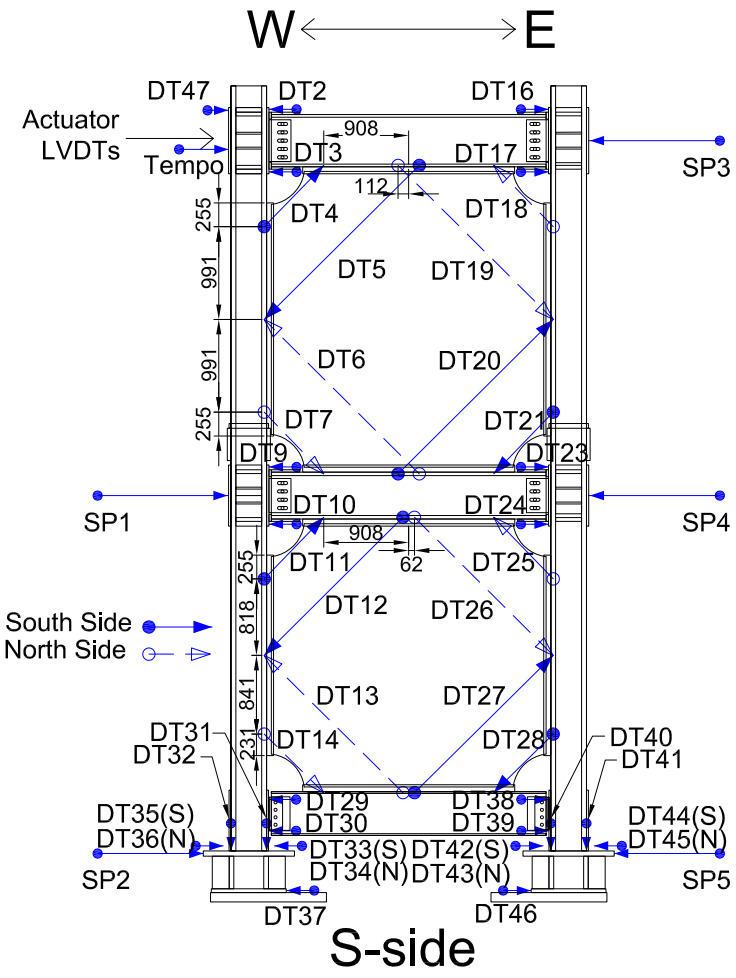

Figure 5.12: Displacement transducer and string potentiometer layout and naming (typical dimensions provided in units of mm)

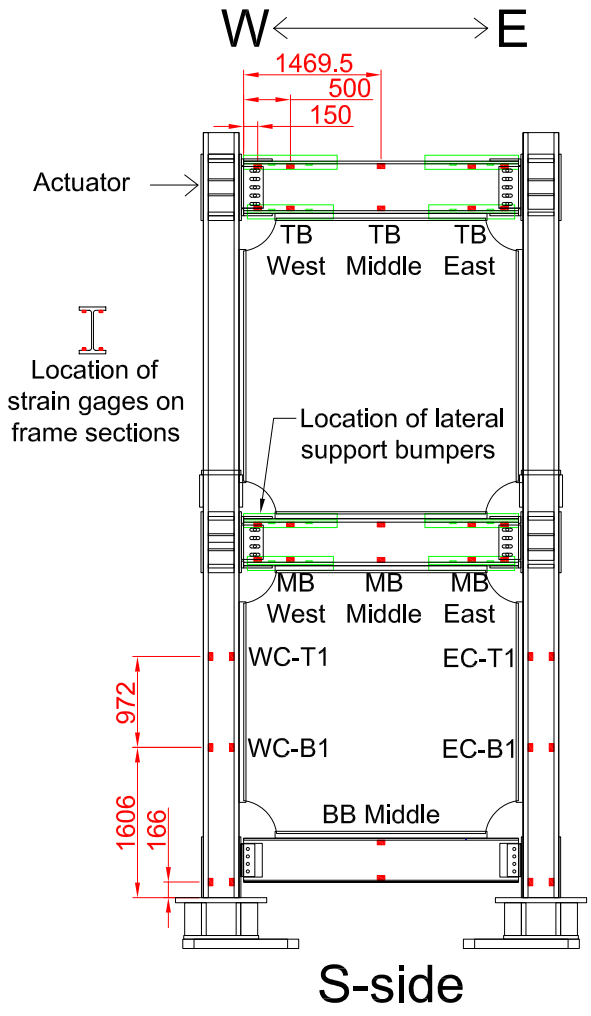

Figure 5.13: Strain gage layout (units are in mm)

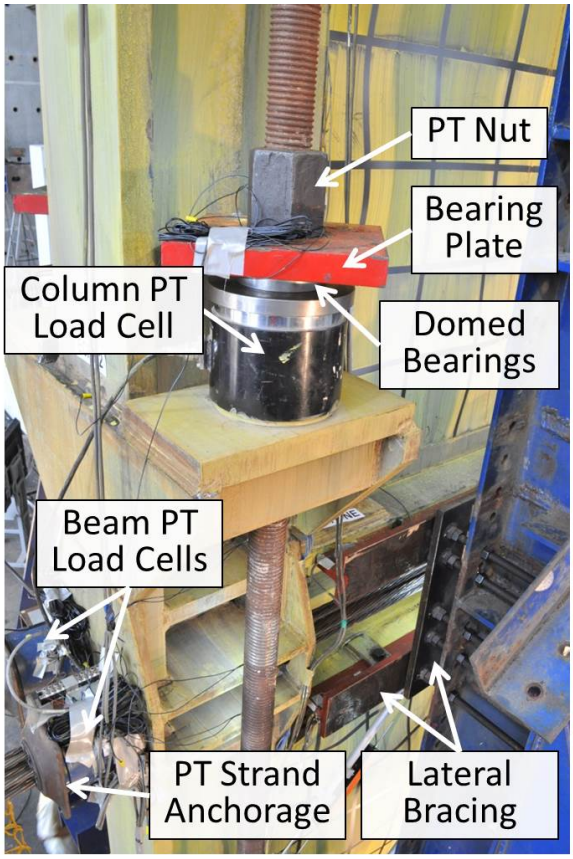

Figure 5.14: Load cells for beam PT strands and column PT bars

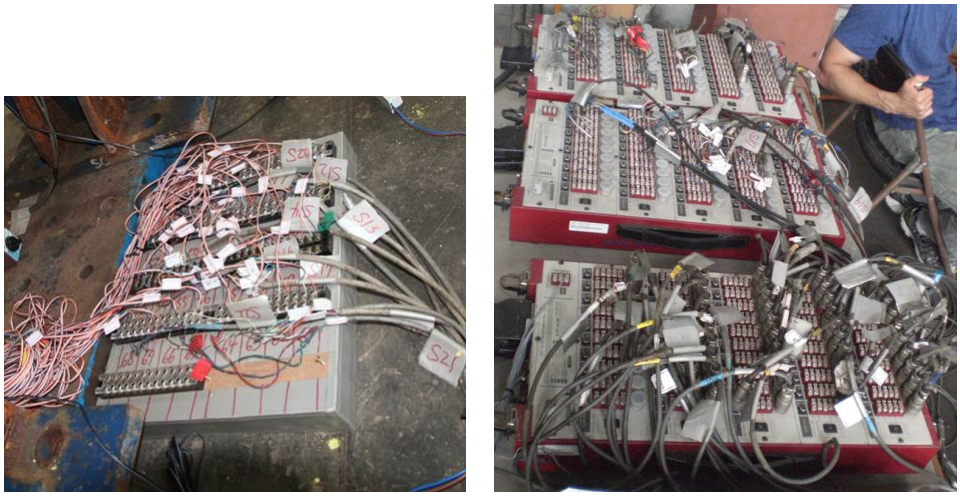

(a) (b)

Figure 5.15: (a) Strain gage panel and (b) switch boxes used to collect instrument data signals

5.3.2.1 Photo and video documentation

Still cameras and video cameras were used to provide continuous documentation of the test. The cameras were located to view critical locations within the specimen while also meeting constraints of camera availability, laboratory layout, and lateral bracing or other laboratory equipment obstructing the view. Based on these constraints the cameras were placed at the following locations (also shown in Fig. 5.16):

- Top Beam-to-column connection, North side, East end (TB-N): video and still cameras
- Middle Beam-to-column connection, North side, East end (MB-N): video and still cameras (shown in Fig. 5.17)
- East Column base connection, North side (EC-N): video and still cameras
- West Column base connection, North side (WC-N): two (2) still cameras (one zoomed into the column base, the other zoomed out to see the bottom beam double-angle connection)
- North overview (N-overview), looking at the specimen from the northeast: video and still cameras
- South overview (S-overview), looking at the specimen from the southeast: still camera only

The video cameras were each manually started and stopped at the beginning and end of testing. The MTS FlexTest GT was used to send a signal to the still cameras to take a photo. A photo was taken during every fifth load step. The signal was sent to the S-overview and EC-N still cameras. A remote triggering system was connected to the EC-N camera to send a trigger to the other cameras (at N-overview, WC-N, MB-N, and TB-N) to take a photo at each of these steps. There was some discontinuity in the photos from these cameras due to loss of battery power in the remote triggering system.

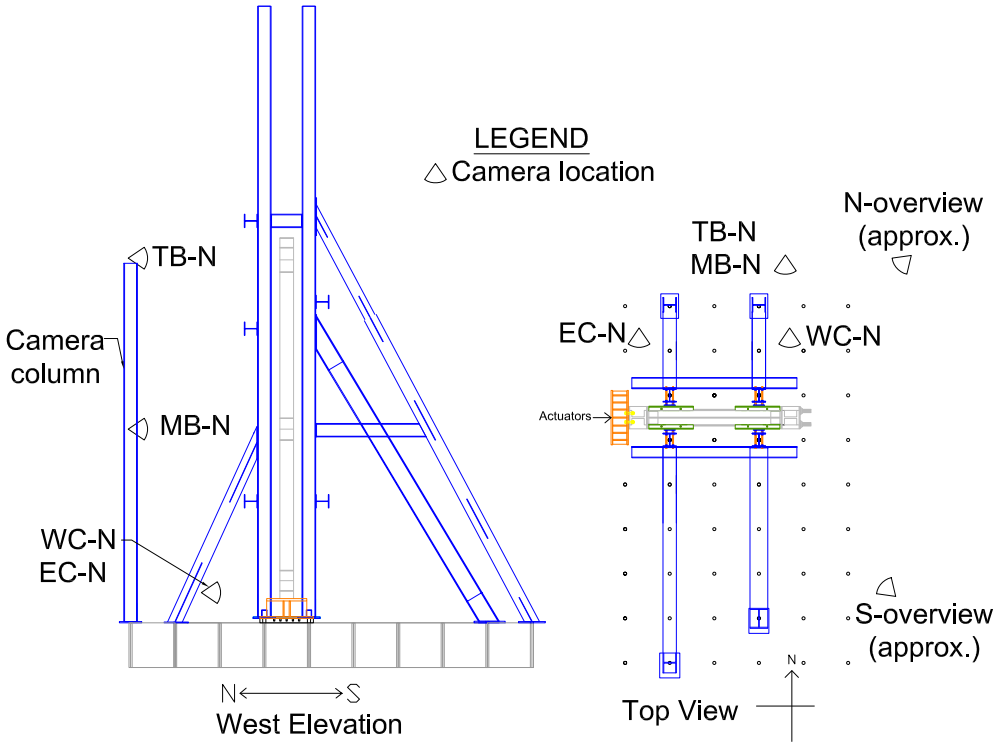

Figure 5.16: Approximate camera locations and directions

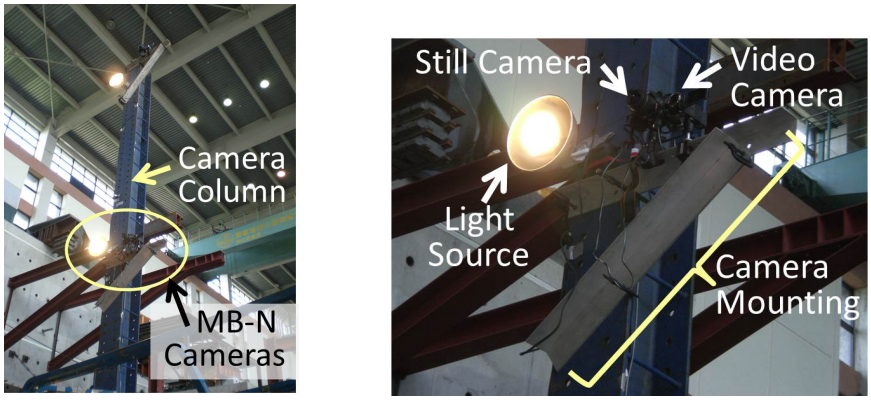

(a) (b)

Figure 5.17: Photos of (a) camera column and (b) close-up of cameras at location MB-N

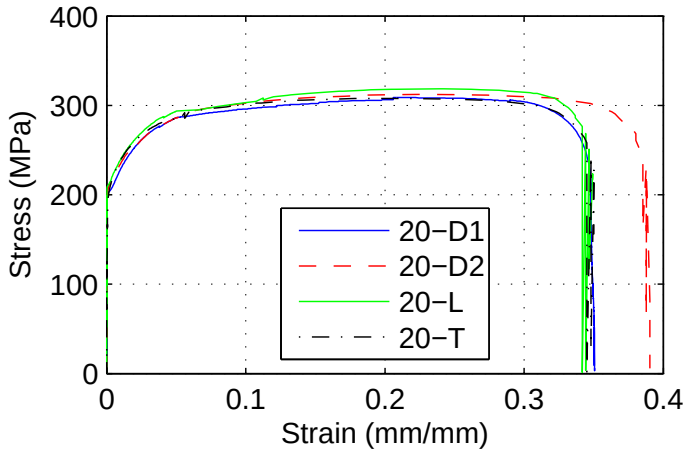

Figure 5.18: Monotonic stress vs. strain response of LYS225 web plate material

5.3.3 Material properties

Monotonic tension tests were conducted on coupons of the 2.7 mm thick web plate material (LYS225). Four coupons were cut from the web plate material: one in the longitudinal direction (20-L), one in the transverse direction (20-T), and two in the 45°-diagonal direction (20-D1 and 20-D2). The nominal gage width of each coupon was 20 mm and the gage length was 80 mm. The coupon tests were conducted in the Yen Tjing Ling Industrial Research Institute at National Taiwan University.

The monotonic stress vs. strain response of each coupon is shown in Fig. 5.18. Because the response of the coupons was similar, the data from 20-L (representing an upper bound of the web plate material properties) was used for determining characteristic material properties. The initial elastic stiffness, E_w, was determined to be 584 GPa, and the yield strength was 208 MPa.

Since the boundary elements and PT strands were designed to remain elastic, tests were not conducted on these materials; however, as previously stated, the materials were specified to be ASTM A992 and ASTM seven-wire Grade 270 prestressing strand, respectively. For analysis, the elastic moduli were taken to be 200 GPa for the boundary elements and 196.5 GPa for the PT strand.

5.4 Loading

The loading for the pseudo-dynamic tests was determined based on prototype building design and expected seismic response. This section outlines the prototype building and SC-SPSW design methodologies that were used as the basis for determining the seismic mass to be used in the tests. Nonlinear response history analyses of the prototype building were conducted to determine median expected response parameters and select appropriate ground motions to represent typical response at the target hazard levels. In this section the nonlinear analyses and selected ground motions are discussed, as well as the pseudo-dynamic loading control algorithm used in the tests.

5.4.1 Prototype design

The seismic mass attributed to the specimen, a key parameter in the dynamic response of the lateral force resisting system, was determined based on preliminary designs of the prototype building. The preliminary prototype building design is presented below. The corresponding final design of the prototype building using as-built specimen properties is also presented.

5.4.1.1 Preliminary prototype design

The seismic mass to be used in the pseudo-dynamic tests was initially estimated prior to knowledge of actual specimen strength properties and was based on preliminary target specimen strength approximations (details described below). This seismic mass could also be determined based on actual specimen strength parameters known at the time of testing, the procedure for which is described in the following section (Sec. 5.4.1.2).

In the preliminary design stages, the exact dimensions and material strengths of the specimen was unknown. Most importantly, the web plate material, which is the driving factor in determining SC-SPSW design strength (see Sec. 2.4.1.2), was being provided by a company in China, China Steel Corporation. The available plate thicknesses and material strength were unknown at the time of the boundary frame design. According to sources at NCREE who had worked with this company in previous SPSW tests, because the web plate

material was donated from material the company had in stock, the available plate thicknesses and material properties varied based on the company's recent production orders. As the web plate properties were unknown and the boundary frame sections had to be ordered prior to acquisition of the web plate material, conservative web plate strength and thickness values were assumed for the boundary frame design.

The SC-SPSW specimen was also designed to have overall dimensions and strengths similar to the previous SPSW test conducted at NCREE (referred to as Specimen NC) [Lee, 2011; Li et al., 2012], such that the same lateral bracing frame and actuator loading method could be used. For preliminary design of the prototype building, the SC-SPSW specimen strength was assumed to be similar to Specimen NC. Here, the strength of Specimen NC at 2% drift (approximately 1400 kN) was taken as the specimen strength under design-level loading[1]. This drift value was used as it is the code-based design-level drift limit [ASCE, 2005] for a regular-use office building. Based on the overstrength factor, $\Omega_o = 2$, for conventional SPSWs, it was assumed that the corresponding design strength of the specimen would have been 700 kN. Because the SC-SPSW specimen was to be designed to have a similar strength as Specimen NC, a design strength of 700 kN was assumed for the SC-SPSW specimen[2].

Assuming that the SC-SPSW specimen had a design strength of approximately 700 kN and that the prototype building had a seismic base shear, $V_{protoype}$, of 2,870 kN (Sec. 5.2), the prototype building was estimated to require four SC-SPSW specimens in each direction (i.e. longitudinal and transverse directions) of the building to resist the seismic loads. Therefore, the tributary mass for an individual SC-SPSW, based on these preliminary estimations, was taken as one-forth of the building seismic mass (approximately 236,500 kg per story). This is the basis for the seismic mass assumed in the pseudo-dynamic tests.

---

[1]The specimen response in Sec. 5.5.4 shows that the SC-SPSW specimen strength at 2% drift was very similar to the 1400 kN strength of Specimen NC at 2% drift, indicating that their strengths were, in fact, similar

[2]In design of SC-SPSWs and conventional SPSWs, the web plate is typically designed to resist the entire seismic lateral force and the boundary frame is capacity designed based on the web plate forces. Assuming that both SC-SPSW and SPSW specimens use a similar web plate material and thickness, it would be reasonable to assume that they both have similar prototype design forces.

5.4.1.2 Final prototype design

Although the tributary seismic mass determined in the preliminary prototype design above was used in the PSD tests, a prototype design based on the actual specimen dimensions and strengths was also determined. Here, the actual web plate thickness, t_w, and yield strength, F_y, w, (provided in Sec. 5.3.1) were 2.7 mm and 208 MPa, respectively.

The web plate nominal strength, $V_{n,web}$, was determined based on the equation [AISC, 2005a]:

$$V_{n,web} = 0.42 F_{y,w} t_w L_{web} \sin(2\alpha) \tag{5.1}$$

where, L_w is the length of the web plate connected to the bottom beam (2.233 m) and α is the angle of inclination of the tension field and was assumed to be 45°. From this equation, the web plate design strength, $\phi V_{n,web}$ was determined to be 474 kN, where ϕ is the strength reduction factor, 0.9.

According to the proposed SC-SPSW performance-based design procedure [Clayton, 2010], the web plate thickness is to be designed to resist the entire seismic lateral load using Eqn. (5.1). Using this method, the prototype building would require six of the SC-SPSW specimens ($V_{prototype}/\phi V_{n,web} = 6.05$) in each direction of the building. This results in a tributary seismic mass per wall that is less than that determined from the preliminary prototype design of four SC-SPSWs and that was used in the PSD tests.

However, if the strength of the PT boundary frame is considered, the number of walls required will be reduced. This method of considering the boundary frame strength and the web plate strength in the design is referred to as a balanced design. Unlike the moment resisting frames used in conventional SPSWs, the PT boundary frame is not intended to reach its yield strength, as the members are designed to remain elastic at large drift demands. Here, a conservative estimation of the PT boundary frame strength due to the strength of the PT connections is used.

As previously described, the decompression moment, M_d, is the moment at which a gap forms in the PT connection and can be taken as:

$$M_d = \frac{d}{2} T_o \tag{5.2}$$

The performance-base seismic design(PBSD) procedure proposed in Clayton [2010], suggests that the initial PT force be designed primarily to prevent connection decompression under wind loading, suggesting that connection decompression will occur at the seismic hazard levels considered in the PBSD procedure. Also, the PBSD procedure proposed that the HBE depth and number of PT strands be designed to provide a positive recentering stiffness considering P-Delta effects, thus the decompressed connection rotational stiffness must be greater than zero. Therefore, it can conservatively be assumed that the PT connection strength at drift-levels associated with seismic loading will be greater than or equal to the decompression moment.

By using a virtual work method, the strength of the PT frame can be determined by equating the internal work (i.e. the flexural rotation of the PT connections) to the external work (i.e. the force applied at the top of the PT frame) based on the schematic shown in Fig. 5.19. The nominal strength of the PT frame, $V_{n,PTframe}$, can be estimated as:

$$V_{n,PTframe} = \frac{\Sigma M_{conn}}{h} \tag{5.3}$$

where, h is the height from the column base to the actuator load (note that this equation only applies to a frame loaded at one point), and ΣM_{conn} is the sum of the moments in all of the PT connections. The moment at connection decompression, M_d, of each of the connections (i.e. two TB connections, two MB connections, and the connections at both column bases) is conservatively assumed as the lower-bound for M_{conn} during an earthquake. Also note that the BB double-angle connections are not considered here, as they are intended to simulate a pinned connection with negligible moment resistance.

The strength reduction factor, ϕ, of 0.9 can also be applied to the PT frame nominal strength. Here, the strength reduction factor does not account for discrepancies in material yield strength, as the boundary frame members are elastic; however, this reduction factor can account for variations in initial PT force (e.g. accounting for PT losses) or variations in the beam rocking depth. Although there is not data to suggest the expected variation in these values, 0.9 is assumed as it is the value commonly applied to flexural strength calculations.

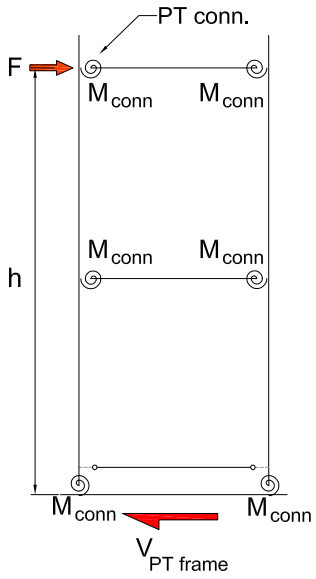

Figure 5.19: Virtual work method for approximating PT frame strength

Using these assumptions and the initial PT forces ($T_{o,MB} = T_{o,TB} = 1000$kN, $T_{o,col}$=2600kN) and member rocking depths[3] (d_{MB}=552mm, d_{TB}=609mm, d_{col}=421mm) described in Sec. 5.3, the PT frame design force, $\phi V_{n,PTframe}$, was determined to be 266 kN. When this conservative estimate of PT frame strength is considered with the web plate strength (i.e. a balanced design), the required number of SC-SPSWs in each direction of the building is four ($V_{prototype}/(\phi V_{n,web} + \phi V_{n,PTframe}) = 3.88$). Using this balanced design approach, the number of walls required in the building matches those determined in the preliminary prototype design that was used in the PSD tests.

Although a balanced design approach is not suggested in the proposed SC-SPSW PBSD procedure [Clayton, 2010], this method provides a reasonable approach to achieve the same seismic mass considered in the PSD tests. It should be noted that the seismic mass attributed to the SC-SPSW specimen was larger (approximately 50% larger) than the mass that would have been attributed to a single wall using the proposed PBSD procedure con-

[3]The member rocking depths include the depth of the flange reinforcing plates and rocking plates attached to the frame members at the connections.

sidering the web plate strength only. Therefore, the results from these tests should be considered to be conservative in that the test specimen was subjected to larger inertial forces than would be experienced by a SC-SPSW designed according to the proposed PBSD procedure.

5.4.2 Prototype building numerical model

To predict the specimen response and determine the ground excitations to be used in the PSD tests, numerical nonlinear response history analyses were conducted. For the ground motion selection, the SC-SPSW was modeled as a component in the prototype building, meaning that gravity loads, gravity frame nonlinearity, and the seismic mass distribution was modeled corresponding to the prototype building. A schematic of this model is shown in Fig. 5.20 and is described below. When used for specimen response prediction, the gravity loads and gravity frame nonlinearity were not included in the model as these were not simulated in the test, and the total seismic mass was lumped at the location where the actuator was connected to the specimen.

The SC-SPSW was modeled in OpenSees using the same methods that will be described further in Sec. 7.2. To account for P-Delta effects, leaning columns were placed symmetrically on either side of the SC-SPSW to simulate the prototype building's tributary gravity loads as described in Clayton [2010] and shown in Fig. 5.20. The tributary gravity load combination considered $1.2DL + 0.5LL$ with four SC-SPSWs in each direction of the building. The dead load, DL, was taken as 4.6 kPa (96 psf) for the floor-level and 4.8 kPa (100 psf) for the roof-level, and the live load, LL, was taken as 0.96 kPa (20 psf) at both levels. The seismic mass, again considering four SC-SPSWs in the each direction of the building, was lumped at the column nodes at the height of the middle and top beams as described in Clayton [2010].

The strip model used to simulate the web plate incorporated the proposed tension-compression strip material (described in further detail in Sec. 7.2) that was developed based on experimental results from the quasi-static cyclic subassembly tests (Chapter 4) that suggested that the web plate has some non-negligible residual strength upon unloading.

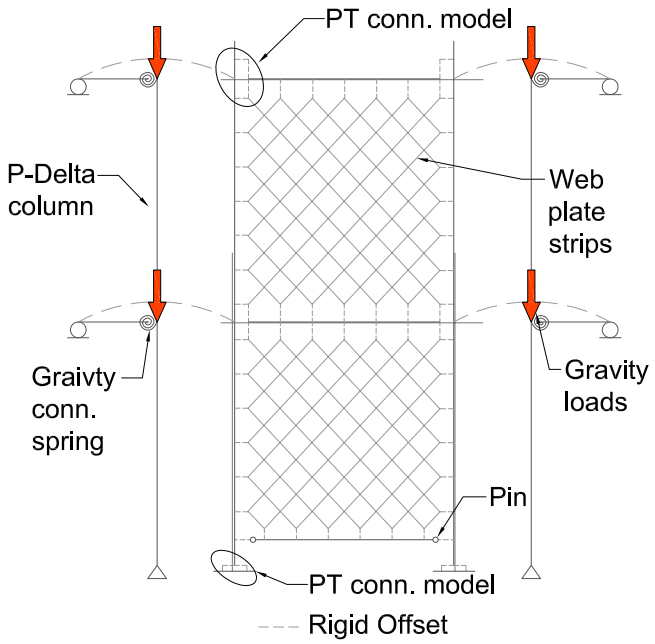

Figure 5.20: Schematic of OpenSees model of prototype SC-SPSW

For purposes of seclecting the ground motion excitation to be used in the PSD tests, and because the magnitude of web plate residual strength was not fully understood at the time of this study, multiple SC-SPSW models were constructed with varying magnitudes of web plate strip compressive strength. The compressive strength varied from 10% to 40% of web plate tensile stength. Further discussion of the magnitude of compressive resistance and the appropriateness of this model will be provided in later chapters. The magnitude of compressive resistance in the stips has two key effects: (1) a large web plate compressive strength can negatively impact recentering and (2) a larger web plate compressive strength increases energy dissipation in the system and may, therefore, reduce drift demands. More detail will also be provided in later chapters on the SC-SPSW numerical modeling methods and comparisons of the experimental and numerical responses.

5.4.2.1 Gravity frame connection model

Unlike the previous numerical studies on SC-SPSWs [Clayton, 2010; Clayton et al., 2012b], the material nonlinearity of the gravity frame was also simulated to account for any resistance that gravity frame yielding may provide against recentering. Here, the gravity frame was modeled with nonlinear flexural springs that were attached to the P-Delta columns as shown in Fig. 5.20. The springs were also connected to essentially rigid horizontal struts that were supported by roller supports. The roller supports restrained displacement in the vertical direction and were constrained to have the same horizontal displacement as the corresponding node of the SC-SPSW column.

The nonlinear spring representing the gravity frame shear connections was adopted from Hsiao et al. [2013] and used the `Pinch04` material model in OpenSees to represent the nonlinear cyclic behavior of shear connections with composite slabs [Lui and Astaneh-Asl, 2004] as shown for a single connection in Fig. 5.22. The connection moment, rotation, and pinching parameters used in the model were based on the procedures and experimental data presented in Lui and Astaneh-Asl [2004] and shown in Fig. 5.21.

The gravity connection springs simulated the gravity bays within the tributary area of the building; therefore, the spring moment strengths were taken as the strength of a single shear connection (shown in Fig. 5.22) times the number of gravity bays in the tributary area (for this model 28 gravity bays were considered in the short, i.e. transverse, direction of the building, with one-forth of those being in the tributary area of the modeled SC-SPSW).

5.4.3 Ground motion selection

The SC-SPSW preliminary prototype model described above was subjected to the suite of sixty ground motions developed as part of the SAC project for the Los Angeles site [Somerville et al., 1997]. This was also the same ensemble of ground motions used in the previous SC-SPSW numerical study [Clayton, 2010]. This ensemble includes twenty ground motions at each of the three hazard levels: 50%, 10%, and 2% probability of exceedance in 50 years (50/50, 10/50, and 2/50, respectively). Further details of the ground motion records and scaling can be found in Somerville et al. [1997] and FEMA [2000b]. The ground

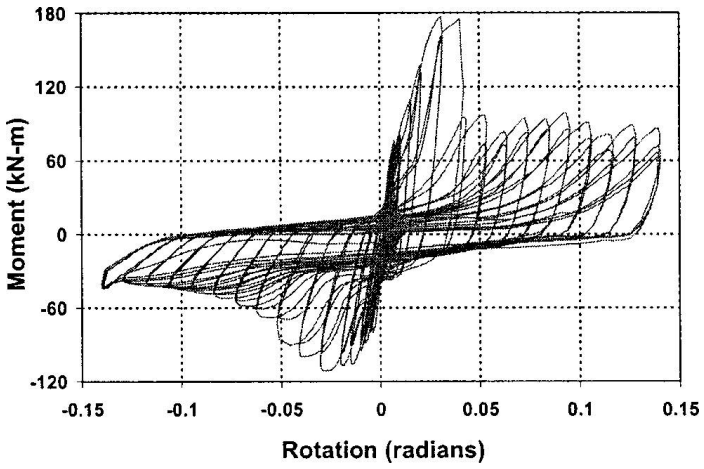

(a)

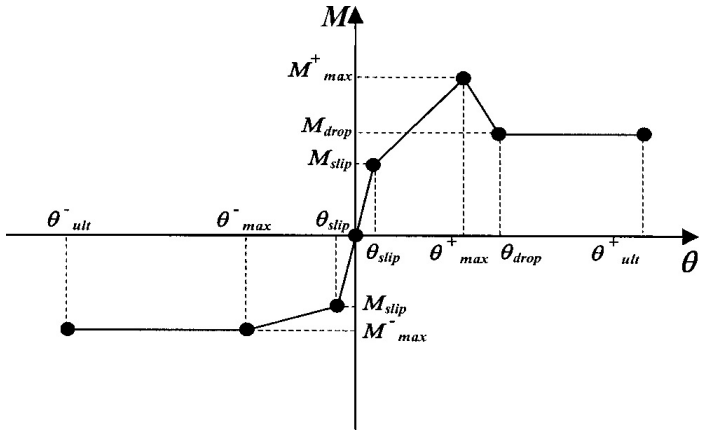

(b)

Figure 5.21: (a) Typical cyclic response of shear connection with composite slab and (b) proposed shear connection backbone model [Lui and Astaneh-Asl, 2004]

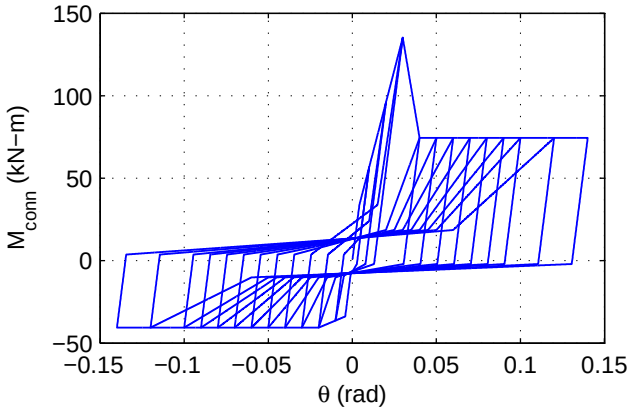

Figure 5.22: Cyclic response of shear connection model used in OpenSees analyses

motions were "scaled such that, on average, their spectral values match with a least square error fit to the United States Geological Surveys (USGS) mapped values at 0.3, 1.0, and 2.0 seconds, and an additional predicted value at 4.0 seconds." [FEMA, 2000a]. These USGS mapped values are those provided in Table 5.1. Rayleigh damping in the preliminary model was assumed to be 2% in the first and second modes.

A summary of the peak roof drift values observed during these preliminary nonlinear response analyses are shown in Fig. 5.23. The results are shown for models with varying magnitudes of web plate strip compressive resistance, σ_{cw}, given as a percentage of web plate tensile yield strength, σ_{yw}. Because these preliminary analyses were conducted before acquisition of the web plates used in the specimen, the web plate thickness and yield strength was estimated based on those used in the previous SPSW tests conducted at NCREE (t_w=2.7 mm, σ_{yw}=245 MPa). These values were later refined for the specimen response prediction models once the actual material properties were known. In Fig. 5.23, the x-axis represents each ground motion (LA#), where LA01 through LA20 are 10/50 records, LA21 through LA40 are 2/50 records, and LA41 through LA 60 are 50/50 records. These ground motion labels correspond to the names given in Somerville et al. [1997] and used in Clayton [2010]. Also, the results of analyses that encountered numerical convergence problems are not shown, although this only occurred in a very small number of analyses.

The ground motion excitations used for the PSD tests were selected from this suite of

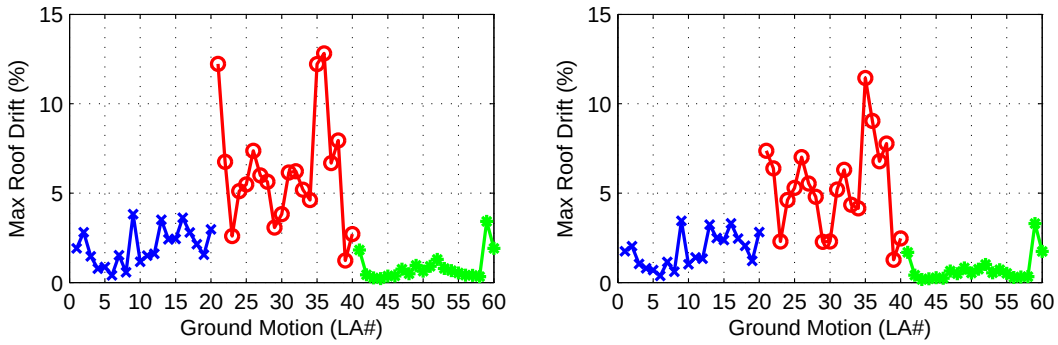

(a) $\sigma_{cw} = 10\%\ \sigma_{yw}$

(b) $\sigma_{cw} = 20\%\ \sigma_{yw}$

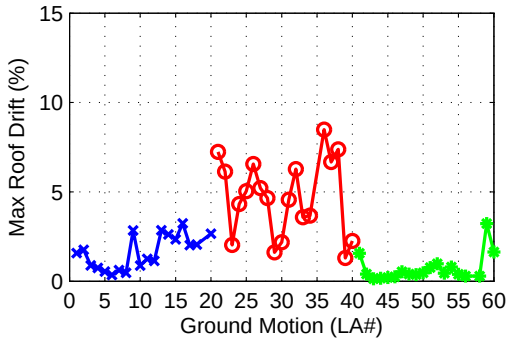

(c) $\sigma_{cw} = 30\%\ \sigma_{yw}$

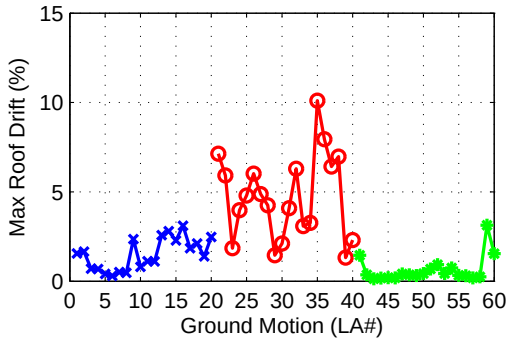

(d) $\sigma_{cw} = 40\%\ \sigma_{yw}$

Figure 5.23: Peak roof drift for each ground motion in preliminary prototype numerical model

records considering the following constraints and preferences:

- Only ground motions derived from actual ground acceleration records (i.e. not simulated) were considered.
- Shorter ground motions were preferred to reduce the total duration of testing.
- The peak drift demand of the numerical model should be similar to the median drift expected for a low-rise SC-SPSW at that hazard level [Clayton, 2010] while conservatively staying below the drift capacity of the test set-up. Target peak drifts of 0.5%, 2%, and 3.5% were assumed for the 50%, 10%, and 2% in 50 year hazard levels.

Due to the limited number of 2% in 50 year ground motions that met all of these criteria, a ground motion with a peak drift smaller than the target drift was selected and was linearly scaled by 1.3 (as shown in Table 5.2) to produce a drift demand that more closely matched the target (results from the additional nonlinear response history analyses used to determine this scale factor are not shown here). From these citeria the LA42, LA01, and LA23 ground motions were selected for the 50/50, 10/50, and 2/50 ground motions, respectively.

The PSD loading used in this experiment was roughly 200 times slower than an actual earthquake, and due to time constraints, it was not feasible to test the full duration of the ground motion. For this reason, only a portion of the ground motions during strong shaking were used. The selected ground excitations are shown in Fig. 5.24. Further numerical simulations showed that using these abbreviated ground motions did not greatly influence the peak drift demands compared to the models subjected to the full ground motion. The beginning and end of the time window selected for the PSD excitation are shown in Table 5.2. The time step, Δt, used in the PSD loading algorithm was 0.01 sec, and the ground accelerations at each time step were linearly interpolated from the SAC ground motion records. A period of free vibration was added to the end of each ground motion to determine response parameters such as residual drift, post-event fundamental period, and damping. The duration of free vibration, given in Table 5.3, was determined by stopping the test when the specimen returned to near-zero displacement after at least 1.5 cycles of free vibration.

Table 5.2: Summary of ground motions used for pseudo-dynamic tests

Name	SAC motion	Time Window (sec) Begin	End	Scale
50/50	LA42	2.59	4.85	1
10/50	LA01	0	15.18	1
2/50	LA23	4.01	14.14	1.3

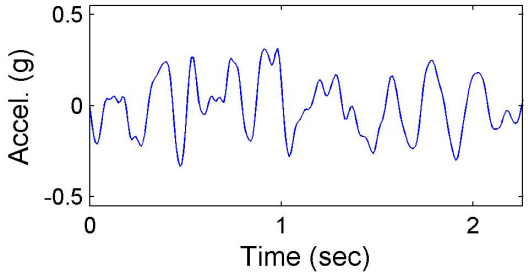

(a) 50/50

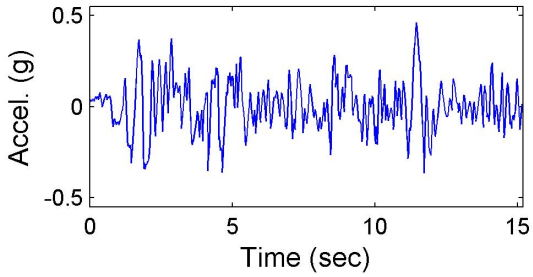

(b) 10/50

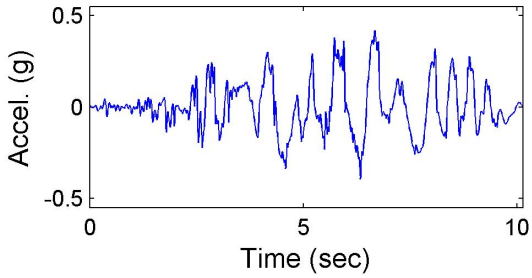

(c) 2/50

Figure 5.24: Ground excitations used in pseudo-dynamic tests

5.4.4 Response spectra

To provide context for the Los Angeles SAC ground motions, the elastic strength demand (acceleration) response spectra for each SAC ground motion in each hazard level is shown in Fig. 5.25, where the median and 84^{th} percentiles are highlighted. These figures are taken directly from FEMA [2000a], and the response spectra were determined with 2% viscous damping assumed. Fig. 5.26 also shows the median elastic strength demand (acceleration) spectra for each hazard level, where the 1994 NEHRP design spectrum (assuming 5% damping) is also shown for comparison. The 1994 NEHRP document [FEMA, 1994] represents the most current design code at the time of the SAC project and associated ground motion emsemble development.

In the FEMA [2000a] research, it was found that the median 10/50 response spectra offered a reasonable, yet conservative (i.e. larger spectral accelerations than the design spectrum) representation of the current design code [FEMA, 1994]. It also notes that the difference in the shapes of the 1994 NEHRP spectra and the median response spectra indicate that the response from the SAC ground motions may differ from those expected based on design code assumptions [FEMA, 2000a]. Although the current target (i.e. design) spectral values for Los Angeles may vary slightly from those used in this study, this ensemble of ground motions provide a realistic representation of various seismic excitations at different hazard levels and are sufficient for general studies of a structural system's viability.

The acceleration response spectra for the excitations used in the PSD tests (using the time windows and scaling shown in Table 5.2) are shown in Fig. 5.27. The target design-basis and maximum credible earthquakes (DBE and MCE, respectively) are also shown. Because these ground motions were not scaled to a specific design code (they were scaled to the USGS target spectral values given in Table 5.1 as described previously and in Somerville et al. [1997]), the MCE spectra accelerations were taken as those for the 2/50 hazard level [FEMA, 2000a]. The MCE short-period and 1sec-period spectral acceleration, S_{MS} and S_{M1}, respectively, were taken as the USGS target spectral accelerations at periods of 0.3 sec and 1 sec, respectively. The DBE spectral accelerations were taken as 2/3 of the MCE spectrum (note that these values are very similar to the 10/50 USGS target spectral values),

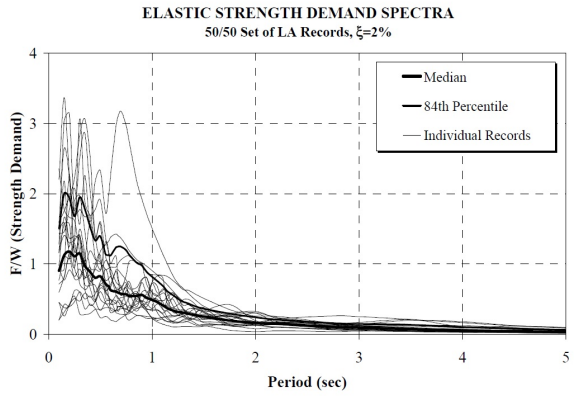

(a) 50/50

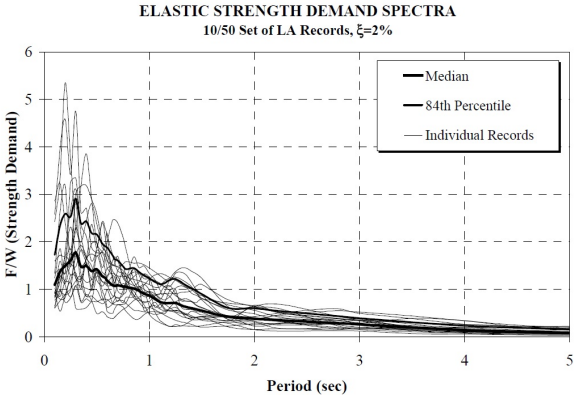

(b) 10/50

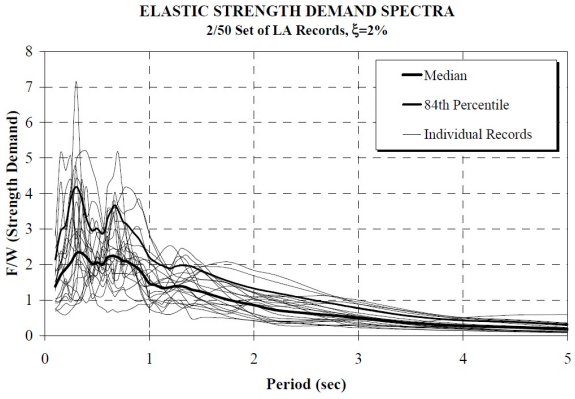

(c) 2/50

Figure 5.25: Elastic strength demand response spectra for all Los Angeles SAC ground motions with median and 84^{th} percentiles shown [FEMA, 2000a]

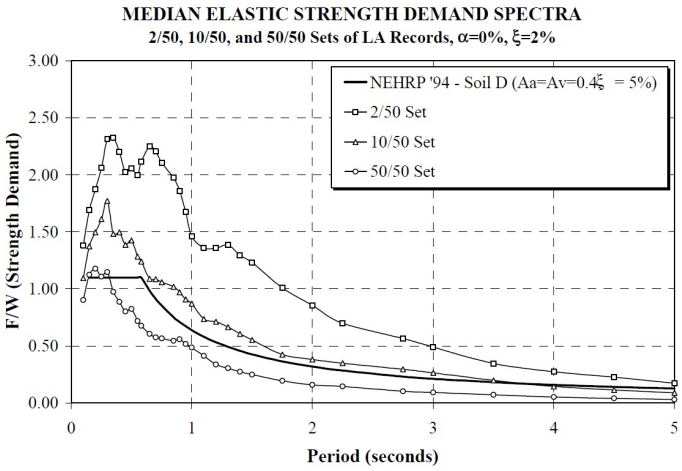

Figure 5.26: Median elastic strength demand spectra for Los Angeles SAC ground motion ensemble [FEMA, 2000a]

and the shapes of the target MCE and DBE spectra were based on current design codes [ASCE, 2005].

For reference, Fig. 5.27 also shows key structural periods of the specimen as vertically dashed lines. The initial fundamental period, $T_{i,exp}$, was estimated from the experimental displacement vs. time response during the elastic free vibration test as 0.6 sec. The fundamental period of the PT boundary frame, $T_{PTframe,exp}$, was estimated from the experimental displacement vs. time response (discussed later in Sec. 6.4.1) during the free vibration following the 10/50 test as approximately 1.5 sec[4]. Note that the web plate still provides some residual strength and stiffness after the 10/50 test; however, the relative strength and equivalent hysteretic damping of the web plate at this point is greatly reduced, and behavior is largely dominated by PT frame response. For the sake of comparison, an approximate fundamental period based only on the recentering stiffness, $T_{r,est}$, of the specimen is shown. Although this period does not represent any real response of the specimen, because the specimen will always have an increased stiffness at small drifts after the PT connections recompress, this is shown for purposes of comparing the large range of stiff-

[4]Note that this fundamental period was determined from free vibration at drift demands that included the nonlinear post-connection decompression response of the PT frame.

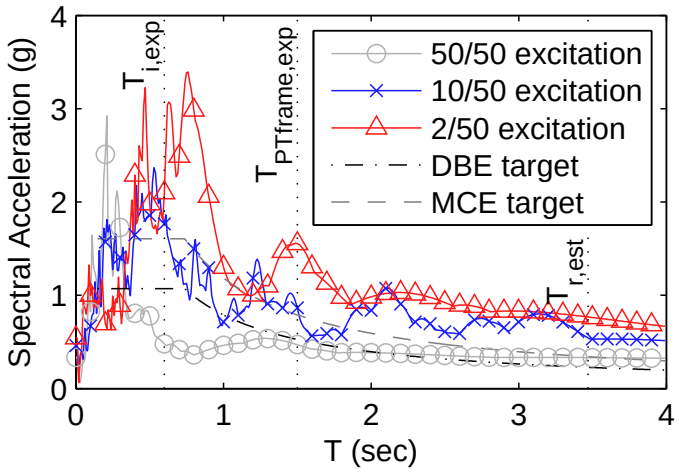

Figure 5.27: Response and target spectra for excitations used in PSD tests

nesses experienced by the SC-SPSW system at different states during a transient, dynamic analysis. The artificial recentering period, $T_{r,est}$, was estimated using the experimentally determined recentering stiffness, K_r, and the seismic mass of the specimen. The results of the PSD tests, from which these fundamental periods were based, will be presented later in Sec. 5.5.

It should be noted that the spectral accelerations for the PSD excitations shown in Fig. 5.27 are within the range of the median and 84^{th} percentile responses from the SAC ground motions ensemble presented in Fig. 5.25. This signifies that the selected records represent a conservative (i.e. larger spectral demands) approximation of the median response for each hazard level. Fig. 5.27 also shows that the spectral response during the 10/50 and 2/50 excitations are larger (sometimes as much as double) than the DBE and MCE target spectra, respectively, at all but very small periods. Again, this signifies that the response due to the excitations used in the PSD tests will be more severe than those suggested by design codes. One should keep these facts in mind when considering the response of the specimen under these excitations.

5.4.5 Loading sequence

A total of six different tests were conducted on Specimen FR (Tables 5.3 and 5.4). These included a small-amplitude (0.13% drift) pseudo-dynamic (PSD) free vibration test, a small amplitude (0.15% drift) static-cyclic test, three PSD tests at three different sesimic hazard levels, and a large amplitude (4.5% drift) static-cyclic test. The three PSD tests, as discussed above, represent each seismic hazard level considered in the SC-SPSW performance-based design procedure proposed by Clayton [2010]: 50/50, 10/50, and 2/50.

After each pseudo-dynamic test the specimen was returned to zero-displacement, and the next pseudo-dynamic was started with an initial analytical displacement, velocity, and acceleration, u_o, $\dot{u}_o$, and $\ddot{u}_o$, respectively, of zero. The ground motions were all run one after the other without any repair to the specimen. This procedure provided a conservative evaluation of SC-SPSW response at the 2% in 50 year hazard level since an actual SC-SPSW would likely have undamaged, elastic web plates prior to an earthquake of this intensity.

Table 5.3: Pseudo-dynamic tests

Name	Order	Hazard Level	PGA (g)	Duration (sec) of Excitation	Duration (sec) of Free Vibration
Free Vibration	1	—	0	—	10
50/50	3	50% in 50 year	0.33	2.26	3.0
10/50	4	10% in 50 year	0.46	15.18	2.73
2/50	5	2% in 50 year	0.54	10.13	7.02

Table 5.4: Quasi-static tests

Name	Order	Drift (%)	No. of Cycles
Elastic	2	0.15	2
Inelastic	6	4.5	2

5.4.6 Pseudo-dynamic loading algorithm

Because the specimen was loaded only at one location (the west column at the top beam) and because the building gravity system was not modeled analytically in the PSD tests (e.g. as in a hybrid simulation), the equations of motions could be solved as a single degree-of-freedom (SDOF) system, where the free DOF was taken to be at the location of the actuator.

Here, the Newmark explicit method was used [Newmark, 1959]. Given the actuator displacement at time n, $u(n)$, as calculated from the Temposonic sensor reading, the analytical velocity at the actuator, $\dot{u}(n)$, the analytical acceleration at the actuator, $\ddot{u}(n)$, the ground acceleration excitation, $\ddot{u_g}$, the analytical seismic mass, m, the time step, Δt, the applied analytical damping coefficient, c, and the measured force applied by the actuator, $R(n)$, the following steps could be taken to apply the Newmark method in the pseudo-dynamic loading protocol:

1. Calculate the displacement for the next time step:

$$u(n+1) = u(n) + \dot{u}(n)\Delta t + \frac{1}{2}\ddot{u}(n)\Delta t^2 \tag{5.4}$$

2. Impose $u(n+1)$ on the specimen.

3. Measure the actuator force at step n+1, $R(n+)$

4. Calculate $\ddot{u}(n+1)$ and $\dot{u}(n+1)$ by simultaneously solving the following two equations:

$$m\ddot{u}(n+1) + c\dot{u}(n+1) + R(n+1) = -m\ddot{u_g}(n+1) \tag{5.5a}$$

$$\dot{u}(n+1) = \dot{u}(n) + \frac{1}{2}\Big(\ddot{u}(n) + \ddot{u}(n+1)\Big)\Delta t \tag{5.5b}$$

5. Let $u(n) = u(n+1)$, $\dot{u}(n) = \dot{u}(n+1)$, and $\ddot{u}(n) = \ddot{u}(n+1)$, and then repeat the previous steps for next time step.

The time step, Δt, ground acceleration, $\ddot{u}_g$, seismic mass, m, and the damping coefficient, c, are all specified a priori by the user. The seismic mass was 473,000 kg and was determined based on the tributary mass attributed to an individual SC-SPSW in the prototype building as described in Sec. 5.4.1[5]. The ground acceleration records used in these tests are described in Sec. 5.4.3. The damping coefficient was taken as zero for these tests based on the inherent damping observed in the free vibration PSD test and described in Sec 5.5.1.

In the PSD tests, a time step, Δt, of 0.01 sec was used. When using an explicit method for determining the next step, a smaller time step can more closely match the actual response; however, because the PSD loading requires data from the Temposonic displacement sensor and the actuator load cell, there is some inherent error associated with those signals. If the time step is too small, the relative error in these readings can cause the numerical solution to diverge form the actual solution. To verify that an explicit time step of 0.01 sec was sufficient in accurately simulating the response, a numerical model of the test specimen (modeled in OpenSees and discussed in later chapters) was subjected to the ground excitation used in the tests. The model was analyzed using an explicit time step of 0.01 sec and using an implicit solution algorithm. Differences in the response of both models were negligible; therefore, 0.01 sec time step was determined to adequately predict the actual response.

The error tolerance for the actuator was 0.01 mm (i.e. the actuator was displaced until reaching within $\pm$0.01 mm of the target displacement). Also, the actuator loading velocity was limited to 4 mm/sec. During the PSD loading, the displacement was measured by the Temposonic and was corrected to estimate the displacement at the actuator height assuming rigid column rotation (i.e. the estimated displacement at the actuators is the Temposonic measurement times the ratio of the height of the Temposonic above the column base over the height of the actuators above the column base). The specimen was loaded with multiple iterations until the estimated actuator displacement was within the aforementioned error tolerance for that load step. During this process, the south actuator displacement was slaved to the displacement of the north actuator. The MTS FlexTest GT was used to gather

[5]Note that the analytical mass used in the pseudo-dynamic tests was 473,000 kg. However, the total seismic mass of the building is 1,912,000 kg, resulting in a tributary mass of 478,000 kg if four SC-SPSWs are used in the building. The difference between these two values is approximately 1% and is therefore considered negligible.

the actuator load, actuator displacement, and the Temposonic displacement measurements; controlling the actuators while iterating to impose the specified displacement; and solving the equations of motion to determine the displacement and the analytical velocity and acceleration for each time step.

5.5 Experimental Observations and Results

This section presents visual observations made during each test of Specimen FR. Observations include the initiation and prorogation of web plate tearing and observed yielding in the PT boundary frame. The actuator force and displacement responses of the specimen will also be shown. The displacement is often normalized and presented as drift. For this specimen, drift is determined as the displacement of the WC measured by the Tempo sensor (Fig. 5.12), normalized by its height above the base of the column (7475 mm). Positive displacement or drift corresponds to the actuator pushing towards the East direction.

5.5.1 Free Vibration Test

The displacement and force time histories and force vs. drift response for the free vibration PSD test are shown in Fig. 5.28. As observed in Fig. 5.28(c), the specimen remained elastic during this test with an initial stiffness of 52 kN/mm. From the displacement history shown in Fig. 5.28(a), the fundamental period was determined to be 0.58 sec. The peak displacement during each cycle appears to decay linearly over time, implying that damping is primarily due to friction.

Although the damping did not appear to be viscous in nature due to the linear decay of oscillation, the equivalent viscous damping ratio, ζ_{eq}, was calculated to provide a relative approximation of damping. An equivalent viscous damping ratio was calculated based on the peak displacement decay between each subsequent cycles per Chopra [2007]. These values ranged from 0.8% to 1.0%, with an average damping ratio of approximately 0.9%. Since equaivalent viscous damping in steel structures is usually assumed to be between 1% to 2%, it was decided that the damping inherent in the test set-up, most likely due to friction within the specimen and actuator and friction between the specimen and the lateral bracing frame, was comparable to, and even a slightly conservative underestimation of, the

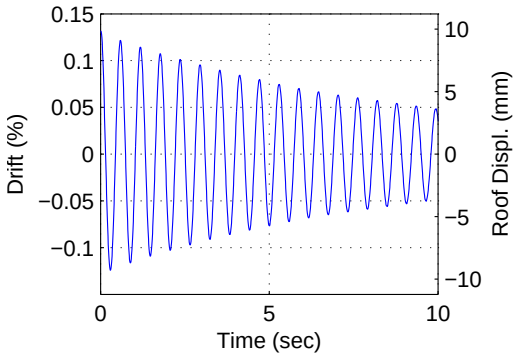

(a) Displacement vs. Time

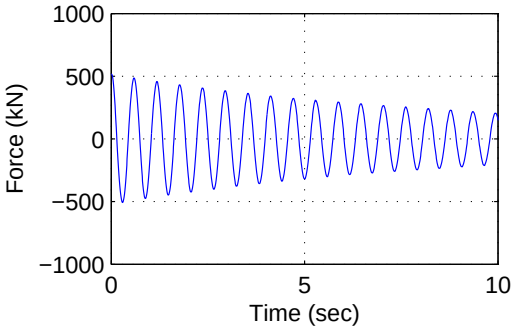

(b) Force vs. Time

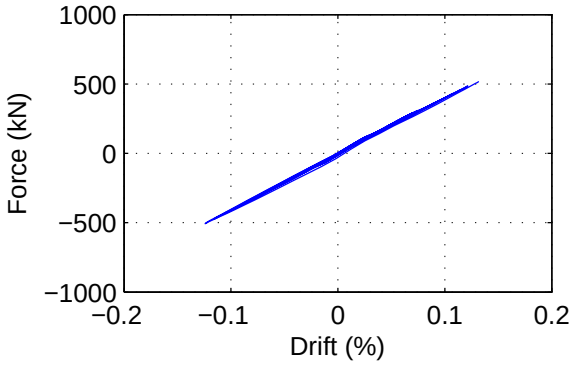

(c) Force vs. drift

Figure 5.28: Free vibration response

damping in actual steel buildings; therefore, no additional analytical damping was added to the following PSD tests. Damping ratios and fundamental periods will be discussed in further detail in Sec. 6.4.

5.5.2 Elastic test

The displacement and force time histories and force vs. drift response for the elastic cyclic test are shown in Fig. 5.29. As observed in Fig. 5.29(c), the specimen remained elastic during this test with an initial stiffness of 51 kN/mm. During the test, elastic web plate buckling was observed and was accompanied by low frequency noises. No damage was observed in the specimen.

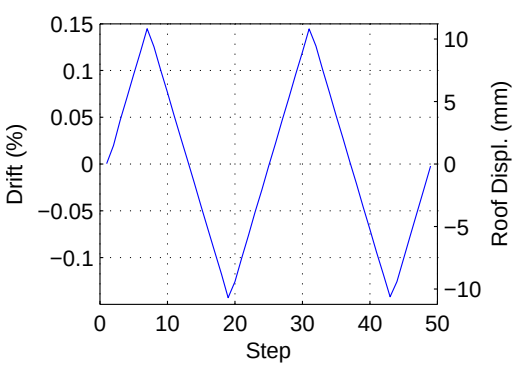

(a) Displacement vs. Time

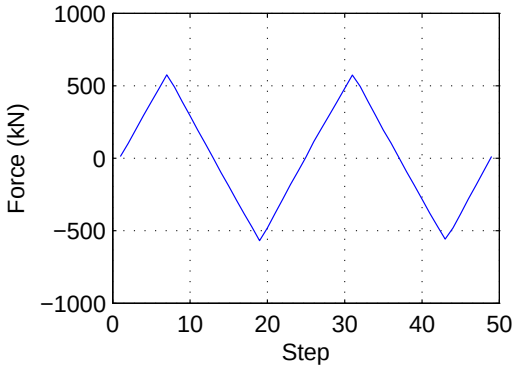

(b) Force vs. Time

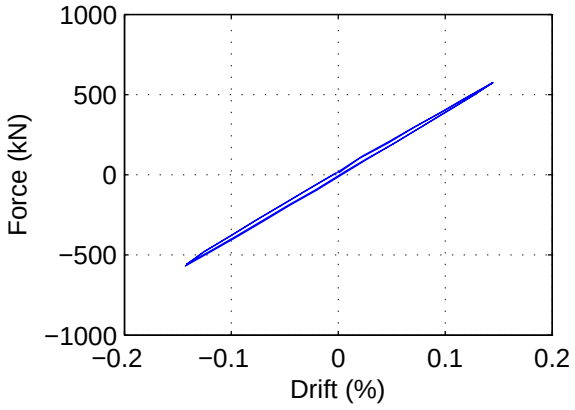

(c) Force vs. drift

Figure 5.29: Elastic cyclic response

5.5.3 50/50 test

The displacement and force time histories and force vs. drift response for the 50/50 PSD test are shown in Fig. 5.30. This test simulated the SC-SPSW response during a 50% in 50 year earthquake. The proposed performance objective at this hazard level is no repair required [Clayton, 2010]; the web plates, boundary frame, and PT elements should remain essentially elastic and the system should be fully recentered. To satisfy the "no repair" performance level, the peak drift should remain less than 0.5%, as this is the median drift at which significant web plate yielding was typcially observed in numerous conventional SPSW experimental studies [Baldvins et al., 2010]. Recentering is determined based on residual drifts less than 0.2% following a seismic event, as this drift corresponds to out-of-plumb tolerances during construction [Clayton, 2010].

As observed in Fig. 5.30(c), the specimen remained essentially elastic during this test with only some minor hysteresis at drifts exceeding approximately 0.17% in the negative direction of loading. Elastic buckling was observed in the web plate. No yielding was visually observed in the boundary frame as there was no flaking of the whitewash. During the test, PT connection decompression was not observed at either the column base or beam-to-column connections. No whitewash flaking or tearing was observed in the web plates; however, some risidual diagonal buckles were observed in the web plates after the 50/50 test, indicating some minor web plate yielding. The web plate yielding was not significant enough to warrant web plate repair or replacement. No other damage was observed in the specimen. The peak drifts during the 50/50 tests were 0.185% and -0.26% in each direction of loading, both of which are below the 0.5% web plate repair threshold [Baldvins et al., 2010]. Also, the residual drift, as indicated by the maximum drift magnitude associated with zero-force in the actuator during the free vibration after the seismic excitation, is -0.02%, well below the 0.2% drift recentering criteria; therefore, the specimen did meet the "no repair" performance objective. Further discussion of residual drifts for each test will be discussed in Sec. 6.4.

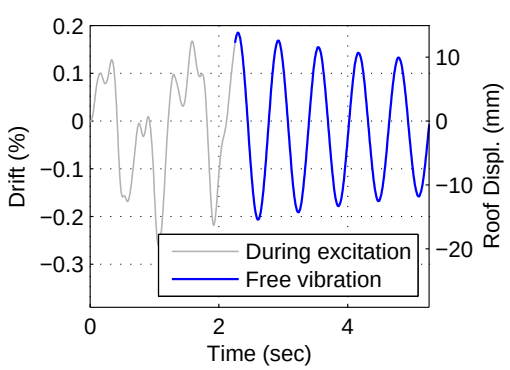

(a) Displacement vs. Time

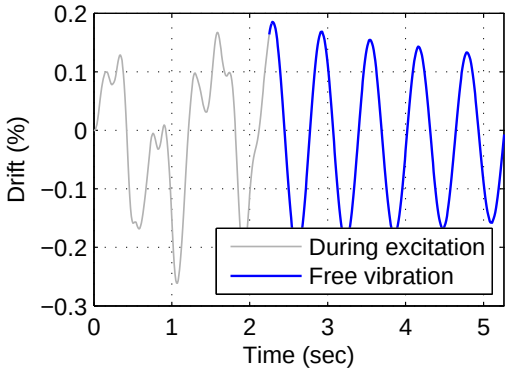

(b) Force vs. Time

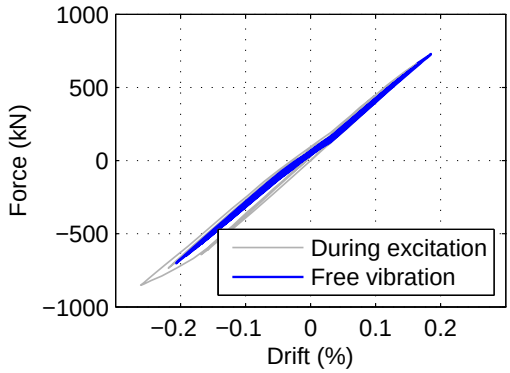

(c) Force vs. drift

Figure 5.30: 50/50 response

5.5.4 10/50 test

This test simulated the SC-SPSW response during a 10% in 50 year earthquake, which is also assumed to be an approximation for a design-level earthquake in the Los Angeles area, although as discussed in Sec. 5.4.4, the response spectrum for the selected ground motion exceeded the DBE spectrum. The proposed performance objective at this hazard level is repair of the web plate only [Clayton, 2010]; the boundary frame and PT elements should remain essentially elastic, the system should be fully recentered, and significant yielding in the web plate is acceptable. If the boundary frame remains undamaged and the system is recentered, replacement of a damaged web plate after the earthquake would be relatively quick and easy compared with repair of other lateral framing systems [Qu et al., 2008]. Also, since the 10% in 50 year hazard level is assumed to be an approximation for the design-basis earthquake (DBE), the peak drifts should be less than the 2% code-based drift limits at this hazard level.

The displacement and force time histories and force vs. drift response for the 10/50 PSD test are shown in Fig. 5.31. Table 5.5 shows the times (where $t = 0$ corresponds to the beginning of the particular ground motion) and corresponding observation name and drifts at which the test was paused to make visual observations around the specimen[6] (also marked in Fig. 5.31(a)). Note that the actuator displacement at observation 10/50R1 taken at a time of 3.04 sec was zero. Just after the local minimum negative loading at 3.04 sec, the hydraulic system suddenly shut down, causing the actuator to unload and return to a near-zero displacement. While the specimen was at zero-displacement, visual observations were made. The test was resumed by returning the specimen to the previous displacement (-1.5% drift) and continuing the pseudo-dynamic loading algorithm using the displacement, velocity, and acceleration history from the previous steps to predict the next step. Therefore, the drop in load caused by the hydraulic system malfunction is not shown in the pseudo-dynamic time-history response. The 0.2% recentering criterion is indicated

[6]The observation naming scheme is the test name, followed by a letter indicating the direction of loading at the observation (e.g. 'N'=negative, 'P'=positive, 'R'=residual or zero), followed by a number indicating the order of the observation to differentiate between multiple observations made in the same direction of loading. For example, 2/50P1 represents the first observation made at a positive displacement in the 2/50 test, 10/50R2 represents the second observation made at a displacement of zero in the 10/50 test.

with vertical dashed lines in Fig. 5.31(c), and the portion of the response associated with free vibration after the imposed excitation is highlighted.

Table 5.5: Observations during pseudo-dynamic testing

Test	Observation Name	Time (sec)	Drift (%)
10/50	10/50R1	3.04	0‡
10/50	10/50N1	11.84	-1.97
10/50	10/50R2	17.91	0
2/50	2/5P1	5.19	4.57
2/50	2/50R1	17.15	0

‡ Observations made when hydraulic system shut down. Drift prior to shut down was -1.5%.

As observed in Fig. 5.31(c), the peak drifts were less than 2% (+1.94% and -1.97%), thus meeting the code-based drift limits for the DBE. As indicated by the large hysteresis in the same figure and as observed by the significant permanent deformation of the web plate after the 10/50 test (Fig. 5.32), the web plate was fully yielded and would require repair after an earthquake of this severity. Connection decompression was observed at the beam ends and at the column bases (examples shown at 10/50N1 in Figs. 5.33(a) and 5.33(b), respectively). Evidence of connection decompression from instrument readings will be discussed in further detail in Chapter 6. No yielding was observed in the PT elements.

Very minor whitewash flaking was observed in the columns near points of large concentrated forces due to the rocking PT connections. These yield lines were first observed just after loading up to -1.5% drift (10/50R1 in Fig. 5.31(a)). The diagonal yield lines typically occured in the column web near the outside flange at the base of the coulmn (as circled in Fig. 5.34(a)). When the column is acting as the compression column to carry the overturning moment (e.g. the EC during positive, or eastward, loading), the outside flange of the column transfers the compression forces to the base pedestal. As the cross-sectional compression forces are transferred to the bearing flange, this area at the web-flange intersection has the highest stress concentrations due to the shear lag effect, resulting in the diagonal yield lines observed here. For similar reasons, slight diagonal yield lines were also observed

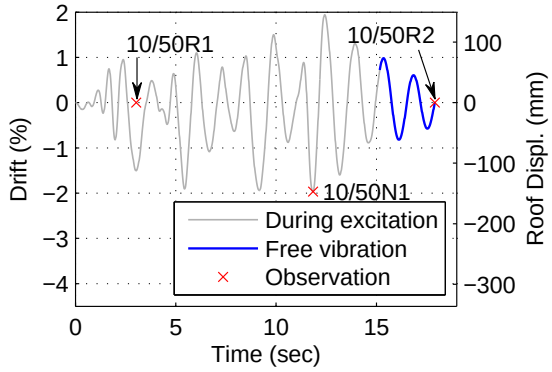

(a) Displacement vs. Time

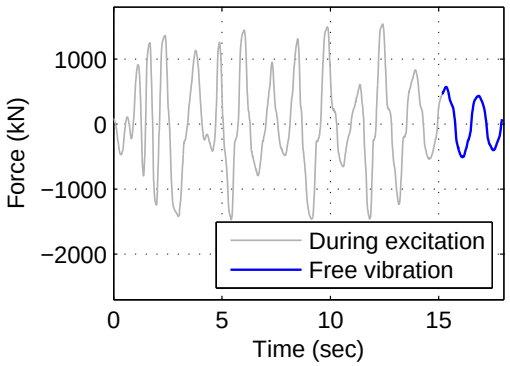

(b) Force vs. Time

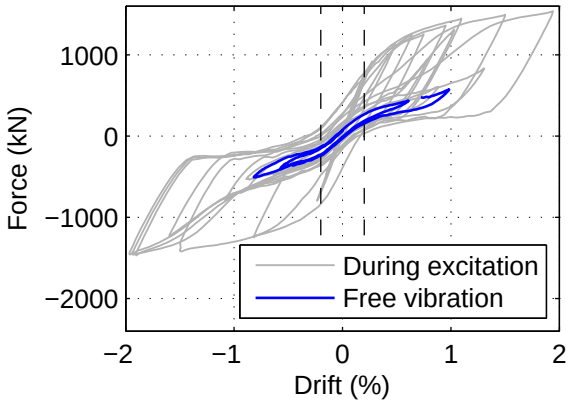

(c) Force vs. drift

Figure 5.31: 10/50 response

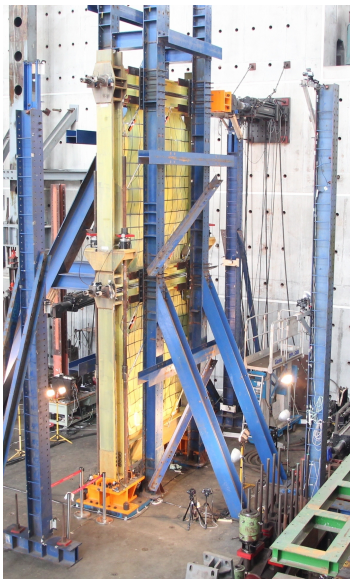

Figure 5.32: Specimen FR after the 10/50 PSD test.

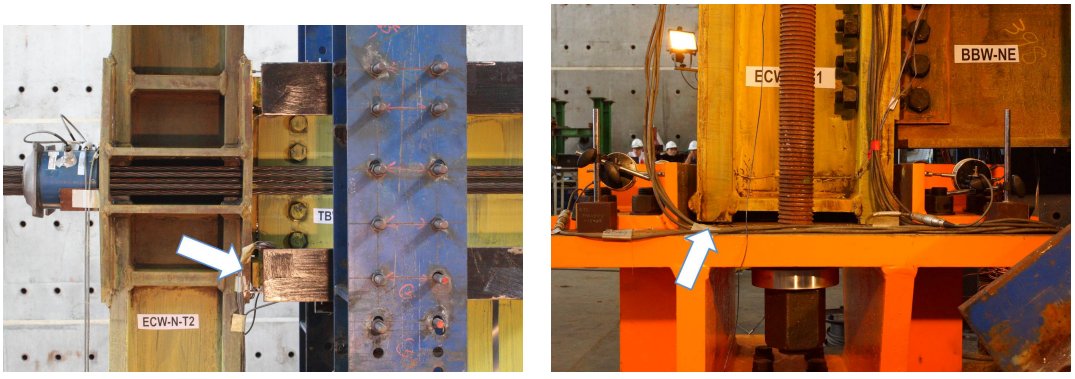

(a) (b)

Figure 5.33: (a) East end of TB and (b) EC base PT connection gap openings at 10/50N1

(a) (b)

Figure 5.34: Minor whitewash flaking in the column webs at the (a) column base and (b) just above the doubler plate in the panel zone during the 10/50 test.

in the column web just below the panel zone web doubler plates as shown in Fig. 5.34(b). Here, the yield lines are a result of stress concentration at the web-flange intersection due to shear lag as the large compressive forces from the beam flange are being transfered to the column cross-section. Minor whitewash flaking and permanent deformations were also observed in the angles connecting the BB to the columns as shown in Fig. 5.35. The whitewash flaking occured at the intersection of the angle legs. At the end of the 10/50 PSD test, the angle legs were permanently offset approximately 1-2 mm from the column face.

Tearing along the edge of the web plate was also minimal and is shown schematically in Fig. 5.36. The first web plate tear was observed just after loading up to -1.5% drift (10/50R1 in Fig. 5.36) as shown in Fig. 5.37. The first tear occurred at the toe of the weld in the top west corner of the first story web plate along the WC fish plate and was approximately 2 mm long. The longest web plate tear at the end of the 10/50 test (10/50R2 in Fig. 5.36, photo in Fig. 5.38) was approximately 13 cm long and was located along the second story WC fish plate nearest the MB. Tearing typically propagated in the web plate (i.e. not in the weld material). All of the web plate tearing during the 10/50 test was localized at the ends of the

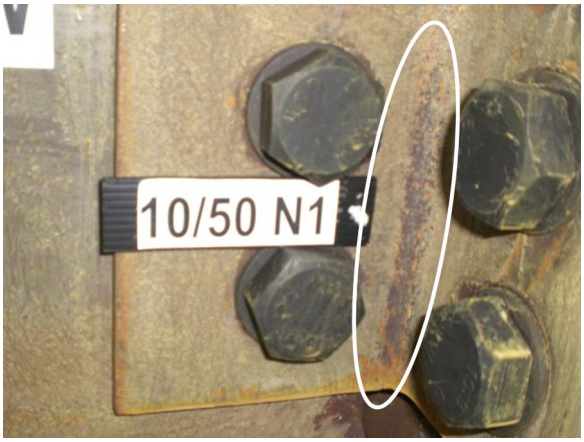

Figure 5.35: Yield lines in BB double angle connections

fish plate near the PT connections where the web plate strains are largest due to connection gap opening. At the web plate corner cutouts, the plastically elongated web plate had to deform out-of-plane as the connection gap closes, creating large curvature strains near the weld due to the out-of-plane deformation as shown in Fig. 5.39. The additional out-of-plane deformation along the unrestrained edge of the web plate corner cutout may have caused increased demands near the weld compared to conventional SPSWs where the web plate is welded along all sides with no unrestrained edges. The total torn length along any web plate edge did not extend over 8% of the edge weld length. The residual drift, as indicated by the maximum drift magnitude associated with zero-force in the actuator during the free vibration after the seismic excitation (shown in Fig. 5.31(c)), is -0.07%, indicating that the SC-SPSW specimen was capable of recentering following a 10% in 50 year event. Thus the specimen was able to meet the "repair of web plates only" performance objective proposed for this hazard level.

It should be noted that during the 10/50 PSD excitation, the maximum drifts at zero-force during the PSD excitation were 0.16% and -0.34% following peak loading in the positive and negative directions, respectively. Upon initial inspection, it would appear that the -0.34% drift (shown at a time of 3.4 sec in Fig. 5.40) at zero-force does not meet the recentering criteria; however, the drifts at zero-force decrease as the specimen oscillates at

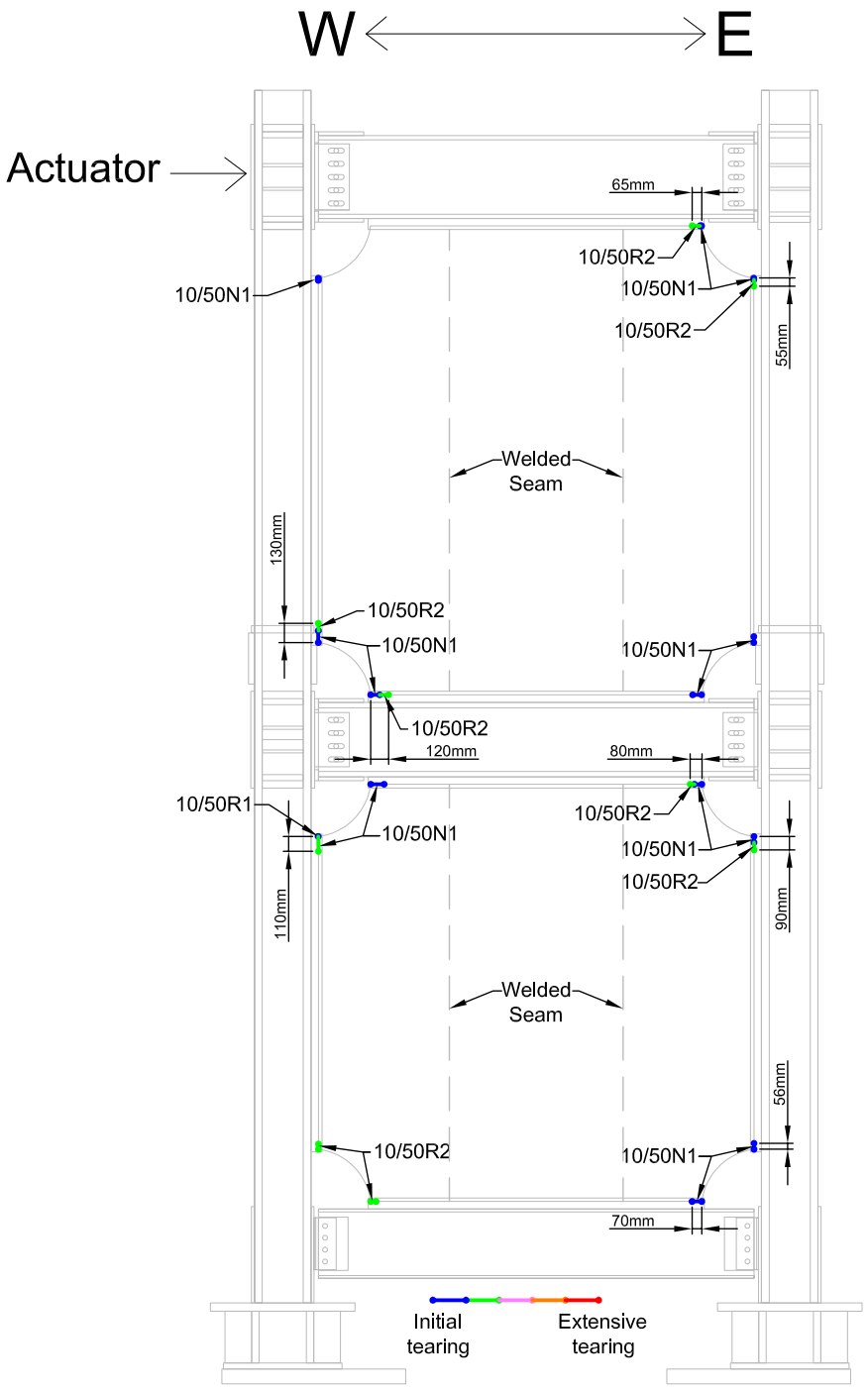

Figure 5.36: Web plate tearing at end of 10/50 test.

Figure 5.37: First web plate tearing (2 mm long) observed along first story of WC fish plate at 10/50R1

Figure 5.38: Longest web plate tear (13 cm long) at the end of 10/50 test

Figure 5.39: Out-of-plane deformation of the web plate at the fish plate near the corner cutouts

lower drift amplitudes and after the earthquake excitation. This drift observed at zero-force is due to the phenomenon of the web plate residual strength observed in the SC-SPSW subassembly tests (described later in Fig. 6.22). The residual strength in the web plate increases following cycles of larger displacement, as more force is required to overcome the plastically buckled web plate upon loading in the reverse direction. However, in the smaller amplitude cycles following the large amplitude cycles, the tension field of the plastically stretched web plate is not fully formed, the web plate has fewer buckles or corrugations that need to be overcome during unloading, resulting in a lower residual force. The residual force that exists in the web plate causes the force vs. displacement curve to intersect the disaplacement-axis at a larger drift than the zero-residual drift that the idealized tension-only web plate behavior implies; however, as the web plate residual force decreases during free vibration or vibration at lower acceleration levels, as does the residual displacement. Thus, the SC-SPSW meets recenting criteria after the seismic excitation. The zero-force drifts during free vibration, as shown at times of 15.75, 16.5, and 17.2 sec in Fig. 5.40, all have magnitues less than 0.06%, singinifcantly below the 0.2% drift recentering criteria. Further discussion of residual drift calculations will be provided in Sec. 6.4.7. Accurate quantification of this penonmenon requires further investigation.

5.5.5 2/50 test

This test simulated the SC-SPSW response during a 2% in 50 year earthquake. The proposed performance objective at this hazard level is collapse prevention [Clayton, 2010]. At this performance level, some minor yielding and residual drift in the PT boundary frame is acceptable; however, substantial yielding in the boundary frame and PT strand rupture are not acceptable, as these events may lead to sudden loss of connection strength and stiffness or formation of a soft story mechanism. The displacement and force time histories and force vs. drift response for the 2/50 PSD test are shown in Fig. 5.41.

As observed in Fig. 5.41(c), the peak drifts were 4.56% and -3.54% in each direction of loading. At the largest positive drift (2/50P1), the longest tears in the web plate were around 50 cm and were located in the top-east and bottom-west corners of the first and

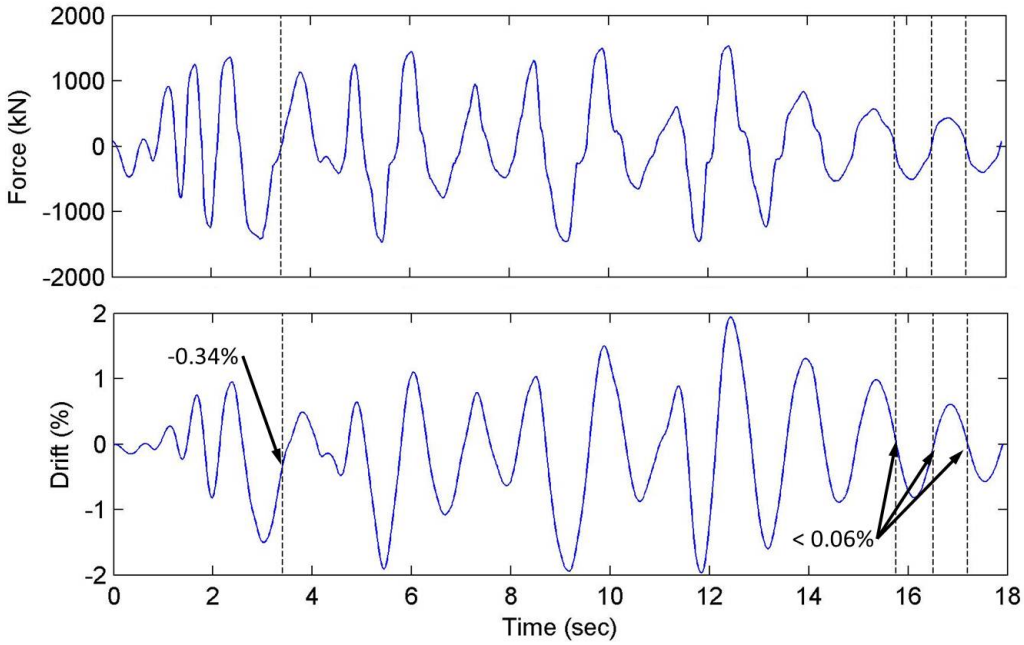

Figure 5.40: Force and drift vs. time for 10/50 test. (Notable times at zero force are marked with vertical dashed lines.)

second story web plates, respectively, and as shown in Fig. 5.42. Photos of the tearing along the HBE and VBE in the top-east corner of the first story web plate at 2/50P1 are shown in Fig. 5.43. Web plate tears at other locations ranged from 1 cm to around 30 cm. Fig. 5.44 shows a photo of the buckled shape of the web plate near the welded fish plate connection. This out-of-plane buckling is believed to be a primary contributing factor in the propogation of web plate tears. The longest tear, located along the HBE in the top-east corner of the first story web plate, propogated to 80 cm long (approximatley 36% of the web plate edge length) by the end of the 2/50 test (2/50R1). Tearing typically propogated just outside of the heat affected zone (HAZ) in the web plate material. As shown in Fig. 5.42, the tears typically propogated parallel to the weld; however, diagonal tears did propogate into the web plate after mutiple large cycles of loading, an example of which is shown in Fig. 5.45. These diagonal tears were typically located near the welded seam running vertically within the web plates.

The extent of whitewash flaking in the boundary frame did not significantly increase be-

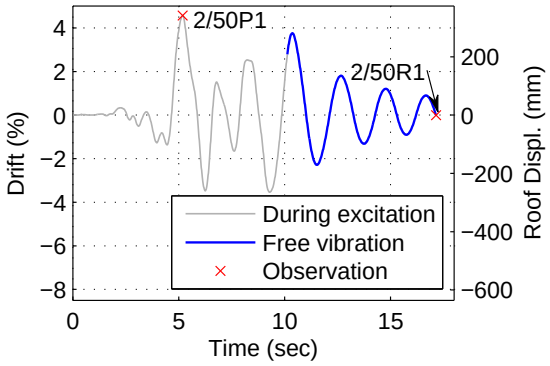

(a) Displacement vs. Time

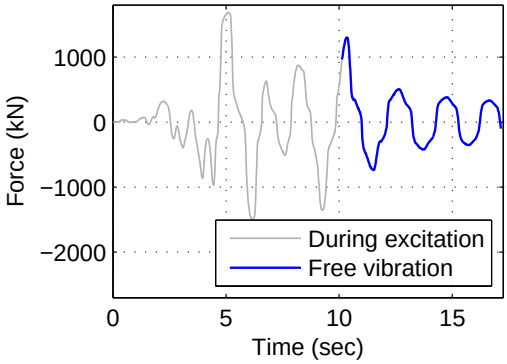

(b) Force vs. Time

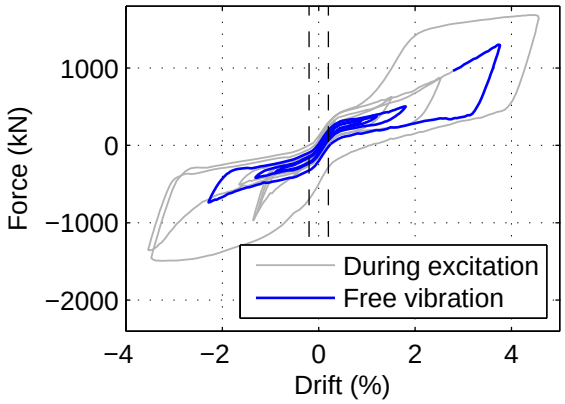

(c) Force vs. drift

Figure 5.41: 2/50 response

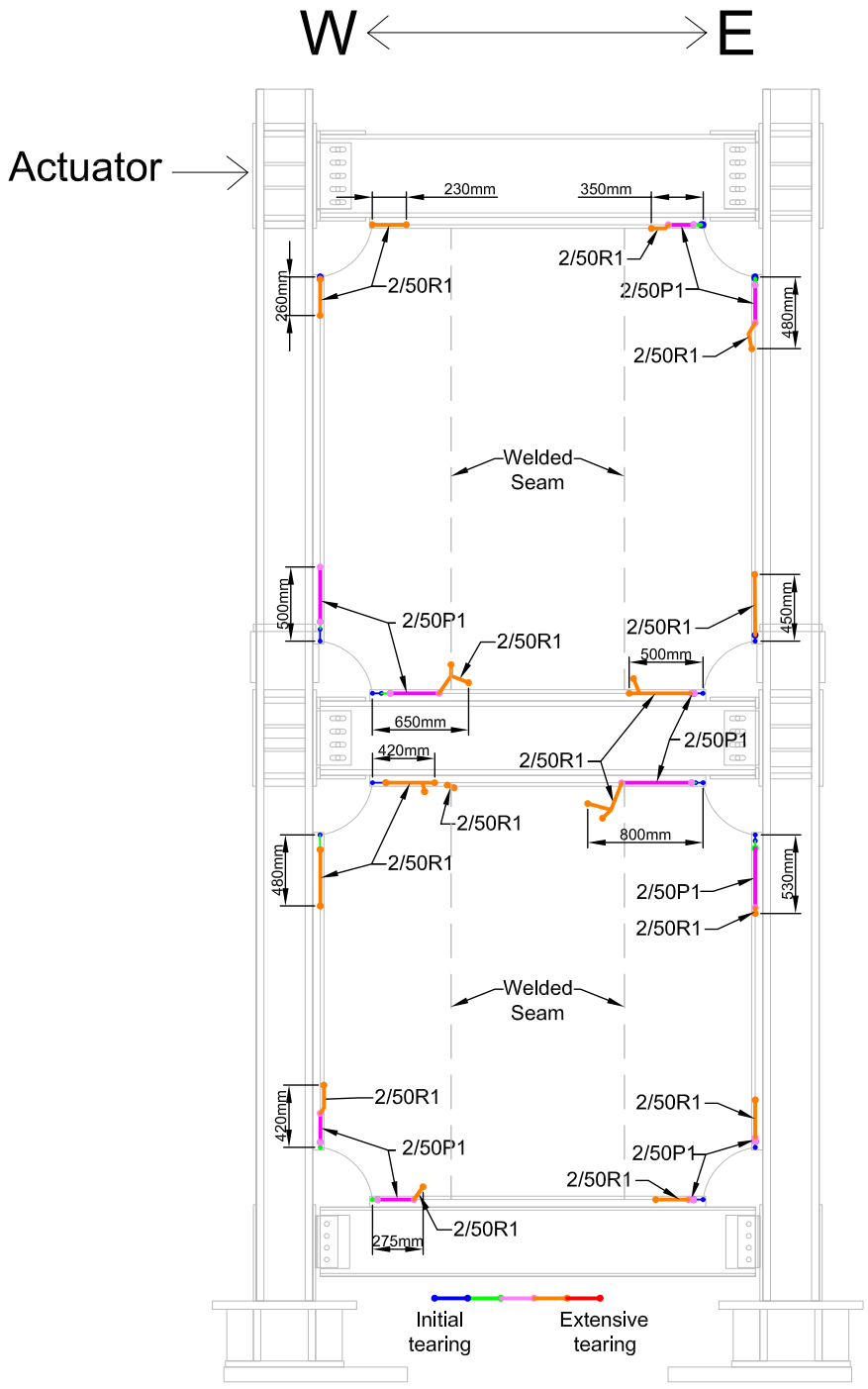

Figure 5.42: Web plate tearing at end of 2/50 test.

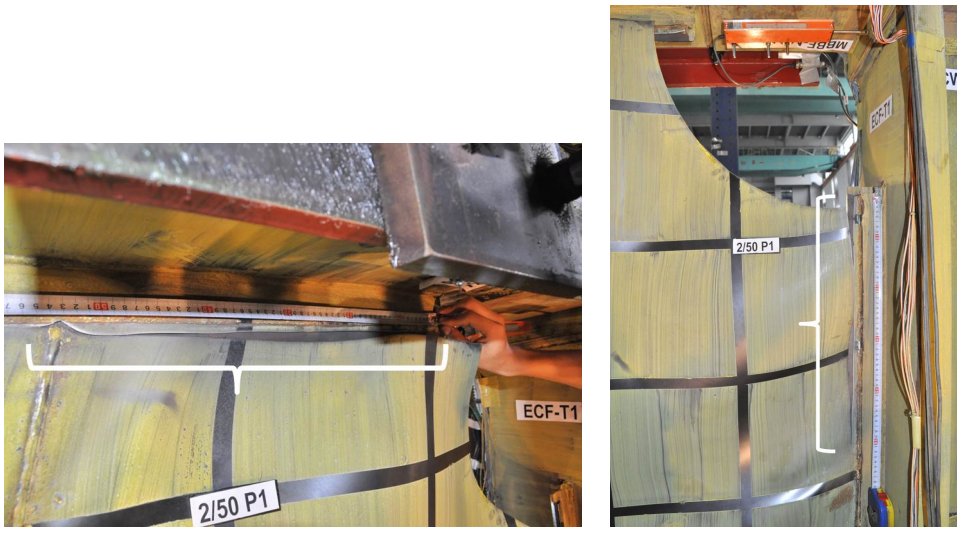

(a) (b)

Figure 5.43: Tearing in top-east corner of first story web plate along (a) HBE and (b) VBE at 2/50P1

Figure 5.44: Out-of-plane buckling of web plate along fish plate

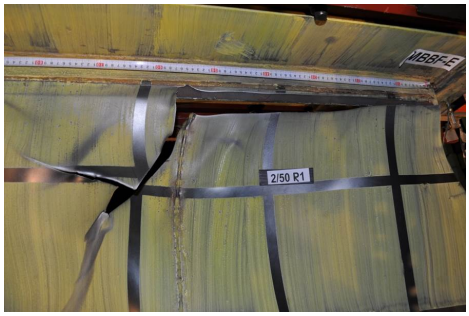

Figure 5.45: Tearing in top-east corner of first story web plate along HBE at 2/50R1

yond those observed after the 10/50 test, and no yielding was observed in the PT elements. Diagonal localized yield lines were observed at the intersection of the column webs and flanges (Fig. 5.46) and are attributed to stress concentrations caused by the shear lag effect near areas of large force concentrations, as describe previously in the 10/50 PSD test. There was some yielding and permanent deformation in the double angles at the BB connections (Fig. 5.47); however, the angle yielding was ductile. Yielding was not observed in the BB itself, and the bolted angles would be relatively easy to replace if the permanent deformations were sever enough to require repair following an earthquake. Some minor rounding was also observed at the outside corner of the base of the column flange reinforcing plates as shown in Fig. 5.48. Based on these observations and the lack of extensive boundary frame yielding, the "collapse prevention" performance objective was achieved.

Although recentering was not a criteria for the collapse prevention performance objective, the residual drift at zero-force during free vibration after the 2/50 excitation was 0.1%, still below the 0.2% recentering criteria (as shown by the veritcal dashed lines in Fig. 5.41(c)). Again, the largest drift at zero-load during the 2/50 excitation was 1.06%. A zero-force drift of this magnitude only occured once, following the largest positive excursion, while the zero-force drift during other cycles remained around or below 0.2%. The reason for this large, one-time, zero-force drift is hypothesized to be due to some part of the specimen getting temporarily "caught" on part of the lateral bracing or column base shear brackets during unloading this large displacement as this unloading response was not observed at any other time during the test (i.e. the unloading response retuned to the expected flag-shaped

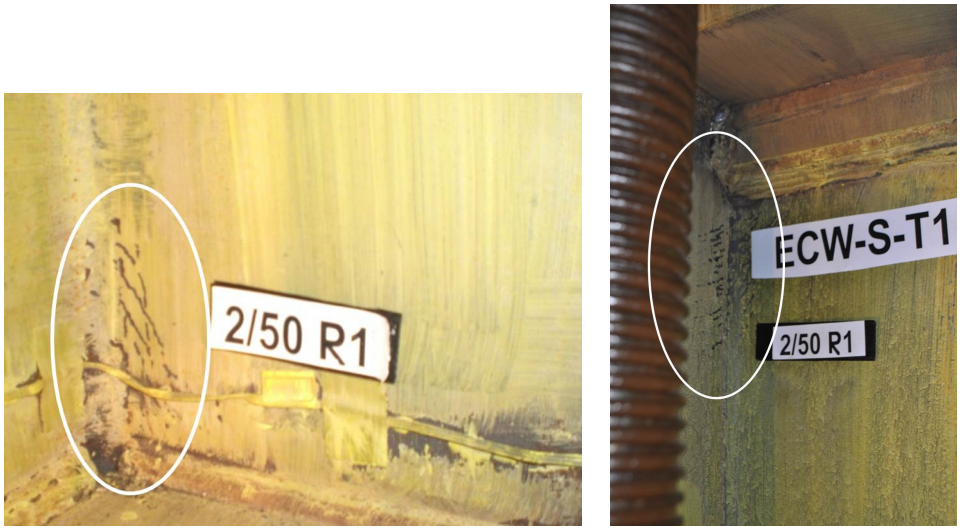

(a) (b)

Figure 5.46: Minor whitewash flaking in the column webs at the (a) column base and (b) just below the doubler plate in the panel zone during the 2/50 test.

(a) (b)

Figure 5.47: (a) Yield lines and (b) angle leg offset in double angles at BB connections.

Figure 5.48: EC exterior flange rounding at 2/50P1

SC-SPSW recentering response after this "cycle").

5.5.6 Inelastic cyclic test

The displacement and force response histories and force vs. drift response for the inelastic cyclic test are shown in Fig. 5.49. The peak strength of the two 4.5% drift cycles were 87% and 79% of the peak strength during the 2/50 PSD test, showing a significant amount of strength and ductility even after three prior seismic events. As shown in Fig. 5.49(c), the residual drifts at zero-force were less than the 0.2% recentering criteria (as indicated by the vertical dashed lines), indicating that the specimen retained its recentering capabilities.

Figs. 5.50 and 5.51 show a photo and schematic, respectively, of the extent of web plate tearing at the end of testing (EOT), after the two inelastic cycles. At the end of the inelastic cyclic test, the longest extent of web plate tearing occurred along the top of the MB with 80 cm and 140 cm tears propagating from the west and east ends, respectively, as shown in Fig. 5.51. The tears at this location extended over approximately 90% of the total web plate edge length.

Observations of yielding in the boundary frame at the end of the inelastic cyclic test were minimal and were not significantly different from observations made during the pseudo-dynamic tests. As previously described, diagonal yield lines were observed in the webs of the

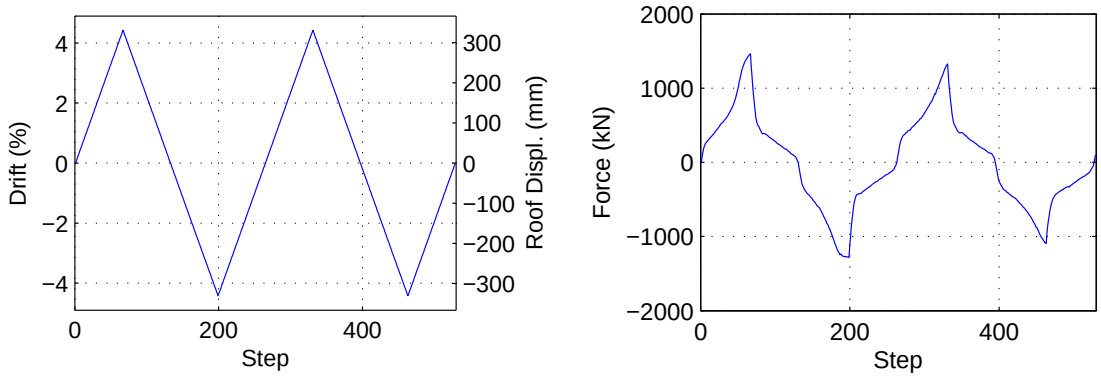

(a) Displacement vs. Time

(b) Force vs. Time

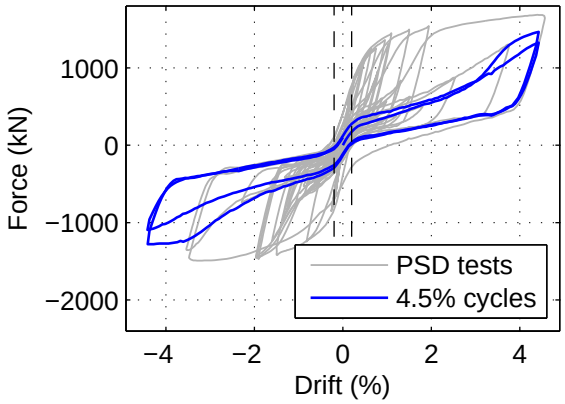

(c) Force vs. drift

Figure 5.49: Inelastic cyclic response

Figure 5.50: Specimen FR after all tests.

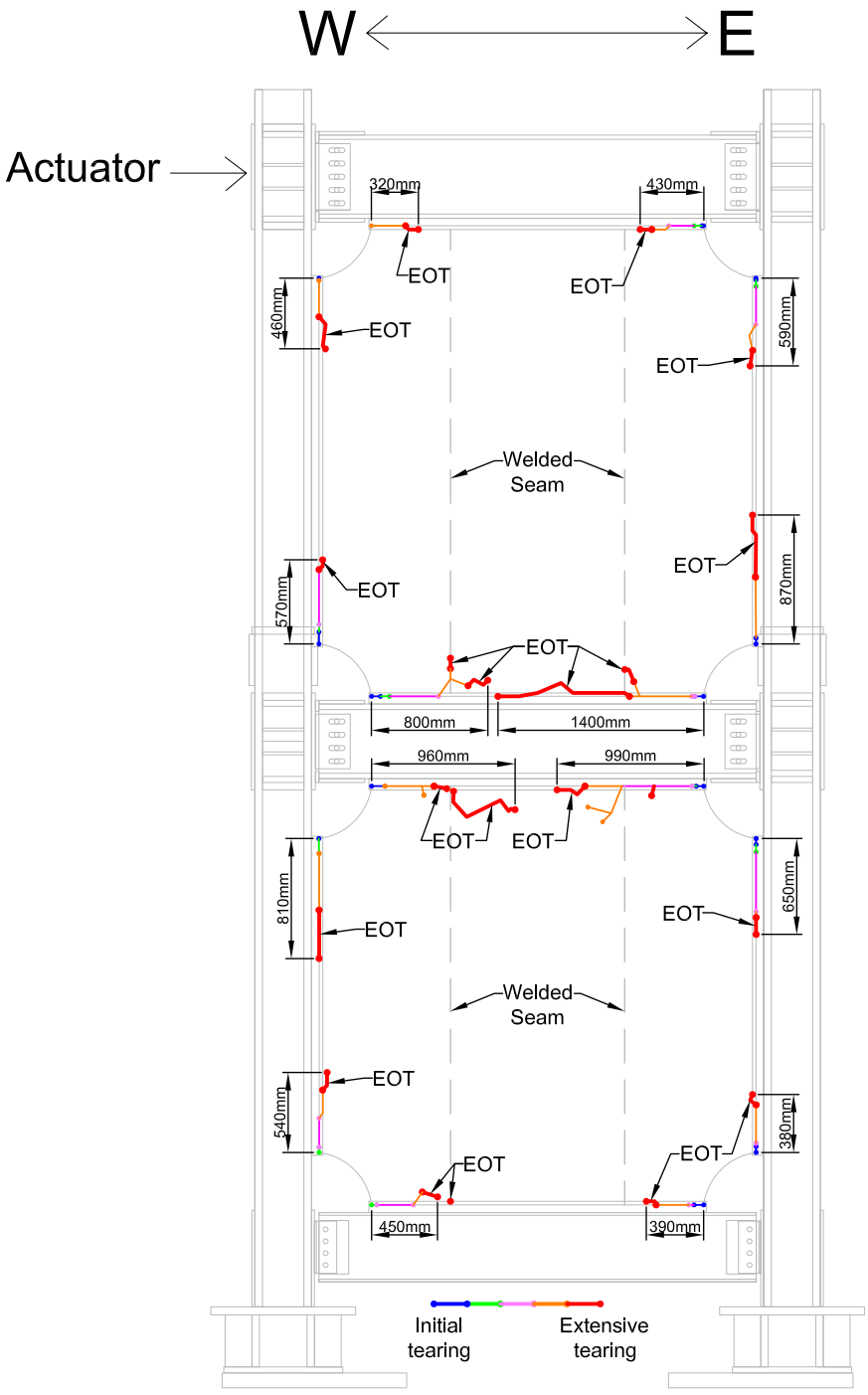

Figure 5.51: Web plate tearing at end of inelastic cyclic test (EOT).

(a) (b)

Figure 5.52: Diagonal yield lines at (a) east and (b) west column base

column bases nearest the outside flange as shown in Fig. 5.52. Similar diagonal yield lines in the column webs just outside of the web doubler plates were also observed, examples of which are shown in Fig. 5.53. These yield lines occurred nearest the inside flange and were observed in both the east and west columns at both the middle and top beam connection regions. The double angles at the bottom beam (BB)-to-column connections also had yield lines and permanent deformation after testing as shown in Fig. 5.54.

Some yield lines in the boundary frame were also observed after testing that had not been previously observed during the PSD tests; however, the yield lines may have been present previously but were not noticed due to obstruction of view in the test set-up. These new observations of yielding include vertical yield lines in the top beam (TB) web near the east end as shown in Fig. 5.55. Also, diagonal yield lines were observed in the north side of the west column web within the middle and top beam connection regions. These diagonal yield lines were in the middle of the web between stiffener and continuity plates and also coincided with the location of the web doubler plate plug welds on the south side of the column; therefore, they may be related to the concentration of residual stresses due to the plug welds along with the transfer of shear stresses between the column web and the doubler plate. A photo of these yield lines and the corresponding plug weld on the opposite side of the web are shown in for the MB connection region in Fig. 5.56 and are similar to the yield lines observed in the TB connection region; however, there were no observations of similar yield lines in the east column at these locations.

(a)

(b)

Figure 5.53: Diagonal yield lines in east column web (a) above and (b) below the web doubler plate at the middle beam location

Figure 5.54: Yielding in the double angle connections at the bottom beam at the end of testing

(a) (b)

Figure 5.55: Vertical yield lines on the (a) south and (b) north sides of the east end of the top beam web

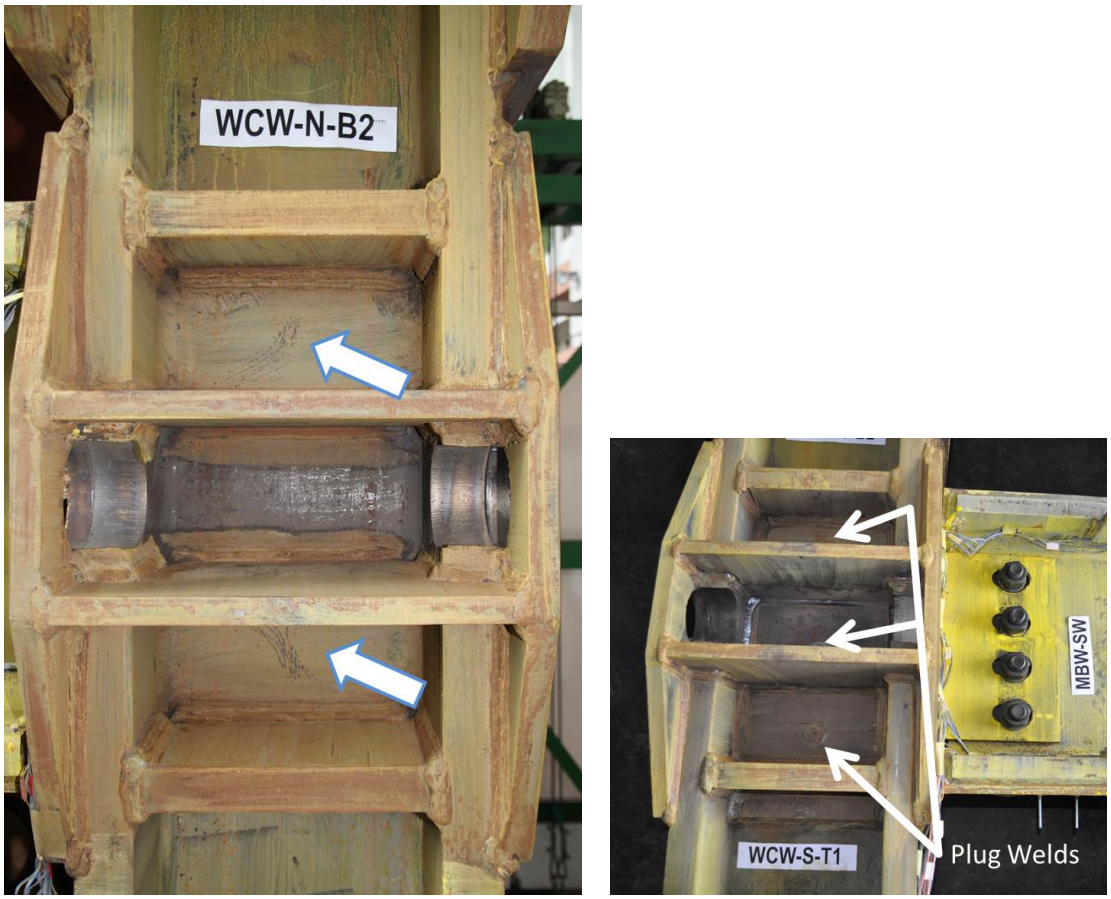

(a) (b)

Figure 5.56: (a) North and (b) south side of the west column web at the middle beam connection (PT stands removed after testing)

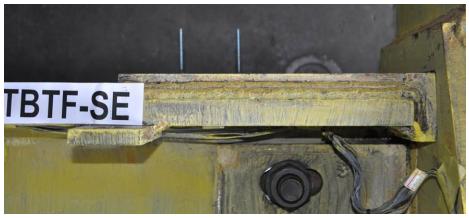

Figure 5.57: Typical flange reinforcing plate (shown here after testing and after removal of PT strands)

Apart from those mentioned above, there were no additional observations of damage in the boundary frame. Although rounding was observed in the column flanges at the base (discussed previously in Fig. 5.48), no rounding or localized permanent deformation was observed in the beam flanges due to the flange bearing reinforcing plates welded to the beam ends (as shown in Fig. 5.57).

5.6 Data Corrections

The DAQ system at NCREE was set up such that it only recorded data during loading; therefore, the data required much less "cleaning" than the data from the subassembly tests at UW described in Sec. 4.4. During the test, some of the diagonal displacement transducers measuring web plate deformations were removed as the out-of-plane deformation of the torn web plate became large enough to touch those transducers. Data from these instruments were removed after they were taken off of the specimen.

Also, because three-wire strain gages were used, the variations due to ambient temperature described in Sec. 4.4 were not observed. Some strain gages either had flat line readings or noisy readings that did not correspond to any physical mechanics of the system. The data from these strain gages[7] were removed. The PT and actuator load cells were also professionally manufactured and produced reliable and stable readings. Any additional corrections of the data for particular calculations will be described as needed in Sec. 6.4.

[7]Strain gage data channels that were removed include: SG34, SG04, SG03, SG46, SG20, SG37. See Fig. A.1 for locations of these gages.

5.7 Summary of Pseudo-dynamic testing

A full-scale, two-story SC-SPSW specimen was tested at NCREE in Taiwan. This specimen (Specimen FR) had PT connection at the ends of the top and middle beam and at the base of the columns. The test program included an elastic free vibration pseudo-dynamic (PSD) test, an elastic quasi-static cyclic test, and PSD excitations representing 50/50, 10/50, and 2/50 seismic hazard levels, followed by quasi-static cycles at 4.5% drift. These tests were conducted sequentially without any repairs to the specimen in between tests. The results of these tests include:

- The specimen met or exceeded the proposed performance objectives at all three hazard levels, including: no web plate yielding after the 50/50 excitation; no significant PT boundary frame yielding, peak drift less than 2%, and recentering after the 10/50 excitation; and negligible PT frame damage and recentering after the 2/50 excitation.

- The specimen had significant residual strength in the 4.5% drift cycles following the 2/50 excitation.

- The only yielding observed in the specimen was ductile yielding of the double-angle shear connections as the bottom beam (as intended) and minor diagonal yield lines in the column webs due to the shear lag effect in areas of high stress concentrations.

- Web plate tearing initiated at the toe of the web plate-to-fish plate weld (first observed at a drift magnitude of 1.5%) and propogated within the web plate material. The web plate tears propogated more severley during the 2/50 test; however, the stiffness of the backbone of the force vs. drift response during the 2/50 test was always positive (i.e. no peak strength degradation due to web plate tearing).

- The magnitude of the web plate residual strength appears to be transient and appears to be related to the peak drift of the previous "cycle." When unloading from a drift exceeding previous peak drifts, the magnitude of the residual web plate strength is larger than when unloading from a peak drift that is smaller than the maximum drift

experienced by the plate. This suggests that web plate residual strength may not have a large impact on recentering capabilities in that during free vibration after an earthquake as the magnitude of drift oscillations decay, so does the magnitude of the web plate unloading resistance.

The PSD loading of the specimen was considered to be more severe compared to design code assumptions for several reasons. These include:

- The spectral acceleration responses of the PSD excitations were greater than the targeted spectral values (Fig. 5.27). The target spectral values were based on USGS target values for the Los Angeles region (Table 5.1), and the PSD excitation was chosen from a set of ground motions scaled to match, on average, those target values.

- The entire seismic mass of both stories was lumped at the top of the specimen (the location of the actuator). This results in larger analytical inertia forces at the top level than would have been present if the seismic mass was evenly distributed at both stories.

- The seismic mass attributed to the specimen was larger than expected based on the proposed design procedure [Clayton, 2010] in which the web plates are designed to resist the entire seismic lateral load. In this case, the seismic mass was determined based on preliminary estimation of the specimen strength and an assumed system overstrength, $\Omega_o = 2$. This method resulted in fours walls being required in each direction of the prototype building to resist the design base shear. This preliminary estimation of the design strength also corresponds to a "balanced design" approach where the resistance of the PT boundary frame is considered. However, if only the web plate strength is considered (which was unknown at the time of the preliminary determination of the seismic mass), then six SC-SPSWs would be required in each direction of the building, resulting in a 33% reduction in the tributary seismic mass than was used in the tests.

- The earthquake simulations were conducted sequentially. No repair was done to the specimen following the 10/50 event, before the 2/50 event. In an actual SC-SPSW, the web plate would likely be elastic and undamaged prior to a 2/50 event.

- No additional analytical damping was considered in the PSD loading equations of motion. The equivalent viscous damping during the elastic free vibration test was estimated to be around 1%, conservatively within the range expected in steel buildings. It was assumed that this damping was due to friction in the test set-up, not within the specimen itself, and could therefore be considered to simulate the damping present in the non-lateral load resisting systems of a real structure. Therefore, no additional analytical damping was added. However, it is possible that the damping observed in this test was due to friction in the specimen (in the rotation connections, etc.)– friction that would be present in the SC-SPSWs of a real building. If this is the case, then the non-lateral load resisting systems would provide additional damping that was not simulated in the analytical PSD equations of motion.

When these points are considered, it suggests that the SC-SPSW specimen was subjected to loading that represents the "worst case" scenario. The fact that the specimen performed so well (i.e. met and even exceeded the proposed performance objectives) under this severe loading suggests the robustness of the SC-SPSW system. Adjusting the tributary seismic mass, analytical damping, excitation spectral responses, etc. to more closely match those suggested by the design procedure would further reduce the specimen demands. However, it should also be noted that the PT boundary frame was designed before web plate material properties were known. They were capacity-designed conservatively for web plate forces approximately 20% larger than what was present in test specimen.

Chapter 6

DATA ANALYSIS AND RESULTS

6.1 Introduction

Experimental data was collected from hundreds of instruments in both SC-SPSW experimental test programs. This chapter expands upon the force vs. drift data presented in the previous chapters. The data has been analyzed to produce more meaningful values such as PT connection gap rotation, member force and moment demands, specimen stiffnesses, and more. The methods used to analyze the data and the interpretation and comparison of those results are presented for each test program.

6.2 Subassembly Test Data Analysis

This section presents the data analysis for the SC-SPSW subassembly tests. Representative example plots are shown to demonstrate certain concepts or results, and in most cases additional plots for the other specimens can be found in Appendix B.

6.2.1 PT force and gap rotation

The gap opening relative rotation, θ_r, was calculated from displacement potentiometers located on the inside of the flanges at both ends of every HBE. The potentiometers measured relative displacement between the HBE flange and the VBE bearing surface. The rotation was calculated as the difference in the potentiometer readings at the top and bottom flanges divided by the distance between the two potentiometers. The distance between the potentiometers was measured with a device with 1/16th inch (1.6 mm) precision. The potentiometers were also assumed to be parallel with the HBE flange. The gap opening vs. drift response and PT force vs. gap opening response for a few representative specimens will be presented. Additional figures for all of the specimens are shown in Appendix B.1.

Fig. 6.1 shows the PT connection gap rotation response for W18-8s100k. As previously

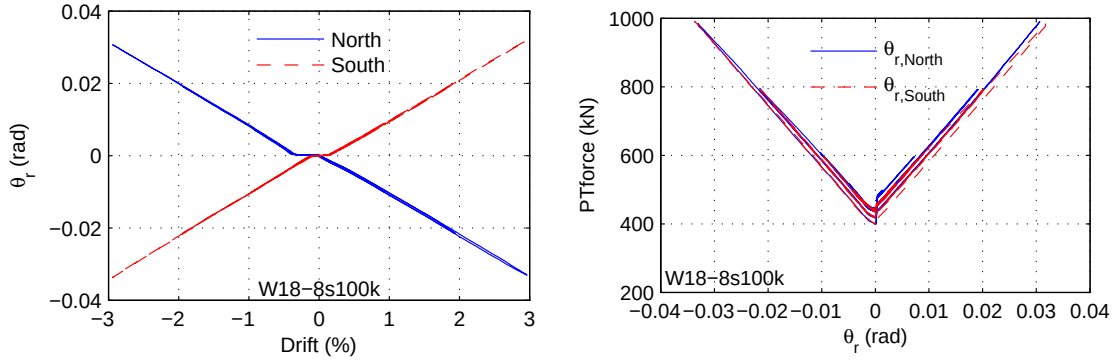

(a) (b)

Figure 6.1: PT connection gap rotation response in middle HBE of W18-8s100k. (a) Gap rotation vs. drift, (b) total PT force vs. gap rotation

discussed, the PT frame behavior is expected to be bilinear. At small drift demands, the PT connection in closed (θ_r=0 as seen in Fig. 6.1(a)). After connection decompression, the gap rotation, θ_r, and the PT force increase linearly as shown in Figs. 6.1(a) and (b), respectively. The sign of θ_r is positive if the end of the HBE is rocking about the top flange corresponding to a positive beam moment at its end, and negative if the HBE is rocking about the bottom flange. Fig. 6.1(a) indicates that connection decompression does not occur at the same drift for both ends of the HBE, as would be expected in an ideal PT frame. This difference is due to uneven bearing surfaces and fabrication tolerances. The PT force also does not increase perfectly linearly just after connection decompression as shown in Fig. 6.1(b). At small values of θ_r, the connection gap is just forming and the HBE may be rocking about some point within the compression flange, not along the outermost edge as assumed in the ideal PT connection behavior, thus producing a slightly lower increase in PT force at small drift demands. Fig. 6.1(b) also appears to have a jump in PT force at θ_r=0. This jump is due to the formation of a gap at one end of the HBE causing the PT to elongate when no gap is present at the other end of the HBE. For example, in Fig. 6.1(a) under negative drift, a gap forms at the south end of the HBE prior to gap formation at the north end; therefore, Fig. 6.1(b) shows a jump in the PT force vs. $\theta_{r,North}$ because the PT strand is elongating while $\theta_{r,North}$=0.

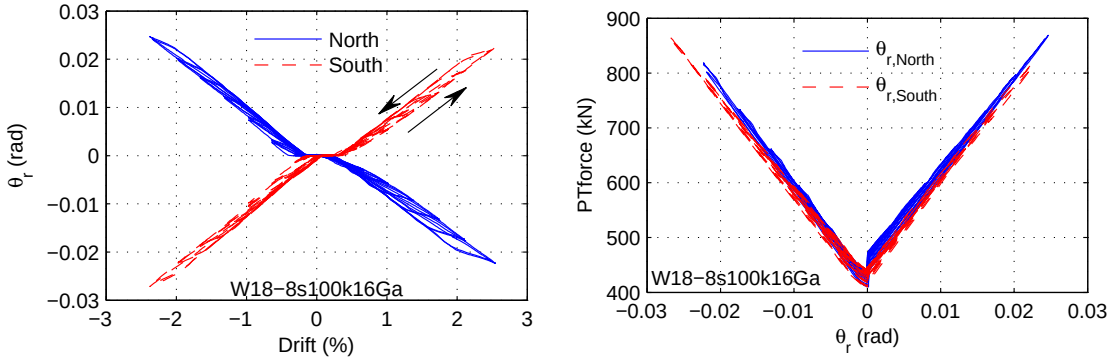

Figure 6.2: PT connection gap rotation response in middle HBE of W18-8s100k16Ga. (a) Gap rotation vs. drift, (b) total PT force vs. gap rotation

Fig. 6.2 shows the PT connection gap rotation response for W18-8s100k16Ga to demonstrate how the web plates affect response compared to the bare PT frame presented in Fig. 6.1. Fig. 6.2(a) shows that the gap opening vs. drift behavior is not as bilinear as that presented for the bare PT frame. Because the web plates are connected to the HBEs and VBEs, they are providing some restraint to gap opening as the specimen is being loaded. This can be observed in Fig. 6.2(a) in that at a given path, the gap rotation during loading has a lower magnitude than the gap rotation at the same drift during unloading. However, the effect of the web plate restraint on gap opening is small; therefore, the assumption that gap opening is approximately equal to the drift is still appropriate to use when estimating HBE demands. As shown in Fig. B.12(a), the specimen with web plates connected to the HBEs only (W14-8s100k16GaHBE), this restraint to gap opening is not present, and the specimen has a bilinear gap rotation vs. drift response, similar to the bare PT frame. Fig. 6.2(b) also shows that with the presence of web plates, the PT force is still linearly related to the gap rotation as indicated in Eqn. (2.3).

Fig. 6.3 shows the gap rotation response for W14-8s100k16Ga. Many of the same conclusions can be drawn from these plots as could be observed in the previous discussion of W18-8s100k16Ga; however, the data for this specimen demonstrates the effects of initial gaps present in the HBE bearing surfaces. As previously discussed, there was an initial gap

present at the top flange of the south end of the middle HBE in the W14 specimens. As shown in Fig. 6.3(a), the north end of the HBE behaves as expected, with θ_r=0 at small drifts and increasing after connection decompression; however, the south connection of the middle HBE has a linear response at zero drift and levels off (i.e. no change in θ_r) around θ_r=0.005 radians at small positive drift demands between approximately 0.5% and 0.9%. This suggests that the initial gap present in the top flange of the south end of the middle HBE was equivalent to a gap rotation of approxiamtely 0.005 radians. This is also evident in the PT response in Fig. 6.3(b). The PT forces should be lowest when both connections are closed at θ_r=0. In this case though, the north and south connections are not both closed simultaneously; therefore, the PT forces are lowest at some point between connections being closed at a θ_r of approximately 0.003 radians and -0.001 radians in the south and north ends of the HBE, respectively.

After observation of the initial gap, a shim was installed at this location to try to fill the initial gap and allow even bearing of the pre-decompressed HBE at this end. The shim was intended to mitigate observed behavior that did not match the idealization. For the W14 subassembly tests, the shim was present for specimens W14-8s100k20Ga and W14-6s75k20Ga only. The shim did help reduce the gap in the initial configuration, but did not close it entirely as can be observed by the W14 gap rotation responses before (Figs. B.10 through B.12) and after (Figs. B.13 through B.14) shim plate installation shown in Appendix B.1. Although the presence of gaps in the initial configuration due to fabrication tolerances does not greatly affect global response, the initially decompressed PT connection responds with a lower stiffness (equal to the post-decompression stiffness). Similarly, the initially decompressed connection will have lower PT force when the initial gap closes, resulting in lower than expected PT forces and PT boundary frame strength. Although the reduction in PT frame strength is not significant, the reduction in initial PT frame stiffness may result in larger deformations under wind loading; therefore, care should be taken during fabrication to avoid uneven bearing surfaces and connection gaps in the initial configuration. Improvements to the PT connection details to avoid uneven bearing were used in the full-scale specimen and are discussed in the detailing considerations in Chapter 9.

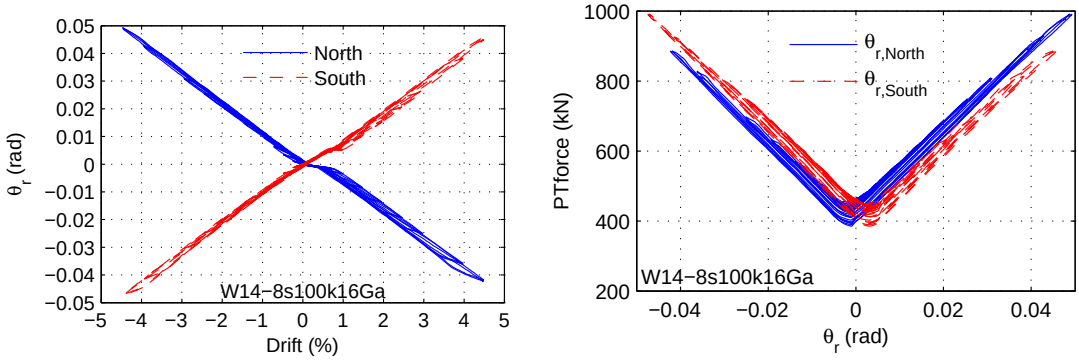

(a) (b)

Figure 6.3: PT connection gap rotation response in middle HBE of W14-8s100k16Ga. (a) Gap rotation vs. drift, (b) total PT force vs. gap rotation

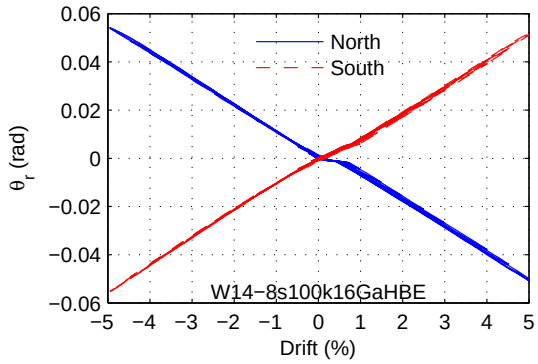

Figure 6.4: Gap rotation vs. drift response in middle HBE of W14-8s100k16GaHBE.

6.2.2 PT losses

As discussed previously (e.g. Figs. 4.15(b), and 6.3(b)), the initial PT force, T_o, prior to connection decompression decreased throughout testing during cycles of increasing displacement. These losses are believed to be due to PT anchorage seating. From experimental PT force data, T_o was determined for each cycle of loading and was taken as the minimum total PT force at each HBE during each cycle of loading. Due to the presence of the initial gap at the top flange of the south end of the middle HBE in many specimens, the minimum PT force may not have occurred at zero-drift (as observed in Fig. 6.3). The T_o determined from the first cycle of loading was taken as the initial pre-decompression PT force, $T_{o,i}$. The loss of pre-decompression PT force, T_{loss}, was taken as the T_o determined for a given cycle minus $T_{o,i}$. Table 6.1 shows the initial PT force in the middle HBE at the beginning of testing, $T_{o,i}$, and the percentage of PT force loss, $T_{loss}/T_{o,i}$. The percentage of PT loss is provided for two demands parameters: the first cycle of loading closest to 2% drift and at the end of the test (the exact drift demands are provided in Table 6.1). In general, PT losses were typically between 4% to 6% of the initial PT force after the first cycle of loading at approximately 2% drift. Total PT force losses were typically between 10% to 20% of the initial PT force at the end of testing (Table 6.1).

Fig. 6.5 shows the PT force loss, T_{loss}, versus the peak drift previously incurred for each HBE in W18-s8100k20Ga-2. The amount of PT anchorage seating is expected to be related to the peak PT force. The PT force demand is related to the PT elongation, which can be calculated as the gap rotation demand, θ_r, times the HBE depth, d (Eqn. (2.3)). Since the PT connection gap rotation can be approximated by the drift demand in radians (Sec. 2.4.1.1), it follows that the PT losses should be proportional to the peak drift demands as shown in Fig. 6.5.

A non-dimensional relationship between PT loss and peak PT demands was determined that was independent of the initial PT force, HBE depth, or number of PT strands. The peak drift demands (in radians) times the HBE depth were used as an approximation of the peak beam growth or PT elongation, $\Delta_{PT,max}$, for each cycle. The amount of PT anchorage seating (i.e. the length by which the PT strands shortened due to anchorage

Table 6.1: Actual initial PT force, $T_{o,i}$, and PT loss (as percentage of T_o) for middle HBE after loading at approximately 2% drift and at end of testing in SC-SPSW subassembly specimens

Specimen	$T_{o,i}$ (kN)	Approx. 2%		End of test	
		$T_{loss}/T_{o,i}$(%)	Drift (%)	$T_{loss}/T_{o,i}$(%)	Peak Drift(%)
W18-8s100k	444	5.6	1.94	6.1	1.94
W18-8s100k20Ga	444	5.0	2.00	14.6	3.66
W18-6s75k20Ga	333	5.4	2.15	12.7	3.66
W18-6s75k16Ga	341	4.0	2.12	12.9	4.16
W18-8s100k16Ga	441	4.6	2.10	6.4	2.54
W18-6s75k	331	2.7	1.92	2.8	1.91
W18-8s100k20Ga-2	443	4.5	1.94	15.9	3.85
W18-8s100k16Ga20Ga	445	6.0	1.93	19.4	4.49
W18-8s100k20GaW	440	4.6	1.94	19.7	4.96
W14-6s75k	326	8.8	2.00	10.8	2.00
W14-8s100k16Ga	461	4.6	1.97	14.0	4.48
W14-8s100k16GaHBE	408	3.3	1.98	11.5	5.00
W14-8s100k20Ga	447	3.7	1.97	13.4	5.01
W14-6s75k20Ga	333	2.3	1.97	8.0	4.51

seating), $\Delta_{PT,loss}$, was calculated as the PT force loss, T_{loss}, for each cycle divided by the axial stiffness of all of the PT strands at a given HBE, k_{PT}. A linear regression of the $\Delta_{PT,loss}$ vs. $\Delta_{PT,max}$ data was conducted for each HBE of each specimen. The slope of these regressions are provided in Table 6.2 and represent an estimation of the amount of PT anchorage seating as related to the peak PT elongation. For example, in the middle HBE of W18-8s100k20Ga-2, the total amount of PT anchorage seating is approximately 8.2% of the peak elongation of the PT strand, as estimated by the drift demand times the HBE depth. These values of PT seating vs. peak elongation tended to range from 5% to 10% for the SC-SPSW subassembly specimens. Eatherton and Hajaar [2010][1] found that the loss in minimum PT force was approximately 14% of the increase in maximum PT

[1]Eatherton and Hajaar [2010] also used 13mm diameter seven-wire PT strands with one end having the same three-wedge barrel PT anchorage; however, the other end of the PT had two-part wedges in conical holes. The PT strands in these tests were on the order of 5m in length.

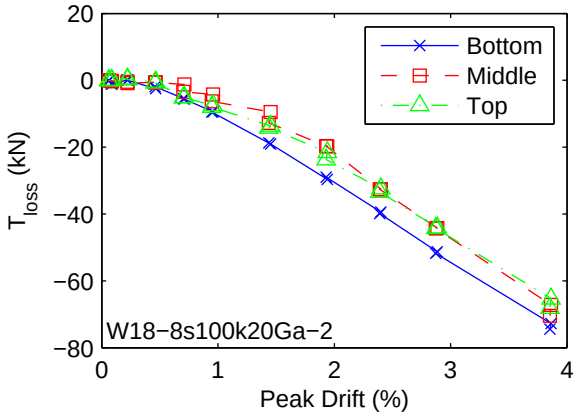

Figure 6.5: PT force loss vs. peak cycle drift for bottom, middle, and top HBEs of W18-8s100k20Ga-2

force for the scaled vertically rocking braced frame specimens. The SC-SPSW subassembly specimens had an average loss in minimum PT force of approximately 8% of the increase in maximum PT force, which is less than that of the Eatherton and Hajaar [2010] tests, but still with a similar order of magnitude. Although these values are representative only of the PT anchorage systems, PT strand length, and PT stressing methods used for this test program, they may be useful to consider in design of SC-SPSWs in which PT demands and losses are expected to be significant or may impact recentering capabilities.

6.2.3 HBE Axial force and moment demands

The axial force and moment demands were determined from the strain gage readings taken at each section along the boundary elements. As previously described, the strain measurements used in these calculations, referred to as the change in strain, $\Delta\epsilon$, were taken as the measured strain minus the initial strain at the beginning of testing. A linear regression of the gage distance from the member centroid vs. $\Delta\epsilon$ was taken at each colinear strain gage section and at every time step. The linear regression used to approximate the strain profile assumes that plane sections remain plane and that flexural and axial stresses are evenly distributed throughout the the entire cross-section. Since the connection region has very localized strains due to the rocking flange-bearing behavior, this assumption was only applied to the

Table 6.2: PT anchorage seating (given as % of approximation of maximum PT elongation) for SC-SPSW subassembly specimens

Specimen	$\Delta_{PT,loss}$ / $\Delta_{PT,max}$ (%) Bottom HBE	Middle HBE	Top HBE
W18-8s100k	7.9	6.5	5.2
W18-8s100k20Ga	9.9	7.8	8.2
W18-6s75k20Ga	8.7	6.7	7.3
W18-6s75k16Ga	8.5	6.6	7.7
W18-8s100k16Ga	7.9	4.7	4.2
W18-6s75k	4.1	3.2	2.4
W18-8s100k20Ga-2	9.1	8.2	8.0
W18-8s100k16Ga20Ga	10.7	9.2	9.0
W18-8s100k20GaW	7.2	7.7	6.2
W14-6s75k	8.6	10.0	9.4
W14-8s100k16Ga	10.9	7.7	7.9
W14-8s100k16GaHBE	11.1	4.9	1.2
W14-8s100k20Ga	9.1	7.5	6.9
W14-6s75k20Ga	6.2	4.3	6.7

strain gage sections along the interior of the members (i.e. not at the connections). The member centroid and other cross-sectional properties (e.g. moment of inertia and area) were determined from the nominal cross-sectional properties of the built-up W-shape that included the section and fish plate(s).

From the linear regression, the strain-intercept, ϵ_o, at the cross-sectional centroid was taken as the constant strain attributed to axial load, and the slope of the linear regression was taken as the curvature, ϕ. The moment demand, M, at that point was calculated as $M = EI\phi$, where E is the nominal elastic modulus of steel (200 GPa) and I is the moment of inertia of the built-up section. The axial load, P, at that point was calculated as $P = EA\epsilon_o$, where A is the cross-sectional area of the built-up section and the other variables are as previously defined.

Since $\Delta\epsilon$ was used to calculate P and M, these represent the change in axial load and moment demand, respectively, from the beginning of the test. To account for the demands at the beginning of testing, the calculated P and M were added to their assumed initial

state. Here, the HBEs are assumed to have no initial moment demands and a constant axial force equal to the initial PT force, T_o. The VBEs were assumed to have negligible axial or moment demands caused by post-tensioning of the frame. The initial HBE demands were based on assumptions that both flanges on both ends of the HBE were bearing equally, resulting in a constant stress distribution in the member. As was discussed previously, there were some imperfections in the flange bearing surfaces due to fabrication tolerances that may have resulted in uneven bearing stresses, and thus a non-constant stress distribution; however, the actual initial moment and axial force distributions due to the uneven bearing surfaces are not believed to differ significantly from the constant axial and zero moment demands assumed.

It should also be noted that the boundary members were design to remain well within their elastic range during the largest demands expected during all of the tests; thus, the measured strains were very small. The determination of the linear strain profile also relied on the exact locations of the strain gages, which were determined using measurement devices with a 1/16th inch (1.6 mm) accuracy. And as noted previously, all of the strain gages were two-wire quarter bridge circuit gages, and the lead wires in many of the gages were spliced and extended to lengths of up to approximately 8 m resulting in a larger lead wire resistance. An increase in lead wire resistance results in an increased loss of measurement sensitivity compared to three-wire strain gage assemblies [Mic, 2010]. The small strain measurements coupled with the reduced gage sensitivity and precision of strain gage location provide an inherent uncertainty in the axial and moment demands calculated from these values. This uncertainty should be considered when comparing these derived demands to expected values.

Axial force and moment demands vs. drift plots help describe how the HBE demands change during web plate loading and unloading and PT gap decompression. A few representative plots will be shown below to discuss characteristic behavior of different specimen types; however, plots from every HBE in every specimen can be seen in Appendix B.2.

Fig. 6.6 shows the moment and axial force demands vs. drift for the middle HBE in W18-8s100k. Fig. 6.7 also shows the moment demands along the length of the middle HBE at maximum positive and negative drift demands for different cycles. For a PT frame without any web plates, a constant axial force distribution and linear moment distribution

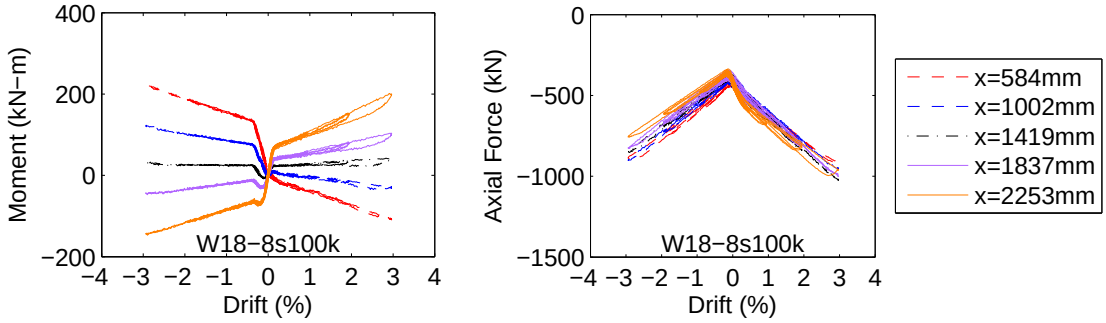

Figure 6.6: (a) Moment and (b) axial force demand vs. drift along middle HBE in W18-8s100k

is expected along each HBE. As seen in Fig. 6.6(b) the axial force is approximately the same as the initial PT force, T_o (445 kN), at zero drift and increases uniformly (i.e. the axial force is approximately the same at each strain gages section for a given drift demand) as the PT connection gap opens and the PT force increases. As expected and as shown in Figs. 6.6(a) and 6.7, the moment along the HBE is approximately equal and opposite for sections symmetric about the HBE midpoint. For example, at a given drift demand, the moment at x=584mm has approximately the same magnitude but opposite sign from the moment at x=2253mm, and so on for the other locations. Note that the section mid-length along the HBE, x=1419mm, has a constant near-zero moment due to the linear HBE moment diagram. Also, as indicated by the idealized PT frame behavior presented in Sec. 1.2.2.2 and shown in Fig. 6.6(a), the moments increase more at small drifts before connection decompression when the idealized PT connection has a stiffness equivalent to a welded moment-resisting connection. After connection decompression, the PT connection responds with a reduced rotational stiffness, resulting in a slower rate of increase in moment demands.

Some observed behaviors that differ from the idealized behavior include the small dip in moment prior to connection decompression from approximately -0.3% to -0.1% drift in Fig. 6.6(a). This small “dip” is beleived to be due to uneven bearing surface at the ends of the HBE due to fabrication tolerances. As previously described, the top flange of the

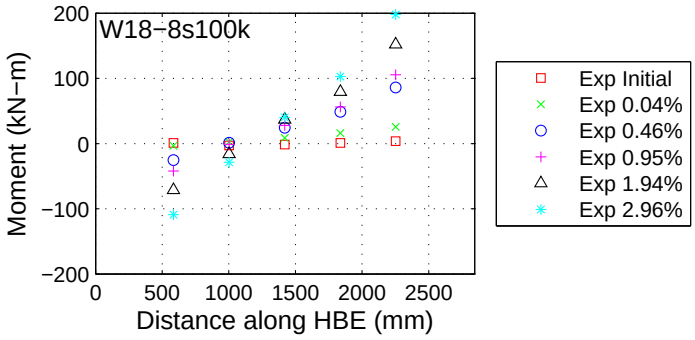

(a)

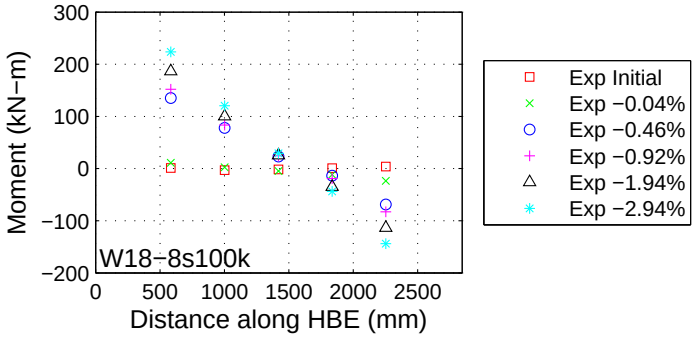

(b)

Figure 6.7: Moment demands along middle HBE in W18-8s100k at certain (a) positive and (b) negative drift demands

south end of the middle HBE was observed to have an intial gap due to the uneven bearing surfaces. To account for the initial gap, an additional shim plate was welded to the VBEs at this location; however, the thickness of the shim plate may not have been sufficient to fully close the initial gap and create an even bearing surface at both flanges. Therefore, there may have been a small initial negative moment in the HBE due to larger bearing forces in the bottom flange on the south end of the middle HBE. However, the effects of the uneven bearing surface should not affect the post-decompression behavior as both ends of the HBE are only bearing on one flange, as demonstrated by the "dip" only occuring pre-decompression. The effects of the uneven bearing surfaces at the HBE ends results in non-idealized behavior; however, these differences are negligible.

Fig. 6.6(b) also shows some slight asymmetry with respect to loading direction at small positive drifts prior to connection decompression (i.e. less than approximately 0.2% drift). In an idealized PT frame, the axial load in the HBE should only increase after decomrpession and should be equal to the increase in PT force. However, in this specimen, the axial compressive demands increase at a higher rate during loading at small positive drifts, resulting in larger axial compressive demands for positive drift demands compared to drifts of equal magnitude in the negative direction. This increase in axial demands during positive direction loading is beleived to be due to the asymmetric loading of the specimen on the South VBE. When loading in the positive direction, the actuator is pushing the specimen, causing a greater compressive force in the HBE, which is not present in the negative drift direction, where the actuator is pulling on the South VBE. Also, there is a slight hysteresis in the moment and axial force demands that is likely due to friction in the lateral bracing and test set-up, similar to the base shear vs. drift hysteresis for the bare PT frame test presented in Fig. 4.15(a).

Fig. 6.8 shows the same axial force and moment demands vs. drift for the middle HBE in a W18-8s100k20Ga-2, which represents typical behavior of SC-SPSW specimens with the same web plate thicknesses above and below the middle HBE and connected to HBEs and VBEs. In an idealized SC-SPSW HBE with web plates of equal strength and thickness above and below, the distributed loads from the web plates above and below the HBE are expected to cancel each other out, resulting in a linear moment distribution and constant

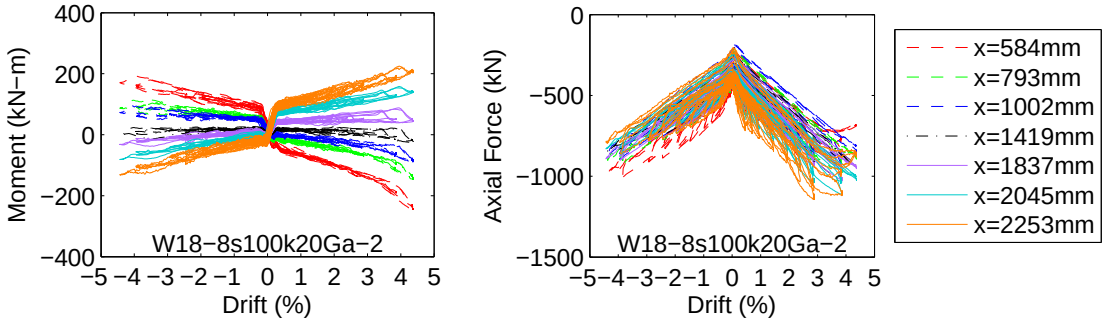

Figure 6.8: (a) Moment and (b) axial force demand vs. drift along middle HBE in W18-8s100k20Ga-2

axial force distribution along the HBE as described in Sec. 1.2.1.1 . The resulting moment and axial force demands along the middle HBE are very similar to those of the bare PT frame (Fig. 6.6) as shown in the moment distributions along the HBE in Fig. 6.9. Unlike a bare PT frame, however, there is an additional axial load in the HBE due to the web plates pulling in on the VBEs, $P_{HBE(VBE)}$. This compressive load due to the web plate creates an additional hysteresis in the axial force and moment demands that is not present in the bare PT frame HBE demands (Fig. 6.6). For example, as the specimen is being loaded in either direction, the compressive axial force demands (Fig. 6.8(b)) increase as the web plate stresses increase and pull in the VBEs. The HBE compressive axial demands then rapidly decrease as the specimen begins unloading. After the web plates are unloaded the axial demands continue to unload following a similar path to the bare PT frame as the PT connection gap closes and PT forces decrease. The HBE moment demands (Fig. 6.8(a)) also show some small hysteresis due to non-idealized web plate behaviors including: slightly different strengths for each web plate, non-constant web plate stress distributions along the HBE, web plate tearing, variations in angles of tension field inclination, etc.

Although the test setup was designed specifically to investigate the middle, or intermediate, HBE, general observations can be made from the axial force and moment demands on the bottom and top HBEs shown in Figs. 6.10 and 6.11, respectively. In general, the unloading potions of the moment and axial force demands follow the same bilinear shape as

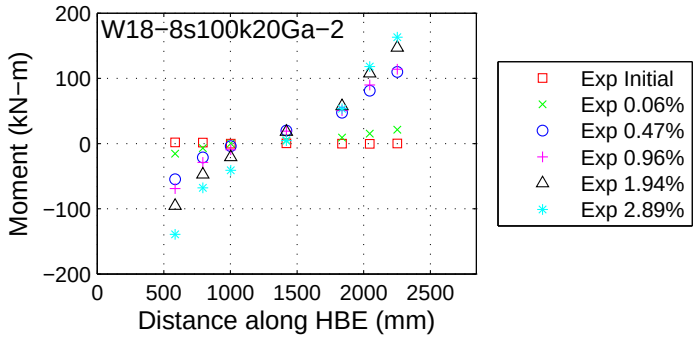

(a)

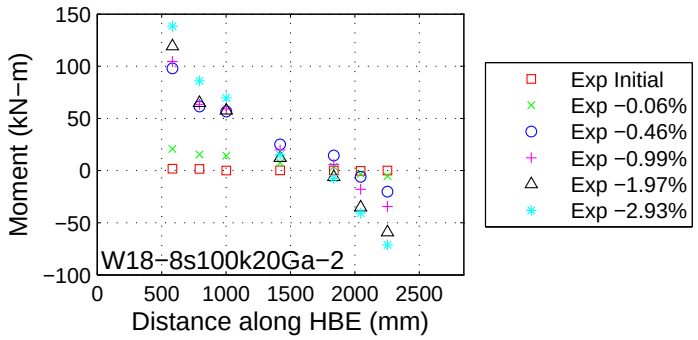

(b)

Figure 6.9: Moment demands along middle HBE in W18-8s100k20Ga-2 at certain (a) positive and (b) negative drift demands

observed in the middle HBE; however, the additional web plate demands during specimen loading result in additional hystereses, or loops in the response, that were not as prevalent in the middle HBE. The web plates only on one side of the HBEs will produce a net upward and downward distributed force on the bottom and top HBE, respectively. The distributed web plate forces will result in additional negative moments in the bottom HBE and positive moments in the top HBE, during web plate reloading and prior to web plate unloading. These additional moments due to distributed vertical web plate demands can be seen in Figs. 6.10(a) and 6.11(a), where the path of the hysteretic loops due to web plate loading and unloading correspond the the expected sign of the moment associated with these distributed loads, and where the unloading paths after web plate unloading follow a similar path as the bare PT frame. The same distributed web plate loading also produces an axial distributed load on the HBEs; however, the effects of this distributed axial loading are difficult to observe in these results, as the magnitude of this load is relatively small compared the the axial forces associated with PT forces and actuator loading.

Another general observation of the axial demands in the bottom and top HBEs (Figs. 6.10(b) and 6.11(b), respectively) are the relative magnitudes of compressive forces during loading in the positive and negative directions. As described previously for the middle HBE, during positive loading, the actuator is pushing the specimen on the South VBE at the top HBE, resulting in larger compressive forces in the top HBE during positive loading as seen in Fig. 6.11(b). Similarly, the compressive forces in the top HBE are reduced during loading in the negative direction when the actuator is pulling the top of the South VBE. These results are opposite for the bottom HBE due to the fact that there is a roller at the base of the North VBE and a pin at the base of the South VBE. Because the roller at the base of the North VBE cannot resist any horizontal load, all of the shear force in the North VBE must travel through the bottom HBE to the pin connection at the base of the South VBE. During positive loading, the actuator force is acting northward. All of the shear force acting in the North column is transferred into axial force in the bottom HBE as shown in Fig. 6.12(a). The axial force attributed to the transfer of North VBE shear forces reduces the compressive forces in the bottom HBE. This axial force is then transfered into shear in the South VBE and combines with the South VBE shear force above the bottom HBE,

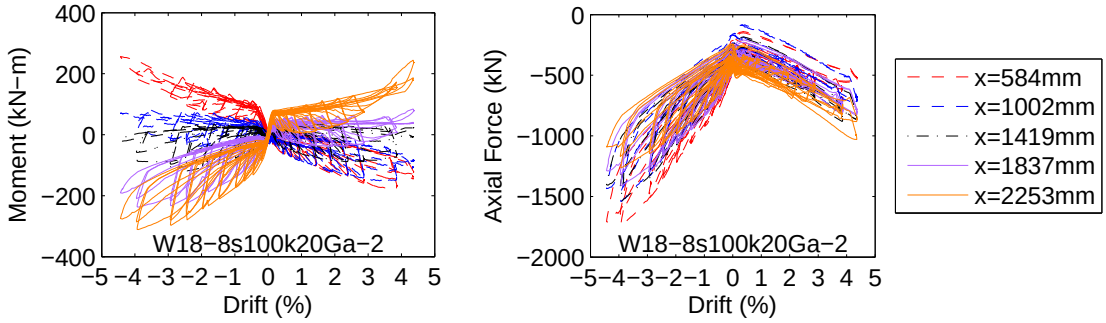

(a) (b)

Figure 6.10: (a) Moment and (b) axial force demand vs. drift along bottom HBE in W18-8s100k20Ga-2

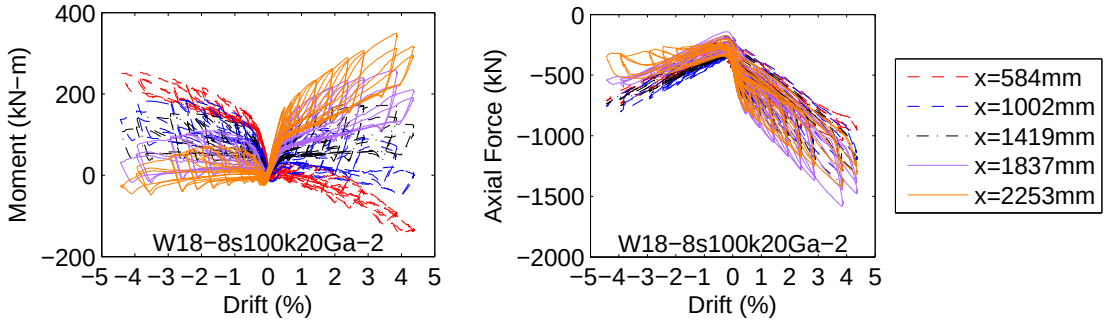

(a) (b)

Figure 6.11: (a) Moment and (b) axial force demand vs. drift along top HBE in W18-8s100k20Ga-2

such that the entire specimen base shear can travel to the reaction blocks via the pin clevis at the base of the South VBE. Similarly, in negative direction loading, the transfer of North VBE shear forces to the pin clevis results in an increase in bottom HBE axial demands as shown in Fig. 6.12(b). The influence of the North VBE shear force transfer through the bottom HBE can be seen in Fig. 6.10(b), where the compressive forces are higher in the bottom HBE during negative direction loading and lower during positive direction loading.

As the middle HBE is the main focus of this test program, the remaining analysis of results will focus on the middle HBE. The results for specimen W18-8s100k16Ga20Ga

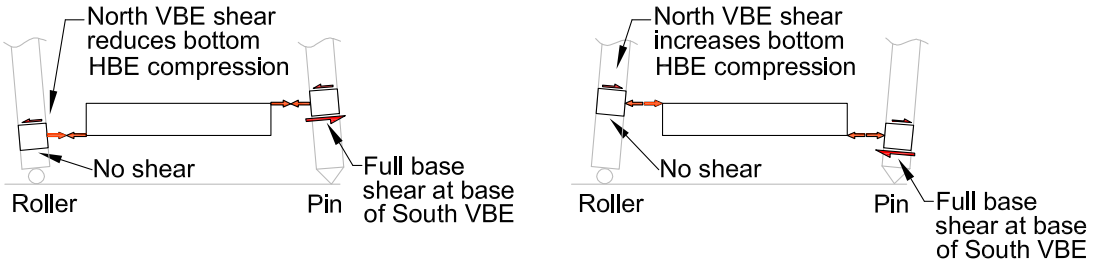

(a) Positive direction loading

(b) Negative direction loading

Figure 6.12: Influence of transfer of North VBE shear forces to pin at base of South VBE (PT and web plate forces not shown for clarity).

demonstrates the effects of different web plate thicknesses above and below the middle HBE. Having a thicker web plate with a larger yield strength below the middle HBE results in a net distributed force acting on the HBE. The net distributed web plate force always acts downwards and acts rightwards (i.e. southwards) during positive direction loading and leftwards (i.e. northwards) during negative direction loading. The net downward distributed web plate force results in a positive moment when the web plate is engaged. In Fig. 6.13(a), the path of the middle HBE moment demands during loading and unloading in both directions show an additional positive moment at all strain gage sections when the web plate is engaged. After the web plate is quickly unloaded, the moment demand follows a path similar to the bare PT frame as discussed previously. The net rightwards (i.e. southwards) axial distributed load during positive direction loading results in an increase in compressive demands in the south end of the HBE (i.e. larger x-values) and a decrease in compressive demands in the north end of the HBE (i.e. smaller x-values), and vice versa for the net northwards force during negative direction loading. This behavior is indicated in Fig. 6.13(b) by the increasing magnitude of compressive forces with larger x-values during positive loading and by the increasing magnitudes of compressive forces for decreasing x-values during negative loading (also shown more clearly in Fig. 6.13(c) for the smallest and largest x-values).

It should be noted that because there is no actuator loading at the middle HBE, the total shear force in the specimen above the HBE must be the same as the total shear force below the HBE. In a multi-story SC-SPSW, a change in web plate thickness between stories is typically associated with the applied lateral load at that floor. The change in web plate thickness is typically designed such that the net horizontal web plate load, $P_{HBE(web)}$, is equal to the applied story shear at that level; however, in this specimen, there is no applied lateral force at the middle HBE where the plate thickness changes. In this specimen, because the thicker first story web plate has larger distributed forces than the thinner second story web plates for similar deformation demands (e.g. the ratio of the distributed web plate forces in the second and first story, i.e. $(t_w F_y)_{Story2}/(t_w F_y)_{Story1}$, is 2.3), equilibrium must be satisfied by a reduction in VBE shear just below the middle HBE, a reduction in the net horizontal load in the first story web plate (i.e. by lower first story drift demands resulting in lower stresses), or a combination of both. In this specimen, the VBEs were relatively stiff. For rigid VBEs, the strain in both web plates would be equal, and the difference in web plate lateral strength between stories would be carried by the the frame. For non-rigid VBEs, the VBE flexibility allows story drifts, and thus web plate strains, to be different at each story relative to the VBE demands (which are larger in the second story). Thus, the second story had more web plate damage due to the slightly larger demands.

Fig. 6.13(c) also shows a slight decrease in axial compressive demands in the leftmost section (x=584mm) during extreme positive loading (i.e. greater than 3% drift) and a decrease in axial compressive demands in the rightmost section (x=2253mm) during extreme negative loading (i.e. less than -3% drift). This decrease in compressive demands only at the ends of the HBE is believed to be due to the larger web plate forces in the first story web plate coupled with the extensive tearing in the second story web plate at the ends of the middle HBE. For example, after extensive web plate tearing, the second story web plate is not providing any distributed force where the web plate is torn. In positive (i.e. northward) direction loading (as shown in Fig. 6.14), where the second story web plate is torn, the first story web plate is reducing compressive forces (i.e. with a righward distributed horizontal force) on the left (i.e. north) end of the HBE as previously discussed, resulting in a larger reduction of the compressive forces at this location. This phenomenon is only evident at

the end of the HBE where the bottom flange is in contact with the column. For example, during positive loading, the north end of the HBE is in contact with the North VBE via the bottom flange. Here, the larger (southward-acting) axial distributed force due to the first story web plates is acting on the bottom flange, the same flange that is transferring all of the compressive forces. The web plate forces acting directly on the flange carrying all of the compressive forces make the redcution in compression more evident. This observation does imply that the sections closest to the HBE ends may not have linear strain profiles as assumed in the calculation. Stress concentrations may be present at these end sections as they are located slightly less than one beam depth, d, away from the connection region. That may also explain why these observations of reduced axial demands in these sections are only noticed at larger drifts where the compressive forces being trasferred through the bearing flanges are larger, and thus the stress concentrations due to shear lag may be present farther from the HBE end. This phenomenon is also evident, although to a lesser extent, in the end sections of some of the other specimens at large drift demand (see App. B.2).

Fig. 6.15 shows the axial force and moment demands vs. drift for the middle HBE in W14-8s100k16GaHBE. The results for this specimen demonstrates the influence of web plates connected to the HBEs only. As shown in Fig. 4.42, releasing the web plate from the VBEs results in development of a partial tension field, where only a portion of the web plates contribute to lateral load resistance. The HBE free-body diagram and demand distributions were presented in Sec. 3.2. In the case of this specimen with the same web plate thicknesses above and below the middle HBE and the length of the partial tension field is equal in both stories, the distributed force, $\omega_{b(i)}$ and $\omega_{b(i+1)}$ are equal and the net axial reaction force due to the web plates, $P_{HBE(web)}$, is zero. Because the partial tension field does not extend along the entire HBE length, there are portions of the HBE where the distributed web plate forces above the HBE are not counteracted by web plate forces below the HBE, and vice versa.

As shown in Fig. 3.4 for rightward (i.e. southward or negative direction) drift, the vertical component of the partial tension field forces above the HBE on the left (i.e. northward) end of the HBE will create an additional negative moment that will effectively reduce the positive moment at the left end of the HBE due to the PT compressive forces acting on

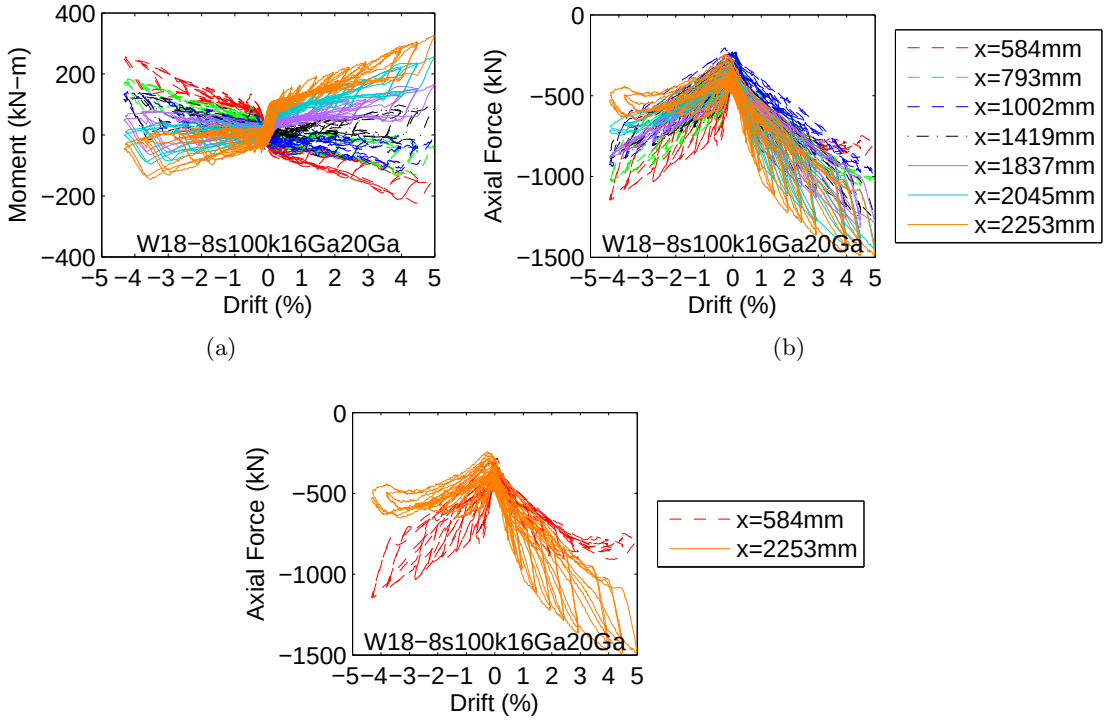

Figure 6.13: (a) Moment and (b,c) axial force demand vs. drift along middle HBE in W18-8s100k16Ga20Ga

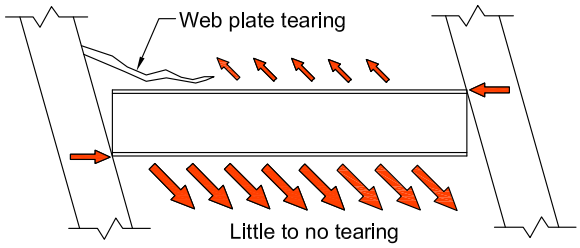

Figure 6.14: Example of reduction in compression at HBE ends at large drift demands in W18-8s100k16Ga20Ga

the top flange. Similarly, on the right (i.e. southern) end of the HBE, the net downward distributed force from the bottom story partial tension field will provide a positive moment to reduce the magnitude of the negative moment attributed to the PT forces acting on the bottom flange. The effect of the unbalanced partial tension field web plate forces are discussed in more detail in Sec. 3.2. When the loading is reversed to the positive direction, the influences are the same. The unbalanced vertical distributed forces produce moments in the opposite direction as the moments developed by PT frame action, effectively reducing the magnitude of the moments along the HBE where the partial tension fields of the web plates above and below the HBE are not balanced. This is evident in Fig. 6.15(a) where the path of the moment demands when the web plate is engaged have lower magnitudes than the moment demands after rapid unloading of the web plates.

General observations can also be made by comparing the axial demands of this specimen with those of other specimens, in which the web plate is connected along all four edges. In other specimens, the web plate forces always cause an increase in the compressive force along the entire length of the middle HBE (see Figs. 6.8(b) and 6.13(b)) due to the web plate pull-in of the VBEs, $P_{HBE(VBE)}$. In W14-8s100k16GaHBE where $P_{HBE(VBE)}$ is not present, the HBE axial demands associated with the web plate forces cause small increases and decreases in compressive demands depending on the location along the HBE.

6.2.4 Energy dissipation

The energy dissipation was calculated for each cycle of loading by summing the area under curve created by plotting the actuator force vs. the displacement of the South VBE at the top HBE (measured by potentiometer pd3s). Because the energy dissipation is dependent on the load history, the energy dissipated per cycle and cumulative energy dissipation were plotted for specimens with similar displacement histories in Figs. 6.16 and 6.17, respectively.

Fig. 6.16(a) shows that the energy dissipation in the bare PT frames that is associated with friction in the specimen PT connections, lateral bracing, and actuator are at least an order of magnitude less than the energy dissipation in SC-SPSW specimens with web plates. Figs. 6.17(b) and 6.17(c) demonstrate the general trend that specimens with thicker web

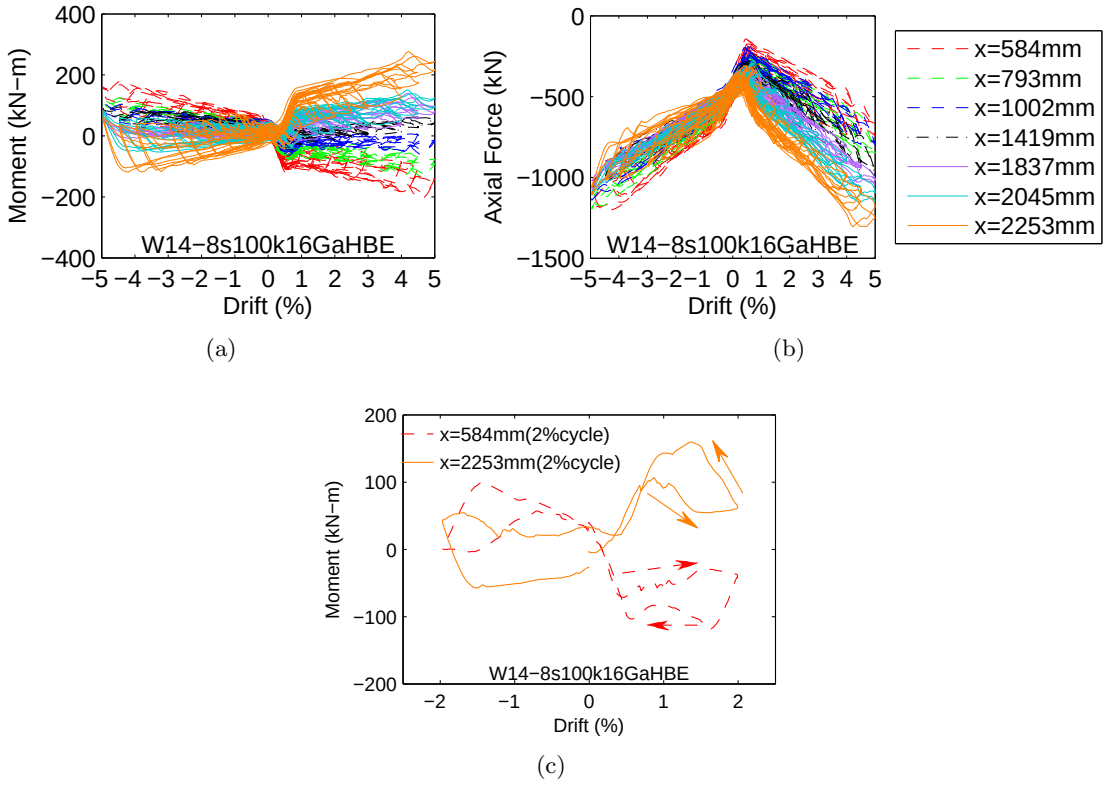

Figure 6.15: (a) Moment and (b) axial force demand vs. drift along middle HBE in W14-8s100k16GaHBE. (c) Selected moment vs. drift demands during 2% drift cycle showing loading direction.

plates dissipate more energy, as expected. Specimens with the same web plate thickness tend to have similar cumulative energy dissipations independent of the number of PT strands, indicating that web plate yielding is the primary mechanism for energy dissipation, also as expected.

Fig. 6.17(c) also shows that the energy dissipation in the specimen with the web plate connected to the HBEs only (W14-8s100k16GaHBE) is less than the energy dissipated by a comparable specimen with web plates connected along all edges (W14-8s100k16Ga). This behavior is expected due to the partial tension field developed in the web plates connected to HBEs only—only a portion of the web plate is yielding and contributing the energy dissipation. It is worth noting, however, that while the web plate strength ($t_w F_y$) of W14-8s100k16GaHBE is approximately 2.2 times that of W14-8s100k20Ga, these specimens have comparable energy dissipation. This result shows that increasing the web plate thickness (or strength) but connecting to the HBEs only results in similar energy dissipation to thinner (or weaker) web plates fully connected to the HBEs and VBEs.

Another observation from Fig. 6.17(c) is a comparison of the energy dissipated by similar specimens with bolted and welded web plate connection details, W18-8s100k20Ga-2 and W18-8s100k20GaW, respectively. Both specimens dissipate similar amounts of energy until cycle 15 (2% drift), when W18-8s100k20GaW begins to dissipate less energy than W18-8s100k20Ga-2 due to the propagation of web plate tearing along the welded connection.

6.2.5 Initial and recentering stiffness

The initial stiffness, K_i, and recentering stiffness, K_r, are important response characteristics that are useful in design and response estimation. Table 6.3 provides the initial stiffness, $K_{i,exp}$, and recentering stiffness, $K_{r,exp}$, determined from the experimental data for each subassembly specimens, as well as the theoretical recentering stiffness, $K_{r,th}$. The derivation of each of these parameters is described below. The force measured from the actuator load cell and the displacement measured from the string potentiometer attached to the South VBE at the location of the top HBE (pds3) were used for determining the experimental stiffnesses.

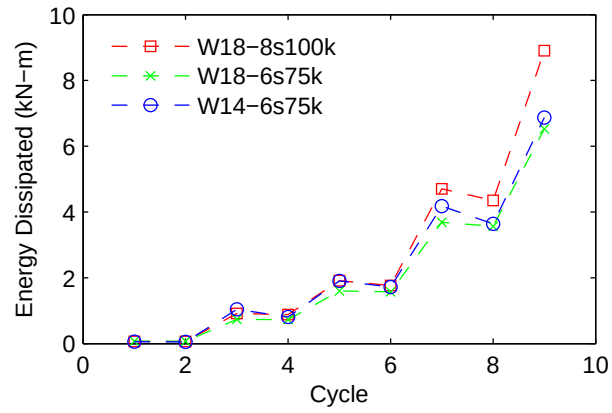

(a)

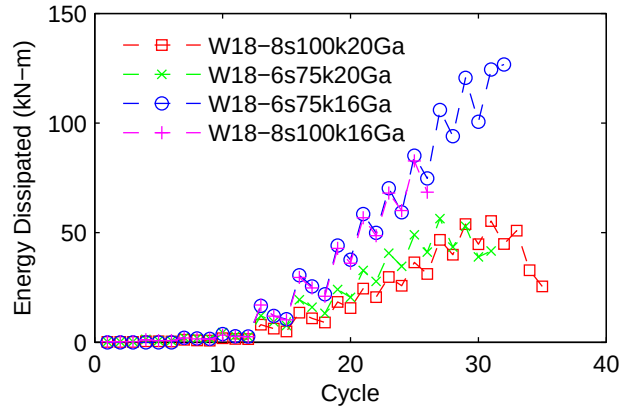

(b)

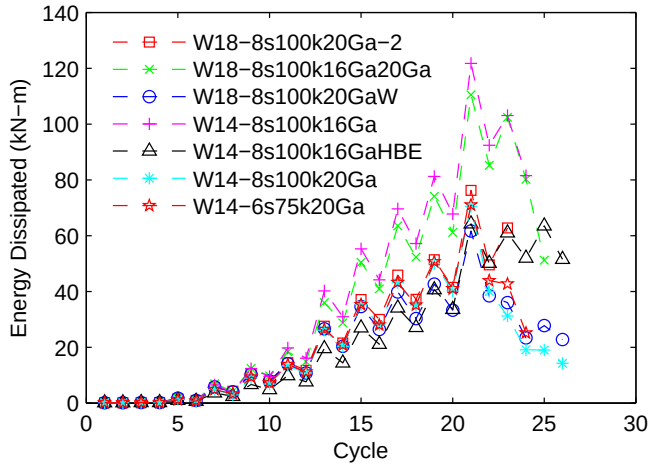

(c)

Figure 6.16: Energy dissipated per cycle for specimens with displacement histories (a) BF, (b) LP1, and (c) LP2

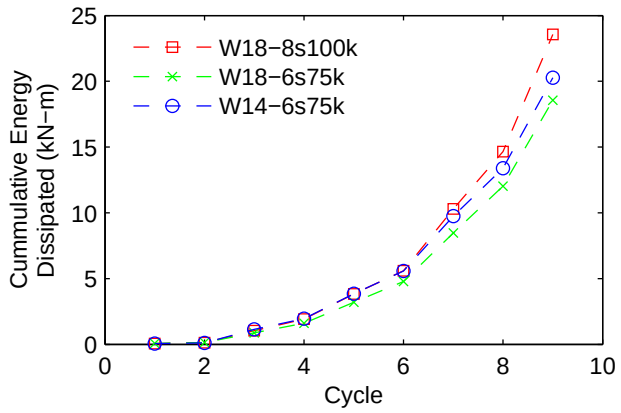

(a)

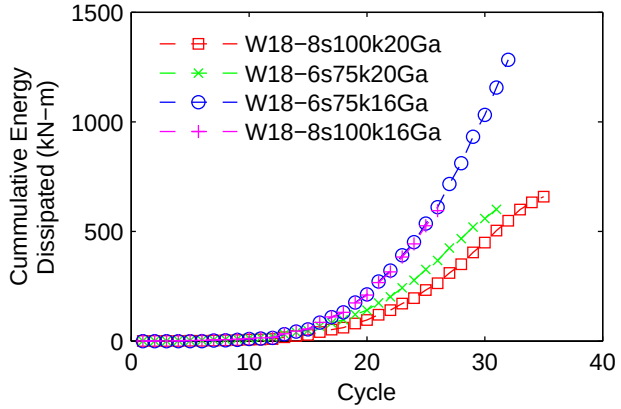

(b)

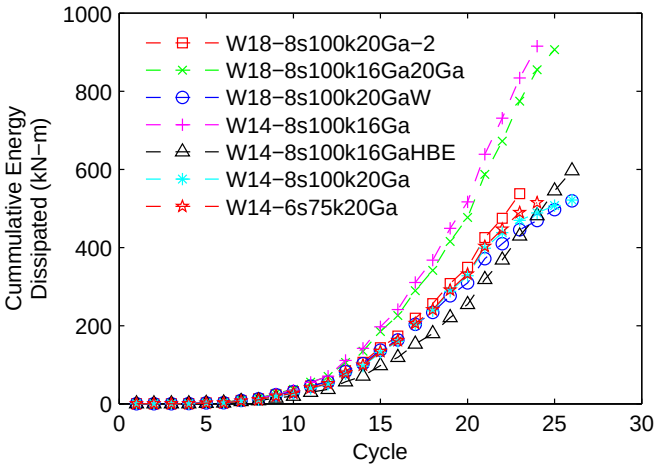

(c)

Figure 6.17: Cumulative energy dissipated per cycle for specimens with displacement histories (a) BF, (b) LP1, and (c) LP2

The theoretical specimen recentering stiffness, $K_{r,th}$, can be calculated as (derived from Eqn. (2.6) [Clayton, 2010]):

$$K_r = \frac{\Sigma k_d^\theta}{H^2} \tag{6.1}$$

where H is the overall height of the specimen and Σk_d^θ is the sum of the post-decompression rotational stiffness of all the PT connection in the frame (Eqn. (2.7)). Eqn. (6.1) ignores P-Delta effects as no gravity loads were applied to the VBEs in these specimens, and it assumes the web plate offers negligible stiffness after unloading.

The initial experimental stiffness was calculated from a linear regression of the force vs. displacement response of the first cycle, in which the specimen remains elastic. The slope of this linear regression is taken as $K_{i,exp}$ (Table 6.3). Examples of the experimentally determined initial stiffness, $K_{i,exp}$, are shown on force vs. displacement responses in Fig. 6.18.

The experimental recentering stiffness was determined from a linear regression of the force vs. displacement response after web plate unloading and before connection recompression. More specifically, the range of data considered for each linear regression began during unloading when the drift reached approximately 1% drift less than the peak cycle drift. This is intended to only consider unloading data after the web plate is fully unloaded, when the response is approximatley linear. The range of considered data ended at approximately 0.8% drift, before the connections begin to recompress and the stiffness increased. To ensure sufficient number of data points in the approxiatley linear recentering range, only cycles with target displacements greater than 2.5% drift were considered. Because of the bilinear response of the bare PT frame specimens, the linear portion of the post-decompression loading curve was considered. Examples of the force vs. displacement data used to determine $K_{i,exp}$ are shown in Fig. 6.18 for a bare PT frame specimen and a SC-SPSW with a web plate. A linear regression was taken for each of these data ranges in both the positive and negative directions of loading for each cycle. The recentering stiffness,, $K_{r,exp}$, was taken as the average of the slopes from each of these linear regressions (Table 6.3).

As suggested by Eqn. (6.1), $K_{r,exp}$ is most dependent on HBE depth and number of

Table 6.3: Initial and recentering stiffnesses of SC-SPSW subassembly specimens

Specimen	$K_{i,exp}$ (kN/mm)	$K_{r,exp}$ (kN/mm)	$K_{r,th}$ (kN/mm)	$K_{r,exp}/K_{r,th}$
W18-8s100k	25.3	2.34	1.89	1.24
W18-8s100k20Ga	45.0	2.08	1.89	1.10
W18-6s75k20Ga	40.6	1.64	1.43	1.15
W18-6s75k16Ga	49.1	1.59	1.43	1.11
W18-8s100k16Ga	57.6	1.90	1.89	1.01
W18-6s75k	17.3	1.53	1.43	1.07
W18-8s100k20Ga-2	34.9	1.89	1.89	1.00
W18-8s100k16Ga20Ga	42.9	1.79	1.89	0.95
W18-8s100k20GaW	48.2	1.84	1.89	0.97
W14-6s75k	9.5	0.80	0.75	1.07
W14-8s100k16Ga	31.1	0.98	0.99	0.99
W14-8s100k16GaHBE	17.1	0.88	0.99	0.89
W14-8s100k20Ga	23.3	0.97	0.99	0.98
W14-6s75k20Ga	20.7	0.79	0.75	1.05

PT strands. Eqn. (6.1) shows that K_r is proportional to the HBE depth squared, d^2, and the PT area per HBE (as part of k_{PT}). For example as shown in Table 6.3, the ratio of $K_{r,exp}$ for W14-6s75k to W18-6s75k, $K_{r,W14-6s75k}/K_{r,W18-6s75k}$, is 0.523. This value is roughly equal to the ratio of their HBE rocking depths squared, d^2_{W14}/d^2_{W18} , 0.525 (Table 4.1). Similarly, the ratio of $K_{r,exp}$ for W18-6s75k20Ga to W18-8s100k20Ga, $K_{r,W18-6s75k20Ga}/K_{r,W18-8s100k20Ga}$, is 0.788, which is similar to the ratio of cross-sectional area of the PT strands, $A_{PT,6s}/A_{PT,8s}$, 0.75. The experimentally determined recentering stiffnesses match well with those predicted by Eqn. (6.1), typically within 10% of the theoretical estimate.

As shown in Clayton [2010], the initial stiffness of an SC-SPSW depends primarily on the stiffness of the web plate, which is a function of the web plate thickness, and the boundary frame flexural stiffness among other things. Because the idealized PT frame has a stiffness equivalent to a fully welded moment-resisting frame prior to decompression, the number of PT strands should not impact the initial stiffness. In Table 6.3, the bare PT frame specimens do have the lowest $K_{i,exp}$ because they lack the additional stiffness provided

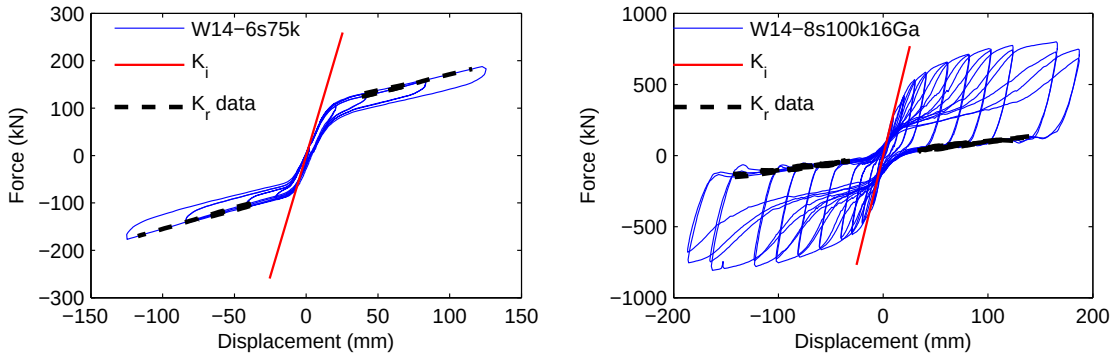

Figure 6.18: Force vs. displacement plots showing $K_{i,exp}$ and data used to determine $K_{r,exp}$ for (a) W14-6s75k and (b) W14-8s100k16Ga

by the web plates. Similarly, specimens with thicker web plates (16Ga) also have larger initial stiffnesses than those with thinner web plates (20Ga). Specimens with smaller, more flexible, HBEs (W14) also have lower initial stiffnesses than otherwise identical specimens with stiffer HBEs (W18). However, unlike an idealized PT frame, there may be some connection rotation in the test specimens even at very small drift demands due to uneven bearing surfaces. Because the non-idealized PT connection may not initially behave as a rigid connection, the initial stiffness may have influence from the PT connection stiffness and the number of PT strands, as seen by the difference in $K_{i,exp}$ of W18-8s100k and W18-6s75k.

6.2.6 Residual drift

The performance-based seismic design (PBSD) procedure presented in Clayton [2010] proposes performance objectives for different hazard levels, including recentering at the 10% in 50 year (10/50) hazard level. The criterion for recentering is a residual drift less than 0.2%, as this corresponds to the out-of-plumb limits in construction [ATC, 2009]. The PBSD procedure also suggests story drifts be limited to the 2% code-based drift limit [ASCE, 2005] at the 10/50 hazard level, as the 10/50 earthquake is an approximation of a design-basis earthquake (DBE) [FEMA, 2000a]. It is important to note that these specimens were not designed according to the proposed PBSD procedure and, therefore, do not represet a pro-

totype building. They also are subjected to displacement-controlled histories which are not representative of the dynamic response and inertial effects of real buildings in earthquakes. However, in order to asses the SC-SPSW recentering cabilities, the residual drift of each specimen was approximated as the drift of the specimen at zero-force. To compare to the performance objectives proposed in Clayton [2010], the specimen residual drift was determined after the cycles of loading at 2% drift to represent residual displacements following 10/50-level demands. Table 6.4 shows the maximum residual drift and the residual drift after loading up to 2% drift for loading in both the positive and negative directions.

Table 6.4: Residual drifts of SC-SPSW subassembly specimens

Specimen	Residual Drift (%) after 2% cycle		Maximum Residual Drift (%)	
	Negative dir.	Positive dir.	Negative dir.	Positive dir.
W18-8s100k	-0.05	-0.01	-0.05	-0.01
W18-8s100k20Ga	-0.15	0.08	-0.19	0.10
W18-6s75k20Ga	-0.15	0.12	-0.19	0.12
W18-6s75k16Ga	-0.33	0.20	-0.37	0.32
W18-8s100k16Ga*	-0.17	0.16	-0.19*	0.17*
W18-6s75k	-0.01	0.03	-0.01	0.03
W18-8s100k20Ga-2	-0.07	0.11	-0.10	0.11
W18-8s100k16Ga20Ga	-0.22	0.02	-0.22	0.08
W18-8s100k20GaW	-0.09	0.03	-0.10	0.13
W14-6s75k	-0.02	0.08	-0.02	0.09
W14-8s100k16Ga	-0.21	0.39	-0.26	0.45
W14-8s100k16GaHBE	-0.10	0.21	-0.14	0.22
W14-8s100k20Ga	-0.13	0.14	-0.13	0.15
W14-6s75k20Ga	-0.15	0.21	-0.15	0.22

* Test was ended prematurely due to PT wire fracture [Winkley, 2011].

Table 6.4 shows that the bare PT frame specimens had very small residual drifts, likely due to friction in the test setup. In general, specimens with thicker web plates (16Ga), lower initial PT forces (75k), fewer PT strands (6s), and smaller HBEs (W14) had larger residual drifts. As observed in Winkley [2011], the web plate residual strength attributed to the buckled web plate's geometric stiffness upon unloading provides some resistance to

recentering. The web plate residual strength, $V_{web,resid}$, causes the SC-SPSW to unload at a lower magnitude force than is assumed by the idealized tension-only web plate behavior. If $V_{web,resid}$ is sufficiently large, it can result in the unloading force-displacement response crossing the displacement axis (i.e. force equal to zero) at a displacement larger than the recentering criterion. Lower initial PT forces reduce the specimen strength at connection decompression/recompression, and fewer PT strands reduce the recentering stiffness, which can also cause larger drifts at zero-force when coupled with the effects of the web plate unloading resistance.

In these subassembly tests, most SC-SPSW specimens were able to recenter (i.e. residual drift magnitudes less than 0.2%) after being subjected to loading up to 2% drift. The two specimens that had the largest residual drifts were W18-6s75k16Ga and W14-6s75k16Ga, with residual drift magnitudes up to 0.33% and 0.39%, respectively, following loading at 2% drift. Both of these specimens had the thickest web plates (16Ga) and the lowest PT connection strengths and stiffnesses (6s75k). There were a few specimens that also had residual drifts slightly larger than 0.2% after the 2% cycle (W18-8s100k16Ga20Ga, W14-6s75k16GaHBE, W14-6s75k20Ga); however, the residual drifts in the other direction of loading were significantly less than 0.2%.

These results suggest that web plate residual strength should be considered when designing the SC-SPSW. The PT connection strength and stiffness should be sufficiently large to overcome the web plate resistance during unloading. To do so, an expression is needed to estimate the magnitude of $V_{web,resid}$, which will be discussed in further detail later in this dissertation. Also, these quasi-static cyclic subassembly tests are not representative of earthquake loading. Further work is required to quantify the affects of web plate residual strength in different load histories, specifically in load histories more representative of the decaying cyclic amplitudes of a real building coming to rest following an earthquake.

6.2.7 Web plate strains

Some of the subassembly specimens were instrumented with strain gages on the web plates. In specimens W18-8s100k20Ga-2, W18-8s100k16Ga20Ga, and W18-8s100k20GaW, uniaxial

strain gages were located in the first story web plate at angles of 45° and 135° with respect to the horizontal (i.e. parallel to the HBE) axis as shown in Fig. 4.7. Uniaxial strain gages were also placed along the corner cutouts nearest the middle HBE in the first story web plate (as shown in Fig. 4.7). In these specimens, all of the uniaxial web plate strain gages were only placed on the top, or ceiling, side of the web plate; therefore, the strain readings may have included some flexural strain at the extreme fiber of the plate thickness due to buckling and out-of-plane deformation of the web plate. Although these readings did not provide the mid-thickness web plate strains, they are still useful for comparison of the magnitude of web plate strains.

The readings from these strain gages are shown in Appendix B.4 with general discussion of the trends presented here. In general, the gages oriented at 45° measured an increase in tensile strain during loading in the negative drift direction as expected due to the direction of the tension field. The response is similar for the strains in the 135° direction increasing in magnitude during loading in the positive drift direction. Similarly, the gages in the corner cutouts measured increasing tensile strains when the gap at that location was opening (e.g. during positive direction drift for the cutout in the southeast corner of the first story plate). The strain gages in the corner cutouts typically had magnitudes less than those along the HBE due to web plate slipping in the bolted connections near the cutouts and early onset of tearing in the welded connection. The "capping" of corner cutout strains due to web plate slip or tearing is shown in Fig. 6.19(a) where the strains in the cutout did not significantly change after approximately 1% drift when the welded web plate-to-fish plate connection had significant tearing near the cutouts. The effects of out-of-plane bending of the web plate in the cutouts can also be observed in Fig. 6.19(b) where the cutout strains vary greatly in the positive or negative strain directions (depending on the if the web plate buckles toward the ceiling or the floor, respectively) when the gap in the connection at that location is closing.

For specimens W14-8s100k20Ga and W14-6s75k20Ga, the web plates were instrumented with strain gage rosettes (in the web plate along the middle HBE) and/or uniaxial gages (in the corner cutouts) as shown in Figs. 4.9 and 4.10, respectively. Here, the gages were placed at approximately the same location on both sides of the web plate such that the readings for each pair of gages (on either side of the web plate in the same location) could be averaged

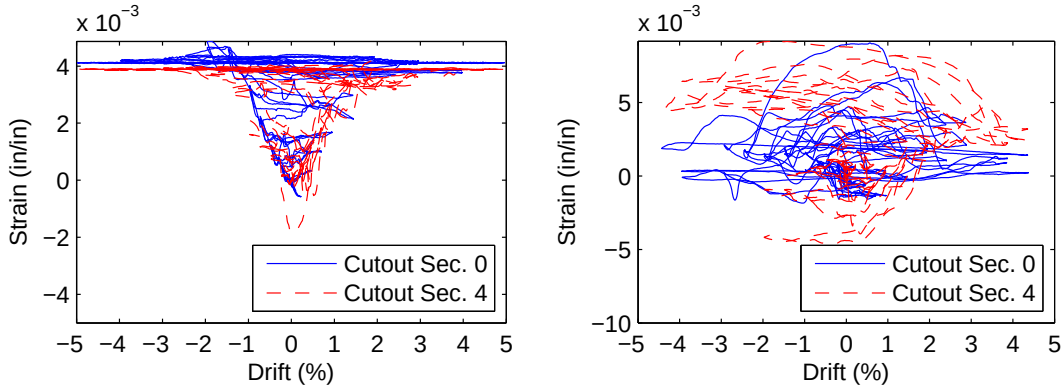

Figure 6.19: Corner cutout strains in (a) W18-8s100k20GaW and (b) W18-8s100k20Ga-2 in 1st story web plate nearest the middle HBE.

to approximate the mid-thickness strain. From these mid-thickness strain approximations[2] in the rosettes, the principal strains and principal strain directions could be determined.

Figs. 6.20 and 6.21 show an example of the principal strain and angle of inclination at peak drifts and the corner cutout strains, respectively (additional plots are provided in Appendix B.4). Note that the section number increases from the north to south end of the HBE. Also, only the principal strains and directions are shown for the first cycle of loading at each drift level when the tension field was fully developed. In general, the principal tensile strain magnitude (Fig. 6.20(a)) increases with increasing drift demands as expected. The rate of this increase decreases at large drift demands when web plate tearing is significant and full tension field action does not develop everywhere in the web plate.

Fig. 6.20(b) shows that the angle of tension field inclination increases (i.e. starting near vertical inclination and becoming shallower) at very small drift levels. The angle of inclination appears to settle near 50° after web plate yielding. This angle is shallower than the 45° typically assumed for tension field inclinations [Webster, 2013]. This is believed to be due to the additional horizontal strain from frame expansion that is present in SC-SPSWs and not in conventional SPSWs from which the inclination angle estimation was

[2]Note that the gages and rosettes may not have been perfectly aligned on both sides of the plate; therefore, the average of the readings are only an approximation of mid-thickness strain.

formulated; however, further investigation is required to verify this hypothesis. Also, as the extent of web plate tearing increases with increasing drift demands, as does the scatter in the measured angle of inclination. This is due to the fact that the tension field is not fully formed across the entire web plate after significant tearing. In some cases the angle of inclination is in the opposite direction from what would be expected (e.g. Sec. 4 having positive inclination angles under extreme negative direction loading), indicating that the tension field is not being developed at that particular location in that direction of loading.

Fig. 6.21 shows the mid-thickness web plate strain in the corner cutouts. In the first story web plate, the cutout at the south end of the middle HBE (i.e. Sec. 4) has increasing tensile strains as the connection gap is opening at this location, and vice versa for strains of the north cutout under negative loading. As mentioned previously, the magnitude of the cutout strains is much smaller than the magnitude of principal strains within the web plate due to web plate slip in the bolted clamping bars near the cutouts. Also note that the mid-thickness cutout strains are relatively constant during unloading, compared to the large fluctuations in extreme fiber (i.e. one side of the plate) cutout strains during unloading shown in Fig. B.71(d). This is because the effects of out-of-plane bending strain are eliminated by taking the average of the gages on both sides of the plate.

6.3 Comparison of Subassembly Responses

This section uses the data analysis presented in the previous section to make comparisons between the different SC-SPSW subassembly specimens. Specifically, comparisons are made to demonstrate the effects of each of the varied test parameters.

6.3.1 Effects of load protocol

Specimens W18-8s100k20Ga and W18-8s100k20Ga-2 were essentially the same but were loaded with different displacement histories, LP1 and LP2, respectively. The differences in the displacement histories were subtle—the main difference being LP2 had eight fewer cycles at small drift amplitudes, less than 2%, than LP1. The target displacements above 1.5% drift in LP2 were based on quasi-static tests of conventional SPSWs [Vian et al., 2009a; Li et al., 2010].

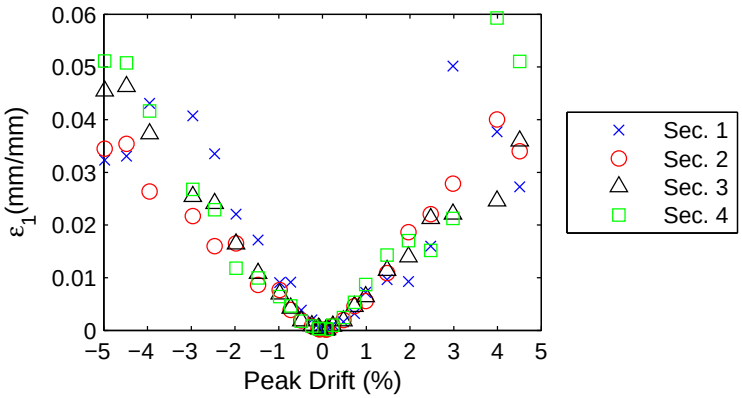

(a)

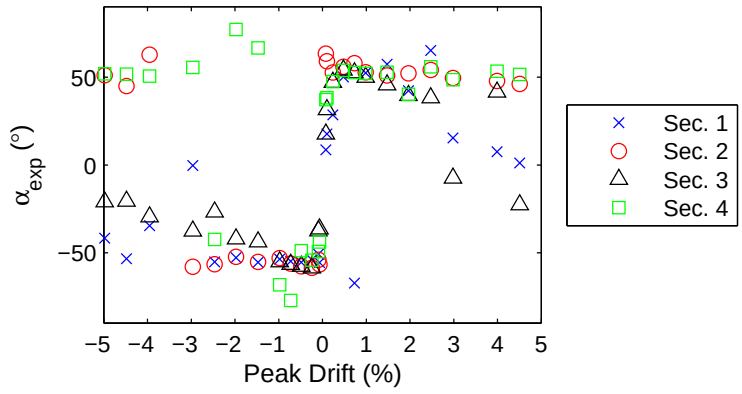

(b)

Figure 6.20: W14-8s100k20Ga: 1st story along middle HBE (a) principal strain and (b) angle of inclination at peak drifts

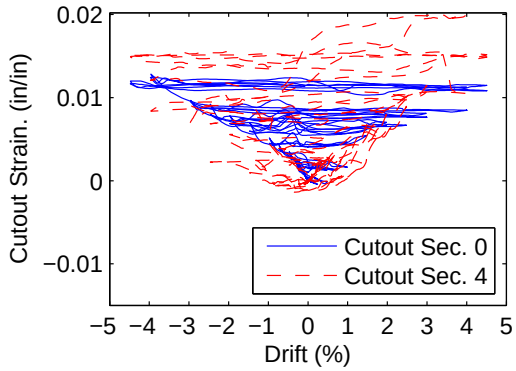

Figure 6.21: Corner cutout strains in W14-6s75k20Ga in 1st story web plate nearest the middle HBE

Both of these specimens showed initial signs of web plate tearing at drifts slightly less than 3% (Table 4.3) and both lost approximately 13% of their peak strength during the second cycles of loading at 3.7% and 3.8% drift for specimens W18-8s100k20Ga and W18-8s100k20Ga-2, respectively. These observations of web plate tearing and strength degredation suggest that web plate damage is not significantly affected by number of cycles at low displacement amplitudes, at least for the the specimens and web plate connection detailing considered here; therefore, the remainder of the tests were conducted using LP2 for simplicity.

6.3.2 Web plate thickness, t_w

As expected, specimens with thicker web plates (W18-6s75k16Ga) had more strength and energy dissipation than specimens with thinner web plates (W18-6s75k20Ga) as shown in Fig. 6.22. Actual web plate behavior exhibited two key differences from the assumed idealized web plate behavior presented in Fig. 1.5. First, the web plate is able to resist load before reaching the peak plastic strain of previous cycles, a characteristic also found by Choi and Park [2010]. This results in more web plate energy dissipation in later cycles than is assumed in the idealized behavior, which is therefore conservative for use in nonlinear response history analyses such as those described in Clayton et al. [2012b]. Second, the residual strength of the web plate during reversal of loading can be significant, as indicated by the increased area below the bare PT frame response (W18-6s75k) in Fig. 6.22 and as found by Webster [2012]. Whereas the idealized web plate response in Fig. 1.5(c) does not show resistance to recentering during system unloading since the residual strength of the thin plate is assumed to be negligible, the actual web plate does have some residual strength that the PT connection must overcome in order to recenter the system. Because of this phenomenon, specimens with thicker web plates, and thus a larger web plate residual stress, did have larger residual drifts after unloading.

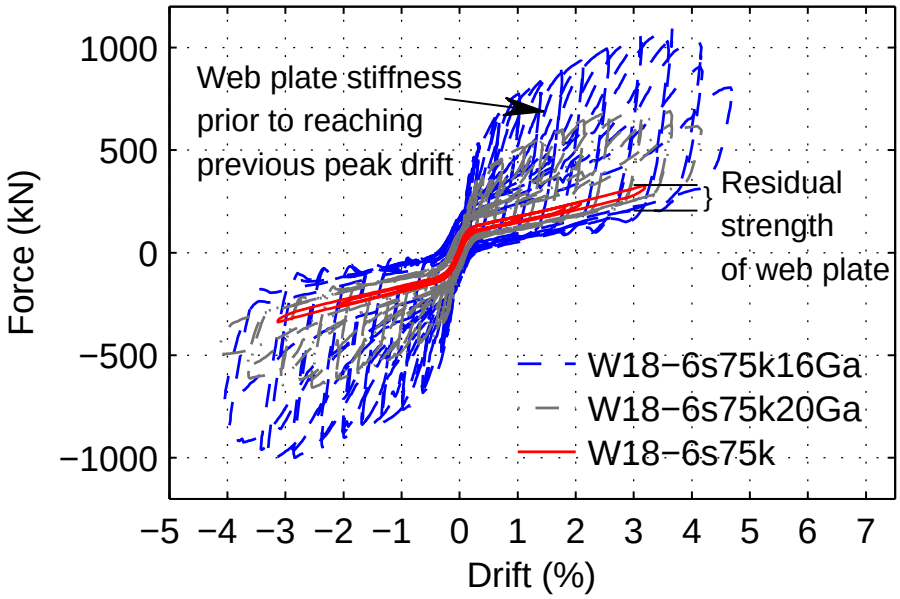

Figure 6.22: Comparison of specimens with different web plate thicknesses.

6.3.3 Number of PT strands, N_s, and initial force, T_o

Increasing the number of PT strands increases the rotational stiffness of the PT connection after decompression [Clayton, 2010] and, subsequently, the system recentering stiffness, K_r, shown in Fig. 1.5(c).

The formula for estimating the specimen recentering stiffness is provided in Eqn. (6.1). In the case of these specimens, where k_{HBE} is significantly larger than k_{PT}, the PT connection rotational stiffness, k_d^θ, is related primarily to d^2 and k_{PT}. Thus an increase in the PT area, which proportionally increases k_{PT}, also causes a proportional increase in K_r. This increase in recentering stiffness due to an increase in the number of PT strands can be observed in Fig. 6.23 and in Table 6.3 where the recentering stiffness of the specimen with eight PT strands (W18-8s100k20Ga) is proportionally larger than the specimen with six PT strands (W18-6s75k20Ga).

While variations in N_s impact the PT frame stiffness, variations in T_o impact the PT frame strength. Increasing T_o increases the PT connection decompression moment, M_d,

and the specimen decompression strength, V_d, as shown in Fig. 1.5(c). This increase in PT frame strength can also be observed in Fig. 6.23 in the specimen strength near zero drift, after web plate unloading and as the PT connections recompress.

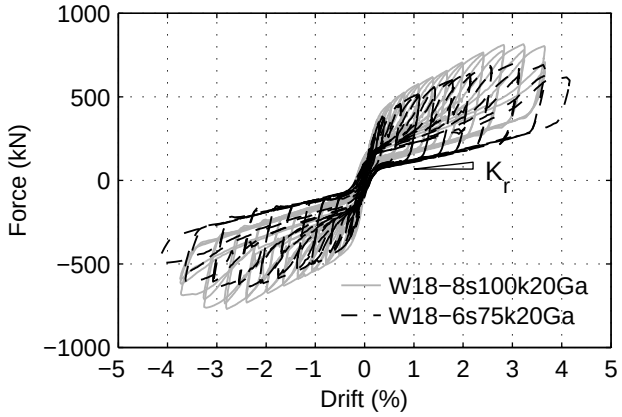

Figure 6.23: Comparison of specimens with different number of PT strands and initial PT force.

6.3.4 Effects of HBE depth

Fig. 6.24 compares the force vs. drift response of two specimens that are essentially identical with the exception of HBE depth, d. As with the change in PT design, a change in the HBE depth primarily affects the recentering stiffness. The HBE depth does impact the decompression strength, V_d, since the PT connection decompression moment, $M_d = \frac{d}{2}T_o$, as indicated by the lower strength at PT recompression of W14-8s100k20Ga compared to that of W18-8s200k20Ga-2 (Fig. 6.24).

The recentering stiffness, K_r, of specimens W14-8s100k20Ga and W18-8s200k20Ga-2 were found to be 0.98 and 1.89 kN/mm, respectively, resulting in a ratio, $K_{r,W14}/K_{r,W18}$, of 0.519. As both specimens had the same number of PT strands, this value is roughly equal to the ratio d^2_{W14}/d^2_{W18} of 0.525, verifying the expected relationship between HBE depth and recentering stiffness shown in Eqn. (6.1).

The effect of HBE depth on PT connection rotational stiffness and recentering stiffness is also illustrated in the PT force vs. drift response for the middle HBE (Fig. 6.25). The PT

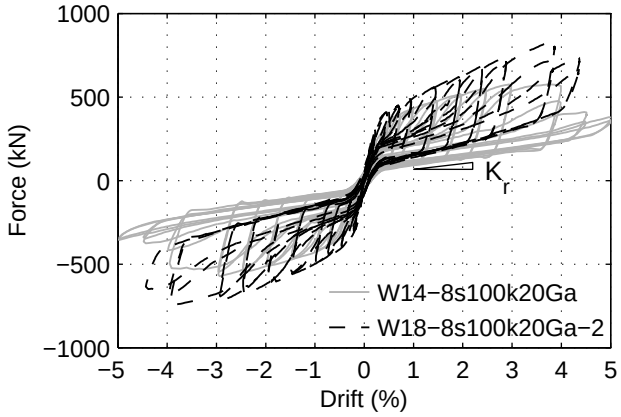

Figure 6.24: Comparison of specimens with different beam depth

elongation, and thus PT force, is larger in the W18 specimen than in the W14 specimen for a given drift demand due to the increase in connection rocking depth. As the development of PT strain energy provides the restoring forces to recenter the frame, the lower PT elongation at a given drift demand caused by a decrease in HBE depth results in a lower recentering stiffness and corresponding PT connection rotational stiffness.

6.3.5 Effects of web plate connection details

Fig. 6.26 shows the force vs. drift response of specimens with bolted (W18-8s100k20Ga-2) and welded (W18-8s100k20GaW) web plate-to-fish plate connection details (both shown schematically in Fig. 4.3). All other specimen parameters were identical between the two specimens. As observed in Fig. 6.26 the two specimens have essentially identical response up to 1.5% drift.

Initial signs of web plate tearing were first observed in specimen W18-8s100k20GaW at 0.7% drift with very small cracks, less than 5 mm, at the toe of the weld along the first story VBE (Table 4.3, Fig. 4.31). All web plate tearing initiated at the toe of the weld and propagated just outside of the heat affected zone (HAZ). Tear propagation was minimal up to 2% drift, with tear lengths not exceeding 10% of the total weld length along a given edge.

In a survey of conventional SPSW tests, all of which used welded web plate connection

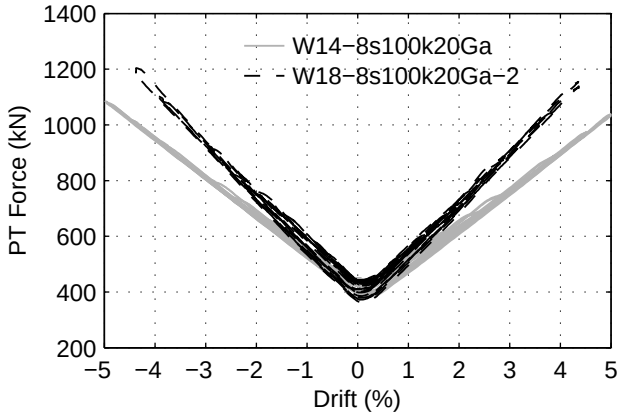

Figure 6.25: Comparison of total PT force in middle HBE for specimens with different beam depth

details, initial web plate tearing was first recorded at a median drift of 1.6% [Baldvins et al., 2010], which is greater than the observation of tearing at 0.7% drift in this specimen; however, it is not outside of the range of conventional SPSWs as some tests did have web plate tearing at lower drift levels [Tromposch and Kulak, 1987; Berman and Bruneau, 2003]. The earlier onset of web plate tearing in SC-SPSWs can be explained by the additional web plate demands resulting from gap opening and out-of-plane web plate deformation along the unrestrained edge of the corner cutouts in SC-SPSWs that are not present in conventional SPSW web plates welded continuously along all edges.

At 2% drift the welded specimen strength was approximately 96% of the bolted specimen, and this ratio decreseased with increasing drift demands. During the second cycle at 4% drift, the first story web plate of W18-8s100k20GaW tore completely through along a VBE edge (Fig. 4.34); however, the specimen retained 91% of its peak strength after two cycles at 5% drift with at least one third of the web plate edge being intact along all of the HBEs. The end-of-test strength is large with respect to peak strength due to two key factors: (1) the peak strength in the welded web plate specimen was smaller than the comparable bolted web plate specimen due to the earlier onset and propagation of web plate tearing, and (2) due to the elastic nature of the PT frame, it contribute larger strength at larger drift demands. This result shows that the increasing strength of a properly detailed (i.e. elastic)

PT frame with respect to drift is beneficial in offsetting the effects of strength degredation associated with web plate tearing.

Tearing was first observed in the specimen with the bolted web plate connection detail (W18-8s100k20Ga-2) at 2.9% drift (Table 4.3, Fig. 4.20); however, minor web plate slip was observed at the ends of the clamping bars as early as 0.75% drift in the 8 cm beyond the outermost bolts where the clamping friction forces were reduced (shown at 2.9% drift in Fig. 4.20). Tearing typically initiated and propagated along the edge of the clamping bars. In specimen W18-8s100k20Ga-2, the tear propagated along the entire length of the bottom HBE after two cycles at 4.4% drift (Fig. 4.22), retaining 81% of its peak strength.

While the peak strength of the specimen with the welded web plate connection was 85% of that with the bolted web plate connection, and the welded connection detail showed signs of web plate tearing prior to the bolted connection detail, both specimens had similar strengths up to 2% drift, within the range of design-level earthquake drift demands [Clayton et al., 2012b]. Interestingly, both specimens had nearly identical unloading strength and stiffness even though they had significantly different peak strengths and web plate tearing characteristics. This observation indicates that the web plate residual strength does not degrade significantly with web plate peak strength and damage, supporting the hypothesis that web plate residual strength is a product of the geometric stiffness of the buckled and plastically deformed web plate as it deforms during unloading.

6.3.6 Effect of web plate configuration

6.3.6.1 Different web plate thicknesses above and below middle HBE

Fig. 6.27 shows the force vs. drift response of specimens with 20Ga (W18-8s100k20Ga-2) and 16Ga (W18-8s100k16Ga) web plates at both stories and the specimen with 16Ga and 20Ga web plates in the first and second stories, respectively (W18-8s100k16Ga20Ga). The strength of W18-8s100k16Ga20Ga is larger than that of W18-8s100k20Ga-2 but smaller than that of W18-8s100k16Ga.

Because the web plates provide the primary lateral load resistance in the SC-SPSW specimens and because the actuator was loading at the top of the specimen only, upon first

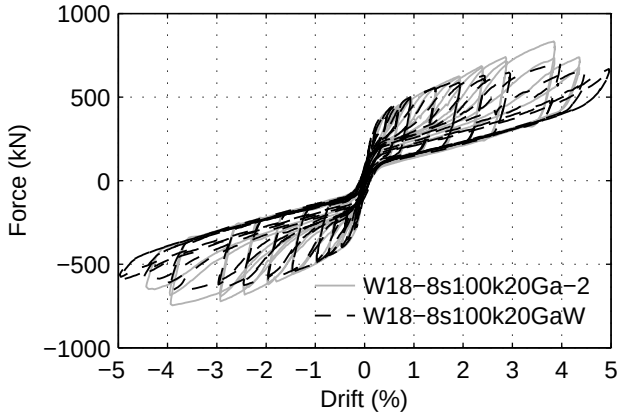

Figure 6.26: Comparison of specimens with bolted (W18-8s100k20Ga-2) and welded (W18-8s100k20GaW) web plate-to-fish plate connection details

inspection one would expect the base shear of W18-8s100k16Ga20Ga to be limited to the strength of the weaker second story plate, based on equilibrium of section cut taken in the second and first stories. However, due to compatibility requirements and the stiff VBEs, the first story web plate was subjected to deformation demands similar to those of the second story, which resulted in yielding in the first story web plate. Due to the difference in web plate thicknesses and yield strengths, yielding in both stories would cause greater web plate forces in the first story. The simultaneous satisfaction of equilibrium, compatibility, and constitutive requirements required that: (1) the VBEs in the second story of the PT frame resist more lateral load than in a comparable 20Ga-only SC-SPSW and (2) the first story (16Ga) web plate forces are lower than those in a comparable 16Ga-only SC-SPSW. The results are a total strength of W18-8s100k16Ga20Ga somewhere in between that of a 16Ga- or 20Ga-only specimen. This result is not very applicable to real SC-SPSWs, as an increase in web plate thickness between stories is always accompanied by an increase in story shear forces due to inertial forces at each floor; however, it does indicate that having stiff VBEs can help resist additional lateral forces to help avoid the formation of soft story mechanisms at large transitions in web plate strength. The impact of the different web plate thicknesses on the middle HBE axial force and moment demands was shown and discussed previously in Fig. 6.13.

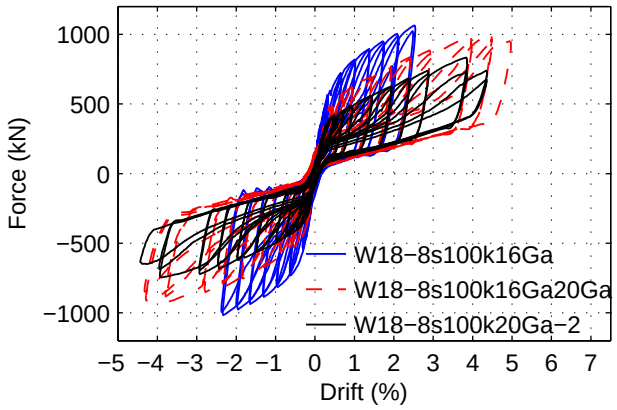

Figure 6.27: Comparison of specimens with 20Ga web plates (W18-8s100k20Ga-2), 16Ga (W18-8s100k16Ga), and both (W18-8s100k16Ga20Ga) web plates

6.3.7 Web plates connected to only HBEs

Fig. 6.28 shows the force vs. drift response of specimens with the web plates connected along all edges (W14-8s100k16Ga) and along the HBEs only (W14-8s100k16GaHBE). Connecting the web plates only to the HBEs delayed the onset of web plate tearing, which was first observed at 4.5% drift in specimen W14-8s100k20GaHBE compared to 3% drift in specimen W14-8s100k20Ga (Table 4.3). Connecting the web plate to the HBEs only similarly increased specimen ductility, with W14-8s100k20GaHBE sustaining two cycles of loading at 5% drift with minimal tearing (less than 33% of the edge length torn along the most damaged edge) while the first story web plate in W14-8s100k20Ga tore completely along the edge of the middle HBE after two cycles at 4.5% drift (Table 4.3).

The strength of the specimens with web plates connected to the HBEs only is significantly less than the specimen with web plates connected to the boundary frame along all edges due to the decrease in the size of the tension field. The total web plate strength, calculated as the peak strength minus the unloading strength of each specimen at 2% drift, for W14-8s100k20GaHBE was 52% of W14-8s100k20Ga. This is consistent with visual observations of the extent of the diagonal buckles of the tension field. Due to lack of restraint along the vertical edges, a partial tension field develops along just over half of the horizontal

edge length and at a steeper angle of inclination [Basler, 1961; Thorburn et al., 1983] in W14-8s100k20GaHBE (Fig. 4.42). This observation can be compared to the tension field developed along the full horizontal edge length and at an approximately 45 degree inclination in specimens with the web plate connected along all edges (e.g. Fig. 4.19). Taking the partial tension field length and angle of inclination provided in Eqns. (3.2) and (3.1), respectively, and an assumed full tension field angle of inclination, α=45°, for the fully-connected web plate, the lateral strength equations for HBE-only connected web plates (Eqn. (3.6)) and for fully-connected web plates (Eqn. (2.2)) suggest that the HBE-only web plate in W14-8s100k16GaHBE would have approximately 56% the stength of the fully-connected web plate in W14-8s100k16Ga, which is comparable to the difference in web plate strength observed in the tests.

Fig. 6.28 also shows that although W14-8s100k16GaHBE has a significantly reduced strength compared to W14-8s100k16Ga due to the partial tension field, the residual web plate strength (i.e. the unloading strength) for both specimens is similar. This similarity in unloading strengths suggests that the web plate residual strength may be a function of the full web plate, not a function of the extent of the tension field (i.e. the full web plate is providing resistance during unloading). Therefore, if an HBE-only web plate is designed to have the same strength as a fully-connected web plate (e.g. by increasing the thickness or yield strength), the HBE-only web plate would have a larger residual strength during unloading, which would provide additional energy dissipation.

By releasing the web plate from the VBEs, the component of axial force in the HBE due to the web plates pulling in the VBEs, termed $P_{HBE,VBE}$ in Sabelli and Bruneau [2007], is eliminated. Fig. 6.30 shows the average axial force, as calculated from strain gage measurements, in the middle HBE during the 2% cycle for the specimens with web plates connected along all edges (W14-8s100k20Ga) and along the HBEs only (W14-8s100k20GaHBE). The HBE axial load is influenced primarily by three components [Clayton, 2010; Dowden et al., 2012]: the increase in PT force as the PT connection gap opens; the difference in web plate thicknesses or strengths above and below the HBE, which is not the case for either of these specimens; and the web plate pull-in of the VBEs. The change in PT force is due primarily to the connection gap opening which can be related to drift. As shown in Fig. 6.29, the

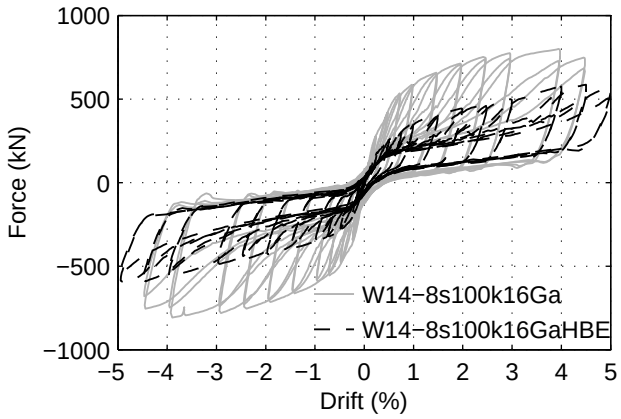

Figure 6.28: Comparison of specimens with web plate connected along all edges (W14-8s100k16Ga) and along the HBEs only (W14-8s100k20GaHBE)

PT force increase with respect to drift is not significantly impacted by the web plate-to-boundary frame conenctivity. As such, the size of the hysteretic loop in the the average HBE axial force response (Fig. 6.30) of W14-8s100k20Ga can be attributed to the VBE pull-in. As the web plate stress and corresponding pull-in of the VBEs increases, as does the HBE axial load (as indicated by the increase in magnitude of compressive forces). The quick reduction in web plate force just as the specimen begins unloading results in a rapid decrease in HBE axial load, the magnitude of which corresponds to $P_{HBE,VBE}$. After the initial unloading of the web plate, the HBE compression demands decrease proportional to the decrease in PT forces. Alternatively, in W14-8s100k20GaHBE, where the VBE pull-in is eliminated, the hysteretic loop is essentially nonexistent. In this specimen, the HBE axial load depends mainly on the PT force.

The significant delay and reduction of web plate tearing in the specimen with the web plate connected to the HBEs only suggests that much of the web plate damage in other specimens can be attributed to the affects of gap opening and frame expansion causing increased horizontal strain demands in the web plate. If the web plate thickness is appropriately designed to resist the required lateral loads, using a HBE-only web plate connection configuration may be desirable in SC-SPSWs for web plate damage mitigation and potential reduction of VBE demands [Xue and Lu, 1994].

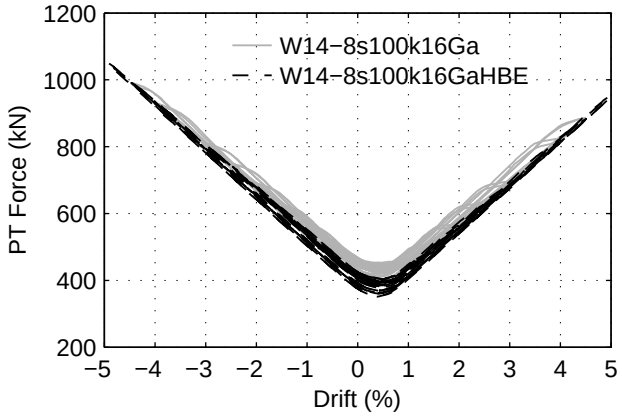

Figure 6.29: Comparison of PT force in middle HBE of specimens with web plate connected along all edges (W14-8s100k16Ga) and along the HBEs only (W14-8s100k20GaHBE)

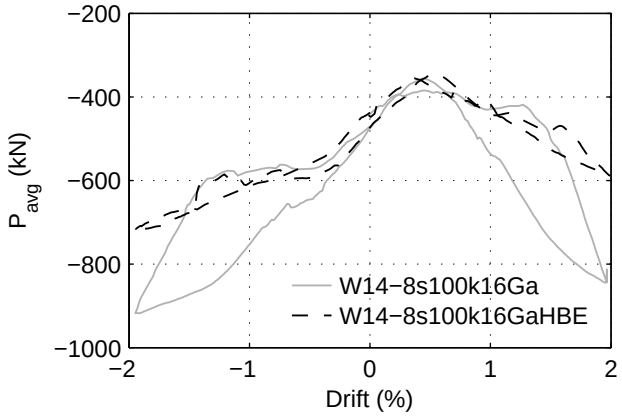

Figure 6.30: Comparison of average measured axial force in specimens with web plate connected along all edges (W14-8s100k16Ga) and along the HBEs only (W14-8s100k20GaHBE) during 2% cycle

6.4 Full-scale Test Data Analysis

This section presents the data analysis for the full-scale specimen. The experimental response parameters analyzed for this specimen are similar to those analyzed in the subassembly tests in the previous sections; however, additional analysis of the dynamic properties of the system are also provided.

6.4.1 Fundamental period and damping

The fundamental period and equivalent viscous damping ratios of the specimen were calculated from the displacement vs. time response of the specimen during the free vibration portion of each PSD test. Note that "time" in this sense refers to earthquake, or analytical, time used in in the equations of motion. The period of the structure, T_n, was determined from finding the difference in time between sequential local maxima or minima. During larger intensity PSD tests when the response during free vibration was nonlinear, the calculated period of the specimen varied depending on the points used for the calculation. Table 6.5 shows the smallest, largest, and average calculated value for the period during free vibration.

Table 6.5: Fundamental period during free vibration of PSD tests

Test	Period, T_n, during free vibration (sec) Max.	Min.	Average
Free Vibration	0.60	0.58	0.58
50/50	0.63	0.62	0.62
10/50	1.50	1.42	1.45
2/50	2.29	1.90	2.10

As expected, the period is smaller and has less variation during the Free Vibration and 50/50 tests when the specimen remained essentially elastic with the high initial stiffness of the undamaged web plate and pre-decompressed PT connections. During the 10/50 and 2/50 tests, the specimen exhibited nonlinear behavior during free vibration (as shown in Figs. 5.31(b)and 5.41(b) due to the large displacement at the beginning of free vibration).

The lower post-decompression stiffness of the PT frame and the lower stiffness of the yielded and damaged web plates resulted in larger periods during the free vibration of these tests. The range of calculated periods was also larger for these tests as the time required for the specimen to oscillate one full nonlinear cycle is dependent upon how much of that cycle the specimen experienced the lower stiffness. For cycles at larger displacements in the range of nonlinear response, the equivalent, or secant, stiffness during that cycle is lower, resulting in longer periods.

The equivalent viscous damping ratio, ζ_{eq}, was calculated by[Chopra, 2007]:

$$\zeta_{eq} = \frac{\delta}{\sqrt{(2\pi)^2 + \delta^2}} \text{ where } \delta = \ln \frac{x_1}{x_2} \tag{6.2}$$

where δ represents the logarithmic decay of the displacement response, and x_1 and x_2 represent the displacements at sequential local maxima or minima. The damping ratio was calculated as described for both local maxima and local minima decay, again resulting in some variation in calculated values. The minimum, maximum, and average of the calculated values of equivalent viscous damping during free vibration are provided in Table 6.6.

Table 6.6: Calculated equivalent viscous damping ratio during free vibration of PSD tests

	Damping ratio, ζ_{eq}, during free vibration (%)		
Test	Max.	Min.	Average
Free Vibration	1.05	0.78	0.91
50/50	1.50	0.94	1.19
10/50	7.66	5.63	6.65
2/50	11.60	4.67	7.48

As described in Sec. 5.5.1, the damping ratio for the Free Vibration PSD test was comparable to the range of viscous damping ratios typically assumed for steel buildings; therefore, no additional analytical damping was assumed in the PSD loading protocol. As the specimen experiences nonlinear response during the free vibration portion of the tests (as shown in Figs. 5.31(b)and 5.41(b)), the calculated damping ratio increases due primarily to the hysteretic energy dissipation of the web plate and the magnitude of the web plate

residual strength.

6.4.2 PT force and gap rotation

The gap rotation was calculated from the relative displacement measured between the displacement transducers at each PT rocking connection divided by the distance between them. The PT force was measured directly by load cells at each PT bar or PT seven-strand bundle. For the following plots, the PT force in each member (e.g. MB, EC, etc.) is taken as the sum of the two PT load cells readings for each PT strand bundle or PT bar in that member.

The gap rotation vs. drift responses for each connection are shown in Fig. 6.31. For purposes of demonstrating rocking PT connection behavior, only the results from the 10/50 PSD test are presented here. Arrows are shown to indicate the direction of the response during loading and/or unloading[3].

Figs. 6.31(a) and 6.31(b) show that during positive, or eastward, loading, the gap at the west end of the beam opens with a positive rotation (i.e. bottom flange decompressing), while the gap at the east end opens with a negative rotation (i.e. top flange decompressing). The loops in these gap rotation vs. drift plots are due to the effects of the web plate. For example, in Fig. 6.31(a) the arrows indicate that as the specimen is being loaded in the negative direction, the magnitude of gap rotation at the west end of the MB for a given drift demand is lower during loading than during unloading. As the gap forms during loading, the web plate provides some restraint to gap opening. As the specimen is loaded to higher drifts, the gap can open unrestrained (i.e. it loads along the unloading path when the web plate tensile forces are negligible) until the plastic strain in the web plate corner cutout is overcome. After the web plate corner cutout reaches its peak plastic strain, tensile forces develop in the web plate and again restrain gap opening, resulting in a slowing increase in gap rotation with respect to drift. This response (e.g. the size of the loops in Fig. 6.31(a)) is symmetric for the MB where the web plate above and below the MB are

[3]Note that in general one can determine the direction of loading and unloading in most of the plots by understanding general web plate behavior, specifically the fact that the web plate forces decrease rapidly upon unloading. For example, the unloading direction can be determined in Fig. 6.31(b) by observing the sharp change in stiffness as the specimen is unloaded from the peak drift. Then after the web plate is rapidly unloaded, the rest of the specimen unloads with a stiffness similar to the loading stiffness. This trend is evident in many different types of response plots for SC-SPSWs.

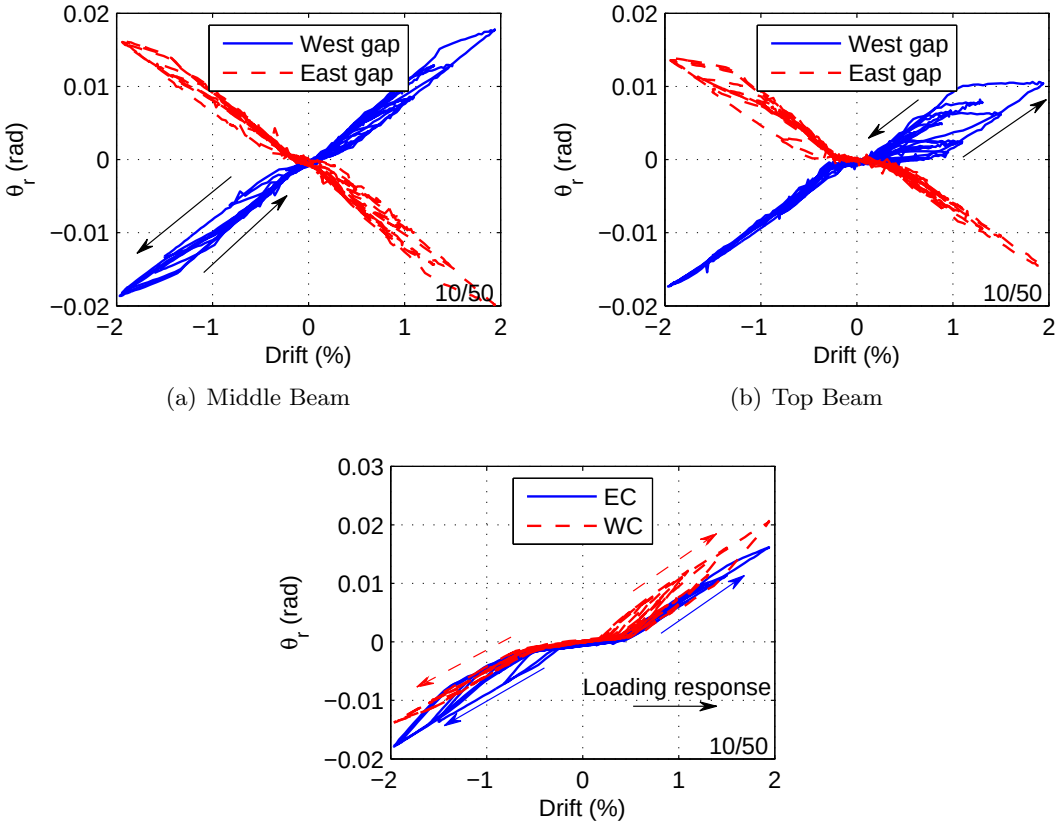

(a) Middle Beam

(b) Top Beam

(c) East and West Columns

Figure 6.31: Gap opening vs. drift during 10/50 PSD test

the same thickness and provide the same restraint to gap opening on both ends of the HBE under both directions of loading. For the TB, these loops are only present in the direction of loading where the bottom flange is decompressed (i.e. the west end of TB during positive direction loading, and the east end during negative direction loading). Because there is no web plate above the TB, there is no restraint to gap opening when the gap forms at the top flange, resulting in a more linear gap rotation vs. drift response at these locations.

Fig. 6.31(c) shows that the PT connection gaps at the base of each column have positive gap rotations (i.e. western flange decompressing) under positive direction loading, and negative rotations for negative direction loading as expected. The loops in the column gap rotation vs. drift response are also due to the effects of web plate loading. The tension column (e.g. the WC during positive direction loading and EC in negative direction loading) decompresses (i.e. increases gap rotation) at a lower drift demand than the compression column (e.g. EC in positive direction loading) due to the upwards distributed web plate forces acting on the columns. Similar to the beam PT connection, at increasing drift demands, the increase in gap rotation due to web plate forces only occurs when the web plate tension field is engaged after reaching the previous peak plastic strain. Also, similarly for the compression column, the downwards distributed web plate forces on the column cause a slightly lower gap rotation.

Fig. 6.32 shows the PT force vs. gap rotation response for each PT connection. Again, the response during only the 10/50 PSD test is shown for purposes of demonstration of behavior. However, Figs. 6.33 through 6.36 show the PT force vs. drift response for each PSD test and the Inelastic cyclic test.

Fig. 6.32(a) shows that the MB PT force is nearly linearly proportional to the gap rotation as suggested by Eqn (2.3). The presence of minor loops in the PT force vs. gap rotation plot in Fig. 6.32(a) may be due to the axial deformation of the beam due to the web plate pull-in of the columns, $P_{HBE(VBE)}$, which is also present in Eqn. (2.3). For example, for any given drift demand, the PT force in the MB during loading is slightly lower than the PT force during unloading because the web plate pull-in is causing the beam to shorten slightly during loading. The PT force vs. gap rotation response in the TB (Fig. 6.32(b)) is not as linear due to the effect of the web plates producing asymmetric gap rotation responses

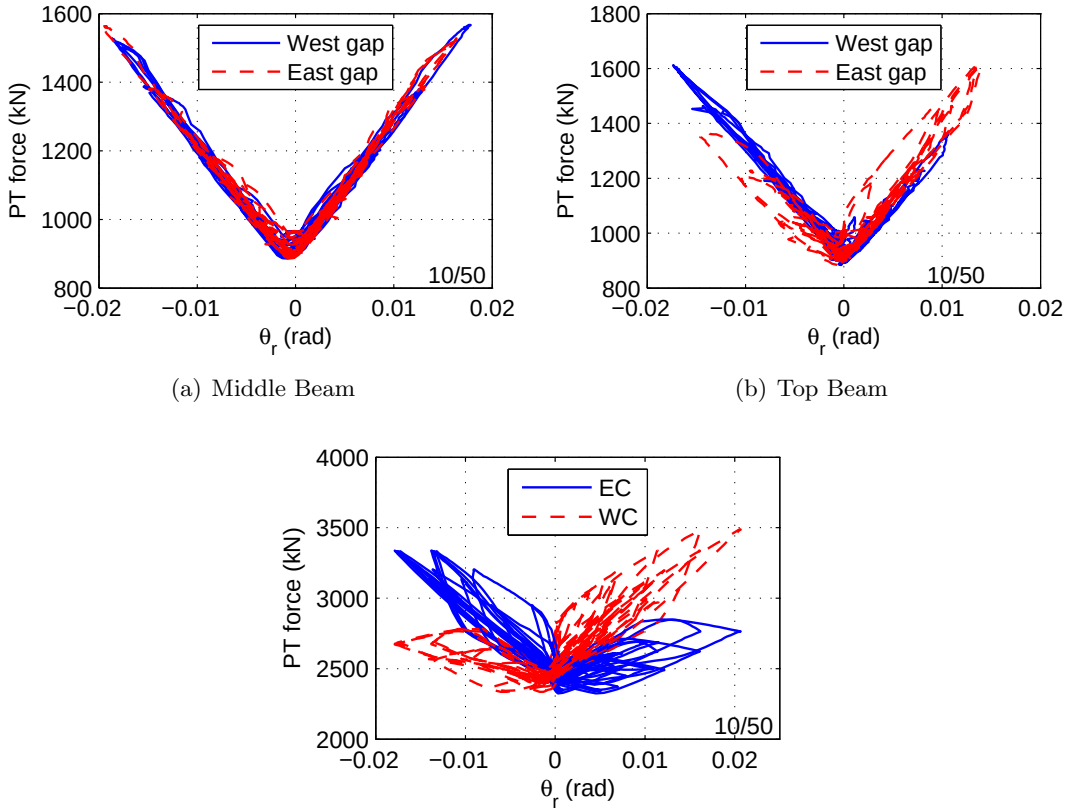

(a) Middle Beam

(b) Top Beam

(c) East and West Columns

Figure 6.32: Gap opening vs. PT force during 10/50 PSD test

on either end of the beam as previously described. However, during unloading when the web plate tensile forces are negligible, the unloading PT force vs. gap rotation response in the TB is linear, and the PT force vs. gap rotation response for the gaps at each end of the HBE (i.e. the two responses plotted in Fig. 6.32(b)) unload along the same path.

Similarly, the PT force response for the column base PT connections are not linear with respect to gap rotation due to the impact of the web plate forces and the overturning moment. For a given gap rotation demand, the PT force will be different depending on the axial loads in the column due to web plate forces (this phenomenon was breifly discussed in Sec. 3.3). For example, when the web plate is pulling upwards on the column (e.g. in the WC during positive direction loading and positive gap rotations) the PT force is larger for a given gap rotation because the PT bars are carrying the uplift force. Similarly, when the web plate is applying a downwards force on the column (e.g. the EC in negative direction loading or negative gap rotation) the PT forces are smaller for a given gap rotation because of axial shortening of the column. Note that after web plate unloading when the impact of the web plate forces is significantly diminished, the WC and EC PT force vs. gap rotations unload along the same linear path.

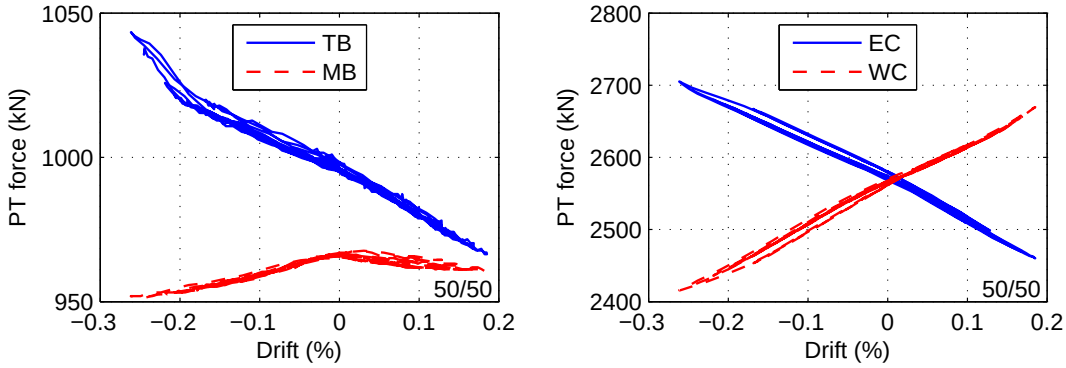

(a) Middle and top beams (b) East and West Columns

Figure 6.33: PT force vs. drift for 50/50 PSD test

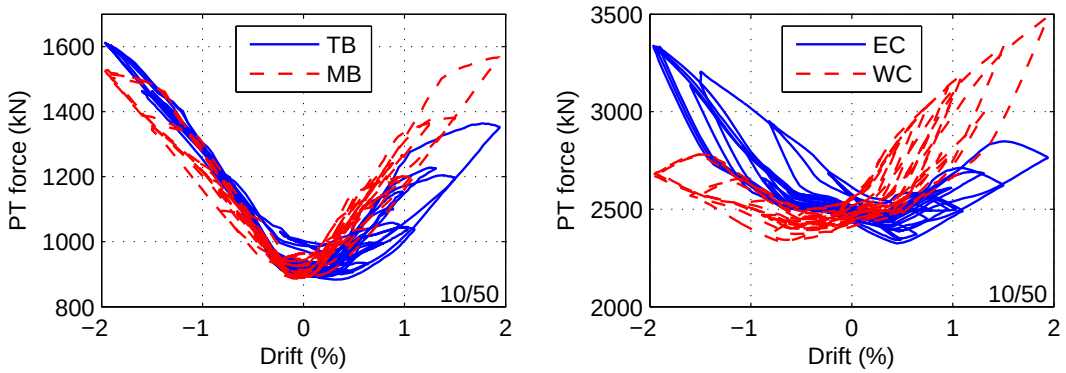

(a) Middle and top beams (b) East and West Columns

Figure 6.34: PT force vs. drift for 10/50 PSD test

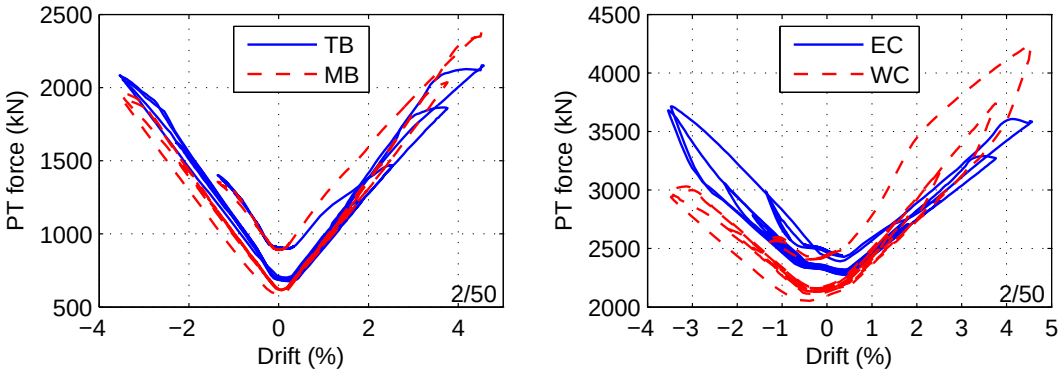

(a) Middle and top beams

(b) East and West Columns

Figure 6.35: PT force vs. drift for 2/50 PSD test

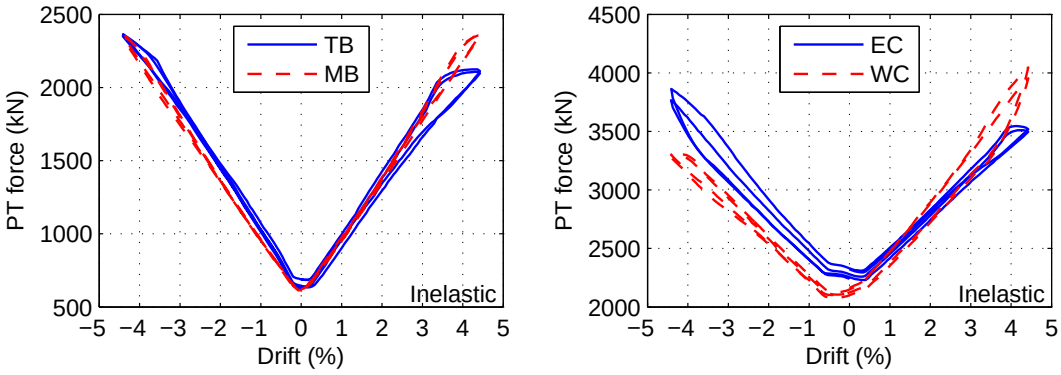

(a) Middle and top beams

(b) East and West Columns

Figure 6.36: PT force vs. drift for Inelastic cyclic test

Fig. 6.33 shows the PT force vs. drift response for the MB, TB, EC, and WC during the 50/50 PSD test, representing the response under essentially elastic loading conditions. The EC and WC (Fig. 6.33(b)) show that the PT force increases linearly with increasing drift demands in the uplift or tension column (e.g. WC in positive direction loading), while the PT force decreases linearly with increasing drift demands in the compression column. As previously described, this is due to axial elongation and shortening of the columns due to the overturning moment. The fact that the PT force vs. drift response is linear indicates that the PT column base connections do not decompress under the drift 50/50 PSD test drift demands.

The TB PT force vs. drift demand in the 50/50 PSD test (Fig. 6.33(a)) shows that under positive direction loading, the PT force decreases and under negative direction loading the PT force increases for small drift demands. This response is due to the actuators loading the specimen only on the WC. As the actuators are pushing on the WC (i.e. in the positive direction), the actuator force is being transfered into compressive force in the TB, resulting in axial shortening of the TB and a reduction in PT forces. Similarly, when the actuators are pulling the WC (i.e. negative direction loading), the PT strands are essentially pulling the EC towards to west resulting in an increase in PT forces. The increase in slope of the PT force vs. drift response at approximately -0.2% drift suggests that at least one of the connections in the TB had decompressed. This is supported by the gap rotation vs. drift response of the TB (e.g. in Fig. 6.31(b)), which indicates that the west connection gap rotation begins to increase in magnitude more rapidly at approximately -0.2% drift.

The MB PT force demand in the 50/50 PSD test (Fig. 6.33(a)) remains relatively constant with respect to drift at low drift levels prior to connection decompression. The MB PT does not exhibit the same linear response as the TB PT at low drift levels, because the axial beam forces induced by the actuator loading at the TB are not present in the MB. The slight decrease in MB PT force at small drift demands is due to the axial shortening of the MB as the web plate forces develop and pull-in the columns.

At the larger drift demands of the 10/50 PSD test, the PT force vs. drift responses (Fig. 6.34) exhibit the expected V-shaped behavior. The MB PT has a symmetric response with the loops in the response due to web plate loading causing axial shortening of the MB.

The TB has an asymmetric response with a larger decrease in PT force during positive loading due to the increased compressive forces in the TB as the actuators load the WC and push the specimen.

The asymmetry of the column PT response (Fig. 6.34(b)) is due to the overturning moment and the web plate forces acting on the columns. As previously described, when the the web plate forces are acting upwards on the column, the column PT forces are larger. When the web plate forces are acting downward, the column PT forces are smaller. Note that at small drift levels in the compression column (e.g. EC in positive drift), the PT forces even decrease to be less than the initial PT force but then begin to increase after connection decompression. Again, after the web plates are fully unloaded, both the EC and WC unload along the same path.

The same behavior can be observed in the PT force responses in the 2/50 PSD test (Fig. 6.35). A key difference is that loops are much less pronounced prior to 2% drift because the web plates have already been yielded up to approximately 2% drift in the previous test. When the web plate is stretching beyone previous peak drift demands, the magnitude of the loops is similar to those observed in the previous tests[4]. PT losses (i.e. the reduction in PT force at zero-drift) also appear to be more prominent in the 2/50 PSD test; however, the magnitude of PT losses will be analyzed in the next section. For the same reasons stated above, the PT force vs. drift response in the Inelastic cyclic test (Fig. 6.36) also have a more linear behavior due to the reduced, but still present, web plate hysteresis.

As verification of the column PT force equations presented in Sec. 3.3, the column PT forces observed in the full-scale test were compared to the column PT force design approximation for presented in Eqn. (3.27). Fig. 6.37 shows a comparison between the WC PT force (note that the WC is the uplift column when loaded in the positive drift direction) from the experiment and as determined using Eqn. (3.27) in two ways: (i) where $\theta_{r,col}$ is taken as the WC gap rotation measured during the test($\Delta_{PT,col} = (d/2)\theta_r$) and (ii) where $\theta_{r,col}$ is taken as the column drift, θ_s ($\Delta_{PT,col} = (d/2)\theta_s$). The approximations of PT demands using Eqn. (3.27) appear to conservatively predict the PT forces for drift demands

[4]Note that the scale of PT force plot in Fig. 6.35 is larger than that of Fig. 6.34.

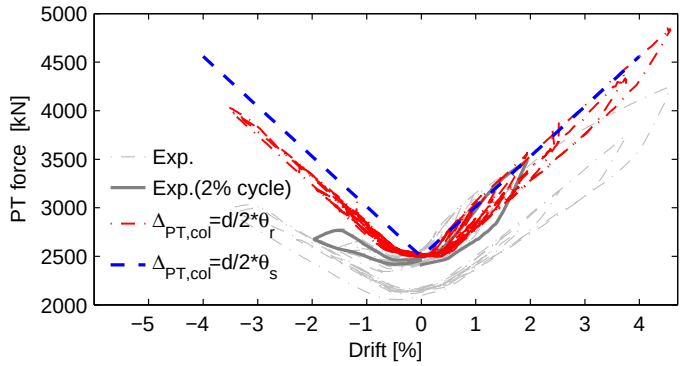

Figure 6.37: Comparison of experimental and analytical column PT force demands.

greater than approximately 1%. Because the PT elements are typically designed to remain elastic at the 2% in 50 year hazard level (at drift demands as much as 4 or 5% according to Clayton [2010]), this equation is a conservative and accurate approximation of PT demands for design. It should be noted that the WC PT experienced approximately 350 kN of loss during the cycle of loading up to 4.7% drift, and the Eqn. (3.27) approximation using θ_s is approximately 450 kN larger than the experimental PT demand at 4% drift, meaning that Eqn. (3.27) is still conservative even without the presence of PT losses. This figure also shows that the approximation assuming $\theta_{r,col} \approx \theta_s$ is accurate when the column is acting as the uplift column as the envelope of the $\Delta_{PT,col} = (d/2)\theta_r$ curve is approximaltely equal to the $\Delta_{PT,col} = (d/2)\theta_s$ approximation in Fig. 6.37.

Fig. 6.37 also shows that Eqn. (3.27) overestimates the column PT demands when the column is acting as the compression column (e.g. negative drift demands for the WC). This overestimation is expected as Eqn. (3.27) intentionally does not account for the additional column shortening due to the increased compression in the column from the web plate forces; however, because the critical case for PT design is when the column is being pulled up by the web plate (i.e. the uplift column), Eqn. (3.27) provides a conservative approximation of PT demands.

6.4.3 PT losses

The PT force loss, T_{loss}, was determined from the PT force at zero-drift after unloading from a new peak drift. For example, because the peak drift magnitude during the 10/50 PSD test was approximately 2% drift, PT loss in the 2/50 PSD test was calculated after the the first cycle of loading beyond 2% drift, which was at approximately 4.6% drift. Because column PT forces are largest when the web plate forces are acting upwards on that column, the PT losses were calculated only after an increase in peak drift in the direction in which the column was uplifting (e.g. after new peak drifts in the positive direction for the WC, and peak negative direction drifts for the EC). Similarly for the TB, the PT loss was calculated after increases in the peak drift magnitudes in the negative direction, beacuse the PT forces are larger in that direction of loading (because of the compressive forces, and thus axial shortening, in the TB due to actuators pushing the WC in the positive direction loading). For the MB, because the PT forces are symmetric with respect to direction of loading, the peak drift magnitudes in either direction of laoding were considered.

The PT force loss was calculated as the PT force at zero-drift following each new peak drift as described above. The PT force loss vs. peak drift for each member is shown in Fig. 6.38. This plot shows similar trends of PT force loss for each member, suggesting that the PT loss is proportional to the peak drift, or peak PT force, demands. This figure also shows that the PT losses that appeared to be so prominent in the 2/50 PSD test in Fig. 6.35 after unloading from 4.6% drift were actually proportional to the amount of PT loss expected based on losses observed at lower drift demands.

Using the same procedure as was used in the subassembly specimens, the percentage of PT force loss, $T_{loss}/T_{o,i}$, after a peak drift of approximately $\pm$2% drift and at the end of the PSD testing is provided in Table 6.7. Even though the magnitude of PT force loss was similar for all PT locations as shown in Fig. 6.38, the percentage of PT force loss was larger for the PT strands in the beams than for the PT bars in the columns for a given drift demand because they had lower initial PT forces. The source of PT loss in the PT strands is likely due to seating in the wedge anchors. The source of PT loss in the PT bars in less clear. Because the PT bars were well within their elastic range (the peak PT force

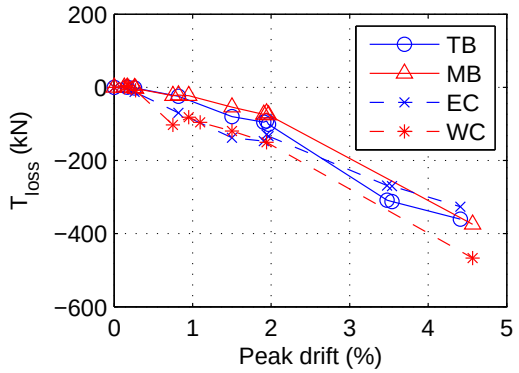

Figure 6.38: PT force loss vs. peak drift in Specimen FR

in the bars was approximately 65% of yield), the loss is not due to plastic deformation of the bars. Other potential sources of loss may be: slipping in the threads of nut anchors or coupler, plastic deformation of the acnhor plates (between the domed nut bearings and the PT load cell), localized plastic deformation at the rocking point at the column base, or settling/shifting of the column during recompression when unloading which could have resulted in a shorter "undeformed" length.

Table 6.7: Actual initial PT force, $T_{o,i}$, and PT loss (as percentage of T_o) for PT in each member after loading at approximately 2% drift and at end of PSD testing for Specimen FR

PT location	$T_{o,i}$ (kN)	$T_{loss}/T_{o,i}$ (%) Approx. 2%	End of PSD tests
MB	967	7.9	38.7
TB	997	10.2	36.1
WC	2562	5.9	18.2
EC	2581	5.2	12.7

Also similar to the calculations made for the subassembly specimens, a non-dimensional expression was calculated to characterize the amount of seating with respect to the total elongation of the PT members. The change in PT element length based on the PT force loss, $\Delta_{PT,loss}$, was plotted vs. the estimated PT member elongation, $\Delta_{PT,max}$, for each peak

drift previously described. Note that, as was done for the subassembly tests, the estimated PT elongation was based on the assumption that the gap opening is approximately equal to the drift, and that the PT elongation due to each gap opening is equal to θ_r times half the rocking depth, and the beam PT has two gaps opening (i.e. total elongation is two times the elongation per gap) while the column PT only has one gap opening. The slope of the linear regression of the $\Delta_{PT,loss}$ vs. $\Delta_{PT,max}$ data (as a percentage) is given in Table 6.8.

The amount of PT loss relative to PT elongation (i.e. the linear regressions of the $\Delta_{PT,loss}$ vs. $\Delta_{PT,max}$ data) for the PT elements in the full-scale specimen (Table 6.8) are larger than those of the subassembly specimens (Table 6.2), but are comparable to the approximate 14% PT loss with respect to maximum PT force increase found in Eatherton and Hajaar [2010]. It should be noted that the percentage of PT loss with respect to initial PT force during the 2% drift cycles in the full-scale and subassembly specimens (Tables 6.7 and 6.1, repsectively) were very similar; however, the PT losses as a percentage of initial PT force at maximum drift demands (between approximately 4 and 5% drifts for the subassembly tests with web plates and 4.6% drift for the full-scale specimen) were much larger for the full-scale specimen comapred to the subassembly specimens. The exact reason for the larger PT losses in the full-scale specimen at larger drift demands is unknown but may be due to the difference in PT anchorage systems used in the subassembly and full-scale systems.

Table 6.8: PT anchorage seating (given as % of approximation of maximum PT elongation) for Specimen FR

PT location	$\Delta_{PT,loss}$ / $\Delta_{PT,max}$ (%)
MB	16.2
TB	16.9
WC	16.9
EC	12.5

6.4.4 Strains near connections

Strain gages were placed in the inside of the TB, MB, EC, and WC flanges near the connections (150 mm and 166 mm from the beam ends and column bases, respectively) as shown in Figs. 5.13 and A.1. Fig. 6.39 shows an example of the raw strain gage data, ϵ_{exp}, vs. gap rotation, θ_r, for the gages located at the base of the WC. Here the strain gage readings are shown for the all of the PSD tests combined (50/50, 10/50, and 2/50). The two gages on the inside flange (e.g. the eastern flange in the WC) are labeled with IF, and the outside flange, OF.

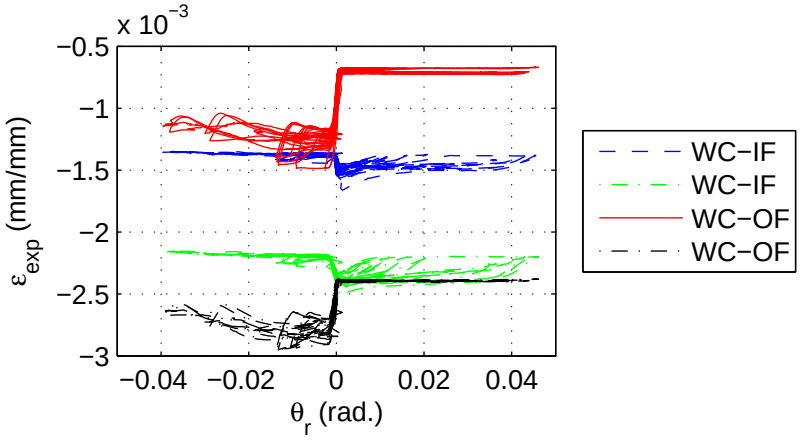

Figure 6.39: Raw strain gage data vs. gap rotation for gages on the inside flange (IF) and outside flange (OF) near base of WC

After connection decompression, the strain at the end of the decompressed flange is expected to be zero. Fig. 6.39 shows that a flat line response (i.e. no change in strain reading with respect to drift) occurs in the inside flange gages during negative gap rotations, when the inside, or eastward, flange is expected to decompressed. Similarly, the outside flanges have a flat line response during positive gap rotations when the outside flange is expected to be decompressed. On the assumption that the strain at the location of the gages should be zero when the flange is decompressed, the strain gage readings can be adjusted such that the flat line response during decompression represents zero-strain. To do so, the flat line strain reading at ±0.02 rad. gap rotation was determined for each gage and the readings

were offset by that amount. The corrected strain gage readings for each flange were then averaged. The corrected and averaged strain gage response, $\epsilon_{corr,avg}$, for each flange at each connection are shown in Figs. 6.40 through 6.42. Strain gage data from some locations are not shown due to faulty readings as described in Sec. 5.6.

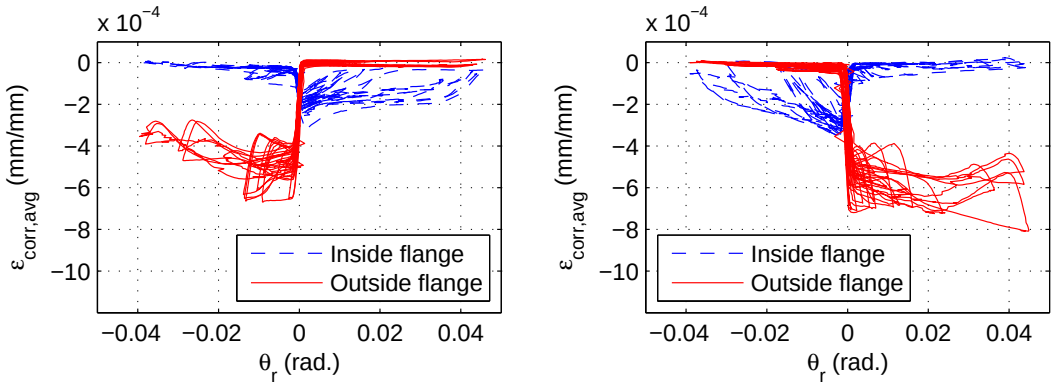

(a) West column (b) East column

Figure 6.40: Corrected and averaged strain gage data vs. gap rotation for each flange near the base of the (a) WC and (b) EC

Fig. 6.40 shows that the compressive strains in the outside flanges near the column bases are larger in magnitude than the strains in the inside flanges. This is because the outside flanges of the columns are compressed (i.e. act as the rocking points) when the column carries the compressive overturning moment (e.g. The WC is the compressive column during negative loading with negative gap rotations). When the inside flange is in contact with the base pedestal, that column is acting tension column (i.e. the web plate forces are acting upwards on that column) and thus has lower compressive strains. Even when the inside flange is acting as the rocking point (e.g. during positive gap rotations for the WC, and negative gap rotations for the EC), the strains on the inside (i.e. the side of the flange closer to the W-shape web) of the inside flange (i.e. the W-shape flange closer to the infill web plate) become zero when the web plate is fully engaged. Zero strains in these locations do not necessarily mean that both flanges are decompressed from the base pedestal. Because the strain gages are placed on the inside of the flanges and the column flanges are relatively

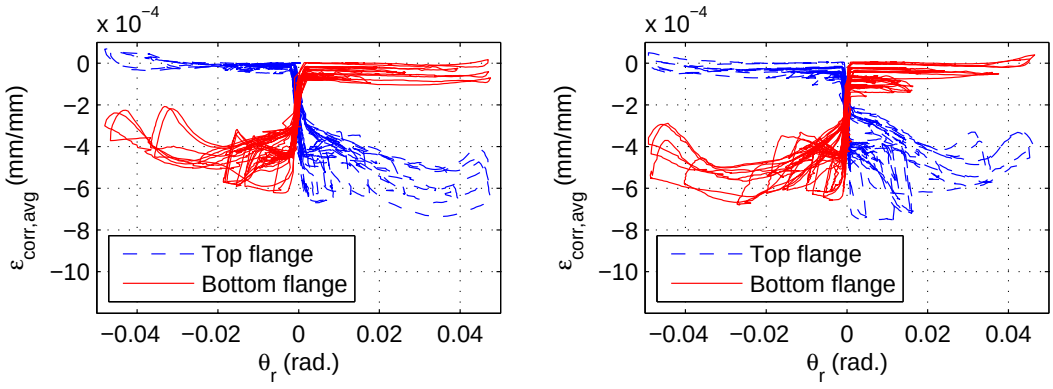

(a) West end (b) East end

Figure 6.41: Corrected and averaged strain gage data vs. gap rotation for each flange near the (a) west and (b) east ends of the MB

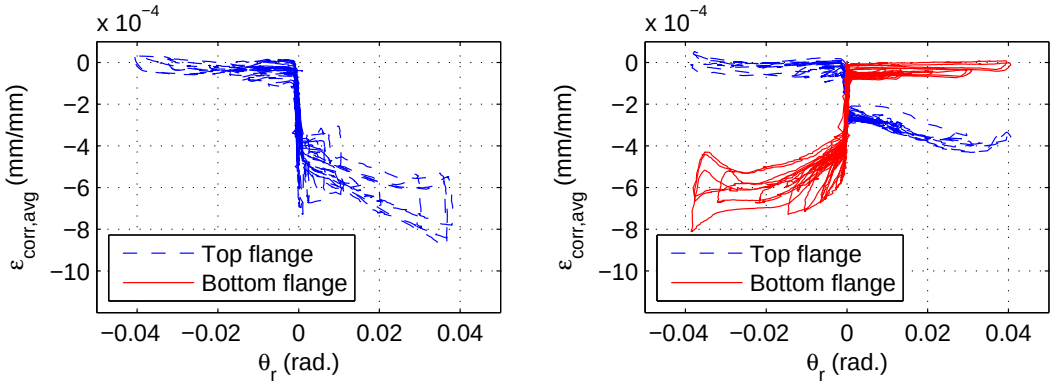

(a) West end (b) East end

Figure 6.42: Corrected and averaged strain gage data vs. gap rotation for each flange near the (a) west and (b) east ends of the TB

thick (approximately 72 mm thick including the flange reinforcing plates), and because the column base rocks about the outermost fiber of the flange, the compressive strains may be concentrated closer to the outside of the flange, leaving zero strains in the inside of the flange.

Fig. 6.41 shows the compressive strains in the top and bottom flanges near the ends of the MB. Again the magnitude of strains are similar for the top and bottom flanges in opposite directions of loading. These plots also show that with increasing gap rotation demands the magnitude of compressive strains in the compressed flanges begins to decrease. As described for the column bases, this does not mean that the total compressive force in the flange is decreasing; but rather the strain becomes concentrated closer to the outside extreme fibers of the flange, thus reducing the strains on the inside of the flange, as the gap rocks open more. Also, at very large rotation demands, near ±0.04 rad., the decompressed flanges may develop small tensile strains. The development of tensile strains at these locations is believed to be due to the increase in magnitude of the moment in the beams. Although the strain must be zero at the decompressed face at the end of the flange, at the location of the strain gage some tensile strains can be developed.

Although the bottom flange strain data is not available for the west end of the TB (Fig. 6.42(a)), Fig. 6.42(b) shows that the magnitude of the compressive strains in the bottom flange in the east end of the TB are larger than the strains in the top flange when compressed. This again is due to the asymmetric loading of the actuators on the WC. During positive direction loading, when the bottom flange is compressed on the east end of the beam and the top flange is compressed on the west end, the TB has larger compressive forces due to the actuators pushing the specimen. In the negative direction of loading when the top flange is compressed on the east end of the TB, the actuators are pulling the specimen, resulting in lower compressive forces and strains in the TB.

6.4.5 Axial force and moment demands

The axial force and moment demands were determined from the strain gage sections along the interior of the beams (i.e. not the strain gages closest to the connections discussed in

the previous section). In the MB and TB, there were three strain gages sections (as shown in Figs. 5.13 and A.1), referred to as the West, Middle, and East sections. The BB had only one section located in the middle of the beam. The axial force and moment demands were calculated using the same method as was described for the SC-SPSW subassembly tests (Sec. 6.2.3). To account for the initial offset in the strain gage readings (as observed in Fig. 6.39), the demands were calculated using the change in strain from the initial strain gage reading, $\Delta\epsilon$, similar to the process used in the subassembly tests. The calculated demands determined from $\Delta\epsilon$ were then adjusted for the assumed demands at the beginning testing: constant axial force along the member equal to the initial PT force, and zero moment along the member.

The calculated axial force and moment demand vs. drift responses are plotted for each section in the BB, MB, and TB in Figs. 6.43(b) through 6.47(b), respectively. The results for all of the tests (50/50, 10/50, 2/50, and inelastic cyclic tests) are combined in each of these figures. The BB has shear connections on both ends, thus behaving as a simply supported beam. The net upwards distributed force from the web plate in both directions of loading results in a negative moment in the middle of the beam, as can be observed in Fig. 6.43(b). If the BB connections are assumed to be pinned, the moment in the middle of the BB due to a constant distributed load acting along the length of the web plate can be determined based on the HBE moment distribution Eqn. (2.4), where d and T_{PT} are are assumed to be zero as there are no rocking PT connections in the BB. Based on this equation and assuming that the tension field angle of inclination, α, is 45° and the web plate stress is approximately 235 MPa (taken from web plate coupon data at ϵ=0.01mm/mm, which corresponds to an approximate drift of 2%), the moment in the middle of the BB at 2% drift is estimated to be -3.25e5 kN-mm, which conservatively estimates the measured moment of -3.02e5 kN-mm at 2% drift shown in Fig. 6.43(b).

The web plate pull-in forces on the columns also cause an increase in compressive axial forces in the beam as can be observed in Fig. 6.43(a). The distributed web plate forces along the BB would also produce a linear axial force distribution; however, the force distribution in the BB cannot be observed as only one strain gage section was used in this member. However, if the distributed axial force is assumed to be symmetric (i.e. $\frac{1}{2}P_{BE(web)}$ acting

on each end of the beam), then the axial force in the middle of the BB can assumed to be equal to the web plate pull-in force, $P_{HBE(VBE)}$ from [Sabelli and Bruneau, 2007]. As was done before, if α=45° is assumed and the web plate stress is assumed to be 235 MPa (corresponding to web plate coupon data at ϵ=0.01mm/mm), $P_{HBE(VBE)}$ at 2% drift is estimated as 305 kN, again conservatively approximating the 301 kN axial force in the BB at 2% drift in Fig. 6.43(a).

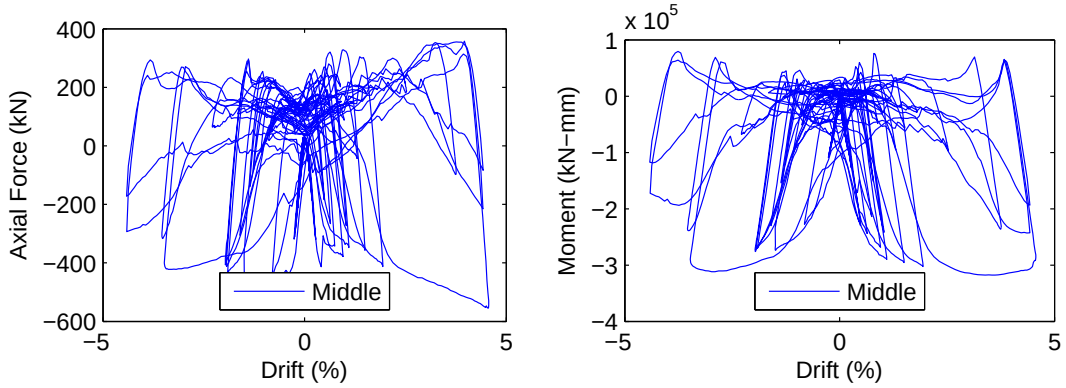

(a) (b)

Figure 6.43: (a) Axial force and (b) moment demands in the strain gage section in the BB

The MB has web plates of the same thickness above and below and no applied story shear force at that level; therefore, the MB is expected to have a linear moment distribution (Eqn. (2.4)) similar to the middle beam in the subassembly tests (Sec. 6.2.3). Under this assumption, the moment in the middle of the MB should remain approximately zero, and the moments should be approximately equal and opposite symmetrically about the center point of the beam, both of which can be observed in Fig. 6.44(b). For comparison, Fig. 6.45 also shows the axial force and moment distributions[5] for selected drift demands when the web plate is engaged and unloaded.

Fig. 6.45(b) also shows a near linear moment distribution with increasing moment magnitudes with larger drift demands (due to the increase in PT forces) and with web plate

[5]Note that the location along the beam starts at zero on the west end of the beam and increases towards the east.

engagement (due to the increase in column pull-in forces). Again, using the theoretical moment distribution given in Eqn. (2.4) and an assumed α=45° and σ_{web}=235 MPa, the moment at the west and east sections at 2% drift is predicted to be ±4.20e5 kN-mm, which is conservatively larger than the 3.22e5 kN-mm and -3.41e5 kN-mm observed in the west and east sections, respectively. The overprediction may be due to several conservative assumptions including the the beam rocking, d, being the distance between extreme flange reinforcement fibers, the assumed angle of tension field inclination, and the assumption that the gap rotation, θ_r can be approximated by the column drift.

The axial force distribution for the MB is also expected to be constant for this case with equal web plates thicknesses above and below (Eqn. (2.5)). In Fig. 6.44(a), although each strain gage section has the same initial force at the beginning of testing (the initial PT force), during the tests the west and middle strain gage sections exhibit some loss of compressive axial force (i.e. a reduction or offset in axial force magnitude at zero-drift) that is not observed, or at least observed to a lesser extent, in the east section. So although the computed axial forces at each section do not remain equal during the test, the magnitude of axial force increase due to web plate loading (i.e. the size of the loops) appear to be similar for each of the sections, as would be expected for the loading condition described above. Fig. 6.45(a) also shows that with the exception of the east end having slightly large compressive forces, the axial force distribution remains relatively constant with larger compressive force magnitudes with increasing drift demands (due to the increase in PT forces) and with web plate engagement (due to the increase in column pull-in forces). For comparison, using an assumed α=45° and σ_{web}=235 MPa as described above, Eqn. (2.5) predicts a constant axial force of approximately 2540 kN in the MB at 2% drift, which compares well with the 2450 kN axial force measured at the middle section at 2% drift.

To demonstrate the effect of the web plate forces on the MB axial force, Fig. 6.46 shows the axial force determined from the strain gages in the middle of the MB minus the MB PT force plotted vs. drift. Because the web plates above and below the MB are the same strength and thickness, the main factors contributing to the MB axial load are PT force and web plate pull-in of the columns. When the effects of the PT force increase are removed from the MB axial force, the result is the axial force due to web plate pull-in of the

columns. Fig. 6.46 shows that as the web plate is engaged, the compression, $P_{HBE(VBE)}$, increases as the web plates pull in the columns. The magnitude of $P_{HBE(VBE)}$ for the MB as calculated per Sabelli and Bruneau [2007] using an assumed α=45° and σ_{web}=235 MPa, is approximately 655 kN at 2% drift, which is less than the $P_{HBE} - P_{PT}$ of 890 kN at 2% drift as shown in Fig. 6.46. The underestimation of $P_{HBE(VBE)}$ is likely due to the assumption that tributary web plate area contributing to $P_{HBE(VBE)}$ is equal to half the story height[6] and that the assumed α=45° does not account for the additional horizontal strain in the web plate due to frame expansion. Note that although $P_{HBE(VBE)}$ is underestimated using the idealized assumptions presented, Eqn. (2.5) still provides a good approximation of the axial force in the MB (as shown above) as it overestimates the PT force using the conservative rocking depth and gap rotation assumptions also as described above. After ±2% drift when tearing was observed the peak magnitude of this pull-in force decreases as the length of tearing increases. Note that when the web plates are unloaded the axial load in the MB due to the web plate actually becomes positive (although the total MB axial load is still in compression). This is due to the compressive, or residual, resistance in the hardened and plastically buckled web plate. Also note the realtive manitudes of the axial load due to column pull-in in the MB (Fig. 6.46) and the axial load (due mostly to column pull-in) in the BB (Fig. 6.43(a)). The magnitude of the web plate pull-in force in the MB is roughly twice that of the compressive forces in the BB, because the MB has twice the tributary area of web plate pull-in forces (i.e. approximately half the story height above and below the MB, compared to only above the BB) acting on the beam.

The TB only has a web plate below and it also has the actuator loading only on its west end. As the web plates are engaged, this loading condition would result in a parabolic moment distribution with a positive moment being produced by the distributed web plate forces. The rocking PT connections would induce a linear moment distribution. Fig. 6.47(b) shows that when the web plates are engaged, the moment at each of the sections becomes

[6]For a two-span continuous beam with a constant distributed load, the middle support (i.e. the MB here) would resist the tributary load of 5/8 of each adjacent span [AISC, 2005b], while the Sabelli and Bruneau [2007] equation for $P_{HBE(VBE)}$ assumes tributary areas of half the adjacent spans. The actual tributary area in this specimen would likley be somewhere in the range of these values and would be dependent upon relative axial stiffness of the beams.

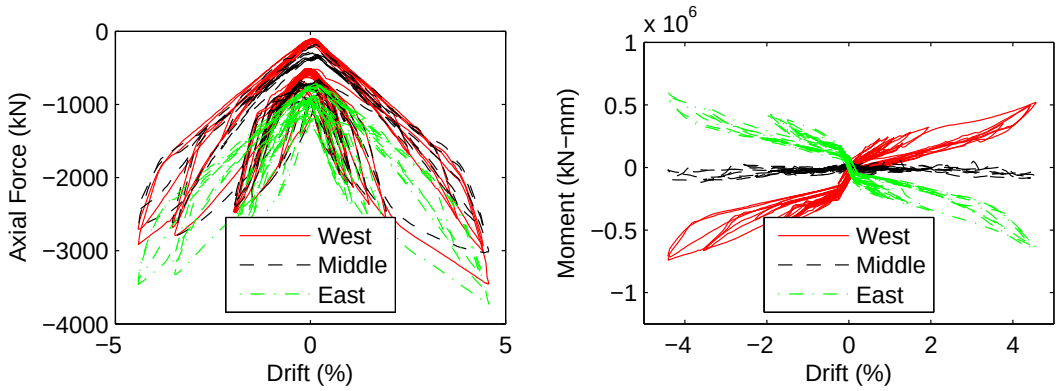

(a) (b)

Figure 6.44: (a) Axial force and (b) moment demands vs. drift in the strain gage sections in the MB

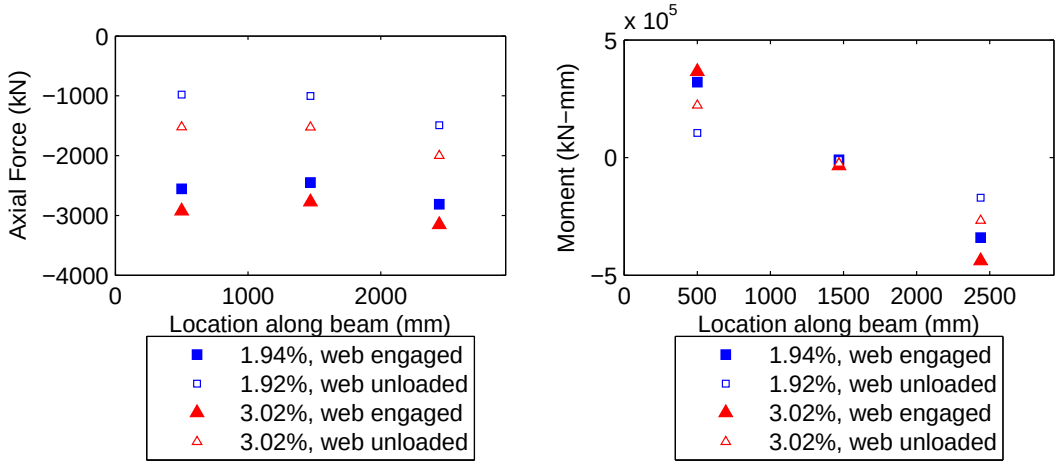

(a) (b)

Figure 6.45: (a) Axial force and (b) moment demand distributions along the MB

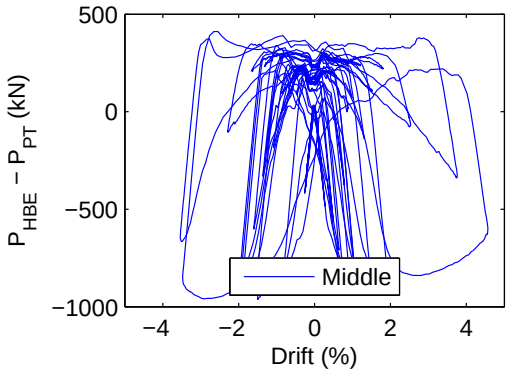

Figure 6.46: Axial force in MB due to web plate forces (i.e. $P_{HBE} - P_{PT}$)

more positive in both directions of loading as expected. For example, according to Eqn. (2.4) and the same assumptions of α and σ_{web} described previously, the moment in the middle of the TB is predicted to the 3.75e5 kN-mm at 2% when the web plates are engaged (this is a conservative approximation of the 3.02e5 kN-mm moment measured at 2% drift). When the web plates are unloaded, the moment at the middle section is near zero, and the west and east sections unload along paths with approximately equal and opposite moments, producing the approximately linear moment distribution as expected. This is also observed in Fig.6.48(b)–when the web plate is unloaded, the moment distribution is near linear and zero in the middle, and the moment demands increase in magnitudes with increasing drift demands. When the web plate is engaged, the moment increases (i.e. becomes more positive) at all locations due to the positive moment from the distributed web plate loading.

Fig. 6.47(a) also shows that the compressive forces measured in the strain gage sections are larger in the TB during positive drift. This is consistent with the actuators loading the WC only, causing larger compressive forces when the TB is pushing the EC in the positive direction and lower compressive forces when the TB PT strands are essentially pulling the EC towards the negative direction. From the HBE free-body diagrams and design equations presented in Clayton [2010] and summarized in Fig. 1.3, the $\pm\frac{1}{2}P_{HBE(web)}$ axial force term acting on each end of the HBE is the member end force due to the net distributed horizontal web plate load acting on the HBE. The total $P_{HBE(web)}$ is also assumed to be equal to the

applied story shear force, and is separated with equal portions of the lateral load applied to each column. Using this assumption, the axial force distribution in Eqn. (2.5) would predict an axial force of approximately 2400 kN in the middle of the TB at 2% drift (using the same α and σ_{web} assumptions as above), which is still a conservative approximation of the measured axial force of 2170 kN at 2% drift. However, in the case of Specimen FR, where all the lateral load is applied on the west column, the distributed axial load will have member end reaction forces of $P_{HBE(web)}$ on the west end and zero on the east end (as opposed to the $\frac{1}{2}P_{HBE(web)}$ on each end as described previously). This can be observed in Fig. 6.48(a). When the web plates are engaged, compared to when they are unloaded, the axial load distribution becomes linear with increasing compressive forces on the west end for positive direction loading due to the net distributed web plate force and actuators loading only on the WC. If this change in axial member end forces were reflected in the design equations, it would produce a more conservative increase in predicted axial force demands (e.g. accounting for asymmetric loading in the design equation as described would predict a more conservative axial force of 2760 kN in the middle of the TB).

Similar to Fig. 6.46 described for the MB above, Fig. 6.49 shows the axial load in the middle of the TB minus the TB PT forces. At the TB, the axial force depends on several factors: the PT force, the distributed axial force on the TB due to the web plate below the beam, the web plate pull-in of the columns, and the axial force due to the actuator pulling or pushing from only one of the columns (a factor that is a result of the asymmetric loading of the test system and was not as prevalent in the MB where there was no actuator). With the PT forces removed, Fig. 6.49 shows the impact of the web plate and actuator forces on the TB axial force. Note that this figure demonstrates the reduction in compressive load (i.e. a positive $P_{HBE} - P_{PT}$) due to the actuator and pulling (i.e. negative drift) the specimen at the TB, and vice versa for the actuator pushing in the positive drift direction. Because it is difficult to quantify the amount of the actuator force that is transferred into axial load in the TB vs. shear force in the WC, it is difficult to dissect the how much of $P_{HBE} - P_{PT}$ is due to each of the above-mentioned factors individually.

As was done for the beams above, the axial force and moment demand response for the WC and EC strain gage sections (B1 and T1 per Fig. 5.13) are shown in Figs. 6.50 and

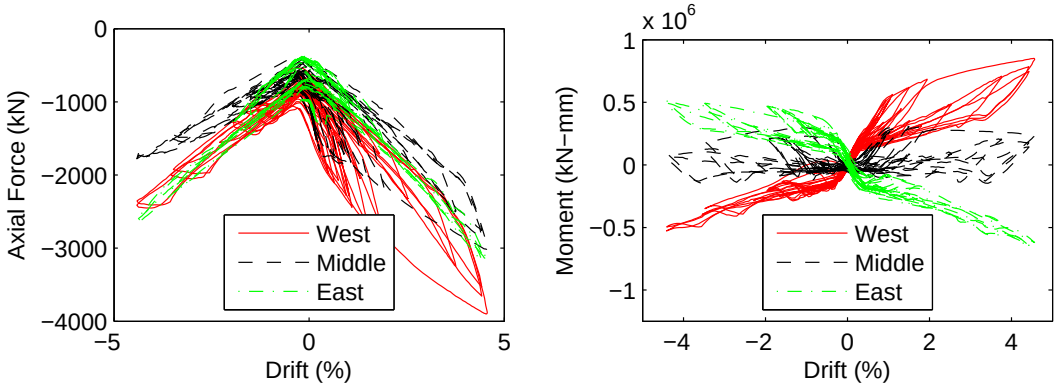

(a) (b)

Figure 6.47: (a) Axial force and (b) moment demands in the strain gage sections in the TB

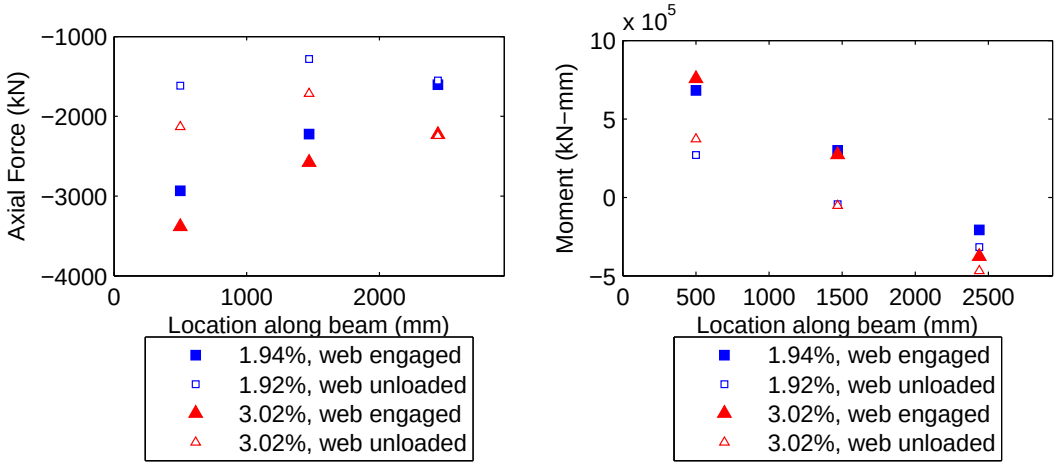

(a) (b)

Figure 6.48: (a) Axial force and (b) moment demand distributions along the TB

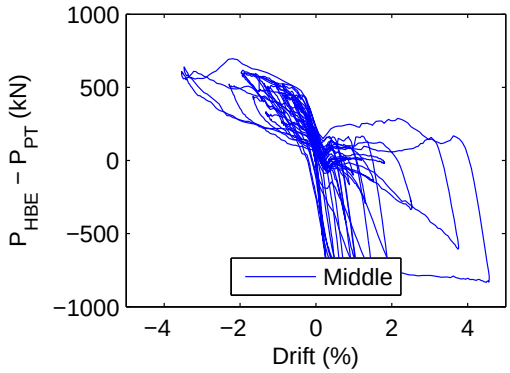

Figure 6.49: Axial force in TB due to web plate and actuator loading forces (i.e. $P_{HBE} - P_{PT}$)

6.51, respectively. Because trends in the response of the WC and EC are roughly the same for opposite directions of loading (e.g. during positive direction loading the WC acts as the uplift, or tension, column, while the EC is the uplift column during negative direction loading) the column axial and moment demands will be discussed primarily in terms of the uplift and compression columns and will refer to the response of the WC (although similar conclusions can be drawn from the EC demands with the opposite loading direction). As was also done for the beams, the column PT forces were removed from the corresponding measured axial force ($P_{VBE} - P_{PT}$) to demonstrate the affect of the web plates and frame action on the column axial demands. These are shown for the WC and EC in Figs. 6.50(c) and 6.51(c), respectively. These values can be compared with the column demands due to web plate forces and frame action (i.e. excluding column PT forces) shown in Fig. 3.14 and derived in Berman and Bruneau [2008]. Using the assumed α=45° and σ_{web}=235 MPa and the procedure outlines in Berman and Bruneau [2008], the axial force excluding column PT forces at the bottom section (i.e. B1) of the WC at 2% drift is predicted to be 2200 kN, which compares well with the $P_{VBE} - P_{PT}$ value of 2160 kN in the WC-B1 section at 2% drift.

A key observation from the column axial demand is that the first story column is always in compression due to the initial column PT force. Upon initial loading, the uplift column compressive force decreases while the compression column compressive force increases due

to the overturning moment; however, after column base PT connection decompression (approximately 0.5% drift) the compressive force in both the uplift and compression columns increase as the PT elongates (Figs. 6.50(a) and 6.51(a)). As the web plate enagaged, the direction of the distributed web plate forces would suggest an increase in compressive forces in the compression column and a decrease in compressive forces in the uplift column. This can be observed for bottom of the first story columns (section B1) in Figs. 6.50(c) and 6.51(c).

While the section near the top of the first story (T1) exhibits similar behavior when acting as the uplift column (i.e. positive drift for WC, negative drift for EC), it does not behave similarly when acting as the compression column. Instead, the top section of the compression column increases in compression upon initial loading prior to column base PT connection decompression, then the compressive force decreases upon further loading. Even during unloading after the web plate forces are unloaded (with the exception of the small residual force in the web plate) the top section of the compression column actually increases in compression as the compression column base gap closes. One would expect that when the compressive force due to the PT elements is removed ($P_{VBE} - P_{PT}$), the axial force in the column after web plate unloading (i.e. negligible web plate forces) would be near zero[7] (as shown in Fig. 6.50(c)) and that the axial forces in both sections of the first story column, B1 and T1, would be similar as there would be no, or negligible, applied load between them. However, this is not the case for the top section of the compression column. The exact reason for this phenomenon is unknown[8].

The moments is the columns are more difficult to evaluate just from intuition alone as the distributed web plate forces produce a parabolic moment diagram, the magnitudes of which depends on the relative stiffnesses of the connections (e.g. for a beam with a distributed load, the shape of the parabolic moment distribution is constant; however, the

[7]Even if the web plate forces were zero, there would still be some axial force in the column due to the shear force in the beams.

[8]As will be discussed in Chapter 7, the unexpected axial load in the section T1 of the compression column was not observed in numerical models of the specimen; therefore, this behavior is thought to be either a byproduct of some (unknown) non-simulated web plate behavior or due to differences in the assumed and actual strain profiles used in the axial force derivations at this location (e.g. due to all of the concentrated forces and shear forces near the PT MB connection and column PT anchorage that is not accounted for in the numerical and analytical Euler-Bernoulli beam theory).

moment distribution is can be shifter up or down based on the beam end stiffnesses and reactions). However, during unloading when the web plate forces are considered to be small, the moment vs. drift response at both first story column sections (B1 and T1) behave in a bilinear elastic response as would be expected of a PT rocking frame (i.e. high stiffness, and therefore more rapid increase in moments, before connection decompression, and lower stiffness after connection decompression). During both directions of loading, the web plate forces pull the columns inward, producing a parabolic moment distribution with a more positive moment and more negative moment[9] in the middle of the WC and EC web plates, respectively. The magnitude of the moment due to the web plate forces is harder to evaluate as previously described; however, the signs of the change in moment due to web plate forces are as expected in both directions of loading (see Figs. 6.50(b) and 6.51(b)). As will be shown later in Chapter 7, the envelope (i.e. design) moment demands predicted by simple numerical models (which are a numerical approximation of the column loading shown in Fig. 3.14) match well with measured demands at these locations.

6.4.6 Initial and recentering stiffnesses

The initial stiffness of the specimen was determined from the experimental actuator force vs. displacement response for each test. Only the initial data where the magnitude of displacements remained less than approximately 11 mm (0.15% drift) was considered as this was within the elastic, pre-connection decompression response range. The slope of the linear regression of these data was taken as the experimental initial stiffness, $K_{i,exp}$, and are provided in Table 6.9. Note that the specimen remained essentially elastic during the Ealstic, Free Vibration, and 50/50 tets; therefore, the initial stiffnesses in the Elastic, 50/50, and 10/50 tests are roughly equal (the percent of the range of variation between the three tests is 2% of the average of the three tests) and represent the initial stiffness of the system with undamaged and unyielded web plates. In later tests, the initial stiffness decreases due to the significant decrease in the lateral stiffness of the already yielded web plate. This initial lateral stiffness of a yielded and torn web plate is reduced even further

[9]Using the same sign convention as the beam but rotated 90° counter-clockwise

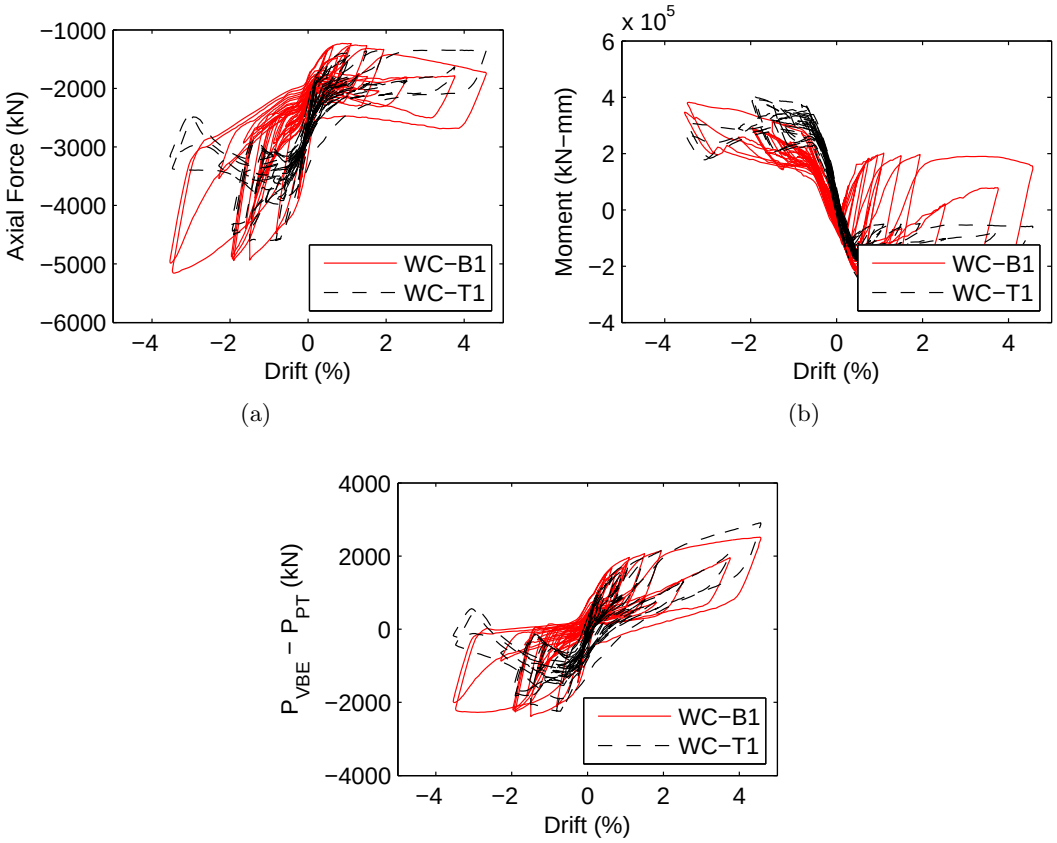

Figure 6.50: (a) Axial force, (b) moment, and (c) axial force without PT contribution ($P_{VBE} - P_{PT}$) demands vs. drift for strain gage sections near bottom (B1) at top (T1) of WC first story

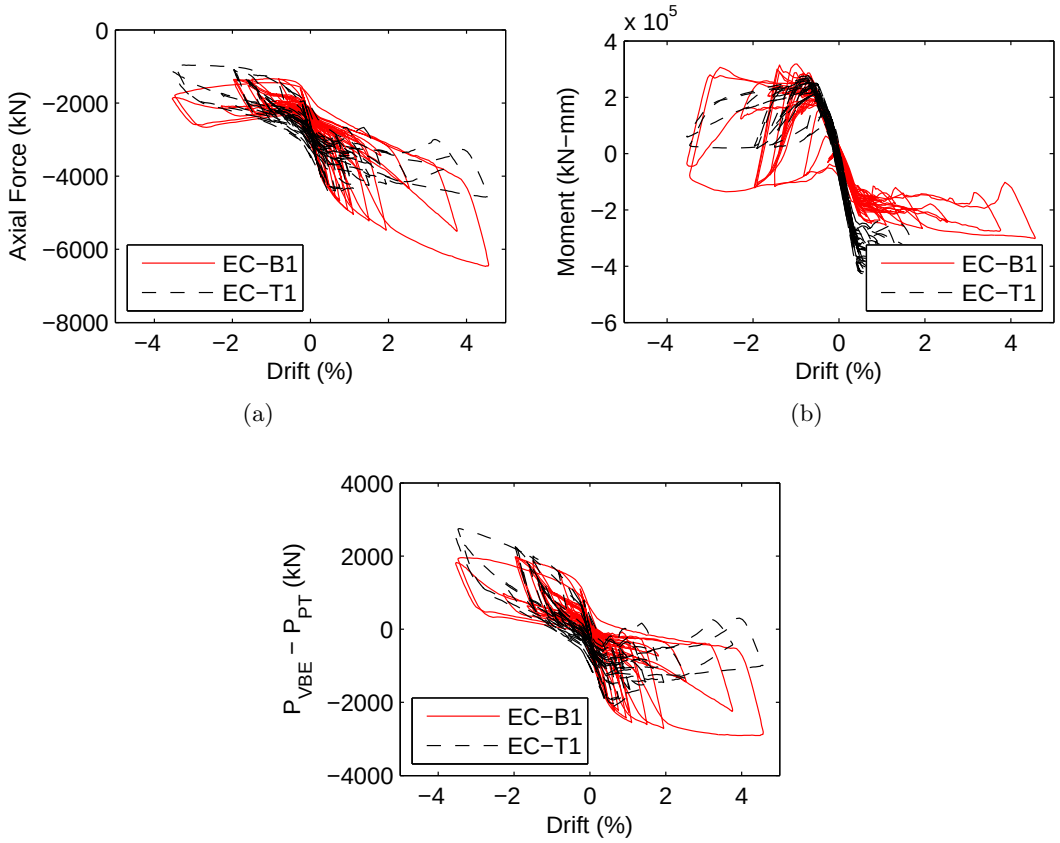

Figure 6.51: (a) Axial force, (b) moment, and (c) axial force without PT contribution ($P_{VBE} - P_{PT}$) demands vs. drift for strain gage sections near bottom (B1) at top (T1) of EC first story

with an increase in the extent of web plate tearing, as in the case of the Inelastic test.

Table 6.9: Initial and recentering stiffnesses of Specimen FR

Test	$K_{i,exp}$ (kN/mm)	$K_{r,exp}$ (kN/mm)
Elastic	50.5	—
50/50	52.0	—
10/50	48.6	1.93
2/50	19.7	1.40
Inelastic	12.6	1.38

The experimentally determined recentering stiffness, $K_{r,exp}$, was also determined for the 10/50, 2/50, and Inelastic tests where the drift demands were large enough to observe the recentering stiffness after web plate unloading and before connection recompression. These values were determined from the portion of the force vs. displacement response that occurred in the range after web plate unloading and before connection recompression. A linear regression was taken for each set of eligible unloading data, and $K_{r,exp}$ was taken as the average of the slopes of the linear regressions from each of these data sets. The data sets that were used and the resulting $K_{r,exp}$ for each of these tests is shown in Fig. 6.52. Note that in the 2/50 test, the unloading response directly following the peak drift at 4.6% drift was not included in the recentering stiffness calculation as the response at that time did not match the expected and characteristic recentering behavior. Also note that the recentering stiffness calculated after the 10/50 is slightly larger than those calculated in the 2/50 and Inealstic tests. Because of the smaller drift demands in the 10/50 test, it was harder to find ranges of data in which the web plate was fully unloaded and prior to the nonlinear response associated with connection recompression; therefore, the portions of response used for calculating the recntering stiffness may still include some influence from the web plates.

6.4.7 Residual drift

In an actual earthquake, the residual drift would be the drift at which the building settles following free vibration and decay of oscillations after the earthquake excitation ends. In

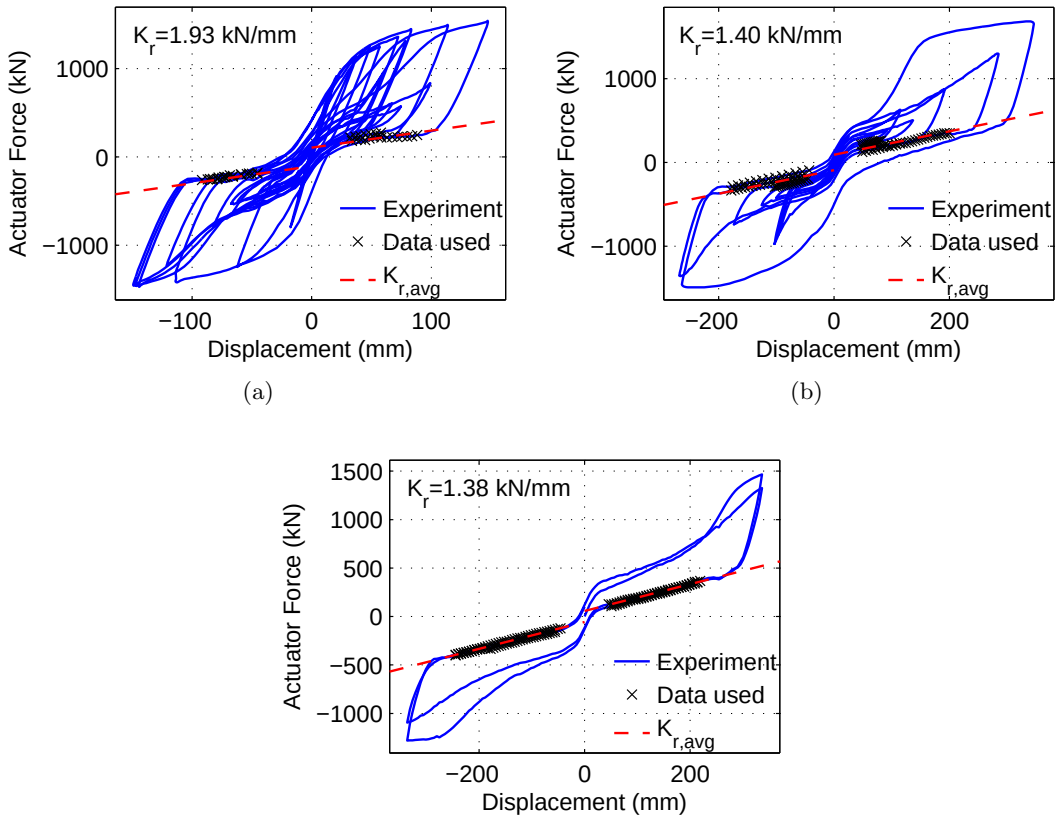

Figure 6.52: Recentering stiffness calculations for (1)10/50, (b) 2/50, and (c) Inelastic tests

these PSD tests, the analytical duration of the free vibration following the excitation was not long enough to allow the specimen to completely settle (i.e. stop oscillating) at a certain displacement[10]. For this reason, the residual displacement must be estimated from the free vibration response data. There are a number of methods to do so:

1. Take the average of the last two peak displacements (one positive and one negative) from the free vibration oscillation. If there is no damping (i.e. in a frictionless vacuum), the average of these peaks will be exactly equal to the residual drift. However, in the presence of damping (friction, hysteric, or otherwise), this value will be biased towards the direction of earlier peak (e.g. if the earlier peak was negative and the latter positive, because the earlier peak will naturally be larger in magnitude, the average will be biased towards the negative direction). If the damping is small (as is the case in this test, see Sec. 6.4.1) it provides a reasonable estimate of the order of magnitude of the residual drift.

2. Determine the residual drift from the last two peak displacements of the free vibration oscillation (the same two peaks described above) considering the amount of logarithmic decay expected between those peaks based on an assumed equivalent viscous damping ratio [Chopra, 2007]. This would provide an exact residual drift for a single degree-of-freedom system with pure viscous damping; however, in this specimen the damping is not purely viscous, and the calculated equivalent viscous damping ratio is dependent on the response history and is not constant from oscillation to oscillation. For this calculation, the average of the equivalent viscous damping ratios, $\zeta_{eq,avg}$, shown for each test in Table 6.6 was assumed.

3. In a real structure, after sufficient time following an earthquake the building would theoretically settle at a displacement in which the system is in equilibrium without the presence of inertial forces (i.e. lateral force equals zero); therefore, the residual

[10]Note that no additional analytical damping was included in the PSD loading algorithm. In the presence of additional damping, as would be the case of an actual building, the oscillations would decay and settle more rapidly.

drift can be taken as the drift at zero force at the end of free vibration. As described previously, the magnitude of drift at zero force decreases over time during free vibration due to the decrease in the web plate residual strength; therefore, it can be assumed that the residual drift must be less than or equal to the last observed drift at zero force. Here, the drift at zero force was determined after unloading from the last two peak displacements (i.e. one positive and one negative) used above, and the maximum of these values was taken as an upper bound for residual drift.

The residual drifts determined using each of these methods ($\theta_{resid,1}$, $\theta_{resid,2}$, and $\theta_{resid,3}$ for methods 1, 2, and 3, respectively, as described above) for each of the PSD tests are given in Table 6.10. Note that for all of these tests, the residual drifts calculated using each of the previously described methods were all well below the 0.2% recenentering drift criterion, indicating that the specimen was able to recenter at each of these seismic hazard levels.

Table 6.10: Residual drifts determined from different methods for each PSD test

Test	Residual drift (%)		
	$\theta_{resid,1}$	$\theta_{resid,2}$	$\theta_{resid,3}$
Free Vibration	-0.001	-0.002	-0.001
50/50	-0.012	-0.015	-0.019
10/50	0.016	-0.045	-0.052
2/50	-0.002	-0.077	0.096

6.4.8 Web plate strains

No strain gages were installed on the web plates in this specimen; however, displacement transducers (DT) were installed on the specimen to estimate the strain in the web plate at locations near the corner cutouts and near the interior, or field, of the web plates. As shown in Fig. 5.12 the diagonal DTs were oriented at 45° and were attached to the flanges of the beams and columns. The web plate strain was estimated by taking the axial deformation measured by these transducers and dividing it by the undeformed distance between the two anchor points (on the beam and column flanges) of the diagonal DT apparatus. The

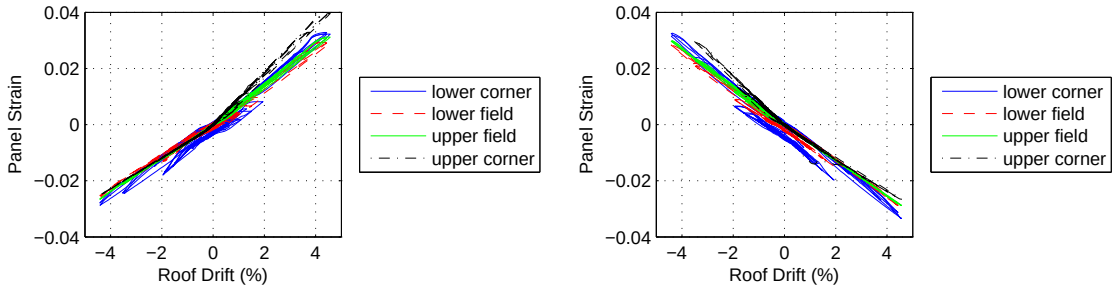

Figure 6.53: Estimated strains in 1st story web plate from DTs on (a) south and (b) north side of the specimen

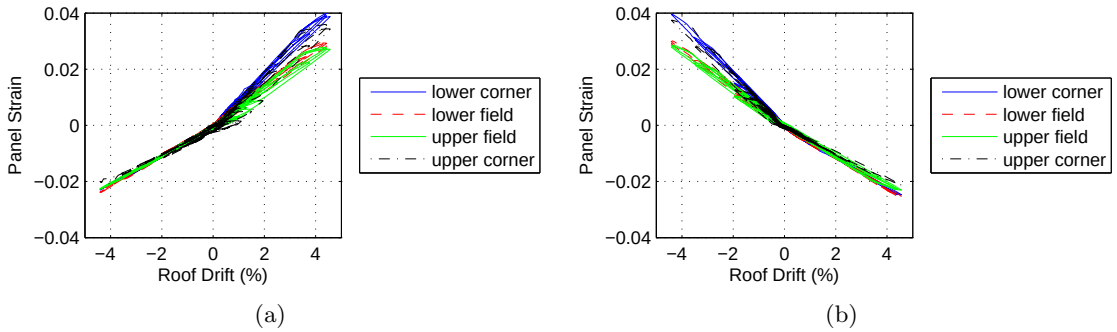

Figure 6.54: Estimated strains in 2nd story web plate from DTs on (a) south and (b) north side of the specimen

estimated web plate strains vs. drift are shown for the first and second stories in Figs. 6.53 and 6.54, respectively. Here, the labels "corner" and "field" refer to the diagonal DTs measuring strains near the corner cutouts and in the interior of the web plate, respectively, and where "lower" and "upper" refer to the DTs that were located near the bottom or the top, respectively, of that particular story. Data from DTs that were removed from the specimen near the end of testing are not shown after the point of removal.

In general, the diagonal DTs on the south side of the specimen are in the approximate direction of the tension field during positive loading, and vice versa for the DTs on the north side of the specimen. As expected, the estimated web plate strains are positive when in the direction of the tension field and negative when the DTs are measuring orthogonal

to the approximate tension field. Also as expected, the strains at the corner cutouts near PT gap openings (e.g. the top corner in the first story and the bottom and top corner in the second story) have larger tensile strains than the interior, or field, strains when the flange nearest the corner cutout is decompressed. The reason for the difference in slopes in positive and negative direction loading is believed to be due to effects of frame expansion introducing a positive horizontal strain in the web plates in both directions of loading. This positive horizontal strain causes a larger increase in positive tension field direction strains and a smaller decrease in compressive strains.

6.5 Comparison with Conventional SPSW

The dimensions and target strength for the SC-SPSW full-scale specimen (Specimen FR) were designed to be comparable to a previous conventional SPSW (Specimen NC) test conducted at NCREE [Li et al., 2012]. To compare the performance between the self-centering and conventional SPSW systems, a summary of the performance of Specimen NC will be described and compared to that of Specimen FR.

Specimen NC was part of a series of three SPSW specimens investigating different methods for design of the bottom columns and allowing hinging to form in the columns at certain target demand levels. Specimen NC was termed so for being designed to have "Normal Columns" that only have column hinging at the base of the column at the MCE-level (assumed to be at 2.5% drift based on Qu et al. [2008]). The other specimens were designed to have weaker columns to promote further hinge development in the columns; therefore, Specimen NC can be taken as a typical SPSW, designed in the current state-of-practice. The dimensions and loading for Specimen NC are shown in Fig. 6.55. A table summarizing the top beam (TB), middle beam (MB), bottom beam (BB), and column (C) frame sizes and the web plate thickness, t_w, for both Specimen NC and FR are provided in Table 6.11 for purposes of comparison[11] Both specimens used the same thickness of web palte, and the boundary frame sizes in Specimen FR were larger than those used in Sepcimen NC. The boundary frame members for both specimens were Grade 50 steel, and the web plates in

[11]Approximate dimensions of Specimen FR boundary frame sizes are given in metric units for purposes of comparison, although US standard sections shapes were used.

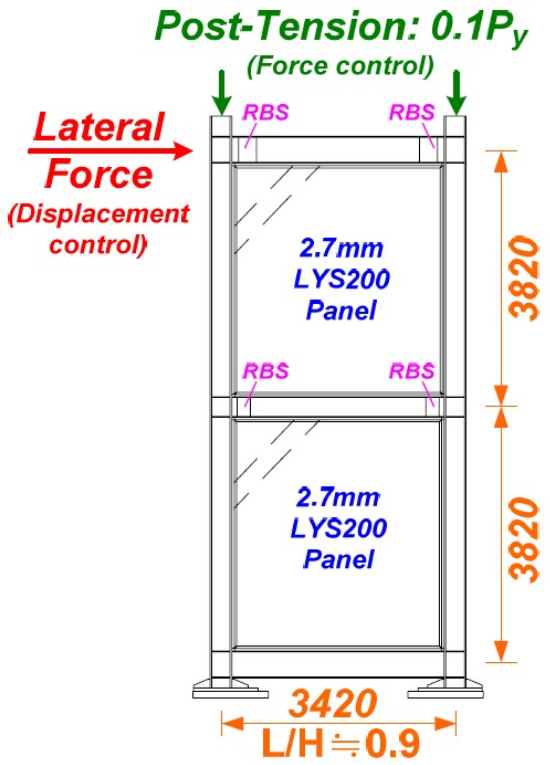

Figure 6.55: Specimen NC [Li et al., 2012]

both specimens were made of LYS225 steel.

Specimen NC was loaded cyclically up to 4.5% drift. Key observations of damage in SpecimenNC included [Li et al., 2012]:

- Reduced-beam section (RBS) beam flange yielding at 0.75% drift.
- Whitewash flaking in the webs of the bottom column and bottom beam at 1% drift, with significant yielding in the lower one-quarter to one-half of the columns at 1.5% drift.
- RBS web local buckling in the top and middle beam at 2.5% drift.

There were no descriptions of the onset of web plate damage (more specifically tearing), although boundary frame damage was the focus of this study. Fig. 6.56 shows typical web

Table 6.11: Comparison of frame and web plate properties for Specimen NC [Li et al., 2012] and Specimen FR [Frame sizes are depth x flange width x web thickness x flange thickness (all units in mm)]

Component	Specimen NC	Specimen FR
TB	H400x200x10x14	560x308x19x29(approx.)
MC	H300x150x10x12	502x286x20x36(approx.)
BB	H400x200x8x13	467x282x12x20(approx.)
C	H320x310x16x25	381x327x33x52(approx.)
t_w	2.7mm	2.7mm

Figure 6.56: Specimen NC Web plate damage typical in corners at end of test [Lee, 2011]

plate damage in the corners (shown specifically at the top flange of the middle beam) of the panel at the end of the test after multiple cycles of loading at 4.5% drift.

Fig. 6.57 compares the force vs. roof drift response of Specimens NC (conventional SPSW) and FR (SC-SPSW). Both specimens notably have very similar peak strengths and backbone responses, with specimen FR having slightly larger strength in the positive direction of loading and roughly equal strength in the negative direction of loading. Because the web plate thicknesses and strengths for both specimens were the same, the equal specimen strengths imply that the boundary frames were contributing similar strengths in both of the specimens. The boundary frame strength of Specimen NC was developed by the plastic capacity of the yielded RBS connections, while the boundary frame strength in Specimen FR was developed by the increase in PT connection forces as gaps opened (i.e. leaving the frame damage free). It should also be noted that Specimen NC did not exhibit significant

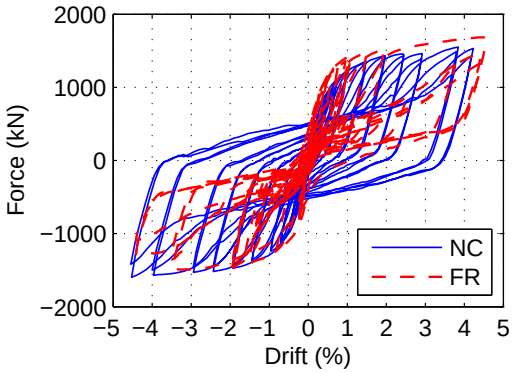

Figure 6.57: Comparison of conventional SPSW (Specimen NC) and SC-SPSW (Specimen FR)

strength loss up to 4.5% drift due to ductile yielding of the frame and only minor tearing in the web plate, while Specimen FR did exhibit some loss of strenth in the negative direction of loading beyond -3.5% drift due to web plate tearing.

A key difference between the response of both specimens is the unloading path. Although both specimens have what would be considered a "pinched" hysteresis die to the nature of the web plate behavior, the Specimen FR response is much more pinched than that of Specimen NC, resulting in much smaller residual drifts upon unloading. Other than general observations of the specimen hysteresis strength and shape and observations of damage, it is difficult to draw many other conclusions from this data due to the difference in types of loading (i.e. cyclic loading vs. pseudo-dynamic loading with a non-uniform drift history).

Overall, these two tests indicate that conventional and self-centering SPSWs designed with the same web plate (thicknesses and strength) can have comparable lateral strengths and drift capacities. Although the SC-SPSW does require significantly larger boundary frame members, the boundary frame damage is negligible after loadings up to 4.5% drift. Alternatively, the conventional SPSW can use smaller boundary frame sizes that will undergo significant yielding and likely need significant repair or replacement after drifts of approximatley 1.5%.

6.6 Summary of Data Analysis

6.6.1 Summary of subassembly testing

Data analysis from the SC-SPSW subassembly tests investigated the effects of various parameters including: web plate thickness, t_w; number of PT strands, N_s; initial PT force, T_o; HBE depth, d; load protocol; bolted and welded web plate-to-fish plate connection details; and web plate-to-boundary frame connection configurations. The results of these analyses include:

- The web plate thickness, t_w, was found to have a significant impact on SC-SPSW strength and energy dissipation as expected. The web plate residual strength, attributed to geometric stiffness of the plastically deformed web plate, was also found to impact the recentering capabilities by increasing the residual drift of the specimen at zero-force.

- The number of PT strands, N_s, and HBE depth, d, had the most significant impact on the specimen recentering stiffness, K_r, as expected from Eqn. (6.1).

- The experimentally determined axial force and moment demands in the HBE followed trends as expected from simple SC-SPSW free-body diagrams and web plate loading and unloading characteristics.

- The theoretical estimations of recentering stiffness, K_r (Eqn. (6.1)), matched well with those determined from the experimental response.

- PT force and connection gap opening responses matched well with the expected response. Some PT force losses due to PT anchorage seating were observed; however, these are only representative of the PT strand lengths and anchorage systems used in this test program and may be smaller in actual building construction when longer PT strands and non-reusable PT anchors are used.

6.6.2 Summary of full-scale testing

A full-scale two-story SC-SPSW was tested under static cyclic and pseudo-dynamic loading to investigate response and performance under different seismic hazard levels. The results of these tests include:

- The equivalent viscous damping ratio in the elastic specimen was found to be approximately 1%, within the range of, if not slightly less than, damping expected in steel buildings. The initial period of the structure was found to be approximately 0.6 sec. The period of oscillation increased to over 2 sec during free vibration following the 2/50 test when the specimen web plates were significantly damaged and yielded.

- The PT force and gap rotation responses were as expected. Nonlinear PT force and gap rotation response with respect to drift can be explained by influences from the web plate forces (either by restraining gap opening or causing boundary frame member axial deformation).

- PT losses were present in all PT elements. Losses in the PT strands in the beams are likely due to anchorage seating; however, the reason for losses in the threaded PT bars in the columns are less certain.

- Axial force and moment demand responses determined from strain gages along the beams correspond to the expected behavior based on web plate and PT element loading and unloading. The axial force and moment distributions along the MB and TB are also similar to the expected distribution trends.

- Because the duration of free vibration was not long enough for the specimen to stop oscillating, the residual drift was estimated based on several different methods. Each method indicated that the residual drift after each of the PSD tests was well below the 0.2% recentering criterion, indicating that the specimen was able to recenter at each hazard level.

- The axial force and moment demands for the beams and columns predicted by capacity design equations presented in Clayton [2010] provided conservative approximations of those measured by strain gage test data based on reasonable approximations of web plate strength and tension field angle of inclination.

Chapter 7

NUMERICAL MODELING

7.1 Introduction

This research project aims at understanding global behavior and local component demands of the SC-SPSW system and how they impact seismic performance. Because the range of physical specimens and loading conditions that can be tested in the laboratory are limited due to resource constraints, numerical models can be used to approximate actual system behavior for a broader range of SC-SPSWs and earthquake loading. More specifically, this research is aimed at evaluating and validating numerical modeling approaches used to simulate SC-SPSW behavior. To conduct the wide range of numerical time history analyses necessary to understand SC-SPSW seismic behavior, various numerical models must be considered and evaluated based on various criteria, including the model's accuracy when compared to experimental results, its numerical robustness (i.e. ability to consistently produce converged and reasonable results), and its computational efficiency. Based on these objectives, a numerical modeling approach can be selected to investigate the SC-SPSW's seismic response and performance (as will be done in Chapter 8).

Numerical models of the subassembly and full-scale specimens were developed using two different web plate modeling methods. The open-source finite element analysis platform OpenSees [Mazzoni et al., 2009] is a robust framework for numerical nonlinear simulations and dynamic response history analyses. Models developed in OpenSees simulated the web plate using the relatively simple and commonly employed strip method, and represent modeling techniques that would be more typically employed in a design office. Various OpenSees models investigated different material models that can be employed in the strip method, including a tension-only material (which is the current state-of-practice for modeling SPSW web plates [Sabelli and Bruneau, 2007]), a simply modified tension-compression material (developed to account for the web plate residual strength that was observed in the ex-

perimental tests presented in Chapter 4), and a more advanced and newly developed web plate strip material model (developed by Webster [2013] to capture various non-idealized web plate behaviors). Alternatively, a more complex and computationally demanding finite element model of the SC-SPSW specimens was developed in ABAQUS [ABAQUS, 2010] in which the web plate was modeled using continuum shell elements.

In this chapter, Sec. 7.2 describes the strip model and various strip materials employed in OpenSees. This section evaluates the global, local, and dynamic response of the tension-only and tension-compression strip material models to the experimental results for validation. Sec. 7.3 describes the shell web plate model employed in ABAQUS and compares its response to experimental results. Sec. 7.4 presents the preliminary results for the newly developed web plate strip material employed in OpenSees, and compares these preliminary results to both ABAQUS and experimental results. Finally, Sec. 7.5 summarizes the findings from evaluating the various models and provides recommendations for which modeling approaches are most appropriate for design and nonlinear response history analyses.

7.2 OpenSees Model

The OpenSees model represents the simpler of the SC-SPSW numerical models discussed in this research. The SC-SPSW is modeled in OpenSees using a combination of beam-column and truss elements. The benefit to using these "simple" elements is that they are more commonly used by practicing design engineers in commercial finite element software and they are more computational efficient compared to shell element-based models. The OpenSees framework also supports parallel execution of multiple dynamic analyses, making it ideal for investigation of the seismic response of the system.

7.2.1 Description of model

The test specimens were modeled in OpenSees [Mazzoni et al., 2009] as shown schematically in Fig. 7.1. The boundary frame elements were modeled using force-based beam-column elements with fiber cross-sections to allow for distributed plasticity, although no yielding was expected. The PT elements were modeled using truss elements with an initial stress and were anchored at points rigidly offset from the boundary element centerline to the location of

the PT anchorage[1]. The boundary frame and PT elements were modeled with the nominal elastic moduli and yield strengths of their respective materials. The web plate was modeled using diagonal strips oriented in both directions of the tension field [Sabelli and Bruneau, 2007]. The strips in the models with web plates connected to HBEs and VBEs were inclined at an angle, α, of approximately 45° according to Eqn. (2.1) [Sabelli and Bruneau, 2007]. For specimen W14-8s100k16GaHBE, the strips were connected to the HBEs only as shown in Fig. 7.2. Here, the strip inclination, θ, was calculated to be approximately 30° from vertical as determined from Eqn. (3.1) [Thorburn et al., 1983]. The cross-sectional area of the strips, A_s, for the fully-connected web plated were determined from the equation in Sabelli and Bruneau [2007] as:

$$A_s = \frac{1}{n}\left(L_{cf}\cos\alpha + h_c \sin\alpha\right) t_w \tag{7.1}$$

where, n is the number of strips and all other variables as previously defined. The strip area for the HBE-only web plate, $A_{s,HBE-only}$, was determined based on the previously presented equation as:

$$A_{s,HBE-only} = \frac{1}{n} L_w \cos_w \tag{7.2}$$

where, L_w is the length of the web plate connected to the HBE. All strips were rigidly offset half of the corresponding boundary element depth from the boundary frame centerline as shown in Fig. 7.1(c). Details of the strip material model will be discussed later. The pin and roller boundary conditions at the base of the VBEs corresponded to those in the physical subassembly experimental model.

7.2.1.1 PT connection model

The PT connection (Fig. 7.1(d)) was modeled using compression-only zero-length elements rigidly offset from the boundary elements to simulate gap opening and closing at the HBE flanges. The compression-only elements were located half the rocking depth from the boundary member centerline. Here, the rocking depth is considered the distance between extreme

[1]The PT anchorage point was assumed to be at the farthest end of the barrel anchor or threaded nut.

fibers of the member's flange reinforcement, with the exception of the column base PT rocking connection in the full-scale specimen. The rocking depth at the column base was taken as the distance between extreme fibers of the column flanges (excluding flange reinforcement) based on visual observation of the column base rocking behavior (Note that the column base rocking depth assumed is approximately 10% less than the distance between extreme fibers of the column flange *reinforcing plates*). Shear forces were transfered from the HBEs to VBEs in the model via vertical displacement constraints between the VBE flange and HBE centerline simulating the horizontally slotted shear tab connection in the physical model. The vertical displacement constraint used here has a behavior similar to the diagonal shear transfer springs used in Clayton et al. [2012b] and produces nearly identical system and connection responses. Note that in Fig. 7.1(d), the PT elements are connected to slave nodes that are located byond the VBE (i.e. ouside of the the PT frame centerline) and are not connected to the VBEs themselves.

7.2.2 Web plate strip models

The diagonal strips simulating the web plate were employed using three different uniaxial material models:

1. Tension-only (TO) material
2. Tension-compression (TC) material
3. SPSW web plate (WP) material [Webster, 2013]

Each of the uniaxial material models are described below.

7.2.2.1 Tension-only model.

Sabelli and Bruneau [2007] recommend modeling the web plate using tension-only strips with a pinched hysteresis under the assumption that web plate shear buckling strength is negligible resulting in immediate formation of the tension field, that web plates have negligible stiffness upon unloading, and that the web plate must reach the previous peak

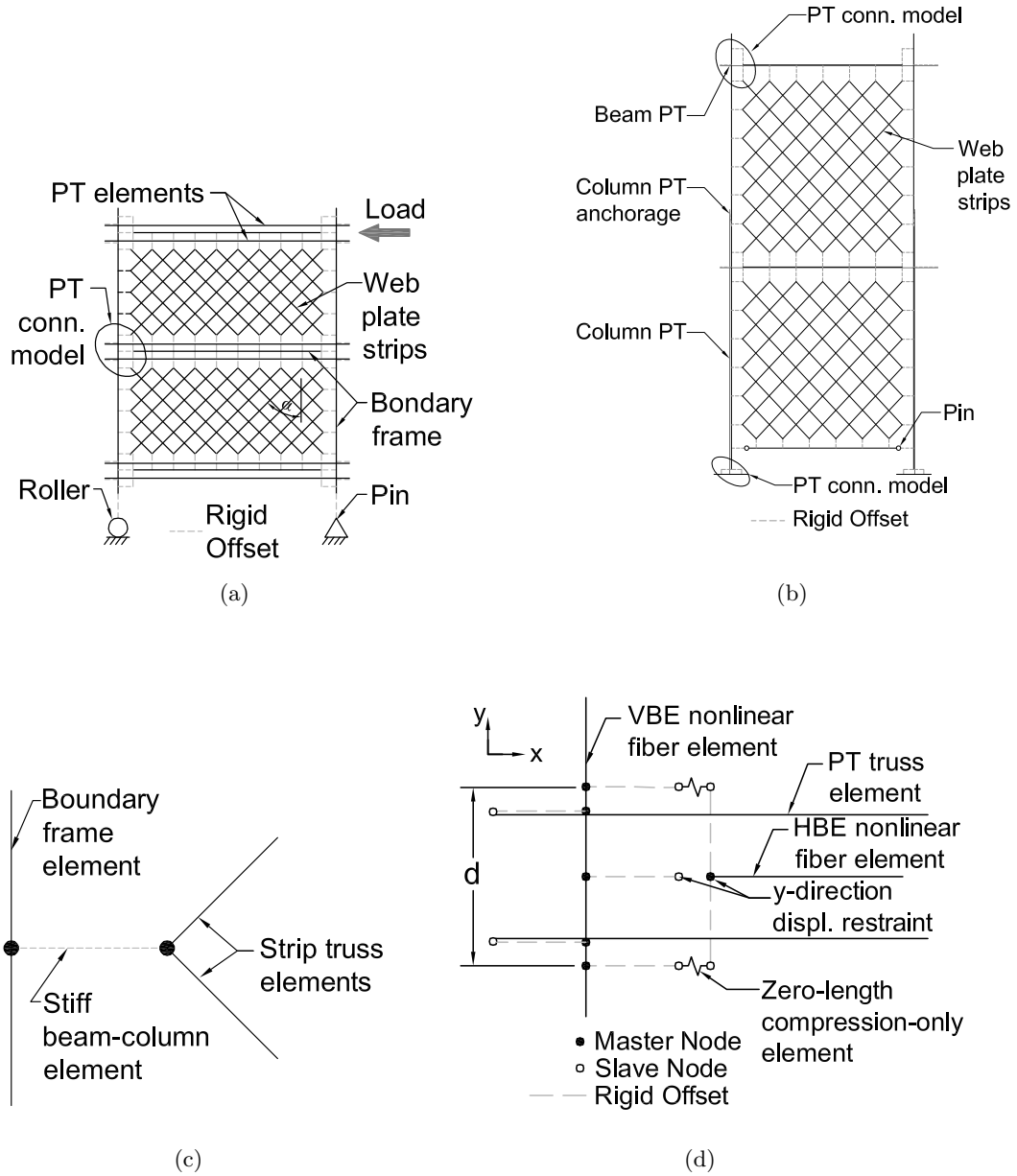

Figure 7.1: Schematic of numerical model of (a) subassembly specimen, (b) full-scale specimen, (c) strip rigid offset, and (d) PT connection

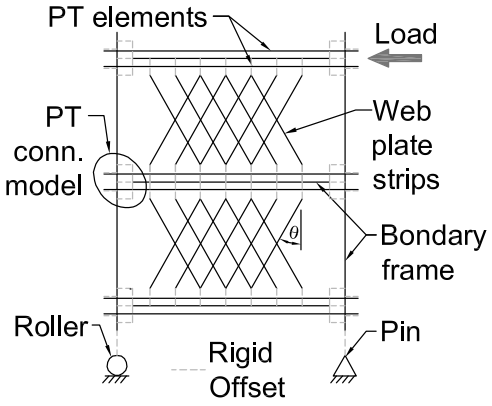

Figure 7.2: Schematic of OpenSees numerical model of specimen with web plate connected to HBEs only.

plastic strain before resisting additional load. This idealized tension-only web plate behavior (shown as Model TO in Fig. 7.6) has been shown to match the initial stiffness, strength, and cyclic response in conventional SPSWs [Sabelli and Bruneau, 2007; Elgaaly et al., 1993; Lubell et al., 2000] with moment-resisting HBE-to-VBE connections reasonably well (as shown in Fig. 7.3).

7.2.2.2 Tension-compression model.

In the first SC-SPSW subassembly tests conducted by Winkley [2011], the specimens were observed to have additional energy dissipation upon unloading that was attributed to the web plate residual strength, $V_{web,resid}$, and was not accounted for in the idealized tension-only behavior shown in Fig. 7.6. This web plate residual strength was also observed in conventional SPSW experiments [Berman and Bruneau, 2005] when assumed boundary frame response was removed from the specimen response to approximate the web plate contribution. However, for conventional SPSWs the impact and magnitude of $V_{web,resid}$ is insignificant in comparison with the supplementary strength and energy dissipation provided by the moment-resisting boundary frame.

In SC-SPSWs, where the PT boundary frame offers no energy dissipative qualities and where unloading strengths of the web plates can have an impact on recentering capabilities,

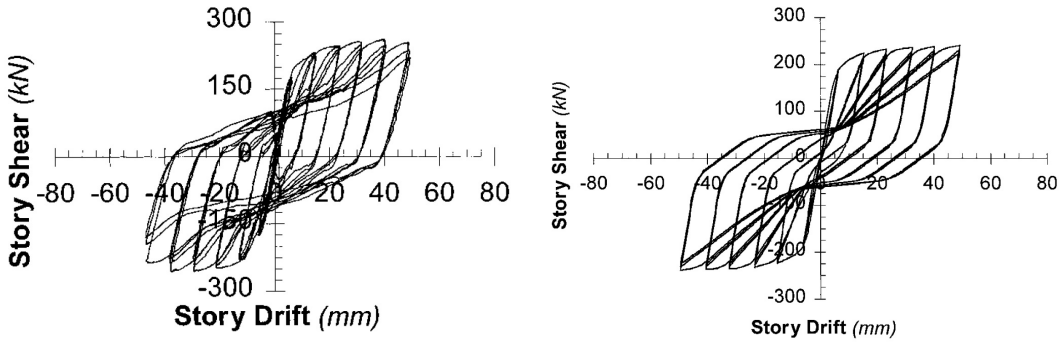

Figure 7.3: (a) Experimental and (b) tension-only strip model numerical response for SPSW specimen [Lubell et al., 2000]

proper modeling of $V_{web,resid}$ is necessary. Previous research [Shishkin et al., 2005] proposed a modified strip model to account for the additional resistance of the "compressive field" in the web plate by including a compression-only diagonal strut with a strength of 8% of the web plate tension yield strength. This 8% compressive strength was calcibrated based on the energy dissipation observed in experimental SPSW tests conducted by and Driver et al. [1998]. However, the results of SC-SPSW testing [Clayton et al., 2012c] show that highr compressive strength values are appropriate.

To simulate the residual strength phenomenon in the current study, a modified strip material was used in which a pinched tension-only material, as described above, and an elastic-perfectly plastic compression-only material were used in parallel. Here, the compression-only material had a compressive strength equivalent to 25% of the web plate tensile yield strength. The value of 25% was selected based on numerical simulations conducted by Webster [2013] in which web plates were modeled with shell elements in a pinned boundary frame to capture the unloading resistance of the buckled web plate. The magnitude of $V_{web,resid}$ (as a proportion of V_y, the web plate yield strength) was investigated for different web plate aspect ratios (panel length over height, L/h) and slenderness ratios (panel height over thickness, h/t) as shown in Fig. 7.4. The h/t vlaues for web plates used in the experimental portion of this study ranged from 740 to 1200 (h/t=740,1200 for 16Ga and 20Ga plates,

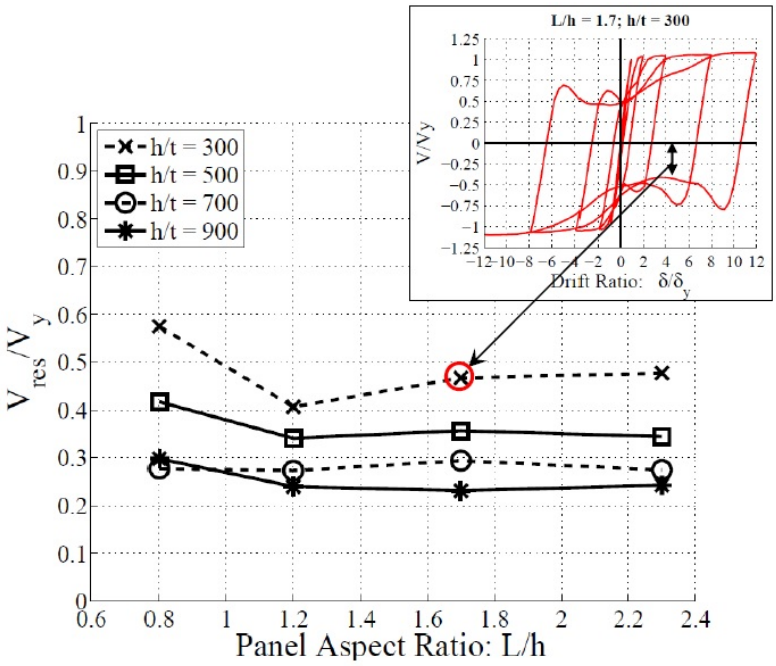

Figure 7.4: Residual strength (V_{res}) normalized by yield strength (V_y) from ABAQUS web plate models [Webster, 2013]

respectively in subassembly tests and h/t=1040,1170 for first and second stories of full-scale specimen,respectively), L/h is approximately 2.4), and the L/h values for these specimens ranged from 0.9 to 2.4 (L/h=2.4 for the subassembly tests and L/h=1.0,0.9 for first and second stories of full-scale specimen,respectively). Web plates with such large slenderness ratios (h/t) tended to have asymptotically approach $V_{web,resid}/V_y$ ratios near 0.25 over a broad range of aspect ratios (L/h). For this reason the compressive strength of 25% fof the yield strength was reasonable for simulating the subassembly and full-scale test specimens.

Since the residual web plate strength phenomenon affects lateral strength during web plate unloading and reformation of the tension field, the strip tensile strength must be reduced by the same 25% such that the peak lateral load resistance of the web plate modeled with strips oriented in both tension field directions is the same as that of the tension-only strip model. The sum of the horizontal components of the strength of the strips simultaneously in tension and compression account for the net web plate lateral reesitance as shown

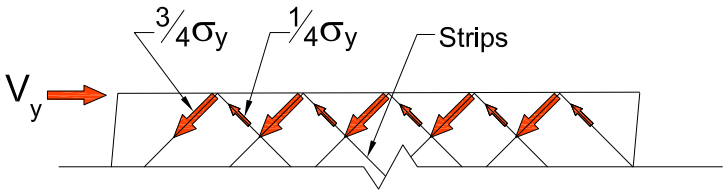

Figure 7.5: Total web plate lateral strength as sum of tension and compression strip resistance

schematically in Fig. 7.5. The cyclic response of the tension-only strip material (Model TO) and the modified tension-compression strip material (Model TC) with compressive strength equal to 25% of the plate material tension yield strength is shown in Fig. 7.6. The yield envelope for each web plate was fit to monotonic tensile tests of coupons taken from each plate, shown for one particular coupon in Fig. 7.6.

It should be noted that the modeled compressive resistance of the web plate strips is constant and is not dependent on material loading history. This tension-compression strip model was developed based on observations made during the subassembly cyclic tests with increasing drift amplitudes where the magnitude of $V_{web,resid}$ appeared to remain constant for each cycle; however, later pseudo-dynamic tests (Chapter 5) provided further insight into web plate residual strength under non-cyclic loading that did not support the constant residual strength assumption. This phenomenon will be discussed in the next material model (Model WP).

7.2.2.3 SPSW web plate model

As previously stated, the research conducted by Webster [2013] found that the web plate residual strength was a function of the web plate aspect and slenderness ratios. From this study, Webster developed a more sophisticated web plate strip material model (Model WP) that determines the web plate residual strength based on various parameters such as web plate geometry.

Similarly, in the pseudo-dynamic full-scale test, it was observed that the magnitude of

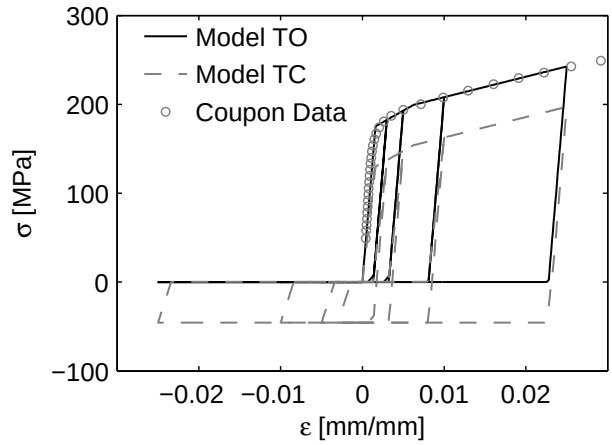

Figure 7.6: Web plate tension-only (Model TO) and tension-compression (Model TC) strip material models fit to monotonic coupon test data

$V_{web,resid}$ decreased during free vibration following the earthquake excitation as the amplitude of oscillation decreased (see Chapter 5). This suggests that the magnitude of the compressive resistance in the strip is dependent on strip load history. This phenomenon was also investigated by Webster [2013] and was incorporated into the new web plate strip material (Model WP) to account for this transient web plate residual strength as well as other aspects of web plate behavior not captured by the TO and TC models. Preliminary results using this new material model are discussed in Sec. 7.4.

Webster [2013] conducted an in depth study of web plate behavior that included experimental tests of web plates in a pinned frame and numerous ABAQUS shell-element models of web plates with a wide range of geometric and material properties and load histories. These experimental and numerical studies were used to characterize web plate behavior. From these results, a mathematical model was developed to represent the uniaxial behavior of a "strip" oriented in the direction of the tension field. When employed in a conventional strip model, this uniaxial material was able to capture complex aspects of web plate behavior. Non-dimensional parameters used to model the uniaxial behavior were based on regressions from the numerical simulations in ABAQUS and tests of web plates in pin-connected frames.

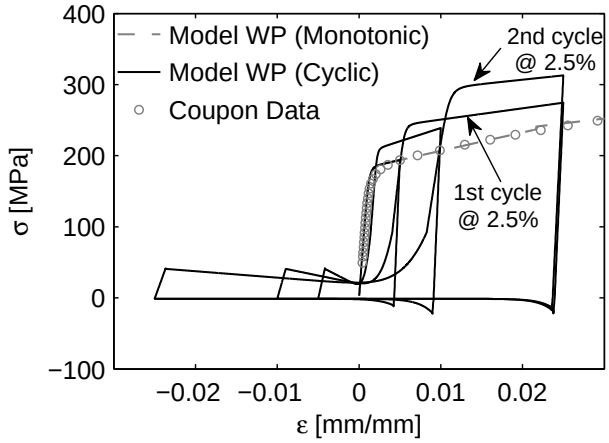

Figure 7.7: SPSW web plate material model (Model WP) under monotonic and cyclic loading fit to coupon data

The new web plate material model developed by Webster [2013] was implemented in OpenSees as the uniaxial material called `SPSW_Web_Plate`. An example of the monotonic and cyclic response of a single strip is shown in Fig. 7.7. In Fig. 7.7, the cyclic loading consists of one cycle each to drift amplitudes of 0.5% and 1%, followed by two cycles to 2.5% (the first and second cycles at this amplitude are denoted in Fig. 7.7). Characteristics of the `SPSW_Web_Plate` material response are described below.

The input values for the `SPSW_Web_Plate` uniaxial material include: the yield stress, σ_y; elastic modulus, E; stress amplification and plastic strain parameters identifying the isotropic hardening envelope; the kinematic hardening modulus (set to zero for all applications in this dissertation); the length, L, and height, h, of the web plate panel (taken as the clear distance between the VBE and HBE inside flanges, respectively); and the thickness of the web plate, t_p [Webster, 2013]. The material model was developed based on in-depth experimental and numerical investigations as previously described. The input parameters for the material hysteresis shown in Fig. 7.7 were based on the monotonic coupon data, plate thickness, and subassembly specimen panel dimensions for one particular web plate sample.

Some of the key response characteristics that are simulated by the `SPSW_Web_Plate`

uniaxial material include (see Webster [2013] for more in-depth descriptions):

- The strip begins reloading in tension at a reloading strain, ϵ_r, that is less than the previous peak plastic strain. The model simulates a curvilinear reloading path, with strength increase initiating at ϵ_r, a strain that is smaller then the previous peak plastic strain. In comparison, the TO and TC models simulate a linear reloading path with strength gain initiating at the peak plastic strain. The reloading strain is determined based on the strip strain history and the web plate slenderness ratio (h/t_p) and aspect ratio (L/h). For example, in Fig. 7.7, the reloading strain for the first cycle of loading at 2.5% is approximately 0.4%, significantly less than the previous peak plastic strain at 1%; the reloading strain for the second cycle of loading at 2.5% is approximately 0.8%, singificantly less than the previous peak plastic strain at 2.5%. This reloading characteristic more accurately captures the web plate energy dissipation and accumlation of plastic strain. It should be noted that if given the same loading protocol, the tension-only material model would have no energy dissipation in the second cycle of loading at 2.5%, and the tension-compression model would only dissipate energy during compressive loading during the second 2.5% strain cycle (as shown in Fig. 7.8).

- The web plate snap-through (F_{ST}), residual (F_{RES}), and tension reloading (F_{TR}) strengths (as indicated schematically in Fig. 7.9) are determined based on web plate slenderness ratio (h/t_p), aspect ratio (L/h), and elastic modulus to yield strength ratio (E/σ_y). The magnitude of F_{ST} also increases with increasing magnitude of the previous drift range (i.e. the difference between the minimum and maximum strain in the previous loading cycle) and decreases with increasing accumulated plastic strain from the entire web plate loading history. The F_{RES} and F_{TR} quantities are, in effect, a more accurate representation of the "compressive strength" in the tension-compression material model (Model TC) described previously that takes into account various parameters to determine the appropriate unloading and reloading strength magnitudes. The unloading and reloading response (e.g. snap-through and residual strength) of Model WP was calibrated to match web plate material tests and numerical

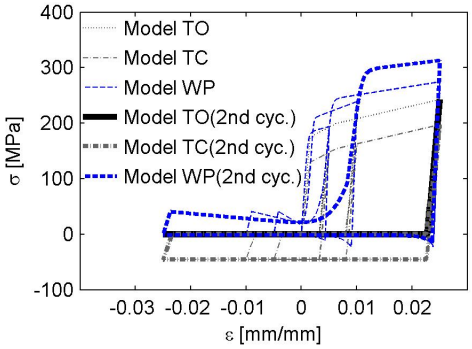

Figure 7.8: Comparison of Models TO, TC, and WP strip response during repeated cycle of loading

models [Webster, 2013].

- The yield surface and hardening rules of this material more accurately account for the plastic strain accumulation associated with plastic contraction and tensile yielding in the direction perpendicular to the tension field. Specifically, tensile strain along the length of the strip is assumed to be accompanied by compressive strain perpendicular to the strip axis, and the accumulated plastic strain in a strip is assumed to include the plastic strain accumulated during tensile loading in the opposite direction. Both are used to determine strength gain due to isotropic and kinematic hardening. For the purposes of this research, where the material hardening characteristic were unknown, the kinematic hardening parameters were assumed to be zero. The results of the modified hardening rules can be seen in Fig. 7.7, where the tension strength developed under cyclic loading exceeds that developed under monotonic loading; this is due to the plastic strain accumulation during cyclic loading and unloading.

7.2.3 Comparison of global response

Fig. 7.10 shows a comparison of the experimental and numerical model force vs. drift responses for specimen W14-8s100k20Ga and is representative of typical subassembly specimens. Fig. 7.11 shows similar force vs. drift response of the full-scale specimen and nu-

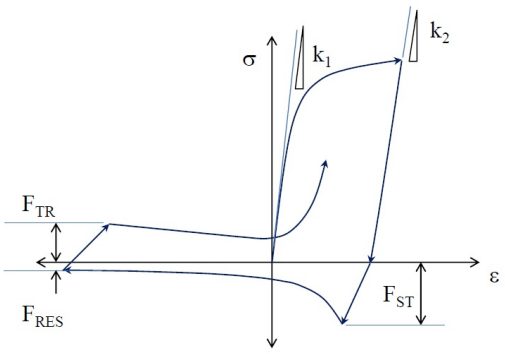

Figure 7.9: F_{TR}, F_{RES}, and F_{ST} in SPSW web plate uniaxial material (Model WP) hysteresis [Webster, 2013]

merical model. Figs. 7.10(a) and 7.11(a) show the numerical results from the model with the tension-only (TO) strips, Figs. 7.10(b) and 7.11(b) show the numerical results for the modified tension-compression (TC) strip model with compressive strength equal to 25% of the web plate yield strength. Note that the preliminary results for Model WP are shown later in Sec. 7.4.

Because the hysteretic behavior of Models TO and TC are dependent only on the previous peak strain, the subassembly test numerical models were subjected to cycles at 1.5% and 2% drift only to more clearly show characteristics of the response envelope (e.g. the 1.5% cycle represents the envelope response of the cycles prior to 2% drift) and the unloading and reloading behavior for a cycle prior to significant web plate tearing (e.g. 2% cycle). The 2% drift cycles (for the numerical models and the experiment) are shown in solid lines for better comparison of a single cycle response.

Because the full-scale specimen was loaded pseudo-dymaically, there was not a specific cycle of loading at ±2%; therefore, the TO and TC models in Figs. 7.11 and 7.12 were subjected to the full displacement history of the specimen during the 10/50 test. For illustration of single cycle response, Fig. 7.11 shows the "cycle" containing the maximum and minimum drift deamnds (+1.94% and -1.97%) as a solid line for comparison of response during larger cycles of loading. The portion of the displacement history included in this "2% cycle" is shown in Fig. 7.11(c). The same potion of the displacement history is used to represent the

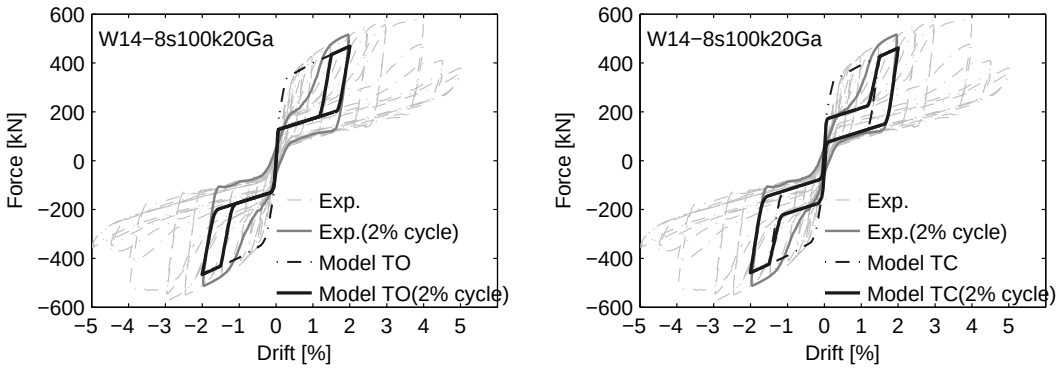

Figure 7.10: Comparison of specimen W14-8s100k20Ga response with (a) tension-only (Model TO) and (b) tension-compression (Model TC) strip model responses

"2% cycle" in figures showing component-level responses later in this chapter. Similarly, to demonstrate Model TO and TC response during free vibration (Figs. 7.12(a) and 7.12(b), repsectively), only the portion of the numerical response during the free vibration portion of the drift history (shown in Fig. 7.12(c)) is shown in comparison with the experimental free vibration response.

7.2.3.1 Initial stiffness

The TO and TC strip numerical models overestimate the initial stiffness as can be observed in Fig. 7.10. Table 7.1 provides the ratio of simulated to observed initial stiffnesses for the TO model. The average $K_{i,TO}/K_{i,exp}$ ratio for all the subassembly specimens is 2.96 (2.50 for specimens with web plates and 4.64 for specimens without web plates) with a coefficient of variation (standard deviation divide by mean) of 0.38 (0.24 for specimens with web plates and 0.25 for specimens without web plates). This overestimation of initial stiffness is likely due to the numerical assumption that the PT connections have a stiffness equivalent to a welded connection prior to decompression [Clayton et al., 2012c; Garlock et al., 2007]; however, the actual connections have uneven bearing surfaces at the HBE flanges

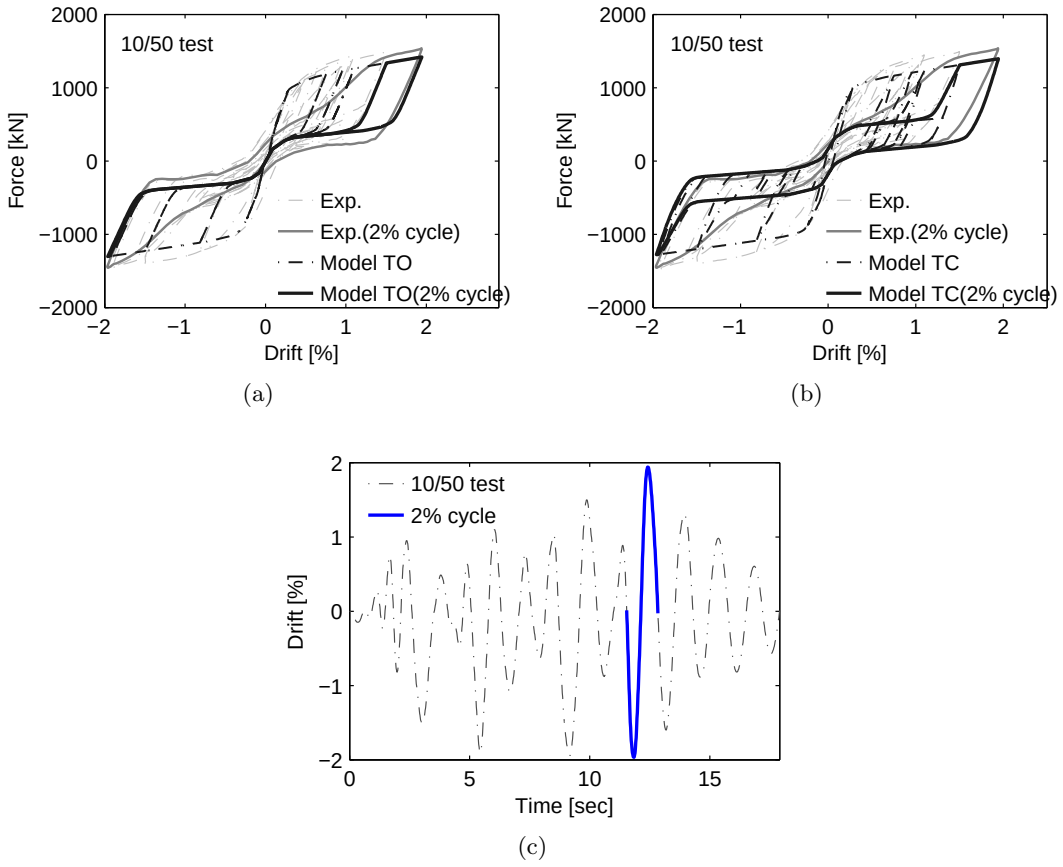

Figure 7.11: Comparison of 10/50 test response with (a) tension-only (Model TO) and (b) tension-compression (Model TC) strip model responses during the (c) 2% cycle

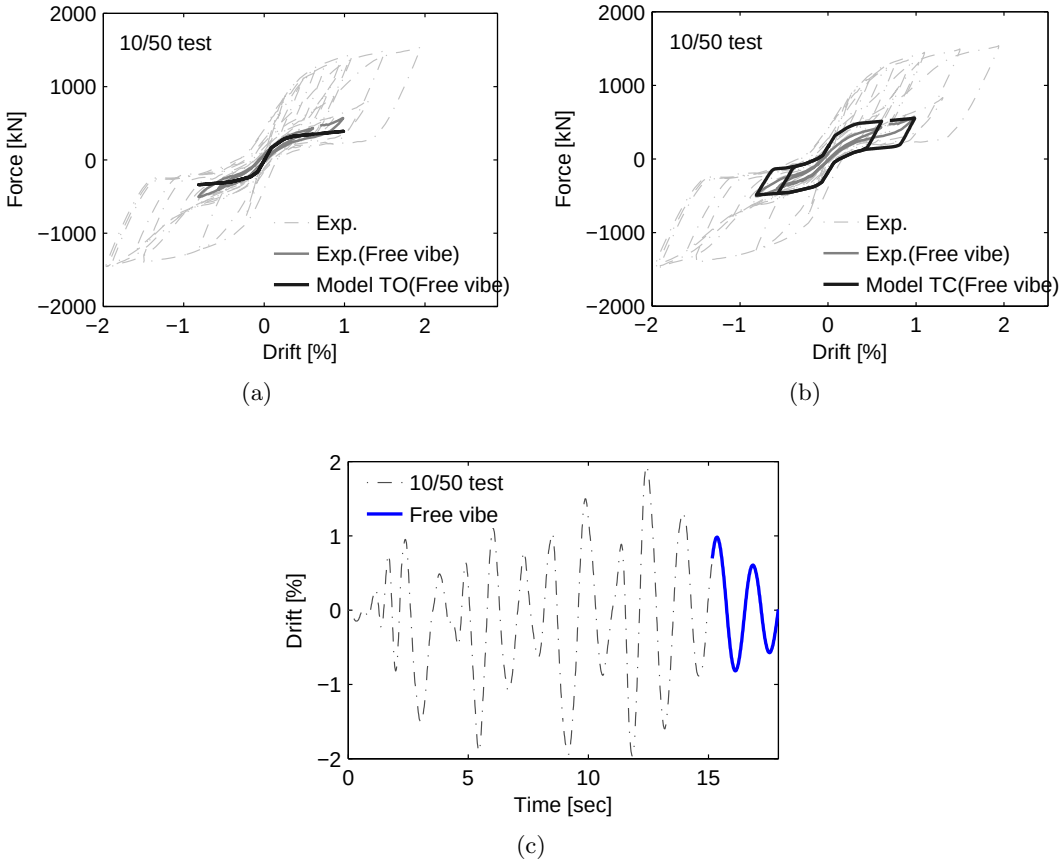

Figure 7.12: Comparison of 10/50 test response with (a) tension-only (Model TO) and (b) tension-compression (Model TC) strip model responses during (c) free vibration

due to construction tolerances[2], allowing for some connection rotation prior to reaching the decompression moment, M_d. It should be noted that due to the uneven bearing surfaces observed in the subassembly tests, the full-scale specimen used flange bearing plates at the ends of the beams to provide an even bearing surface which reduced the effects of this problem. This flange bearing plate detail, along with specification of fabrication tolerances, is recommended in Chapter 9 to ensure sufficient initial stiffness. Therefore, modeling the connections as idealized, evenly bearing, connections in the full SC-SPSW models in Chapter 8 is appropriate.

Table 7.1: Initial and recentering stiffnesses of OpenSees models (Model TO)[‡] of specimens compared with experimental results

Specimen	$K_{i,TO}$ (kN/mm)	$K_{r,TO}$ (kN/mm)	$K_{i,TO}/K_{i,exp}$	$K_{r,TO}/K_{r,exp}$
W18-8s100k	85.5	2.04	3.38	0.87
W18-8s100k20Ga	96.4	2.04	2.14	0.98
W18-6s75k20Ga	97.3	1.55	2.38	0.94
W18-6s75k16Ga	110.7	1.655	2.25	1.04
W18-8s100k16Ga	105.7	2.04	1.84	1.07
W18-6s75k	85.9	1.55	4.97	1.01
W18-8s100k20Ga-2	96.4	2.04	2.76	1.08
W18-8s100k16Ga20Ga	103.6	2.04	2.41	1.14
W18-8s100k20GaW	96.4	2.04	2.00	1.11
W14-6s75k	53.0	0.87	5.58	1.09
W14-8s100k16Ga	67.9	1.15	2.18	1.17
W14-8s100k16GaHBE	67.9	1.15	3.97	1.31
W14-8s100k20Ga	60.9	1.15	2.61	1.19
W14-6s75k20Ga	62.2	0.87	3.00	1.10
FR	55.5	1.40	1.10*	1.00+

‡ Because the initial and recentering stiffnesses for each of these models are, by design, not significantly different, Model TO is shown here for comparison.
* $K_{i,exp}$ is taken from the elastic cyclic test.
+ $K_{r,exp}$ is taken from the 2/50 PSD test where the linear recentering stiffness region was better pronounced.

[2]The uneven flange bearing surfaces is more pronounced in the subassembly tests, and particularly in the W14 subassembly specimens as can be observed in the $K_{i,TO}/K_{i,exp}$ values in Table 7.1. Due to the uneven bearing surfaces observed in the subassembly tests, the full-scale specimen used flange bearing plates at the ends of the beams which reduced the effects of this problem.

It is also worth noting that if one were to account for the presence of initially decompressed connections in the subassembly specimens, the initial analytical stiffness reduces significantly. To demonstrate this, a simple model of the subassembly specimens was constructed to simulate the initial stiffness of each connections (Fig. 7.13). For this purpose, beam-to-column connections that were assumed to be fully compressed with even bearing surfaces were simulated as rigid connections, while connections that were assumed to be initially decompressed (due to uneven bearing surfaces or misaligned beams) were simulated with a rotation spring with a stiffness equal to the decompressed connection stiffness, k_d^θ, as given in Eqn. 2.7.

Three different boundary frame models were assumed to represent a range of possible initial configurations. From observations and data analysis, it is clear that the middle HBE had initially decompressed connections (most notably and visually evident at the top flange of the south end of the HBE, although also present to a lesser extent on the north end of the middle HBE). This scenario was simulated as shown in Fig. 7.13(a). Although visual observations of initial decompression were not made at other locations during the test, the θ_r vs. drift response at the north end of the bottom beam (shown for W18-8s100k16Ga in Fig. 7.14 but typical for other subassembly specimens) suggest that when initially loaded from zero drift, the connection almost immediately becomes decompressed as indicated by the increase in θ_r (compare this to an idealized PT connection behavior with near zero θ_r at small drifts when the connection should remain closed). Based on this observation, it is possible that during initial small cycles, this connection may also have a stiffness equivalent to a decompressed connection; therefore, another boundary frame model as shown in Fig. 7.13(b) was used to assess this initial stiffness condition. Finally, a (Fig. 7.13(c)) frame model representing the worst-case scenario where all PT connections were initially decompressed was considered.

Each of these frame models were used with appropriate web plate TO strip models to assess the range of initial stiffnesses in each specimen due to non-idealized PT connection initial configuration. The initial stiffnesses determined from these models are given in Table 7.2 and are compared to the observed experimental initial stiffness. In this table, the three boundary frame models (Fig. 7.13(a), (b), and (c), respectively) are referred to as the

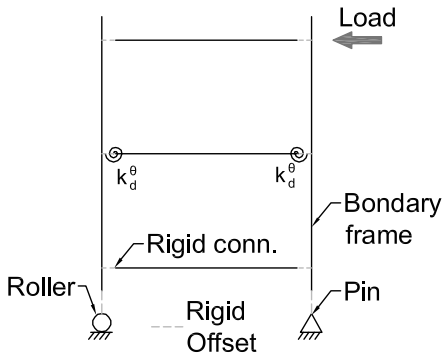

(a) Middle HBE connections decompressed

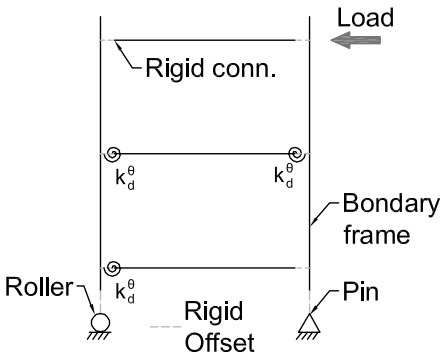

(b) Three connections decompressed

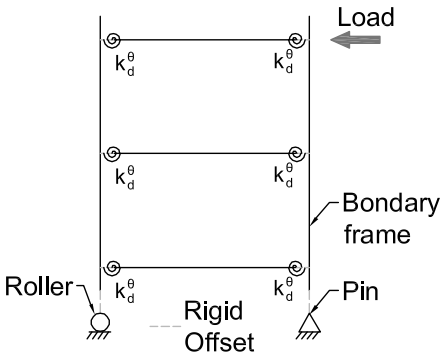

(c) All connections decompressed

Figure 7.13: Boundary frame models to estimate initial stiffness with non-idealized initial PT connection stiffness (Web plate strips not shown for clarity).

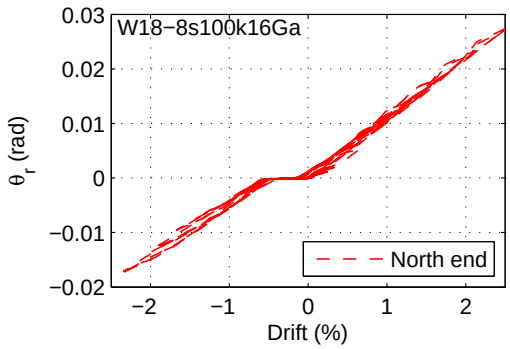

Figure 7.14: Typical gap rotation vs. drift response north end of bottom beam (shown for W18-8s100k16Ga).

"2 conn. decomp.", "3 conn. decomp.", and "All conn. decomp." models, representing the number of initially decompressed connections. Table 7.2 shows that the boundary frame models with two or three connections assumed to be initially decompressed (as supported by visual observation and data analysis) do a better job of matching the initial stiffness of the specimen.

As noted in the table, the web plate numerical model (i.e. tension strips oriented in the tension field direction) may not be particularly suitable for comparing to the measured initial stiffness in W14-8s100k16GaHBE. In this specimen, because the web plate was unsupported along the vertical edges, there was much more initial sag in the web plate due to installation in the horizontal configuration (i.e. with the self-weight of the plate acting perpendicular to the pane of the frame) compared to other specimens; therefore, the tension field was developed at larger drifts than other specimens.

These supplemental boundary frame models demonstrate that imperfections in the initial bearing configuration of the PT connection (due to fabrication tolerances) are likely the cause for the discrepancy between experimental and numerical initial stiffnesses using the idealized PT boundary frame model; however, because these supplemental boundary frame models are only representative of initial conditions (i.e. they do not contain rocking PT connections to represent cyclic behavior), the results of numerical models employing the traditional PT connection boundary frame model presented in Fig. 7.1(d) will be used in

the following sections. Also, as previously stated, detailing recommendations that were employed in the full-scale test appear to alleviate these initial imperfections, making the traditional PT connection model appropriate for use in modeling of SC-SPSW with these improved details.

Table 7.2: Initial stiffnesses of OpenSees models (Model TO) of specimens assuming non-idealized initial PT connection response compared with experimental results

	2 conn. decomp.		3 conn. decomp.		All conn. decomp.	
Specimen	$K_{i,TO}$ (kN/mm)	$\frac{K_{i,TO}}{K_{i,exp}}$	$K_{i,TO}$ (kN/mm)	$\frac{K_{i,TO}}{K_{i,exp}}$	$K_{i,TO}$ (kN/mm)	$\frac{K_{i,TO}}{K_{i,exp}}$
W18-8s100k	36.7	1.45	22.2	0.88	2.04	0.08
W18-8s100k20Ga	47.6	1.06	33.1	0.73	12.9	0.29
W18-6s75k20Ga	48.1	1.18	33.6	0.83	13.0	0.32
W18-6s75k16Ga	61.5	1.25	47.0	0.96	26.3	0.54
W18-8s100k16Ga	56.9	0.99	42.4	0.74	22.2	0.39
W18-6s75k	36.7	2.12	22.2	1.28	1.55	0.09
W18-8s100k20Ga-2	47.6	1.36	33.1	0.95	12.9	0.37
W18-8s100k16Ga20Ga	54.8	1.28	40.3	0.94	20.1	0.47
W18-8s100k20GaW	47.6	0.99	33.1	0.69	12.9	0.27
W14-6s75k	26.7	2.81	15.4	1.63	0.87	0.09
W14-8s100k16Ga	41.9	1.35	30.3	0.98	16.1	0.52
W14-8s100k16GaHBE*	41.9	2.45	30.3	1.77	16.1	0.94
W14-8s100k20Ga	34.9	1.50	23.3	1.00	9.05	0.39
W14-6s75k20Ga	35.9	1.73	24.6	1.19	10.1	0.49

* In this test, the web plate did have significant initial sag as it was not supported along the vertical edges. The initial sag likely results in a lower initial stiffness than is assumed in the numerical model which assumes immediate development of the tensdion field in the web plate.

7.2.3.2 Response envelopes

Models TO and TC have similar response envelopes that accurately simulate initial web plate yielding but underestimate strain hardening as drift demand increases. This underestimation of peak strength is present in the subassembly and full-scale specimen models.

The underestimation of strain hardening is due to the continuum nature of the web plate not simulated in the strip model—as the web plate yields in the tension field direction plastic

strain is accumulated in the tension field direction for a unit area of the plate to yield. As the web plate is loaded in the opposite direction, that same unit area of plate yields in the opposite tension field direction, such that the total accumulated plastic strain in the plate is related to the tensile plastic strain incurred in both directions of loading[3] [Webster, 2013]. This accumulation of plastic strain in both directions of loading increases the rate of strain hardening compared with the traditional strip model. Depending on the experimental drift history, the true accumulated plastic strain can be up to four times that computed using the strip model [Webster, 2013]. Depending on the hardening properties of the web plate material (e.g. isotropic, kinematic, or a combination of both) and the load history, this increase in plastic strain accumulation can result in tensile stresses typically around 20-30% higher than the stress assumed in a traditional strip model [Webster, 2013]. This difference corresponds to the magnitude by which the TO and TC strip models underestimate the web plate strength as shown in Fig. 7.10; for example, in Fig. 7.10(a) the web plate strength at 2% drift (taken as the peak strength minus the strength of the PT frame at 2% drift) for the actual web plate is approximately 22% larger than the the tension-only model web plate strength.

The TO and TC strip model underestimation of web plate strength was typical in subassembly specimens with bolted web plate-to-fish plate connections in which tearing was initiated after 2% drift (see Appendix C) and in the full-scale specimen where web plate tearing was not significant during the 10/50 test. In the subassembly specimen with welded web plate connections (W18-8s100k20GaW) where tearing was observed prior to reaching 2% drift, the strip model overestimation is not apparent. Although these current strip modeling methods (i.e. Models TO and TC) are conservative in predicting web plate srength (i.e. underestimate actual strength), these methods may be unconservative when estimating peak web plate demands for capacity design of the boundary frame members.

[3]There is additional plastic strain accumulation in the plate due to normal plastic contraction (NPC) of the plate due to Poisson's effect; however, the tensile plastic strain accumulated during reverse loading has a larger impact on the rate of strain hardening [Webster, 2013].

7.2.3.3 Recentering stiffness

The TO and TC strip models simulate well observed unloading stiffness (K_r). Table 7.1 provides the recentering stiffness of Model TO for each specimen model, $K_{r,TO}$, and compares it with the experimentally determined $K_{r,exp}$ from Chapter 6 and shown in Fig. 6.18. The stiffness results for Models TO and TC are very similar since the various material models account primarily for the web plate unloading strength and each have negligible web plate stiffnesses following unloading. The average $K_{r,TO}/K_{r,exp}$ ratio for all the subassembly specimens is 1.08 with a coefficient of variation (standard deviation divide by mean) of 0.10.

7.2.3.4 Cyclic history

By intent, each of the strip models have different strengths during unloading (and subsequent reloading in the next cycle) due to the hysteretic behavior of the material models. The unloading and subsequent reloading of the tension-only model (Model TO) follow the same path (i.e. same strengths for a given drift demand as shown in Figs. 7.10(a) and 7.11(a)). However, for the tension-compression model (Model TC), the unloading strength is less than that of the tension-only model and the reloading strength is greater; this is consistent with experimental data. This results in the TC model simulating significantly more energy dissipation than the TO model (as shown in Figs. 7.10(b) and 7.11(b)). The data in Figs. 7.10(b) and 7.11(b) show that Model TC somewhat underestimates observed strength gain upon reloading; thus the TC model does slightly underestimate observed energy dissipation.

The unloading strength of Model TC is similar to that of the experimental specimen when unloading from a peak drift (with a residual strength approximately 25% of the tension field strength) as shown in Fig. 7.11(b). However, when the full-scale specimen oscillates during free vibration following the peak drift, the magnitude of the web plate residual strength decreases; this is not simulated in Model TC as shown in Fig. 7.12(b).For this phase of the displacement history, the tension-only strip model (Model TO) is able to better approximate the specimen unloading strength during smaller cycles of loading after significant web plate

yielding (i.e. during free vibration) as shown in Fig. 7.12(a). Thus, the TC model is suitable for estimating the effect of the web plate residual strength under cyclic loading of increasing drift amplitudes and conservatively estimates residual drift during oscillation decay (i.e. free vibration).

While the web plate strip material model (Model WP) developed by Webster [2013] is able to better simulate this complex web plate behavior (preliminary results discussed in Sec. 7.4), when comparing the TO and TC model, Model TC is better at capturing the cyclic response. Additionally, Model TC provides a conservative underestimation of energy dissipation and stiffness during web plate reloading and provides a conservative overestimation of residual drift during free vibration.

7.2.3.5 Strength loss

The experimental response in Fig. 7.10 also shows that the reloading strength of the specimen decreases as the extent of web plate tearing increases at large drifts. At the 5% drift cycles where the web plate was torn completely along the VBEs and along the majority of the HBEs, the reloading strength approaches that of the tension-only model (Fig. 7.10(a)). Due to the considerable web plate tearing along the boundary elements, the tension field cannot developed during reloading, which is representative of the tension-only strips that cannot resist additional load until reaching the peak plastic strain from previous cycles. However, in these cycles after significant tearing the specimen unloads with a lower strength, closer to the unloading curve of the tension-compression model. This behavior indicates that although the tension field cannot develop to resist lateral load during reloading, the severely damaged web plate still provides some resistance, and thus energy dissipation, upon unloading. This unloading resistance is attributed to the work required to return the hardened, deformed web plate to zero-displacement, indicating that web plate resdiual strength is related to the full web plate stiffness and not the development of the tension field.

7.2.3.6 HBE-only web plate simulation

Fig. 7.15 shows a comparison between the experimental and numerical response for W14-8s100k16GaHBE, where the web plate is connected only to the HBEs, with tension-compression strips. As was the case for the specimens with web plates connected to HBEs and VBEs, the TO and TC strip models underestimate strain hardening and the response envelope in the specimen for reasons previously described, and the strip model simulates well the reloading strength of the web plate while the TO model underestimates the reloading strength. However, while the TC model provides reasonably accurate simulation of unloading/residual strength for SC-SPSWs with plates connected to the HBEs and VBEs, for HBE-only connected web plates the TC model under-predicts the unloading/residual strength. If the web plate residual strength is taken as the difference between the unloading strength and the simulate bare PT frame strength, Model TC predicts a web plate residual strength that is 54% of the experimental web plate residual strength. This is attributed to the fact that the model does not account for the additional unloading resistance provided by the portions of the web plate not included in the partial tension field model. This observation is consistent with the theory that the web plate residual strength is a function of the entire web plate geometric stiffness as described previously. The tension-compression strip model (Fig. 7.2), which only models the portion of the web plate contributing to the tension field, is able to accurately capture the peak and reloading strengths that depend on tension field action. For the current study, the roughly 50% error in simulated web plate residual strength (which is still only a portion of the total lateral strength) is deemed acceptable for investigating behavior of HBE-only connected SC-SPSWs.

7.2.4 Comparison of boundary element demands

The previous section compared experimental and numerical strip model global response, while this section investigates boundary element demands. In order to assess the adequacy of proposed boundary frame design methodologies, the numerical models should be able to accurately and conservatively approximate boundary frame demands. Based on the global response comparisons presented previously, Model TC appears to more accurately represent

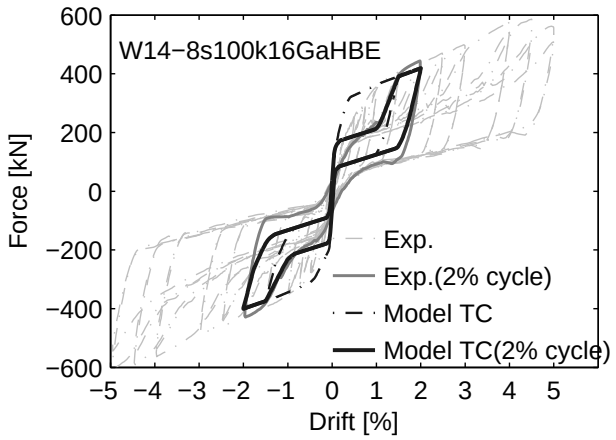

Figure 7.15: Comparison of specimen W14-8s100k16GaHBE response and numerical model with tension-compression (Model TC) strips

web plate behavior compared to Model TO. For this reason, the following results discussing component demands will be shown for Model TC. Additional plots for Model TO are shown in for the subassembly tests in Appendix C and for the full-scale test in Appendix D.

7.2.4.1 Subassembly tests

One of the purposes of the subassembly tests was to assess the middle HBE (representing intermediate HBE) demands; thus, the HBEs were heavily instrumented with strain gages to enable the estimation of the axial force and moment demands (Figs. 4.7 through 4.10). Fig. 7.16 compares the moment distribution as computed using analytical formulas derived in Clayton [2010], from the numerical model, and from experimental strain gage data (shown here for specimens W18-8s100k20Ga-2 and W14-8s100k20Ga at 2% drift). The linear shape of the moment distribution in Fig. 7.16 is due to fact that the web plate distributed force above and below the middle HBE are approximately the same. In the case where web plate thicknesses and story shears above and below an HBE are unequal, the moment distribution will have a parabolic shape as illustrated in Clayton [2010]. The experimentally determined moments are derived using the curvature calculated from a linear regression of the strain gage data at a given location along the HBE length, the elastic modulus of steel

(200 GPa), and nominal cross-sectional moments of inertia of the beam. The moments calculated analytically per Clayton [2010] and Dowden et al. [2012] assumed a constant web plate stress distribution based on the web plate tension yield strength oriented at an angle, α, of 45 degrees. Additional comparisons of the experimental and numerical global and component responses for the subassembly specimens can be found in Appendix C.

The data in Fig. 7.16 shows that the analytical and simulated moment distribution match well with the OpenSees numerical model. When the 25% compressive strength is included in the numerical strip material model (Model TC), the magnitude of the peak moments reduces by approximatly 5% compared to the tension-only; thus, the web plate material model (Model TO vs. Model TC) does not appear to have a significant impact on moment distributions. The jumps in the simulated (e.g Model TC) moment distribution is due to the strip being rigidly offset from the HBE element, resulting in a conentrated moment on the beam at each strip connection; these jumps in moment are not present in the real HBE where web plate forces are continuously distributed.

Some variation between the analytical, OpenSees simulated, and experimental HBE moment distributions may be due to differences in the assumed and actual tension field inclination and stress distribution, web plate strain hardening and PT losses, difference in axial load during positive and negative excursions due to actuator loading on one column (instead of symmetric loading on both columns as assumed in the analytical derivations), and inherent uncertainty in deriving moments from very small strain measurements. In general, the experimental moments calculated from strain gages followed similar trends and had similar magnitudes as the numerical and analytical approximations, demonstrating that the design formulas and modeling methods presented previously in Clayton [2010] adequately predict the HBE demands.

7.2.4.2 Full-scale test

The full-scale specimen also had strain gage sections along the boundary frame members to enable calculation of axial force and moment demands (Fig. 5.13 shows strain gage locations). The axial force and moment demand response histories at these locations along the

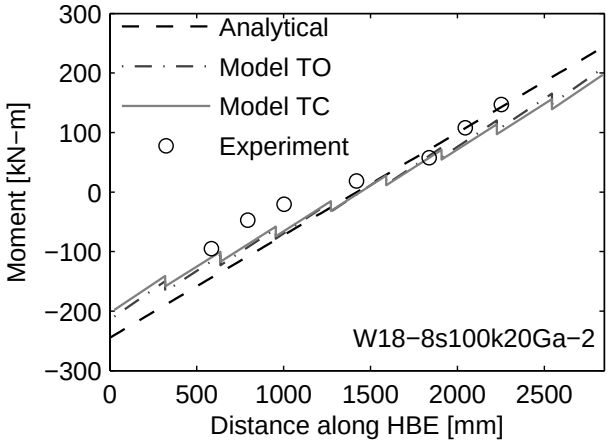

(a)

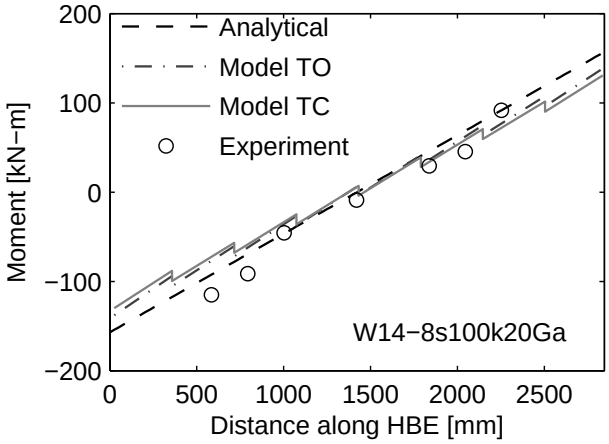

(b)

Figure 7.16: Moment distribution at 2% drift for specimens (a) W18-8s100k20Ga-2 and (b) W14-8s100k20Ga

beam members are compared with those from the OpenSees numerical model in Figs. 7.17 and 7.18, respectively. Numerical results are shown for Model TC in this chapter and for Model TO in Appendix D. These figures show the results for the entire displacement history (aa shown by the dashed lines), with the 2% cycle (as shown in Fig. 7.11(c)) shown with solid lines as was done in Fig. 7.11. In general, the shape and magnitudes of the experimentally determined axial and moment demand histories correspond well to those of the OpenSees model. The OpenSees TC model is able to reasonably approximate peak demands, reloading and unloading shapes, and residual demands at zero-drift. Differences between the measured and simulated responses are likely due to assumptions that were used to calculate experimental demands from strain gage data (Sec. 6.4.5). For example, the BB was assumed to have zero moment at the beginning of the test; however, the BB likely had an initial possitive moment due to the PT forces at the MB and TB pulling the columns toward the center of the SC-SPSW. If it was possible to compute this initial positive moment, then the experimental BB moment demands (Fig. 7.18(e)) would be offset from zero at zero-drift and would match the numerical results more closely.

Two strain gage sections were also placed within the height of the first story of the columns to measure axial and moment demands (see Fig. 5.13 for strain gage locations). The axial and moment demand vs. drift responses are shown for these discrete locations along the columns in Figs. 7.19 and 7.20, respectively; data is presented as was done for the beams. The OpenSees numerical model is able to adequately capture the column axial and moment response histories and magnitudes. For most of the locations, the peak axial or moment demands are approximately the same as or slightly (and conservatively) larger than the experimental demands calculated from strain gage data, suggesting that the OpenSees strip model is sufficient for estimating beam and column demands in design. The primary discrepancy between the numerical model and experimental results is the TC model's inability to capture the complex web plate reloading response (e.g. the web plate resisting load prior to the previous peak plastic strain).

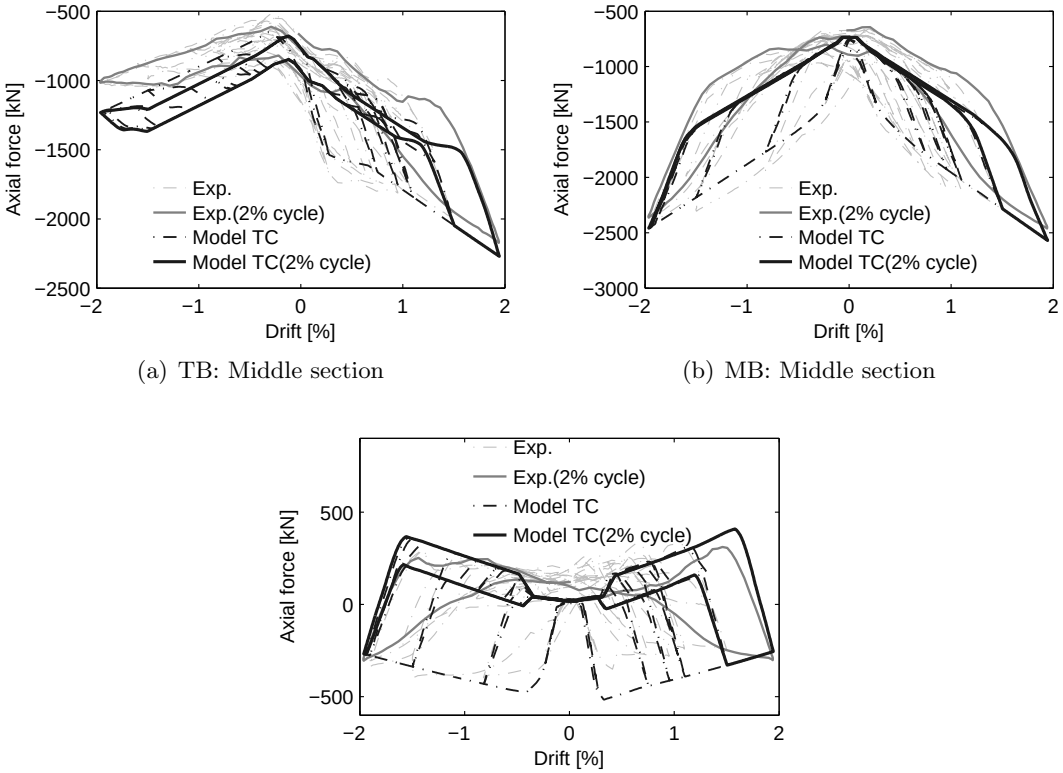

(a) TB: Middle section

(b) MB: Middle section

(c) BB: Middle section

Figure 7.17: Comparison of experimental (10/50) and numerical (Model TC) axial force vs. drift demands for certain locations in full-scale specimen beams

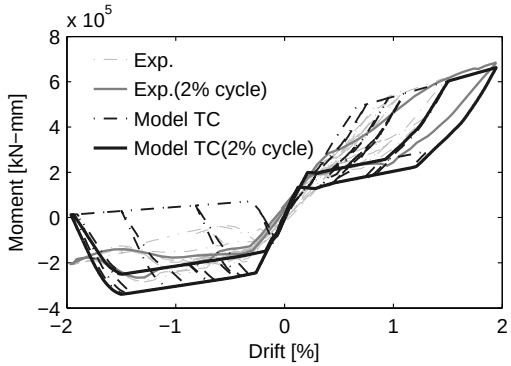

(a) TB: West section

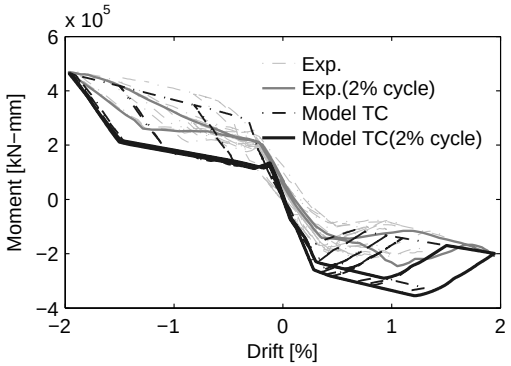

(b) TB: East section

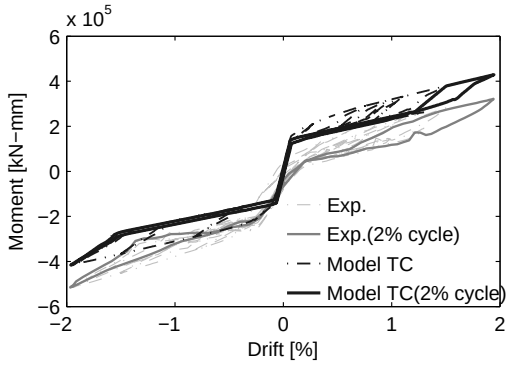

(c) MB: West section

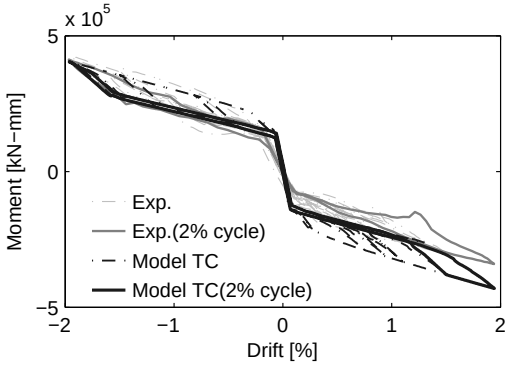

(d) MB: East section

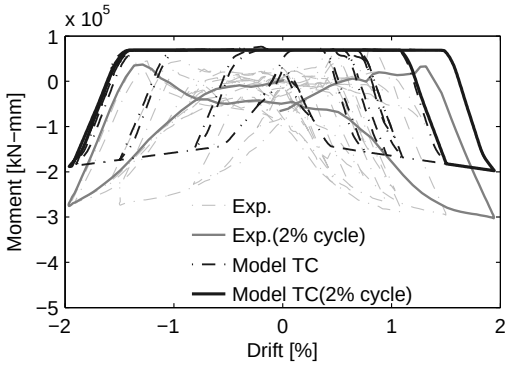

(e) BB: Middle section

Figure 7.18: Comparison of experimental (10/50) and numerical (Model TC) moment vs. drift demands for certain locations in full-scale specimen beams

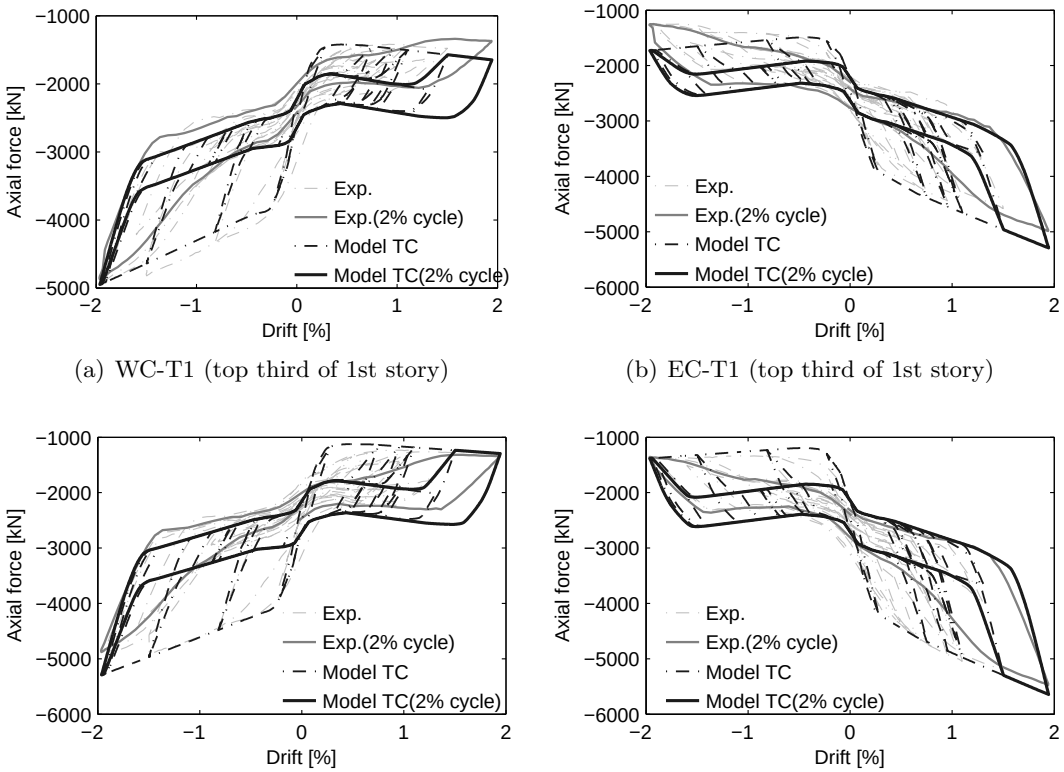

(a) WC-T1 (top third of 1st story)

(b) EC-T1 (top third of 1st story)

(c) WC-B1 (bottom third of 1st story)

(d) EC-B1 (bottom third of 1st story)

Figure 7.19: Comparison of experimental (10/50) and numerical (Model TC) axial force vs. drift demands for certain locations in full-scale specimen columns

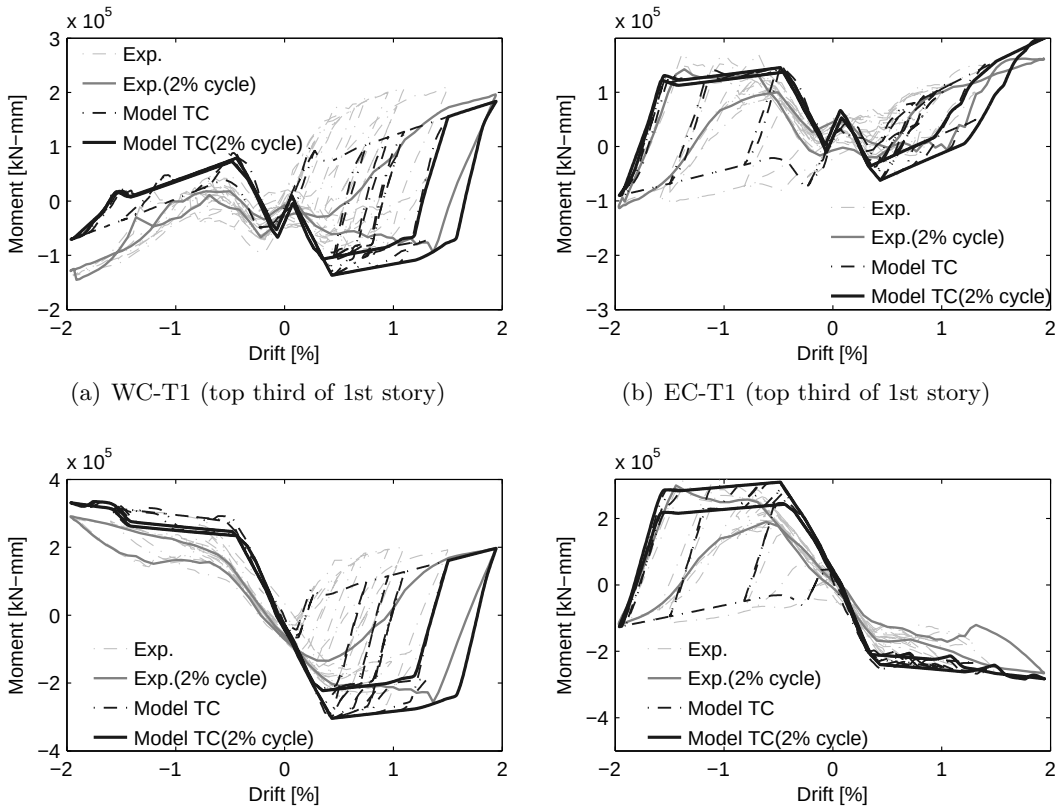

(a) WC-T1 (top third of 1st story)

(b) EC-T1 (top third of 1st story)

(c) WC-B1 (bottom third of 1st story)

(d) EC-B1 (bottom third of 1st story)

Figure 7.20: Comparison of experimental (10/50) and numerical (Model TC) moment vs. drift demands for certain locations in full-scale specimen columns

7.2.5 Comparison of PT and connection responses

7.2.5.1 Subassembly tests

The PT connection response is characterized by the HBE moment at the connection vs. relative rotation in the decompressed connection, θ_r. Although the moment at the connection cannot be measured directly in the experiment, it can be estimated using simplifying assumptions. Specifically, the moment at the connection can be estimated as the average axial force calculated from strain gage data times half the beam depth, $d/2$ [Clayton, 2010; Dowden et al., 2012] if (1) the web plate stress distribution along the HBE is assumed to be constant, (2) the web plates above and below the HBE have similar thicknesses and yield strengths, as is the case for all of the subassembly specimens except W18-8s100k16Ga20Ga, and (3) the HBE is assumed to rock about the outside edge of its flanges. The connection rotation is calculated directly from displacement potentiometers located on each flange at the ends of the HBE. In Fig. 7.21, the experimentally estimated connection response is compared with the numerical connection response for W18-6s75k16Ga at the south end of the middle HBE during the 2% cycle. The estimated experimental response matches well with relative magnitudes and hysteretic trends of the numerical connection response. The presence of a hystertic loop in the experimental connection moment vs. rotation response at small rotations is also observed in the Model TC response (and not the Model TO response), suggesting that Model TC provides a more appropriate approximation of connection response.

Fig. C.5(a) shows the PT force vs. drift response for the middle HBE during the 2% cycle. Note that the web plate strip model (Model TO vs. Model TC) does not have a significant impact on PT force response. The numerical model shows similar loading and unloading paths and loops compared with the experimental PT force. The model also slightly overestimates the observed PT response. Possible reasons for this overprediction include the rocking depth assumed in the model and not accounting for flexibility or seating in PT anchorage. Further disscussion of PT force response will be discussed in the following section regarding the full-scale test specimen PT force response. Additional PT force vs. drift and connection moment vs. rotation data are provided for all the subassembly specimens

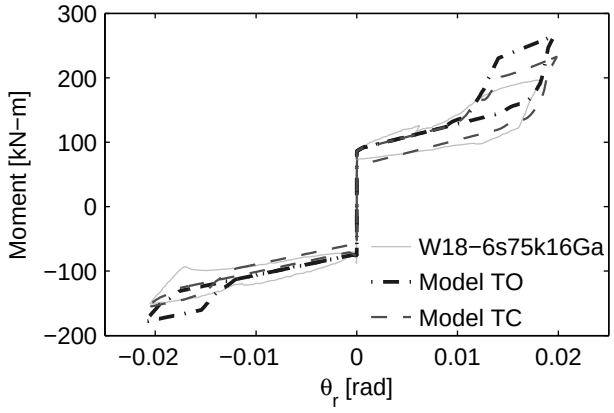

Figure 7.21: Comparison of experimental and numerical PT connection response during 2% cycle

in Appendix C.

7.2.5.2 Full-scale test

Figs. 7.23 and 7.24, respectively, show the PT force vs. roof drift, gap rotation vs. roof drift, and PT force vs. gap rotation responses for the PT beam-to-column connections and the PT column base connections of the full-scale test specimen. In each of these figures, the results from Model TC are shown; however, similar results for Model TO are shown in Appendix D. As was done for the subassembly data, the 10/50 PSD experimental and numerical results are shown for the full displacement history with dashed lines, and the 2% drift "cycle" is shown as a solid line for easier comparison. For the MB and TB PT force vs. gap rotation response (Figs. 7.23(e) and 7.23(f), respectively), the average gap rotation (from the west and east connections) is shown. Figs. 7.23(c) and 7.23(d) also show the gap rotation from both the east and west connections for the MB and TB, respectively. For clarity in only these figures, the full displacement history is shown (i.e. the 2% cycle is not highlighted).

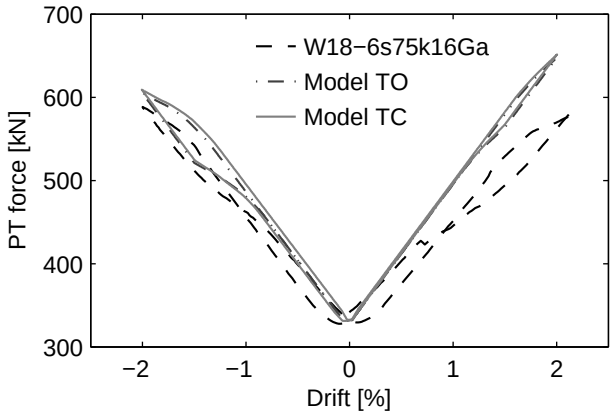

Figure 7.22: Comparison of experimental and numerical PT force response during 2% cycle

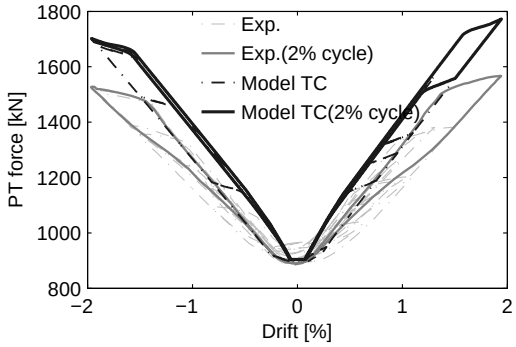

(a) MB: PT force vs. drift

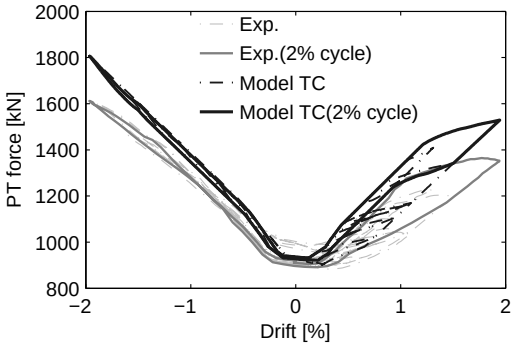

(b) TB: PT force vs. drift

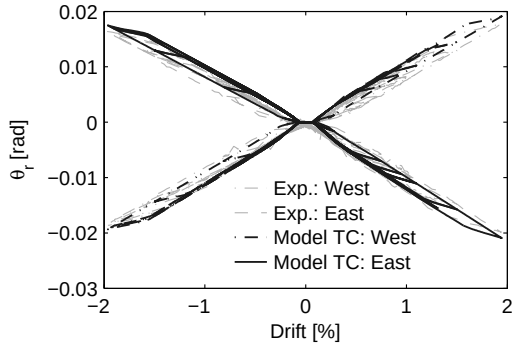

(c) MB: Gap rotation vs. drift

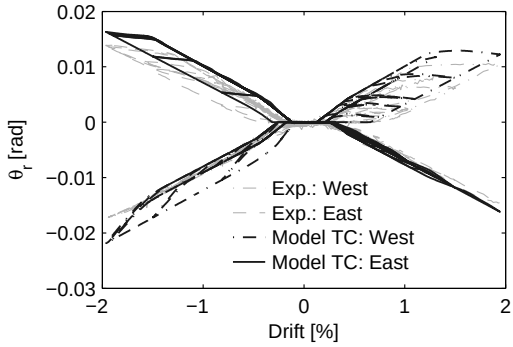

(d) TB: Gap rotation vs. drift

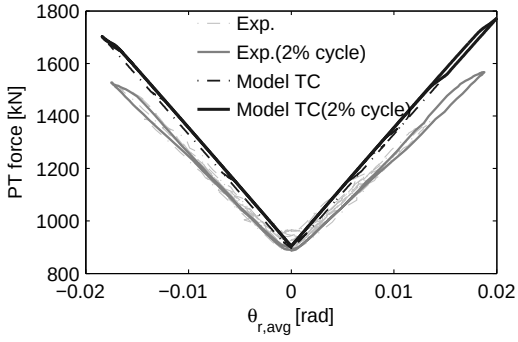

(e) MB: PT force vs. gap rotation

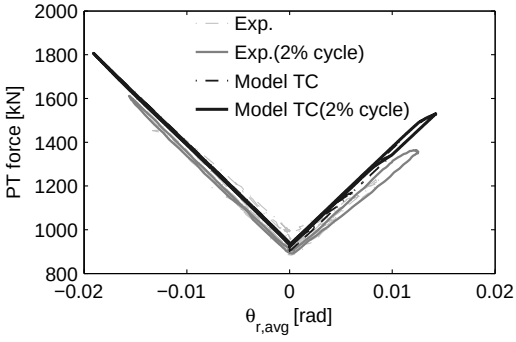

(f) TB: PT force vs. gap rotation

Figure 7.23: Comparison of numerical (Model TC) and experimental (10/50 test) responses of beam PT connections for full-scale specimen

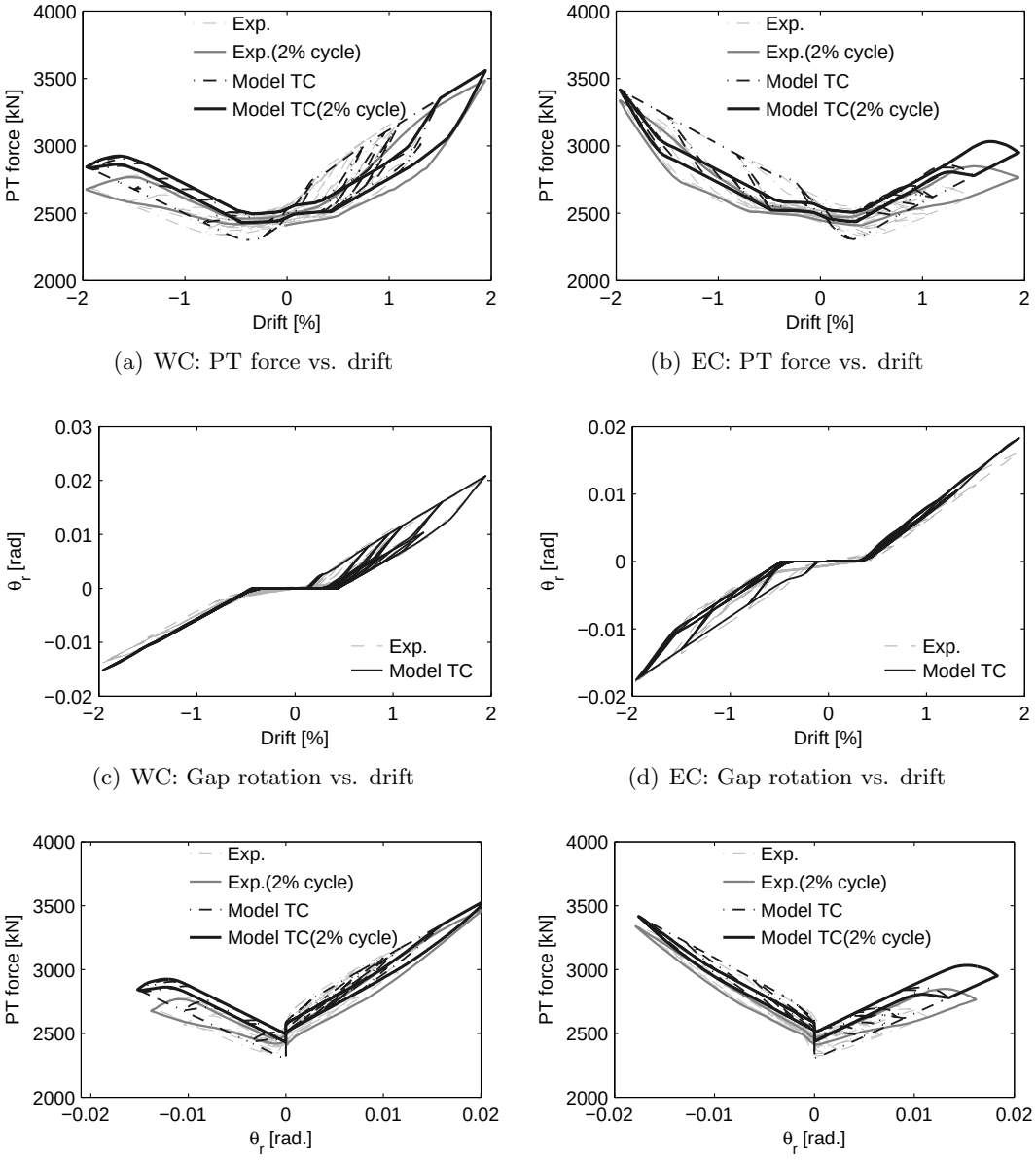

(a) WC: PT force vs. drift

(b) EC: PT force vs. drift

(c) WC: Gap rotation vs. drift

(d) EC: Gap rotation vs. drift

(e) WC: PT force vs. gap rotation

(f) EC: PT force vs. gap rotation

Figure 7.24: Comparison of numerical (Model TC) and experimental (10/50 test) responses of column base PT connections for full-scale specimen

The data in Figs. 7.23 and 7.24 show that, in general, the numerical model overestimates the PT force for a given drift demand (Note that this is also true for the subassembly models shown in Appendix C). This is likely due to one or more of the following:

- The model assumed the boundary frame member rocks about its extreme fiber[4], whereas the rocking point (or more accurately, the centroid of the bearing surface) may be somewhere within the flange depth.

- The model assumes that the PT anchorage is rigidly offset from the appropriate boundary element. There may be some flexibility in the physical PT anchorage assembly (e.g. the anchorage bearing plates, load cells, nut or wedge anchorages, etc.) that is not accounted for in the model.

- As shown in Fig. 7.23, the numerical model slightly overestimates the amount of gap rotation for a given drift demand. There may be some additional restraint to gap opening in the physical model that is not included in the numerical model. Potential sources of gap opening restraint may be due to the web plate corner cutouts or friction in the bolted shear tab connections.

- The model does not account for PT losses due to anchorage seating. This means that if comparing the PT force response during the 2% cycle, the experimental specimen would be starting with an lower PT force than the numerical model, as PT anchorage seating occured during cycles earlier in the response history.

Because the exact rocking depths and PT anchorage assembly flexibilities were not known and to maintain simplicity and conservativism in the model, no changes were made to the model to simulate these sources of flexibility.

Although the numerical model conservatively overestimates the PT demands, it is able to capture the general behavior and trends of the PT connection response. For example,

[4]The beam PT connections are assumed to rock about the extreme fiber of the flange bearing plates (Sec. 7.2.1.1); similarly, the column connections are assumed to rock about the extreme fiber of the column flange (i.e. not including the flange reinforcing plates due to observed rocking behavior).

the relative size and shape of the loops in the PT force or gap rotation response histories for both the beam and column connections are similar to those from the experiment (As previously discussed, the loops are due to axial shortening of the boundary members or restraint from the web plates when the tension field is engaged).

7.2.6 Comparison of dynamic response histories

Previous sections compared experimental results with OpenSees models subjected to static cyclic loading. Here, the OpenSees models are used to simulate response to dynamic loading, using the same ground motions as used in the full-scale pseudo-dynamic tests. In the simulations, the ground motions were executed sequentially (as they were in the tests) with enough free vibration between motions for the response to decay to approximate the zero displacement, velocity, and acceleration initial conditions of each of the pseudo-dynamic tests. However, the numerical response is only shown during the duration of the experimental test including the excitation and free vibration duration used in the test (as given in Table 5.3).

In the OpenSees simulations, Model TC was used with the compressive strength of 25% of the web plate yield strength and no numerical damping (as no additional analytical damping was provided in the test). Because Model TO does not have any energy dissipation in smaller cycles following larger cycles of web plate yielding, 2% damping was added to Model TO to control peak drift deamnds and free vibration oscillation responses. Details of damping in the test speciment are discussed in Sec. 6.4.1.

Figs. 7.25, 7.26, and 7.27 show the drift vs. time and force vs. drift response of Model TO, TC, and the test specimen during the 50/50, 10/50, and 2/50 PSD tests, respectively. The maximum and minimum drifts observed in the experiments and numerical dynamic analyses for each of the three tests or excitations are shown in Table 7.3.

Fig. 7.25(a) shows that during the 50/50 test, when the specimen exhibited near-elastic behavior, Model TO very accurately predicts the drift vs. time response including peak drifts and decay during free vibration. Model TC does have minor differences in the drift time history response and slight overestimation of the energy dissipation, resulting in more

Table 7.3: Peak (min. and max.) drift demands in PSD tests and dynamic analyses

	Experiment		Model TO		Model TC	
Hazard Level	Min. (%)	Max. (%)	Min. (%)	Max. (%)	Min. (%)	Max. (%)
50/50	-0.26	0.19	-0.23	0.21	-0.27	0.16
10/50	-1.97	1.94	-2.86	3.16	-1.97	2.10
2/50	-3.54	4.56	-4.59	4.32	-4.17	3.93

decay in oscillations during free vibration (Fig. 7.25(b)); however, it provides reasonable approximations of peak demands (Table 7.3).

Fig. 7.26 shows that Model TO greatly overestimates the peak drift demands compared with Model TC in the 10/50 test. Fig. 7.26(b) and Table 7.3 shows that Model TC provides reasonable approximations of peak drift magnitudes compared with the 10/50 experimental response. Both the model provide reasonable approximations of the experimental response up to approximately 2.5 seconds. In the first four seconds, Models TO and TC have very similar responses. After this time both models tend to have peaks and troughs in the drift vs. time response (Fig. 7.26(a)) at similar times; however, the magnitude of those local minima/maxima is lower for Model TC. Again, Model TC overestimated the hysteretic damping (i.e. oscillatory decay) during free vibration at the end of testing (due to the constant web plate compressive strength in the model that becomes negligible in the real web plate during free vibration). Although the free vibration response of Model TC does decay more rapidly during free vibration compared to the actual test, it still accurately captures, if not conservatively estimates, the residual drift. Similar observations can be made for the 2/50 response shown in Fig. 7.27.

Comparison of simulated and measured drift histories show that Model TO predicts much larger (i.e. conservative) drift demands during excitations inciting web plate yielding than observed in the actual test specimen. The additional energy dissipation and residual strength provided by Model TC is better able to capture peak drift demands observed in the actual test specimen. Although Model TC does assume a constant web plate residual strength resulting in more damping during free vibration compared to the actual web plate

with diminishing residual strength during free vibration, it is still able to conservatively and reasonably estimate (i.e. overestimate) the residual drift. Based on this set of PSD tests, Model TC appears to be reasonable for predicting key response parameters in nonlinear dynamic analyses. Further is needed to validate these claims for a range of web plates of various thicknesses and geometries.

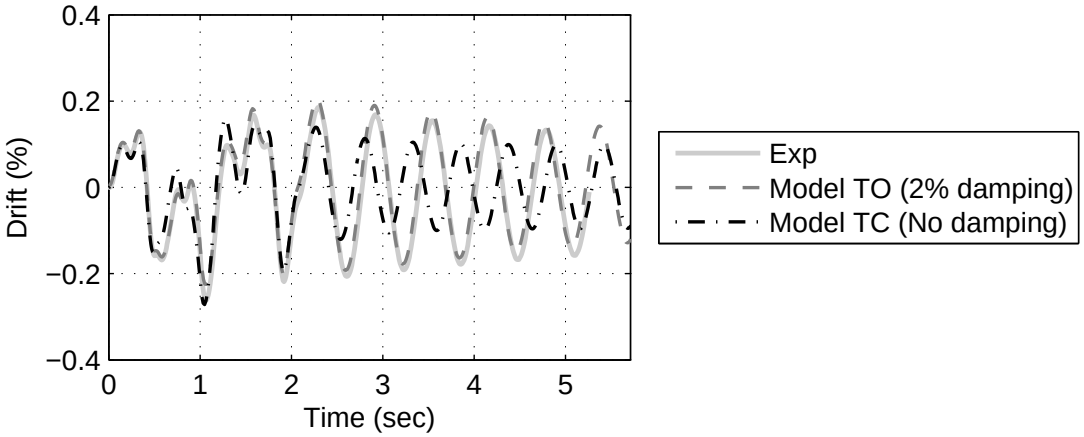

(a) Drift vs. time

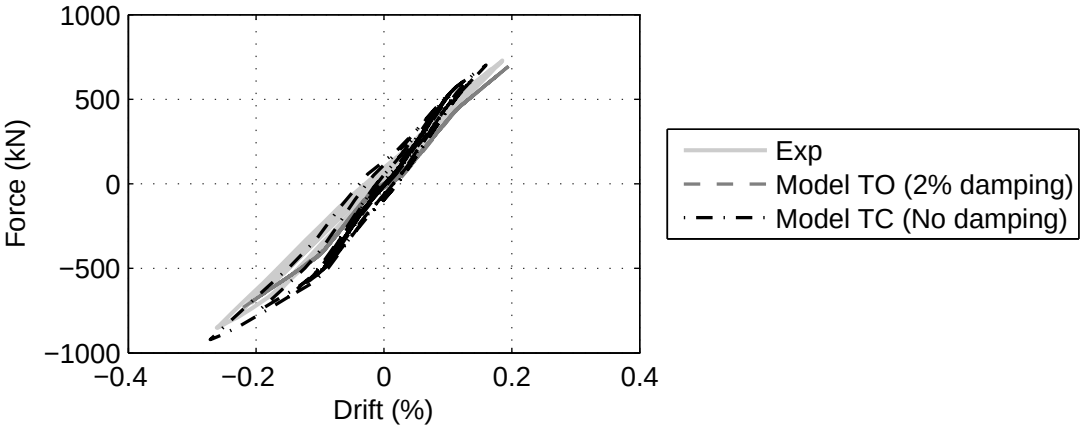

(b) Force vs. drift

Figure 7.25: Comparison of responses of different OpenSees models for 50/50 PSD test

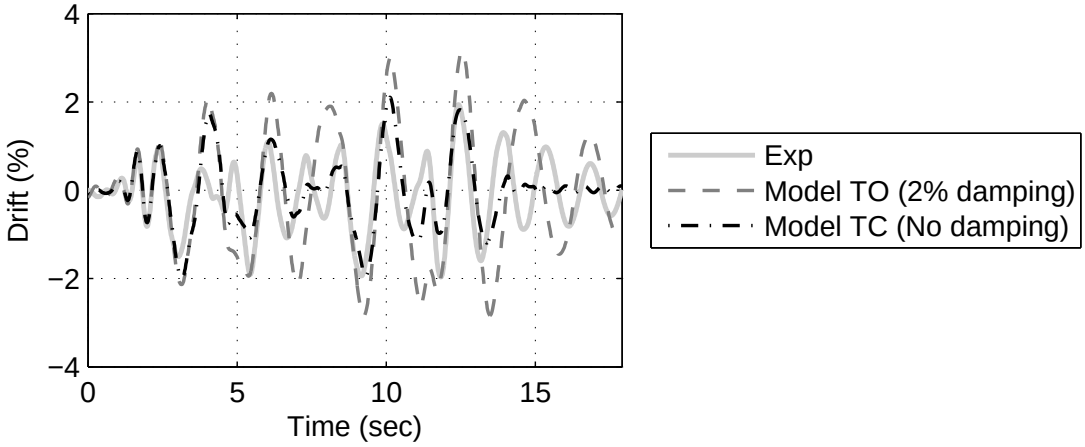

(a) Drift vs. time

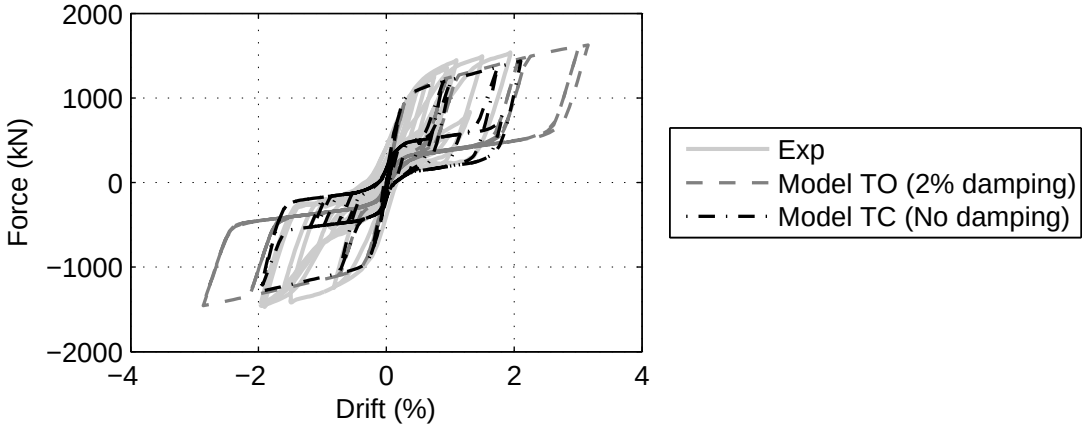

(b) Force vs. drift

Figure 7.26: Comparison of responses of different OpenSees models for 10/50 PSD test

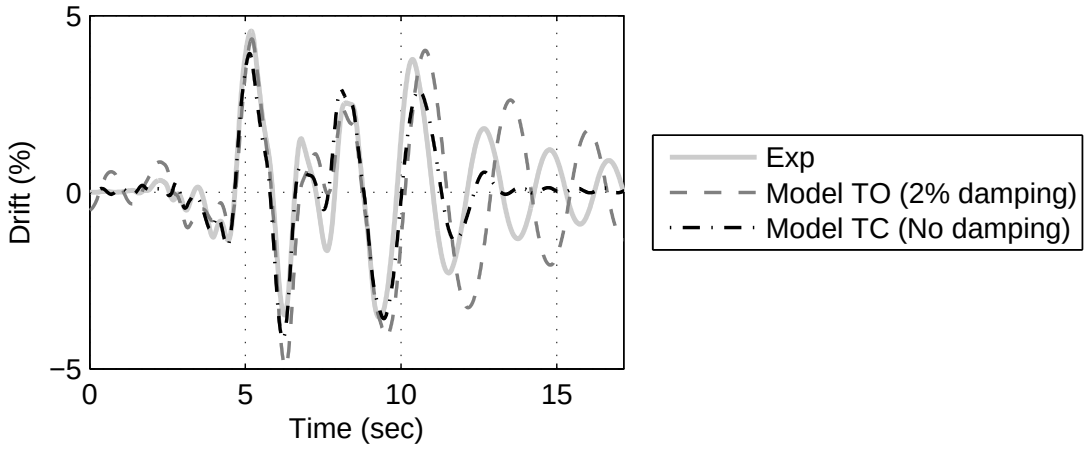

(a) Drift vs. time

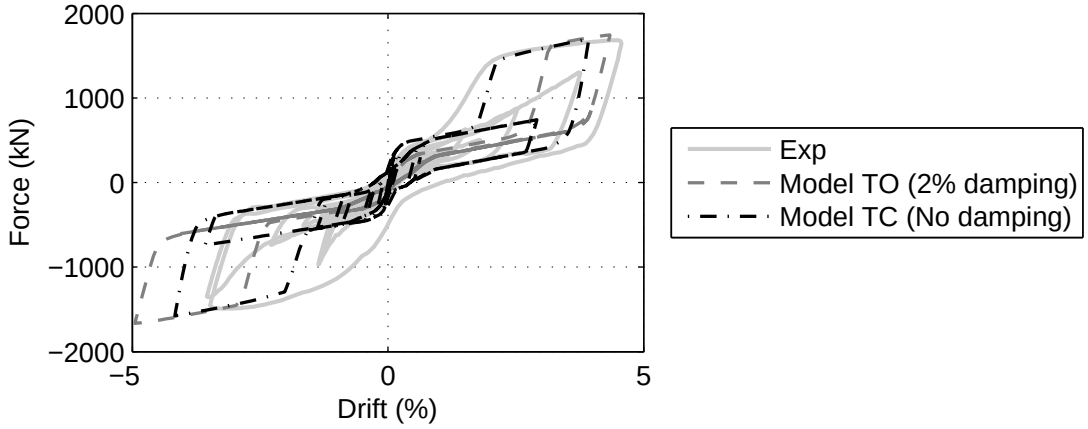

(b) Force vs. drift

Figure 7.27: Comparison of responses of different OpenSees models for 2/50 PSD test

7.3 ABAQUS Model

In comparison with the OpenSees model, the ABAQUS model provides a greatly enhanced representation of web plate response. The web plate is modeled using nonlinear shell elements enabling simulation of material nonlinearity as well as web plate buckling and snap-through; behavior that is not explicitly simulated using the OpenSees models. The added complexity of the ABAQUS model results in significantly increased computational demand, making ABAQUS analysis run-times long and impractical for lengthy displacement or time histories. However, use of the ABAQUS model enables investigation of the impact of web plate and other design parameters on response; this type of investigation cannot be accomplished using simple OpenSees models. The purpose of these ABAQUS models are to understand the complex web plate behavior and how it affects SC-SPSW behavior; thus, more refined models were used for the web plate, while the PT boundary frame was modeled using simpler methods. A description of the ABAQUS model and comparisons with experimental results are presented below.

The modeling approach used in ABAQUS is based on the modeling recommendations developed by Webster [2013]. Webster conducted a series of experimental tests on web plates in pinned boundary frames. Experimental data such as global force and deformation, web plate buckled shape, principal strains, and boundary frame demands were used to validate the ABAQUS modeling approach. The modeling approach used in this study for the boundary frame members, web plate, web plate-to-boundary frame connection, mesh size, and explicit solution algorithm are based on the recommendations provided by Webster.

7.3.1 Description of model and analysis

The finite element analyses were conducted using ABAQUS version 6.9, which is produced by the Dassault Systemes Simulia Corp. [ABAQUS, 2010]. The details of the model and the analysis methods are described below.

7.3.1.1 Boundary frame model

The boundary frame was modeled using three-node linear beam (B31 element in ABAQUS) and two-node truss (T3D2 element in ABAQUS) elements. The PT boundary frame model was very similar to the PT frame model developed in OpenSees and described in Sec. 7.2. The PT connections were modeled using a similar method of stiff compression-only springs rigidly offset from the boundary element centerlines to transfer forces between the beam flanges and the column flange, while shear transfer was provided by y-direction displacement restraints at the beam ends (as shown in Fig. 7.1(d)). The main purpose of this numerical study was to understand the complex web plate behavior and how it affects SC-SPSW behavior. Because the PT boundary frame response is relatively well understood, these simpler modeling techniques were sufficient in simulating its behavior.

Preliminary studies were conducted in ABAQUS where the boundary frame members (i.e. beams and columns) were modeled using shell elements. Here, the rocking behavior of the PT connections was simulated with contact and friction between the face of the column flange (shell elements) and the solid brick elements located at the ends of the beams. When tested on a single connection, this method was able to capture the rocking behavior; however, it required numerous small elements and multiple opening and closing contact surfaces, both of which considerably increased the computational demands. When incorporating this shell/solid element PT connection model into a frame with multiple PT connection, the computation times were very long. Therefore, it was decided that because the simpler PT connection model (Fig. 7.1(d)) was able to adequately simulate the PT connection rocking behavior (see Sec. 7.2.3) with substantially less computational effort than the shell/solid connection model, the simpler model would be employed. Also, because the boundary elements were expected to remain elastic during the simulations, beam elements were satisfactory in representing the boundary frame member response. If significant yielding is expected in the boundary frame, the boundary frame members should be modeled using shell elements to understand the progression and localization of yielding within the members.

The beams and columns were modeled as beam elements (B31 as described above)

with the cross-sectional and material properties (E_s = 200 GPa, ν=0.3) corresponding to the nominal W-shape. The PT members were modeled as single truss elements for each boundary frame member (e.g. one truss to represent all of the PT strands in each beam, or one truss element to represent the two PT bars in each column) with cross-sectional areas, modulus of elasticities ($E_{PTstrand}$ = 196.5 GPa, E_{PTbar} = 204.8 GPa, ν = 0.3), and yield strengths ($F_{y,PTstrand}$ = 1689.2 MPa, $F_{y,PTbar}$ = 827.4 MPa) corresponding to the nominal, manufacturer-provided, properties. The "rigid offset" elements used in the PT connection model (described above) were beam elements with large cross sectional areas and moments of inertias with the elastic modulus of steel material (200 GPa). The "compression-only springs" at the beam flanges were modeled using axial connectors with nonlinear behavior representing a high elastic stiffness in compression and very low elastic stiffness in tension. The y-displacement restraint between the beam end and the rigid offset from the column centerline was modeled with a Kinematic coupling constraint between the y-direction degrees-of-freedom between the two nodes. This restraint provided shear transfer, similar to the vertical restraint used in the OpenSees PT connection model (Fig. 7.1(d)). A similar PT connection model was used for the PT connection at the column bases in the full-scale specimen; however, the y-displacement restraint at the beam end was replaced by a boundary condition fixing the x-direction displacement of the nodes at the base of the column to simulate the shear brackets restraining lateral displacement of the column base. In the ABAQUS model of the subassembly specimens, the column base boundary conditions matched those of the physical specimen—y- and z-displacement restrained under the North VBE and x-, y-, and z-displacements restrained under the South VBE.

During the tests, the specimen boundary frames were restrained out-of-plane at discrete points that were stationary with respect to the ground; however, because no out-of-plane deformation was observed in the boundary frames in any of the SC-SPSW tests, out-of-plane restraint was provided in the ABAQUS model at the nodes in the connection regions (e.g. nodes at the ends of the rigid offset elements, PT anchorage, beam ends, etc.). In the full-scale specimen, the double-angle shear connection at the ends of the BB were simulated with a pin connection (i.e. kinematic coupling of x-, y-, and z-displacement of the nodes at the beam end and column face).

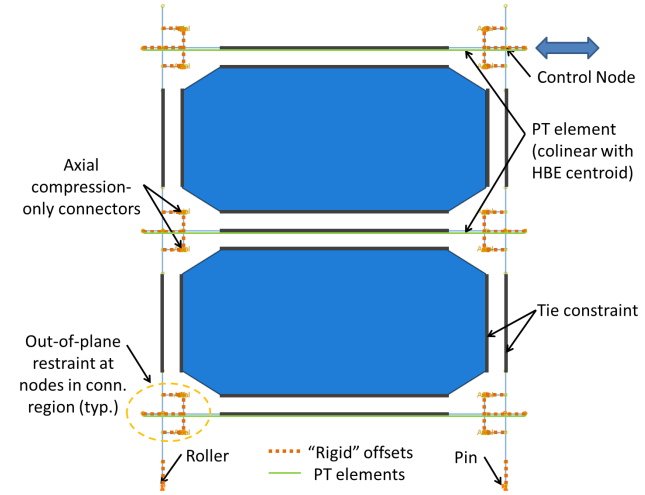

(a)

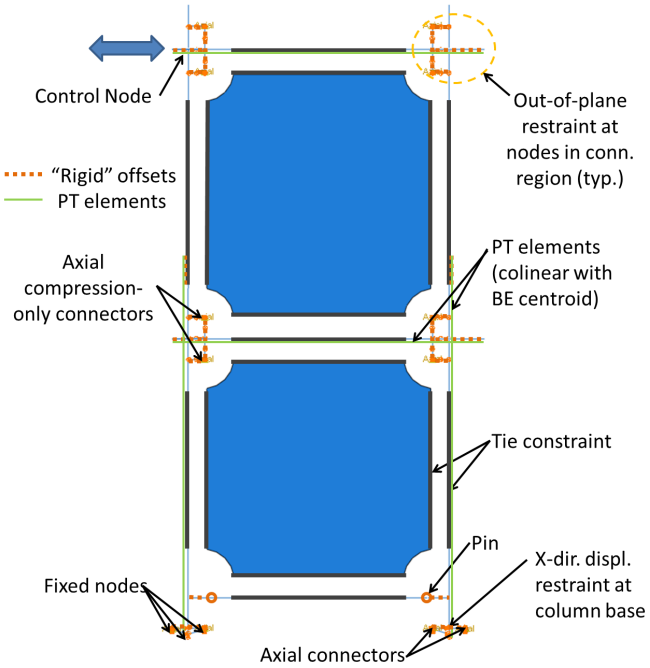

(b)

Figure 7.28: Schematic of ABAQUS model for (a) subassembly specimen and (b) full-scale specimen

7.3.1.2 Web plate model

Schematics of the ABAQUS finite element (FE) models for the subassembly and full-scale test specimens are shown in Fig. 7.28. The web plates were modeled using four-node quadrilateral shell elements with reduced integration (S4R elements in ABAQUS) with five Gauss integration points through the thickness of the shell. The web plates were modeled with initial out-of-plane imperfections to facilitate web plate buckling and development of tension field action. The initial imperfections were determined from an eigenvalue buckling analysis of the model with a unit lateral load applied at the location of the actuator. The web plates were seeded with the nodal displacements of the first ten modes from the eigenvalue buckling analysis, scaled to a peak amplitude of 5 mm based on the recommendations provided by Webster [2013].

The web plate extended to the centerline of the bolts in the bolted clamping bar web plate connections and the edge of the weld in the welded web plate connection detail. The edge of the web plate was attached to the boundary frame via tie constraints (as shown in Fig. 7.28), with the web plate degrees-of-freedom being slaved to those of the boundary frame elements.

7.3.1.3 PT model

The initial stress was applied to the PT elements via a constant predefined temperature field on the PT elements. The PT material was given an arbitrary isotropic thermal expansion coefficient, and the predefined temperature was adjusted in each member to achieve the desired initial PT force. The temperature "load" was applied in the first analysis step, prior to any other loading to apply the initial PT force and was held constant during subsequent loading steps.

7.3.1.4 Web plate material properties

The web plate material properties used in ABAQUS were determined based on the web plate coupon results. The modulus of elasticity, E_w, and yield strengths, σ_{yw}, from the subassembly test specimens in Table 4.2 were used for each respective web plate in the

subassembly models. For the full-scale specimen model, the yield strength was taken from coupon data as 208 MPa (as described in Sec. 5.3.3). The elastic modulus found from the monotonic testing of these web plate coupons from the full-scale specimen (584 GPa as given in Sec. 5.3.3) was much larger than expected for LYS plates; this was attributed to the fact that the E_w was computed from linear regression of very few points within the elastic range of the material. Therefore, a more appropriate nominal value of E_w for steel (200 GPa) was used in the ABAQUS model for only the full-scale specimen (subassembly specimens used E_w as given in Table 4.2).

The plastic response of the web plate material was defined by parameters defining the yield surface and material strain hardening parameters. Webster [2013] investigated modeling plastic web plate response in ABAQUS and found that (1) the material hardening parameters (e.g. Isotropic, Kinematic, or combined hardening rules) had a significant impact on the cyclic response and lateral strength of the web plate, (2) the hardening parameters varied for different materials and different gage thicknesses, and (3) assuming isotropic hardening tends to better represent actual hardening observed in experimental web plate tests and provides a slightly conservative approximation (i.e. slight overestimation) of the web plate strength. Thus, isotropic hardening was assumed in the analyses presented here.

The yield surface was defined based on the Cauchy (true) stress, σ, vs. logarithmic plastic strain, ϵ_{pl}, response of the monotonic coupon data. The Cauchy stress and log-plastic strains were derived from the engineering stress and strain, σ_{eng} and ϵ_{eng}, respectively, as follows

$$\sigma = \sigma_{eng}(1 + \epsilon_{eng}) \tag{7.3}$$

$$\epsilon_{pl} = \ln(1 + \epsilon_{eng}) - \frac{\sigma_{eng}}{E_w} \tag{7.4}$$

where σ_{eng} and ϵ_{eng} were determined from the monotonic coupon tests of the web plate material. The yield surfaces that were defined in ABAQUS were based on data from one of the coupons from each plate, typically the coupon which represented the most typical or "average" response from the set of coupons taken from that particular plate. An example of the yield surface (True σ-ϵ_{pl}) for one web plate from the subassembly tests is shown in Fig. 7.29. Here, the corresponding engineering stress-strain behavior is also shown for

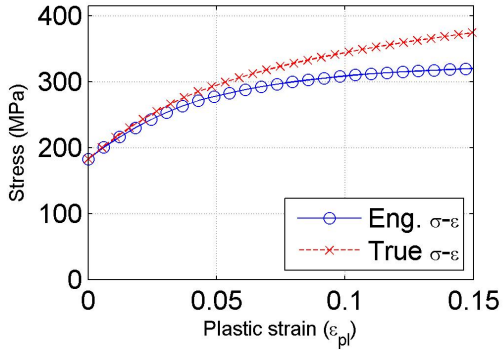

Figure 7.29: Example of engineering stress vs. plastic strain yield surface from the monotonic coupon test and the true stress vs. logarithmic plastic strain yield surface used in ABAQUS web plate material model (shown here for second story of subassembly specimen W18-8s100k20Ga)

comparison.

7.3.1.5 Analysis methods

ABAQUS/Explicit was used to conduct all of the numerical simulations. The explicit central-difference solution algorithm was used because of its ability to capture the snap-through behavior of the buckling web plate that is difficult to capture with implicit methods in ABAQUS/Standard [Webster, 2013].

In explicit solution algorithms, the time step must be very small to maintain numerical stability and better approximate the actual response. To ensure numerical stability, the time step must be less than the critical time step, Δt_{cr}, which is related to the time it would take a wave to propagate through an element, making it a function of the element length and the wave velocity associated with the material:

$$\Delta t_{cr} \propto L_{min}\sqrt{\frac{\rho}{E}} \tag{7.5}$$

where L_{min} is the minimum element length, ρ is the material density, and E is the material's modulus of elasticity. Using very small elements or very large material stiffnesses can result in very small time steps and long computational run times. Similarly, to decrease the

computational demands by reducing the number of steps required in a given load history, the critical time step can be increased through mass scaling. Essentially, as shown in Eqn. (7.5), increasing the mass (or density, ρ) of the material by a factor of f^2, the explicit time step used in the analysis, Δt, is increased by a factor of f.

Unless stated otherwise, a mass scale of fifty was used for the web plate, beam, column, and PT elements. The "rigid" beam column elements were modeled with material with the same elastic modulus of steel (200 GPa) but with cross-sectional properties that were much larger than (approximately 20-50 times larger) than those of the W-shape sections used in the test; therefore, the masses of these elements were not amplified.

Unless otherwise stated, the numerical models were subjected to a displacement history, which was applied to the node where the actuator was loading the specimen. In order to simulate quasi-static loading, the time scale (i.e. the amount of time for the specimen to be loaded to a prescribes displacement) of the applied loading was made long enough to ensure that inertial effects were negligible in the model, typically such that the inertial forces remained less than 1% of the expected peak strength.

7.3.2 Comparison with subassembly experimental results

In the analyses of the subassembly specimen models, the displacement history was an abbreviated version of the experimental displacement histories. The models were loaded cyclically up to approximately 2.5% drift. This was the drift at which web plate tearing was typically first observed in the lab; as web plate tearing was not simulated in the ABAQUS model, comparison of simulated and observed response at drift levels beyon 2.5% was not appropriate. To reduce the computation time of the analyses, the initial elastic cycles were excluded such that the displacement history applied to the models began with cycles of approximately 0.5% drift.

The ABAQUS shell-element web plate model was used to provide enhanced simulation of complex web plate response. However, some simplifying assumptions were made to facilitate web plate modeling. These assumptions include:

1. The web plates were assumed to be tied to the boundary frame, rigidly offset from the

frame member centerline to the fish plate connection location; therefore, the phenomena of web plate slip in the clamping bars and web plate tearing were not simulated.

2. The web plate was assumed to exhibit pure isotropic hardening. Webster [2013] found that web plate hardening parameters (e.g. isotropic, kinematic, and combined) can vary from plate to plate depending on material classification, production batch, and thickness; however, isotropic hardening was suggested for web plate model as it provides slightly conservative (i.e. overestimation) of peak strengths.

Although these assumptions result in model error, the error is assumed to have negligible impact on the overall simulated response.

The deformations of the web plates in the ABAQUS model qualitatively matched well with the buckled shapes observed in the experiment. Figs. 7.30 through 7.32 show comparisons of some specimens at ±2.5% drift and at zero drift following the 2.5% cycle. In these figures the ABAQUS deformed shape is plotted, and the color contours represent the out-of-plane deformation. The results discussed in the following sections compare the numerical data recorded in these analyses to experimental data.

(a) Specimen at +2.5% drift

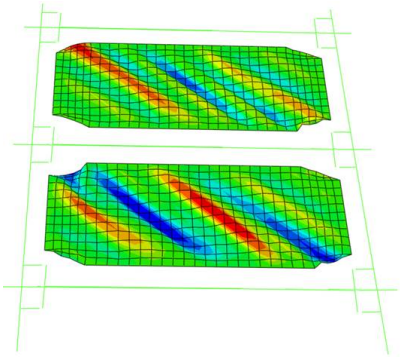

(b) ABAQUS at +2.5% drift

(c) Specimen at zero drift following 2.5% cycle

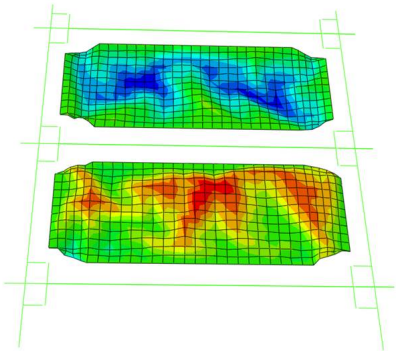

(d) ABAQUS at zero drift following 2.5% cycle

Figure 7.30: W18-8s100k20Ga-2 web plate deformation in experiment and ABAQUS model

(a) Specimen at -2.5% drift

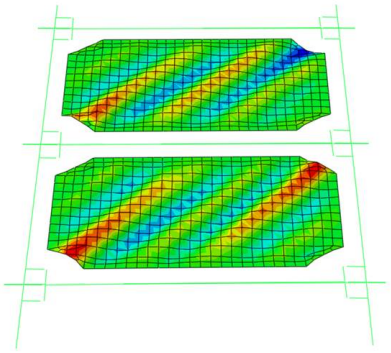

(b) ABAQUS at -2.5% drift

(c) Specimen at zero drift following 2.5% cycle

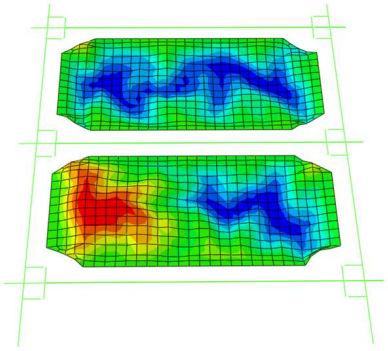

(d) ABAQUS at zero drift following 2.5% cycle

Figure 7.31: W14-8s100k16Ga web plate deformation in experiment and ABAQUS model

(a) Specimen at -2.5% drift

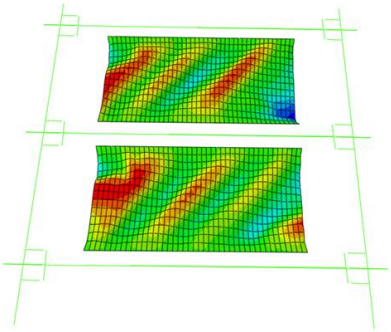

(b) ABAQUS at -2.5% drift

(c) Specimen at zero drift following 2.5% cycle

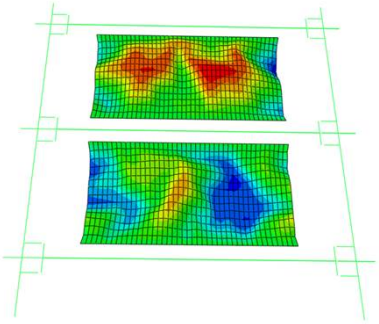

(d) ABAQUS at zero drift following 2.5% cycle

Figure 7.32: W14-8s100k16GaHBE web plate deformation in experiment and ABAQUS model

7.3.2.1 Comparison of global response

Fig. 7.33 shows the experimental and finite element model force vs. drift responses of four subassembly specimens. For easier comparison of single cycle behavior, the first cycle of loading at approximately 2% drift is highlighted for both the experiment and the numerical model. These specimens were selected as representative of typical Phase I W18 specimens (W18-8s100k20Ga), Phase II W18 (W18-8s100k20Ga-2) and W14 (W14-8s100k20Ga) specimens, and the specimen with the web plate connected to the HBEs only (W14-8s100k16GaHBE). These specimens also had no observed tearing and minimal plate slipping in cycles prior to 2.5% drift; however, it should be noted that some web plate slip was observed near the corner cutouts at the end of the clamping bars as early as 0.75 and 1% drift. Similar figures for all of the SC-SPSW subassembly specimens are shown in App. E.

In general, the ABAQUS models were able to capture the unloading and reloading strength of the specimen, as well as the additional energy dissipation as the web plate resisted load prior to reaching the previous peak plastic strain, a behavior that the OpenSees tension-compression strip model was not able to simulate (e.g. see Fig. 7.10(b)). Like the OpenSees models, the ABAQUS models also have a higher initial stiffness than the test specimen; however, this is largely influenced by flexibility in the initial configuration of the PT connections (e.g. due to uneven bearing in the connections and initial gaps present in the middle HBE) that is not present in the assumed PT connection spring model in which the connection behaves like a rigid connection prior to decompression. This was discussed previously for the OpenSees subassembly models in Sec. 7.2.3.1 showing that the presence of initially decompressed connections significantly reduce the initial stiffness using boundary frame models in OpenSees that are very similar to those used in ABAQUS.

The ABAQUS models also typically match or overestimate the peak strength and backbone response of the specimen. Unlike the OpenSees tension-only and tension-compression strip models which tended to underestimate the peak strength, the ABAQUS web plate shell model is able to accumulate plastic strain and harden due to plastic contraction orthogonal to the tension field direction. The overestimation of the peak strength in the ABAQUS model may be due to a combination of the assumed isotropic hardening and web plate slip

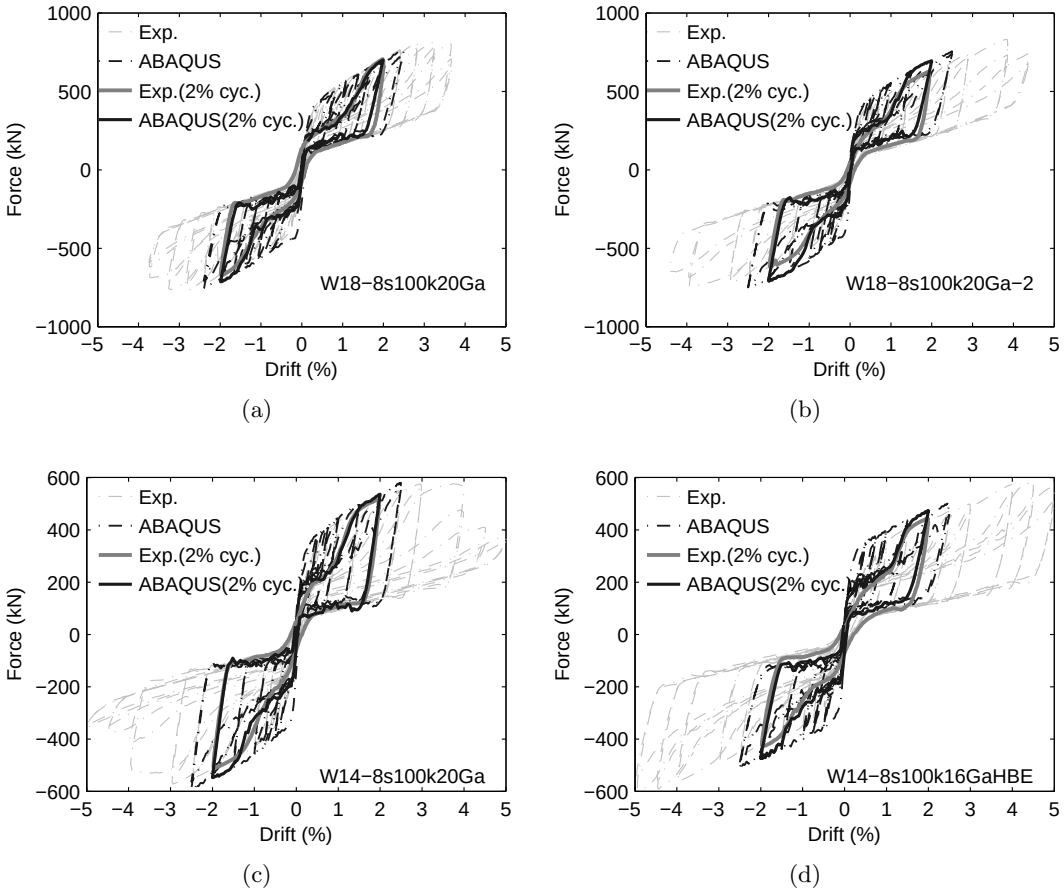

Figure 7.33: Comparison of experimental and finite element model force vs. drift responses for specimens (a) W18-8s100k20Ga, (b) W18-8s100k20Ga-2, (c) W14-8s100k20Ga, and (d) W14-8s100k16GaHBE

in the bolted clamping bar connections present in the physical model that was not simulated in the numerical model.

7.3.2.2 Investigation of E_w on response

The residual web plate strength in the ABAQUS model was dependent on the elastic modulus defined for the web plate material. In preliminary models of the subassembly specimens, in order to better approximate the web plate yield surface, the web plate elastic modulus was assumed to be the secant stiffness passing through the the following points: zero stress and strain (0,0), and the yield stress and strain associated with the yield stress based on the monotonic coupon tests (ϵ_y=$\epsilon(\sigma_y)$,σ_y). Because the light gage plates used in these tests had a rounded yield surface without a distinct yield plateau, this secant stiffness was significantly less than the initial tangential stiffness of the web plate (E_w in Table 4.2 and used in the final ABAQUS model).

Fig. 7.34 shows an example of preliminary force vs. displacement results from the numerical model of specimen W14-8s100k20Ga using this secant web plate stiffness[5]. Note that the model using the secant elastic stiffness (Fig. 7.34) provides a slightly more accurate approximation of the backbone response at lower drift demands compared to the model using the initial stiffness (Fig. 7.33(c)), because the secant stiffness model assumes the actual web plate strain associate with the yield stress rather than ϵ_y=σ_y/E_w. However, the reduction in initial stiffness when using the secant web plate stiffness still does not account for all of overestimation in the specimen's initial stiffness as the numerical boundary frame that does not simulate the initial decompression and uneven bearing that was present in the actual PT connections for this specimen.

As the model is unloaded, because the web plate unloads with the elastic modulus specified in the web plate material model, the secant stiffness model underestimates the unloading web plate stiffness. Additionally, because the residual web plate strength is related to the material stiffness, the secant stiffness model also underestimates the web plate residual strength, resulting in an unloading strength that is similar to that of the

[5]All other aspects of the model other than the elastic modulus of the web plate material were identical.

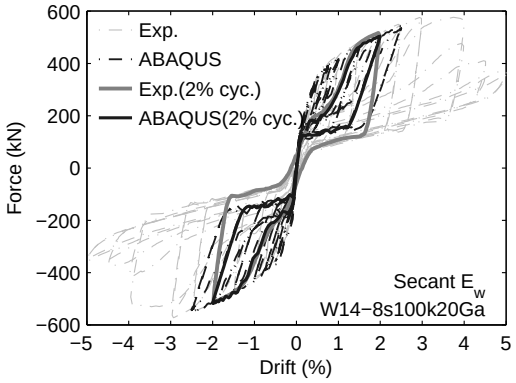

Figure 7.34: Preliminary results of W14-8s100k20Ga ABAQUS model with lower web plate elastic modulus

tension-only strip model (Fig. 7.10(b)). Although the models using the initial web plate stiffness, E_w, overestimate the backbone response for smaller cycles of loading (partly due to the initial web plate stiffness and partly due to the idealized representation of the boundary frame connections), it is able to better capture the web plate unloading stiffness and residual strength, which are important factors in determining SC-SPSW energy dissipation and recentering capabilities. This demonstrates the importance of accurate modeling of the web plate elastic properties, even though the elastic range of loading is limited to only very small drift demands.

7.3.2.3 Comparison of HBE and PT demands

By modeling the web plate as a continuum using shell elements, the distributed web plate demands acting on the boundary frame elements should, in theory, be more accurate than the discrete loading simulated by the strips employed in the OpenSees model. To investigate this, Fig. 7.35 shows the middle HBE moment distribution for specimens W18-8s100k20Ga-2 and W14-8s100k20Ga at the first cycle of loading at approximately 2% drift for the ABAQUS model, the OpenSees tension-compression strip model (OS Model TC), and the experimental specimen. Similar plots comparing moment distributions at approximately ±2% drift are shown for each of the subassembly specimens in App. E.

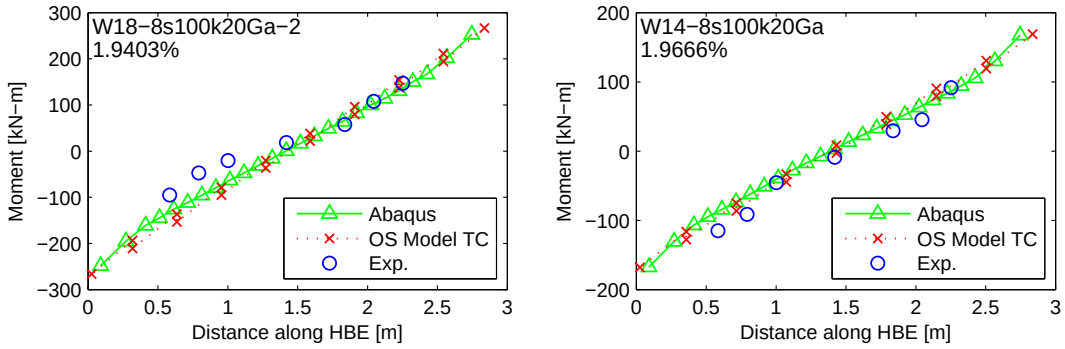

(a) (b)

Figure 7.35: Comparison of ABAQUS, OpenSees, and experimental middle HBE moment distributions at approx. 2% drift for (a) W18-8s100k20Ga-2 and (b) W14-8s1000k20Ga

The moment distributions from the ABAQUS models match, on average, those from the OpenSees strip model and the experimental results. Most importantly, the maximum moments, which occur at the ends of the beam in this case with equal plate thicknesses above and below, are very similar for the OpenSees and ABAQUS models. Thus the OpenSees strip model, while approximating the continuous nature of the web plate with discrete element, is sufficient for estimating peak moment demands.

Fig. 7.36 shows a typical comparison of the PT force and connection gap opening vs. drift responses for the middle HBE in specimen W18-8s100k20Ga (results are provided for all specimens in App. E) for the entire displacement history. Although the PT force and gap rotation responses from the ABAQUS model match well with those observed in the test there are some minor deviations. The PT force response in the numerical model is slightly larger than in the experiment (also typical of the OpenSees models); however, this is expected as PT force loss due to anchorage seating and additional flexibility in the PT anchorage system (e.g. axial stiffness of PT load cells, adjustable spacers, etc.) is not simulated. The gap rotation demands in the numerical and physical models are also similar. One key difference is the drift at which gap opening was first observed (i.e. a change in slope in the gap rotation vs. drift response). As stated previously, the numerical model overestimates the stiffness of the PT frame, which means the connections reach their decompression moment at a lower

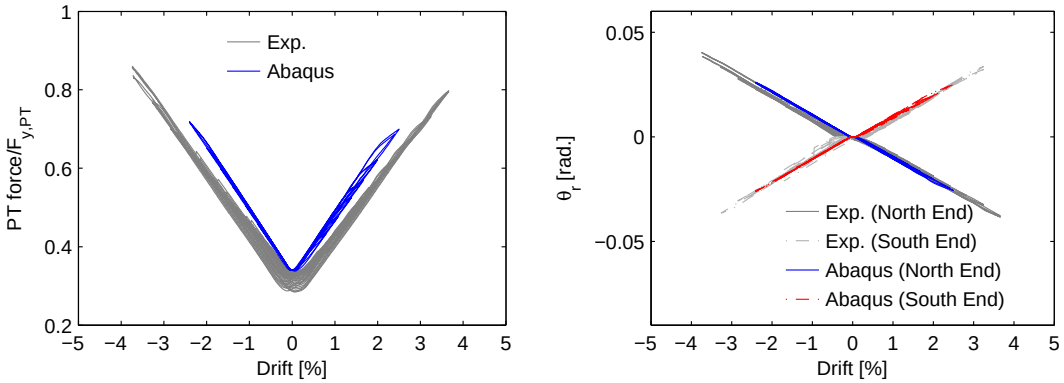

Figure 7.36: (a) PT force and (b) gap rotation vs. drift response for middle HBE in W18-8s100k20Ga

drift than in the more flexible physical specimen; therefore, the connection decompresses earlier in the numerical model.

7.3.3 Comparison with full-scale experimental results

To further evaluate the ABAQUS model, it was used to simulate the response of the full-scale specimen subjected to the same displacement history as observed in the 10/50 PSD test. The 10/50 PSD test was chosen as during this test the full-scale specimen experienced significant web plate yielding but did not exhibit significant web plate tearing. Thus, the ABAQUS model could be expected to provide accurate simulation of response.

Fig. 7.37 shows the deformation of the web plates for the specimen during the peak positive (+1.94%) and negative (-1.97%, also at the observation point 1050N1) drift demands and at the end of the 10/50 PSD test (at the observation point 1050R2). Scales representing the magnitude of out-of plane web plate deformation (in units of meters) are provided. Because the out-of-plane bracing frame obscured quality photos of the web plate deformation (as seen in Fig. 5.32), no experimental photos are provided for comparison; however, the general web plate deformation observed in ABAQUS corresponds to the visual observations made during the test.

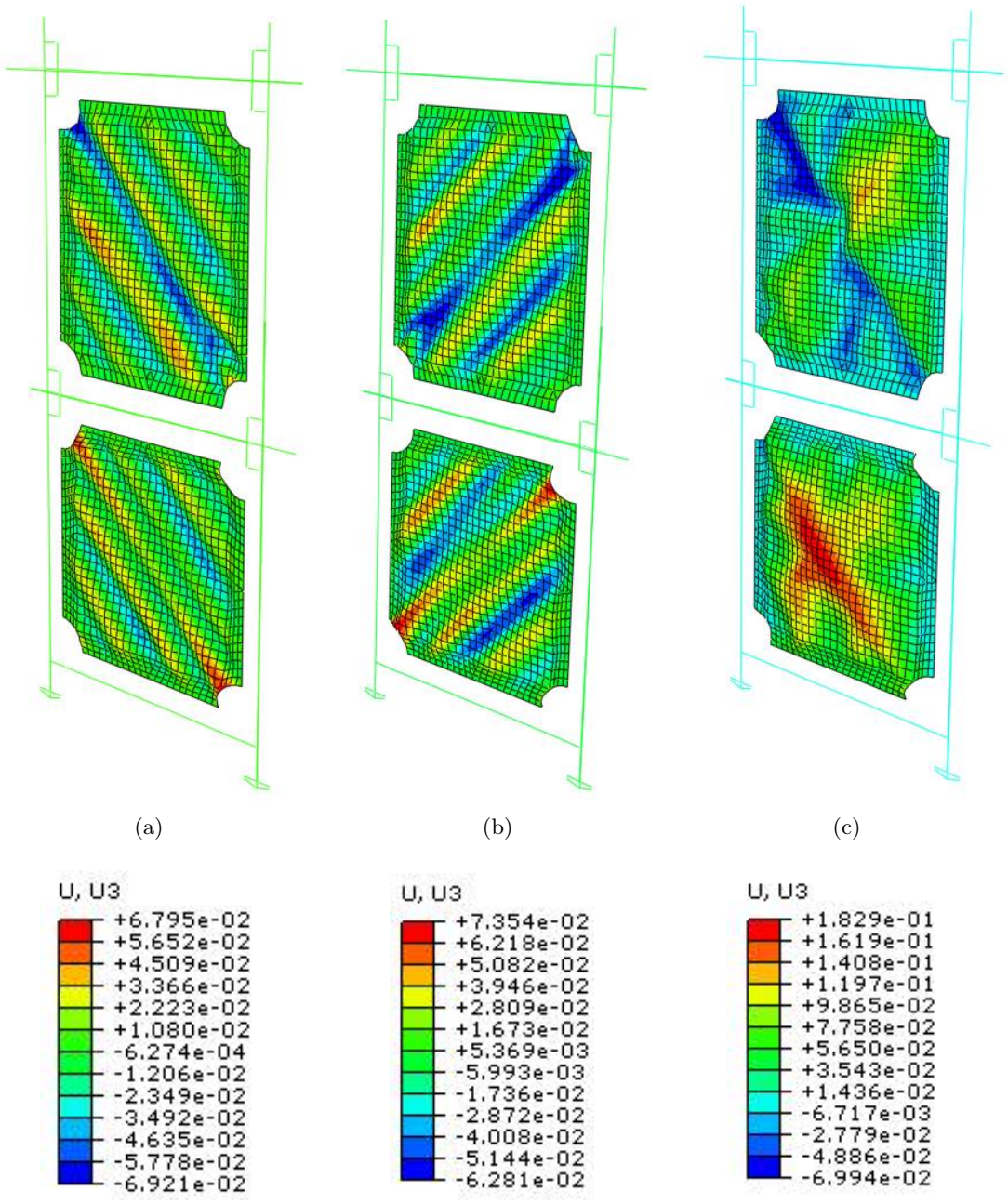

Figure 7.37: Full-scale specimen web plate deformation at (a) the peak negative drift, at (b) the peak positive drift, and at (c) the end of the 10/50 displacement history

7.3.3.1 Comparison of global response

Figs. 7.38(a) and 7.38(b) show the drift and force histories of the full-scale specimen and the ABAQUS model under the 10/50 PSD displacement history. Note that although the displacement history from the 10/50 PSD test was applied as a boundary condition to the the ABAQUS model under displacement control, there is some very minor differences between at the local minima and maxima (Fig. 7.38(a)). This difference between the numerical and experimental drifts at local maxima/minima is less than 1% difference, and is deemed to be negligible. Here, the finite element model force history matches very well with that of the experimental specimen.

The full force vs. drift response is shown in Fig. 7.39, where Fig. 7.39(a) highlights the cyclic response at the peak drift cycle, and Fig. 7.39(b) highlights the cyclic response during free vibration. Fig. 7.39(a) shows that the finite element model is able to capture the reloading and unloading path and the yield surface of the specimen very well, especially when compared to the Model TO and Model TC responses in OpenSees (Fig. 7.11).

7.3.3.2 Comparison of HBE and PT connection demands

As was done previously for the OpenSees models (Secs. 7.2.4.2 and 7.2.5.2), key response parameters from the ABAQUS model were compared with those from the 10/50 PSD experimental results. Figs. 7.40 and 7.41 show the beam axial and moment responses, respectively, while Figs. 7.42 and 7.43 show the beam axial and moment responses, respectively, for those locations where boundary frame demands were measured.

Fig. 7.40 shows that the ABAQUS model over-predicts the axial demands in the middle of the beams compared to those derived from strain gage readings in the specimen. This is attributed, at least partially, to the over-prediction of PT froce due to under-prediction of PT loss. However, the shape and response characteristics of the finite element model and the specimen are similar. It is reasonable that the shell web plate model would result in larger beam axial forces that similar strip web plate plate models in the SC-SPSW, as the continuous shell model accounts for the net horizontal strain in the web plate due to frame expansion that is not accounted for in the discrete strip model (as will be discussed

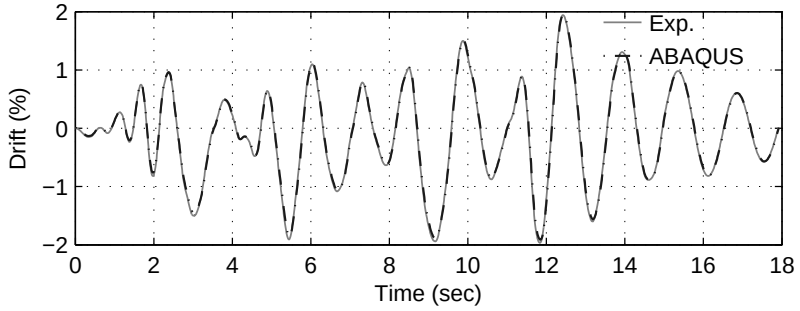

(a)

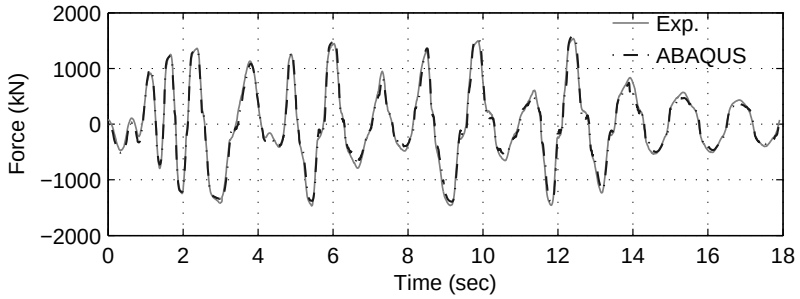

(b)

Figure 7.38: (a) Drift and (b) force time histories of ABAQUS and experimental results for 10/50 PSD

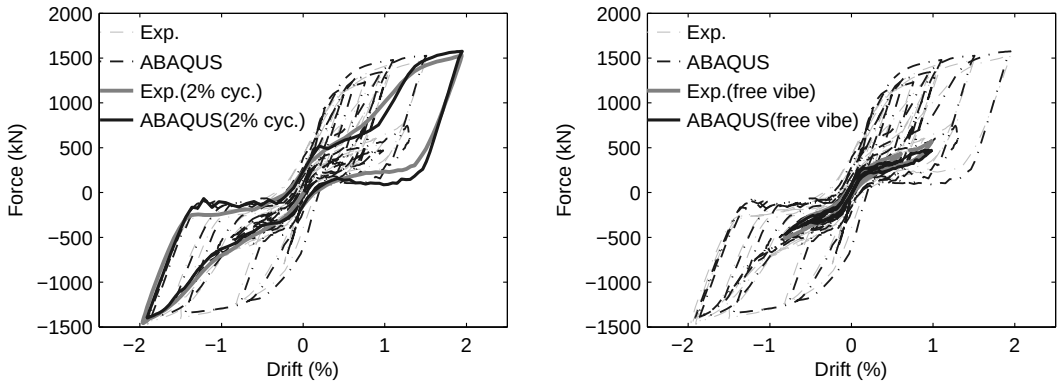

(a) (b)

Figure 7.39: Force vs. drift response of ABAQUS and experimental results for 10/50 PSD highlighting the (a) peak cycle and (b) free vibration responses

in further detail later in Sec. 8.3.3). Although the exact reasons why the ABAQUS shell model over-estimates the experimental results are unclear.

The beam moment demands predicted in the finite element model (Fig. 7.41) match well in shape and magnitude with the experimental results, with the exception of the moments at the West section in the TB, particularly in the negative loading direction (which was also observed in the OpenSees model). This difference between the finite element model and the numerical results may be due to the simplified model of the actuator loading (modeled as a concentrated load on the west column at the TB centerline) in the stick element boundary frame model in ABAQUS and OpenSees models. This simplified modeling approach for the boundary frame and loading may impact the relative stiffness of the WC at the loading location and may impact how the load is transfered to the TB and WC (e.g. in the real specimen, the additional stiffness and load distribution provided by the loading beam may help keep the connection closed, whereas the point load in the simplified boundary frame model may allow for larger concentrated column deformations in the connection region), which would affect the local demands near that location.

The column axial (Fig. 7.42) and moment (Fig. 7.43) demands also match well in shape and relative magnitude with the experimental results. The ABAQUS model does over-predict the compressive axial forces in the compression columns (e.g. WC in negative drifts) and slightly under-predicts the compressive axial forces and over-predicts the moments in the tension columns (e.g. WC in positive drifts).

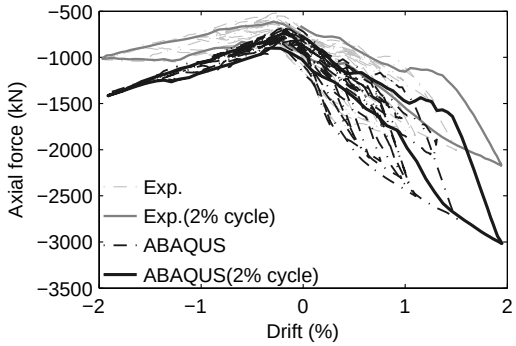

(a) TB: Middle section

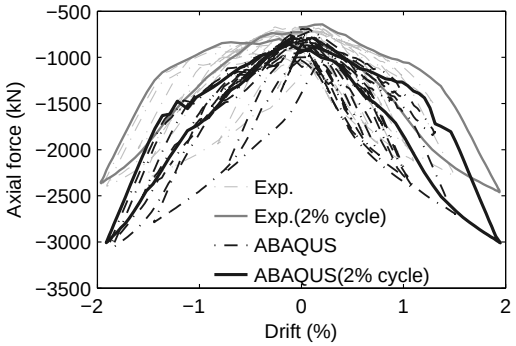

(b) MB: Middle section

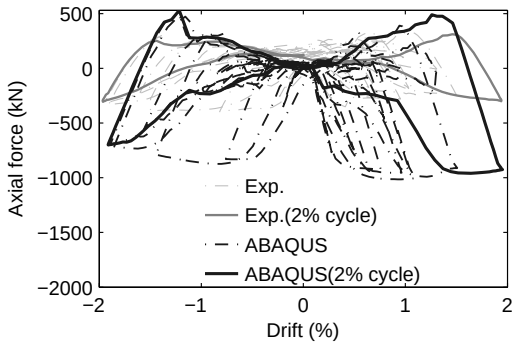

(c) BB: Middle section

Figure 7.40: Comparison of ABAQUS model and experimental (10/50 test) axial force vs. drift demands for certain locations in full-scale specimen beams

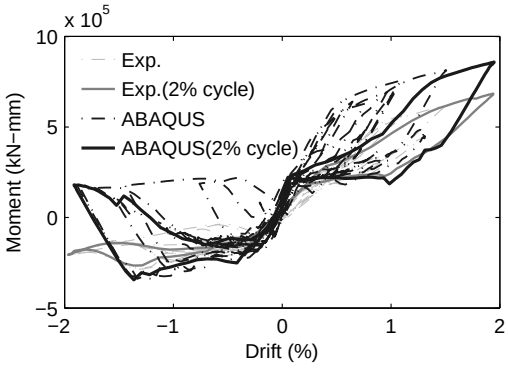

(a) TB: West section

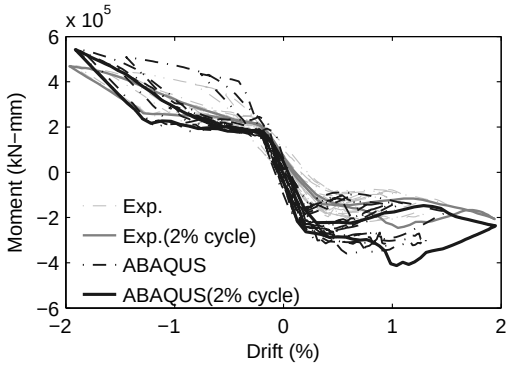

(b) TB: East section

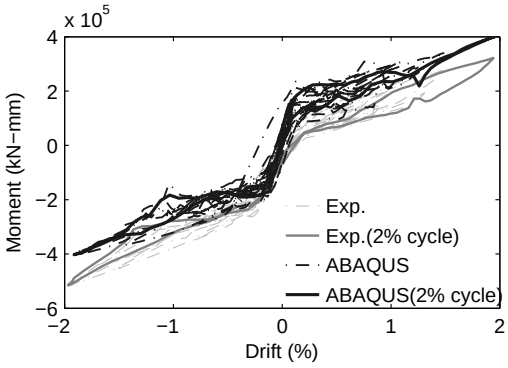

(c) MB: West section

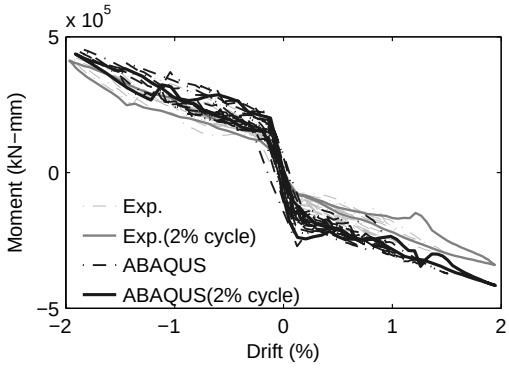

(d) MB: East section

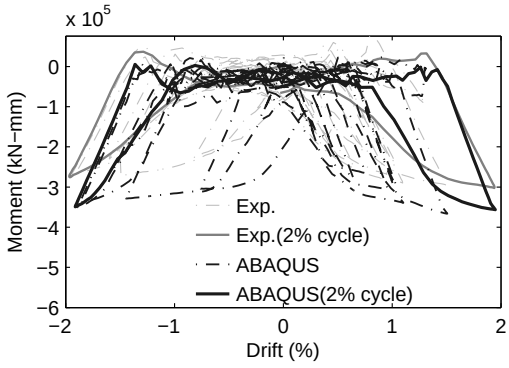

(e) BB: Middle section

Figure 7.41: Comparison of ABAQUS model and experimental (10/50 test) moment vs. drift demands for certain locations in full-scale specimen beams

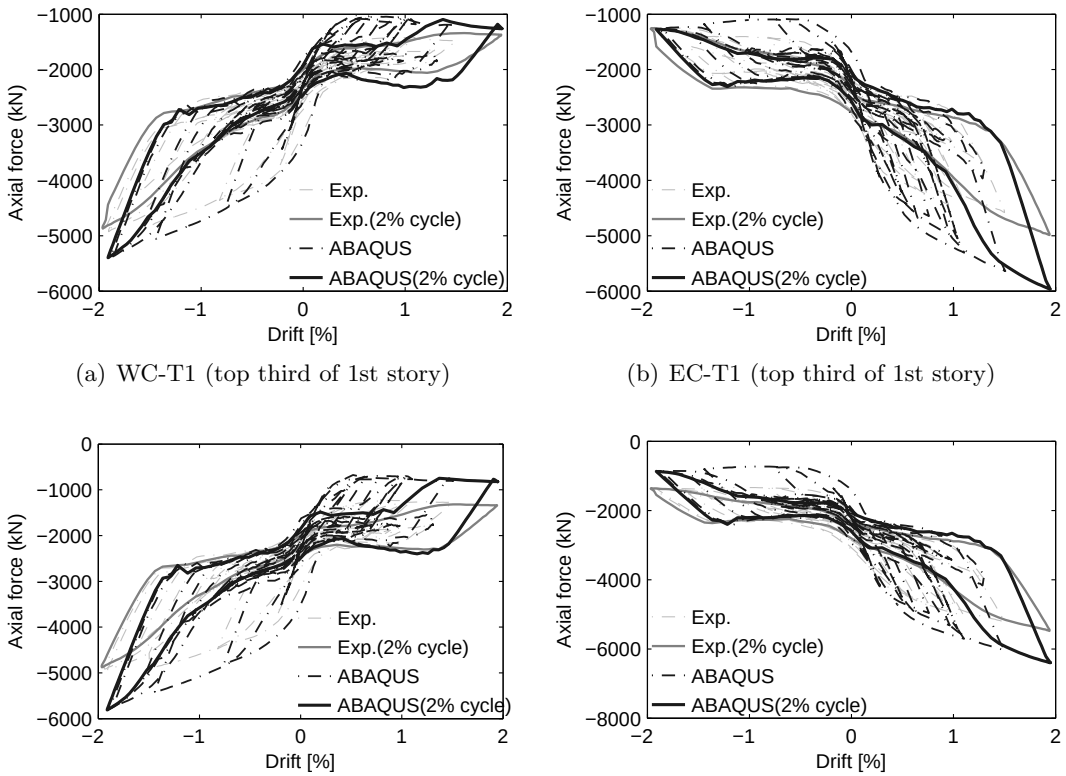

(a) WC-T1 (top third of 1st story)

(b) EC-T1 (top third of 1st story)

(c) WC-B1 (bottom third of 1st story)

(d) EC-B1 (bottom third of 1st story)

Figure 7.42: Comparison of ABAQUS model and experimental (10/50 test) axial force vs. drift demands for certain locations in full-scale specimen columns

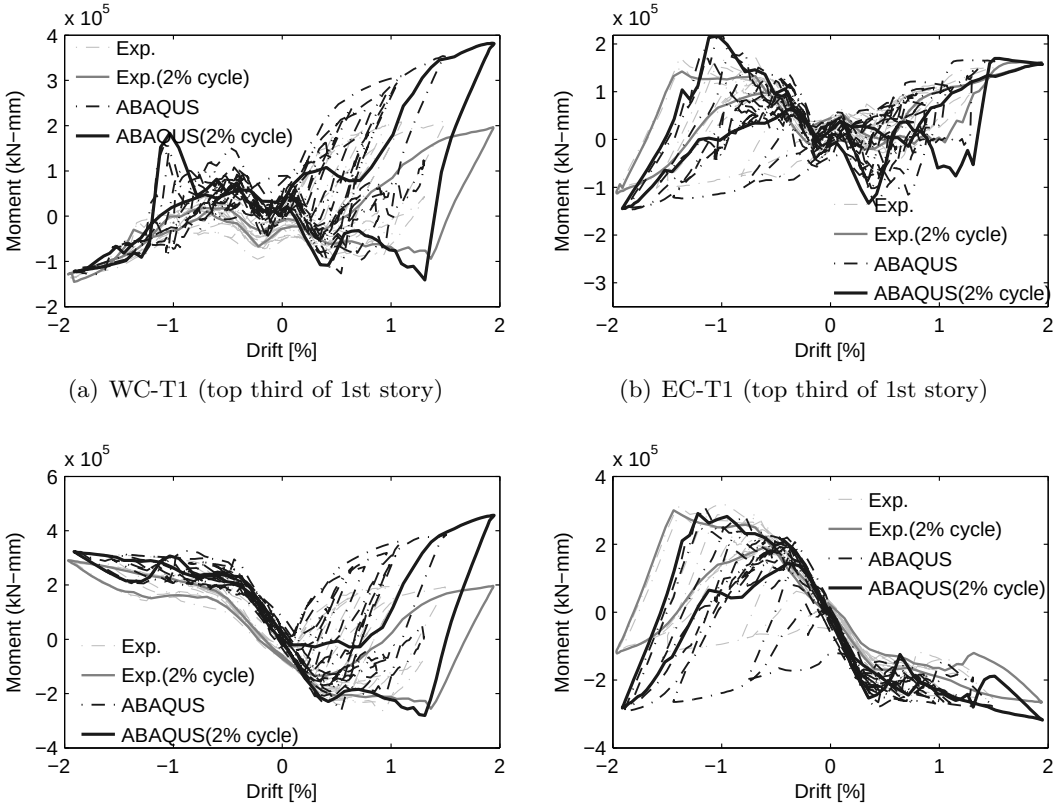

(a) WC-T1 (top third of 1st story)

(b) EC-T1 (top third of 1st story)

(c) WC-B1 (bottom third of 1st story)

(d) EC-B1 (bottom third of 1st story)

Figure 7.43: Comparison of ABAQUS model and experimental (10/50 test) moment vs. drift demands for certain locations in full-scale specimen columns

Figs. 7.44 and 7.45 show a comparison between the ABAQUS model and experimental PT force and gap rotation responses for the beams and columns, respectively. These figures show that the ABAQUS model over-predicts the PT forces for a given drift or rotation demand, which was very similar to the OpenSees numerical model. Because both the ABAQUS and OpenSees models used a simplified boundary frame model, the discprepencies between the numerical and experimental PT connection response are likely due to similar reasons as described previously in Sec. 7.2.5.2.

It should be noted that even with the discrepencies in the local component demands of the numerical model and the actual specimen, the global responses of both match well. And in most cases, the simplified boundary frame model used in the ABAQUS models result in conservative predictions of component demands.

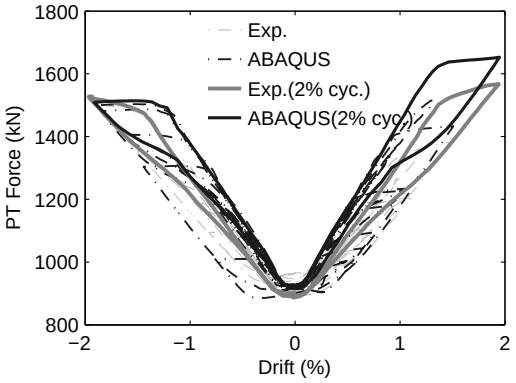

(a) MB: PT force vs. drift

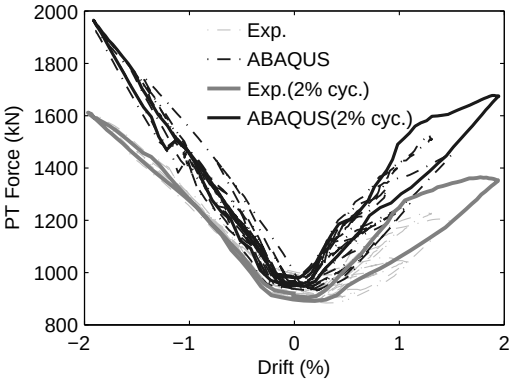

(b) TB: PT force vs. drift

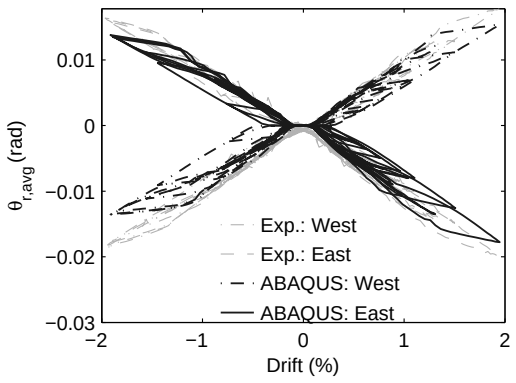

(c) MB: Gap rotation vs. drift

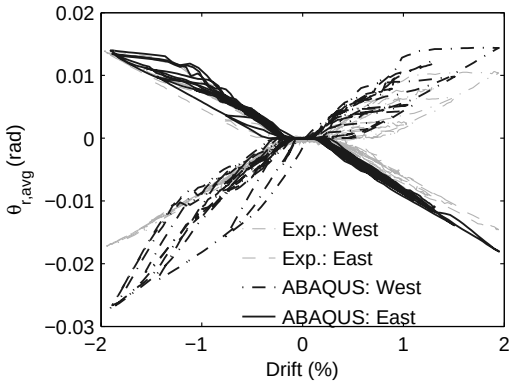

(d) TB: Gap rotation vs. drift

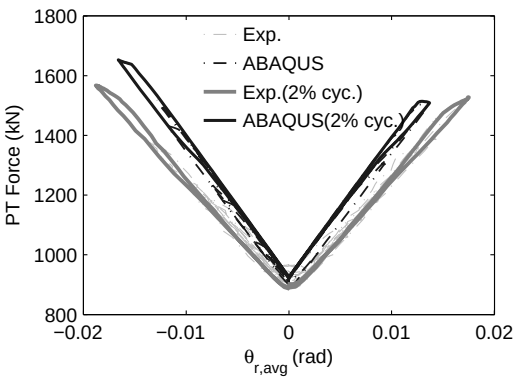

(e) MB: PT force vs. gap rotation

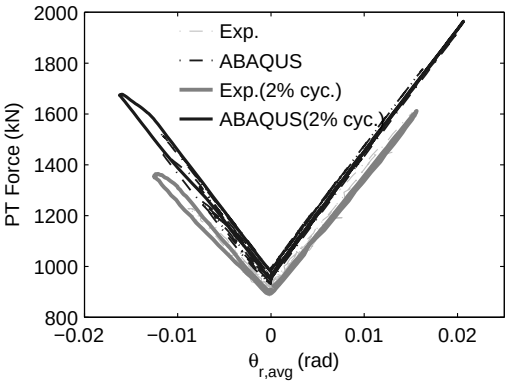

(f) TB: PT force vs. gap rotation

Figure 7.44: Comparison of ABAQUS model and experimental (10/50 test) responses of beam PT connections for full-scale specimen

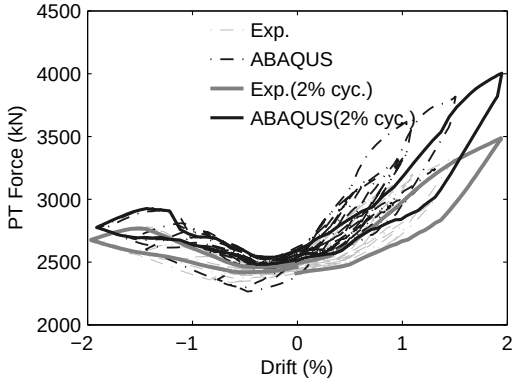

(a) WC: PT force vs. drift

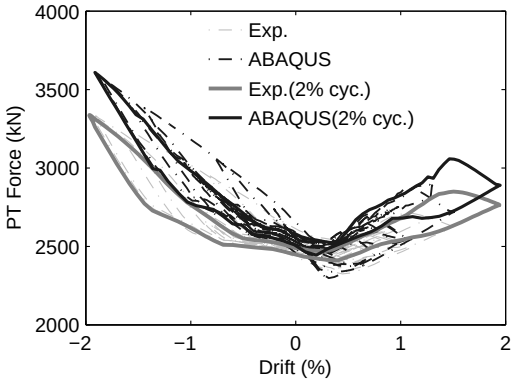

(b) EC: PT force vs. drift

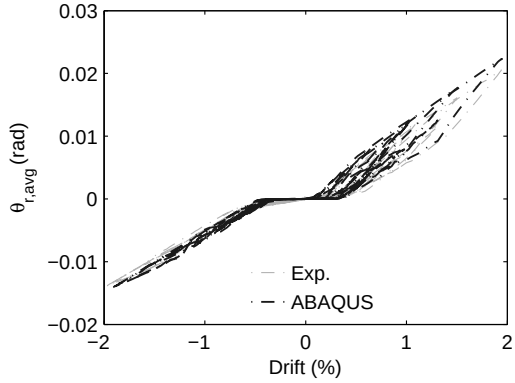

(c) WC: Gap rotation vs. drift

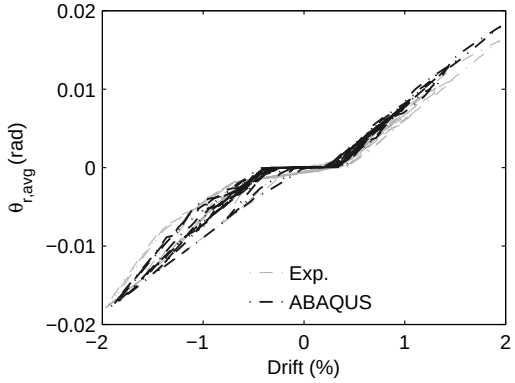

(d) EC: Gap rotation vs. drift

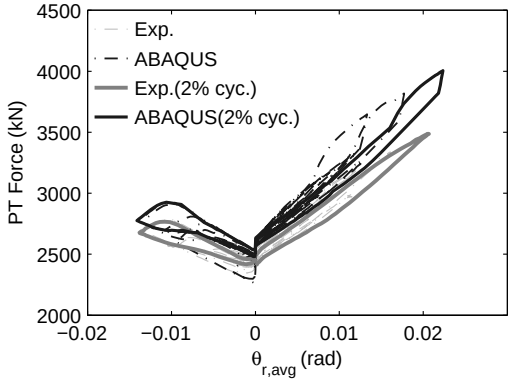

(e) WC: PT force vs. gap rotation

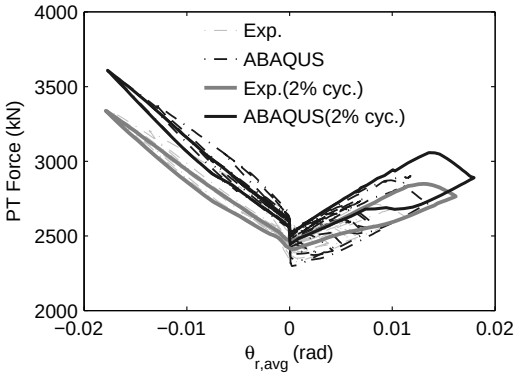

(f) EC: PT force vs. gap rotation

Figure 7.45: Comparison of ABAQUS model and experimental (10/50 test) responses of column base PT connections for full-scale specimen

7.3.3.3 Comparison with web plate damage

Web plate and weld tearing were not simulated in the ABAQUS model. Additionally, the mesh of the web plate was relatively coarse compared to the magnitude of web plate tear lengths in the 10/50 PSD test (approximate 10cm element edge length with maximum tear lengths of 12cm at the end of the 10/50 PSD test), making it difficult to compare local stresses, strains, and out-of-plane deformations close to the welds. The mesh size was selected based on the ABAQUS web plate model recommendations discussed in Webster [2013] and to produce a reasonable critical time step for explicit analysis to reduce the computation time. The main purpose of this model was to evaluate global and component strengths and demands, and simulation of local response was a secondary concern.

Even with the relatively coarse mesh near the web plate welds, the ABAQUS model was able to qualitatively show peak plastic strain demands in locations corresponding to those where web plate tearing was first observed. Experimental observations (Chapters 4 and 5) suggest that web plate tearing was due to low-cycle fatigues as the web plate undergoes significant strain demands during formation and reformation of the tension field in multiple cycles of loading. For this reason, the cumulative equivalent plastic strain (PEEQ) is used as a scalar representation of the amount of plastic deformation the element has undergone. The PEEQ parameter is calculated in ABAQUS as

$$PEEQ = \int_0^t \sqrt{\frac{2}{3}\epsilon_{ij}^{pl}\epsilon_{ij}^{pl}}dt \tag{7.6}$$

where PEEQ is integrated over the full time or displacement history, t, and ϵ_{ij}^{pl} is the plastic strain components summation over the three i, j=1,2,3 directions.

Figs. 7.46 and 7.47 show the PEEQ contours, plotted on the deformed shape, in two areas where web plate tearing was observed during the 1050N1 observation point (see Fig. 5.31(a)). Fig. 7.46 shows the upper-west corner of the first story web plate, while Fig. 7.47 shows the lower-east corner of the first story web plate (both are shown as if looking from the south side of the specimen). These figures also show photos of the web plate tearing observed in those locations with approximate tear lengths indicated. These can be compared qualitatively to

the PEEQ concentrations. For comparison, the element edge lengths in the ABAQUS plots are approximately 10cm.

If localized stresses and strains near the welds were to be investigated in more detail, the model should have a much finer mesh near the welded connection (with element lengths on the order of the observed local deformations such as the out-of-plane bending of the plate shown in Fig. 5.39). Also, because out-of-plane deformation due to buckling appears to be a driving factor in initiation of web plate tearing, the web plate and weld material along the welded connection should be modeled with solid elements to better capture the additional strains associated with out-of-plane flexure (and the solid elements should be appropriately tied to the shell elements at the transition). If a dynamic explicit analysis of the full-scale specimen was done, accurate simulation of localized (i.e. element lengths on the order of millimeters and centimeters) response would require extremely long run-times.

7.4 Preliminary Results for Model WP

Model WP is a newly developed web plate strip material implemented in OpenSees to provide a more accurate simulation of web plate behavior [Webster, 2013]. The material behavior was discussed previously in Sec. 7.2.2.3. This section will present preliminary results comparing Model WP to experimental test and ABAQUS results. Here, the global response will be the focus of discussion as changes in the web plate strip material did not appear to have a significant effect on maximum HBE or PT demands in the OpenSees models.

7.4.1 Comparison with experimental results

Fig. 7.48 shows the force vs. drift response of Model WP and the test results for subassembly specimens W18-6s75k20Ga, W14-6s75k20Ga, and W14-8s100k20Ga. Unlike the previous OpenSees models, the numerical models were subjected to the same displacement histories as the specimens up to a drift of approximately 3%, because the web plate strain hardening in Model WP is history dependent (unlike Models TO and TC). The cycle at 2% drift for both the experiment and the numerical simulation are hilighted for better comparison of single-cyle response.

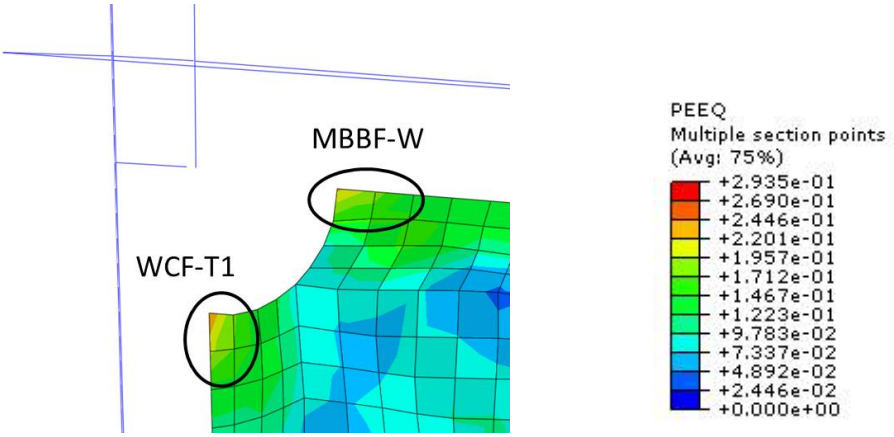

(a) PEEQ contours

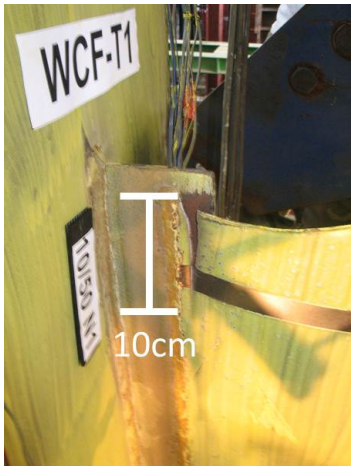

(c) Photo along WC

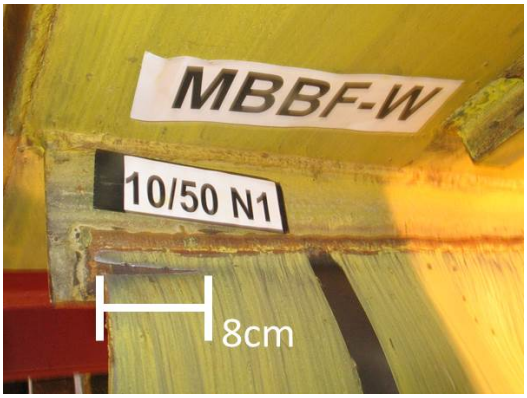

(d) Photo along MB

Figure 7.46: PEEQ and corresponding tearing in upper-west corner of 1st story web plate at 1050N1

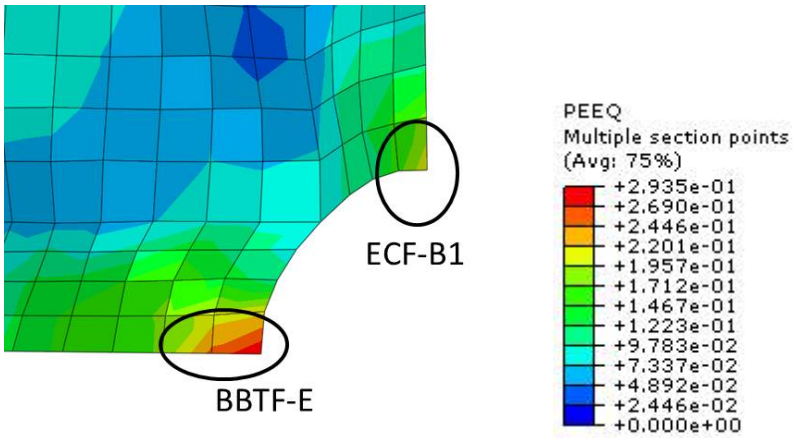

(a) PEEQ contours

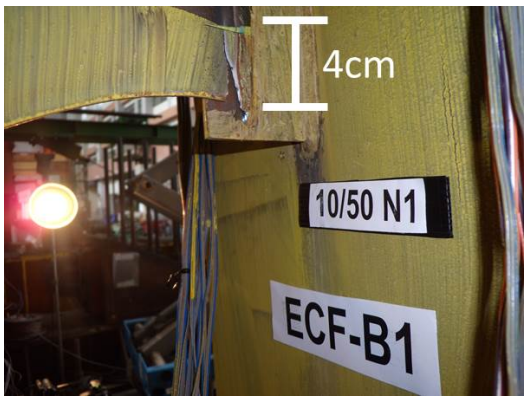

(c) Photo along EC

(d) Photo along BB

Figure 7.47: PEEQ and corresponding tearing in lower-east corner of 1st story web plate at 1050N1

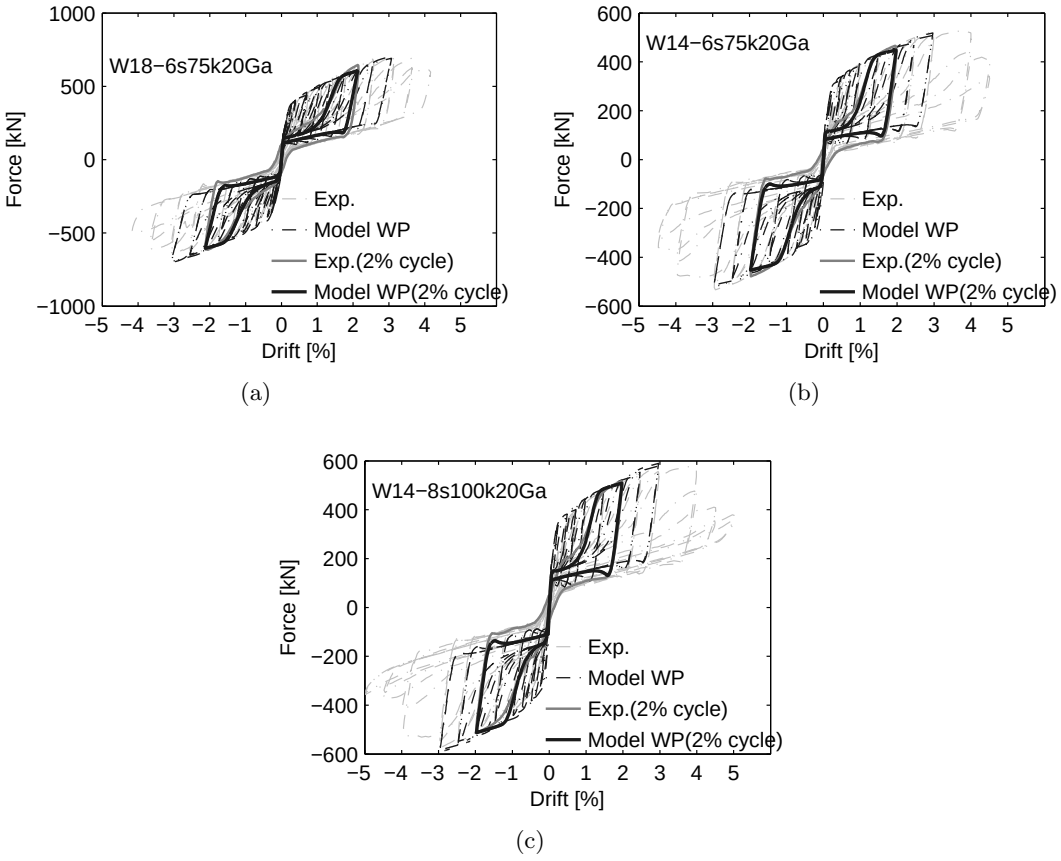

Figure 7.48: Comparison of specimen (a) W18-6s75k20Ga, (b) W14-6s75k20Ga, and (c) W14-8s100k20Ga response with SPSW web plate (Model WP) strip model responses

Fig. 7.48 shows that Model WP better captures the yield envelope compared with Models TO and TC (Figs. 7.11(a) and 7.11(b)). The better approximation of the yield envelope is due to Model WP accounting for an increased rate in strain hardening associated with plastic contraction perpendicular to the tension field.

Also unlike Models TO and TC, Model WP has an unloading snap-through and tension reloading strength that is dependent upon geometric parameters of the plate and the plate drift history. Although it appears that Model WP is able to accurately capture the snap-through strength of the web plate immediately upon unloading, it seems to slightly underestimate the residual strength of the web plate as shown in Fig. 7.48, particularly for the subassembly specimens. The underestimation of the asymptotic residual strength in Model WP may be due to the fact that the large aspect ratio (L/h) of these specimens is outside of the range of those allowed in SPSW design and outside of the range for which the web plate material model was calibrated [Webster, 2013]. Alternatively, the underestimation of the residual strength may be due to additional resistance in the web plate corner cutouts during unloading or due to the effects of frame expansion on the web plate that were not present in the SPSW web plate tests and simulations conducted by Webster [2013].

Model WP is also able to better capture the strain at which tension reloading occurs and better matches the reloading path of the web plate. The improvements in capturing web plate reloading better predict the cyclic energy dissipation compared to Models TO and TC. Model WP also overpredicts the specimen's initial stiffness due to non-idealized initial PT connection behavior that was not accounted for in the boundary frame model, as was described previously for the other ABAQUS and OpenSees models.

7.4.2 Comparison with ABAQUS model

Sec. 7.3.2.1 showed that the ABAQUS models were very accurate in predicting the global response of the SC-SPSW specimens. Additionally, Model WP was calibrated and validated in Webster [2013] with a broad set of experimental tests and ABAQUS simulations. The intent of Model WP was to accurately simulate web plate behavior with the accuracy of an (ABAQUS) shell model and with the computational efficiency of an (OpenSees) strip model;

therefore, Model WP response should be comparable to the response of the ABAQUS shell model.

Fig. 7.49 compares the force vs. drift response from Model WP, ABAQUS, and the experiment for subassembly specimen W14-8s100k20Ga. For clarity in comparing single cycle response, Figs. 7.49(b) through 7.49(d) show the glabal cycles for individual cycles at 1.5%, 2% and 2.5% drifts. The differences between the ABAQUS and Model WP responses are minor, although some of the differences are similar to those between the Model WP and experimental results. For example, Model WP predicts a slightly smaller web plate residual strength than ABAQUS possibly due to the reasons presented above for the experimental test comparison.

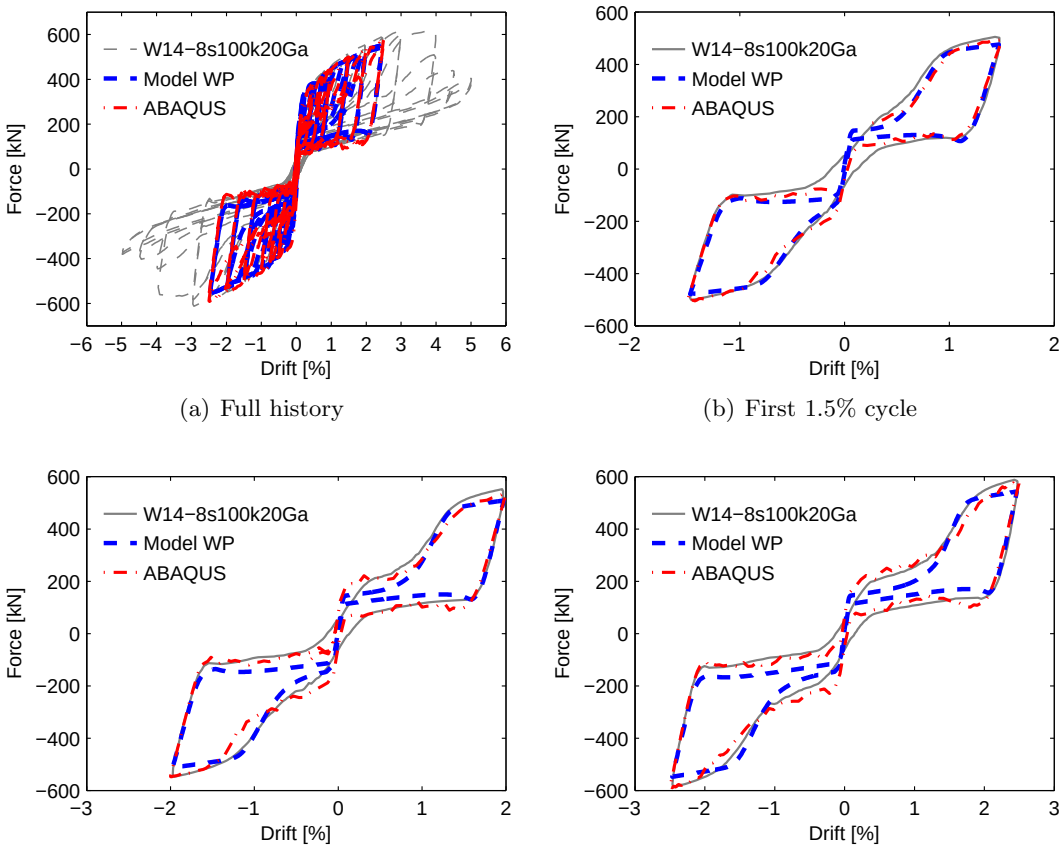

(a) Full history

(b) First 1.5% cycle

(c) First 2% cycle

(d) First 2.5% cycle

Figure 7.49: Comparison of experimental, Model WP, and ABAQUS force vs. drift response

These results indicate that Model WP provides an accurate approximation of web plate behavior. It offers improvements in capturing web plate strain hardening, residual strength, reloading strength, reloading strain, and energy dissipation compared to the previous tension-only and tension-compression strip materials. Although further work should be done testing and validating Model WP in a variety of SC-SPSW applications, these preliminary comparisons suggest improvements in simulating web plate behavior compared to previous web plate strip modeling methods.

7.4.3 Comparison of energy dissipation with Model TC

Sec. 7.2.6 showed that Model TC was able to reasonable predict peak drift demands in the full-scale pseudo-dynamic test even though it is known to under-predict web plate energy dissipation early in the ground motion (due to web plate reloading occurring at the previous peak strain) and it is known to over-predict energy dissipation during the smaller cycles at the end of or following a ground motion (due to the assumption of constant web plate residual strength). Model WP, considered a more accurate albeit more complex strip material model, was developed to account for the larger web plate energy dissipation associated with earlier tension reloading and to account for the decrease in energy dissipation associated with decreasing web plate residual strength as the oscillations become smaller. To assess the accuracy of Model TC in predicting the energy dissipation in the web plate, the energy dissipation in a single strip of Model TC and Model WP are compared for the same strain history.

The strip strain history was taken from the full-scale pseudo-dynamic tests as approximately one-half of the drift demand (based on assumed tension field angle of 45°) as shown in Fig. 7.50(a). Here, all the pseudo-dynamic tests were appended sequentially to create one long time history. The vertical dashed lines separate the excitations at different hazard levels. The two example strips (Model TC and Model WP) had material properties based on the same web plate coupon data and were defined as outlined in Sec. 7.2.2. The resulting stress vs. strain response for each strip material is shown in Fig. 7.50(b). The dissipated strain energy (i.e. the area under the stress vs. strain plot) for each material is shown in

Fig. 7.50(c). This figure shows that at the end of the 10/50 test both materials have nearly equal cumulative strain energy dissipation, although Model WP tends to accumulate more energy dissipation earlier in the ground motion, while Model TC "catches up" towards the end of the ground motion, due to reasons described above. This indicates that Model TC provides a reasonable approximation of cumulative energy dissipation. However, because Model WP does dissipate more energy early in the motion, it is possible this could reduce peak drift demands (i.e. result in a strain history different from Model TC) in a dynamic analysis.

Fig. 7.50(c) also shows that the energy dissipation in Model TC during the 2/50 motion is greater than that of Model WP. This is likely due to the fact that the 2/50 test was conducted following the 10/50 test such that the web plates had initial plastic strain prior to the excitation. Therefore, Model TC overestimates energy dissipation in these post-yield 2/50 cycles due to the assumption of constant web plate residual strength, similar to how it does during free vibration cycles. However, in real earthquakes the web plate is expected to be elastic prior to the ground motion, and the energy dissipation characteristics are expected to be similar those observed in the 10/50 test (because energy dissipation and web plate yielding in the 50/50 excitation was negligible representing an essentially elastic web plate prior to the 10/50 event).

7.5 Summary of Numerical Models and Recommendations

7.5.1 Summary of Numerical Models

Numerical models of various complexity were used to simulate SC-SPSW behavior. Due to the predictable bilinear elastic response of the PT boundary frame, each model utilized a stick-element boundary frame model with nonlinear springs to simulate the rocking PT connection behaviors as described in Sec. 7.2.1.1. The different numerical models employed different web plate models. The web plate models, in order of increasing complexity, were:

1. Tension-only strip model (Model TO), which is commonly used in practice and is suggested in Sabelli and Bruneau [2007]. (employed in OpenSees)

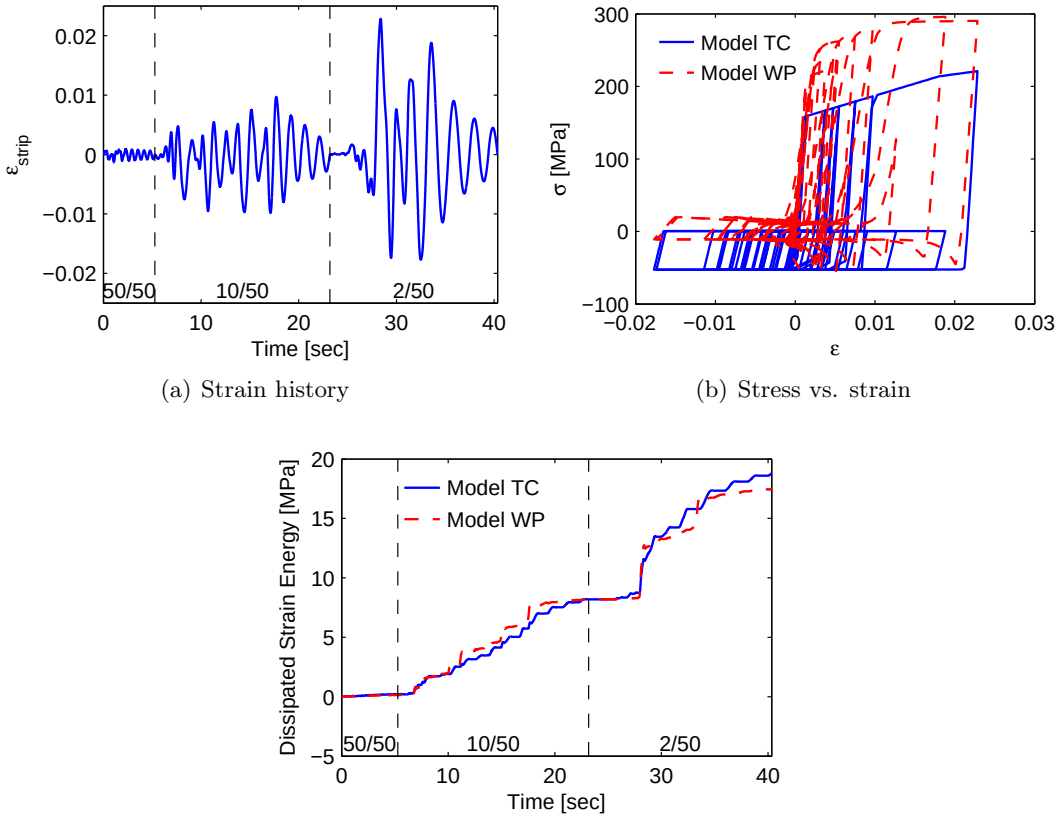

(a) Strain history

(b) Stress vs. strain

(c) Strain energy dissipation

Figure 7.50: Comparison of Model TC and Model WP strip response

2. Tension-compression strip model (Model TC), where compressive resistance is added to the tension strip according to the estimated web plate residual strength as a function of web plate aspect and slenderness ratios [Webster, 2013]. (employed in OpenSees)

3. SPSW web plate uniaxial material strip model (Model WP) developed by Webster [2013] to capture the complex reloading, snap-through, residual strength, and strain hardening aspects of web plate panels as functions of web plate aspect and slenderness ratios and drift histories. (employed in OpenSees)

4. Shell web plate model (Shell model), where the web plate is modeled as a continuum with shell elements that buckle and develop tension field action. (employed in

ABAQUS)

None of the web plate models simulated tearing or subsequent web plate strength degradation. Strength properties of the web plate models were based on web plate monotonic tensile coupon test data.

The following observations were made about the different modeling techniques:

- The stick-element **boundary frame** and nonlinear spring PT connection models were able to accurately capture the bilinear elastic response of the bare PT frame subassembly tests (Fig. C.1(a)). The PT frame model did over-predict the initial stiffness due to the assumption of connections acting as fixed connections prior to decompression, which was not observed in the physical test specimens where uneven flange bearing surfaces allowed for some connection rotation upon initial loading.

- Models TO and TC simulate similar **web plate backbone strengths** by intent and slightly underestimate the backbone strength of the test specimens. This is attributed to the inability of the models to simulate accumulation of plastic strain that occurs in the test specimen due to plastic contraction normal and cyclic tensile loading to the direction of the tension field. Due to the continuum nature of the real web plate, the plastic strain accumulation is dependent on the drift history [Webster, 2013], which is not simulated in the simple TO and TC strip models. Model WP and the Shell Model simulate this phenomenon and thus better match the experimental backbone strengths.

- Model TO does not simulate **web plate residual strength**. In this simple model, the web plate is assumed to have negligible strength upon unloading and reloading to the previous peak plastic strain. This idealized behavior results in significantly less energy dissipation than an actual web plate and provides no energy dissipation during cycles of loading less than the previous peak drift.

- Model TC was able to capture the **reload and unload strengths** of the SC-SPSW subsassembly specimens under cyclic loading to increasing drift demands. Model TC

was able to capture the lower-bound unload strength and stiffness for the full-scale specimen; however, it did not capture the reduction in web plate residual strength that occurred in smaller cycles of loading following the peak drift demands (e.g. during free vibration). Model TC underestimated the web plate energy dissipation and reloading stiffness (i.e. the stiffness at lower drift demands during reloading) for both the subassembly and full-scale specimens due to the assumption that tension reloading only occurs after reaching the previous peak plastic strain.

- Model WP was able to better capture the **reloading and unloading path** of the SC-SPSW specimens. Model WP slightly underestimated the residual web plate strength for the subassembly specimens, which may be due to the fact that the high aspect ratio (L/h=2.4) of the subassembly specimen panels was outside of the range for which the web plate strip material model was calibrated. However, Model WP was able to capture the unloading snap-through response of the plate that was visible in the tests but was ignored in other strip models (Models TO and TC).

- The Shell model force vs. drift responses matched well with the subassembly and full-scale test specimens. It was able to capture the **reloading and unloading paths** well and was able to simulate the decrease in web plate residual strength as observed during free vibration in the full-scale pseudo-dynamic test. However, the computational time required to run the Shell model was orders of magnitude longer than the time required to run the same displacement history for the OpenSees strip models.

- The **HBE moment and axial force demands** (and VBE axial and force demands from the full-scale model) from each of the numerical models matched well with those measured from strain gages on the experimental specimens. The different web plate strip models did not have a significant impact on the peak demands in the HBE or their distribution. The Shell Model did have a slight impact on the demand distribution, especially near the ends of the HBE at the web plate cutouts; however, the magnitudes of the demands were still similar to those of the strip models and experi-

mental specimens. In some cases, the numerical models did slightly overestimate the demands determined from the strain gages on the specimens; however, this difference was reasonable and conservative.

- All of the numerical models slightly overestimate the PT force demands measured during both the subassembly and full-scale tests. This overestimation was conservative and likely due to to ignoring axial flexibility in the PT anchorage system, using manufacturer-provided elastic modulus information for the PT strands, and conservative assumptions of PT frame rocking points.

- The Shell Model was able to accurately simulate the global response and component demands for the subassembly specimen with **web plates connected to the HBEs only**. The strip models (Models TO and TC) provided reasonably accurate simulation of component demands and global backbone strengths. While Model TC was able to simulate some of the residual web plate strength upon unloading, it underestimated the residual strength as the strip model only considered the resistance of the portion of the web plate contributing to the partial tension field. The Shell Model was better able to capture the specimen's unloading strength, and the compressive resistance of the full plate was considered.

7.5.2 Modeling Recommendations

Below are recommendations for the best applications for each modeling approach:

- Model TO is desirable for design in estimating SC-SPSW peak strength, component demands, and recentering stiffness. The tension-only strip model has been the preferred method of SPSW web plate modeling for decades [Sabelli and Bruneau, 2007] and can be implemented in most commercially-available software. Recent research [Webster, 2013] has shown that web plates undergo more strain hardening, due to the continuum nature of web plates, that is ignored in the tension-only strip model; therefore, the designer may wish to use an amplification factor for modeling the web plate peak strength according to recommendations provided in Webster [2013]. This

modeling approach may be used for dynamic analyses; however, because the tension-only strip underestimates web plate energy dissipation, dynamic analyses may result in conservatively large drift demands. Because the web plate does respond in an essentially tension-only mode during small cycles following peak drift demands (i.e. during free vibration), the tension-only strip could be expected to provide reasonably accurate predictions of post-event response (e.g. recentering drifts).

- Model TC, like Model TO, is appropriate for determining peak strength, component demands, and recentering stiffness for design, making it the preferred approach to modeling web plate behavior. Additionally, Model TC also has the ability to be easily implemented in commercially-available analysis software. If the compression component of the tension-compression strip is appropriately modeled, Model TC has the added benefit of predicting the lower-bound strength during SC-SPSW unloading, which is important for estimating the maximum potential residual drift from static analyses (i.e. the drift at zero-load). Model TC is also appropriate for simulating quasi-static cyclic tests, as the model predicts the constant web plate residual strength observed in lab tests. However, Model TC does not capture some key features of observed response, including reloading at a plastic strain smaller than the peak unloading strain and the accumulation of strain hardening due to normal plastic contraction of the web plate. Model TC is appropriate for dynamic analyses as the additional energy dissipation in the material model (in comparison with Model TO) produces reasonable approximations of peak drift demands. Although the assumption of a constant web plate residual strength overestimates the amount of energy dissipation in later cycles, this typically occurs after peak drift demands occur and could be expected to provide conservative overestimates of residual drifts.

- Model WP better estimates reloading response (including the reloading stiffness and strain at which tension reloading occurs) and strain hardening of the web plate, both of which can greatly impact SC-SPSW strength and energy dissipation in dynamic analyses. Model WP is more computationally expensive and requires a full displace-

ment history to predict demands under certain loads. Due to the material model complexity, it may not be as numerically robust as Model TO and TC. Currently, this strip material model is only available in the OpenSees framework; however, the C++ source code is provided in the open-source framework and could be modified for use with other structural analysis software packages. While this model is not necessary for design purposes, it provides accurate simulation of dynamic SC-SPSW behavior with a moderate increase in computational demand.

- The shell model is the most computationally expensive of all the models presented here. Because the previous strip models can accurately simulate static cyclic and dynamic responses, the shell model is only recommended for use when detailed stress and strain concentrations in the web plate or PT connections (if frame members are modeled using shell elements) are desired. For example, if a designer is looking at web plate cutout details to mitigate strain concentration and damage in the web plate or is investigating the effects of local buckling, shear lag, or localized yielding in the (shell-based) PT connection regions, this modeling approach be desirable.

7.5.3 Future improvements

Although each of the modeling methods studies was able to adequately capture the SC-SPSW response with varying levels of accuracy, there are some improvements that can be made given additional experimental and numerical investigation:

- In these models, PT anchorage is simulated as "fixed". There is some flexibility in the PT anchorage system that can be incorporated into the model. Most importantly, proper simulation of PT losses due to anchorage seating should be simulated to capture PT frame strength degradation over long duration and severe shaking. PT losses can be modeled by incorporating gap spring elements at the PT anchorage nodes to simulate PT loss and anchorage seating. Further experimental investigation is required to better understand the magnitude of PT losses for a wide range of load histories, PT lengths, PT stressing procedures, and anchorage types.

- All of the web plate models ignored web plate tearing and associated strength degradation. Extensive finite element numerical simulations should be conducted to understand the tensile and out-of-plane flexure strains in the web plate near the fish plate connection and correlate these to occurrences of web plate tearing. Because the occurrence of tearing is highly dependent on the type of connection (e.g. bolted vs. welded, thin web plate "roll-over bead" weld vs. thicker plate fillet weld, etc.), the experimental studies used to calibrate a web plate tear degradation model should be conducted on full-scale web plate connection details that are typically employed in practice. Furthermore, unlike conventional SPSWs where the web plates are essentially welded all the way around, SC-SPSW web plates have a larger susceptibility to tearing due to out-of-plane bending at the unrestrained corner cutout edge. Therefore, studies investigating web plate tear models for SC-SPSWs should also incorporate this out-of-plane deformation demand at the web plate connection.

- A shell model of PT boundary frame can be incorporated into the ABAQUS model to investigate local stress concentrations near connections that are not captured in beam-column elements (e.g. local flange buckling, shear lag, web crippling/yielding, etc.). This may be used to inform better connection detailing and reinforcement practices.

Chapter 8

NUMERICAL INVESTIGATION OF BUILDING RESPONSE

8.1 Introduction

Clayton [2010] presented a numerical proof-of-concept study investigating SC-SPSW seismic performance of SC-SPSWs to verify that the system was able to meet proposed performance objectives. This numerical study focused on 3- and 9-story buildings in the Los Angeles, California area with SC-SPSWs fully connected to the HBEs and VBEs. In this study, the web plates were modeled using the tension-only strip method suggested in SPSW design guidelines [Sabelli and Bruneau, 2007]. The numerical study presented in this chapter builds upon this previous proof-of-concept study to further investigate SC-SPSW performance, including the effects of connecting the web plates only to the HBEs and the effects of including web plate residual strength in the model. The tension-compression (TC) model was selected from those investigated in the previous chapter as the most appropriate model for simulating the effects of web plate residual strength with numerical robustness and efficiency. Thus, the TC model will be used in the analyses presented in this chapter. Most of the analyses presented in this chapter were complete using computational resources on the Open Science Grid [Pordes et al., 2007].

Experimental and analytical investigation suggested that connecting the web plates to the HBEs only may delay web plate tearing (Sec. 4.3.7) and may reduce column demands (Sec. 3.2), resulting in more ductile and economic designs. To evaluate the seismic performance and potential for cost savings, several SC-SPSWs with web plates connected only to the HBES were designed to have strengths equal to the fully-connected web plate prototype SC-SPSWs presented in Clayton [2010]. The boundary frame member sizes are compared. Nonlinear response history analyses of these HBE-only SC-SPSWs are conducted using the same tension-only strip method assumed in Clayton [2010] for direct comparison of key seismic response parameters.

The experimental subassembly tests also suggested that the web plate residual strength can be a significant portion of the yield strength (Sec. 6.3.2). Later pseudo-dynamic testing suggested that the magnitude of the residual web plate strength is largest during early cycles of loading and decays as the oscillatory response decays to smaller drift values (Sec. 5.5). To investigate the effects of the residual strength in SC-SPSW response, nonlinear response history analyses were conducted using web plate strip models incorporating varying degrees of compressive strength. These analyses were conducted for SC-SPSWs with both fully-connected and HBE-only connected web plates for comparison with the previous tension-only web plate responses. The results of each of these numerical studies on web plate connectivity and web plate residual strength will be presented in this chapter.

8.2 Prototype Building

The prototype buildings presented in Clayton [2010] serve as the basis for the numerical study presented here. Below the design parameters, member sizes, and critical response parameters for the prototype SC-SPSWs investigated in Clayton [2010] are summarized. This information is provided for direct comparison with the following numerical investigations. Further details on the original prototype designs and seismic response can be found in Clayton [2010].

8.2.1 Building and site information

The prototype building is based on the 3- and 9-story SAC buildings located near Los Angeles, California [Gupta and Krawinkler, 1999], representing some of the largest seismic hazards in the U.S. The target response spectra values for the 50%, 10%, and 2% in 50 year hazard levels are shown in Table 8.1. The buildings had assumed story heights of 3.96m, with plan dimensions, seismic masses, and loading equivalent to those of the SAC buildings. The SC-SPSW bay width was assumed to be 4.57m.

Table 8.1: Response Spectra Values (in units of g) for Site Class D for 5% Damping Level in Los Angeles area (from Somerville et al. 1997)

	Period (sec)	
Hazard Level	0.3	1.0
2% in 50 year	1.610	1.190
10% in 50 year	1.070	0.680
50% in 50 year	0.510	0.288

8.2.2 SC-SPSW designs and member sizes

The SC-SPSW designs that resulted from implementation of the performance-based design procedure described in Clayton [2010] are shown in Tables 8.2 and 8.3 for the 3- and 9-story buildings respectively. The naming convention for the SC-SPSW designs is the number of stories ('3' or '9'), followed by the web plate design methodology ('5050' represents web plates designed to remain elastic under 50/50 demands, and '1050' represents web plates designed to resist the code-based reduced design forces, $V_{10/50}/R$[1], where the response modification factor, $R = 7$, was assumed), followed by the number of SC-SPSWs in each direction of the building. For this study, the web plates were designed to resist the entire story shear (i.e. without considering additional strength from the boundary frame), and the web plate thicknesses were chosen from commonly available thicknesses of ASTM A36 steel. The PT strands were assumed to be 13mm (0.5in) diameter, Grade 270, seven-wire strands. For design 9-5050-10, built-up column box sections were required to resist the capacity design forces. The column sizes are given in Table 8.3 as the outer box dimensions (e.g. 610mmx6110mm) followed by the plate thickness (e.g. 51mm), all in units of mm. All boundary frame members were assumed to be made of Grade 50 steel.

8.2.3 Results of nonlinear response history analyses using tension-only strips

The numerical models assumed pinned connections at the column bases and included two P-Delta columns, located on each side of the SC-SPSW, to simulate the effects of gravity

[1]For the Los Angeles location, the 10/50 spectral acceleration is approximately equal to the 2/3MCE design-level spectral acceleration.

Table 8.2: Design parameters for 3-story prototype designs [Clayton, 2010]

Name	Story	t_w (mm)	T_o (kN)	# of PT strands	HBE size	VBE size
3-5050-6	1	7.94	231	16	W24x229	W14x605
	2	6.35	503	12	W30x211	W14x605
	3	4.18	467	32	W36x302	W14x605
3-1050-4	1	3.18	356	24	W24x176	W14x342
	2	2.66	191	16	W24x117	W14x342
	3	1.90	703	20	W30x173	W14x342
3-1050-6	1	2.66	245	16	W24x131	W14x283
	2	1.90	178	12	W24x94	W14x283
	3	1.59	658	16	W30x148	W14x283

loads as the building sways. The PT connections were simulated using the same methods presented in Sec. 7.2.1, and the web plates were simulated using the tension-only strip method (Model TO). Each model was subjected to the suite of sixty ground motions developed as part of the SAC project [Somerville et al., 1997] for this building site. The suite contains twenty ground motions at each seismic hazard levels considered in the design: 50%, 10%, and 2% in 50 year (50/50, 10/50, and 2/50, respectivly). The motions were scaled by Somerville et al. [1997] such that on average they match the spectral parameters in Table 8.1 with weighting factors as described in FEMA [2000a].

Some of the key response parameters that were used to evaluate seismic performance were the peak story drift, $\theta_{s,max}$, maximum story residual drift, $\theta_{resid,max}$, and HBE and VBE demand-capacity ratios, D_{HBE} and D_{VBE}, which were taken as the evaluation of the interaction equations per *AISC Specifications* Eqn. H1-1 [AISC, 2005a]. Recenetering was established as residual drifts less than 0.2%. The response parameters for each of the tension-only SC-SPSW models considered in this study [Clayton, 2010] are given in Appendix F. Table F.1 shows the statistical results (median, $\mu_{1/2}$, and 84th percentile) for the three hazard levels for the maximum story drift, maximum residual story drift, and the HBE and VBE damage values. In this table, the model name has been appended with '-TO' to signify that it employed the tension-only strip model (Model TO). Figs. F.1 through F.4 (taken from Clayton [2010]) show the median and 84^{th} percentile response for each of these

Table 8.3: Design parameters for 9-story prototype designs [Clayton, 2010]

Name	Story	t_w (mm)	T_o (kN)	# of PT strands	HBE size	VBE size
9-5050-10	1	11.11	565	22	W30x357	610x610x127
	2	9.53	516	18	W30x292	610x610x127
	3	9.53	449	16	W30x292	610x610x127
	4	9.53	458	20	W24x279	610x610x127
	5	9.53	369	16	W24x279	610x610x76
	6	7.94	289	14	W24x229	610x610x76
	7	6.35	200	10	W24x192	610x610x51
	8	5.31	752	16	W24x192	610x610x51
	9	3.42	939	30	W30x292	610x610x51
9-1050-6	1	6.35	867	34	W33x354	W36x800
	2	6.35	859	30	W30x292	W36x800
	3	6.35	761	26	W30x261	W36x800
	4	6.35	641	24	W30x261	W36x800
	5	4.76	534	20	W30x211	W36x487
	6	4.76	489	22	W24x192	W36x487
	7	4.76	338	16	W24x162	W36x395
	8	3.18	178	12	W24x117	W36x395
	9	2.66	907	26	W30x211	W36x395
9-1050-8	1	4.76	734	26	W30x261	W14x730
	2	4.76	658	24	W30x235	W14x730
	3	4.76	583	20	W30x211	W14x730
	4	4.76	592	24	W24x207	W14x730
	5	3.42	494	20	W24x162	W14x500
	6	3.18	383	16	W24x131	W14x500
	7	3.18	262	12	W24x117	W14x500
	8	2.66	663	10	W24x117	W14x500
	9	1.59	463	16	W30x148	W14x500
9-1050-10	1	3.42	601	22	W30x211	W14x730
	2	3.42	538	18	W30x191	W14x730
	3	3.18	569	24	W24x176	W14x730
	4	3.18	485	20	W24x176	W14x500
	5	3.18	405	16	W24x131	W14x500
	6	2.66	307	14	W24x131	W14x500
	7	2.66	271	16	W18x106	W14x426
	8	1.90	227	10	W18x76	W14x426
	9	1.59	596	16	W30x132	W14x426

response parameters for each of the three seismic hazard levels. The response parameters are shown for each story to indicate how the response varies up the height of the building.

The results of the nonlinear response history analyses on SC-SPSWs using tension-only strip web plate models with fully-connected web plates are summarized below (taken from Clayton [2010]):

- Buildings designed to meet the enhanced performance objective 2 (designed using $V_{50/50}$) were able to meet all performance objectives.

- Performance of buildings not designed to meet performance objective 2 (designed using $V_{10/50}/R$) varied depending on building height. The 3-story SC-SPSWs had significantly larger story drifts than the 9-story buildings, were not able to meet the 2% code-based drift limit in the 10% in 50 year earthquake, meant to represent the DBE, and had cases of structural collapse in the 2% in 50 year earthquake. The 9-story SC-SPSWs were able to meet the 2% code-based drift limit and no cases of structural collapse were observed.

- There were no cases of PT yielding in the 10% in 50 year earthquakes, and all buildings were able to recenter at this hazard level. For buildings designed using $V_{10/50}/R$, although there were cases of recentering at the 2% in 50 year hazard level, PT yielding was observed in 20% to 50% of the ground motions. For these buildings, frame yielding was present in at least the 84th percentile, and for some models (3-1050-4 and 9-1050-6) at the 50th percentile.

- For buildings designed using $V_{10/50}/R$, story drifts at the 2% in 50 year hazard level were larger than the 4% limit assumed in the design procedure (at the median level for 3-story buildings and at the 84th percentile for 9-story buildings).

- Frame yielding was primarily observed at the first floor HBE-to-VBE connection, where demands are larger due to the fixity at the base of the VBE providing restraint against gap opening at this level.

- Varying the number of SC-SPSW bays did not have a significant effect on building performance, although buildings with lower number of bays did have less conservatively designed members due to the number of available sections with sufficient capacity, which lead to more cases of frame yielding in these buildings.

8.3 HBE-only Web Plate Connectivity Investigation

To investigate potential material savings associated with connecting the web plates to the HBEs only, the same prototype SC-SPSW buildings were redesigned assuming this web plate connectivity. The design assumptions and resulting designs are shown below for comparison with the fully connected web plate SC-SPSW designs. Nonlinear response history analyses of models of the HBE-only designs were conducted using the same methodologies of the Clayton [2010] study. The results are presented to better understand how variation of web plate connectivity may affect SC-SPSW performance.

8.3.1 Design process and assumptions

8.3.1.1 Web plate thickness

To facilitate direct comparison between the responses of the fully connected and HBE-only web plate models, the web plates in these HBE-only SC-SPSWs were designed to have the same lateral resistance as those in the previous study; therefore, the web plate thicknesses may not represent actual available thicknesses. Although connecting the web plates to the HBEs only does require thicker web plates to provide the same lateral strength, use of HBE-only web plates will reduce boundary frame demands, resulting in savings in boundary frame section sizes. The web plate thicknesses were determined based on the partial tension field length, L_{PTFA}, and angle of inclination, θ, of the web plates connected to the HBEs only. As each of these values depend on the web plate aspect ratio, L_{cf}/h_c, which may vary slightly for subsequent stories due to changes in HBE depth, the web plate thicknesses in the HBE-only designs may not be constant in subsequent stories as they were in some of the fully connected web plate designs (Table 8.3). The web plate material was assumed to be A36 steel.

The ratio of web plate thickness required in an HBE-only connected web plate to provide the same lateral strength as a fully connected web plate, $\beta_{web} = t_{w,HBE-only}/t_{w,full}$, can be determined based on the design lateral strength, V_n, equations provided for HBE-only and fully connected web plates in Eqns. (3.6) and (2.2), respectively.

$$\beta_{web} = \frac{t_{w,HBE-only}}{t_{w,full}} = \frac{L_{cf}\sin(2\alpha)}{L_{PTFA}\sin(2\theta)} \tag{8.1}$$

where, L_{cf} is the clear distance between VBEs and α (Eqn. (2.1)) is the angle of inclination for the fully-connected web plate, L_{PTFA} (Eqn. (3.2)) is the length of the partial tension field and θ (Eqn. (3.1)) is the angle of inclination of the HBE-only connected web plate, and the yield strength of both plates are assumed to be equal. For an assumed $\alpha = 43°$, β_{web} can be determined based on the web plate aspect ratio, L_{cf}/h_c as shown in Fig. 8.1. The *AISC Sesismic Provisions* [AISC, 2005a] limit SPSWs to aspect rations of 0.8 to 2.5. For common aspect ratios between 1 and 2, the thickness for HBE-only web plates would need to be approximately 1.5 to 2.5 times thicker than those for fully-connected web plates to provide the same lateral strength. For SC-SPSWs with wider bays (i.e. larger L_{cf}), the required increase in thickness for HBE-only web plates is less. Fig. 8.1 suggests that narrower bays (i.e. smaller L_{cf}/h_c) may not be as efficient for HBE-only web plate connectivity as they would require a significantly larger increase in plate thickness to provide the same lateral resistance; whereas, the efficiency of utilizing HBE-only web plates in wider bays (i.e. larger L_{cf}/h_c) is increased as the required increase in web plate thickness is less.

8.3.1.2 HBE depth and number of PT strands

To maintain similar PT connection stiffnesses between the two building types (i.e. fully connected and HBE-only web plates), the same HBE depth, d, and number of PT strands were assumed for each floor. These parameters are largely determined from the design requirement to maintain a positive recentering stiffness when P-Delta effects are considered. The recentering stiffness, K_r, depends on the PT connection post-decompression rotation stiffness during unloading, when the web plate stiffness is considered to be negligible; therefore, the web plate connectivity and strength did not impact these parameters.

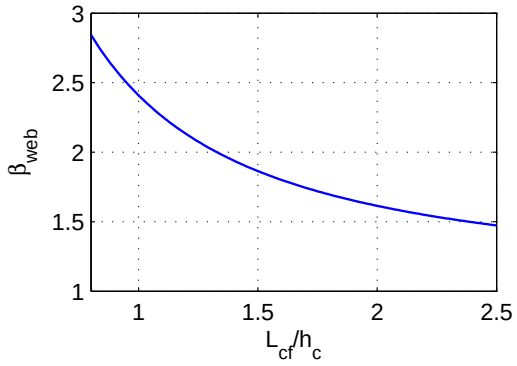

Figure 8.1: Approximate increase in plate thickness, $\beta_{web} = t_{w,HBE-only}/t_{w,full}$, with respect to web plate aspect ratio

8.3.1.3 Initial PT force

The initial PT force was determined to ensure that connection decompression does not occur under wind and gravity loading. In these calculations, web plate forces are not considered and are therefore the same for both building types. Clayton [2010] discussed an additional design constraint requiring the maximum moment to occur at the ends of the HBE at some target drift level (assumed to be 4% in Clayton [2010]) to prevent in-span hinging [Dowden et al., 2012]. This design requirement was based on numerical evaluation of conventional SPSWs with fully connected web plates in which flexural hinging occured along the length of the HBE [Purba and Bruneau, 2010]. The results of this numerical study suggested that in-span hinging could result in large HBE plastic deformations that led to partial yielding of the web plates (shown in Fig. 8.2), resulting in less than expected lateral strengths. To shift the maximum moment closer to the HBE ends, the initial PT force could be increased such that the linear moment distribution due to the PT forces (as shown in Fig. 1.4) was larger than the parabolic moment distribution due to the net vertical web plate forces. This design constraint typically only controlled at the top HBE and at some intermediate HBEs where large changes in web plate thicknesses occured.

Because the tension field angle for the HBE-only partial tension field is steeper, the web plate forces have a larger vertical component for the same horizontal resistance; therefore,

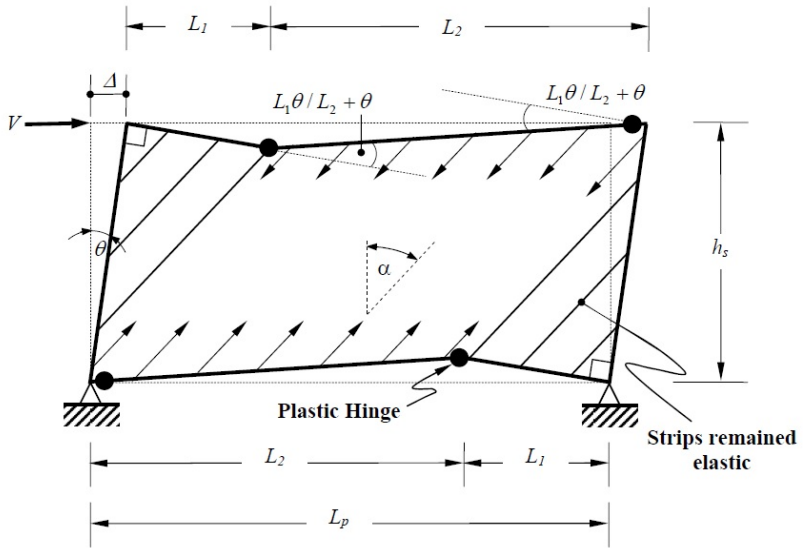

Figure 8.2: Plastic collapse mechanics for single-story SPSW with in-span hinge [Purba and Bruneau, 2010]

the moment due to vertical web plate forces may be larger for HBEs with web plates connected only to the HBEs than for fully-connected web plates. However, due to the already conservative nature of designing the HBEs to remain elastic up to at least 4% drift, it is beleived that the shakedown effects due to in-span hinging observed in the Purba and Bruneau [2010] study on conventional fully-connected SPSWs will not be as severe in the HBE-only SC-SPSWs. In the Purba and Bruneau [2010] study, veritcal displacements in HBEs that exhibited in-span hinging were as much as four times greater than the vertical displacements of HBEs with hinging at the ends at 2% drift. The vertical displacements in HBEs with in-span hinging progressively increased during cyclic loading in both directions, eventually causing the strips in the corners of the web plates (i.e. those spanning from a column to beam) not to defrom enough to develop yield forces. The loss of tension field and degradation of lateral strength associated with the HBE vertical displacement at lower drift levels were thought to have the potential to lead to collapse during earthquake ground motions [Purba and Bruneau, 2010]. In the HBE-only SC-SPSW, the potential effects of in-span HBE hinging are not expected to be as severe, because:

1. Hinging will not occur in the HBEs until drifts greater than 4%; therefore, for design-level earthquakes and many MCE-level earthquakes [Clayton, 2010], the HBEs will remain elastic. Futhermore, for severe shaking when HBEs may yield in drifts greater than 4%, the number of cycles for which the ratcheting of the HBE (or shakedown effect [Purba and Bruneau, 2010]) will lead to a growth in HBE vertical diaplacements will be less than for those HBEs in conventional SPSWs in which in-span hinging occured as early as 2.5% drift [Purba and Bruneau, 2010].

2. A main concern of in-span hinging is the loss of lateral strength associated with the loss of tension field acting in the corners of the web plates (Fig. 8.2). For HBE-only web plates, the partial tension field already excludes the portion of the plate in the corners (i.e. no strips are connected to the columns); therefore, if the effects of in-span hinging are similar for HBE-only web plates as they were for fully connected web plates [Purba and Bruneau, 2010], then the loss of lateral strength will not be as significant as a large portion of the HBE-only partial tension field will still be activated. Further research should be done on in-span HBE hinging in HBE-only connected web plates to verify this hypothesis.

For these reasons, the design constraint requiring the maximum moment to occur at the HBE ends at 4% drift was not strictly enforced for this particular study. The initial PT force, T_o, in the HBE-only SC-SPSWs were taken as the same as that for the fully connected web plate designs to ensure that the PT frame strength was roughly equal for the corresponding SC-SPSWs with the two different web plate connectivitlies (i.e. to investigate the effects of web plate connectivilty, not PT frame strength). In most cases, the initial PT force was controlled by the connection decompression requirement, which was the same for both building types. At the top HBEs and HBEs with larger transitions in web plate thickness, where the moment due to the net vertical web plate load is the largest, the maximum moment for the HBE-only SC-SPSW did occur near the middle of the HBE for the T_o determined from the fully-connected web plate design.

8.3.1.4 HBE design

The HBE was designed to remain elastic up to 4% drift, an approximate drift associated with MCE-level events [Clayton, 2010]. As stated previously, the design requirement to ensure that the maximum moment occurred at the end of the HBE at 4% drift was released such that the same initial PT force from the previous SC-SPSW study could be used; therefore, the location and magnitude of the local in-span maximum moment was determined from Eqns. (3.23) and (3.20), respectively and was compared to the magnitude of the moments at the connections (Eqn. (3.21)) to determine the maximum moment demand in the HBE.

The maximum axial force was taken as the axial force in the interior of the HBE between Zones 1 and 2 (Fig. 3.12) as given in Eqn. (3.17). Although the maximum axial force and maximum moment are unlikely to occur at the same location along the length of the HBE, they were assumed to be coincidental (i.e. occurring at the same location) for conservative design of the HBE.

8.3.1.5 VBE design

The VBEs were designed to have the same nominal depths as those of the corresponding fully-connected SC-SPSW design. The VBE moment, shear, and axial force demands were determined using the procedures outlined in Berman and Bruneau [2008] and summarized in Sec. 3.2.4. The VBE section was selected such that the *AISC Specification* [AISC, 2005b] interaction equitations (Eqn. H1-1) for every point along the height of the column was less than or equal to 1.0. The same nominal VBE depth was used for sections up the height of the building in order to facilitate splicing, and VBE splices, where necessary, were assumed to be located approximately one-quarter of the story height above the floor level.

For purposes of comparison, Figs. 8.3 and 8.4 show the design axial, shear, and moment distributions for the left and right VBEs, respectively, determined using the same procedure [Berman and Bruneau, 2008]. In these figures, the demands are shown for the same SC-SPSW (3-1050-6) designed to have fully-connected web plates[2] and HBE-only connected web plates. The demands shown here are estimated for rightward 5% drift. Here, the web

[2]The VBE demands for this SC-SPSW were shown in Appendix B of Clayton [2010].

plate thicknesses in the HBE-only design have been increased to provide the same lateral strength as the fully-connected web plate as described in Sec. 8.3.1.1 above. Because the HBE depth and PT forces are the same for both SC-SPSWs (as described previously), the difference in the VBE demands are only due to the difference in web plate thicknesses, length of the full or partial tension field, and tension field angle of inclination.

Note the key differences in the HBE-only and fully-connected web plate VBE demands in Figs. 8.3 and 8.4:

1. The axial and shear force distributions for the HBE-only web plate are constant at each story compared to the linear distribution in each story for the fully-connected web plate that imposes distributed x- and y-direction loading on the VBEs. Similarly, the moment distribution for the HBE-only web plate is linearly distributed in each story compared to the parabolic distribution for the fully-connected web plate.

2. The changes in VBE axial force at each HBE level is greater for the HBE-only web plates than for the fully-connected web plates. The larger change in VBE axial force is due to the larger HBE shear reaction forces for the HBE-only, which is caused by the thicker plates and the steeper angle of inclination, θ. Similarly, the VBE axial forces in the left VBE are smaller for the HBE-only web plate compared to the fully-connected web plate due to the unbalanced vertical distributed load along the HBEs to the the partial tension field action causing larger shear reactions at the right ends of the HBEs (similarly causing larger VBE axial forces in the right VBE for the HBE-only web plates).

3. The VBE shear force mid-height in each story is roughly the same for both the HBE-only and fully-connected web plates. The change in VBE shear force at each floor level is due to the axial reaction at the ends of the HBEs. The larger change is VBE shear at each floor in the fully-connected web plate is due to the additional HBE compressive force cause by web plate pull-in of the VBEs, $P_{HBE(VBE)}$, which is not present in the HBE-only web plates. Note that for the HBE-only web plates, the left and right VBEs have roughly the same shear forces at the base; whereas, the left and

right VBEs with the fully-connected web plates have different shear forces at their base based on the direction of the horizontal distributed web plate forces acting on the VBEs. Even though the base shear forces in each column are different for both types of web plate designs, the sum of the column base shears (an indicator of lateral strength) is roughly the same for both web plate connectivity types; therefore, the two web plate designs appear to have similar lateral strengths as intended.

4. The change in VBE moment at each floor level is due to the moment at the ends of the HBEs. The HBE end moments are slightly larger for the fully-connected web plated due to the additional compression at the rocking point due to VBE pull-in, $P_{HBE(VBE)}$. The maximum moments in the VBEs with fully-connected web plates often occurred within each story height, while they occurred at the floor levels for the HBE-only web plates.

5. In general the axial, shear, and moment demands for the VBEs with HBE-only connected web plates were lower in magnitude than those of the fully-connected web plates as determined by the procedure presented in Berman and Bruneau [2008].

8.3.2 HBE-only SC-SPSW designs

The 3- and 9-story designs were modified for HBE-only connected web plates according to the methods presented in the previous section. The resulting 3- and 9-story designs are provided in Tables 8.4 and 8.5, respectively. The columns on the right side of the table show the percentage change in the weight of the HBE and VBE members sizes compared with the comparable fully-connected web plate designs (Tables 8.2 and 8.3). Note that the name of the design has been appended with a 'HBE' to indicate the different web plate connectivity. These design parameters can be compared directly with those of the fully-connected web plate designs given in Tables 8.2 and 8.3. It is worth noting again that the web plate designs may not represent real, commonly available web plate thicknesses, but were determined to provide the same lateral strength as the original fully-connected web plate SC-SPSW designs.

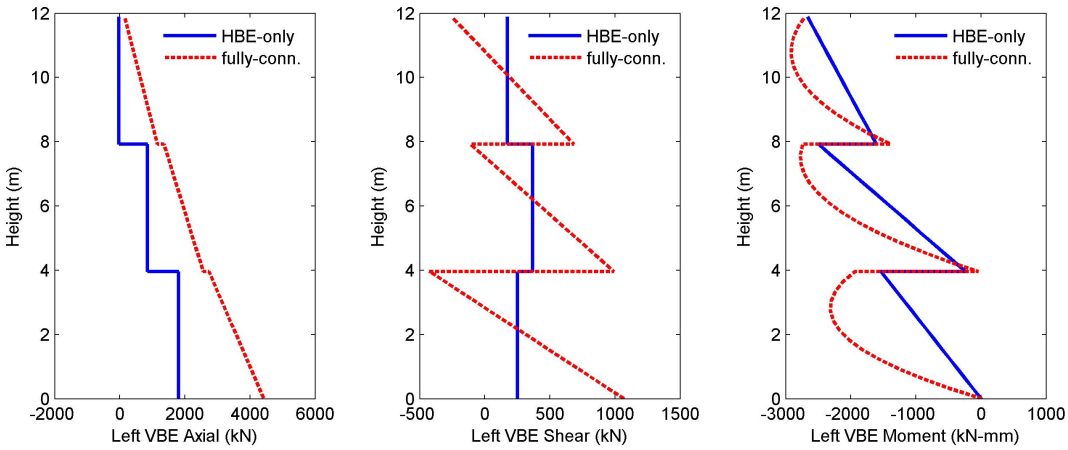

(a) (b) (c)

Figure 8.3: Design force diagrams for left VBE from 3-1050-6HBE (HBE-only) and 3-1050-6 (fully-conn.) at 5% drift

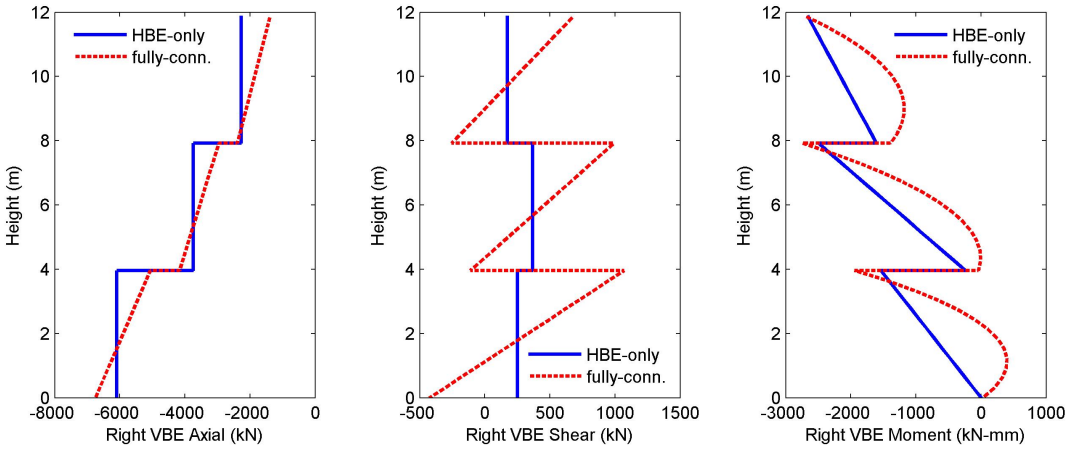

(a) (b) (c)

Figure 8.4: Design force diagrams for right VBE from 3-1050-6HBE (HBE-only) and 3-1050-6 (fully-conn.) at 5% drift

Table 8.4: Design parameters for 3-story HBE-only web plate designs

Name	Story	t_w (mm)	T_o (kN)	# of PT strands	HBE size	VBE size	% Wt. change HBE	% Wt. change VBE
3-5050-6HBE	1	17.76	231	16	W24x250	W14x455	9.2	-25
	2	13.20	503	12	W30x211	W14x455	0	-25
	3	8.44	467	32	W36x302	W14x455	0	-25
3-1050-4HBE	1	7.02	356	24	W24x146	W14x283	-17	-17
	2	5.55	191	16	W24x104	W14x283	-11	-17
	3	3.91	703	20	W30x173	W14x283	0	-17
3-1050-6HBE	1	5.85	245	16	W24x117	W14x211	-11	-25
	2	3.95	178	12	W24x76	W14x211	-19	-25
	3	3.25	658	16	W30x148	W14x211	0	-25

Some of the web plate thicknesses in the HBE-only web plate designs are also very thick (e.g. 25mm in 9-5050-10HBE). Web plates of this thicknesses may require special detailing to connect to the boundary frame and have not been properly tested and validated in experimental tests of real SPSWs; however, for purposes of comparison, the numerical study will still evaluate the performance of these SC-SPSWs assuming the same tension field assumptions. In reality, a designer would likely reduce the required plate thickness by introducing more SC-SPSWs in the building. Also note that although some designs require very thick web plates to provide the same strength as the their fully-connected counterparts, many of the designs still use readily available thin plates.

8.3.3 Modeling validation

Little research has previously been done on HBE-only web plate connectivity in SPSWs, thus the numerical modeling methods for this web plate connectivity configuration have not been validated for a broad range of design parameters as they have been for fully-connected web plate models. Only one test specimen (W14-8s100k16GaHBE as described in Chapter 4) in the SC-SPSW experimental program investigated the HBE-only web plate connectivity; therefore, there is limited experimental data to validate the numerical models. To employ a numerical model in further applications (e.g. conducting response history analyses of full-scale SC-SPSWs with HBE-only web plates), the model should be able to accurately

Table 8.5: Design parameters for 9-story HBE-only web plate designs

Name	Story	t_w (mm)	T_o (kN)	# of PT strands	HBE size	VBE size	% Wt. change HBE	% Wt. change VBE
9-5050-10HBE	1	25.23	565	22	W30x326	610x610x89	-8.7	-30
	2	19.97	516	18	W30x235	610x610x89	-20	-30
	3	20.01	449	16	W30x235	610x610x89	-20	-30
	4	20.29	458	20	W24x229	610x610x50	-18	-61
	5	20.56	369	16	W24x279	610x610x50	0	-34
	6	17.16	289	14	W24x250	610x610x50	9.2	-34
	7	13.77	200	10	W24x192	610x610x38	0	-25
	8	11.55	752	16	W24x207	610x610x38	7.8	-25
	9	7.30	939	30	W30x235	610x610x38	-20	-25
9-1050-6HBE	1	15.19	867	34	W33x291	W36x800	-18	0
	2	13.97	859	30	W30x235	W36x800	-20	0
	3	14.12	761	26	W30x211	W36x800	-19	0
	4	14.13	641	24	W30x211	W36x800	-19	0
	5	10.62	534	20	W30x148	W36x361	-30	-26
	6	10.79	489	22	W24x162	W36x361	-16	-26
	7	10.26	338	16	W24x162	W36x247	0	-37
	8	7.33	178	12	W24x103	W36x247	-12	-37
	9	6.04	907	26	W30x173	W36x247	-18	-37
9-1050-8HBE	1	10.52	734	26	W30x191	W14x605	-29	-17
	2	9.75	658	24	W30x173	W14x605	-26	-17
	3	9.77	583	20	W30x148	W14x605	-30	-17
	4	9.90	592	24	W24x192	W14x426	-7.3	-15
	5	7.21	494	20	W24x117	W14x426	-28	-15
	6	6.72	383	16	W24x104	W14x426	-21	-15
	7	6.73	262	12	W24x104	W14x283	-11	-43
	8	5.63	663	10	W24x117	W14x283	0	-43
	9	3.31	463	16	W30x132	W14x283	-11	-43
9-1050-10HBE	1	7.54	601	22	W30x173	W14x500	-18	-32
	2	7.00	538	18	W30x132	W14x500	-31	-32
	3	6.60	569	24	W24x131	W14x500	-26	-32
	4	6.69	485	20	W24x117	W14x370	-34	-26
	5	6.70	405	16	W24x117	W14x370	-11	-26
	6	5.61	307	14	W24x84	W14x370	-36	-26
	7	5.69	271	16	W18x130	W14x257	-23	-40
	8	4.13	227	10	W18x76	W14x257	0	-40
	9	3.36	596	16	W30x132	W14x257	0	-40

capture the global force vs. drift response and provide a reasonable approximation of the HBE and VBE demands.

To provide some verification of the validity of the numerical models, the following steps were taken:

1. The results (particularly the global force vs. drift and middle HBE moment distribution) of the two test specimens that were identical with exception of web plate connectivity (W14-8s100k16Ga and W14-8s100k16GaHBE) are compared to the numerical models (OpenSees and ABAQUS).

2. The web plate thickness in the HBE-only specimen models (OpenSees and ABAQUS) were increased according to Eqn. (8.1) to provide the same lateral strength as the fully-connected web plate models.

3. The global force vs. drift response, as well as, the HBE and VBE moment and axial force distributions of all of the models were compared to one another to verify that that an increase of web plate thickness produced the intended increase in lateral strength produced reasonable and similar changes in the boundary frame demands for both models.

The following sections discuss each of these steps and the results of this numerical validation.

8.3.3.1 Comparison of experimental and numerical results

The force vs. drift response of the OpenSees (Model TC[3]) and ABAQUS numerical models are compared with the experimental response of specimen W14-8s100k16GaHBE in Figs. 7.15 and 7.33(d), respectively. These figures show that the OpenSees model slightly underestimates the peak strength and magnitude of web plate residual strength upon unloading, while the ABAQUS model slightly overestimates the peak strength of the specimen

[3]Model TC is the OpenSees model used in this section as it provides better approximations of global response than Model TO and is more stable for use in dynamic analyses than Model WP; therefore, references to OpenSees in this section (Sec. 8.3.3) imply Model TC

and slightly underestimates the magnitude of the web plate residual strength (a more detailed comparison of the responses for both types of numerical models are provided in Chapter 7). Similar trends in numerical model agreement with experimental results can be observed in the force vs. drift responses of the fully-connected web plate specimen (W14-8s100k16Ga) shown in the appendix Figs. C.1(s) and E.1(h).

Fig. 8.5 compares the moment distributions from the ABAQUS model, OpenSees model, and experimental strain gage data for the middle HBE at approximately +2% drift for the two similar specimens with fully-connected (W14-8s100k16Ga) and HBE-only connected (W14-8s100k16GaHBE) web plates. Both models show a reasonable approximation of the experimentally derived moments[4]. While both models show similar moment distributions, slight disparities can be attributed to a number of minor differences between the models including web plate material strain hardening[5] and differences in the angles of tension field inclination; however, these differences are very minor. It should be noted that for this figure and for others in this section comparing OpenSees and ABAQUS boundary frame deamnds, the number and location of the elements useds to model the boundary frame members were slighly different for both models. The general shape and magnitude of the demand distributions can be compared; however, direct comparisons at exact points cannot be made as the models did not record demands at exactly the same locations.

8.3.3.2 HBE-only web plate with increased thickness

Sec. 8.3.1.1 and Eqn. (8.1) provide methods for estimating the required increase in web plate thickness for HBE-only connectivity configurations to provide the same lateral strength as their fully-connected counterparts. Using Eqn. (8.1) and assumed angles of inclination of $\alpha = 45°$ and $\theta = 30°$, the β_{web} factor came out to 2.31. This means that the HBE-only web plate for this particular frame geometry must be 2.31 times the thickness (or 3.51mm, in this case) of the corresponding fully-connected web plate to provide the same lateral

[4]See Sec. 6.2.3 for a more detailed discussion of experimentally derived moment demands.

[5]It should be noted that the ABAQUS model in Fig. 8.5(a) was subjected to the full experimental displacement history; therefore, the plastic strain accumulation in the ABAQUS model is larger than in the OpenSees model for reasons described in Sec. 7.3.2.1.

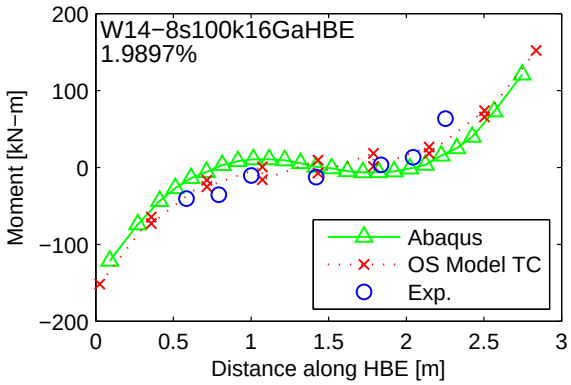

(a) Fully-connected web plates

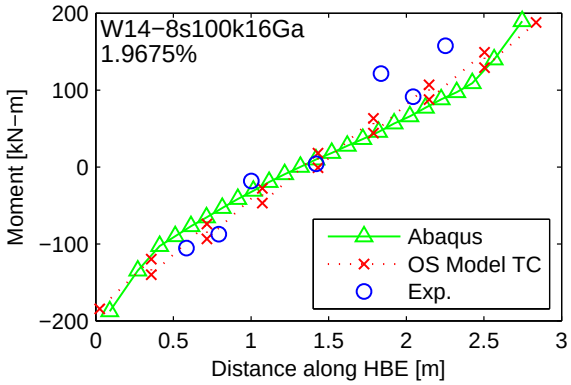

(b) HBE-only connected web plates

Figure 8.5: Comparison of OpenSees, ABAQUS, and experimental moment distributions for middle HBE at approx. +2% drift

strength.

8.3.3.3 Comparison of models

The web plate thickness was increased in the HBE-only model to verify the expected increase in lateral strength, while no other aspects of the model were changed. A comparison of the cyclic force vs. drift response for all of the models are shown in Fig. 8.6(a). Here, the models are names 'OS' or 'AB' according to OpenSees or ABAQUS, respectively; 'HBE-only' or 'fully-conn.' according to the web plate connectivity; and, 't' or '2.31t' indicating the original (1.52mm) or the modified (multiplied by 2.31) web plate thickness, respectively.

Global Response Fig. 8.6(a) shows that increasing the web plate thickness according to Eqn. (8.1) for the HBE-only web plate results in approximately the same lateral strength as the fully-connected web plate for both model types. However, as was observed in numerical models of all of the test specimens (Chapter 7), the ABAQUS models have larger peak strengths than the OpenSees models due to the additional strain hardening associated with plastic contraction normal to the tension field that is not accounted for in the strip method. To compare the strengths without the effects of this additional strain hardening, Fig. 8.6(b) compares the OpenSees cyclic results (for which the peak strength envelope is not dependent on load history) to the ABAQUS model pushed monotonically in the positive direction. Here, the peak strength envelopes for both the OpenSees and ABAQUS models are very similar, verifying that the difference in lateral strength between models can largely be attributed to the cyclic plastic strain accumulation in the shell model. The ABAQUS model still has slightly larger envelope strengths (3-7% larger) than the OpenSees model, but this difference is relatively small and may be due to slight differences in model assumptions or angles of tension field inclination.

Fig. 8.6 also shows that the OpenSees models of the fully-connected and thicker HBE-only web plate models have both the same peak strength and unload strength; however, the cyclic response in Fig. 8.6(a) shows that while the ABAQUS models of the fully-connected and thicker HBE-only web plate models have similar peak strengths, the magnitude of the web plate residual strength in the thicker HBE-only web plate model ('HBE-only:2.31t') is

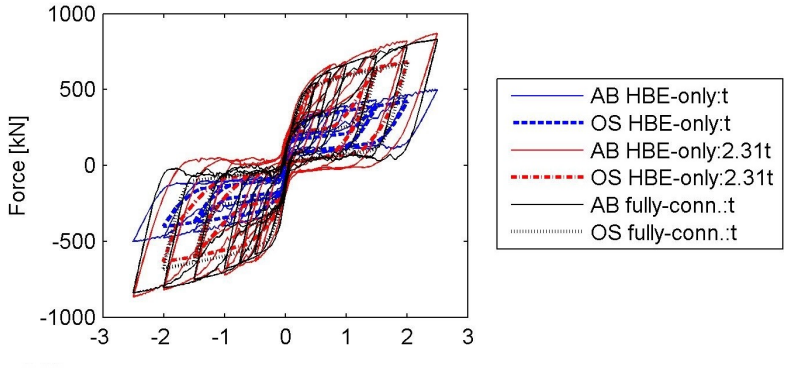

(a)

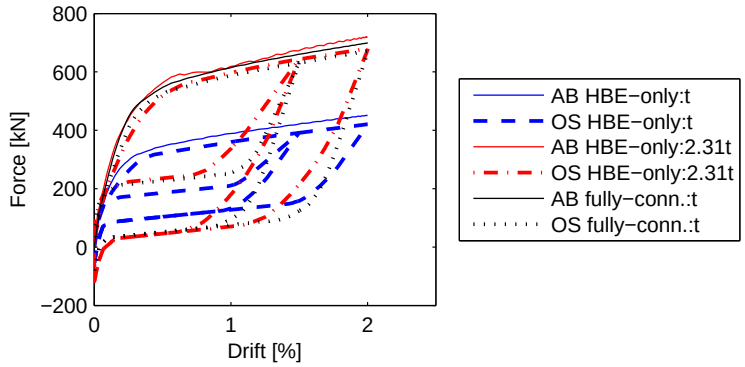

(b)

Figure 8.6: Comparison of (a) cyclic and (b) monotonic OpenSees and ABAQUS models with different web plate connectivities and thicknesses

larger (i.e. the unloading strength is lower) than that of the thinner fully-connected web plate model. Note that this result is only observed in the ABAQUS cyclic model, as the OpenSees strip model does not account for the unloading resistance of the full web plate in the HBE-only partial tension field strip models. This observation is consistent with the Webster [2013] observation that web plate residual strength increases for decreasing web plate height to thickness (h_c/t_w) ratios. This is another aspect of web plate behavior that is ignored in the tension-compression strip model (Model TC) with an assumed compressive resistance of 25% of yield; however, data from Webster [2013] can be used to estimate a more appropriate compressive strength contribution for different values of h_c/t_w and L_{cf}/h_c as shown in Fig. 7.4.

HBE demands For comparison of boundary frame demands, the monotonic ABAQUS models were considered as the web plate strengths without cyclic strain hardening were more comparable to those in OpenSees. The axial force and moment demands were compared at +2% drift (which represents a leftward sway for the subassembly test setup). Fig. 8.7 compares the demands along the middle HBE.The moment distributions of each of the ABAQUS and OpenSees models match well to one another. The moment distribution for the HBE fully-connected web plate SC-SPSW (with equal plate thicknesses above and below) is approximately linear as expected, and the HBEs with web plates connected to the HBEs only have double curvature moment distributions with the influence of the parabolic portions increasing with increasing plate thicknesses, also as expected. For this example, the moment demands at the ends of the middle HBE for both modeling approaches were largely unaffected by the changes in the web plate connectivity (Note that for the fully-connected web plate model in this example with a large L/h ratio, the $P_{HBE(VBE)}$ term is relatively small compared to the PT force; therefore, its effects are not as obvious in the connection moment).

The axial force distributions for the ABAQUS and OpenSees also have similar shapes as one another. For example, in the fully-connected web plate specimen (with equal plate thicknesses above and below), the axial force distributions of both models are approximately linear as expected, and in the HBE-only web plate specimens, the axial force distributions

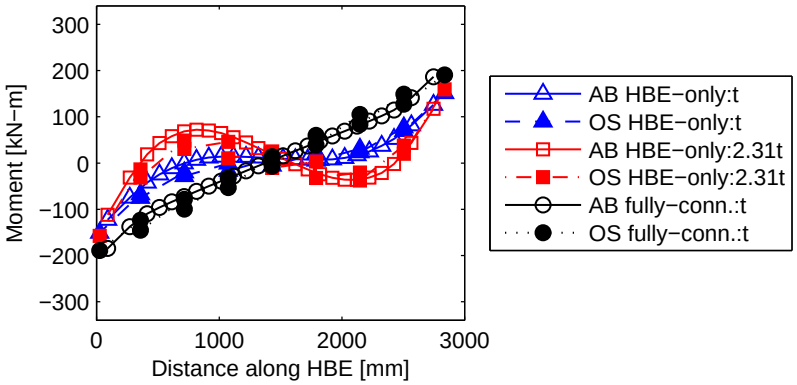

(a)

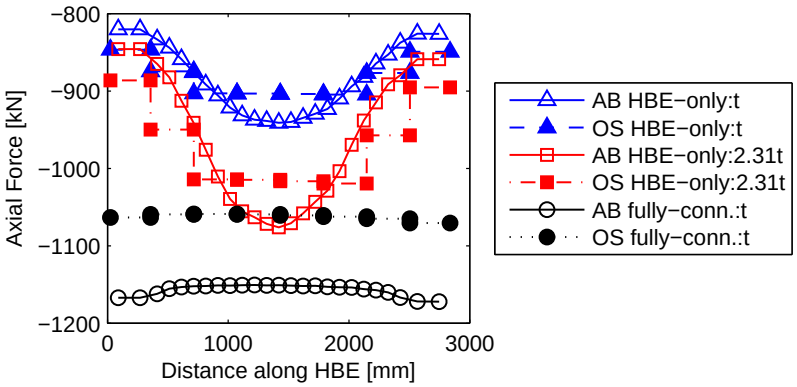

(b)

Figure 8.7: Middle HBE (a) moment distributions and (b) axial force at 2% drift for models with different web plate connectivities and thicknesses

are approximately trilinear and largest near midspan as predicted in Fig. 3.12. Both the ABAQUS and OpenSees models suggest that, at least for this particular example, providing an HBE-only web plate with the same lateral strength of a thinner fully-connected web plate results in lower axial demands in an intermediate HBE. This makes sense as the releasing the web plate from the columns removes the $P_{HBE(VBE)}$ compressive force.

The magnitude of the compressive axial force for the fully-connected web plate model is larger in the ABAQUS model than in the OpenSees model. This observation of larger HBE axial forces was generally true for all ABAQUS models (e.g. compare the HBE axial force responses for OpenSees and ABAQUS in Figs. 7.17 and 7.40, respectively). A likely cause for the larger axial forces in the fully-connected ABAQUS web plate model is due to the horizontal strain that can develop in the shell web plate model due to frame expansion that is not captured as well in the fixed strain inclination angle of the OpenSees strip model. As the columns spread apart, the continuous web plate shell model connected to both columns develops a horizontal tension component due to the expansion, resulting in larger compressive forces being transfered to the HBE; however, in the strip model, frame expansion is primarily resisted by the strips that are connected to the HBE and VBE at the opening gap. The horizontal component of the additional strain in the strip due to connection gap opening (i.e. frame expansion) is transferred as a compressive force into the HBE and is less than the horizontal strain caused by frame expansion in the continuous web plate model. The fact that the ABAQUS models for the HBE-only web plates (for which the web plates offer no direct column-to-column resistance to frame expansion) do no not have the same net increase in compressive force further supports this hypothesis. To better simulate this phenomenon in the strip model, a horizontal strip could be incorporated spanning between the two VBEs to simulate the web plate's resistance to frame expansion; however, further research would be necessary to validate this approach.

The axial force distributions for the corresponding HBE-only web plate ABAQUS and OpenSees models appear to have similar average axial forces as one another; however, the ABAQUS models tend to have slightly lower compressive forces at the HBE ends, larger compressive forces in the middle, and tend to have more of a curved axial force distribution rather than the trilinear response assumed in Sec. 3.2.3 and exhibited in the OpenSees

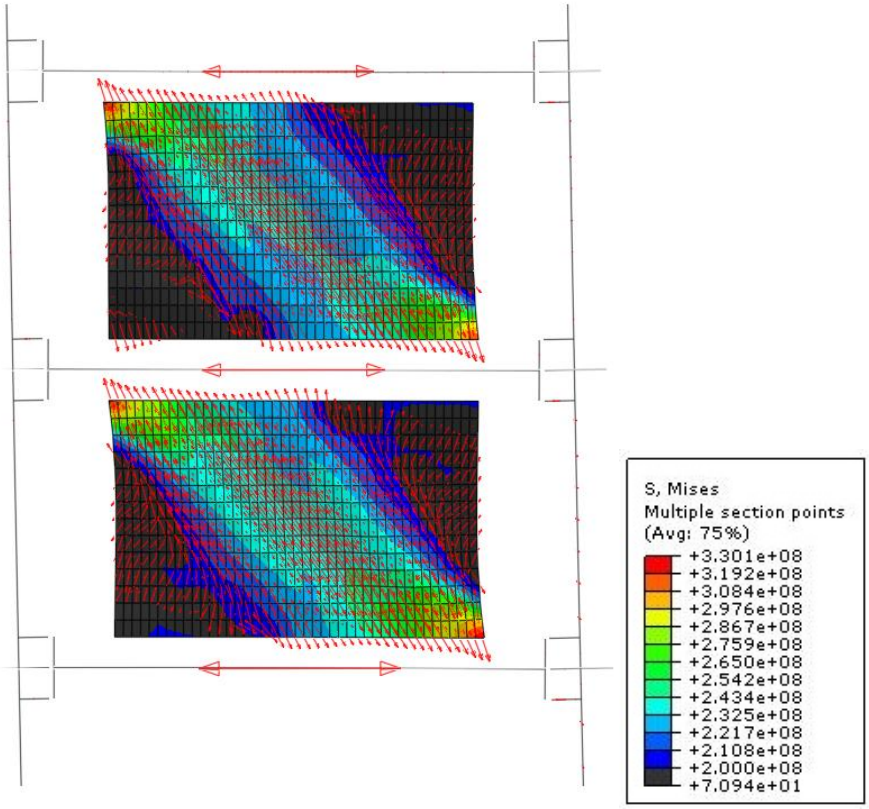

Figure 8.8: Von Mises stress contours and vectors for HBE-only web plate

model. This difference is due to the nonlinear web plate force distribution along the partial tension field as shown in Fig. 8.8. Here, the web plate stress closer to the ends of the HBE are larger and decrease closer to the interior edge of the partial tension field. The analytical derivation and the strip model assumed a constant angle of inclination and web plate stress along the entire length of the partial tension field. The approximate effects of the assumed and actual web plate force distributions are shown in Fig. 8.9, resulting in similar differences in distribution as seen in Fig. 8.7(b).

VBE demands Fig. 8.10 compares the moment and axial force demands along the left VBE and Fig. 8.11 compares the demands along the right VBE. In the VBE demand distributions, only the demands outside of the PT connection are shown (i.e. beginning just

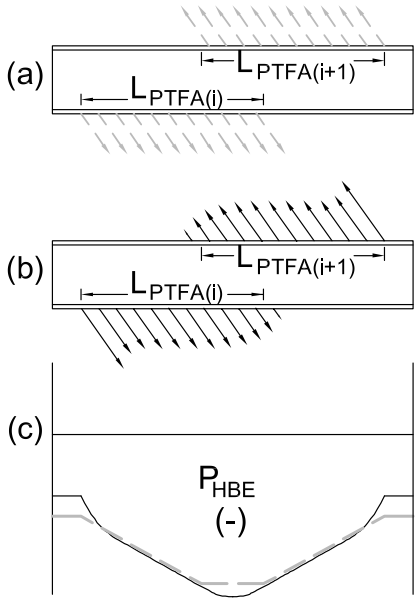

Figure 8.9: (a) Assumed constant web plate demands, (b) actual nonlinear web plate demands, and (c) approximate HBE axial distributions for HBE-only web plate

above and just below the connections) for clarity. Similar to the HBE demands, the moment distributions of the ABAQUS and OpenSees models agree well with one another. There is some difference in the influence of the web plate demands on the columns for the fully-connected web plate. The ABAQUS model appears to have a larger parabolic moment contribution which corroborates the larger horizontal strain in the continuous web plate model compared to the strip model as described previously with respect to the HBE axial demands.

The magnitudes of the VBE axial force distributions do differ between the ABAQUS and OpenSees models. For this SC-SPSW, the OpenSees models tend to predict lower compressive forces in the left VBE and larger tension forces in the right VBE compared to the ABAQUS models. However, the different web plate connectivities and thicknesses appear to have similar effects on the axial force distributions within the same modeling framework. For example, in left VBE for both the ABAQUS and OpenSees models individually, the axial force at the top of the VBE in the 'HBE-only:t' model is approximately equal to that in the 'fully-conn.:t' model, while at the bottom of the 2nd story, the axial demand in the 'HBE-only:t' model is approximately equal to that in the 'HBE-only:2.31t' model.

As discussed previously with regards to VBE design in Figs. 8.3 and 8.4, increasing the thickness of the HBE-only web plate to have the same lateral strength as a thinner fully-connected web plate results in similar VBE moment magnitudes at the connections; however, the fully-connected web plate produces a parabolic moment distribution within the height of each story which can affect peak moment demands in the columns. Similar to what was also observed in the previously discussed VBE design demands, using the thicker HBE-only web plate as opposed to the thinner fully-connected web plate does not significantly affect the axial demand in the compression column (in this example it did produce a slightly larger compressive force in the left VBE) but does significantly reduce the axial demand in the tension column. Also note that the boundary conditions for this particular example are different than the assumed pinned bases in the VBE design demand assumptions. In the test set-up be modeled in this example, the right VBE was pinned at its base, while the left VBE had a horizontal roller to simulate column spreading that would be present in an intermediate story.

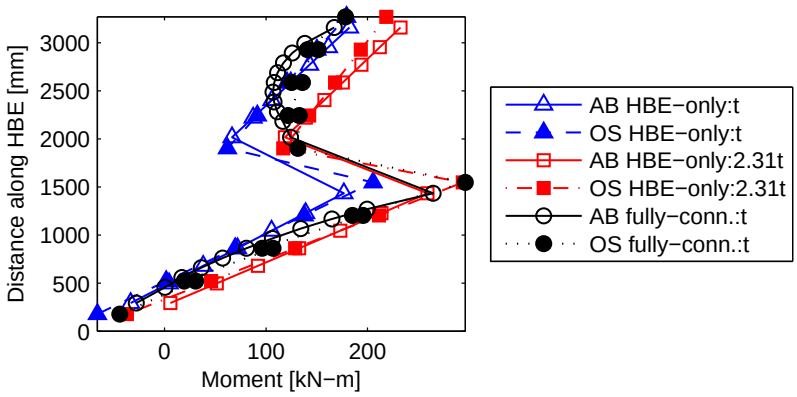

(a)

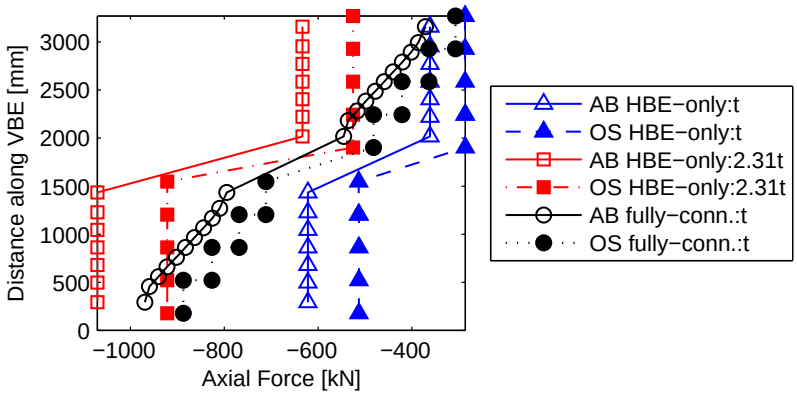

(b)

Figure 8.10: Left VBE (a) moment distributions and (b) axial force at 2% drift for models with different web plate connectivities and thicknesses

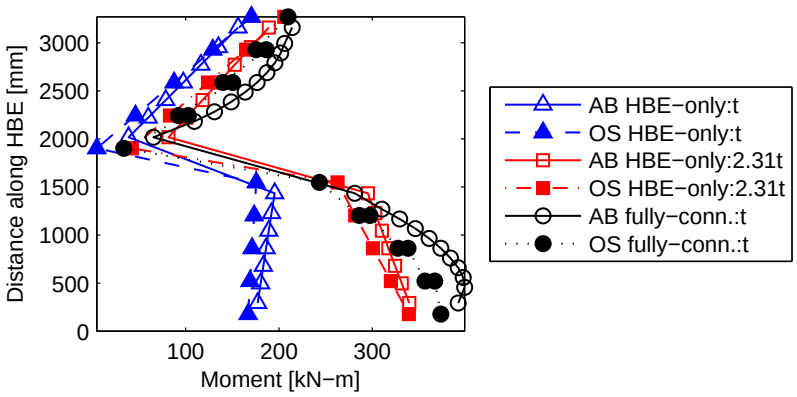

(a)

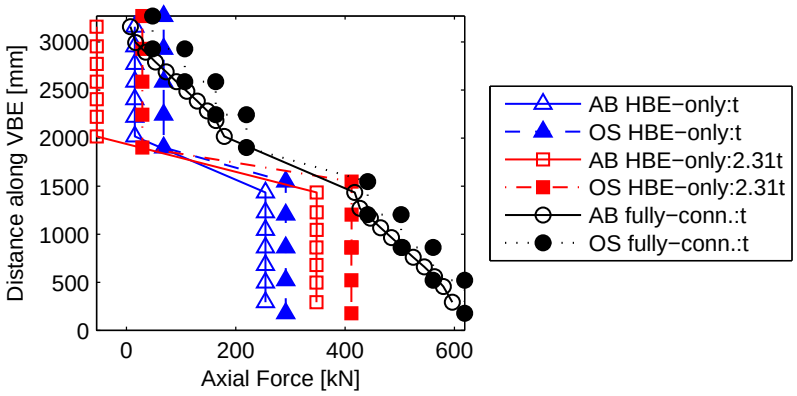

(b)

Figure 8.11: Right VBE (a) moment distributions and (b) axial force at 2% drift for models with different web plate connectivities and thicknesses

8.4 Web Plate Residual Strength Investigation

Sec. 7.2.6 compared the results from nonlinear dynamic analyses of Models TO and TC to the experimental pseudo-dynamic response. These results showed that for this two-story specimen, Model TC (with web plate compressive strength of 25% of yield) was able to reasonably predict peak drift demands, while Model TO overestimated peak drift demands. Model TC was also able to conservatively estimate residual drift demands after a short duration of free vibration (due to the additional hysteretic damping provided by the constant compressive strength in the web plate). Because the SC-SPSW component demands (e.g. PT, VBE, HBE) are proportional to drift demands, accurate approximation of peak drifts is needed to properly assess performance.

The results from nonlinear dynamic analyses of 3- and 9-story SC-SPSWs employing Model TO in Clayton [2010] demonstrated that the system was able to meet all performance objectives including recentering and peak drifts less than code-based limits at the 10/50 hazard level. Given the experimental studies and aforementioned dynamic analyses indicating the importance of accounting for web plate residual strength (and the energy dissipation associated with it), it is believed that the results from the Clayton [2010] numerical study may have been conservative in estimating (i.e. overestimating) the peak drift demands. The dynamic analyses in Sec. 7.2.6 suggest that Model TC may provide a more accurate estimation of peak demands, which may indicate even better performance than the Model TO SC-SPSW models in Clayton [2010].

8.4.1 Modeling assumptions

This section explains the web plate strip material models and the SC-SPSW buildings that were considered to assess the impact of web plate residual strength in SC-SPSW building performance.

8.4.1.1 Web plate material models

In Chapter 7, Model TC had a compressive strength of 25% of the yield strength. This value was based on the L/h and h/t ratios of the web plates used in the experimental

specimens with which the models were being cmapred. The 25% compressive strength also represents the lower bound on $V_{web,resid}$ for the range of L/h and h/t ratios shown in Fig. 7.4. Therefore, using tension-compression models with 25% compressive strength should be accurate for relatively thin web plates (h/t > approximately 700[6]) and should represent a lower bound (i.e. conservative estimate) on the amount of energy dissipation provided by thicker web plates. In the following discussions of SC-SPSW building response, Model TC with 25% compressive strength is labelled as 'TC25' to indicate the compressive contribution. For models with other values of web plate compressive strength that were constant for all web paltes in the SC-SPSW (e.g. those of the prototype building for the full-scale SC-SPSW test in Sec. 5.4.3), they are labelled as 'TCxx', where 'xx' represents the magnitue of σ_{cw}/σ_{yw} in percent.

Fig. 7.4 also shows that for thicker web plates (h/t<700), particularly for aspect ratios (L/h) less than one, the residual web plate strength can reach up to approximately 60% of the yield strength. In some of the SC-SPSW designs, particularly for those with thicker web plates connected to the HBEs only (Tables 8.4 and 8.5), the web plates did have h/t values less than 700. It should be noted that although the web plate residual strengths determined in Webster [2013] were based on web plates connected to the HBEs and VBEs, Model TC still showed a conservative underestimation of the web plate residual strength (Fig. 7.15) compared to the experimental results, as the strip model did not account for the additional unloading resistance of the portions of the web plate not included in the partial tension field. To assess how this increase in web plate residual strength impacts building response, some models used strip compressive strengths that were dependent on the web plate geometry and were larger than 25% of yield. These models are labelled as 'TCv' to indicate tension with variable compression.

For purposes of comparison, only two SC-SPSW 3-story models with the TCv web plate model were considered; these were 3-1050-4HBE and 3-1050-6HBE. Design 3-5050-6HBE was not considered in the Model TCv analyses as the h/t values in this SC-SPSW ranged

[6]Fig. 7.4 onlsy considers web plates with h/t up to 900; however, the V_{res}/V_y values appear to converge to approximately 0.25 for h/t>700. Although some of the web plates used in the SC-SPSW building designs have h/t>900, the web plate residual strength is still assumed to be 25% of yield. Further work should be done to assess this value for very thin web plates (e.g. h/t>1000)

Table 8.6: Strip compression strength considered in tension-variable compression (TCv) models

Model	Story	h_c/t_w	L_w/h_c	σ_{cw}/σ_{yw}
3-1050-4HBE-TCv	1	521	1.14	0.35
	2	603	1.24	0.32
	3	838	1.27	0.25
3-1050-6HBE-TCv	1	625	1.14	0.32
	2	849	1.25	0.25
	3	1001	1.28	0.25

from approximately 200 to 370. Values of h/t<300 were not considered in Fig. 7.4. Unlike larger h/t values that converged to a V_{res}/V_y of approximately 0.25, smaller values of h/t do not appear to converge to an upper bound V_{res}/V_y; therefore, only the 3-story HBE-only web plate SC-SPSWs with h/t values greater than 300 are considered. Table 8.6 shows the web plate h_c/t_w, L_w/h_c, and assumed approximations of normalized strip compressive strength, σ_{cw}/σ_{yw}, for each story in these particular SC-SPSWs.

8.4.2 SC-SPSW buildings considered

To assess the effects of including web plate residual strength using a tension-compression strip method (Model TC), the dynamic response of several SC-SPSWs employing Model TC will be compared to their tension-only (Model TO) counterparts. Each 3- and 9-story SC-SPSW with fully-connected and HBE-only connected web plates (Tables 8.2, 8.3, 8.4, and 8.5) will be modeled using Model TC25 (with a constant 25% compressive strength in all web plates. Additionally 3-1050-4HBE and 3-1050-6HBE will be modeled using different (larger) values of compressive strength in each plate corresponding to its geometric properties (Model TCv) as explained in the previous section (Table 8.6).

Results from the dynamic analyses of the two-story prototype building (see Sec. 5.4.2 for more details) are also shown for σ_{cw}/σ_{yw} values of 10%, 20%, 30%, and 40% (TC10, TC20, TC30, and TC40, respectively). The two-story prototype building had fully-connected web plates; thus, it is only used to investigate the impact of web plate presidual strength, not

web plate-to-boundary frame connectivity.

8.5 Nonlinear Response History Results

A summary of the nonlinear response history results will be presented in this section. As was shown for the prototype buildings in Sec. 8.2, key response parameters that were used to evaluate seismic performance were the peak story drift, $\theta_{s,max}$, maximum story residual drift, $\theta_{resid,max}$, and HBE and VBE demand-capacity ratios, D_{HBE} and D_{VBE}, respectively. Recentering was established as residual drifts less than 0.2%. The model names correspond to the SC-SPSW design (e.g. 3-1050-6 corresponds to three-story, web plates desgind for $V_{10/50}/R$, and six SC-SPSWs in each direction of the building), where an 'HBE' appended to the design name corresponds to HBE-only web plate connectivity, and the final part of the name corresponds to the web plate material model employed (e.g. 'TO' is tension-only, 'TC25' is tension-compression with compression equal to 25% of the yield strength, and 'TCv' is tension-compression with compressive strengths that vary per story corresponding to the web plate geomety per Fig. 7.4).

Unless otherwise noted, each of these models was subjected to the suite of sixty ground motions developed for the Los Angeles site in the SAC project [Clayton, 2010], with twenty ground motions representing each of the three seismic hazard levels (50/50, 10/50 and 2/50). The ground motions were developed by Somerville et al. [1997] to match, on average, the target spectral values for the Los Angeles prototype building; therefore, no additional scaling was done to the ground motions. A brief discussion of response spectra characteristics can be found in Sec. 5.4.4.

The results are separated into sections based on the SC-SPSW building: two-story, three-story, and 9-story. In each of these sections key response parameters such as peak story drift, $\theta_{s,max}$, maximum story residual drift, $\theta_{resid,max}$, and HBE and VBE interaction values, D_{HBE} and D_{VBE} are presented. The median, $\mu_{1/2}$, and 84^{th} percentile for each of the data sets are provided at each hazard level. For easier comparison, much of the data is presented in multiple places so that it can be viewed beside the results with which they are being compared (e.g. when comparing Model TO to Model TC25, the results for Model TO will be shown even though they were already shown in Figs. F.1 through F.4).

8.5.1 Two-story models

The results of the dynamic analyses conducted on the two-story prototype building for the full-scale tests (details of the model and preliminary results are discussed in Sec. 5.4.1) are compiled and presented. These analyses investigate the impact of varying the magnitude of compressive resistance on response parameters. For comparison, the results presented in the following figures have been normalized to the maximum Model TO response parameter for that particular data set. For example, when plotting the 84^{th} percentile of the peak story drift response at the 10/50 hazard level, the results for each of the models is normalized by the maximum 84^{th} percentile peak story drift in Model TO at the 10/50 hazard level. Therefore, values of one indicate response equal to the Model TO response, values less than one indicate a decrease in the response parameter compared to Model TO, and values greater than one indicate a similar increase in the response parameter.

Fig. 8.12 shows the normalized peak story drift and residual story drift responses separately for the median and 84^{th} percentile response for each hazard level. The addition of even a little compression in the web plate material model (TC10) significantly reduces (by approximately 20% or more) peak story drift demands compared to Model TO at all hazard levels (Fig. 8.12(a)). Increasing the compressive resistance beyond 10% further reduces peak drift demands, although not as singificantly as the difference between Models TO and TC10.

Fig. 8.12(b) shows the normalized residual story drift at each hazard level. At the 50/50 hazard level, the SC-SPSW remains essentially elastic resulting in residual drifts near zero; therefore, there is no apparent correlation between web plate residual strength and residual drift at this hazard level. At the 10/50 event, it appears that web plates with larger residual strength have larger residual drifts (particularly in the upper story); however, the residual drifts are still less than the 0.2% recentering criterion. At this hazard level, the boundary frame remains elastic and the residual drift depends more on the web plate residual strain at zero-force. At the 2/50 hazard level, web plate models incorporating any residual strength have significantly reduced residual drift. At this hazard level, the axial-flexural hinges formed in the boundary frame in Model TO due to peak drift demands

larger than the target drifts for which members were designed to remain elastic. Including web plate residual strength reduced the drift demands enough to prevent or significantly reduce yielding in the boundary frame, resulting in smaller residual drifts.

Fig. 8.13 shows the normalized HBE and VBE interaction values separately for the median and 84^{th} percentile response for each hazard level. As the boundary frame demands are largely influenced by drift demands, the same trends that were observed for the peak story drift response also apply here. Note that the magnitude of the web plate residual strength has a larger influence on HBE interaction values than the VBE interaction values, as HBE demands (particularly the PT demands) are more heavily influenced by drift compared the peak VBE demands that are controlled more by web plate forces (which do not change significantly after yielding). Also note that because this investigation of the two-story prototype building only investigated the impact of residual web plate strength, the columns remained the same size in all analyses (i.e. the peak design forces remained the same), unlike the comparison of three- and nine-story SC-SPSW responses with fully-connected and HBE-only connected web plates where the column sizes changed based on different design demands.

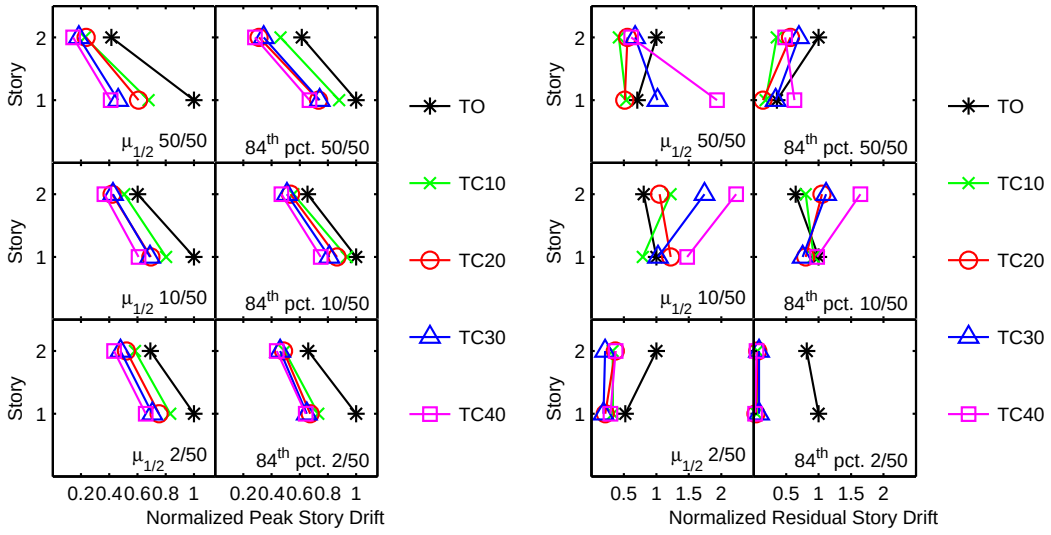

Figure 8.12: Normalized $\mu_{1/2}$ and 84^{th} percentile (a) peak story drifts and (b) residual story drifts at each hazard level for two-story SC-SPSW

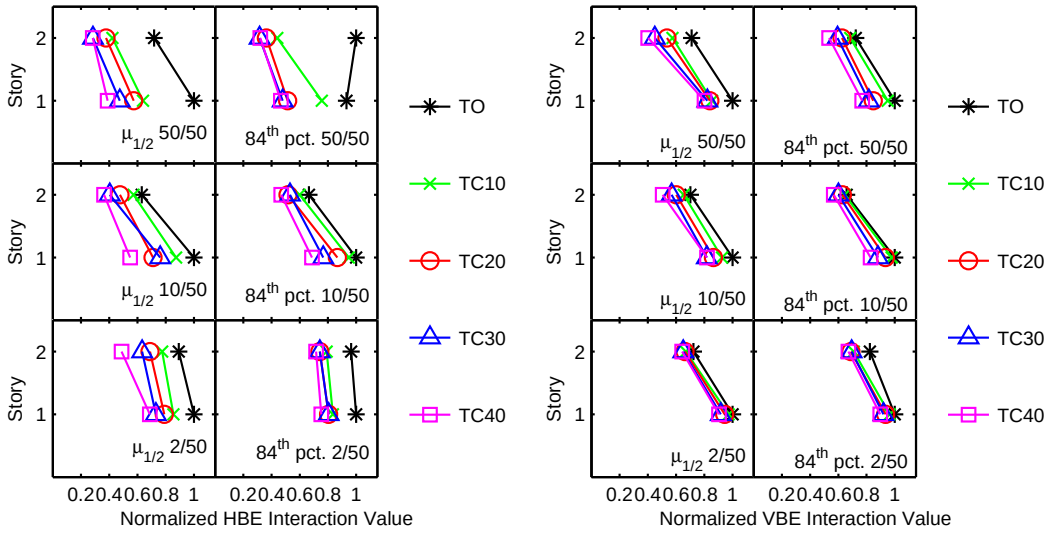

Figure 8.13: Normalized $\mu_{1/2}$ and 84^{th} percentile (a) HBE and (b) VBE interaction values, D_{HBE} and D_{VBE}, at each hazard level for two-story SC-SPSW

8.5.2 Three-story models

The response parameters for the three-story SC-SPSWs are discussed below. Tabular results are provided in Sec. 8.5.2.1 for the models that were done as part of this reasearch (i.e. not including the results from the analyses presented in Clayton [2010] and summarized in Sec. 8.2). The response parameters are then shown visually to compare how variations in the web plate connectivity (Sec. 8.5.2.2) and variations in web plate residual strength (Sec. 8.5.2.3) affect SC-SPSW response.

8.5.2.1 Tabular results

The median and 84^{th} percentile results for the key response parameters are provided in tabular form for the models of three-story SC-SPSWs with web plates connected to the HBEs only in Table 8.7 (TO and TC25 models) and for the three-story SC-SPSW with fully connected web plates and Model TC25 in Table 8.8 (These can be compared to the response parameters of the TO fully-connected web plate models from Clayton [2010] and shown in Appendix F).

Table 8.7: Summarized response parameters for 3-story SC-SPSWs with web plates connected to the HBEs only

Model	Response Parameter	50% in 50 yr		10% in 50 yr		2% in 50 yr	
		$\mu_{1/2}$	84th %	$\mu_{1/2}$	84th %	$\mu_{1/2}$	84th %
3-5050-6 HBE-TO	$\theta_{s,max}$ (%)	0.66	1.62	1.80	5.00	3.31	7.26
	$\theta_{resid,max}$ (%)	0.003	0.24	0.088	1.91	0.35	3.89
	D_{HBE}	0.68	0.99	0.97	1.21	1.00	1.22
	D_{VBE}	0.53	0.83	0.85	1.07	1.03	1.13
3-1050-4 HBE-TO	$\theta_{s,max}$ (%)	1.41	2.59	3.21	4.80	8.14	14.32
	$\theta_{resid,max}$ (%)	0.043	0.21	0.16	0.75	2.68	10.7
	D_{HBE}	0.88	0.92	0.94	1.00	1.13	1.19
	D_{VBE}	0.63	0.93	0.90	1.04	1.19	1.30
3-1050-6 HBE-TO	$\theta_{s,max}$ (%)	1.24	2.51	3.10	4.19	7.04	10.95
	$\theta_{resid,max}$ (%)	0.058	0.30	0.19	1.85	2.95	6.22
	D_{HBE}	0.86	0.91	0.90	0.97	1.10	1.92
	D_{VBE}	0.70	0.81	0.84	1.05	1.14	1.37
3-5050-6 HBE-TC25	$\theta_{s,max}$ (%)	0.60	0.91	0.47	1.61	1.11	1.88
	$\theta_{resid,max}$ (%)	0.004	0.022	0.020	0.11	0.056	0.33
	D_{HBE}	0.49	0.75	0.61	0.81	0.79	0.81
	D_{VBE}	0.36	0.56	0.38	0.68	0.59	0.93
3-1050-4 HBE-TC25	$\theta_{s,max}$ (%)	0.51	0.86	2.27	3.41	5.40	8.74
	$\theta_{resid,max}$ (%)	0.010	0.043	0.071	0.30	0.42	2.05
	D_{HBE}	0.52	0.67	0.70	0.70	0.90	0.99
	D_{VBE}	0.27	0.39	0.65	0.91	1.00	1.15
3-1050-6 HBE-TC25	$\theta_{s,max}$ (%)	0.46	0.79	1.71	3.02	4.82	7.23
	$\theta_{resid,max}$ (%)	0.009	0.020	0.055	0.14	0.25	1.10
	D_{HBE}	0.48	0.66	0.67	0.69	0.82	0.91
	D_{VBE}	0.23	0.33	0.53	0.71	0.96	1.07
3-1050-4 HBE-TCv	$\theta_{s,max}$ (%)	0.49	0.71	1.94	3.23	4.74	8.00
	$\theta_{resid,max}$ (%)	0.013	0.066	0.060	0.16	0.27	0.90
	D_{HBE}	0.46	0.55	0.59	0.60	0.82	0.97
	D_{VBE}	0.24	0.35	0.56	0.76	0.98	1.14
3-1050-6 HBE-TCv	$\theta_{s,max}$ (%)	0.40	0.92	1.37	2.68	4.98	7.31
	$\theta_{resid,max}$ (%)	0.012	0.034	0.062	0.14	0.41	1.32
	D_{HBE}	0.40	0.65	0.65	0.66	0.77	0.87
	D_{VBE}	0.25	0.35	0.41	0.65	0.98	1.11

Table 8.8: Summarized response parameters for 3-story SC-SPSWs with fully-connected web plates and with tension-compression web plate models

Model	Response Parameter	50% in 50 yr		10% in 50 yr		2% in 50 yr	
		$\mu_{1/2}$	84th %	$\mu_{1/2}$	84th %	$\mu_{1/2}$	84th %
3-5050-6 -TC25	$\theta_{s,max}$ (%)	0.10	0.21	0.18	0.36	0.34	0.64
	$\theta_{resid,max}$ (%)	0.015	0.032	0.021	0.054	0.037	0.16
	D_{HBE}	0.19	0.29	0.16	0.42	0.46	0.58
	D_{VBE}	0.33	0.48	0.14	0.29	0.40	0.66
3-1050-4 -TC25	$\theta_{s,max}$ (%)	0.29	0.58	0.98	2.34	3.52	4.91
	$\theta_{resid,max}$ (%)	0.017	0.16	0.12	0.44	0.17	1.82
	D_{HBE}	0.29	0.39	0.45	0.60	0.92	1.02
	D_{VBE}	0.51	0.58	0.58	0.69	0.86	1.03
3-1050-6 -TC25	$\theta_{s,max}$ (%)	0.45	1.04	1.06	2.12	2.99	4.31
	$\theta_{resid,max}$ (%)	0.13	0.26	0.14	0.22	0.49	1.16
	D_{HBE}	0.33	0.80	0.34	0.55	0.77	1.05
	D_{VBE}	0.33	0.56	0.34	0.57	0.73	0.97

8.5.2.2 Comparison of web plate connectivity

The following figures present the median and 84^{th} percentile of the response parameters for each hazard level at each story. Figs. 8.14 through 8.17 compare the peak story drift, residual story drift, HBE and VBE interaction values for SC-SPSWs with fully-connected and HBE-only web plates employing Model TO. Fig. 8.14 shows that the HBE-only SC-SPSWs have much larger drifts compared to their full-connected counterparts. As was observed in the fully-connected web plate SC-SPSWs [Clayton, 2010], the drifts for the SC-SPSWs with web plates designed to remain elastic during a 50/50 event (3-5050-*) are much lower than those with code-based web plates (3-1050-*) and have median drifts less than 2% during the 10/50 event and less than 4% during the 2/50 event. The HBE-only web plates designed for code-based forces and modelled using TO strips have drifts larger than the code-based limit of 2% at the 10/50 hazard level and have drifts in excess of 7% and 8% in the 2/50 event indicating a greater prbability of collapse and detrimental nonstructural damage. These large drifts in the HBE-only code-designed Model TO web plates result in extensive boundary frame yielding and residual drifts in the 2/50 event; however, these SC-SPSWs are still able to meet the 0.2% recentering criteria at the median level in the 10/50 event.

Although the web plates and boundary frames were designed to have the same strengths, the larger drifts in the HBE-only web plate SC-SPSWs are believed to be due to the portion of the web plates (i.e. the individual strips) that are connected to both the HBE and the VBE. Strips that span from HBE to VBE provide some resistance to connection rotation, thus reducing drift demands. In previous conventional SPSWs studies [Tromposch and Kulak, 1987] where the web plates are connected along the entire HBE and VBE lengths (i.e. no corner cutouts), the web plate provide enough resistance to connection rotation that simple bolted (i.e. "pinned") beam-to-column connections essentially behaved as fixed connections at lower drift levels. In the HBE-only web plate models, no strips are connected to both the HBEs and VBEs; therefore, the web plates are not directly contributing to PT connection gap closing.

Figs. 8.18 through 8.21 show the same comparison between SC-SPSWs with fully-

connected and HBE-only web plates, but here are shown for the more appropriate TC25 models. For these models, the same observation of HBE-only drifts being larger than their fully-connected counterparts; however, the drifts in these models are significantly less than those of Model TO (comparison between Model TO and Model TC to be discussed in further detail later). When the residual web plate strength is considered, the SC-SPSWs with HBE-only code-based web plates (3-1050-*HBE) are able to meet the proposed performance objectives including drifts less than the 0.5% web plate yielding criterion at the 50/50 hazrd level, drifts less than (or slightly over) the 2% code-based limit at the 10/50 hazard level, recentering at the 10/50 (and even at the 2/50) hazard level, and only minor yielding in the boundary frame at the 2/50 hazard level. It is important to note that the 25% compression included in the tension strip model still underestimates the web plate residual strength for HBE-only web plates as shown in Fig. 7.15 as it does not consider the unloading resistance of the portion of the plate outside of the partial tension field. Further modification of the tension-compression model to account for this additional unloading resistance in the HBE-only web plate would provide more energy dissipation and would even further reduce the drift demands.

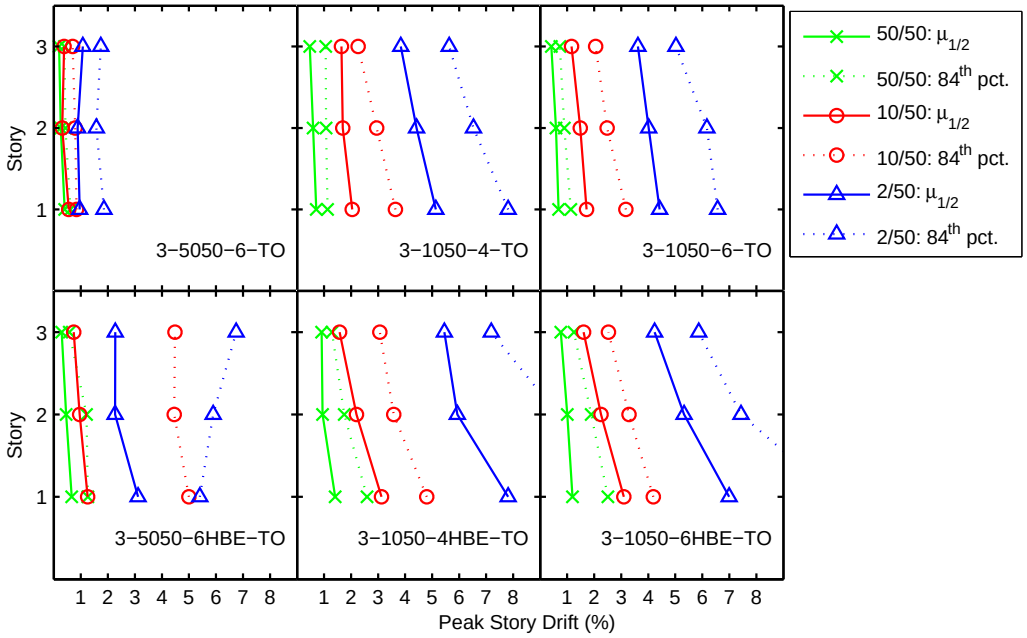

Figure 8.14: Peak story drift response for SC-SPSWs with fully-connected and HBE-only web plates (Models TO)

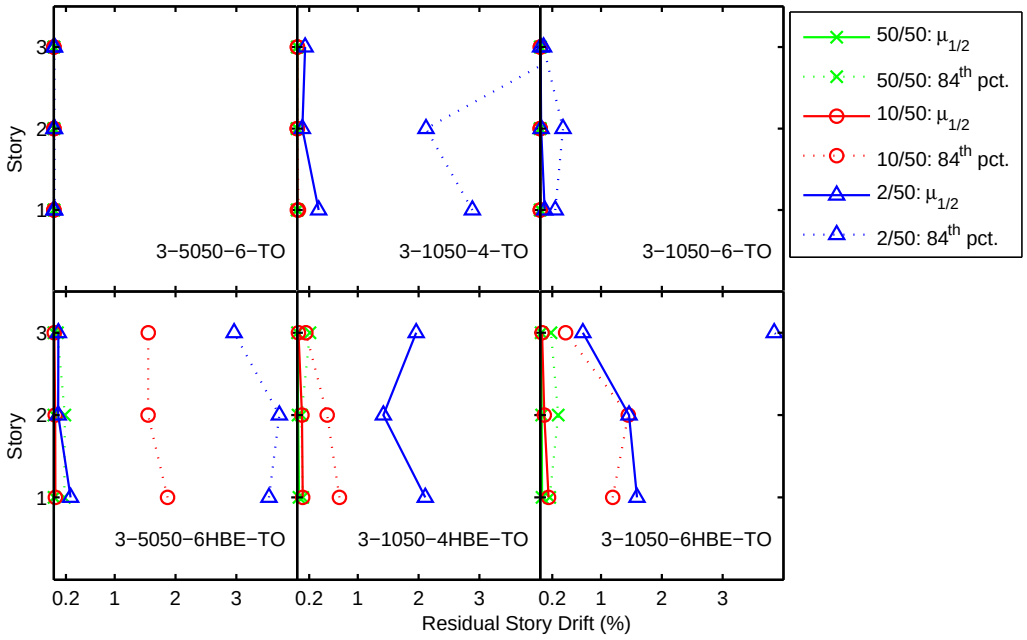

Figure 8.15: Residual story drift response for SC-SPSWs with fully-connected and HBE-only web plates (Models TO)

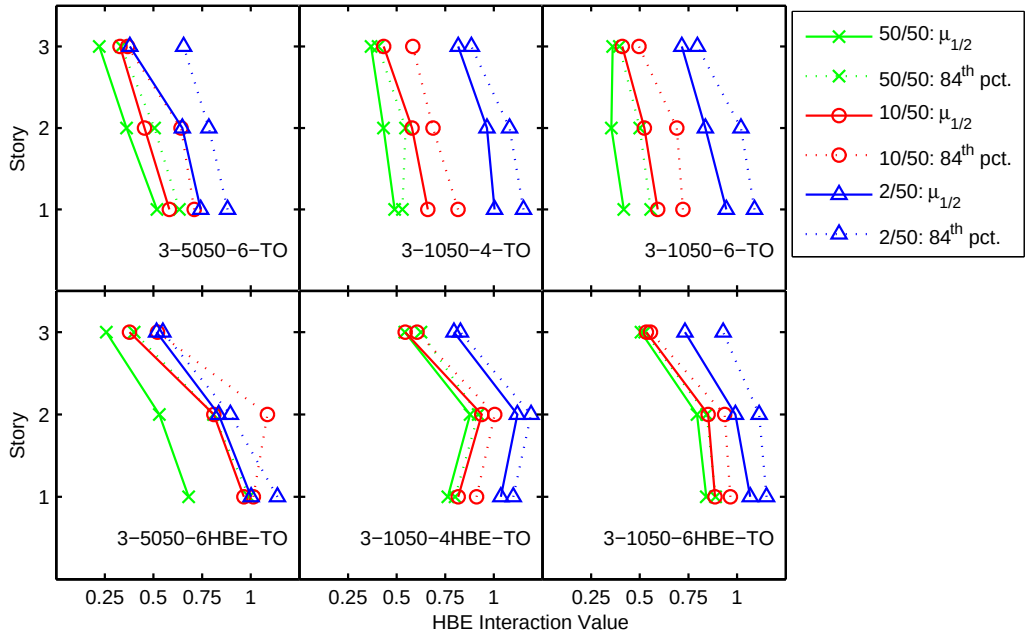

Figure 8.16: HBE damage value for SC-SPSWs with fully-connected and HBE-only web plates (Models TO)

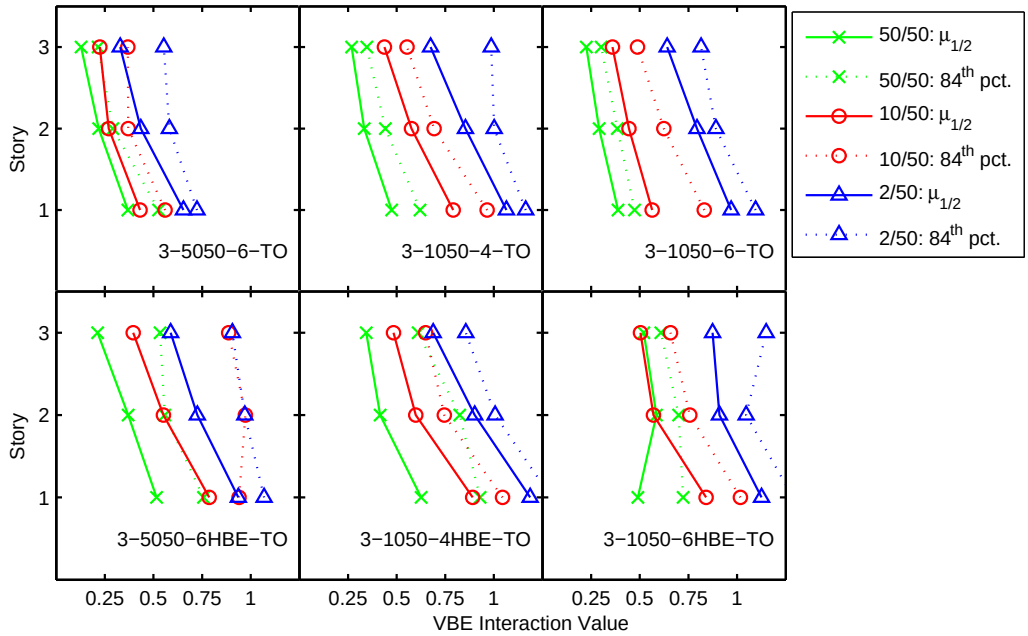

Figure 8.17: VBE damage value for SC-SPSWs with fully-connected and HBE-only web plates (Models TO)

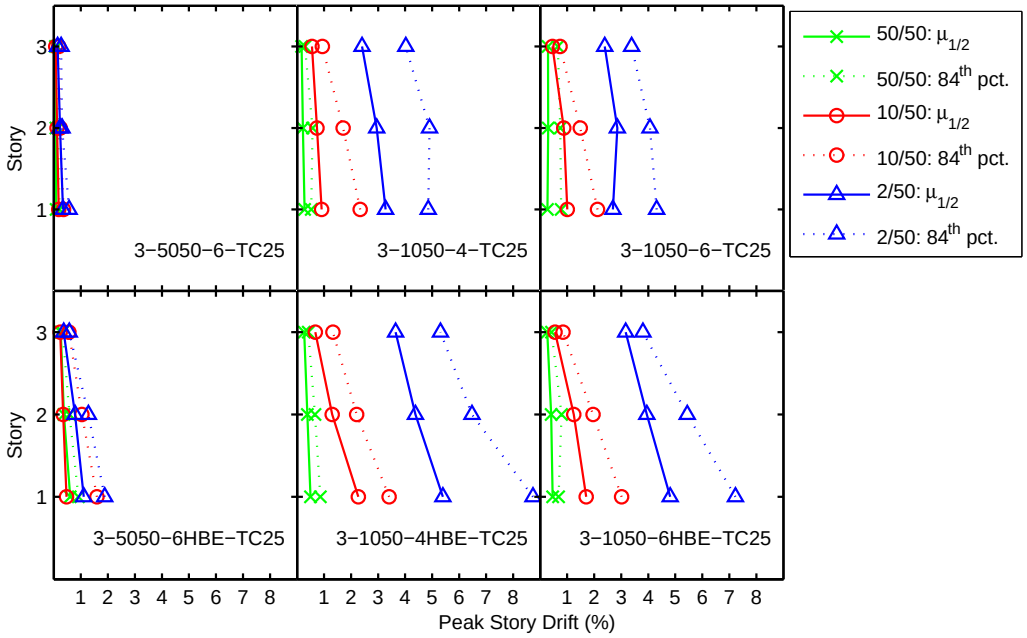

Figure 8.18: Peak story drift response for SC-SPSWs with fully-connected and HBE-only web plates (Models TC25)

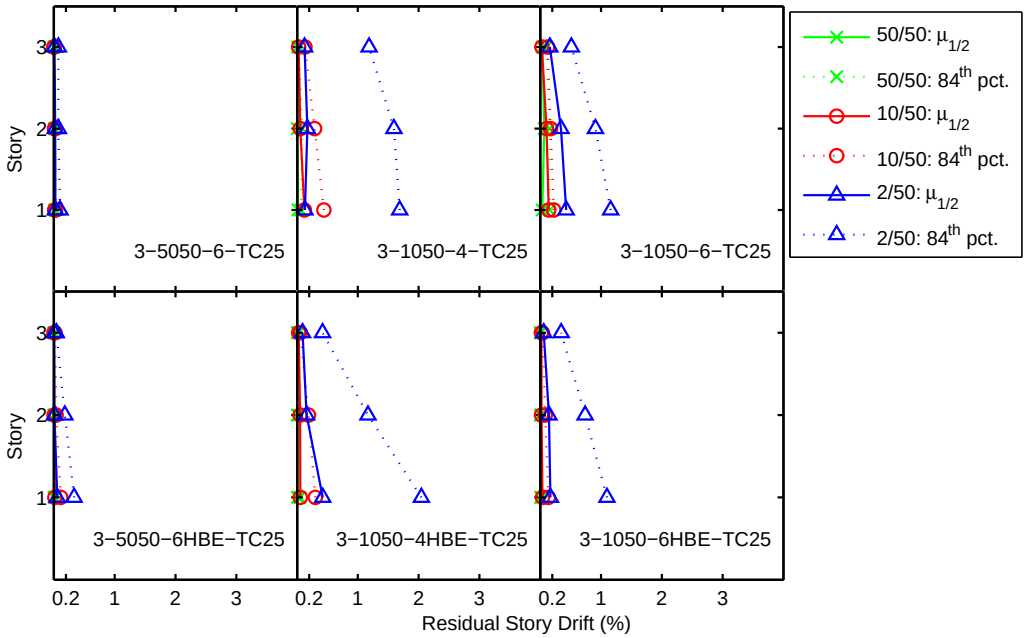

Figure 8.19: Residual story drift response for SC-SPSWs with fully-connected and HBE-only web plates (Models TC25)

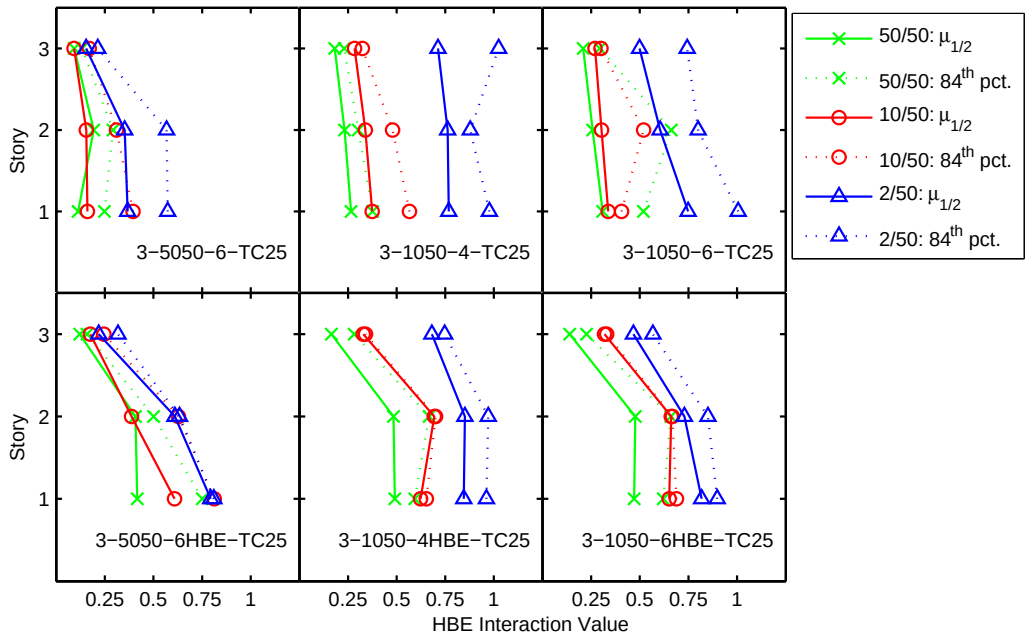

Figure 8.20: HBE damage value for SC-SPSWs with fully-connected and HBE-only web plates (Models TC25)

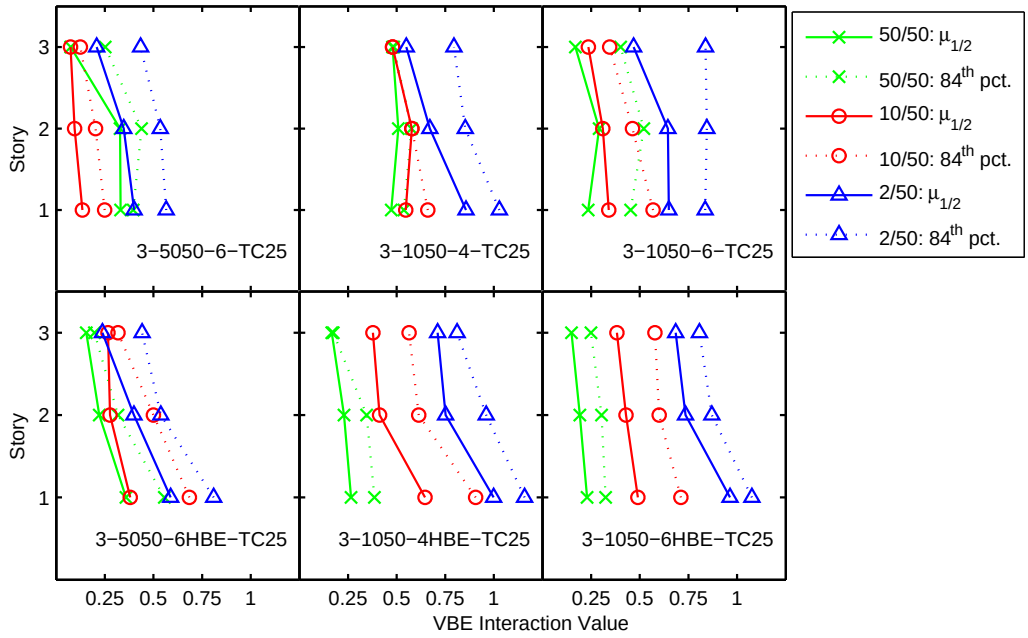

Figure 8.21: VBE damage value for SC-SPSWs with fully-connected and HBE-only web plates (Models TC25)

8.5.2.3 Comparison of web plate residual strength

Figs. 8.22 through 8.25 show comparisons of the key response parameters for fully-connected web plate models employing Model TO and Model TC25. As was briefly discussed in the previous section, considering web plate residual strength (Model TC25) greatly reduces the drift demands compared to the commonly employed tension-only (Model TO) (Fig. 8.22). This reduction in drift demands can be as much as 50%. Although the median residual drifts (Fig. 8.23) in these models (both TO and TC25) meet the recentering criterion at the 10/50 (and even at the 2/50) hazard level, Model TC25 does have larger 84^{th} percentile residual drifts at the 10/50 and 2/50 hazard levels due to the larger web plate strain at zero-force (the residual drifts are not due to boundary frame yielding as HBE and VBE interaction values are typically less than or near one for the TC25 models as shown in Figs. 8.24 and 8.25.).

Figs. 8.26 through 8.29 compare the response parameters for SC-SPSWs with web plates connected to the HBEs only and modeled with Models TO, TC25, and TCv (for those applicable). Similar trends apply when web plate residual strength is considered in the model, including significantly reduced drift demands, reduced residual drift demands (due to the reduction in boundary frame yielding), and reduced HBE and VBE interaction values. For the TCv models, which included additional compression beyond 25% of the tension strength in certain plates with h/t values less than 700 based on Fig. 7.4, the response parameters were even further reduced.

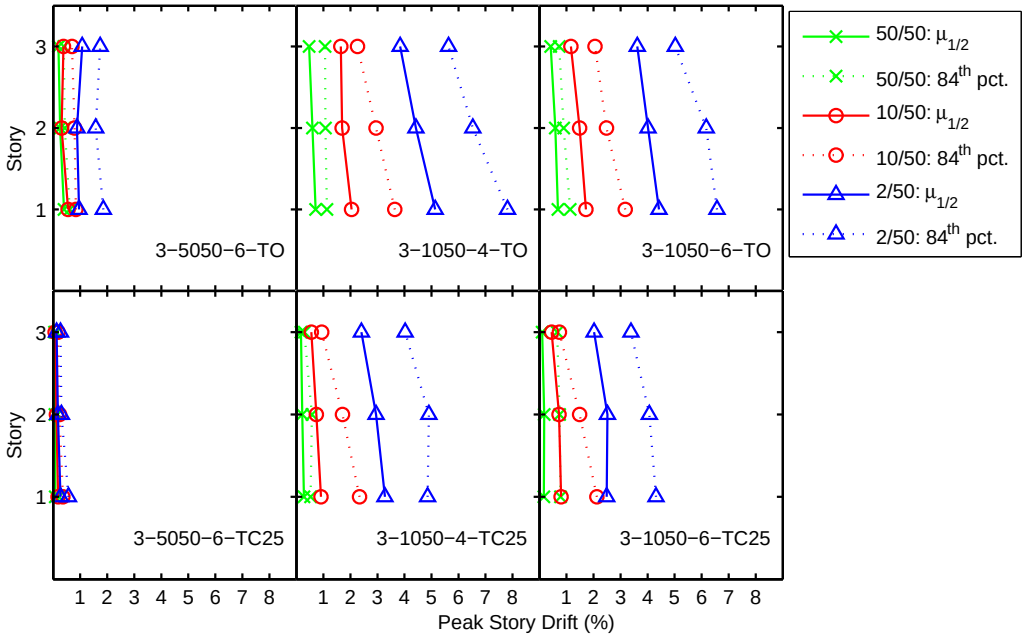

Figure 8.22: Peak story drift response for SC-SPSWs with fully-connected web plates (Models TO and TC)

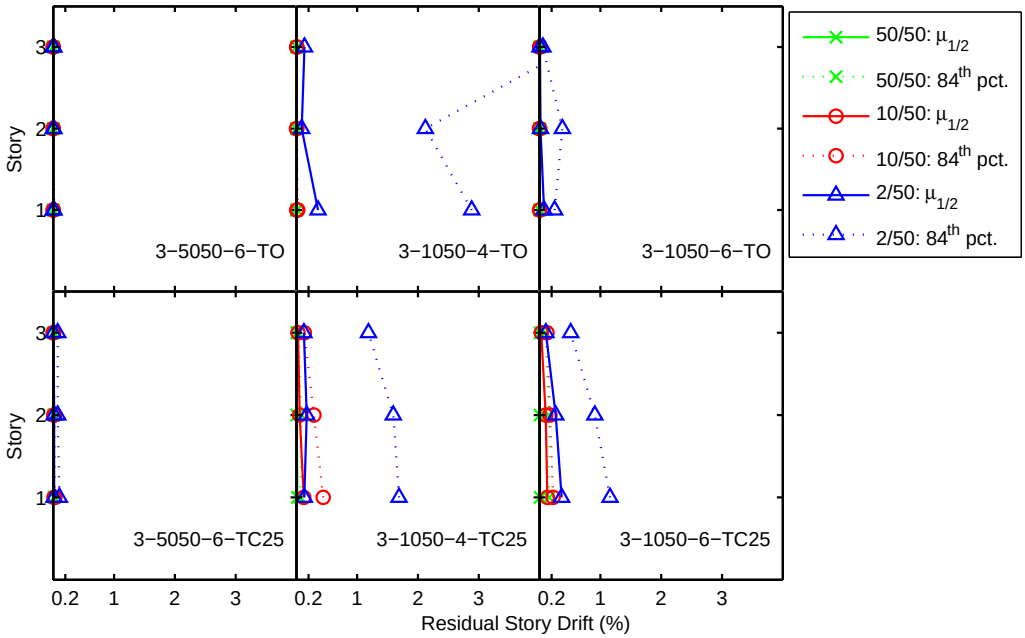

Figure 8.23: Residual story drift response for SC-SPSWs with fully-connected web plates (Models TO and TC)

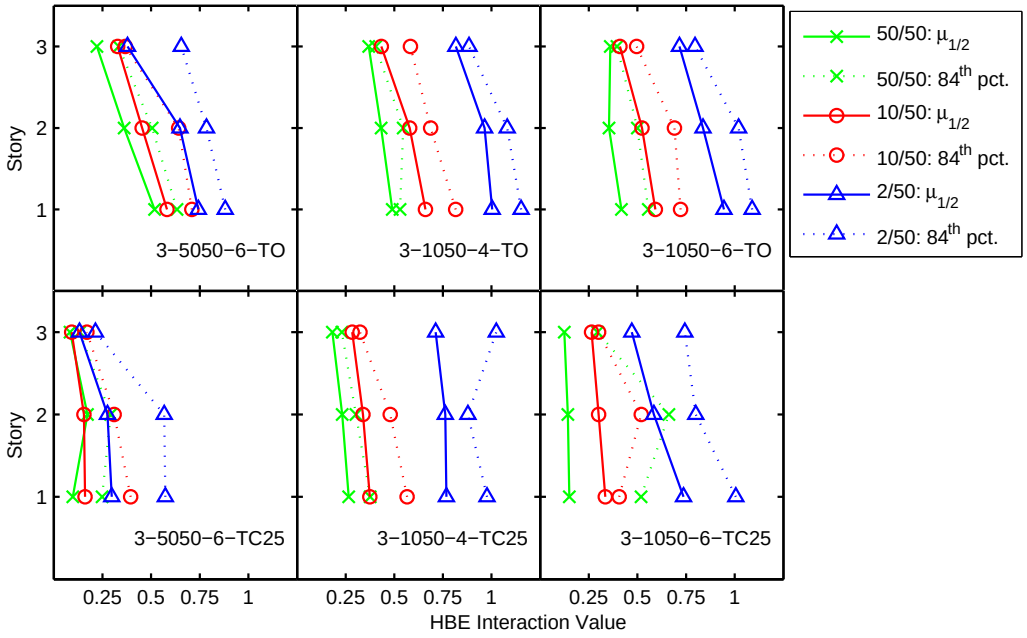

Figure 8.24: HBE damage value for SC-SPSWs with fully-connected web plates (Models TO and TC)

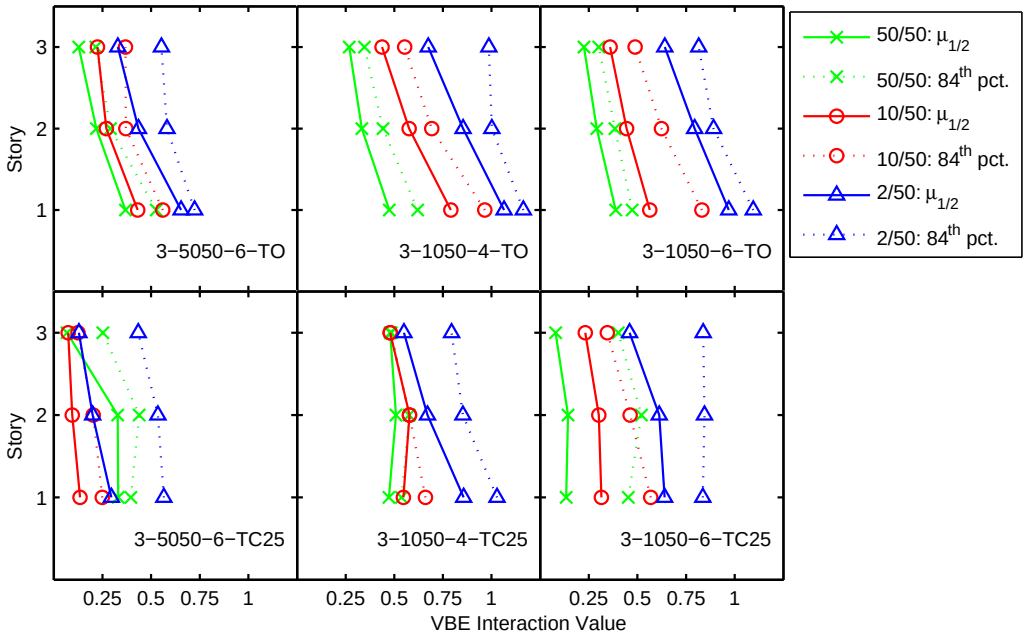

Figure 8.25: VBE damage value for SC-SPSWs with fully-connected web plates (Models TO and TC)

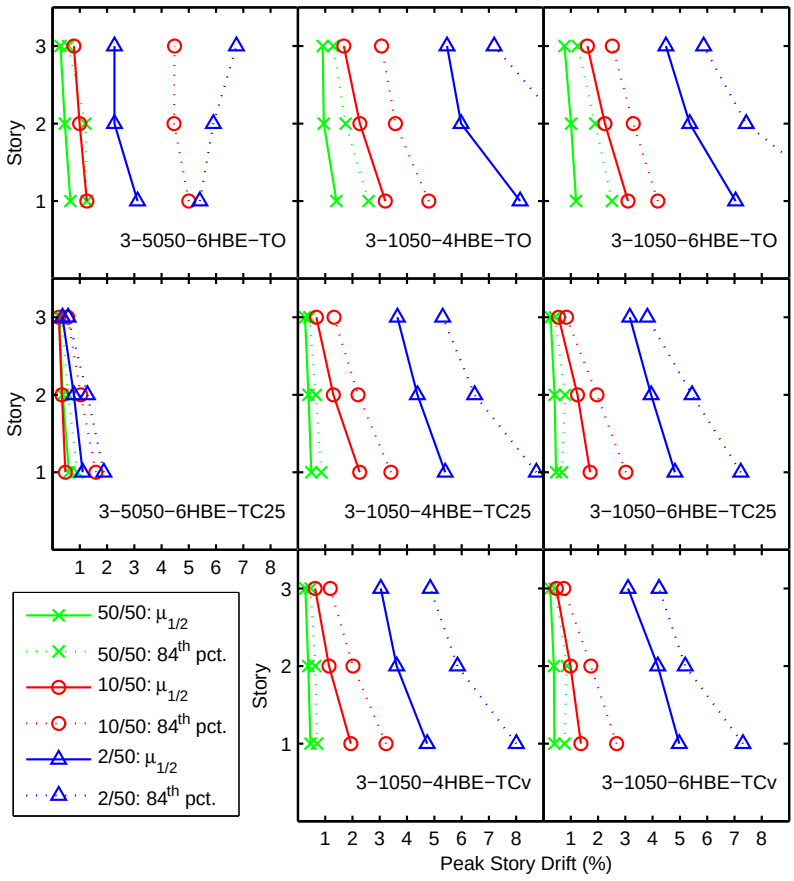

Figure 8.26: Peak story drift response for SC-SPSWs with web plates connected to HBEs only (Models TO and TC)

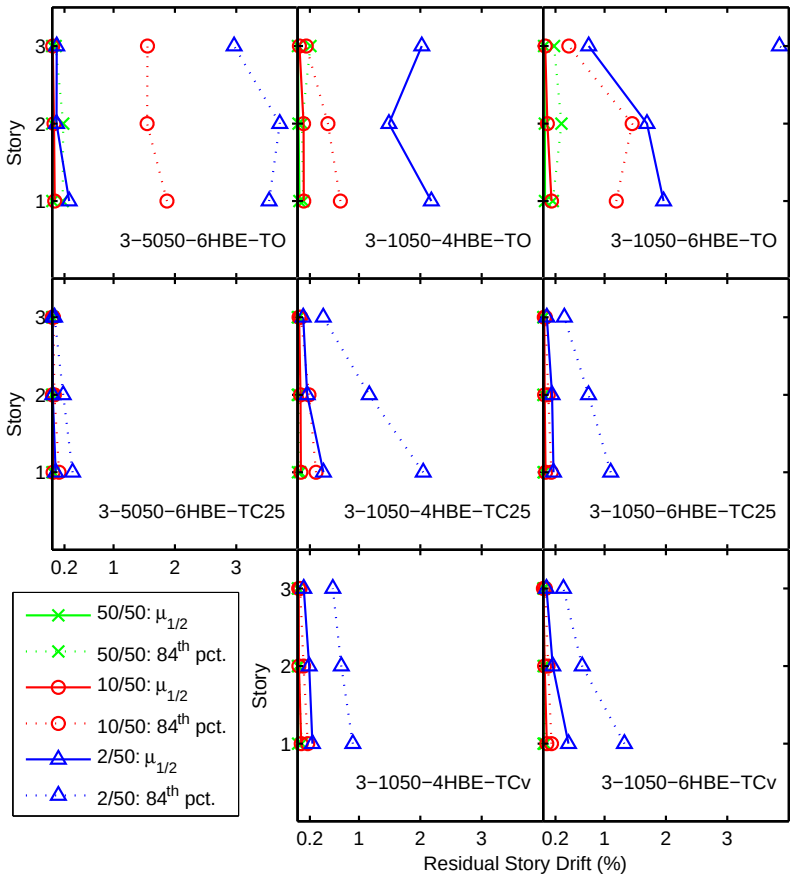

Figure 8.27: Residual story drift response for SC-SPSWs with web plates connected to HBEs only (Models TO and TC)

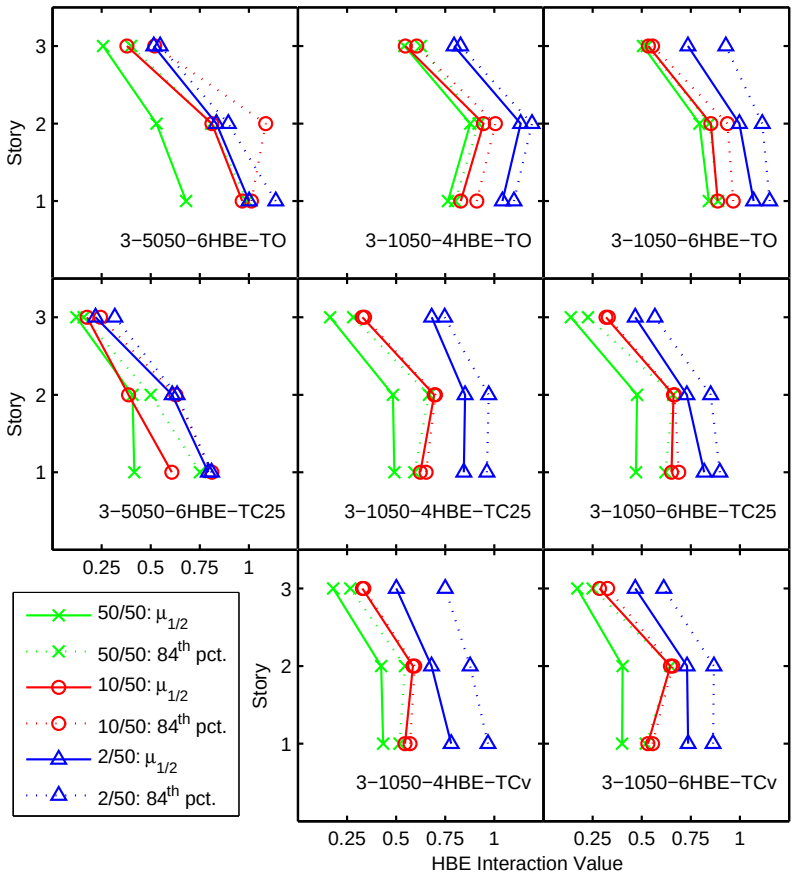

Figure 8.28: HBE damage value for SC-SPSWs with web plates connected to HBEs only (Models TO and TC)

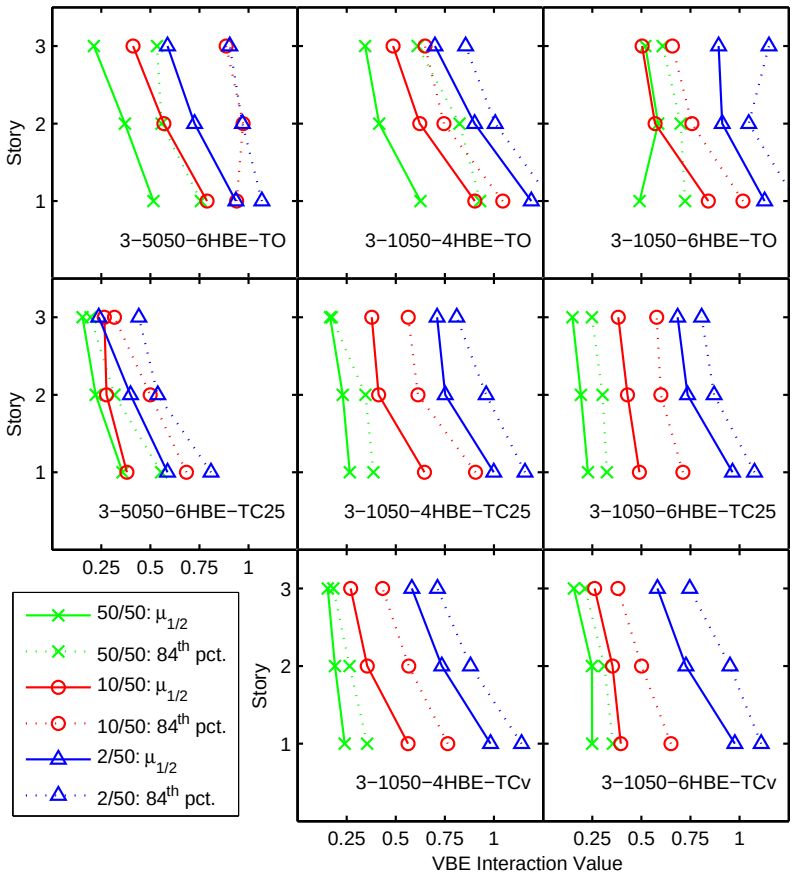

Figure 8.29: VBE damage value for SC-SPSWs with web plates connected to HBEs only (Models TO and TC)

8.5.3 Nine-story models

This section discusses preliminary results for the nine-story SC-SPSW models. Due to limitations of computing resources, only the nine-story SC-SPSWs with web plates designed using the $V_{10/50}/R$ design criteria were considered, as the nine-story walls designed to remain elastic during the 50/50 hazard level far exceeded performance objectives even with the tension-only web plate model (see Table F.1) and were deemed to be overly conservative. Furthermore, only a subset of ten ground motions at each hazard level are considered for each of these models. The selection criteria for the ground motions in each subset included preference for ground motions with shorter duration (to reduce computation time) and ground motions that typically resulted in near-median drift responses. The ground motions that were used in each hazard level are given in Table 8.9. Further details on each motion can be found in Clayton [2010] and in FEMA [2000a]. When comparing results to those from the Model TO study in Clayton [2010], only ground motions from the same subset will be considered.

Table 8.9: Ground motions selected for 9-story analyses

Hazard Level	50/50	10/50	2/50
Ground Motions	LA41	LA01	LA23
	LA42	LA02	LA24
	LA43	LA03	LA25
	LA44	LA04	LA26
	LA51	LA05	LA31
	LA52	LA06	LA32
	LA53	LA11	LA33
	LA54	LA12	LA34
	LA55	LA15	LA35
	LA56	LA16	LA36

The three-story analyses indicated that considering web plate residual strength in the numerical model results in more realistic and greatly reduced peak drift demands. For this reason, the nine-story HBE-only web plate SC-SPSWs will be modeled only with Model TC; however, the Model TC results for the fully-connected web plate SC-SPSWs will be com-

pared to the Model TO results from Clayton [2010] to demonstrate the effects of considering web plate residual strength for the nine-story walls.

8.5.3.1 Tabular Results

Tables 8.10 through 8.12 summarize the results of the analyses for the 9-1050-6, 9-1050-8, and 9-1050-10 SC-SPSWs, respectively. Each table shows the results of the tension-only fully-connected web plate (TO), tension-compression fully-connected web plate (TC25), and tension-compressions HBE-only web plate (HBE-TC25) models side-by-side for comparison. The response parameters are given for each ground motion in the subset. Due to the small sample size in each hazard level subset, only the median response value ($\mu_{1/2}$) for each subset if provided (i.e. the 84th percentile is not given).

Table 8.10: Response parameters for 9-1050-6 SC-SPSWs with fully-connected web plates (TO and TC25) and HBE-only web plates (HBE-TC25)

Hazard Level	Ground Motion	$\theta_{s,max}$(%)			$\theta_{resid,max}$(%)			D_{HBE}			D_{VBE}		
		TO	TC25	HBE-TC25	TO	TC25	HBE-TC25	TO	TC25	HBE-TC25	TO	TC25	HBE-TC25
50/50	LA41	1.07	1.08	1.00	0.002	0.022	0.023	0.74	0.48	0.56	0.89	0.77	0.66
	LA42	0.27	0.47	0.50	0.029	0.010	0.009	0.38	0.14	0.32	0.39	0.34	0.24
	LA43	0.15	0.35	0.36	0.003	0.011	0.018	0.28	0.13	0.24	0.36	0.15	0.24
	LA44	0.12	0.28	0.23	0.006	0.005	0.008	0.20	0.10	0.16	0.18	0.12	0.14
	LA51	1.20	0.68	0.76	0.003	0.010	0.226	0.81	0.27	0.54	0.65	0.42	0.61
	LA52	0.32	0.47	0.77	0.033	0.002	0.005	0.58	0.21	0.42	0.54	0.28	0.39
	LA53	0.55	0.62	0.73	0.025	0.008	0.005	0.51	0.19	0.44	0.73	0.38	0.46
	LA54	0.44	0.53	0.83	0.066	0.004	0.005	0.52	0.18	0.53	0.57	0.36	0.51
	LA55	0.45	0.73	0.61	0.004	0.007	0.008	0.54	0.23	0.35	0.58	0.43	0.40
	LA56	0.47	0.83	0.61	0.003	0.007	0.013	0.54	0.24	0.33	0.76	0.55	0.44
	$\mu_{1/2}$	0.45	0.58	0.67	0.005	0.008	0.008	0.53	0.20	0.38	0.57	0.37	0.42
10/50	LA01	0.76	0.93	1.14	0.072	0.111	0.013	0.71	0.28	0.65	0.79	0.59	0.72
	LA02	0.98	0.97	0.93	0.465	0.027	0.050	0.67	0.30	0.65	0.84	0.65	0.72
	LA03	0.49	0.77	0.94	0.020	0.124	0.023	0.67	0.32	0.50	0.91	0.68	0.60
	LA04	0.48	0.62	0.55	0.003	0.007	0.010	0.52	0.21	0.37	0.64	0.40	0.35
	LA05	0.34	0.76	0.84	0.003	0.006	0.025	0.54	0.23	0.43	0.79	0.44	0.59
	LA06	0.24	0.50	0.47	0.008	0.010	0.008	0.35	0.17	0.25	0.42	0.34	0.30
	LA11	0.65	1.29	1.55	0.059	0.106	0.050	0.66	0.47	0.63	0.85	0.72	0.79
	LA12	0.84	0.85	0.93	0.272	0.035	0.015	1.25	0.33	0.50	0.49	0.42	0.47
	LA15	1.03	1.20	1.68	0.379	0.278	0.065	0.66	0.45	0.65	0.84	0.73	0.91
	LA16	1.51	1.55	1.71	0.083	0.503	0.366	0.80	0.63	0.64	0.95	0.83	0.83
	$\mu_{1/2}$	0.71	0.89	0.94	0.066	0.070	0.024	0.67	0.31	0.57	0.82	0.62	0.66
2/50	LA23	0.61	0.82	1.15	0.009	0.023	0.115	0.51	0.30	0.59	0.74	0.64	0.75
	LA24	3.09	2.10	2.45	1.75	0.310	0.086	1.39	0.81	0.85	1.15	1.00	0.99
	LA25	1.90	2.09	2.42	1.37	0.366	0.103	0.82	0.63	0.66	1.02	0.92	0.98
	LA26	2.87	2.56	2.98	2.79	0.476	0.090	1.07	0.87	0.98	1.11	1.02	0.98
	LA31	2.21	3.28	2.65	0.163	0.455	0.042	0.91	0.85	0.66	1.10	0.87	0.94
	LA32	2.75	2.15	2.68	0.219	0.733	0.701	1.04	0.70	0.87	1.19	1.06	1.01
	LA33	3.03	2.30	2.61	0.123	0.116	0.097	1.16	0.78	0.90	1.09	0.94	1.03
	LA34	1.86	2.12	2.31	0.093	0.130	0.060	0.92	0.76	0.82	1.06	0.99	1.04
	LA35	5.61	5.00	5.52	3.03	0.655	0.964	1.10	1.02	1.06	1.24	1.19	1.19
	LA36	5.54	4.67	5.39	2.06	0.538	0.715	1.32	1.05	1.04	1.26	1.21	1.20
	$\mu_{1/2}$	2.81	2.23	2.63	0.796	0.411	0.100	1.06	0.80	0.83	1.10	1.00	1.00

Table 8.11: Response parameters for 9-1050-8 SC-SPSWs with fully-connected web plates (TO and TC25) and HBE-only web plates (HBE-TC25)

		$\theta_{s,max}(\%)$			$\theta_{resid,max}(\%)$			D_{HBE}			D_{VBE}		
Hazard Level	Ground Motion	TO	TC25	HBE-TC25	TO	TC25	HBE-TC25	TO	TC25	HBE-TC25	TO	TC25	HBE-TC25
50/50	LA41	1.15	1.08	2.09	0.004	0.022	0.046	0.64	0.68	0.89	0.71	0.62	0.77
	LA42	0.41	0.47	0.43	0.004	0.010	0.003	0.47	0.21	0.33	0.56	0.42	0.39
	LA43	0.16	0.35	0.37	0.010	0.011	0.024	0.27	0.18	0.29	0.22	0.19	0.31
	LA44	0.13	0.28	—*	0.011	0.005	—*	0.22	0.15	—*	0.13	0.18	—*
	LA51	1.34	0.68	1.39	0.005	0.010	0.045	0.67	0.35	0.66	0.59	0.56	0.83
	LA52	0.30	0.47	0.62	0.013	0.002	0.018	0.48	0.31	0.65	0.35	0.35	0.74
	LA53	0.58	0.50	1.43	0.010	0.009	0.014	0.52	0.25	0.69	0.62	0.29	0.64
	LA54	0.53	0.40	0.88	0.067	0.009	0.024	0.49	0.25	0.77	0.55	0.29	0.94
	LA55	0.42	0.59	0.62	0.017	0.022	0.023	0.46	0.28	0.85	0.50	0.40	0.87
	LA56	0.41	0.63	1.13	0.004	0.003	0.040	0.45	0.25	0.46	0.55	0.39	0.62
	$\mu_{1/2}$	0.42	0.49	0.88	0.010	0.009	0.024	0.48	0.25	0.66	0.55	0.37	0.74
10/50	LA01	1.10	0.93	1.11	0.591	0.111	0.182	0.65	0.39	0.75	0.71	0.74	0.59
	LA02	1.43	0.97	0.93	0.708	0.027	0.109	0.69	0.52	0.65	0.61	0.89	0.66
	LA03	0.58	0.77	1.03	0.008	0.124	0.393	0.61	0.55	0.96	0.76	0.96	0.72
	LA04	0.59	0.62	0.52	0.020	0.007	0.108	0.54	0.31	0.67	0.60	0.50	0.90
	LA05	0.32	0.76	0.87	0.005	0.006	0.018	0.49	0.33	0.65	0.65	0.55	0.52
	LA06	0.23	0.50	0.84	0.004	0.010	0.679	0.32	0.25	0.55	0.38	0.41	0.86
	LA11	0.82	1.29	1.82	0.004	0.106	0.068	0.68	0.68	0.76	0.77	1.02	0.73
	LA12	1.10	0.85	0.70	0.074	0.035	0.068	0.69	0.38	0.55	0.35	0.55	0.57
	LA15	1.63	1.20	2.28	0.129	0.278	0.080	0.64	0.64	0.73	0.68	0.97	0.70
	LA16	1.63	1.55	2.49	0.416	0.503	0.330	0.70	0.90	0.74	0.74	1.01	0.68
	$\mu_{1/2}$	0.96	0.89	0.98	0.047	0.070	0.108	0.65	0.46	0.70	0.67	0.81	0.69
2/50	LA23	0.66	0.82	1.38	0.008	0.023	0.212	0.60	0.52	0.76	0.64	0.68	0.70
	LA24	3.59	2.10	4.57	1.33	0.310	0.897	0.93	0.61	0.75	0.96	1.10	1.06
	LA25	2.45	2.09	2.61	1.36	0.366	0.146	0.70	0.91	0.94	0.86	0.84	1.20
	LA26	3.20	2.56	3.49	0.377	0.476	0.273	0.81	0.95	0.94	0.86	0.89	0.79
	LA31	5.79	3.28	2.63	0.122	0.455	0.308	0.97	1.03	0.86	0.83	0.86	0.85
	LA32	2.79	2.15	2.42	0.232	0.733	0.414	0.90	1.00	0.75	0.85	0.82	0.95
	LA33	1.94	2.30	4.37	0.098	0.116	0.700	0.69	0.55	0.81	0.84	0.87	1.07
	LA34	2.80	2.12	3.01	0.017	0.130	0.187	0.79	0.70	0.73	0.98	0.92	0.97
	LA35	6.49	5.00	6.18	2.82	0.655	2.15	0.97	1.00	0.82	1.19	1.12	1.11
	LA36	6.48	4.67	6.88	2.15	0.538	0.361	1.00	0.97	0.85	1.17	1.12	1.13
	$\mu_{1/2}$	3.00	2.23	3.25	0.304	0.411	0.334	0.85	0.93	0.81	0.86	0.88	1.01

* Analysis did not finish due to convergence failure. Results from this particular analysis are not included.

Table 8.12: Response parameters for 9-1050-10 SC-SPSWs with fully-connected web plates (TO and TC25) and HBE-only web plates (HBE-TC25)

Hazard Level	Ground Motion	$\theta_{s,max}(\%)$			$\theta_{resid,max}(\%)$			D_{HBE}			D_{VBE}		
		TO	TC25	HBE-TC25	TO	TC25	HBE-TC25	TO	TC25	HBE-TC25	TO	TC25	HBE-TC25
50/50	LA41	1.12	1.23	1.18	0.004	0.066	0.339	0.56	0.32	0.64	0.50	0.47	0.88
	LA42	0.31	0.34	0.42	0.012	0.006	0.005	0.34	0.16	0.28	0.39	0.12	0.50
	LA43	0.18	0.27	0.35	0.008	0.023	0.115	0.26	0.13	0.29	0.17	0.10	0.70
	LA44	0.13	0.24	0.55	0.003	0.005	0.249	0.20	0.13	0.36	0.11	0.10	0.77
	LA51	1.20	0.49	0.62	0.003	0.018	0.285	0.59	0.20	0.88	0.45	0.14	0.74
	LA52	0.28	0.46	0.62	0.002	0.004	0.328	0.36	0.23	0.79	0.22	0.13	0.60
	LA53	0.64	0.41	0.60	0.065	0.010	0.294	0.52	0.19	0.90	0.48	0.15	0.78
	LA54	0.79	0.46	0.76	0.004	0.010	0.099	0.53	0.20	0.60	0.46	0.16	0.77
	LA55	0.46	0.49	0.70	0.004	0.027	0.423	0.48	0.24	0.61	0.44	0.35	0.89
	LA56	0.83	0.77	0.80	0.003	0.028	0.124	0.54	0.42	0.65	0.48	0.34	0.53
	$\mu_{1/2}$	0.55	0.46	0.62	0.004	0.014	0.267	0.50	0.20	0.63	0.45	0.15	0.76
10/50	LA01	0.99	0.66	0.95	0.767	0.016	0.234	0.56	0.25	0.88	0.53	0.39	0.74
	LA02	1.46	0.73	0.91	0.832	0.031	0.084	0.69	0.27	0.64	0.47	0.41	0.77
	LA03	0.70	0.42	0.89	0.004	0.207	0.151	0.61	0.26	0.76	0.60	0.40	0.76
	LA04	0.72	0.56	0.71	0.079	0.010	0.071	0.50	0.19	0.54	0.45	0.15	0.82
	LA05	0.41	0.40	0.78	0.034	0.012	0.064	0.47	0.22	0.61	0.48	0.28	0.52
	LA06	0.24	0.40	0.42	0.007	0.013	0.015	0.31	0.23	0.34	0.21	0.20	0.43
	LA11	0.92	1.38	2.48	0.004	0.133	0.155	0.63	0.97	0.88	0.57	0.46	0.93
	LA12	1.02	0.67	0.75	0.035	0.020	0.451	0.68	0.29	0.87	0.33	0.17	0.95
	LA15	1.23	1.10	1.78	0.039	0.166	0.142	0.62	0.31	0.76	0.49	0.44	0.59
	LA16	2.17	2.12	1.97	0.037	0.493	0.542	0.81	0.55	0.79	0.65	0.53	0.63
	$\mu_{1/2}$	0.95	0.67	0.90	0.036	0.026	0.146	0.62	0.27	0.76	0.49	0.39	0.75
2/50	LA23	0.97	0.81	1.50	0.120	0.058	0.548	0.55	0.28	0.91	0.52	0.43	1.23
	LA24	3.73	2.57	5.21	0.850	0.132	0.605	0.93	0.63	0.79	0.84	0.61	1.01
	LA25	2.20	2.15	2.35	0.292	0.298	0.141	0.69	0.54	0.85	0.60	0.55	0.78
	LA26	3.13	2.82	2.58	1.48	0.288	0.218	0.89	0.70	1.13	0.75	0.66	0.89
	LA31	3.02	2.04	2.42	0.144	0.391	0.059	0.94	0.69	0.82	0.75	0.54	0.78
	LA32	2.93	2.19	2.87	0.060	0.713	0.206	0.80	0.56	0.79	0.78	0.63	0.92
	LA33	2.27	2.03	4.29	0.108	0.172	0.153	0.68	0.54	0.79	0.62	0.59	0.99
	LA34	3.04	2.50	3.30	0.140	0.325	0.074	0.84	0.62	0.79	0.74	0.64	0.89
	LA35	6.56	5.57	6.71	3.59	0.578	1.95	1.07	0.93	0.85	1.06	0.86	1.09
	LA36	6.89	5.81	7.06	1.41	1.74	0.630	1.08	0.97	0.84	1.07	0.98	1.07
	$\mu_{1/2}$	3.03	2.35	3.08	0.218	0.312	0.212	0.86	0.63	0.83	0.75	0.62	0.96

8.5.3.2 Comparison of web plate connectivity

Due to the relatively small number of ground motions in each subset, responses from individual ground motions (as opposed to median and 84th percentile responses) will be compared. The figures below compare (a) roof drift, (b) first story drift, and (c) ninth story drift time histories, as well as the (d) maximum drifts and (e) residual drifts at each story and (f) base shear vs. roof drift responses. Figs. 8.30 through 8.32 compare responses from a representative 50/50 ground motion (LA43) of fully-connected and HBE-only connected web plate SC-SPSWs (both modeled with Model TC) for the 9-1050-6, 9-1050-8, and 9-1050-10 SC-SPSWs, respectively. Similarly, Figs. 8.33 through 8.35 show response of the same SC-SPSWs during a representative 10/50 ground motion (LA11), and Figs. 8.36 through 8.38 show response of the same SC-SPSWs during a representative 2/50 ground motion (LA24).

These results show that for the same web plate material model (TC in this case), using beam-only connected web plates typically results in larger peak story drifts compared to the fully-connected web plates, as was also observed in the three-story buildings. The peak story drift when using beam-only connected web plates typically ranged from 6% to 50% larger than those with fully-connected web plates. Even with the increase in peak story drift demands, the nine-story SC-SPSWs with beam-only connected web plates are still able to meet the proposed performance objectives, including median 10/50 peak drifts less than 1%, significantly less than the 2% code-based drift limit. Additionally, the median peak residual story drift from the selected ground motions at the 10/50 was less than 0.2%, the recentering criterion. The median HBE and VBE damage values (D_{HBE} and D_{VBE}) were near or less than 1.0 at the 2/50 hazard level indicating minimal occurances of boundary frame yielding, and the peak story and residual drift demands at this hazard level were not excessivly large to suggest collapse. These results suggest that SC-SPSWs designed using beam-only connected web plates (and thus smaller boundary frame members) are suitable for meeting the propsed performance objectives for buildings of this height.

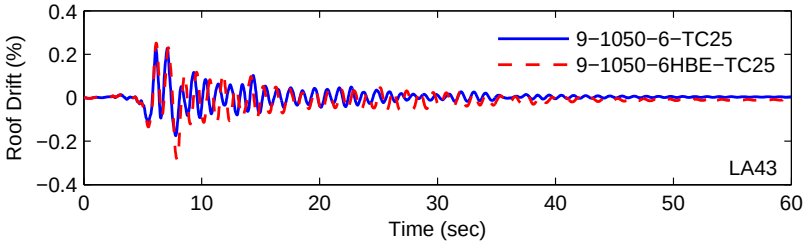

(a) Roof drift vs. time

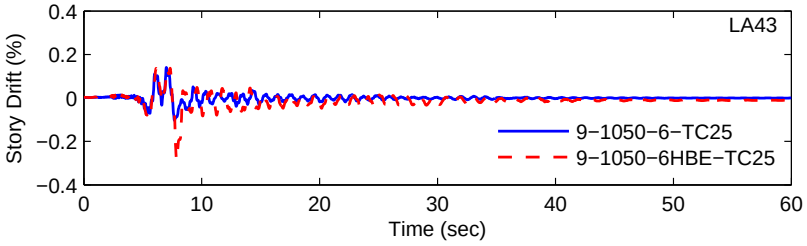

(b) 1^{st} story drift vs. time

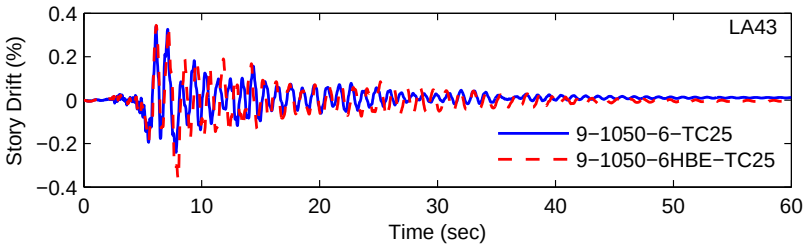

(c) 9^{th} story drift vs. time

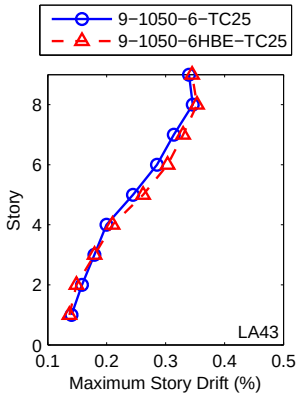

(d) Maximum Story Drifts

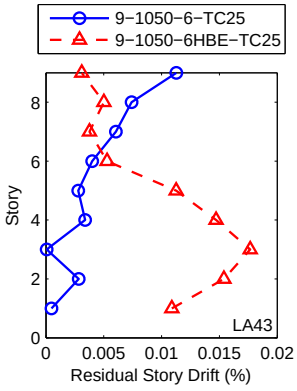

(e) Residual Story Drifts

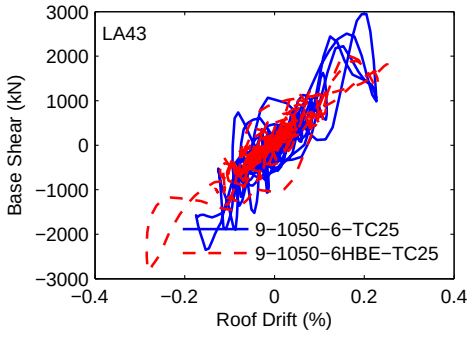

(f) Force vs. drift

Figure 8.30: Representative 50/50 (LA43) responses for 9-1050-6-TC25 and 9-1050-6HBE-TC25

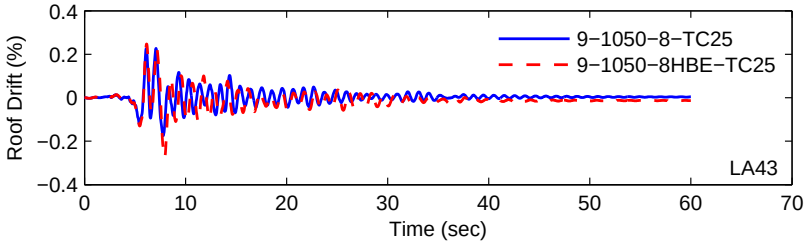

(a) Roof drift vs. time

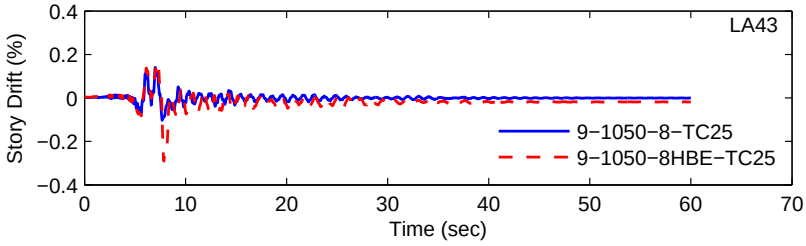

(b) 1^{st} story drift vs. time

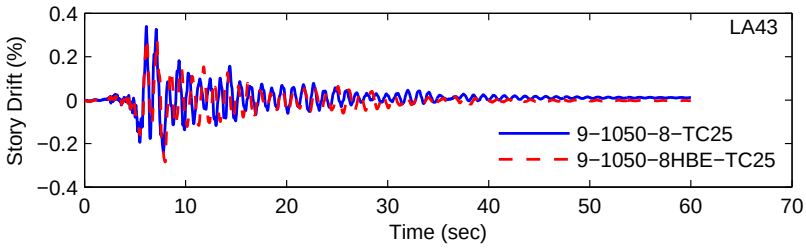

(c) 9^{th} story drift vs. time

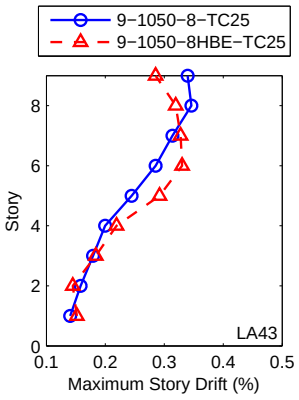

(d) Maximum Story Drifts

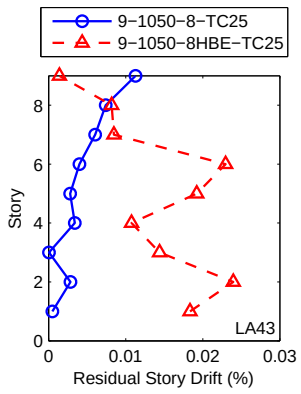

(e) Residual Story Drifts

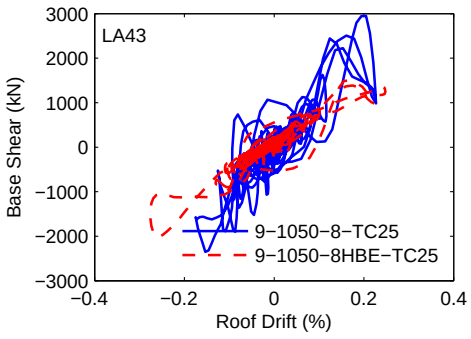

(f) Force vs. drift

Figure 8.31: Representative 50/50 (LA43) responses for 9-1050-8-TC25 and 9-1050-8HBE-TC25

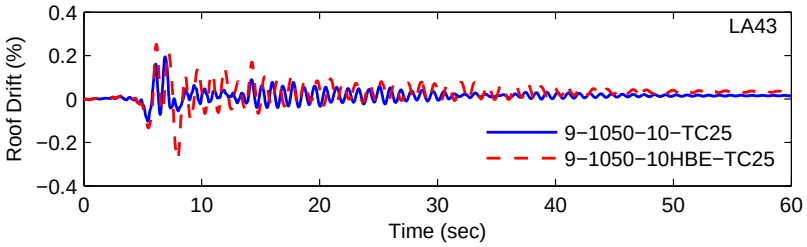

(a) Roof drift vs. time

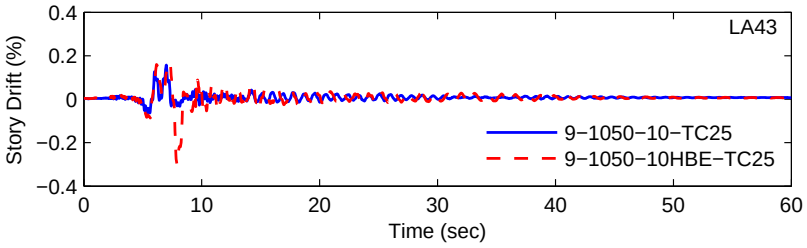

(b) 1^{st} story drift vs. time

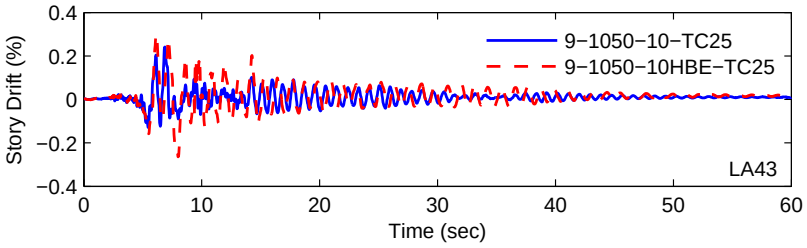

(c) 9^{th} story drift vs. time

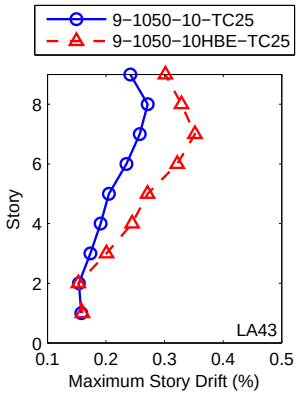

(d) Maximum Story Drifts

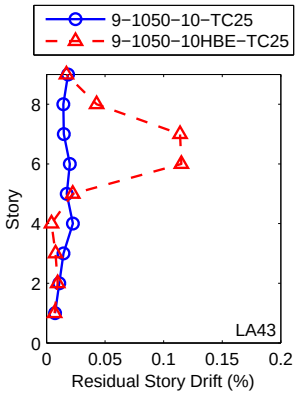

(e) Residual Story Drifts

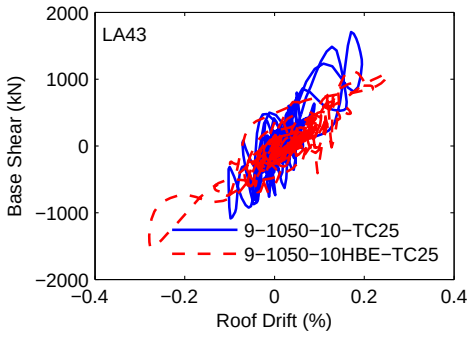

(f) Force vs. drift

Figure 8.32: Representative 50/50 (LA43) responses for 9-1050-10-TC25 and 9-1050-10HBE-TC25

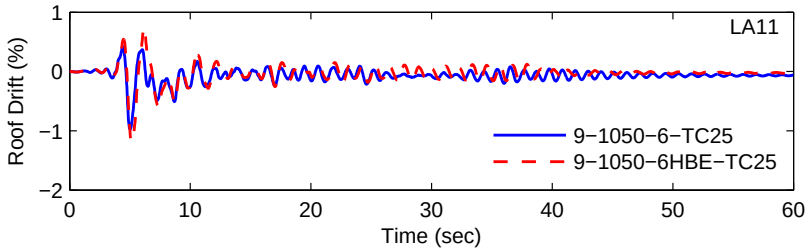

(a) Roof drift vs. time

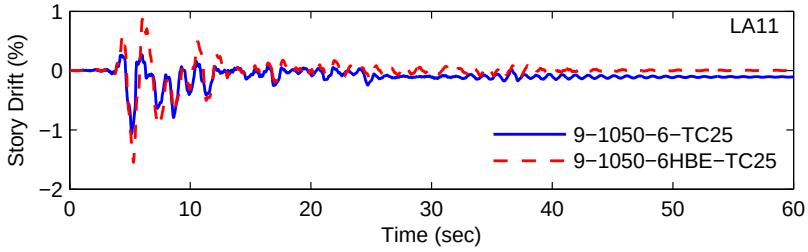

(b) 1^{st} story drift vs. time

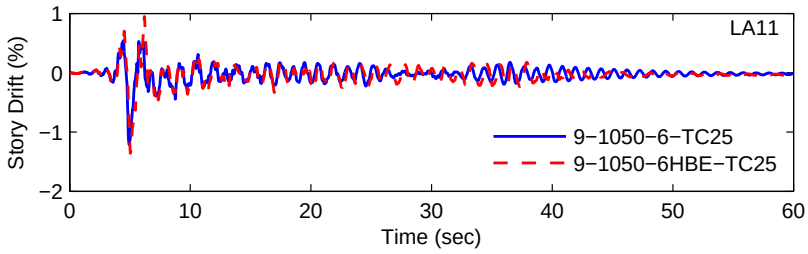

(c) 9^{th} story drift vs. time

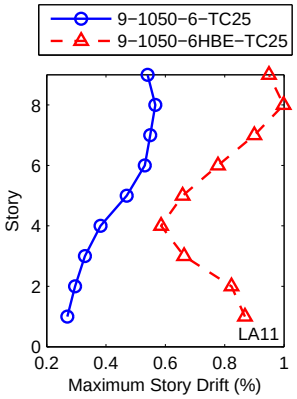

(d) Maximum Story Drifts

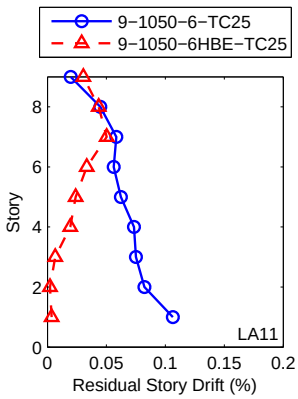

(e) Residual Story Drifts

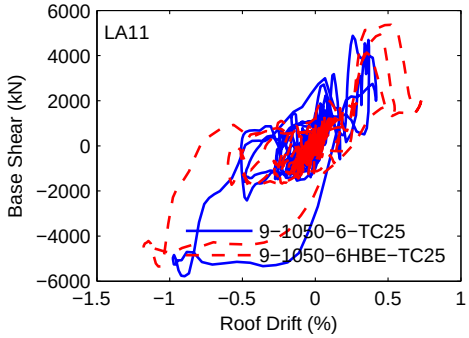

(f) Force vs. drift

Figure 8.33: Representative 10/50 (LA11) responses for 9-1050-6-TC25 and 9-1050-6HBE-TC25

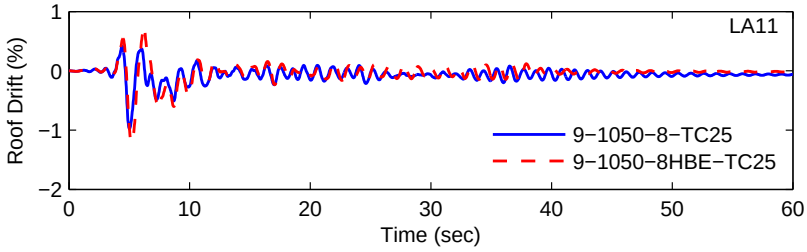

(a) Roof drift vs. time

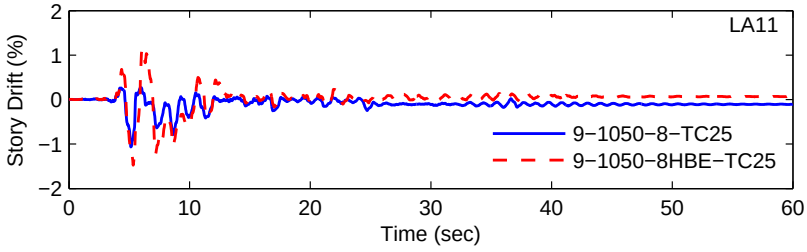

(b) 1^{st} story drift vs. time

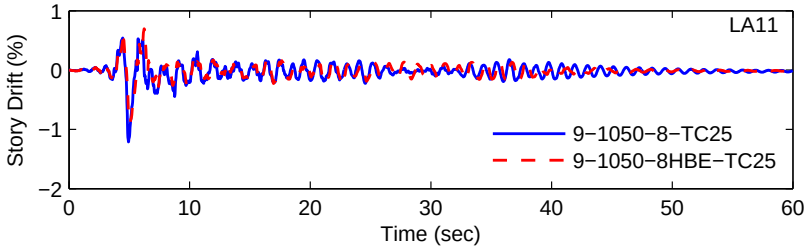

(c) 9^{th} story drift vs. time

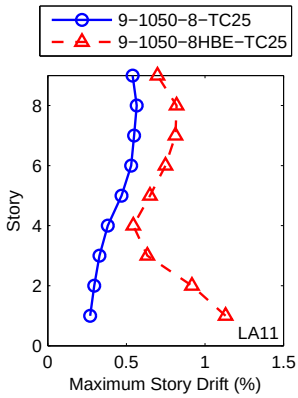

(d) Maximum Story Drifts

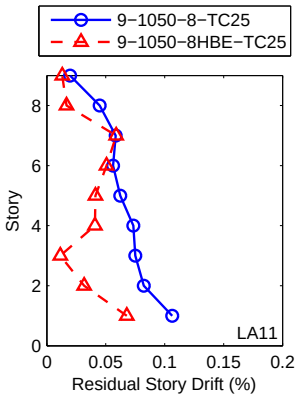

(e) Residual Story Drifts

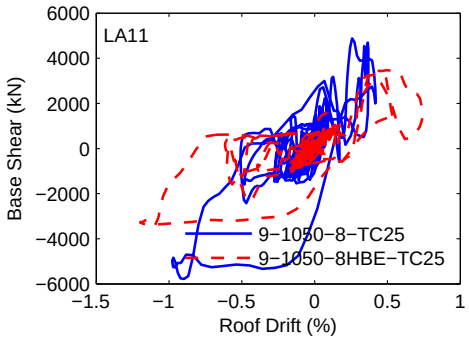

(f) Force vs. drift

Figure 8.34: Representative 10/50 (LA11) responses for 9-1050-8-TC25 and 9-1050-8HBE-TC25

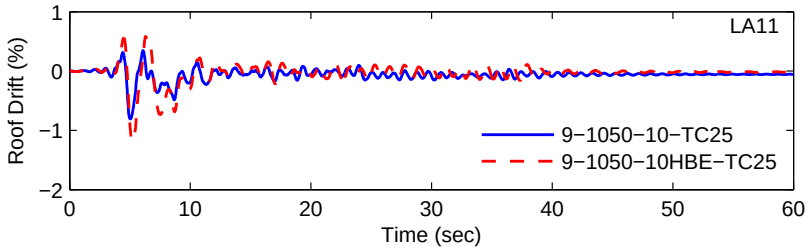

(a) Roof drift vs. time

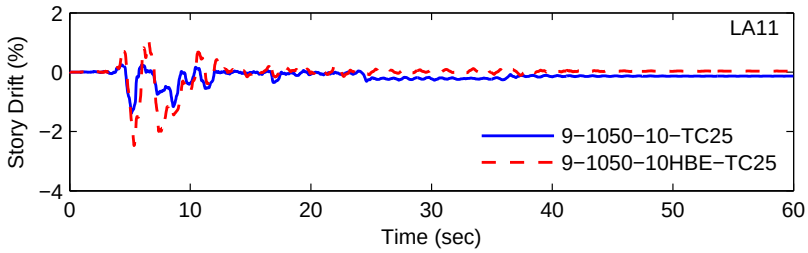

(b) 1^{st} story drift vs. time

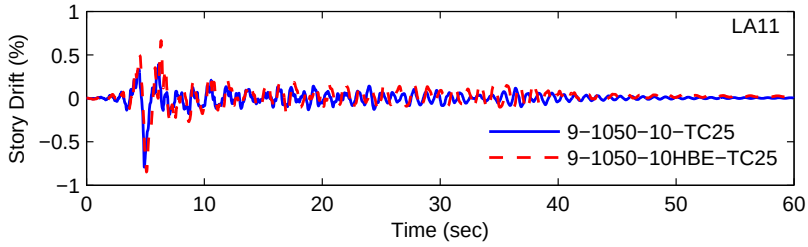

(c) 9^{th} story drift vs. time

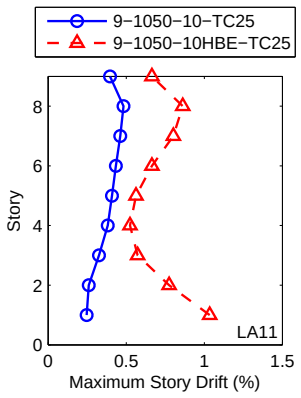

(d) Maximum Story Drifts

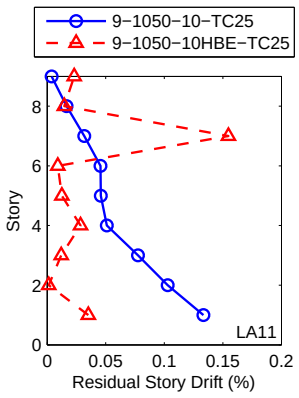

(e) Residual Story Drifts

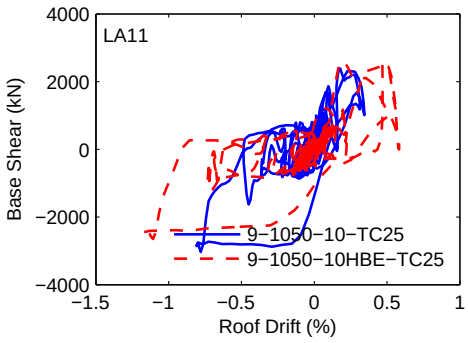

(f) Force vs. drift

Figure 8.35: Representative 10/50 (LA11) responses for 9-1050-10-TC25 and 9-1050-10HBE-TC25

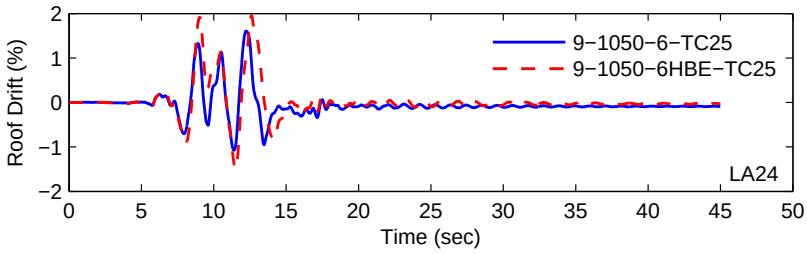

(a) Roof drift vs. time

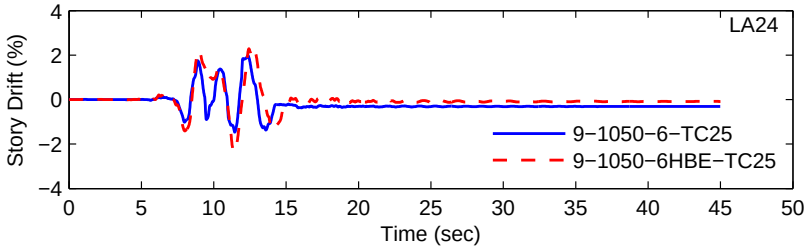

(b) 1^{st} story drift vs. time

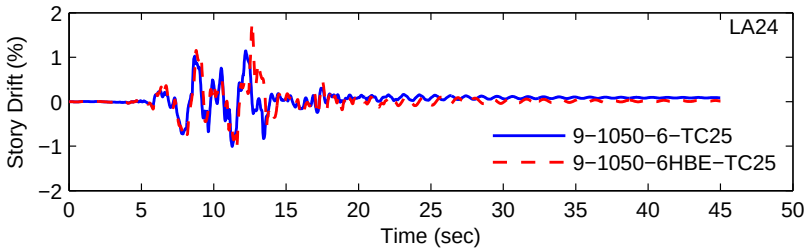

(c) 9^{th} story drift vs. time

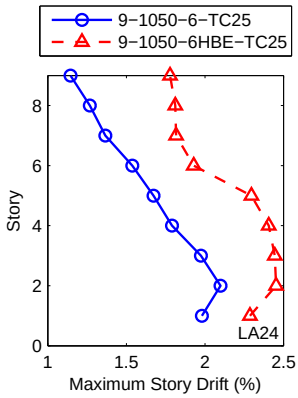

(d) Maximum Story Drifts

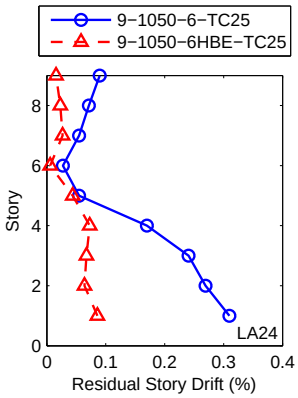

(e) Residual Story Drifts

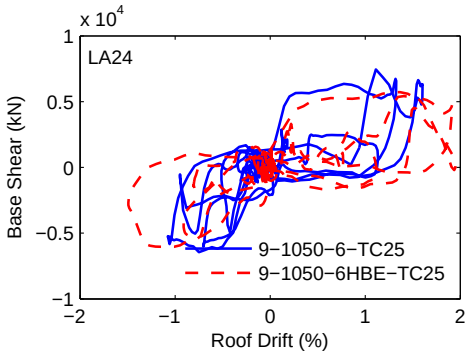

(f) Force vs. drift

Figure 8.36: Representative 2/50 (LA24) responses for 9-1050-6-TC25 and 9-1050-6HBE-TC25

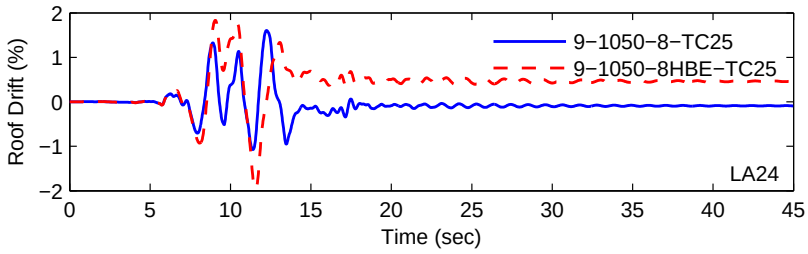

(a) Roof drift vs. time

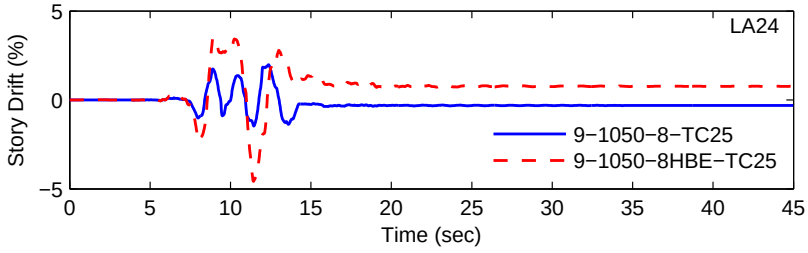

(b) 1^{st} story drift vs. time

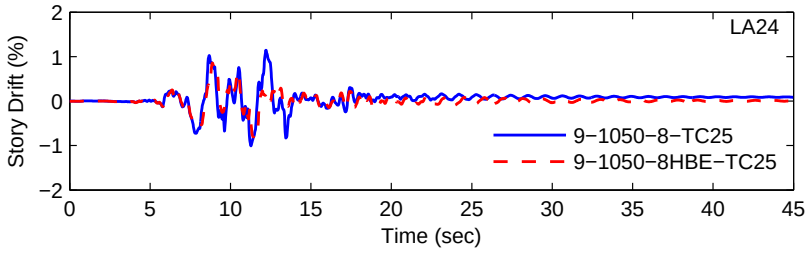

(c) 9^{th} story drift vs. time

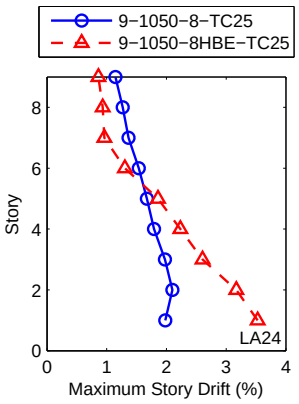

(d) Maximum Story Drifts

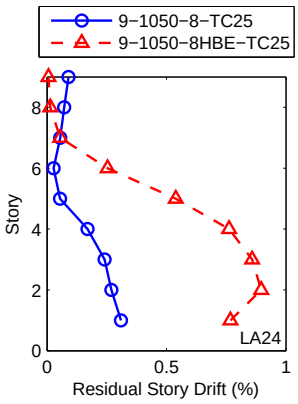

(e) Residual Story Drifts

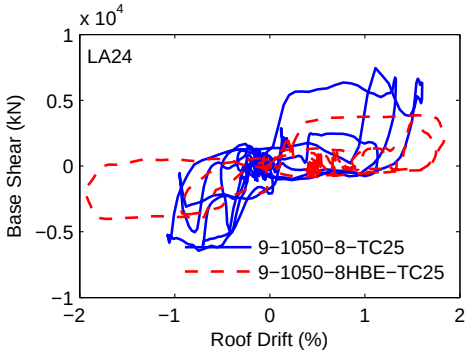

(f) Force vs. drift

Figure 8.37: Representative 2/50 (LA24) responses for 9-1050-8-TC25 and 9-1050-8HBE-TC25

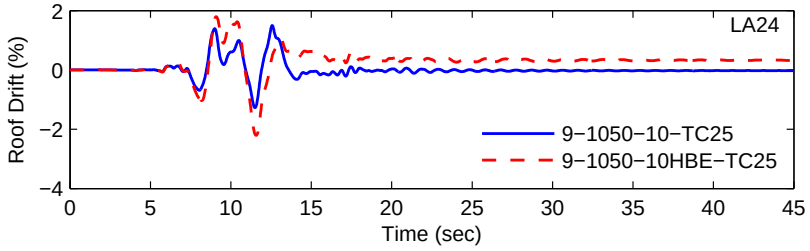

(a) Roof drift vs. time

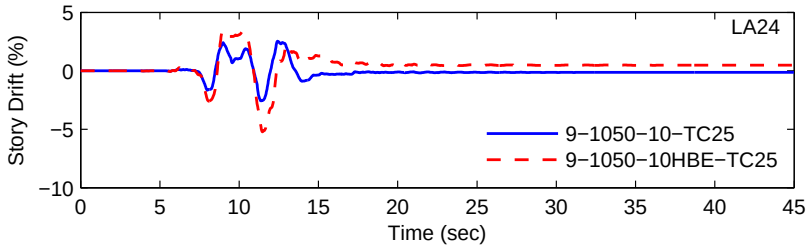

(b) 1^{st} story drift vs. time

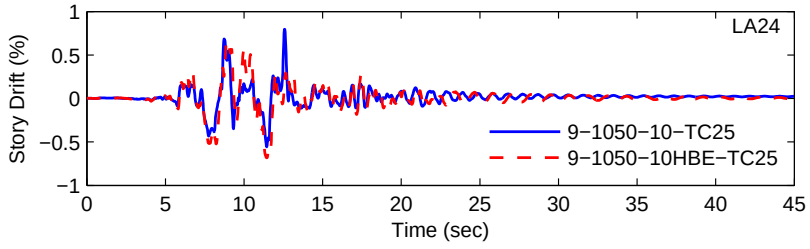

(c) 9^{th} story drift vs. time

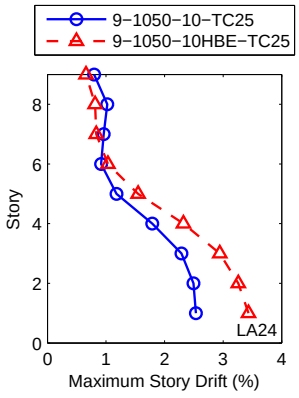

(d) Maximum Story Drifts

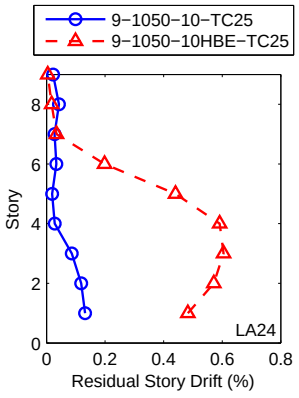

(e) Residual Story Drifts

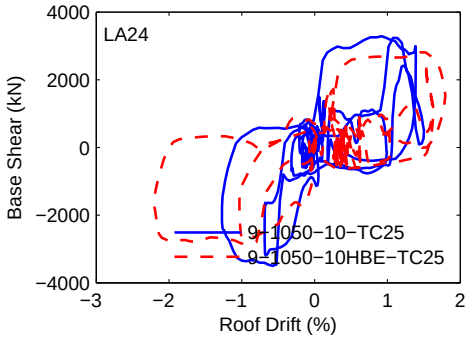

(f) Force vs. drift

Figure 8.38: Representative 2/50 (LA24) responses for 9-1050-10-TC25 and 9-1050-10HBE-TC25

8.5.3.3 Comparison of web plate residual strength

As was done in the previous section, Figs. 8.39 through 8.41 compare responses from a representative 50/50 ground motion (LA43) of a SC-SPSW with fully-connected web plates modeled using the TO and TC models for the 9-1050-6, 9-1050-8, and 9-1050-10 SC-SPSWs, respectively. Similarly, Figs. 8.42 through 8.44 show response of the same SC-SPSWs during a representative 10/50 ground motion (LA11), and Figs. 8.45 through 8.47 show response of the same SC-SPSWs during a representative 2/50 ground motion (LA24).

These results show that for SC-SPSWs that remain essentially elastic (e.g. during 50/50 motions as shown in Figs. 8.39 through 8.41), the web plates employing the TC model actually had larger peak drift demands than the exact same SC-SPSW employing the TO model. For these SC-SPSWs, the larger story drifts in the TC models were located at the upper stories, while the TO models typically had smaller upper story drift demands; however, the peak roof drift demands were similar for both the TO and TC models for these smaller ground motions. During ground motions that caused web plate yielding (e.g. in most of the 10/50 and all of the 2/50 motions as shown in Figs. 8.42 through 8.47, the TC model resulted in smaller peak story drifts on the order of 10% to 30% less than those of the TO model. This reduction in peak story drifts is expected and was observed in the three-story SC-SPSWs due to the additional energy dissipation in the TC model.

Even though the TC model has been shown to provide conservative overestimations of residual drift demands (Sec. 7.2), the median peak residual story drifts in the 10/50 ground motions were well below the 0.2% recentering criterion. The reduction in peak drift demands and the effects of the compressive web plate forces acting on the boundary frame members in the TC models often resulted in lower HBE and VBE damage values (D_{HBE} and D_{VBE}). However, unlike the three-story SC-SPSWs where the TC model resulted in significant decreases in boundary frame demands for fully-connected web plates, the reduction in boundary frame demands were not as significant for the nine-story SC-SPSWs, suggesting that the current VBE and HBE design methdologies (e.g. target drift demands used for capacity design) may be appropriate for mid-rise SC-SPSWs with fully-connected web plates.

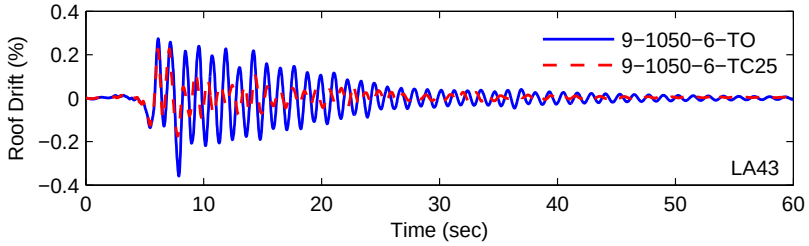

(a) Roof drift vs. time

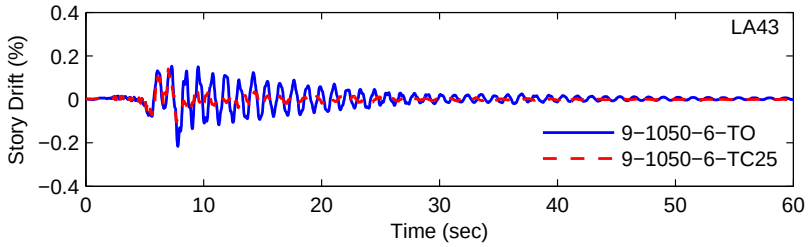

(b) 1^{st} story drift vs. time

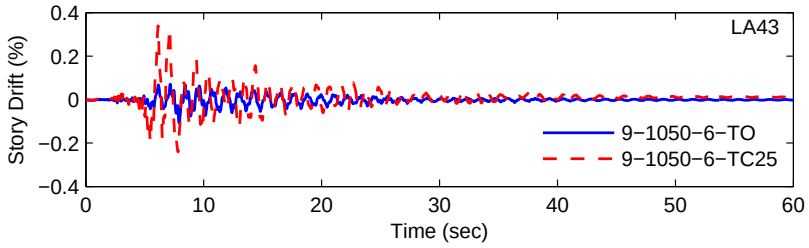

(c) 9^{th} story drift vs. time

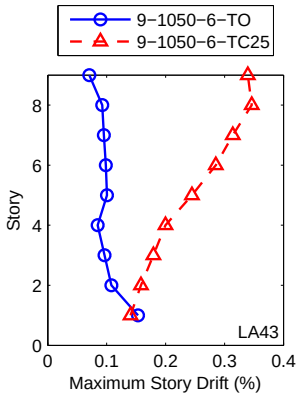

(d) Maximum Story Drifts

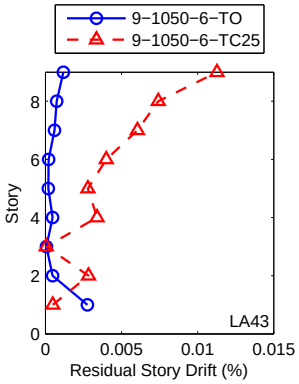

(e) Residual Story Drifts

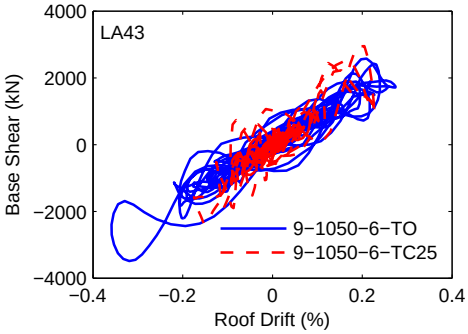

(f) Force vs. drift

Figure 8.39: Representative 50/50 (LA43) responses for 9-1050-6-TC25 and 9-1050-6-TC25

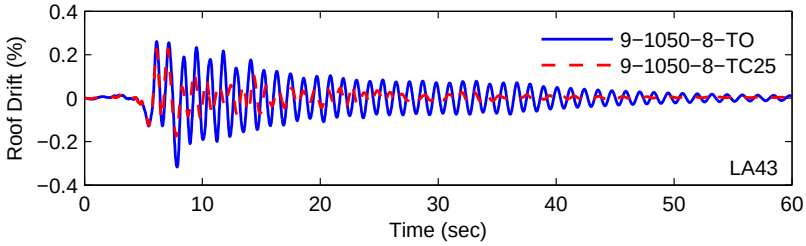

(a) Roof drift vs. time

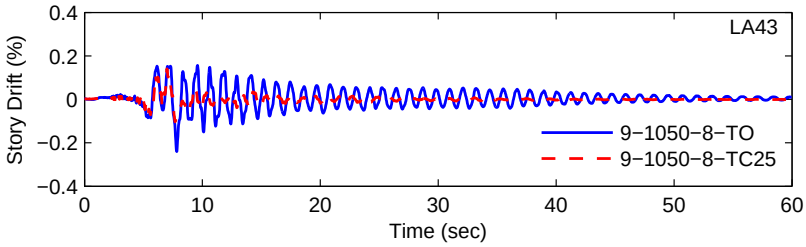

(b) 1^{st} story drift vs. time

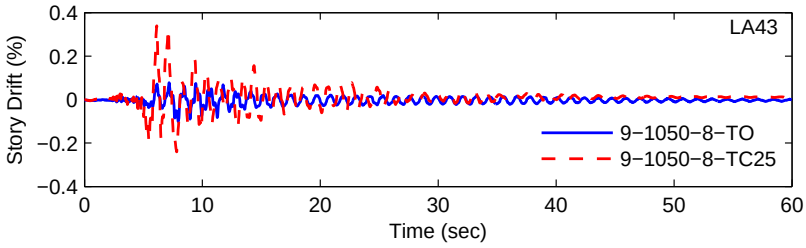

(c) 9^{th} story drift vs. time

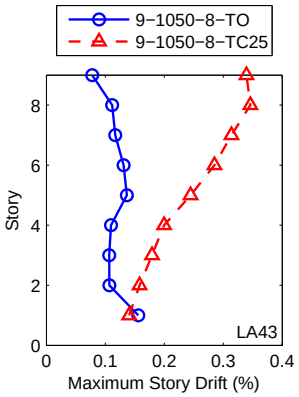

(d) Maximum Story Drifts

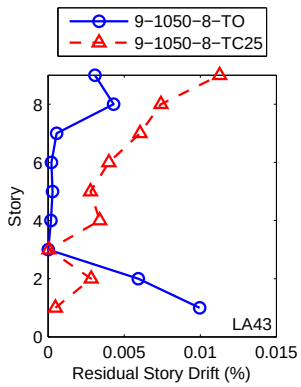

(e) Residual Story Drifts

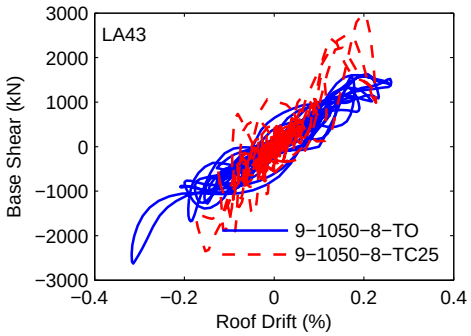

(f) Force vs. drift

Figure 8.40: Representative 50/50 (LA43) responses for 9-1050-8-TC25 and 9-1050-8-TC25

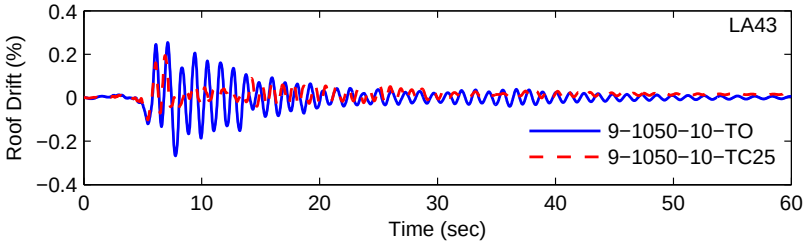

(a) Roof drift vs. time

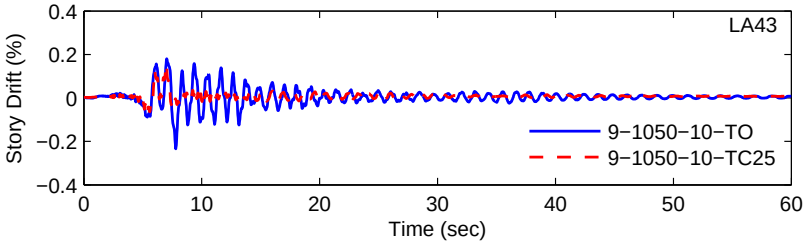

(b) 1^{st} story drift vs. time

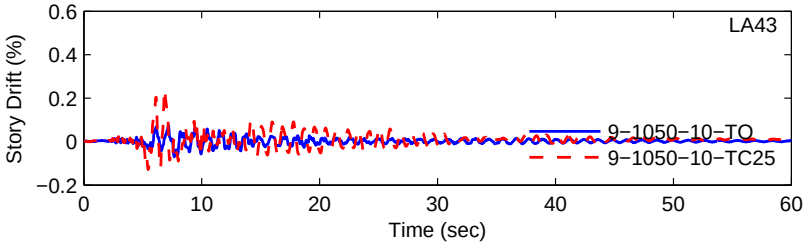

(c) 9^{th} story drift vs. time

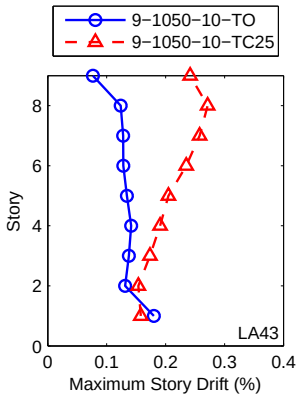

(d) Maximum Story Drifts

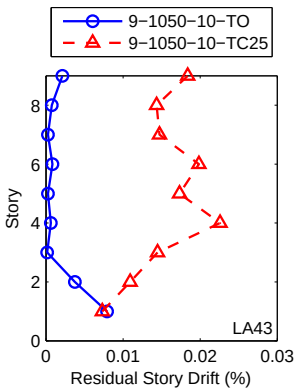

(e) Residual Story Drifts

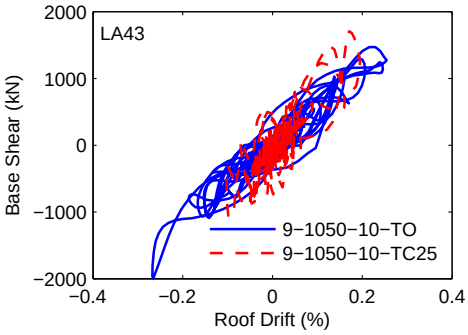

(f) Force vs. drift

Figure 8.41: Representative 50/50 (LA43) responses for 9-1050-10-TC25 and 9-1050-10-TC25

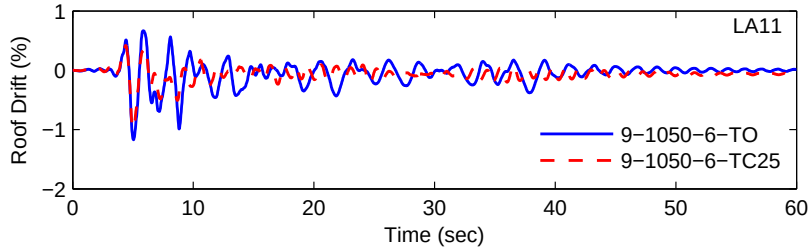

(a) Roof drift vs. time

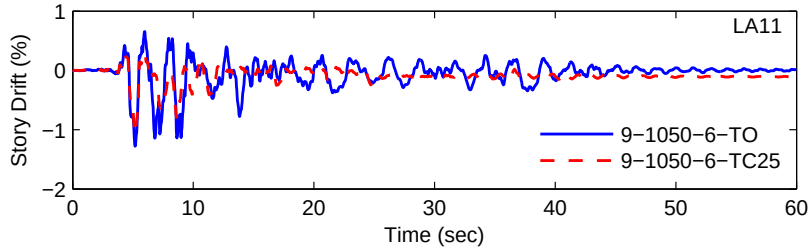

(b) 1^{st} story drift vs. time

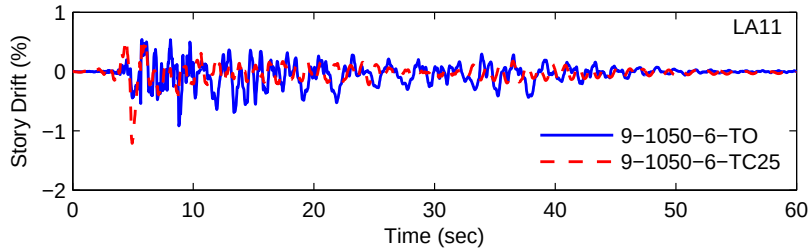

(c) 9^{th} story drift vs. time

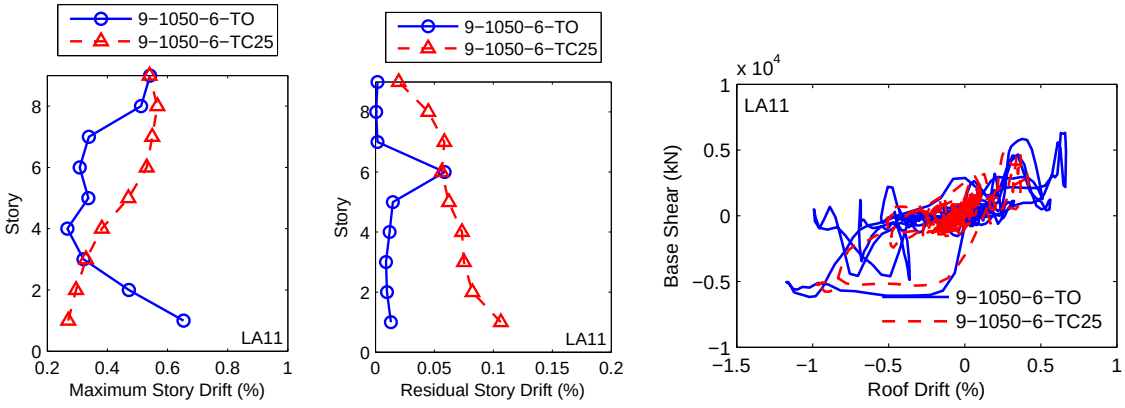

(d) Maximum Story Drifts (e) Residual Story Drifts (f) Force vs. drift

Figure 8.42: Representative 10/50 (LA11) responses for 9-1050-6-TC25 and 9-1050-6-TC25

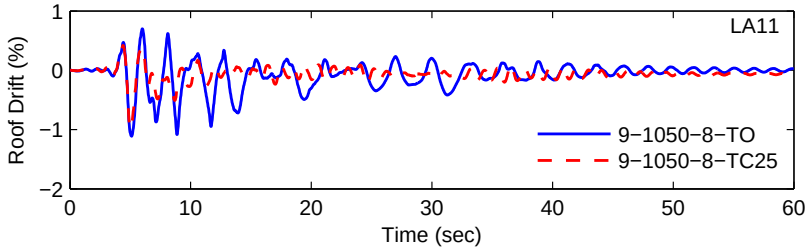

(a) Roof drift vs. time

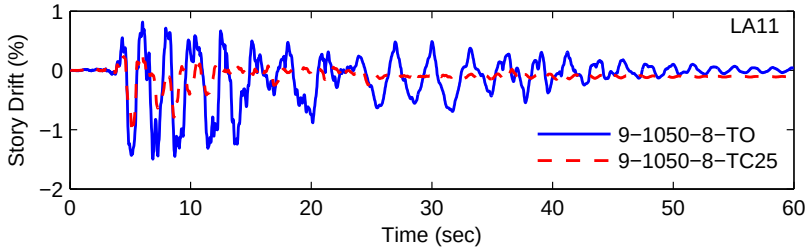

(b) 1^{st} story drift vs. time

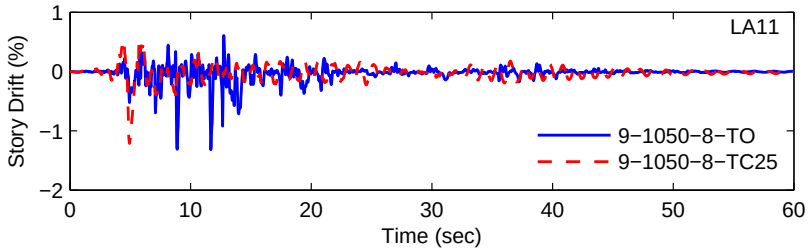

(c) 9^{th} story drift vs. time

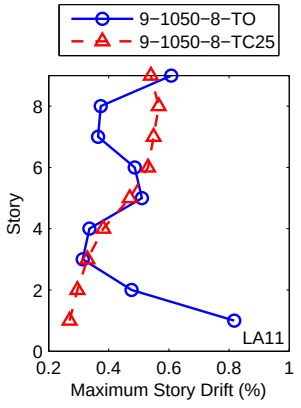

(d) Maximum Story Drifts

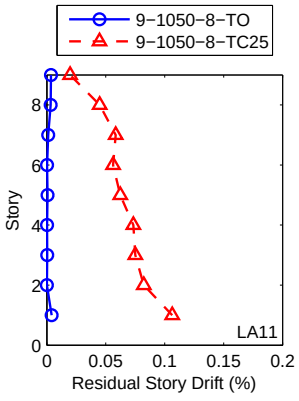

(e) Residual Story Drifts

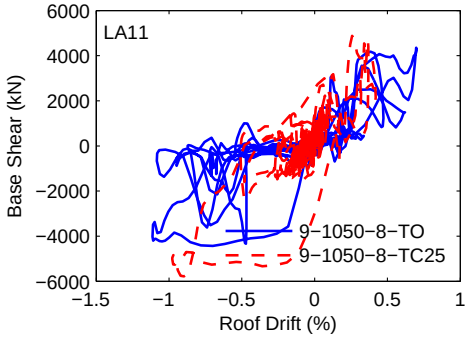

(f) Force vs. drift

Figure 8.43: Representative 10/50 (LA11) responses for 9-1050-8-TC25 and 9-1050-8-TC25

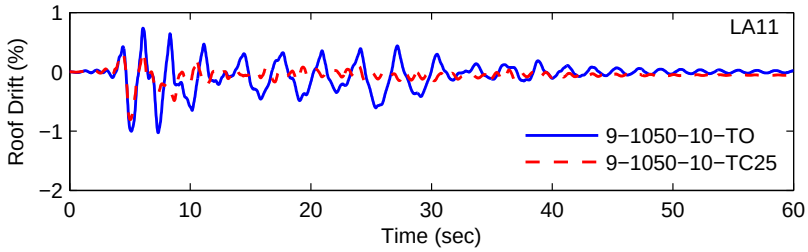

(a) Roof drift vs. time

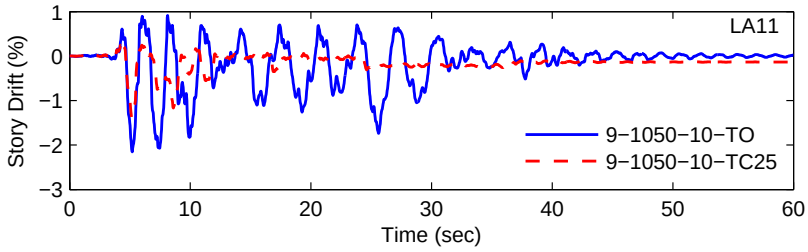

(b) 1^{st} story drift vs. time

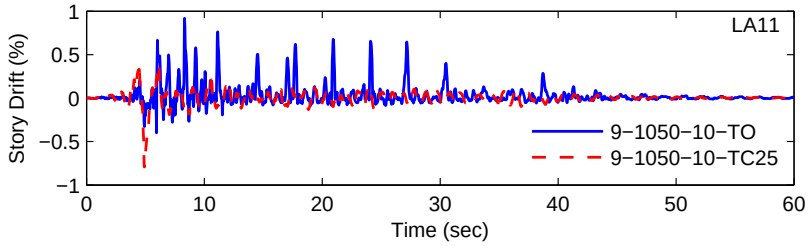

(c) 9^{th} story drift vs. time

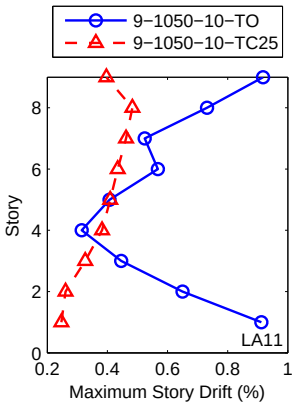

(d) Maximum Story Drifts

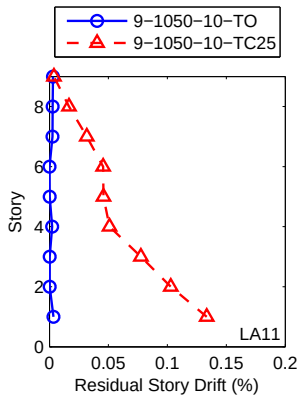

(e) Residual Story Drifts

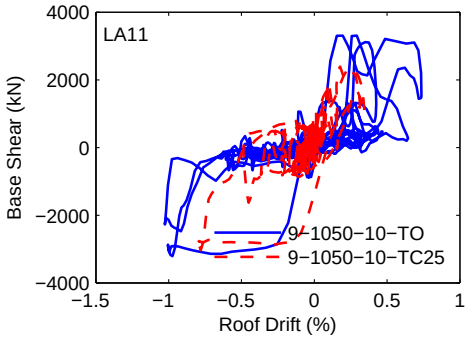

(f) Force vs. drift

Figure 8.44: Representative 10/50 (LA11) responses for 9-1050-10-TC25 and 9-1050-10-TC25

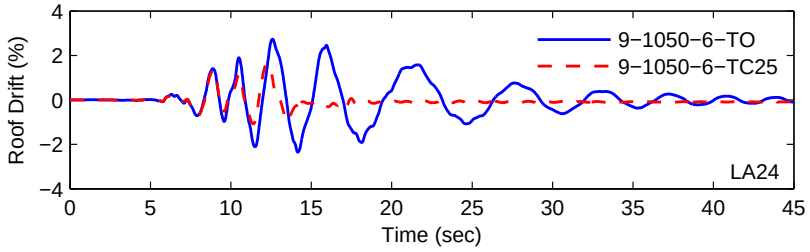

(a) Roof drift vs. time

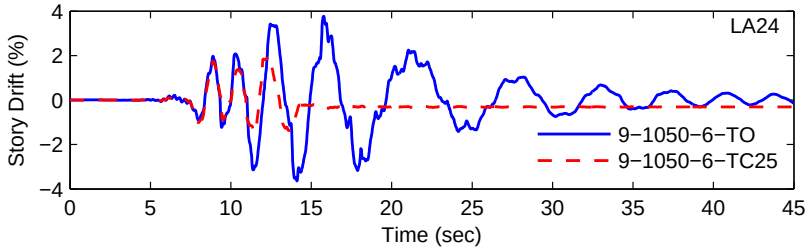

(b) 1^{st} story drift vs. time

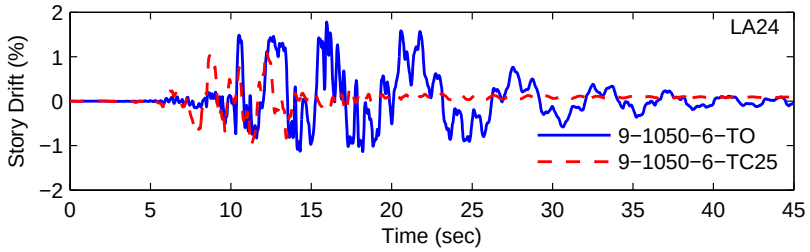

(c) 9^{th} story drift vs. time

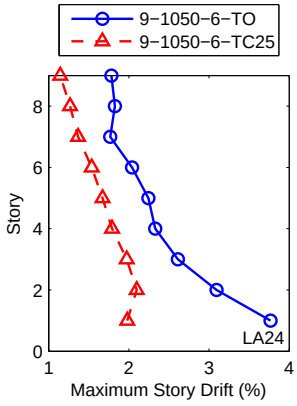

(d) Maximum Story Drifts

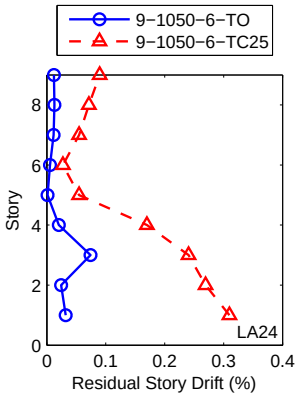

(e) Residual Story Drifts

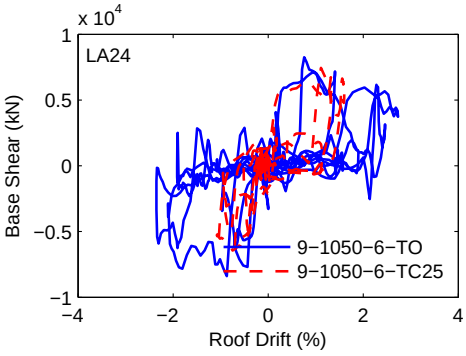

(f) Force vs. drift

Figure 8.45: Representative 2/50 (LA24) responses for 9-1050-6-TC25 and 9-1050-6-TC25

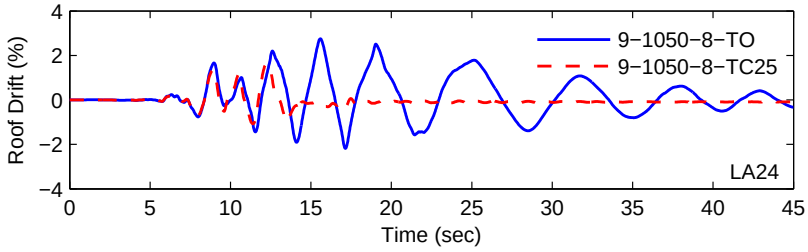

(a) Roof drift vs. time

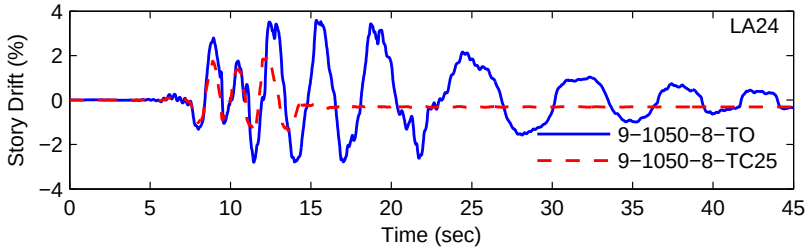

(b) 1^{st} story drift vs. time

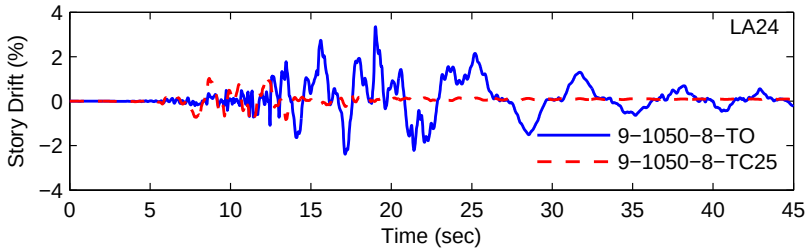

(c) 9^{th} story drift vs. time

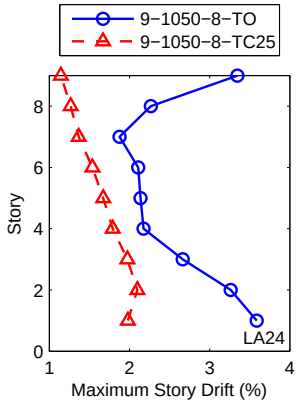

(d) Maximum Story Drifts

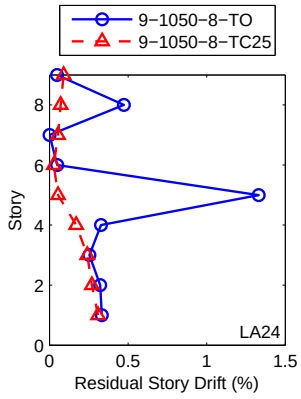

(e) Residual Story Drifts

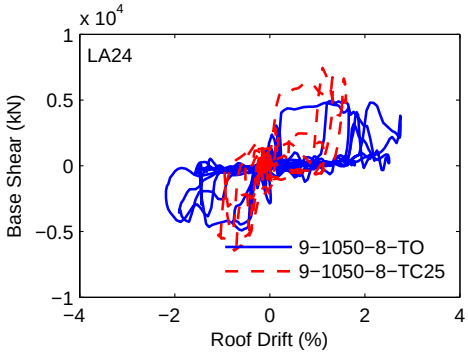

(f) Force vs. drift

Figure 8.46: Representative 2/50 (LA24) responses for 9-1050-8-TC25 and 9-1050-8-TC25

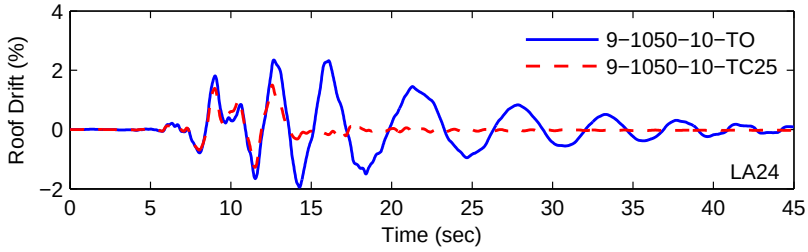

(a) Roof drift vs. time

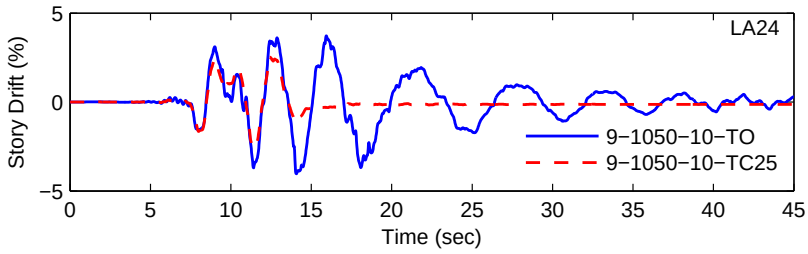

(b) 1^{st} story drift vs. time

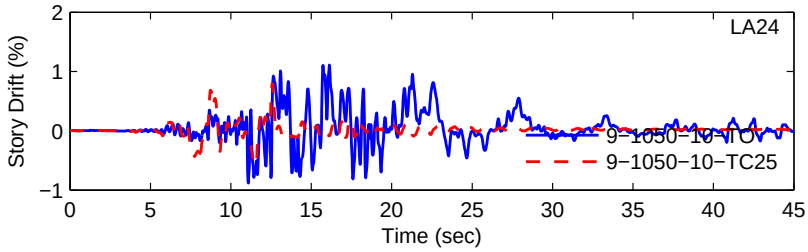

(c) 9^{th} story drift vs. time

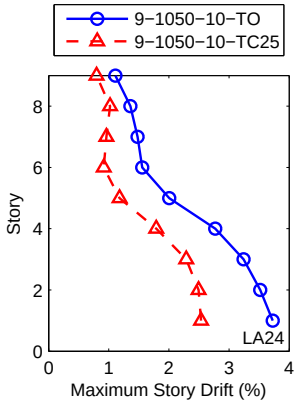

(d) Maximum Story Drifts

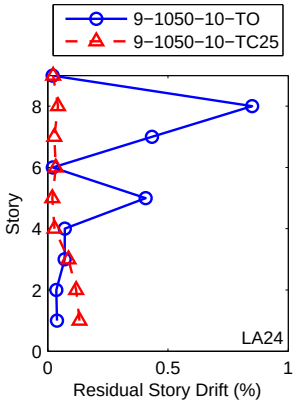

(e) Residual Story Drifts

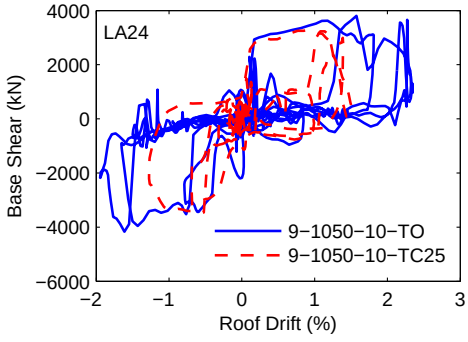

(f) Force vs. drift

Figure 8.47: Representative 2/50 (LA24) responses for 9-1050-10-TC25 and 9-1050-10-TC25

8.6 Effects of Web Plate Connectivity on Design and Response

This sections compares the HBE-only and fully-connected web plate SC-SPSW designs presented in Secs. 8.3 and 8.2, respectively. Comparisons are made of both the design parameters (e.g. web plate thicknesses and frame member sizes) and the seismic response from nonlinear response history analyses.

8.6.1 Comparison of designs

One of the purposes of investigating the HBE-only web plate connectivity was to investigate the potential for reducing frame member sizes. In order to maintain the same lateral strength with the reduced tension field of the HBE-only web plates, thicker (or stronger) plates we required. How the larger web plate demands acting over a shorter portions of the HBEs would affect HBE and VBE member sizes were not known a priori from the analytical derivations in Sec. 3.2; therefore, the actual member sizes resulting from similar design methodologies must be compared to evaluate the impact of web plate connectivity on frame member design.

8.6.1.1 Web plate thickness

As previously described, the web plate thicknesses in the HBE-only designs had to be increased in order to provide the same lateral resistance as the fully-connected web plate designs. The increase in web plate thicknesses ranged from 2 to 2.4 time thicker for the HBE-only designs. The gain in web plate material weight (represented as a negative savings in Table 8.13) for each of the HBE-only deisngs compared with fully-connected web plate designs is given in Table 8.13.

8.6.1.2 Beam sizes and PT design

The number of PT strands and initial PT force did not change between the two designs. The number of PT strands is largely controlled by providing a sufficient amount of connection rotational stiffness to overcome P-Delta effects during recentering, which is not affected by the web plate resistance. The initial PT force, T_o, is often controlled by providing sufficient

decompression moment to prevent connection decompression under wind and gravity loads. In some cases, specifically at the top HBEs and at HBEs between large transitions in web plate thickness, T_o in the fully-connected web plate designs were controlled by the design requirement to force the maximum moment to the ends of the HBEs at 4% drift (a design requirement intended to reduce the potential for in-span HBE yielding and associated loss of full tension field action [Purba and Bruneau, 2010]). This design requirement was not strictly enforced for the HBE-only web plate designs as it would require much larger T_o forces in some cases due to the large unbalanced vertical demands of the web plates; therefore, the same T_o values were assumed for the HBE-only designs such that the PT frames in both designs had similar strengths[7].

The HBEs in the HBE-only web plate SC-SPSW designs were designed to have the same depths as those in the fully-connected web plate designs to maintain similar PT frame strength and stiffness in both designs. In many cases, the HBE members designed according to the HBE-only web plate demands were smaller than those of the fully-connected web plate designs. The smaller HBE sizes resulted from lower compressive demands in the HBEs (due to the elimination of the $P_{HBE(VBE)}$ term) and web plate vertical demands that produced moments with opposite signs of the moments produced by the PT connections as demonstrated in Fig. 3.13 (particularly for HBEs with similar web plate thicknesses above and below). However, the top HBEs typically remained the same size or were only sightly smaller due to the large unbalanced web plate load and larger PT demands at this level. The typical reduction of the weights of individual intermediate HBE W-sections ranged from approximately 10% to 36%. There were only a few cases (e.g. Floor 1 of 3-5050-6HBE, Floor 7 of 9-1050-10HBE) where the HBE increased slightly in size. The overall reduction in HBE weight (taken as the sum of the HBE weights from the HBE-only design divided by the sum of the HBE weights in the fully-connected design) for each SC-SPSW is shown in Table 8.13. In one case (3-5050-6HBE) there was a very small overall increase in HBE weights, but in the other SC-SPSWs, HBE weight savings ranged from 8% to 20%

[7]Using the T_o values assumed in the HBE-only web plate designs, in the most extreme cases of the top HBEs, the maximum moment would occur at the ends of the top HBE at drifts of 5.9% or less (assuming the HBE remains elastic).

Table 8.13: Approximate savings in boundary frame member, web plate, and total SC-SPSW weights for HBE-only web plate designs compared with fully-connected web plate designs (negative values represent increases in weight)

Name	HBE savings (%)	VBE savings (%)	Web plate savings (%)	Approx. total savings (%)
3-5050-6	-2.8	24.8	-112	1.8
3-1050-4	9.2	17.3	-113	3.2
3-1050-6	8.6	25.2	-113	8.3
9-5050-10	9.0	34.7	-113	19
9-1050-6	17.7	17.6	-126	1.6
9-1050-8	19.6	27.3	-109	12
9-1050-10	17.9	31.9	-111	20

using the HBE-only web plate connectivity compared to the fully-cnnected web plates.

8.6.1.3 Column sizes

The VBEs were capacity designed for the demands at 5% drift. Due to the elimination of distributed web plate forces acting on the VBEs (and slight changes in the HBE-to-VBE connection demands) the VBE demands for HBE-only web plate connectivity were less than those for the fully-connected web plates. The reduction in demands by connecting the web plates only to the HBEs resulted in VBE weight savings (taken as the summ of the VBE weights for the HBE-only designs divided by the sum of the VBE weights for the fully-connected designs) ranging from 17% to 35% for various SC-SPSWs as shown in Table 8.13. This exercise in designing SC-SPSWs with comaprable strength for with two different web plate connectivity configurations demonstrates that the HBE-only web plate connectivity can result in significant reductions in VBE and HBE member sizes.

8.6.1.4 Total weights

Connecting the web plates to the HBEs only requires thicker web plates to resist the same lateral load. Although SC-SPSWs with thicker HBE-only web plates tend to have smaller boundary frame member sizes compared with comparable fully-connected web plate designs,

the increase in web plate thickness may lessen the net weight savings of the entire SC-SPSW. The total weight savings, taken as the sum of the boundary frame and web plate weights[8] for the HBE-only designs compared with the "original" fully-connected designs, is shown for each of the SC-SPSWs in Table 8.13. The total SC-SPSW weight savings range from 1.6% (representing only a modest reduction in weight from the fully-connected to the HBE-only connected design) to 20% (representing a significant reduction in weight). Overall, using HBE-only web plates did provide at least some savings in the total weight of all the SC-SPSWs; although in some cases, particularly the three-story SC-SPSWs, this savings was small. The nine-story SC-SPSWs typically had larger net savings in total steel weight, partially due to the larger savings in HBE weights.

Additionally, the weight may not be the only indicator of potential savings in overall SC-SPSW cost. Even for those SC-SPSWs in which using HBE-only web plates resulted in only modest savings in total weight, there may be some cost advantages to using SC-SPSWs HBE-only web plate designs. These potential advantages include being able to use smaller column W-shapes that are more widely available from steel mills thus reducing special orders and transportation costs for extremely large W-shapes, reduction in additional reinforcing required in the PT connections due to the decrease in boundary frame demands, and reduction in field welding costs as only two of the four web plate edges must be welded to the boundary frame. From a cost perspective, the savings from using HBE-only vs. fully-connected web plates should be assessed on a case-by-case basis.

8.6.2 Comparison of response

8.6.2.1 Peak story drift demands

The SC-SPSWs with web plates connected to the HBEs only did have larger drift demands than comparable SC-SPSWs with fully connected web plates, typically on the order of 50% larger for the three-story SC-SPSWs and 10-50% larger for the nine-story SC-SPSWs. Even though both types of web plates were design to have the same strength, releasing

[8]The weight of steel used for stiffeners and flange reinforcement detailing was not considered in the total weight.

the web plate from the VBE removes some of the resistance to frame expansion and gap opening, creating a more flexible system. The same reasons that the HBE-only web plate is prefereable from a web plate damage mitigation point-of-view (e.g. reducing strains associated with frame expansion and gap opening) are the same reasons that contribute to its overall flexibility. Additionally, the smaller column sizes result in a more flexible response.

8.6.2.2 Residual story drift demands

Larger residual story drifts seemed to correlate more with boundary frame yielding than with web plate connectivity. For example, the HBE-only web plate designs that were modeled with Model TO and had peak drift demands larger than the target drifts used in boundary frame design tended to have larger residual drifts. However, the HBE-only web plates modeled with Model TC had much lower drifts, within the boundary frame design parameters, resulting in residual drifts that were comparable to the fully-connected web plate designs.

8.6.2.3 HBE and VBE interaction values

The HBE and VBE interaction values again are correlated to the peak drift demands. For HBE-only designs with drifts exceeding the design target drifts, more boundary frame yielding was observed (HBE and VBE interaction values greater than one), even at the 10/50 hazard level where the frame is expected to remain damage-free. However, for those HBE-only designs modeled with Model TC, the peak drifts in the 2/50 hazard level were near the 4-5% drift range assumed in HBE and VBE design, resulting in HBE and VBE interactions that were less than or approaching one. This result shows that the HBE-only design methodology for HBEs and VBEs is adequate, assuming that the target drift values used in design are good approximations of expected 2/50 drift demands. In this case, for the HBE-only web plates modeled with Model TC, which still provides a conservative underestimation of web plate residual strength but provides much of its beneficial energy dissipating effects, the peak drifts in the 2/50 event corresponded well with the 4-5% used

in design; therefore, these design limits seem to be appropriate for HBE-only web plate designs.

8.7 Effects of Web Plate Residual Strength

This section provides an overview of the effects of including (or not including) the web plate residual strength in nonlinear dynamic response history analyses based on the analyses presented above. Conclusions are based on the results of both fully-connected and HBE-only web plate SC-SPSWs.

8.7.1 Peak story drift demands

Including web plate residual strength resulted in a significant reduction in peak drift demands in the SC-SPSWs of all heights (with the exception of nine-story SC-SPSWs that remained elastic during the ground motion, in which case the TC models had larger drifts in the upper stories). For the two-story SC-SPSW presented in Sec. 8.5.1 considering only small amounts of web plate residual strength (e.g. 10% of yield strength) typically resulted in an 20% reduction in median peak drift at all hazard levels compared to tension-only models. Further increasing the residual strength further reduced the peak drift demands, with reductions up to 40% at the 10/50 and 2/50 hazard levels compared to the tension-only model. The three-story buildings (with both HBE-only and fully-connected web plates) had similar results with peak drift demands in the tension-compression models being approximately 50% of the drift demands in the tension-only models. The nine-story buildings with fully-connected web plates using Model TC had approximatley 20-30% reduction in peak story drifts when web plate yielding was observed compared to the tension-only models. As previously mentioned, the Model TC nine-story SC-SPSWs that remained elastic during smaller ground motions (e.g. 50/50) had larger upper story drifts than the same Model TO SC-SPSW due to some higher order effects in the elastic response that were not present in the inelastic response during stronger shaking. Overall, accounting for web plate residual strength (i.e. using Model TC as opposed to Model TO) resulted in lower peak drift demands for all SC-SPSWs; however, this reduction was more signifcant for low-rise SC-SPSWs.

8.7.2 Residual story drift demands

As was stated previously with respect to HBE-only web plate designs, residual drift was largely influenced by the presence of boundary frame yielding. For SC-SPSWs with drifts greater than the target design drifts, excessive yielding resulted in larger residual drifts. For models that had smaller drifts and did not experience severe frame yielding (i.e. interaction values less than one), the residual drifts were typically less than the 0.2% recentering limit, even at the 2/50 hazard level. When comparing designs with boundary frame designs that remained elastic in both the Model TO and Model TC simulations (e.g. at the 10/50 hazard level), inclusion of web plate residual strength did result in slightly larger residual drifts; however, this effect was small and typically resulted in residual drifts that were still less than the recentering criterion. Therefore, modeling web palte residual strength does not significantly impact residual drift demands apart from reducing peak drift demands which may reduce the potential for boundary frame yielding.

8.7.3 HBE and VBE interaction values

As was stated previously, the largest impact of including web plate residual strength was in reducing drift demands. And since drift demands are related to PT, HBE, and VBE demands, the web plate residual strength in turn reduced the boundary frame demands. The effects of considering the web plate residual strength on the moment and axial distributions in the HBEs and VBEs was not considered here; however, any potential increase or decrease in boundary frame demands associated with this compressive component in the web plate stress appears to be far outweighed by the reduction in demands associated with the reduction in drift demands.

For the fully-connected web plate designs of three-story SC-SPSWs, including the web plate residual strength in the simulations reduced the peak drifts such that HBEs and VBEs had median interaction values near or less than 0.75 at the 2/50 hazard level. These low demands during such a rare and extreme event suggest that the design methodology can be revised to design the HBEs and VBEs for lower drift levels, perhaps near 3% drifts as this corresponds to the median drift for the three-story buildings at the 2/50 level for fully-

connected web plates modeled with tension-compression strips. Further work should be done to investigate appropriate drift demands based on the consideration of various web plate residual strengths and how sensitve peak drifts are to magnitudes of residual strength. The reduction in HBEs and VBEs had median interaction values for the nine-story SC-SPSWs when using Model TC was not as significant at the 2/50 hazard level; therefore, the target design drift damands for taller buildings may not be able to be reduced as much as those for the three-story buildings. Again, further research is necessary to assess more approriate target drift demands that result in designs capable of meeting the proposed performance objectives.

It should be noted that the larger drift demands in the HBE-only web plate SC-SPSW designs resulted in median HBE and VBE interaction values near 1.0 (suggesting minor boundary frame yielding), meaning that the 4% target drift used in HBE design (and 5% drift in VBE design) appear to be appropriate for HBE-only web plate SC-SPSW designs. Reducing the target drift in SC-SPSWs with fully connected web plates will result in smaller boundary frame member sizes, which may lessen the impact or advantages of employing HBE-only web plates strictly for the benefits of member size reduction.

8.8 Summary of Numerical Study

This chapter presented two sets of 3- and 9-story SC-SPSW designs: one set designed with web plates fully connected to the HBEs and VBEs [Clayton, 2010], one set with web plates connected to the HBEs only and designed to have the same strength as the comparable fully-connected web plates SC-SPSWs. The SC-SPSWs with web plates connected to the HBEs only were designed for drift demands equal to those considered in the fully-connected web plate SC-SPSW design, which resulted in boundary frame members that were typically significantly smaller (i.e. lower weight) than their fully-connected web plate counterparts.

Because little previous research has been done on HBE-only connected web plates and little experimental data exists for these types of specimens, a numerical study was done to compare the HBE-only web plate modeled using the strip model in OpenSees with the those modeled using shell elements in ABAQUS and the one SC-SPSW subassembly specimen with HBE-only connected web plates. These studies showed that the OpenSees strip model of

the HBE-only web plates were equally as accurate in predicting the global and component responses as the widely-accepted strip models for fully-connected web plates; therefore, the HBE-only web plate strip model was considered acceptable to be used in dynamic analyses of SC-SPSW buildings.

Nonlinear dynamic response history analyses were conducted on all of the 3- and 9-story SC-SPSW designs previously mentioned. Each of these SC-SPSWs was modeled using the tension-only (Model TO) and tension-compression (Model TC) strip models. Each model was subjected to a suite of ground motions representing the 50/50, 10/50, and 2/50 hazard levels. The results of these analyses were used to assess the impacts of web plate connectivity (e.g. fully-connected vs. HBE-only connected) and modeling of web plate residual strength (e.g. Model TO vs. Model TC) in SC-SPSW seismic response.

The results of the response history analyses showed that the HBE-only web plate designs tended to have larger drift demands than their fully-connected web plate counterparts. In some cases (particularly where Model TO was employed) the drift demands were larger than those for which the boundary frame was designed, resulting in severe yielding and residual drifts at the 2/50 hazard level. However, when the web plate residual strength was considered in the model (Model TC), the drift demands were significantly reduced (as was also the case for fully-connected web plate models), such that the overall performance of the fully-connected and HBE-only connected web plate SC-SPSWs were comparable. When web plate residual drift is considered, the HBE-only web plate SC-SPSWs were able to meet all proposed performance objectives including drifts less than the 0.5% web plate yielding criterion at the 50/50 hazard level (for the three-story SC-SPSWs only)[9], drifts less than (or slightly over for some of the three-story SC-SPSWs) the 2% code-based limit at the 10/50 hazard level, recentering at the 10/50 (and even often at the 2/50) hazard level, and only minor yielding in the boundary frame at the 2/50 hazard level.

In fully-connected web plate SC-SPSWs modeled with Model TC (which more accurately simulated the additional energy dissipation in the web plate upon unloading and reloading), the reduction in drift demands also significantly reduced HBE and VBE demands. These

[9]Note that this was an optional perfermance objective. Those SC-SPSWs named xx-1050-x were not explicitly designed to meet this objective.

analyses suggest that the SC-SPSW performance-based design procedure may be modified to capacity design HBEs and VBE at target drift levels less than the 4% and 5%, respectively that is assumed, particularly for the low-rise SC-SPSWs where the reduction in peak drift demands is most significant. Reducing the HBE and VBE target drift demands will result in smaller member sizes and may greatly improve economy of the structure without having a negative impact on performance. Future research should be done to better assess the impact of smaller column sizes and web plate models incorporating web plate residual strength on seismic performance of the system.

Chapter 9

DESIGN CONSIDERATIONS AND RECOMMENDATIONS

9.1 Introduction

This chapter presents considerations and recommendations for SC-SPSW design. Many of the design considerations presented in this chapter address detailing for PT column base, web plate-to-boundary frame, and SC-SPSW-to-diaphragm connections. Included in these recommendations are discussions of potential advantages and disadvantages to certain detailing or design methodologies that are based on the experimental and numerical results presented previously. The recommendations are also presented as an addendum to the performance-based seismic design (PBSD) procedure presented in Clayton [2010]. An updated PBSD design procedure (based on the aforementioned procedure) incorporating some of the SC-SPSW design options presented in this dissertation is included at the end of the chapter.

9.2 PT Column Base Connection

Sec. 3.3 presented the basic behavior of a post-tensioned column base connection. This section also provided expressions for determining component demands such as PT force, moment in the connection, connection stiffness, etc. Chapter 5 presented a physical implementation of the PT column base connection in a full-scale two-story SC-SPSW test specimen. The results of this test showed that the PT column base connection performed as intended, eliminating column axial-flexural hinging and returning to its undeformed configuration after a series of earthquake simulations and cyclic loadings reaching maximum roof drifts of 4.7%. Column PT forces measured in the test also showed the PT force design equations presented in Eqn. (3.27) accurately predicted the maximum PT forces at design-level drift demands (Fig. 6.37).

These previous discussions demonstrate the concept and feasibility of the PT column

base connection in an idealized and laboratory setting; however, further research should be done to investigate the complexities of practical application of the PT column base in actual buildings. Below is a discussion of some of the practical aspects that should be considered for implementation. An outline of how to incorporate PT column base connections into the previous SC-SPSW performance-based seismic design procedure [Clayton, 2010] is also provided. A brief discussion of the limitations to the application of PT column base connection is also presented.

9.2.1 PT column base configurations

As with many structural systems, the most difficult and critical design aspect is how to connect structural components together or to the foundation. Here, the intent of the rocking column base PT connection and its components are simple: the column can rock about its base, the vertical PT elements elongate to provide restoring forces, compression is transferred directly to the foundation through the bearing column flanges, the PT bar tension forces are transfered to the foundation by some sort of anchorage system, and the shear in the column base can be transferred to the foundation via some sort of direct bearing mechanism (e.g. shear brackets or "keeper" plates). However, these component functions can be accomplished in many different ways. In this section, several alternative PT column base connection configurations will be presented and the advantages and disadvantages of each will be presented. As with any structural system, the designer will need to understand the mechanics and behavior of each of these configurations (or combination of configurations) to choose the best design for the particular application. Fig. 9.1 shows some possible PT column base connection configurations, and each will be discussed individually below.

Fig. 9.1(a) shows a configuration similar to what was tested in the full-scale SC-SPSW test (Sec. 5.3.1). Here, the column sits atop a pedestal which transfers all of the base shear, PT tension, and column flange compression forces to the foundation. The first story web plate is anchored to a beam that is attached to the columns above the rocking interface via shear connection that can allow for rotation in the connection. The column PT is anchored somewhere along the height of the first story column (unlike the full-scale test

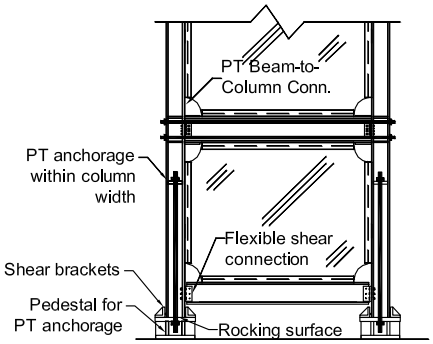

(a) Pedestal with anchor beam above rocking interface

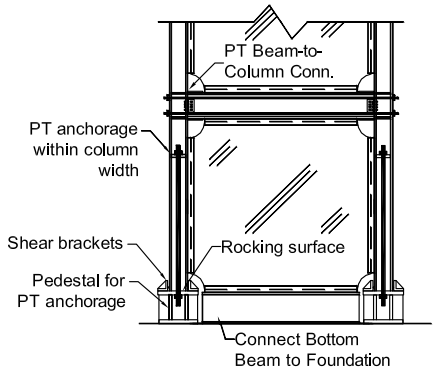

(b) Pedestal with anchor beam below rocking interface

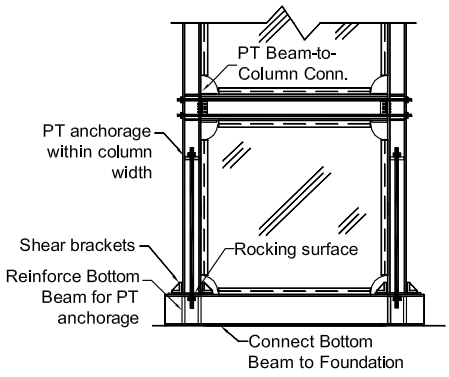

(c) Anchor beam acting as PT anchorage

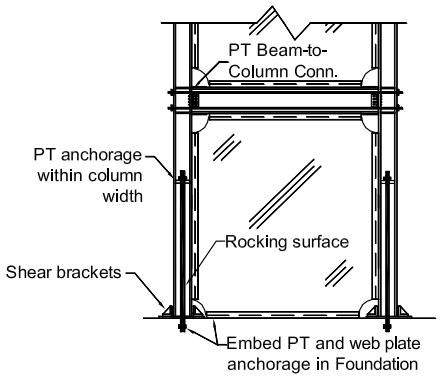

(d) PT and web palte anchored in foundation

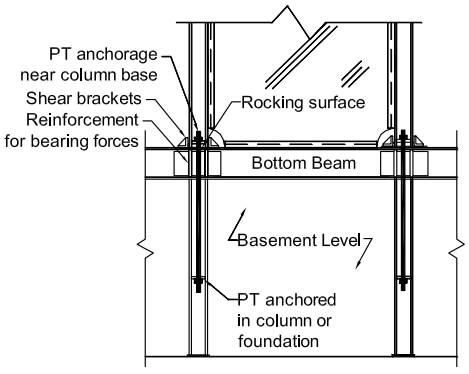

(e) PT anchored in basement level

Figure 9.1: Possible column base PT connection configurations

set-up where the PT was anchored in the second story to due limitations in the capacity of the the available load cells, which would not be present in the actual building). In this configuration, all of the force in the SC-SPSW must be transferred though the pedestals to reach the foundation, resulting in relatively large pedestal design[1]. Because there are only two pedestals to transfer all of the SC-SPSW forces to the foundation, there is less redundancy in the system (i.e. each pedestal is critical to the load path). An advantage to this configuration is that the web plate anchor beam is above the rocking interface; therefore, the corner cutouts at the bottom of the first story web plate do not have additional stress concentrations due to the gap formed by the rocking column.

Fig. 9.1(b) shows another configuration where the PT forces and column shear and compression forces are still transferred via pedestals under the column base; however, the web plate is anchored to a beam that is anchored directly to the foundation along its entire length. Here, the base shear and distributed upwards forces attributed to the first story web plate are transferred directly to the foundation through the anchor beam, which reduces the pedestal demands compared to the previous configuration. In this configuration the web plate corner cutouts at the base will have additional strain concentrations as the column connection rocks open; however, this is not detrimental as the corner cutouts at the other PT beam-to-column connection undergo similar localized deformations due to gap opening. Also, the shear transfer mechanism at the column base (e.g. shear brackets) must be designed to fit within the web plate cutouts, which, depending on the transfer mechanism used, may be difficult in terms of construction fit-up and accessibility.

Fig. 9.1(c) is similar to the previous configuration except that instead of a pedestal beneath the column, the web plate anchor beam is extended to also serve as the PT anchorage and column support. Here, the anchor beam will require lots of additional reinforcement under the column (e.g. continuity/stiffener plates beneath the column flange to transfer the large compressive forces or reinforcing plates on the flanges where the PT is anchored). And

[1]Note that this type of configuration was used in the full-scale test instead of the other possible configurations due to limitations in the strong floor anchorage systems (e.g. it was desirable to use the existing anchorage plates that had been used in numerous previous SPSW tests to connect the columns to the strong floor, therefore the pedestals were design to transfer all specimen forces to the strong floor via the existing anchor plates.)

like the configuration above, the first story web plate cutouts would need to accommodate the column uplift and the column base shear transfer mechanism would need to be designed to fit within the cutouts. One particular advantage of this configuration is that because the column anchorage is integrated into the continuously anchored web plate anchor beam, the column shear and uplift forces can be transfered to the foundation over a longer length, which may be desirable if a bolted anchor connection is being used. However, care should be taken in design of the anchorage beam which will be subjected to large local forces from the PT and column bases as well as global overturning and shear forces.

Fig. 9.1(d) shows a configuration where the PT and web plate anchorage are embedded in the foundation. The fish plate anchorage system can easily be embedded into the foundation concrete. Embedding the PT anchorage system in the foundation is not as easy and may be impractical after the required reinforcement is considered. The concrete around the embedded PT anchorage must be able to resist large pull-out forces, and the top of the foundation just underneath the column flanges should be reinforced with steel plates to reduce the potential for concrete crushing under the large concentrated compressive bearing forces of the rocking flange. The PT bars or strands should be placed in ducts to prevent bonding with the concrete, and care should be taken that the anchorage detail accommodated the amount of rotation necessary as the columns undergo lateral sway. For PT strands, this may not be an issue, but for PT bars, this may be accommodated using domed bearings (which would need to somehow be anchored in the concrete while still free to rotate) as was done in the full-scale test (Sec. 5.3.1). In this configuration, if the PT elements are yielded or damaged during an earthquake, repair may be more difficult. For damaged PT bars, new bars can be installed and connected to shorter lengths of PT bars anchored in the foundation via bar couplers; however, for PT strands, replacement may be more difficult as the anchorage system embedded in the foundation would be inaccessible. The benefits to this configuration are that the forces in the SC-SPSW are transferred directly to the foundation, eliminating the need to design another built-up member to resist all of the SC-SPSW base reactions and then anchoring that into the foundation.

Fig. 9.1(e) shows the final configuration in which the SC-SPSW is sitting above a basement level. Here, the PT elements can be extended into the floor below, as was suggested

by previous SC-MRF PT column base connection research [Chi, 2009]. This allows the PT column anchorage to be closer to the base of the column, which reduces the compressive forces for which the columns must be designed; instead, the column can be heavily reinforced in the short length near and below the PT anchorage instead of using much larger column sections up the entire height. As with the anchor beams and pedestals shown previously, the bottom beam, or grade beam, must be designed and detailed to resist the flexural forces from the SC-SPSW web plate, as well as the large bearing and shear forces from the rocking columns[2]. The column or bearing wall in the basement level below must also be designed for the compressive forces of the SC-SPSW above and the PT bars anchored within its height. For performance objectives to be achieved, the bottom beam and basement level must also be designed to have no damage in the 10/50 event and should limit severe damage leading to collapse in the 2/50 event.

All of these configuration are presented as ideas for the designer. As with many structural systems, connection of the superstructure to the foundation is often a challenging part of building design. The advantages and disadvantages of each of these configurations may be more evident in certain SC-SPSW applications. As with any new structural system, the designer should fully understand the intended behavior and desired response of the system and each component in order to properly design and detail it. The following sections will focus on methodologies for design of the SC-SPSW system and overall column PT design; however, detailing of the PT anchorage and SC-SPSW-to-foundation interface requirements would be determined at the discretion of the well-informed designer.

9.2.2 Column PT design

The design methodology for the column PT connections should be similar to that of the performance-based design methodology for beam-to-column PT connections presented in Clayton [2010]. The beam-to-column PT connection design (as part of the larger SC-SPSW design procedure) methodology followed these general steps:

[2]In this case, as was the case in the SC-MRF in Chi [2009], the bottom beam is design to transfer the base shear forces from the lateral load resisting system out to the ground around it.

1. Determine $A_{PT,min}$ and d to ensure a positive recentering stiffness under P-Delta effects from gravity loads.

2. Determine $T_{o,min}$ to prevent connection decompression under wind or gravity loads.

3. Ensure that the PT elements remain elastic up to the target drift (typically associated with 2/50 earthuake hazard demands). This can be done by increasing A_{PT} or L_{PT} when possible.

4. Detail flange reinforcement to prevent yielding in the bearing flange.

5. Design the horizontally-slotted shear tab connection to transfer the expected shear loads.

A similar design methodology will be used for the PT column base connection and is presented below. The following design methodology and considerations may be incorporated into the SC-SPSW system performance-based seismic design procedure (discussed in more detail later) for those cases where PT column base connections are included.

9.2.2.1 Determine $T_{o,col,min}$ for wind loading

Conservatively estimate the column uplift forces associated with the design wind loads for the building. Although the column base will have some flexural resistance prior to decompression, the exact amount of resistance at the column base is dependent upon the flexural stiffness of the system and the columns themselves, which are not know a priori during the preliminary design phase; therefore, the columns can conservatively be assumed to have no flexural resistance at the base (i.e. assume pinned column base). In this case (shown schematically in Fig. 9.2), the lateral wind loads, V_{wind}, acting along the height of the building (at an effective height, h_{eff}) are resisted by the web plate and column shear forces at the base, V_{base}, and the tension-compression moment couple developed in the columns, F_{col}. The minimum PT force in the column, $T_{o,col,min}$, should conservatively

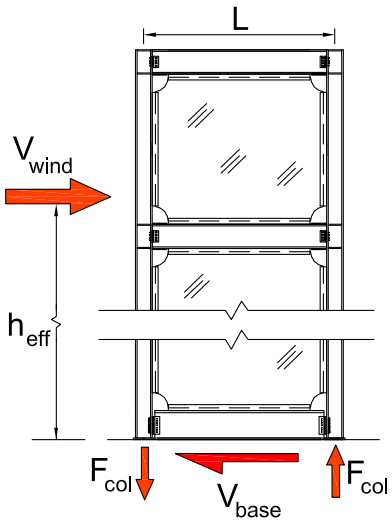

Figure 9.2: Estimation of column base forces due to wind loading

be taken as the tension force produced by the couple to prevent uplift of the column under wind loading.[3]

Where the SC-SPSW design is near its final stages, an analytical model of the SC-SPSW including the PT column base connection can be used to better estimate the uplift and moment demands at the column base under wind loading. The initial PT force in the columns, $T_{o,col}$, may be adjusted based on the demands predicted in this model such that decompression does not occur under wind loading and such that all other design requirements are met.

9.2.2.2 Prevent PT yielding under expected drift demands and uplift forces

The column PT should be designed to remain elastic in the following scenarios:

[3]In the seismic design procedure presented in this dissertation, the columns are to be designed to remain elastic up to drifts associated with a 2/50 seismic hazard level. It is possible that the column sizes can be reduced to allow for some yielding at this hazard level. In this case where the columns are allowed to yield, the designer may wish to ensure that the maximum moment in the column occurs in the bottom quarter of the bottom story, as proposed by Li et al. [2012], to prevent hinging in the upper portion of the column and formation of a soft-story mechanism. Therefore, the designer may also establish a $T_{o,col,min}$ to ensure that the maximum moment occurs in the columns at one-quarter of the story height above the base at a specified target drift level at which the column may begin to yield. A similar approach for designing the initial PT force in the beams to ensure a maximum moment at the beam end at a target drift level was presented in Clayton [2010] and Dowden et al. [2012] and can be modified for this purpose.

1. Under the expected connection rotation demands for the rocking column base connection (i.e. when one column flange is still in contact with the "ground")

2. Under the maximum uplift forces expected in the column for the case where the column is not in contact with the "ground"

The axial force in the column PT in the rocking connection is given in Eqn. (3.25). For purposes of design, the VBE axial stiffness can be considered to be much larger than the column PT axial stiffness, and the column PT force due to connection rocking can be simplified to:

$$T_{PT,col} = T_{o,col} + k_{PT,col}\frac{d_{col}}{2}\theta_{r,col} = T_{o,col} + \left(\frac{EA}{L}\right)_{PT,col}\frac{d_{col}}{2}\theta_{r,col} \tag{9.1}$$

In the event that the column base completely lifts off of its support (i.e. the uplift forces in the column becomes greater than $T_{PT,col}$ due to rocking) the column PT elements resist all of the uplift force in the columns. The column uplift force due to the yielded web plates and beam-to-column connection demands (shown as R_{yl} in Figs. 3.14 and 3.15 for fully connected and HBE-only web plates, respectively) can be found using the methods outlined in Berman and Bruneau [2008] and summarized in Sec. 3.2.4. For purposes of design, the minimum PT area, $A_{PT,col,min}$, can first be determined such that the column PT will not yield when subjected to the column uplift forces due to the web plates and beam-to-column connection demands (R_{yl} above).

Given the preliminary $A_{PT,col,min}$ and a preliminary column depth, d_{col}, the minimum column PT length, $L_{PT,col,min}$, can be determined based on the demands under the expected connection rotation from Eqn. (9.1) above. Here, the connection rotation, $\theta_{r,col}$, can be approximated as the target drift for which the VBEs are designed (taken as 5% drift in Clayton [2010]). Unlike the beam PT design, where the PT length is essentially set for a given bay width, for the columns, the PT length can be set by the designer at any point along the height of the column (or into the basement below). Therefore, the designer may adjust both the PT length and area to achieve the same goal based on PT bar or stand

availability and potential PT anchorage locations[4].

As the design is revised, $L_{PT,col,min}$ and $A_{PT,col,min}$ should be adjusted as the column rocking depth and initial PT force changes. The column rocking depth can initially be taken as the dimension between extreme fibers of the column flanges. If bearing "shoes" (similar to the beam end bearing plates in Specimen FR as shown in Fig. 5.2) or flange reinforcement plates are welded to the column flanges at its base, the column rocking depth should be adjusted accordingly.

9.2.2.3 Check post-decompression stiffness for recentering

Clayton [2010] proposed that the PT connection stiffness should be designed such that the recentering stiffness, K_r, of the SC-SPSW remained positive under the influences of P-Delta effects due to gravity loads. For multi-story SC-SPSWs, closed-form determination of the system recentering stiffness was difficult to determine; therefore, Clayton [2010] proposed checking this design criteria on a story-by-story basis such that the sum of the post-decompression stiffnesses of the PT beam-to-column connections at each story were greater than the reduction of stiffness due to gravity loads at that story.

Similarly, it is difficult to assess the recentering stiffness of multi-story SC-SPSWs with complex lateral loading. Clayton [2010] assumed that meeting the recentering criteria on a story-by-story basis at each beam level would ensure that the system was able to meet the global recentering criteria, enabling the designer to explicitly determine the connection stiffness required at each story. Thus, the additional recentering stiffness provided by the PT column base should only enhance the recentering capabilities. For complex systems, the recentering criteria can be checked globally using a numerical model in which the PT beam-to-column connection and the column base connections are either modeled with PT

[4]Although bars or strands may be used for the vertical PT, the designer should consider the ductility of each in their design. While high-strength PT strands have a larger yield capacity, they are more prone to brittle failure; while high-strength PT bars may yield at lower demands, they have a longer yield plateau. Because the column PT elements are the only mechanism for resisting column uplift forces, non-ductile failure of this element during an earthquake may result in catastrophic loss of lateral strength. Whereas potential brittle failure of beam PT elements may not be as catastrophic, because the shear tabs act as a redundancy to transfer connection forces. If non-ductile PT elements are used in the columns, additional factors of safety should be included to prevent brittle failure.

connections explicitly using methods presented in Chapter 7 or with flexural springs with rotational stiffnesses equivalent to those of the decompressed PT connections. Additionally, a conservative approximation of the global recentering stiffness can be determined using the virtual work method (as presented in Clayton [2010]) and the assumed design (or first mode) lateral load distribution up the height of the SC-SPSW; however, this method could only be used to check the recentering stiffness of a preliminary SC-SPSW design.

For simple SC-SPSW system, such as the two-story SC-SPSW specimen with lateral loading at only one story, the recentering stiffness can be estimated directly as

$$K_r = \frac{\Sigma k^{\theta}_{d,beam} + \Sigma k^{\theta}_{d,col}}{h^2} - \frac{P}{h} > 0 \tag{9.2}$$

where $\Sigma k^{\theta}_{d,beam}$ is the the sum of the post-decompression stiffnesses of the PT beam-to-column connections given in Eqn. (2.7), $\Sigma k^{\theta}_{d,col}$ is the sum of the post-decompression stiffnesses of the PT column base connections given in Eqn. (3.29), P is the gravity load, and h is the height of the applied lateral load. When this equation is used to predict the recentering stiffness of the two-story specimen (for which the gravity loads were zero), it yields a $K_r = 1.39$kN/mm, which corresponds well with the recentering stiffnesses taken from the experimental data ($K_{r,exp}$ in Table 6.9).

If the recentering stiffness is found to be insufficient to overcome the stiffness reduction associated with P-Delta effects, parameters affecting the PT connection rotational stiffness, namely the connection depth, PT cross-sectional area, and PT length, can be adjusted.

9.2.2.4 Detail flange reinforcement

The VBEs should be detailed with flange reinforcing plates according to procedures established in Garlock [2002] and Christopoulos et al. [2002a] to prevent local yielding or buckling at the target drift level. For the SC-SPSWs presented in this study in which the columns sections are designed to remain elastic up to 2/50 seismic hazard levels, the reinforcing plates should extend a minimum of one column depth away from the column base connection where the axial forces are concentrated in the bearing flange. Garlock [2002] offers additional guidance for determining flange reinforcing plate length considering yield strain

at the end of the plate for the case where some frame member inelasticity is expected.

9.2.2.5 Design shear restraint

The shear restraint at the base of the column is designed to transfer the shear forces from the SC-SPSW columns to the foundation. The shear demands at the base of the column are dependent on the SC-SPSW-to-foundation connection configuration. For example, in a configuration where the bottom anchor beam is located above the column base rocking interface (as shown in Fig. 9.1(a)), the shear restraint must be designed to resist the entire lateral load of the SC-SPSW system; however, in a configuration where the first story web plate is anchored directly to the foundation or grade beam (as shown in Figs. 9.1(e) through 9.1(c)), the shear restraint at the column base must only resist the shear in the columns. Column base shear demands can be determined using methods similar to those described in Berman and Bruneau [2008] for conventional SPSWs or can be determined using analytical or numerical models.

It should also be noted that unlike moment frame systems where the column shear forces are often assumed to be symmetrically distributed to each column (at least for interior columns), the columns in a SC-SPSW do not share equal portions of the total base shear due to the distributed loads of the web plate tension field acting on the columns. Fig. 9.3 shows schematically how the the distributed web plate forces cause an increase in the shear force in the uplift column, $V_{col,u}$, while the reducing the shear force in the compression column, $V_{col,c}$. Because the maximum column base shear forces are expected in the uplift column, frictional forces should not be relied upon to transfer shear at the column base; therefore, the shear transfer mechanism must be designed to resist the entire design shear forces. The shear transfer mechanism must also be able to accommodate the expected rotation and vertical uplift of the column while still adequately resisting the design shear forces. Because the column base shear is asymmetric with respect to direction of lateral loading, the designer may wish to design shear transfer mechanisms with different capacities on the inside and outside flanges based on the expected shear in the column in each direction of loading.

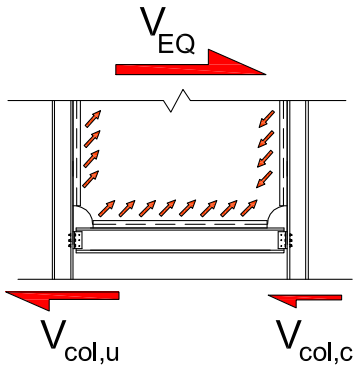

(a)

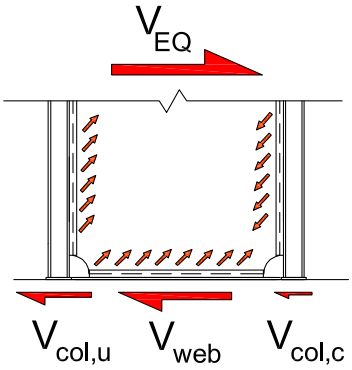

(b)

Figure 9.3: Example of unequal column base shear forces for configurations where (a) the first story web plate forces are transfered to the columns and where (b) the web plate is anchored to the foundation. (Only horizontal forces at the base are shown for simplicity.)

9.2.2.6 Check PT element anchorage and detailing

The column PT anchorage should be detailed to accommodate the expected rotation of the PT members under the expected drift demands. This is particularly important when bars, instead of strands, are used for the vertical post-tensioning as they are less slender and may yield due to curvature demands. To prevent bar bending during lateral sway, it is suggested to use domed bearings at the PT bar anchorage such that the bar is allowed to rotate freely to maintain a straight line between anchorage points (i.e. so that the PT bar always acts as a truss member) within the expected range of drift demands, as shown schematically in Fig. 9.4. The moving interface between domed bearing surfaces should be properly greased to reduce friction.

Examples of domed bearings that can be used to accommodate rotation are shown in Fig. 9.5. The type of domed bearing surface (e.g. concave vs. convex) impacts the location of the center of rotation of the connection as shown in Fig. 9.5. The center of rotation is located at the center of the radial bearing surface (i.e. the location of the center of rotation is dependent upon the radius of curvature in the bearing surface). The location of the center of rotation will impact the clearance required in the holes cutout from bearing plates that support the PT anchorage. For example, thicker plates will require larger holes if the center of rotation is farther away from the plate, but may require smaller holes if the center of rotation in closer to the plate. The domed bearing surfaces can be designed according to these principles, and the designer should ensure sufficient clearance in through each of the interfaces that the PT bar passes through to ensure free rotation.

9.2.3 Limitations of PT column base connections implementation

As stated previously in Sec. 9.2.2.2, the column PT should be designed to remain elastic under the following two events: (1) the largest expected column connection rotation demands and (2) potential uplift of the column (i.e. complete decompression of both flanges). From the latter event, the minimum PT area can be determined, and from the former event the minimum PT length for a given cross-sectional area can be determined. Because the column PT length can vary up to the height of the building, some combination of $A_{PT,col}$,

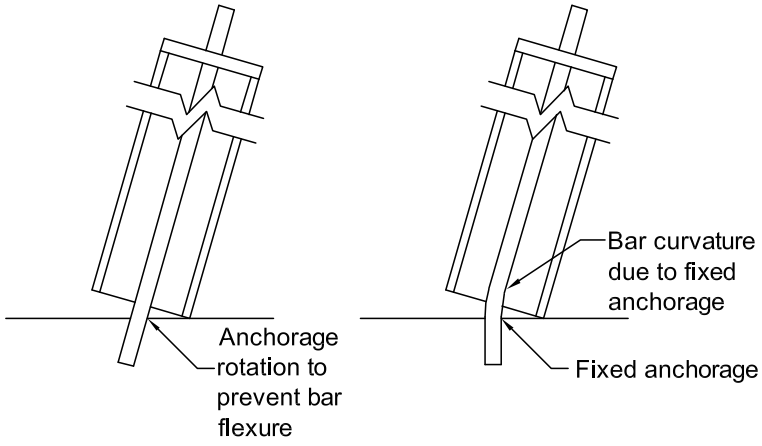

Figure 9.4: Examples of PT anchorage that is free to rotate (left) and is fixed (right). (Deformations are exaggerated)

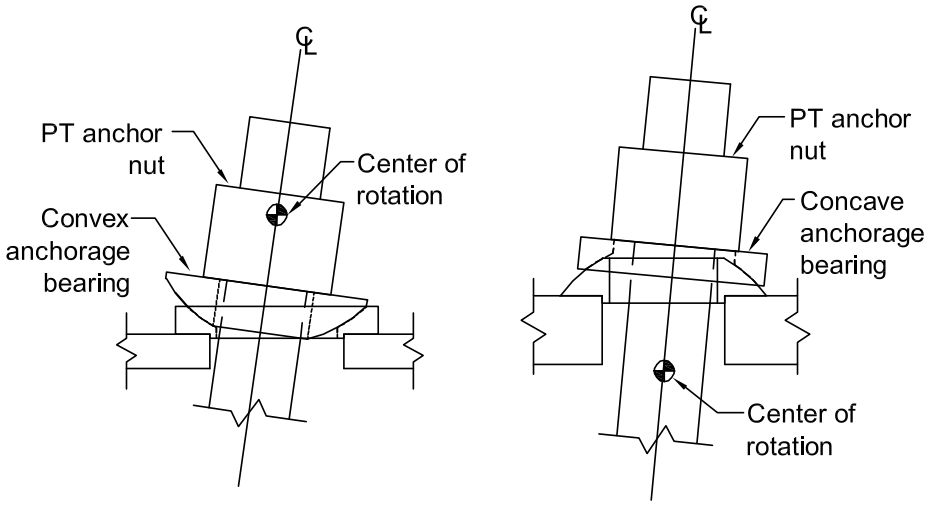

Figure 9.5: Examples of convex (left) and concave (right) domed PT anchorage bearings

$L_{PT,col}$,and d_{col} can be found to satisfy the requirements for event (2).

However, event (2) requires sufficient PT strength to resist the total uplift forces in the column. For very tall SC-SPSWs or SC-SPSWs with very thick plates, this can require a substantial number of PT bars. For this reason, there are some limits on SC-SPSW designs for which PT column base connections can reasonably be employed. Here some simplifying assumptions are made to provide guidance on building-types when PT column base connections may not be feasible.

To capacity design the column PT to resist the maximum column uplift force, details of the web plate and beam-to-column PT connection strengths must be determined. To approximate the column uplift force in a general sense (i.e. not particular to a certain design), the column uplift force was estimated using some very simplified assumptions of earthquake loading and expected web plate overstrength. The following assumptions were made:

1. The earthquake load distribution can be approximated as an inverted triangle, such that the total lateral load acts at an effective height of two-thirds of the building height.

2. The total seismic weight for each story, w, was approximated as 10450 kN. This corresponds to the seismic mass of each floor level for the 9-story SAC building [FEMA, 2000a].

3. The building was assumed to be located in the Los Angeles area with the same spectral values presented in Table 5.1 [Somerville et al., 1997]. The natural period of the building is conservatively assumed to be in the short-period (0.3sec), constant spectral acceleration region.

4. The web plates are assumed to be designed for the design-level earthquake demands, which are taken here as the 10/50 demands divided by a response modification factor, R, of 7 (corresponding to SPSWs).

5. The SC-SPSW is assumed to have an overstrength factor, Ω_o, of 2 (corresponding to SPSWs). For capacity design of the column PT elements, the maximum column demands will be those due to design-level seismic loading times the overstrength factor.

From these assumptions the column uplift force, F_{col}, can be determined from the simplified free-body diagram in Fig. 9.6. In this figure, V represents the total lateral force applied to a particular SC-SPSW, and can be taken as:

$$V = \frac{C_s w n_s}{n_w} \tag{9.3}$$

where C_s is taken as 0.153 as calculated per ASCE [2005] based on the assumptions above, w is the seismic weight per story (taken as 10450 kN from the assumptions above), n_s is the number of stories, and n_w is the number of SC-SPSWs in each directions of the building. The web plates were assumed to be designed to resist this force, meaning that for capacity design, the maximum lateral load that the SC-SPSW can resist is assumed to be $\Omega_o V$[5].

This lateral force is acting at an assumed effective height, $h_{eff} = \frac{2}{3} h_s n_s$, where h_s is the height per story, taken here to be 3.96 m, consistent with the buildings presented in Chapter 8. This lateral load acting at this effective height produces an overturning moment that is resisted by a tension-compression couple in the columns. The maximum force in the uplift column, F_{col}, can be taken as:

$$F_{col} = \frac{\Omega_o V h_{eff}}{L} = \frac{\Omega_o C_s w n_s \left(\frac{2}{3} h_s n_s\right)}{n_w L} \tag{9.4}$$

where L is the bay width. The column PT bars bars must be able to resist this force such that $F_{col} < \sigma_{y,PT} A_{PT,col}$, where $\sigma_{y,PT}$ is the yield strength of the column PT elements. For this study, $\sigma_{y,PT}$ was taken as 830 MPa, or approximately 80% of the ultimate strength of ASTM A722 Grade 150 threaded bar.

The above equations can be combined to estimate the maximum number of stories for

[5]When actually designing the PT to resist uplift forces, the expected web plate strength, $R_y F_y$, and the actual PT connection strength at the expected drift would be used to determine the actual maximum column forces.

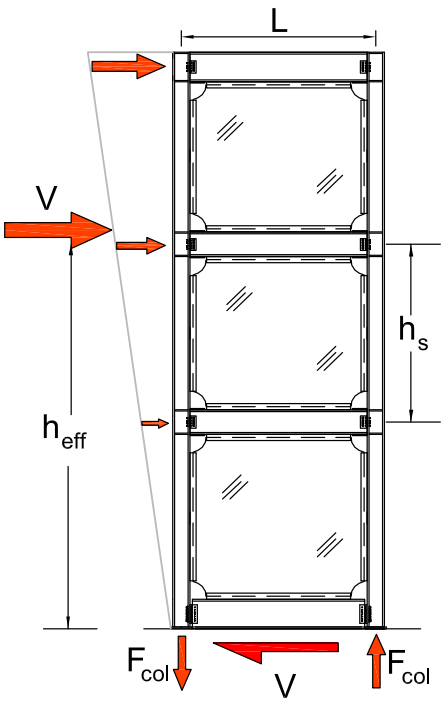

Figure 9.6: Simplified free-body diagram for estimating maximum column uplift forces

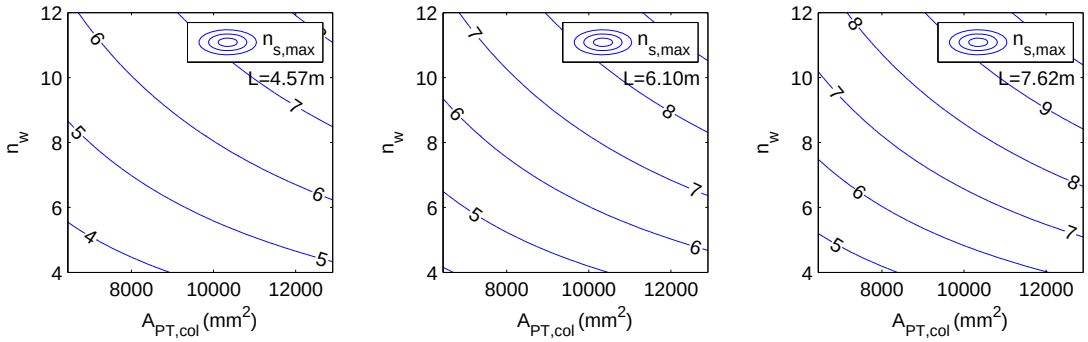

(a) $L = 4.57$m (b) $L = 6.10$m (c) $L = 7.62$m

Figure 9.7: Approximate limits for employing PT column base connections

a given set of design parameters:

$$n_s < \sqrt{\frac{\sigma_{y,PT} A_{PT,col} n_w L}{\frac{2}{3}\Omega_o C_s w h_s}} \tag{9.5}$$

Fig. 9.7 shows the maximum number of stories plotted against the number of SC-SPSWs in each direction of the building, n_w, and the PT area, $A_{PT,col}$ for various bay widths (L=4.57m, L = 6.10m, and L=7.62m). Note that L=4.57m is the bay width that was used in the SC-SPSW designs in Chapter 8. Also note that the two 69 mm diameter threaded bars used in each column of the full-scale test (Chapter 5) had a combined cross-sectional area of 6,700 mm^2, and more PT bars could reasonably be accommodated within the depth of the column.

Fig. 9.7 and Eqn. (9.5) show that increasing the column PT area and increasing the number of SC-SPSWs in the building increases the height of the building for which column PT base connections can reasonably be employed, as would be expected. Similarly, increasing the bay width also increases the maximum number of stories for which PT column bases connections can be used. For example, using only two 69 mm diameter threaded bars in each column, four SC-SPSWs in the each direction of the building, and a bay width of 3.42 m, all corresponding to the prototype for the full-scale specimen, the building could be up to three stories tall using this conservative approximation. However, if increasing the bay width to

5 m, using four 69 mm threaded bars per column ($A_{PT,col}$ = 13,400 mm^2), and assuming ten SC-SPSWs in each direction of the building, the building can be up to approximately eight stories tall before PT column base connections become impractical. These values only represent conservative approximations, and determination of actual column demands based on the actual SC-SPSW design parameters may result in different values.

9.3 Web Plate Detailing

As with all SPSW systems, the web plate-to-boundary frame connections should be detailed to adequately resist the expected yielded web plate forces and the expected deformations. Below are discussions of different web plate detailing considerations.

9.3.1 Corner cutout

Unlike conventional SPSWs with welded connections, the web plate in a SC-SPSW must accommodate the additional deformation in the corners associated with connection gap opening. To reduce the large localized tensile strains in the web plate due to gap opening, cutouts should be provided in the corners. The cutouts should be sufficiently large such that the tensile strain along the edge of the cutout due to the expected drift and gap opening is less than the web plate tensile rupture strain. Further discussion for determining the minimum cutout distance can be found in Dowden [2014].

The cutouts can be either radial or diagonal corner cutouts, as were used in the sub-assembly (Fig. 4.2) and full-scale (Fig. 5.2) tests, respectively. Radial corner cutouts were first selected to "protect" the end of the weld from the largest tensile stresses that form tangent to the radial cutout as shown in Fig. 9.8. Alternatively, for the diagonal corner cutout (also shown in Fig. 9.8), the maximum tensile strains that occur along the cutout edge are transfered directly to the ends of the fish plate connection, where the weld may be particularly vulnerable to crack initiation.

Although the radial cutouts may reduce the tensile demands at the end of the web plate-to-fish plate connection, observations during the experimental studies (of both radial and diagonal cutouts and bolted and welded web plate connection details) found that most of the web plate tearing did initiate at the ends of the fish plate but were due primarily to the

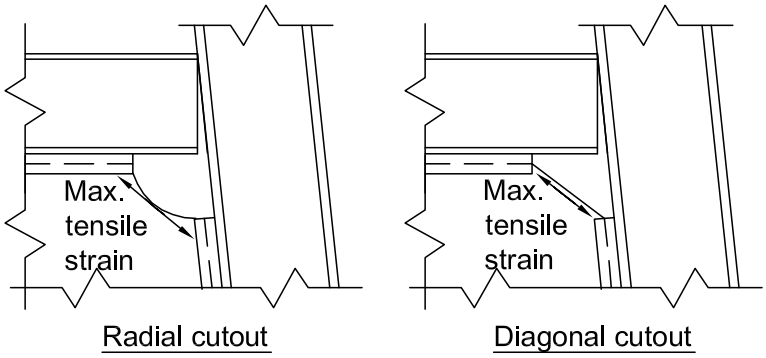

Figure 9.8: Schematic showing the location of the maximum tensile strains at the web plate corner cutouts (PT and shear connection components not shown for clarity)

out-of-plane deformation of the web plate along the free edge of the plastically elongated corner cutout (as previously described and shown in Fig. 5.39). The large out-of-plane deformations along the free edge of the buckled web plate in the corners where the PT connection gap was closed resulted in large localized inelastic curvature demands at the end of the welded or bolted connection, where tear initiation was typically first observed. Therefore, use of radial cutouts, as opposed to diagonal cutouts, may not be as beneficial as originally assumed to prevent crack initiation at the end of the weld. The designer may select the cutout shape according to the geometry of the panel (e.g. the large aspect ratio in the subassembly tests were better suited for diagonal cutouts, because radial cutouts would have resulted in very short lengths of web plate connected to the columns).

9.3.2 Bolted vs. welded connection

Although the bolted web plate-to-fish plate connection used in the SC-SPSW subassembly tests was developed to facilitate quicker turnaround between tests and reuse of the same boundary frame for multiple tests, the tests demonstrated that the bolted connection was

able to adequately transfer web plate forces with web plate damage progression comparable to conventional welded SPSW web plate connections. Alternatively, the welded web plate connection details have been used successfully in a wide range of SPSW applications for multiple decades and had adequate performance at and beyond the 2/50 seismic hazard level in the full-scale SC-SPSW test presented in Chapter 5.

Although welded web plate connection details are suggested for most SC-SPSW applications due to their relative ease of construction and familiarity, there may be some scenarios where using bolted web plate connection details may be beneficial:

- When very thin web plates are required, making conventional welding methods difficult or prone to defect. For example, for the thin web plates used in the SC-SPSW subassembly tests, the web plate was too thin to produce typical fillet welds without burning through the web plate material (as described in Sec. 4.2.2.1); therefore, special care and additional practice was taken by the welder to produce a weld bead that would roll over onto the web plate material. Also, the MIG (GMAW) welding process was used in this case as it was more preferable for welding such thin web plate material. This welding process may not be as common or desirable for field welding applications as external tanks of shielding gas are required. For these reasons, a bolted web plate connection detail may be desirable for thin web plate material.

- For low-rise buildings where the SC-SPSW can be assembled on- or off-site in the horizontal configuration on the ground and lifted into place during erection. For construction sequences that allow for assembling the SC-SPSW in the horizontal configuration, both the bolted and welded web plate connection details are easier to execute compared to doing so in the vertical configuration; however, the additional difficulty of aligning web plate bolt holes in the vertical configuration is reduced, thus reducing the relative difficulty of executing the bolted connection details compared to the welded detail.

9.4 PT Connection Flange Detailing

The current SC-SPSW design procedure only requires that sufficient flange reinforcement be provided to prevent yielding in the bearing flange that transfers the compressive force during rocking. This reinforcement may be provided in multiple ways. For example, flat plates can be welded directly to the outside of the flange as was done in the subassembly tests (Fig. 4.2), or bearing "shoes" can be used to provide a bearing surface at the end of the flange as was done for the beams in the full-scale test (Fig. 5.2). Each of these serves the intended purpose but can impact construction fit-up.

The ends of the beams (or the post-tensioned member) must be cut such that both flanges can bear evenly on the supporting surface (e.g. the column face or foundation). If the ends of the member cannot rest evenly on the bearing surface, the connection may be in an initially decompressed state as was observed in the subassembly tests (Sec. 4.3). This initial decompression results in a reduced initial stiffness and an asymmetric PT connection response (as discussed in Sec. 6.2). Although it does not greatly impact the overall SC-SPSW lateral strength, it may impact SC-SPSW response in the elastic range (pre-connection decompression and pre-web plate yielding). The lower initial stiffness may increase deformations under wind loading or 50/50 seismic events. For these reasons, care should be taken to ensure even bearing at the ends of the member during construction and frame post-tensioning. If necessary, the bearing surface can be fitted with thin steel shims welded to the bearing member (i.e. column flange in the case of PT beam-column connections) prior to post-tensioning to close the initial gap

Additionally, flange reinforcing plates must also be aligned flush with the end of the flange. If the flange reinforcing plates do not align with the edge of the flange, as the connection rocks open, it may transition between bearing surfaces from the edge of the flange to the edge of the reinforcing plate. This transition between unaligned bearing surfaces will result in a PT connection response different than the bilinear elastic response assumed. For example it may become trilinear to represent the different connection stiffnesses when rocking about different points. Although this effect may not have a significant effect on the overall SC-SPSW behavior, it should still be considered to ensure intended behavior.

Using the flange reinforcing "shoe" prevents this problem by providing a single even bearing surface.

9.5 Diaphragm Connection Detailing

One of the complexities that arises with self-centering systems, particularly those that rely upon frame expansion to develop restoring forces, is tying the lateral resisting frame to the diaphragm and gravity framing systems. The diaphragm-to-lateral system connection must be able to perform a number of key functions. It must:

1. Transfer inertial forces from the story to the SC-SPSW

2. Accommodate frame expansion while limiting significant damage to the floor slab (in keeping with the performance objectives)

Previous research (as discussed in Sec. 2.2.3) have proposed diaphragm details, including flexible collector beams to deform as the frame expands [Garlock and Li, 2007], sliding slab-framing interfaces and discontinuous slabs [Kim and Christopoulos, 2008; Chou and Chen, 2011a]. These details were developed primarily for SC-MRF frames; however, they may be extended to other self-centering systems.

One key difference between the SC-SPSW and SC-MRF systems that have been previously researched is the fact that the SC-MSF consists of several bays of SC-MRF in a single frame. Because beam growth accumulates within the frame (i.e. if each bay expands by $\Delta_{gap} \approx \theta_r d$, the relative deformation between the slab and SC-MRF that must be accommodated at the outermost columns is $\frac{1}{2} n \Delta_{gap}$, where n is the number of SC-MRF bays in that frame), the diaphragm connection detail may need to accommodate significant deformation. For example, for a SC-MRF with beam depths of approximately 450 mm, maximum drifts of approximately 0.05 radians, and four bays in each SC-MRF frame (and maybe two SC-MRF frames in each direction of the building, although that does not affect frame expansion), the total frame expansion would be approximately 90 mm, or ±45 mm at the outermost columns. For the SC-SPSW, the SC-SPSW bays are not continuous (i.e. the PT elements do not extend over multiple bays) and slab detailing (as shown and discussed

later in Figs. 9.9 and 9.10) can be provided to accommodate the frame expansion of each SC-SPSW bay itself; thus, beam growth in each bay is not cumulative. So for comparison with the previous example, for a SC-SPSW (which may have four or more separate SC-SPSW bays in each direction) with similar 450 mm deep beams at 0.05 radians, each individual SC-SPSW bay will grow a total of approximately 22 mm, or ±11 mm at each SC-SPSW column. Therefore, the slab connection detail used at each SC-SPCW would only need to accommodate ±11 mm, as the adjacent gravity frames would have slotted and sliding connections such that they would not be affected by beam growth in the SC-SPSW. By separating the "growing" bays in the SC-SPSW, the amount of expansion that the diaphragm detail must accommodate is smaller than in the SC-MRF applications.

Figs. 9.9 and 9.10 show some schematics of possible diaphragm connections. Those from Fig. 9.10 have elements that are borrowed from previous SC-MRF research [Kim and Christopoulos, 2008; Chou and Chen, 2011a]; however, those from Fig. 9.9 were developed particularly for the SC-SPSW as it benefits from the single-bay nature of the system. Each of these schematics are shown for an interior SC-SPSW; however, similar detailing can be used for exterior SC-SPSWs or those adjacent to slab openings (e.g. around stair or elevator cores). Each of these proposed details will be discussed below.

All of the schematics shown in Figs. 9.9 and 9.10 have a few similarities. In each of the proposed connection methods, the diaphragm forces are transferred only to the SC-SPSW columns. As was presented in Clayton [2010], the HBE axial force and moment demands are quite complex due to the distributed web plate loading and rocking connection behavior. All of the expressions for HBE axial force and moment demands assume that the story forces are delivered at the columns (particularly in Clayton [2010], it was assumed that the story forces were delivered symmetrically to both SC-SPSW columns) and are not delivered to the beams; therefore, all of the proposed diaphragm connection schemes transfer story forces through the columns. Gravity loads are also carried to the beams perpendicular to the SC-SPSW such that no beams frame directly into the SC-SPSW beams.

Each of these schematics also include slab blockouts in the immediate vicinity of the SC-SPSW that allow the columns to move relative to the slab without inducing slab cracking. Unless noted otherwise in the schematic drawings or discussed later, the floor diaphragm

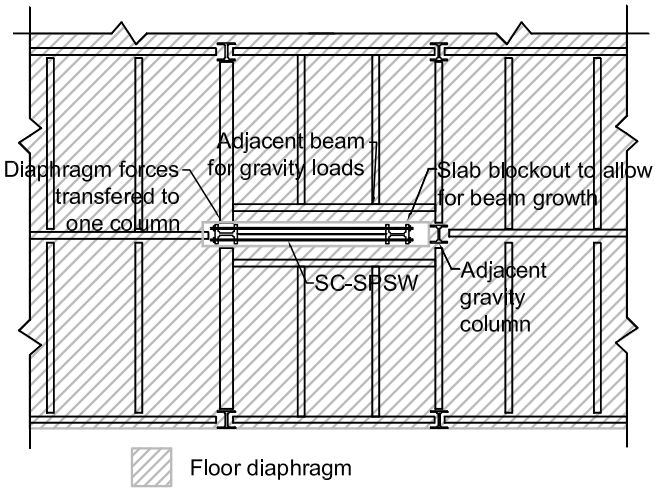

(a) With dummy column to support gravity

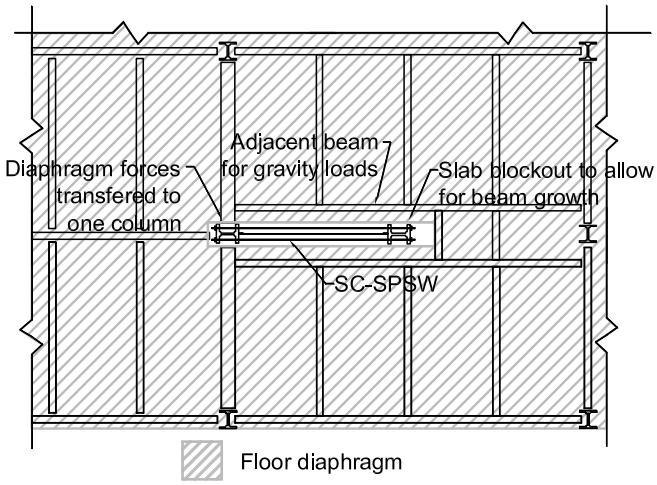

(b) With additional framing to support gravity

Figure 9.9: Schematic of diaphragm connection (one-column configurations)

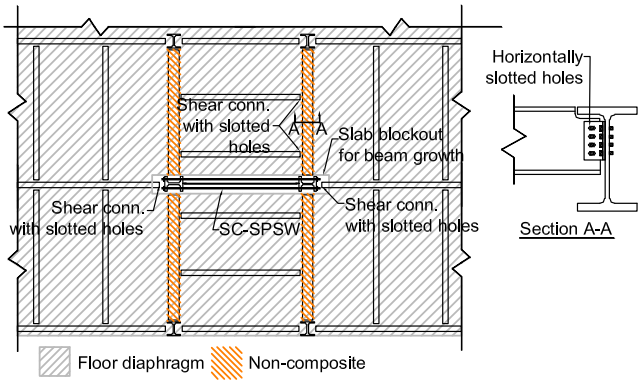

(a) With non-composite collectors

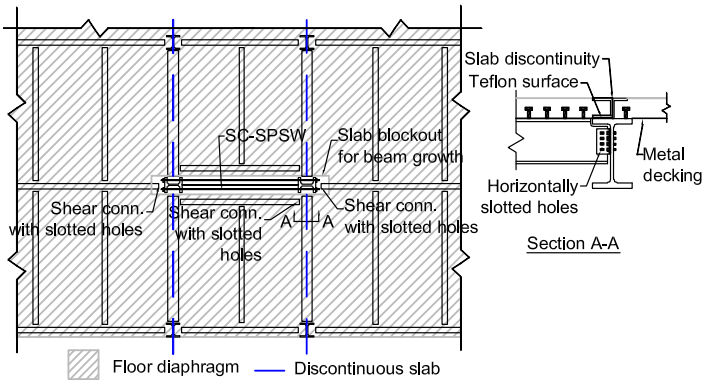

(b) With slab breaks above collectors (perprindicular framing)

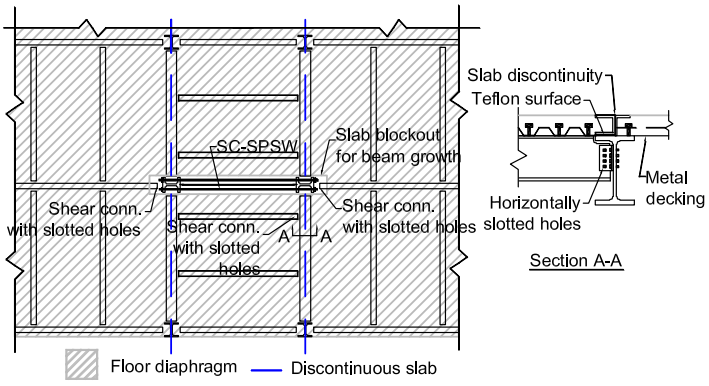

(c) With slab breaks above collectors (parallel framing)

Figure 9.10: Schematic of diaphragm connection (two-column configurations)

(indicated by the gray diagonal hatching) acts as a composite slab meaning that shear connectors are provided between the slab assembly (metal decking and concrete) and the gravity steel framing as indicated.

9.5.1 Single-column loading configurations

Fig. 9.9 shows diaphragm connection details in which the story forces are transferred only to one column. These details are most similar to the loading conditions in both the sub-assembly and full-scale tests where the actuators were attached to one column. This loading configuration is most suitable for individual-bay lateral framing systems (e.g. transferring all of the story shear into a single column of a multi-bay SC-MRF may not be able to adequately distribute the shear forces to all the bays). It is also ideal for the flange rocking SC-SPSW where the beam PT elements are always in tension and can help "pull" the frame when the column is loaded in the direction away from the web plate (as described in the experimental results)[6].

In both of the single-column loading configurations in Fig. 9.9, the gravity loads are transfered to adjacent frames, and the slab is blocked out to allow the unloaded column to expand to accommodate the total expected frame expansion. The key difference between Figs. 9.9(a) and 9.9(b) are how the gravity loads are carried to adjacent framing. SC-SPSW bays are typically of smaller width than typical gravity framing [Clayton, 2010]. Fig. 9.9(a) shows an example of an additional gravity column, or "dummy" column, being placed outside of the SC-SPSW column at a smaller than typical gravity bay spacing, while Fig. 9.9(b) shows an example of using additional gravity framing around the slab blockout to carry gravity loads to the adjacent, regularly-spaced gravity columns. The intent of both of these details is to decouple the gravity framing of the bays adjacent to the SC-SPSW

[6]For other PT connections details in which the PT elements may lose tension, such as those that rock about only the top flange where PT elements on one end of the beam elongate as the gap opens while the PT elements on the other end may go slack as the connection gap closes [Dowden and Bruneau, 2011], this loading configuration may not be as desirable. In this case when the loaded column is pulling the SC-SPSW in the direction away from the web plate, the PT elements nearest that column may also be slack due to gap closing. This may cause the beam to separate from the column which may result in loss of the intended rocking behavior; however, it may not be detrimental to the performance. More research should be done on this load scenario if used in this application.

from the SC-SPSW itself. In both of these cases, the additional dummy column or framing must be placed far enough away from the free SC-SPSW column to prevent pounding under the largest expected frame expansion demands.

The single-column loading configurations are ideal in that as long as the slab blockout is provided to decouple the gravity framing from the SC-SPSW, no additional special detailing or sliding interface details are required. The frame is allowed to expand without damaging the slab due to differential column sway, and the detail does not require special consideration for the complex kinematics associated with simultaneous frame expansion of SC-SPSWs in perpendicular directions of loading (as would be the case for a real 3-D earthquake loading scenario). However, the collector beams and beam-to-column connections should be designed to adequately transfer the inertial forces into the column, which may result in large collector beams and struts.

9.5.1.1 Modification of HBE demands for single-column loading

Although all of the experimental specimens in this SC-SPSW were loaded on a single column and were shown to perform as designed, further investigation is required to better understand the effects of the single-column loading on system mechanics and force transfer.

As previously stated, the HBE demand expressions developed in Clayton [2010] assumed that the story shear forces were transferred symmetrically to both columns. In this simplified derivation, the applied story shear force that is transfered to the HBE is equal to the net horizontal load from the difference in web plate thicknesses above and below the HBE, $P_{(HBE,web)}$. This net horizontal load is distributed symmetrically to the HBE with a horizontal web plate reaction forces of $\frac{1}{2}P_{(HBE,web)}$ acting on each end of the HBE (as shown in Fig. 1.2).

Thus, it follows that in the case where the story shear forces are only transferred to one column, the HBE member end forces due to the net horizontal web plate loading would be distributed according to the story shear loading (i.e. member end forces of $P_{(HBE,web)}$ at end of the HBE attached to the loaded column and zero at the unloaded column side). Using this assumption, the HBE free-body diagrams and axial and moment distributions

derived in Clayton [2010] and summarized in Secs. 1.2.1.1 and 2.4.1.1 can be modified by replacing the $\frac{1}{2}P_{(HBE,web)}$ web plate horizontal member end forces with $P_{(HBE,web)}$ on the loaded end of the HBE and zero on the other.

This approximation of HBE demands is an idealization extended from common assumptions made in conventional SPSW design [Sabelli and Bruneau, 2007]; however, further numerical simulations are required to fully understand how the story shear forces acting on a single column are transfered to the HBEs and VBEs and how they may affect HBE moment and axial demand distributions.

9.5.2 Two-column loading configurations

The diaphragm details shown in Fig. 9.10 all represent configurations where the story shear forces are transferred to both columns of the SC-SPSW. Fig. 9.10(a) shows the collector beams that transfer the story shear to the columns are non-composite meaning that no shear studs are provided on these beams such that they can move relative to the slab above. In this case some sliding interface (e.g. Teflon below steel decking) should be provided to allow for this differential movement. By releasing the slab from collector beams, the beams can rotate with the column expansion (i.e. making the collector beams non-parallel); however, to accommodate the collector beam deformation, the members framing into it (which can still be connected to the slab with shear connectors) should have horizontally slotted holes to allow for this beam growth while still being able to transfer shear forces. Similarly, the shear connections between the SC-SPSW columns and the adjacent gravity beams in line with the SC-SPSW should also have some sort of horizontally slotted holed to accommodate the column expansion. In these cases the horizontally slotted holes should be able to accommodate half of the total frame expansion, while accommodation required in the previously mentioned slotted connections decrease linearly with distance from the SC-SPSW.

Figs. 9.10(b) and 9.10(c) show an alternative where a slab break, or discontinuity, is introduced along the line of the collector beams framing into the SC-SPSW. The difference in these two details is the direction of the metal decking and framing in the gravity framing

adjacent to the SC-SPSW. At the slab discontinuities, one side of the slab is connected to the collector beam via shear studs, while on the other side of the slab break, the slab is allowed to slide on top of the collector beam. Again, because the beams framing into the collector beams are acting compositely with the slab, horizontally slotted holes should again be provided at those shear connections where the slab sliding interface is provided to allow for the slab and gravity framing to move relative to the collector beam. In this configuration as the SC-SPSW bay expands a gap will form at the slab break and will close upon recentering. At least two edges of each slab segment are connected to the collector framing, while the other edges are free to slide. Another disadvantages with this configuration is that these slab breaks must extend over the entire width of the building; therefore, it is preferential if the SC-SPSWs in a single building are in-line to reduce the number of required slab breaks. Also, because the slab breaks must be provided for the SC-SPSWs in both directions of loading the three-dimensional detailing of the floor slab can get complex.

9.5.3 Further research required

These proposed diaphragm connection methods are only presented schematically. Further research is required to fully evaluate the feasibility of transferring such large inertial forces in this manner and understand the flow of the inertial forces through the SC-SPSW when loaded in these ways. Experimental validation is also required to ensure that these diaphragm connections and gravity framing details behave as intended. Ideally, experimental validation could be conducted on three-dimensional specimens considering deformations in perpendicular loading directions as the diaphragm detailing and accommodation of frame expansion becomes particularly complex when considering three-dimensional loading.

9.6 Reduction in Column Sizes

Design of the 3- and 9-story SC-SPSWs in Clayton [2010] and design of the 2-story full-scale specimen in Chapter 5 showed that the current SC-SPSW performance-based and capacity design procedures result in large column member sizes. The minimal damage observed in the columns of the full-scale specimen at the 2/50 seismic hazard level also suggest that there

is room for potential reductions in column member sizes while still meeting the proposed performance objectives[7].

9.6.1 Benefits from reducing column sizes

Apart from the obvious benefits of reducing material costs and reducing the potential for needing built-up or hard-to-find column sections, there are other aspects of SC-SPSW behavior and performance that may benefit from, and even necessitate, a reduction in column size. These aspects of SC-SPSW performance that may be impacted by column size include:

- If columns are too stiff, they cannot accommodate differential beam growth at adjacent levels. For example, if the columns and beams are assumed to be rigid, the columns will rotate to accommodate the frame expansion of the deeper (or more axially stiff) beam as shown in Fig. 9.11 where the boundary frame member sizes are exaggerated for purposes of demonstration. In this case, the smaller beam above will lose contact with the columns as they spread apart due to the deep beam below. The beam essentially is "hanging" by the shear connections (not shown in Fig. 9.11 for clarity) or, in very extreme cases, acting as a tension member in the case that it reached the limits of the shear tab's horizontally slotted holes and no longer has any flexural resistance at the beam ends. Although this is an exaggerated example with rigid boundary frame members and drastic differences in adjacent beam depths, it demonstrates the potential for loss of SC-SPSW intended behavior in the presence of especially stiff columns. More flexible columns would be able to bend to accommodate this difference in beam growth at each story (additionally, beam axial flexibility would help reduce the difference in differential beam growth, but at the expense of reducing PT elongation and the associated recentering benefits).

- The intent of this research was to develop a lateral load-resisting system that could reduce the economic impact of earthquakes. When assessing SC-SPSW performance

[7]It should be restated that because the actual web plate material propertied were unknown at the time of column design, the columns in the full-scale specimen were conservatively designed for an assumed web plate strength approximately 25% larger than the actual web plates used in the test (see Sec. 5.3 for further details).

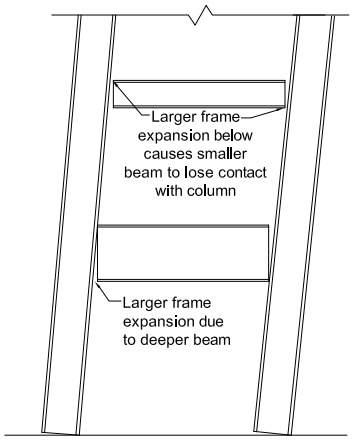

Figure 9.11: Schematic of the stiff column effect (PT elements and web plates not shown for clarity)

from the perspective of reducing overall economic impacts, the expected upfront cost of the structure as well as the expected cost of repairs following a seismic event should be considered. Having overly-conservative, expensive columns that are undamaged following an earthquake with a return period of 2,500 years may not be meeting the intended goal of reducing economic impacts. Assessment of SC-SPSW performance from an economic perspective considering the upfront cost versus the probabilistic repair costs may indicate that this overly-conservative column design approach is not "performing" as intended. To assess and improve performance in an economic sense, an investigation of the probabilistic occurrence of SC-SPSW column damage and repair costs for a given seismic hazard should be incorporated into a lifetime cost analysis of the building and should be compared with similar assessments for conventional SPSW systems to demonstrate the potential for overall economic savings.

9.6.2 Possible approaches to reducing column sizes

Two potential methods for reducing column sizes are presented below. These methods include: (1) reassessing the target drift demands for which columns are designed and (2) connecting the web plates to the beams only.

9.6.2.1 Reconsider column design target drift levels

To improve the structural efficiency and economy of the columns, the column capacity design assumptions should be reconsidered. The target drifts for column design may be reconsidered based on two premises:

1. The target drifts previously proposed in Clayton [2010] were based on a numerical study on SC-SPSWs using tension-only strips. Actual drifts in the 2/50 event when considering the additional energy dissipation in the web plate that is ignored in the idealized tension-only model may be lower than these assumed target drifts.

2. The target drifts used in the performance-based design are intended to prevent column yielding at the 2/50 hazard level in order to provide collapse prevention performance. This design approach may be overly conservative if collapse prevention can be attained when some column yielding is allowed.

Each of these premises is briefly discussed below.

Reducing drift based on actual SC-SPSW drift demands: The numerical studies in Chapter 8 showed that when web plate residual strength is considered, the peak drift demands are reduced significantly (by as much as 50% for the thee-story SC-SPSWs) compared to the conventional tension-only model. These results suggest that for low-rise C-SPSWs designed with web plates that are fully-connected to the HBEs and VBEs the target drift demands for HBE and VBE cpacity design may be reduced to as low as 3% drift[8]. Reducing the target drift demand based on the median 2/50 peak drift demand

[8]Note that this potential reduction in target drift only applies to SC-SPSWs with fully-connected web plates, and the reduction of target drift demands may not be as large for mid- to high-rise SC-SPSWs.

will reduce boundary frame demands used for capcity design (due to the decrease in PT demands) and may significantly reduce frame member sizes. Using a revised target drift demand based on more realistic 2/50 peak drift demands still assumes the boundary frame will remain essentially elastic in the 2/50 event.

Reducing drift to allow some column yielding: The intent of the design methodology is to prevent formation of a soft story by capacity designing the columns remain elastic up to a drift demand larger than that which the beams are designed, typically taken as drift demands associated with the 2/50 seismic hazard level. In Clayton [2010] and in the full-scale SC-SPSW test, the columns were designed to remain elastic up to 5% drift. However, the intended performance objective at this hazard level was collapse prevention. Collapse prevention implies that structural members may be severely yielded but in a ductile manner that prevents collapse and allows for occupant egress. The intended performance and design assumptions for this hazard level seem incongrent. Perhaps the columns can be designed for drift levels greater than those expected in a design-level or 10/50 event, but less than those expected for a 2/50 event, such that the yielding still results in ductile building performance. Further research should be done to investigate what design drift levels provide adequate collapse prevention performance.

Part of the reasoning for establishing conservative 2/50 target drifts was the uncertainty of SC-SPSWs response following significant yielding and potential loss of PT connection strength and stiffness. In order to effectively reduce the column sizes, numerical and experimental research should be done to assess how the system performs following PT yielding, beam or column flexural-axial hinging, or boundary frame local flange or web buckling. No previous SC-SPSW research and little research on self-centering systems in general has been conducted to investigate performance under these extreme loading and damage scenarios.

Numerical models representing the cyclic response associated with these damage states should be calibrated and validated to better simulate the strength and stiffness degradation that may lead to collapse. Nonlinear dynamic analyses should be conducted to assess the system's probability of collapse using procedures such as incremental dynamic analyses (IDA) presented in FEMA [2009].The results of such numerical studies can be used to

assess appropriate design drift levels to be used in column design such that the probability of collapse at the 2/50 hazard level is still under an acceptable threshold.

9.6.2.2 Connecting the web plates only to the beams

Sec. 8.3 showed that connecting the web plates to the beams only (referred to as HBE-only connectivity) can result in a significant reduction in column member size, as well as some potential reduction in beam member sizes). Here, the SC-SPSWs with HBE-only web plate connectivity were designed to have the same strength as comparable fully-connected web plate SC-SPSWs, and the boundary frame members were designed using the same capacity design methodologies. The results of nonlinear response history analyses on SC-SPSW models with both types of web plate connectivity showed that the SC-SPSWs with HBE-only web plates had larger peak drifts demands than their fully-connected web plate counterparts; however, when web plate residual strength was considered in the model, the peak drifts, residual drifts, and HBE and VBE demand-capacity ratios were within the proposed performance objectives, including elastic web plates (i.e. story drifts less than 0.5%) at the 50/50 level, recentering (i.e. residual drifts less than 0.2%) and peak drift demands below or near the 2% code-based limit at the 10/50 level, and minimal HBE and VBE yielding at the 2/50 level.

Potential benefits of connecting the web plates to the HBEs only include:

- Reducing the flexural and axial demands in the columns by eliminating the distributed loading from the web plates.

- Eliminating the additional horizontal strain in the web plate due to frame expansion and the localized tensile strain at the opening connection gaps which can mitigate the occurrence of web plate tearing and damage, as demonstrated in the single subassembly test conducted (W14-8s100k16GaHBE) in this configuration.

- Reducing difficulty in construction and fit-up as only two of the four web plate edges must be connected to the boundary frames (This is especially true if bolted web plate-

to-fish plate connections are used in which bolt hole alignment is particularly difficult along four edges).

- Allowing for longer HBE-to-web plate connection lengths. Because corner cutouts are not required to accommodate the additional strains associated with gap opening, the fish plate can be extended essentially to the end of the HBE[9] to increase the partial tension field area.

Due to the limited amount of experimental data on SPSWs or SC-SPSWs with web plates connected only to the HBEs, further experimental and numerical research should be done to further validate assumptions of partial tension field angle of inclination, distribution of web plate forces on the HBE, and web plate residual strength. Given the improved performance (with respect to web plate damage) exhibited in the SC-SPSW subassembly test with web plates connected only to the HBEs (W14-8s100k16GaHBE) and the results of the response history analyses for SC-SPSWs designed using this web plate connectivity, this method of attaching the web plate to the boundary frame seems to be promising for SC-SPSW applications.

9.7 Updated Performance-based Seismic Design Procedure

Below is a summary of the SC-SPSW performance-based seismic design (PBSD) procedure based on the one presented in Clayton [2010] with modifications and additions based on the findings presented in this document. Further details of the design procedure can be found in Clayton [2010] and as indicated below.

1. Determine the seismic loads and lateral load distribution. The load distribution should account for high-mode effects per Chao et al. [2007]. In the modified lateral load distribution presented in Chao et al. [2007], the story force at floor i can be calculated as:

$$F_i = C'_{vi} V \tag{9.6}$$

[9]There should still be a sufficient gap between the HBE fish plate and the column such that the fish plate along the bearing flange in the PT connection does not touch the column during rotation of the connection.

where,

$$C'_{vi} = (\beta_i - \beta_{i+1}) \left(\frac{w_n h_n}{\sum_{j=1}^{n} w_j h_j} \right)^{\alpha T^{-0.2}} \quad \text{when } i = n, \beta_{n+1} = 0 \tag{9.7}$$

$$\beta_i = \frac{V_i}{V_n} = \left(\frac{\sum_{j=1}^{n} w_j h_j}{w_n h_n} \right)^{\alpha T^{-0.2}} \tag{9.8}$$

where, β_i is the shear distribution factor at level i; V_i and V_n, respectively, are the story shear forces at level i and at the top (nth) level; w_j is the seismic weight at level j; h_j is the height of level j from the base; w_n is the weight at the top level; h_n is the height of roof level from the base; T is the fundamental period; F_i is the lateral force at level i; V is the total design base shear; and α is assumed to be 0.75 based empirically on the results of nonlinear dynamic analyses [Chao et al., 2007].

2. Design the web plates for the design-level story shear forces, V_{des}. The design story shear force, V_{des}, can be taken as the code-based design forces (i.e. design-level forces, $\frac{2}{3}$ MCE force, reduced by a response modification factor, R[10]). However, if the option performance objective of ensuring fully-elastic behavior at the 50/50 hazard level (PO2 in Clayton [2010]) is considered, V_{des} can be taken as the shear forces associated with the 50% in 50 year target spectral values.

   The nominal web plate strength for web plates connected to the HBEs and VBEs can be taken as (Eqn. (2.2)):

$$V_n = 0.42 F_y t_w L_{cf} \sin(2\alpha)$$

   where, F_y is the yield strength of the web plate, t_w is the web plate thickness, L_{cf} is the clear distance between VBEs, and α is the tension field angle of inclination found in Eqn. (2.1).

   The nominal web plate strength for web plates connected to the *HBEs only* can be

[10]The prototype buildings in this building were located in Los Angeles, where the 10/50 spectral acceleration is approximately equal to $\frac{2}{3}$ of the MCE or 2/50 spectral acceleration. For other locations where this relationship may not hold, the design force should be taken as $\frac{2}{3}$ MCE force to ensure that it meet code requirements; however, further research would be required to investigate buildings in different regions of seismicity to ensure that this design requirement results in adequate performance at the 10/50 and 2/50 seismic hazard levels.

taken as (Eqn (3.6)):

$$V_n = 0.42 F_y t_w L_{PTFA} \sin(2\theta)$$

where, L_{PTFA} is the length of the partial tension field found in Eqn. (3.2), and θ is the angle of inclination of the partial tension field found in Eqn. (3.1).

From these equations, the required t_w and F_y of the web plates can be determined such that $V_n > V_{des}$.

3. Determine the minimum initial PT forces in the HBE-to-VBE and column base connections ($T_{o,min}$ and $T_{o,col,min}$, respectively) to prevent connection decompression and column uplift under wind loads. The minimum initial PT forces in the HBE-to-VBE connections should also be designed to prevent connection decompression under gravity loads. The connection moment demands under gravity and/or wind loading can be determined using any preferred analytical or numerical method.

   For an assumed HBE depth, d, the connection decompression moment for the HBE-to-VBE PT connection can be taken as:

$$M_d = \frac{d}{2} T_o$$

   and for an assumed column depth, d_{col}, the decompression moment for the column base PT connection can be taken as:

$$M_{d,col} = \frac{d_{col}}{2} T_{o,col}$$

4. Design the PT connections to have sufficient stiffness to ensure a positive recentering stiffness, K_r, under the influence of P-Delta effects. The recentering stiffness is controlled by the PT post-decompression flexural stiffness. The HBE-to-VBE PT connection stiffness is most influenced by A_{PT}, L_{PT} (which is largely dictated by the bay size), and d (Eqn. (2.7)). Similarly, the PT column base connection stiffness is most influenced by $A_{PT,col}$, $L_{PT,col}$, and d_{col} (Eqn. (3.29)). Typically, the designer

would select the smallest member depth, d or d_{col}, that can reasonably accommodate the PT area (A_{PT} or $A_{PT,col}$) required to provide sufficient stiffness.

For mid- to high-rise SC-SPSWs, the recetering stiffness associated with the HBE-to-VBE PT connections at each floor level can be checked on a story-by-story basis with the following equation:

$$K_r = \frac{\Sigma k_d^\theta}{h^2} - \frac{P}{h} \geq 0$$

where, h is the story height, P is the portion of the p-delta load that must be resisted by the SC-SPSW at a particular story, and Σk_d^θ is the sum of the post-decompression rotational stiffnesses of the connections at a particular story and may be calculated using Eqn. (2.7). If PT column base connections are used, the system recentering stiffness including the PT column base connection contribution can be can be checked using methods discussed in Sec. 9.2.2.3.

5. Capacity design the horizontal PT and HBE to remain elastic and prevent in-span hinging up to 4% drift. This may require adjusting the beam depth or PT area, in which case you shoud reinterate Steps 3 and 4 above to verify satisfaction of both stiffness and strength criteria.

   The HBE axial force and moment demands for HBEs with fully-connected web plates are given in Eqns. (2.5) and (2.4), respectively; and the same demands are given for HBEs with web plates connected to the HBEs only in Eqns. (3.16), and (3.20), respectively. The HBE demands depend primarily on the distributed loads of the yielded web plates and the PT demands. The PT force demands are given in Eqn. (2.3) and depend largely on PT connection geometry and the specified connection rotation demand, which is typically approximated to be equal to the drift demand.

6. Capacity design the VBEs and the vertical PT elements to remain elastic up to 5% drift [Berman and Bruneau, 2008], or another appropriate target drift greater than that drifts expected during 10/50 events. This may require adjusting the column depth or column PT area or length, in which case you shoud reiterate Steps 3 and 4 above

to verify satisfaction of both stiffness and strength criteria. A summary of the VBE demands presented in Berman and Bruneau [2008] is given in Sec. 3.2.4. Methods for designing column PT to remain elastic under expected gap rotation demands and column uplift demands is provided in Sec. 9.2.2.2.

7. All connection regions should be detailed appropriately to transfer expected compressive forces through bearing flanges in the PT connections, to allow for PT rotation where required, and to adequately transfer shear and axial forces at all connections.

8. Check the design feasibility and iterate.

9.8 Summary of Design Recommendations

The preliminary performance-based seismic design (PBSD) procedure for the SC-SPSW was presented in Clayton [2010] and was summarized in Sec. 2.4.1.2. Design considerations that were developed or considered in this body of research were summarized to serve as an addendum to the design methodologies established in Clayton [2010]. In particular, the key design considerations that were presented in this chapter that were not addressed in Clayton [2010] include:

- Design of the PT column base and possible PT column base layouts and configurations.

- Web plate detailing, including the use of welded vs. bolted connection details and radial vs. diagonal corner cutouts.

- Diaphragm connection details that eliminate or mitigate the negative effects of PT frame expansion on the slab floor system.

- Motivation for and potential methodologies for reducing column sizes including adjusting the target drift for which columns are designed and connecting the web plates only to the beams.

To create a more cohesive body of work on SC-SPSWs, a summary of the SC-SPSW PBSD procedure including the additional considerations developed from this work was also provided.

Chapter 10
SUMMARY AND CONCLUSIONS

10.1 Summary

The purpose of this research was to expand upon the preliminary SC-SPSW proof-of-concept study presented in Clayton [2010] to better understand the behavior of the SC-SPSW system and its components. This research consisted of a parametric subassembly experimental program, a full-scale pseudo-dynamic test program, and a series of finite element analyses with various levels of computational complexity. This section presents a summary of each topic covered in this dissertation.

10.1.1 Subassembly testing

The SC-SPSW subassembly test program can be summarized as follows:

- An approximately half-scale, two-story, one-bay specimen was constructed to investigate SC-SPSW cyclic behavior and the demands on an intermediate HBE (i.e. an HBE with web plates above and below) mid-height up a building (i.e. not affected by restraint at the column base).

- Parameters were varied to investigate their effects of response and component demands. The parameters include: web plate thickness, t_w; number of PT strands, N_s; initial PT force, T_o; HBE depth, d; web plate connection detail (e.g. bolted and welded); and web plate connection configuration (e.g. connected to the boundary frame along all four edges and connected to the HBEs only).

- The test program used the same VBEs for all specimens and two sets of HBEs (one for each HBE depth investigated)

- The load protocol consisted of two or more cycles of loading up to drifts of 5%

Key results from the subassembly tests include:

- The subassembly specimens exhibited the desired flag-shaped hysteretic response, and in most cases had residual drifts less than 0.2% (the recentering criteria) upon unloading.

- Although web plate tearing in the bolted web plate connections was first observed at larger drift demands than the welded web plate connection, specimens with different web plate connection types exhibited similar strengths up to 2% drift.

- Web plate tearing (in both web plate connection types) was believed to be due largely to the out-of-plane deformation of the buckled web plate, particularly at the unrestrained edge of the corner cutout, where tear initiation was typically first observed.

- Connecting the web plates to the HBE only resulted in a reduced specimen strength (compared to web plates of the same thickness connected along all four edges) but also delayed and reduced the initiation and prorogation of web plate tearing.

- Thicker web plates resulted in an increase in specimen strength and energy dissipation. Specimens with thicker web plates also tended to have larger residual drifts due to the increase in the web plate residual strength.

- An increase in number of PT strands and HBE depth resulted in an increase of specimen recentering stiffness, K_r.

- An increase in the initial PT force, T_o, resulted in an increase in the specimen strength at connection decompression and recompression. Specimens with lower T_o also tended to have larger residual drifts.

- Experimentally determined axial force and moment distributions in the intermediate HBE matched well with those determined from theoretical free-body diagrams presented in Clayton [2010].

- Actual SC-SPSW behavior does differ from the idealized SC-SPSW behavior presented in Clayton [2010] largely due to the complex web plate behavior. Key differences from the assumed tension-only behavior include: non-negligible residual strength upon unloading (which appeared to be constant in the cyclic tests of increasing drift magnitude presented here) and tension reloading occurring prior to reaching the peak plastic strain from the previous cycles.

10.1.2 Full-scale testing

The full-scale test program can be summarized as follows:

- A full-scale two-story SC-SPSW was constructed with PT beam-to-column connections at the middle and top beams, and PT connections at the base of both columns.

- This specimen was part of the NEESR research project in collaboration with researchers at NCREE and University at Buffalo. Two full-scale specimens were tested as part of this project: one with PT connections that rock about the top and bottom flanges (as presented in this dissertation, for which the author was the primary researcher) and one with PT connections that rock only about the top flanges of the beams (for which Daniel Dowden from the University at Buffalo was the primary researcher).

- The specimen loading consisted of: elastic cyclic loading, pseudo-dynamic (PSD) free vibration testing at elastic demands, PSD excitation representing the 50/50, 10/50, and 2/50 seismic hazard levels (with no specimen repair or modification between tests), followed by quasi-static cycles at 4.5% drift.

- The excitation at each seismic hazard level was selected from the SAC Los Angeles ground motion ensemble to represent the median roof drift demands expected at each hazard level. The excitations used in the PSD tests were modifications of the selected SAC ground motions to reduce test duration and achieve target drift demands.

Key results from the full-scale testing include:

- The specimen was able to meet and exceed the intended performance objectives at the three seismic hazard levels, including: essentially elastic behavior at the 50/50 level; web plate yielding, system recentering, and drifts less than 2% at the 10/50 level; and minor localized yielding in the boundary frame and significant strength and energy dissipation in the presence of web plate tearing at the 2/50 level.

- During the free vibration following each PSD excitation, the magnitude of the residual web plate strength reduced as the drift amplitude of the oscillations decreased. This suggested that the residual web plate strength may be dependent on peak drift demands in previous cycles and may not have as much of an impact of recentering capabilities following an earthquake as suggested in the quasi-static cyclic subassembly tests.

- Web plate tearing was first observed around a magnitude of 1.5% drift during the 10/50 PSD test. The tears propagated more severely during the 2/50 PSD test, but the specimen maintained signfigant strength and energy dissipation porperties following the 2/50 test.

- This test represented a "worse-than-expected" loading scenario for the prototype SC-SPSW due to the following: the seismic mass attributed to the specimen was more than would be expected based on the current proposed design procedure (due to the method of determining the design base shear), the seismic mass for the specimen was lumped at the roof level (where the actuator was loading) instead of being distributed at each story, the response spectra of the ground excitations were larger than the target spectra at the respective hazard level, the specimen experienced no repair between earthquake simulations, and the specimen did not have any additional analytical damping to simulate damping that would be present in the actual building.

10.1.3 Numerical modeling approaches

Four numerical modeling approaches were proposed. Each employed a boundary frame model using beam-column elements and nonlinear springs to represent the rocking PT con-

nection behavior. The web plate models in order of increasing complexity were:

1. A tension-only strip model (Model TO) that is commonly used by practitioners

2. A tension-compression strip model (Model TC) that adds compressive resistance to the strips to approximate the web plate residual strength and could be easily incorporated into traditional models used in practice

3. A newly developed web plate strip model (Model WP) employed in OpenSees that simulates the complex loading, unloading, and reloading states of the web plate and is dependent upon load history

4. A shell model employed in ABAQUS that simulates the actual buckling and tension field action in the web plate

Each of these models were compared with experimental results. Key findings include:

- Model TO and Model TC underestimated the backbone strengths of the specimens as they only accounted for the monotonic strength of the web plate material and did not account for the additional strain hardening due to plastic contraction of the web plate under cyclic loading. Model WP, which was calibrated with experimental and numerical shell-based models, and the shell model were able to account for this additional strain hardening and better match the backbone strength of the experimental specimens.

- Model TO and TC were able to reasonably estimate the peak component demands and recentering stiffness to be used in design. Model TC was also able to estimate a lower-bound strength of the specimen upon unloading.

- Model WP and the shell model, while more computationally expensive, were able to better match the reloading response and energy dissipation of the specimens compared to Models TO and TC.

- The shell model did slightly overestimate the specimen strength in some cases. This may be due to the assumed pure isotropic hardening of the material or web plate slip that was not simulated.

10.1.4 Numerical investigation of building response

A numerical study was done to investigate the effects of connecting the web plates connectivity (i.e. connected to HBEs and VBEs vs. connected to HBEs only) and web plate residual strength (i.e. Model TO vs. Model TC) in SC-SPSW seismic response.

To assess the effects of web plate connectivity, 3- and 9-story SC-SPSWs with HBE-only web plates were designed to have the same strength as the fully-connected web plate SC-SPSWs presented in Clayton [2010]. These designs, although requiring thicker web plates, had HBE and VBE member sizes that were on the order of 10-20% and 17-32% lower than their fully-connected counterparts, respectively, indicating that connecting the web plates to the HBEs only offers some potential for improving economy (i.e. structural weight) of the system.

The fully-connected and HBE-only connected web plate SC-SPSWs were modeled in OpenSees using both the tension-only (Model TO) and tension-compression (Model TC) with different levels of compression. The results of these nonlinear response history analyses showed:

- Including web plate residual strength, even only small amounts, greatly reduces peak drift demands by as much as 50% for still conservative estimates (i.e. underestimations) of web plate residual strength and energy dissipation. This reduction in peak drift demands is largest in low-rise SC-SPSWs, which typically have larger peak drift demands than taller (e.g. nine-story) SC-SPSWs. Therefore, it is import to include web plate residual strength in nonlinear dynamic modeling of SC-SPSWs, even if the residual strength is conservatively approximated.

- SC-SPSWs with web plates connected to the HBEs only had larger peak drift demands than comparable fully-connected web plate designs. When modeled using tension-only

strips, the drifts, and associated boundary frame demands were excessive; however, when the web plate residual strength was considered (Model TC) the peak drift demands, residual drifts, and HBE and VBE interaction values were able to meet the proposed performance objectives.

- The reduction in drift demands associated with consideration of web plate residual strength suggest that SC-SPSWs with fully-connected web plates may be designed for smaller target drift demands without negatively impacting performance. The potential reduction in target design drifts will reduce boundary frame members; however, further research should be done to verify that the SC-SPSW can still meet proposed performance objectives with smaller column sizes for a broad range of SC-SPSWs. Additionally, the target design drift limits should not be reduced for the HBE-only web plate designs as they current target drifts correspond well to those observed in the 2/50 event when web plate residual strength is considered.

It should be noted that the SC-SPSWs investigated in this numerical study were assumed to be located in the Los Angeles area (where the 10/50 hazard level is approximately equal to the design-level, or $\frac{2}{3}$MCE). The seismic hazards at this location, where earthquakes occur relatively frequently, may differ significantly from a location such as Seattle, where very large earthquakes can occur but with a much longer return period. Further research is required to assess the performance of SC-SPSWs designed using the current design procedure for areas of different seismicity, such as Seattle, Boston, or near-fault locations.

10.1.5 Design recommendations

The following SC-SPSW design-related recommendations were presented:

- Design equations, configurations, and procedures for the PT column base connection that are meant to be an addendum to the SC-SPSW mechanics and design methodologies presented in Clayton [2010].

- Considerations in web plate detailing including web plate cutouts, web plate-to-fish plate connection details, and web plate-to-boundary frame connection configurations.

- Possible diaphragm connection details that can accommodate or eliminate the effects of PT frame expansion.

- Motivation and potential methods for reducing column sizes in SC-SPSWs.

10.2 Conclusions

The research further validated the SC-SPSW as a viable lateral force-resisting system to provide enhanced performance in seismic events. Experimental programs at the subassembly and full-scale system levels verified the constructability, recentering capabilities, strength, and energy dissipating properties of the system. These experimental studies can inform designers of best-practices for construction and detailing, and also inform future research aimed at further improving the system's performance and economy.

Data from these experiments were compared to and were used to validate various numerical models of varying complexity. The numerical models were able to adequately capture key design parameters such as strength, component demands, and recentering stiffness. Models of increasing complexity had increasing accuracy in capturing the complex unloading and reloading behavior of the SC-SPSW web plate. This information may be used to inform designers of the benefits of various modeling approaches to be used in different numerical analysis applications.

The validated numerical models were also used to investigate the impact of web plate residual strength and using fully-connected vs. HBE-only connected web plates on SC-SPSW response. These results showed that using even a simple tension-compression model to simulate web plate residual strength significantly decreases peak drift demands compared with the traditional tension-only web plate material model. Additionally, these analyses showed that SC-SPSWs with HBE-only connected web plates have higher peak drift demands than comparable SC-SPSWs with fully-connected web plates. When web plate residual strength is considered in the numerical model, all SC-SPSWs investigated (HBE-only and fully-connected web plate designs) were able to meet the proposed performance objectives. The seismic performance of SC-SPSWs with fully-connected web plates also suggest that the current design procedure may be be overly conservative. The information

resulting from this numerical study may be used to inform designers of the anticipated performance of the system and investigate potential methods for improving SC-SPSW performance or efficiency.

Recommendations were also provided to inform designers of additional aspects of SC-SPSW design that must be considered for proper implementation and performance. Although these recommendations were based on findings made in this research, many of the recommendations serve only as that, and not as hard rules to be followed in design. Much of the SC-SPSW design and detailing is largely dependent on the SC-SPSW layout in the building (e.g. how it is connected to the floor slab, how it is connected to the foundation, etc.); therefore, the designer should fully understand the system mechanics and behavior presented here and in Clayton [2010] to inform proper building system design and detailing.

REFERENCES

SAP2000 Version 14.1.0 [Computer Software].

ABAQUS, *ABAQUS version 6.10 documentation*, Simulia, 2010.

AISC, *Specification for Structural Steel Buildings, ANSI/AISC 360-05*, American Institute of Steel Construction, Chicago, IL, 2005.

——, *Seismic Provisions for Structural Steel Buildings, ANSI/AISC 341-05*, American Institute of Steel Construction, Chicago, IL, 2005.

R. G. and Driver, G. L. Kulak, D. J. L. Kennedy, and A. E. Elwi, "Cyclic test of four-story steel plate shear wall," *Journal of Structural Engineering*, vol. 124, no. 2, pp. 112–120, February 1998.

ASCE, *Minimum Design Loads for Buildings and Other Structures*, A. S. of Civil Engineers, Ed. Reston, VA: ASCE/SEI 7-05, 2005.

ATC, "Guidelines for seismic testing of components of steel structures," Applied Technology Council, Redwood City, CA, Tech. Rep. 24, 1992.

——, "Guidelines for seismic performance assessment of buildings: ATC-58 50% draft," Applied Technology Council, Washington, D.C., Tech. Rep., 2009.

N. Baldvins, J. W. Berman, L. N. Lowes, and T. Janes, "Development of damage prediction models for steel plate shear walls," *Earthquake Spectra*, 2010, (submitted).

K. Basler, "Strength of plate girders in shear," Lehigh University, Fritz Laboratory, Bethlehem, Pennsylvania, Fritz Laboratory Report 251-20, 1961.

J. W. Berman and M. Bruneau, "Experimental investigation of light-gauge steel plate shear walls for the seismic retrofit of buildings," Multidisciplinary Center for Earthquake Engineering Research, Buffalo, New York, Technical Report MCEER-03-0001, 2003.

——, "Capacity design of vertical boundary elements in steel plate shear walls," *Engineering Journal*, vol. 45, no. 1, pp. 57–71, First Quarter 2008.

——, "Experimental investigation of light-gauge steel plate shear walls," *Journal of Structural Engineering*, vol. 131, no. 2, pp. 259–267, February 2005.

V. Caccese, M. Elgaaly, and R. Chen, "Experimental study of thin steel-plate shear walls under cyclic load," *Journal of Structural Engineering*, vol. 119, no. 2, pp. 573–587, February 1993.

Canadian Standards Association , *Limit states design of steel structures*, CAN/CSA S16-01, Willowdale, Ontario, Canada, 2001.

S.-H. Chao, S. C. Goel, and S.-S. Lee, "A seismic design lateral force distribution based on inelastic state of structures," *Earthquake Spectra*, vol. 23, no. 3, pp. 547–569, August 2007.

H. Chi, "Development of post-tensioned column base connection for self-centering seismic resistant steel frame," Ph.D. dissertation, School of Civil Engineering, Purdue University, West Lafayette, IN, 2009.

H. Chi, J. Liu, and M. Garlock, "Design and analytical validation of post-tensioned column bases," in *Proceedings of the 2008 Structures Congress—Structures Congress 2008: Crossing the Borders*, vol. 314, Vancouver, BC, Canada, April 2008.

I.-R. Choi and H.-G. Park, "Hysteresis model of thin infill plate for cyclic nonlinear analysis of steel plate shear walls," *Journal of Structural Engineering*, vol. 136, no. 11, pp. 1423–1434, November 2010.

A. K. Chopra, *Earthquake Dynamics of Structures: Theory and Applications to Earthquake Engineering*, 3rd ed. Prentice Hall, 2007.

C.-C. Chou and J.-H. Chen, "Analytical model validation and influence of column bases for seismic responses of steel post-tensioned self-centering mrf systems," *Engineering Structures*, vol. 33, pp. 2628–2643, June 2011.

——, "Seismic design and shake table tests of a steel post-tensioned self-centering moment frame with a slab accommodating frame expansion," *Earthquake Engineering and Structural Dynamics*, vol. 40, pp. 1240–1261, 2011.

——, "Development of floor slab for steel post-tensioned self-centering moment frames," *Journal of Constructional Steel Research*, vol. 67, pp. 1621–1635, 2011.

C.-C. Chou, J.-H. Chen, Y.-C. Chen, and K.-C. Tsai, "Evaluating performance of post-tensioned steel connections with strands and reduced flange plates," *Earthquake Engineering and Structural Dynamics*, vol. 35, pp. 1167–1185, 2006.

C. Christopoulos, R. Tremblay, H.-J. Kim, and M. Lacerte, "Self-centering energy dissipative bracing system for the seismic reistance of structures: development and validation," *Journaml of Structural Engineering*, vol. 134, pp. 96–107, January 2008.

C. Christopoulos, A. Filiatrault, and B. Folz, "Seismic response of self-centring hysteretic sdof systems," *Earthquake Engineering and Structural Dynamics*, vol. 31, pp. 1131–1150, 2002.

C. Christopoulos, A. Filiatrault, C.-M. Uang, and B. Folz, "Posttensioned energy dissipating connections for moment-resisting steel frames," *Journal of Structural Engineering*, vol. 128, no. 9, pp. 1111–1120, September 2002.

P. M. Clayton, "Self-centering steel plate shear walls: Development of design procedure and evaluation of seismic performance," Master's thesis, Civil and Environmental Engineering Dept., University of Washington, Seattle, WA, 2010.

P. M. Clayton, J. W. Berman, and L. N. Lowes, "Seismic design and performance of self-centering steel plate shear walls," *Journal of Structural Engineering*, vol. 138, pp. 22–30, 2012.

P. M. Clayton, D. M. Dowden, T. B. Winkley, J. W. Berman, M. Bruneau, and L. N. Lowes, "Experimental investigation of self-centering steel plate shear," in *Proceedings of the 2012 Structures Congress*, vol. 318, Chicago, IL, March 2012.

P. M. Clayton, T. B. Winkely, J. W. Berman, and L. N. Lowes, "Experimental investigation of self-centering steel plate shear walls," *Journal of Structural Engineering*, vol. 138, pp. 952–960, July 2012.

D. Dowden, "Resilient self-centering steel plate shear walls," Ph.D. Dissertation, Dept. of Civil, Structural and Environmental Engineering, University at Buffalo, Buffalo, NY, 2014.

D. M. Dowden and M. Bruneau, "NewZ-BREAKSS: Post-tensioned rocking connection detail free of beam growth," *AISC Engineering Journal*, pp. 153–158, Second Quarter 2011.

D. M. Dowden, R. Purba, and M. Bruneau, "Behavior of self-centering steel plate shear walls and design considerations," *Journal of Structural Engineering*, vol. 138, pp. 11–21, January 2012.

M. Eatherton, J. Hajjar, G. Deierlein, H. Krawinkler, S. Billington, and X. Ma, "Controlled rocking of steel-framed buildings with replaceable energy-dissipating fuses," in *Proceedings of the 14th World Conference on Earthquake Engineering*, Beijing, China, October 2008.

M. Eatherton and J. Hajaar, "Large-scale cyclic and hybrid simulation testing and development of a controlled-rocking steel building system with replaceable fuses," Newmark Structural Engineering Laboratory Report Series, University of Illinois at Urbana-Champaign, Urbana, Illinois, Report Report No. NSEL-025, 2010.

M. Elgaaly, V. Caccese, and C. Du, "Postbuckling behavior of steel-plate shear walls under cyclic loads," *Journal of Structural Engineering*, vol. 119, no. 2, pp. 588–605, February 1993.

FEMA, "Recommended seismic design criteria for new steel moment-frame buildings," SAC Joint Venture for the Federal Emergency Management Agency, Washington, D.C., Tech. Rep. 350, 2000.

——, "State of the art report on systems performance of steel moment frames subject to

earthquake ground shaking," Helmut Krawinkler, Team Leader, SAC Joint Venture for the Federal Emergency Management Agency, Washington, D.C., Tech. Rep. 355c, 2000.

——, "FEMA P-695 quantification of building seismic performance factors," Applied Technology Council for the Federal Emergency Management Agency, Washington, D.C., Tech. Rep. P-695, 2009.

——, "1994 Edition: NEHRP recommended provisions for seismic regulations for new buildings and other structure," Building Seismic Safety Council for the Federal Emergency Management Agency, Washington, D.C., Tech. Rep. 222A, 1994.

M. M. Garlock, R. Sause, and J. M. Ricles, "Behavior and design of posttensioned steel frame systems," *Journal of Structural Engineering*, vol. 133, no. 3, pp. 389–399, March 2007.

M. Garlock, "Design, analysis, and experimental behavior of seismic resistant post-tensioned steel moment resisting frames," Ph.D. dissertation, Civil and Environmental Engineering Dept., Lehigh University, Bethlehem, PA, 2002.

M. E. M. Garlock and J. Li, "Steel self-centering moment frames with collector beam floor diaphragms," *Journal of Constructional Steel Research*, vol. 64, pp. 526–538, 2007.

L. Guo, Q. Rong, X. Ma, and S. Zhang, "Behavior of steel plate shear wall connected to frame beams only," *International Journal of Steel Structures*, vol. 11, no. 4, pp. 467–479, 2011.

A. Gupta and H. Krawinkler, "Seismic demands for performance evaluation of steel moment resisting frame structures," John A. Blume Earthquake Engineering Center, Stanford University, Stanford, CA, Tech. Rep. 132, 1999.

P.-H. Hsiao, D. E. Lehman, C. W. Roeder, and P.-C. Chen, "Evaluation of the response modification coefficient and collapse potential of special concentrically braced frames," *Earthquake Engineering and Structural Dynamics*, 2013.

J. Iyama, C.-Y. Seo, J. Ricles, and R. Sause, "Self-centering mrfs with bottom flange friction devices under earthquake loading," *Journal of Constructional Steel Research*, vol. 65, pp. 314–325, 2009.

H.-J. Kim and C. Christopoulos, "Seismic design procedure and seismic response of post-tensioned self-centering steel frames," *Earthquake Engineering and Structural Dynamics*, vol. 38, pp. 355–376, 2008.

N. Kristeva, "Trimming the fat," *AISC Modern Steel Construction*, 2010.

G. L. Kulak, D. J. L. Kennedy, and R. G. Driver, "Discussion of 'Experimental study of thin steel-plate shear walls under cyclic load' by V. Caccese, M. Elgaaly and R. Chen," *Journal of Structural Engineering*, vol. 120, no. 10, pp. 3072–3073, October 1994.

H.-C. Lee, "A study of capacity design for vertical boundary elements in steel plate shear walls," Master's thesis, Department of Civil Engineering, National Taiwan University, Taipei, Taiwan, 2011.

C.-H. Li, K.-C. Tsai, C.-H. Lin, and P.-C. Chen, "Cyclic tests of four two-story narrow steel plate shear walls. part 2: Experimental results and design implications," *Earthquake Engineering and Structural Dynamics*, vol. 39, pp. 801–826, 2010.

C.-H. Li, H.-C. Lee, K.-C. Tsai, and C.-H. Lin, "Experimental investigations on seismic behavior and design of bottom boundary column in steel plate shear walls," in *Proceedings of the 15th World Conference on Earthquake Engineering*, Lisbon, Portugal, September 2012.

C.-H. Lin, K.-C. Tsai, B. Qu, and M. Bruneau, "Sub-structural pseudo-dynamic performance of two full-scale two-story steel plate shear walls," *Journal of Constructional Steel Research*, vol. 66, pp. 1467–1482, 2010.

Y.-C. Lin. (2012, October) NEES project warehouse: Self-centering damage-free seismic-resistant steel frame systems. [Online]. Available: http://nees.org/warehouse/project/77

Y.-C. Lin, J. Ricles, and R. Sause, "Earthquake simulations on a self-centering steel moment resisting frame with web plate friction devices," in *Proceedings of the 14th World Conference on Earthquake Engineering*, Beijing, China, October 2008.

A. Lubell, H. Prion, C. Ventura, and M. Rezai, "Unstiffened steel plate shear wall performance under cyclic loading," *Journal of Structural Engineering*, vol. 126, no. 4, pp. 453–460, April 2000.

J. Lui and A. Astaneh-Asl, "oment-rotation parameters for composite shear tab connections," *Journal of Structural Engineering*, vol. 130, no. 9, pp. 1371–1380, 2004.

S. Mazzoni, F. McKenna, M. Scott, and G. Fenves, *Open System for Earthquake Engineering Simulation User Command-Language Manual - OpenSees Version 2.0*, Pacific Earthquake Engineering Research Center, University of California, Berkeley, Berkeley, CA, 2009.

The Three-Wire Quarter-Bridge Circuit, Micro-Measurements, Vishay Precision Group, November 2010.

A. B. Monnier and A. P. Harasimowicz, "Shear strength," *AISC Modern Steel Construction*, 2007.

S. D. Nakaki, J. F. Stanton, and S. Sritharan, "An overview of the PRESSS five-story precast test building," *PCI Journal*, vol. 44, no. 2, pp. 26–39, 1999.

N. M. Newmark, "A method of computation for structural dynamics," *Journal of Engineering Mechanics*, vol. 85, no. EM3, pp. 67–94, 1959.

R. Pordes *et al.*, "The open science grid," in *J. Phys. Conf. Ser. 78*, 2007, p. 012057.

V. Prakash, G. Powell, and S. Campbell, *DRAIN-2DX base program description and user guide, Version 1.0*, Structural Engineering Mechanics and Materials, University of California, Berkeley, Berkeley, CA, 1993.

M. J. N. Priestly, "An overview of PRESSS research program," *PCI Journal*, vol. 36, no. 4, pp. 50–57, 1991.

R. Purba and M. Bruneau, "Impact of horizontal boundary elements design on seismic behavior of steel plate shear walls," Multidisciplinary Center for Earthquake Engineering Research, Buffalo, New York, Technical Report MCEER-10-0007, 2010.

B. Qu and M. Bruneau, "Design of steel plate shear walls considering boundary frame moment resisting action," *Journal of Structural Engineering*, vol. 135, no. 12, pp. 1511–1521, December 2009.

B. Qu, M. Bruneau, C.-H. Lin, and K.-C. Tsai, "Testing of full-scale two-story steel plate shear wall with reduced beam section connections and composite floors," *Journal of Structural Engineering*, vol. 134, no. 3, pp. 364–373, March 2008.

J. M. Ricles, R. Sause, and M. M. Garlock, "Experimental studies of full-scale posttensioned steel connections," *Journal of Structural Engineering*, vol. 131, no. 3, pp. 113–121, February 2001.

K. Robinson and D. Ames, "Library seismic upgrade," *AISC Modern Steel Construction*, 2000.

P. Rojas, "Seismic analysis, design, and evaluation of posttensioned friction damped connections for steel moment resisting frames," Ph.D. dissertation, Civil and Environmental Engineering Dept., Lehigh University, Bethlehem, PA, 2003.

P. Rojas, J. M. Ricles, and R. Sause, "Seismic performance of post-tensioned steel moment resisting frames with friction devices," *Journal of Structural Engineering*, vol. 131, no. 4, pp. 529–540, April 2005.

R. Sabelli and M. Bruneau, *Design Guide 20: Steel Plate Shear Walls*, American Institute of Steel Construction, Chicago, IL, 2007.

A. Schumacher, G. Y. Grodin, and G. L. Kulak, "Connection of infill panels in steel plate shear walls," Dept. of Civil Engineering, University of Alberta, Edmonton, Alberta, Canada, Structual Engineering Report 217, 1997.

I. F. Seilie and J. D. Hooper, "Steel plate shear walls: Practical design and construction," *AISC Modern Steel Construction*, 2005.

J. J. Shishkin, R. G. Driver, and G. Y. Grodin, "Analysis of steel plate shear walls using the modified strip model," Dept. of Civil Engineering, University of Alberta, Edmonton, Alberta, Canada, Structual Engineering Report 261, 2005.

P. Somerville, N. Smith, S. Punyamurthula, , and J. Sun, "Development of ground motion time histories for phase 2 of the FEMA/SAC steel project," SAC Background Document, Tech. Rep. SAC/BD-97/04, 1997.

J. F. Stanton and S. D. Nakaki, "Design guidelines for precast concrete seismic structural systems," Seattle, Washington, Tech. Rep. PRESSS Report No. 01/03-09, UW Report No. SM 02-02, February 2002.

J. F. Stanton, W. C. Stone, and G. S. Cheok, "A hybrid reinforced precast frame for seismic regions," *PCI Journal*, vol. 42, no. 2, pp. 20–32, March–April 1997.

L. J. Thorburn, G. L. Kulak, and C. J. Montgomery, "Analysis of steel plate shear walls," Dept. of Civil Engineering, University of Alberta, Edmonton, Alberta, Canada, Structual Engineering Report 107, 1983.

P. A. Timler and G. L. Kulak, "Experimental study of steel plate shear walls," Dept. of Civil Engineering, University of Alberta, Edmonton, Alberta, Canada, Structual Engineering Report 114, 1983.

E. W. Tromposch and G. L. Kulak, "Cyclic and static behaviour of thin panel steel plate shear walls," Dept. of Civil Engineering, University of Alberta, Edmonton, Alberta, Canada, Structual Engineering Report 145, 1987.

K.-C. Tsai, C.-H. Li, C.-H. Lin, C.-Y. Tsai, and Y.-J. Yu, "Cyclic tests of four two-story narrow steel plate shear walls. part 1: Analytical studies and specimen design," *Earthquake Engineering and Structural Dynamics*, vol. 39, pp. 775–799, 2010.

K.-C. Tsai, C.-C. Chou, C.-L. Lin, P.-C. Chen, and S.-J. Jhang, "Seismic self-centering steel beam-to-column moment connections using bolted friction devices," *Earthquake Engineering and Structural Dynamics*, vol. 37, pp. 627–645, 2008.

C. Vatansever and N. Yardimci, "Experimental investigation of thin steel plate shear walls with different infill-to-boundary frame connections," *Steel and Composite Structures*, vol. 11, no. 3, pp. 251–271, 2011.

D. Vian, M. Bruneau, K. C. Tsai, and Y.-C. Lin, "Special perforated steel plate shear walls with reduced beam section anchor beams. I: Experimental investigation," *Journal of Structural Engineering*, vol. 135, no. 3, pp. 211–220, March 2009.

——, "Special perforated steel plate shear walls with reduced beam section anchor beams. II: Analysis and design recommendations," *Journal of Structural Engineering*, vol. 135, no. 3, pp. 221–228, March 2009.

D. Webster, "The behavior of un-stiffened steel plate shear wall web plates and their impact on the vertical boundary elements," Ph.D. Dissertation, Civil and Environmental Engineering Dept., University of Washington, Seattle, WA, 2013.

——, "The behavior of un-stiffened steel plate shear wall web plates and their impact on the vertical boundary elements," Ph.D. General Exam, Civil and Environmental Engineering Dept., University of Washington, Seattle, WA, 2012.

T. B. Winkley, "Self-centering steel plate shear walls: Large scale experimental investigation," Master's thesis, Civil and Environmental Engineering Dept., University of Washington, Seattle, WA, 2011.

M. Wolski, J. M. Ricles, and R. Sause, "Experimental study of a self-centering beamcolumn connection with bottom flange friction device," *Journal of Structural Engineering*, vol. 135, no. 5, pp. 479–488, May 2009.

M. Xue and L. W. Lu, "Interaction of infilled steel shear wall panels with surrounding frame members," in *Proceedings of the Structural Stability Research Council Annual Technical Session*, Bethlehem, PA, 1994, pp. 339–354.

Appendix A

ADDITIONAL FIGURES FOR FULL-SCALE TEST SPECIMEN AND INSTRUMENTATION

A.1 Fabrication Drawings

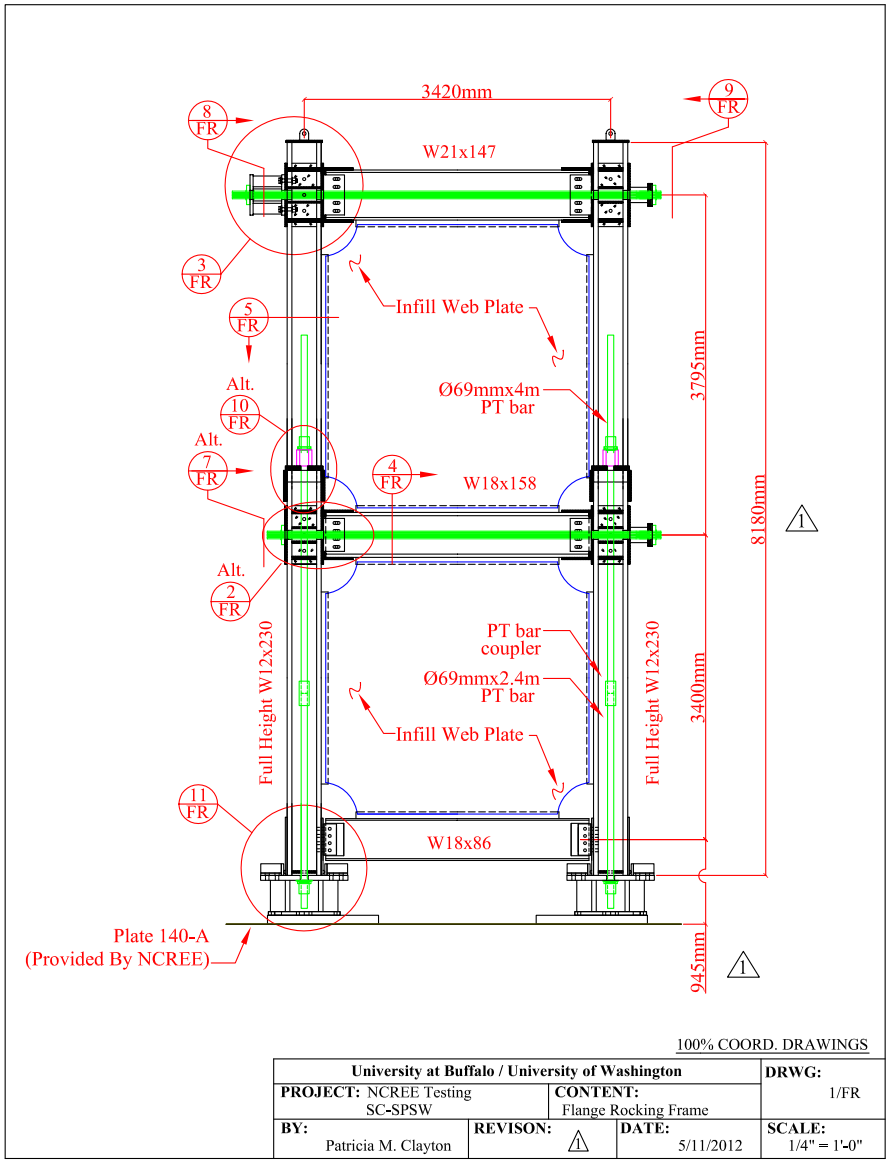

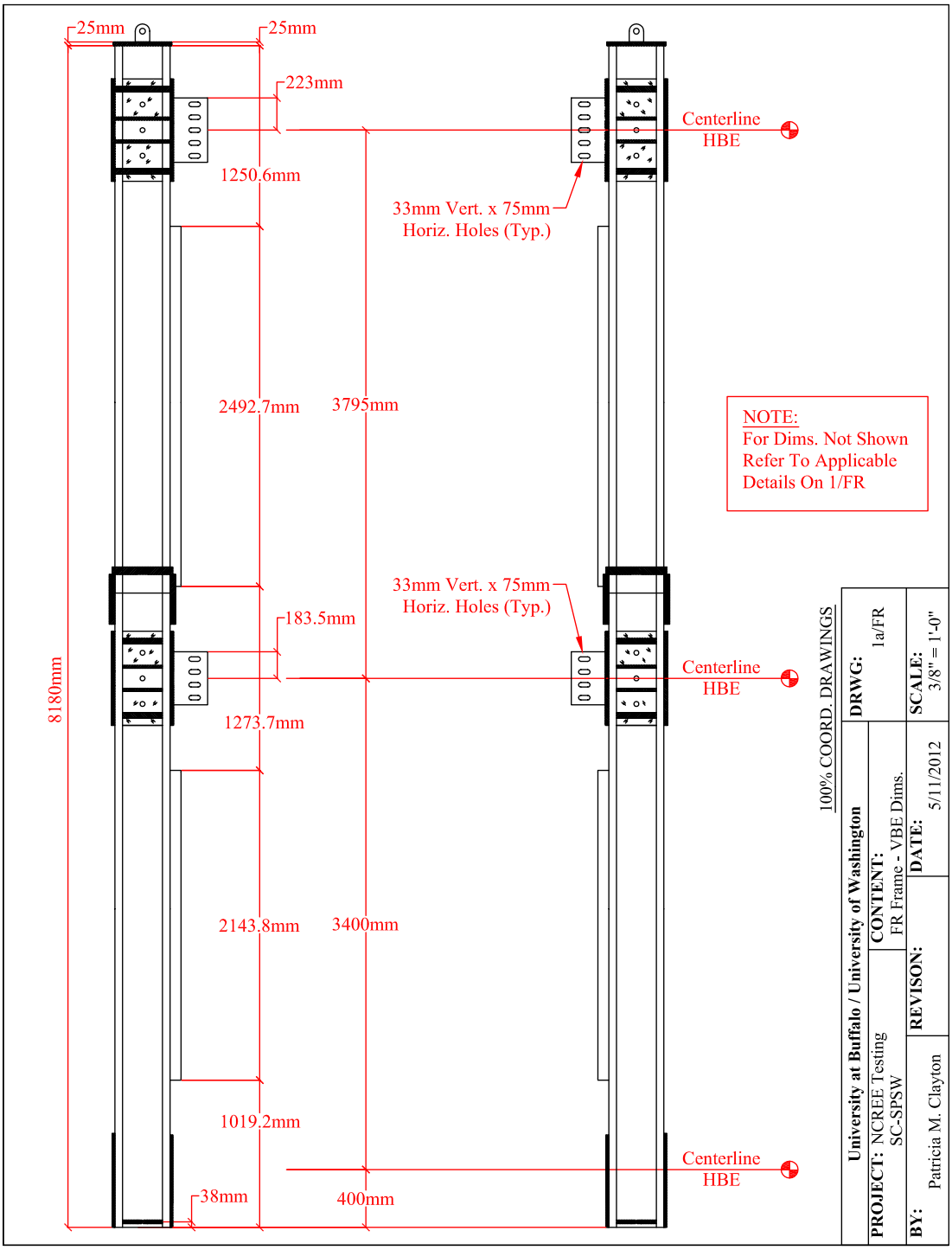
25mm
25mm
223mm
Centerline
HBE
1250.6mm
33mm Vert. x 75mm
Horiz. Holes (Typ.)
2492.7mm
3795mm
NOTE:
For Dims. Not Shown
Refer To Applicable
Details On 1/FR
33mm Vert. x 75mm
Horiz. Holes (Typ.)
183.5mm
8180mm
Centerline
HBE
1273.7mm
2143.8mm
3400mm
1019.2mm
Centerline
HBE
38mm
400mm
100% COORD. DRAWINGS
University at Buffalo / University of Washington
DRWG: 1a/FR
PROJECT: NCREE Testing
SC-SPSW
CONTENT:
FR Frame - VBE Dims.
SCALE: 3/8" = 1'-0"
BY: Patricia M. Clayton
REVISON:
DATE: 5/11/2012

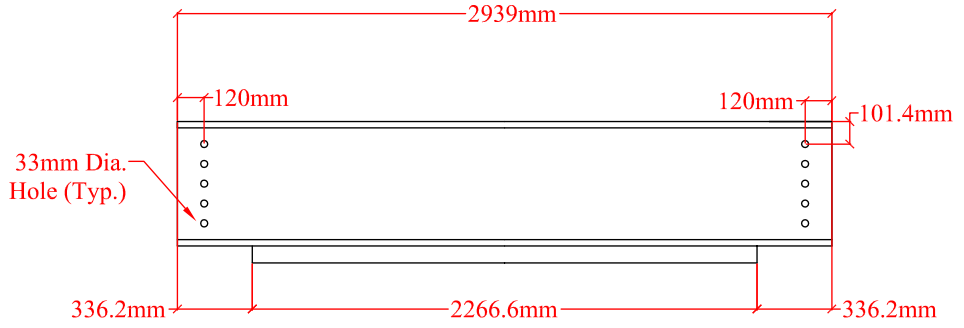

FR Frame - Level 2 HBE - W21x47

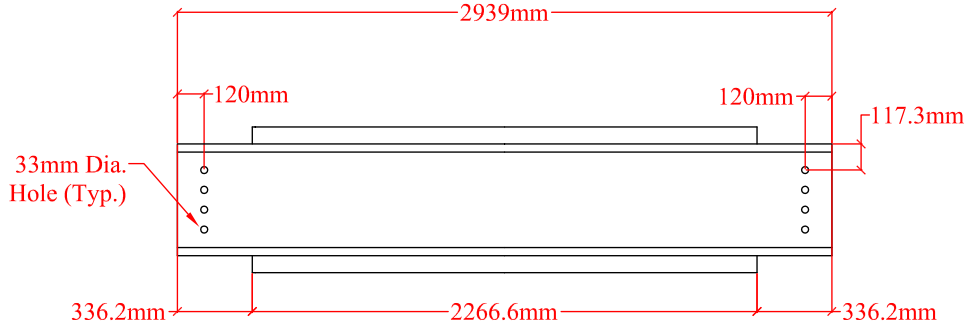

FR Frame - Level 1 HBE - W18x158

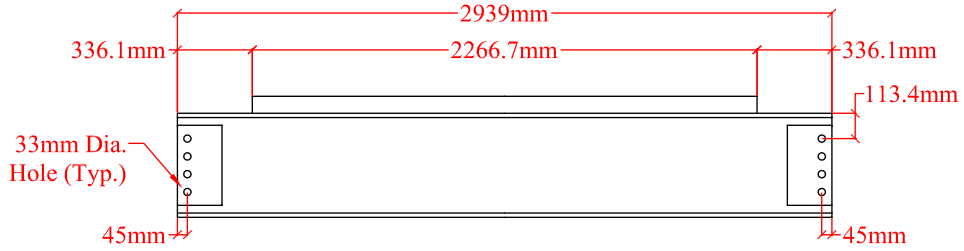

FR Frame - Level 0 HBE - W18x86

NOTES:

1) For Dims. Not Shown Refer To Applicable Details On 1/FR

2) Flange Reinforcement Plate Not Shown For Clarity

100% COORD. DRAWINGS

University at Buffalo / University of Washington			DRWG:
PROJECT: NCREE Testing SC-SPSW	CONTENT: FR Frame - HBE Dims.		1b/FR
BY: Patricia M. Clayton	REVISON:	DATE: 5/11/2012	SCALE: 1/2" = 1'-0"

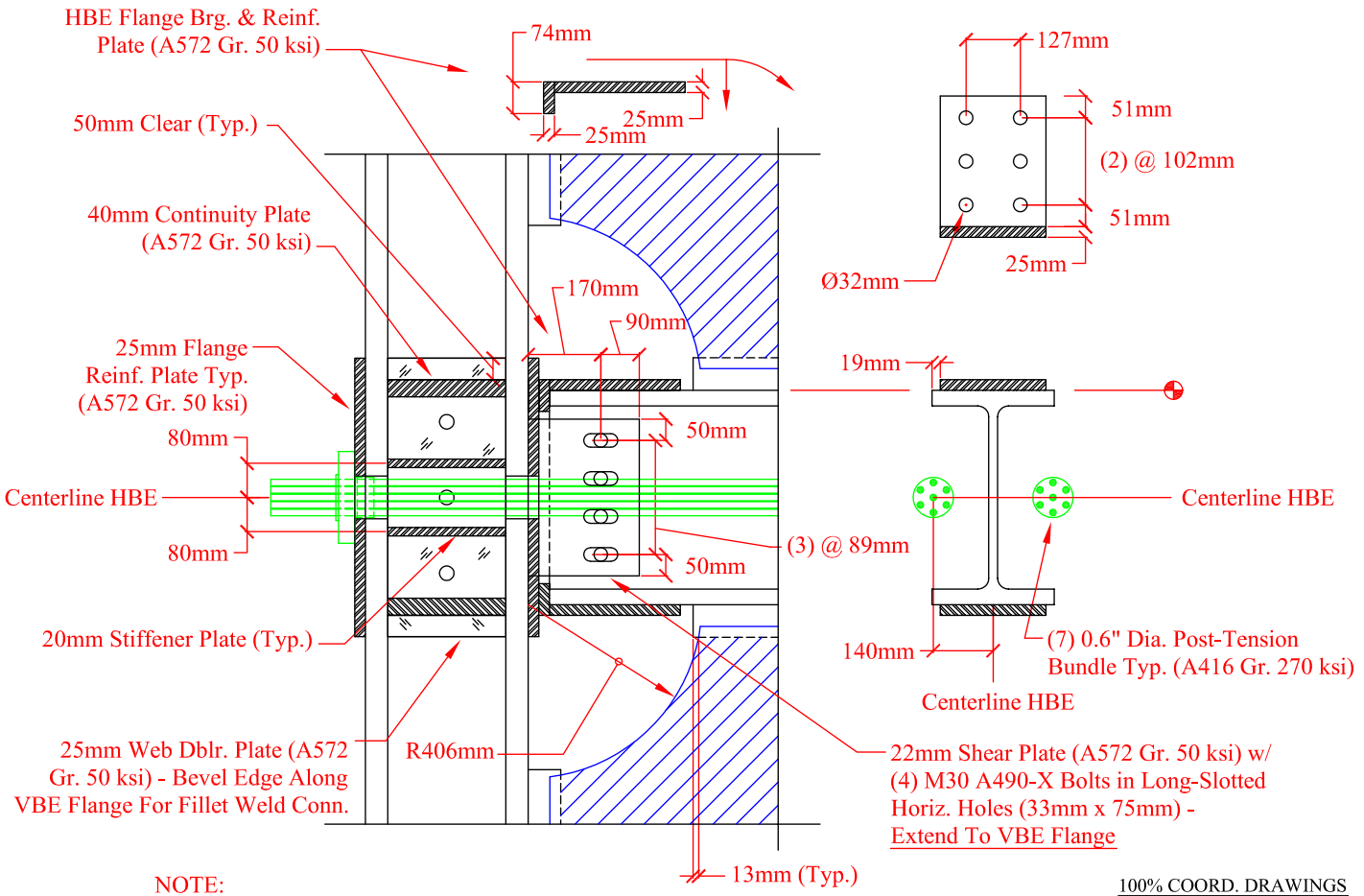

NOTE:
For Weld Details See 2a Alt/FR

100% COORD. DRAWINGS

University at Buffalo / University at Washington			DRWG:
PROJECT: NCREE Testing SC-SPSW	CONTENT: Flange Rocking Joint Detail		2Alt/FR
BY: Patricia M. Clayton	REVISON:	DATE: 5/11/2012	SCALE: 1" = 1'-0"

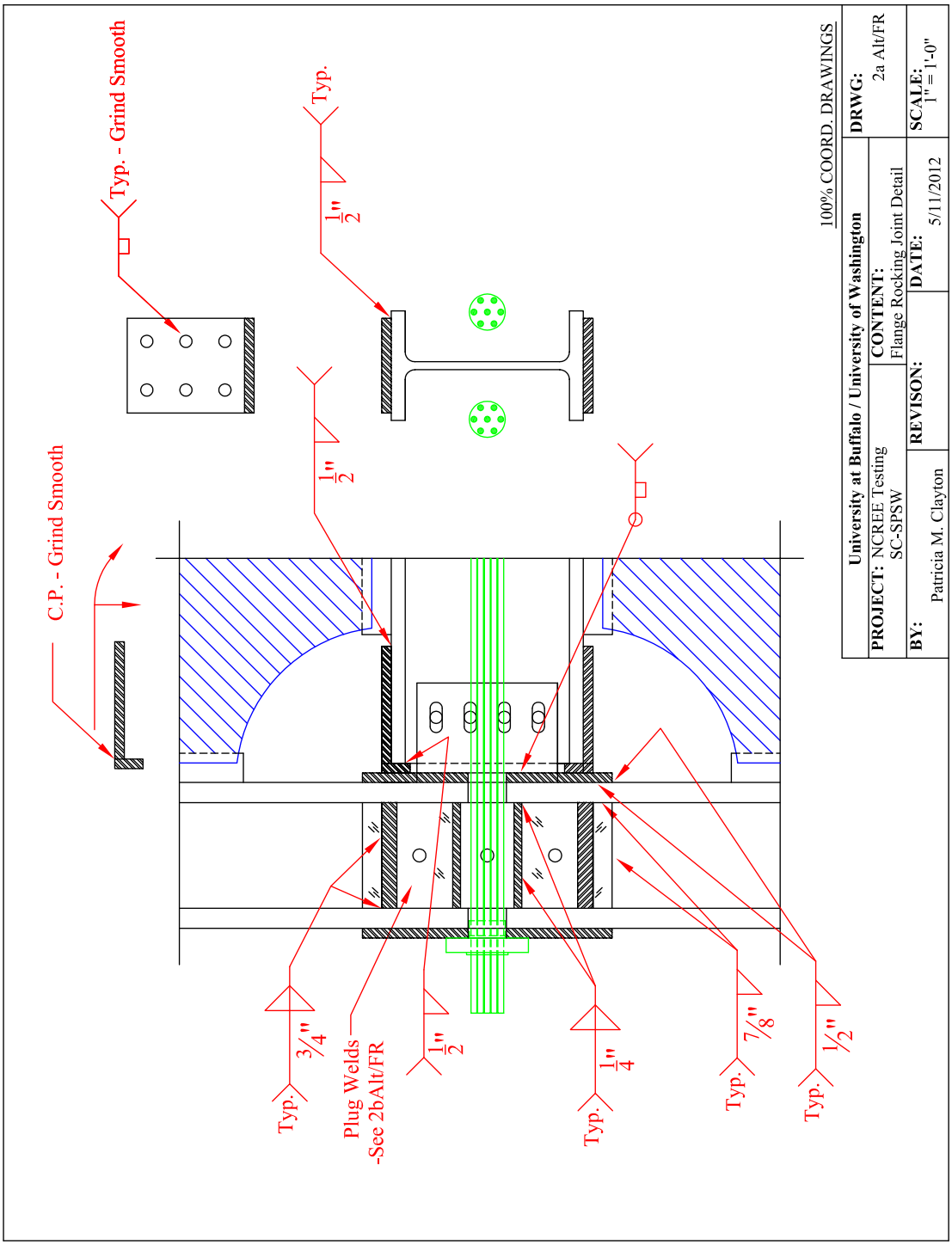
C.P. - Grind Smooth
Typ. - Grind Smooth
Typ.
1/2"
1/2"
Typ.
3/4"
Plug Welds
-See 2bAlt/FR
1/2"
Typ.
1/4"
Typ.
7/8"
Typ.
1/2"
100% COORD. DRAWINGS
University at Buffalo / University of Washington
DRWG: 2a Alt/FR
PROJECT: NCREE Testing SC-SPSW
CONTENT: Flange Rocking Joint Detail
BY: Patricia M. Clayton
REVISON:
DATE: 5/11/2012
SCALE: 1"= 1'-0"

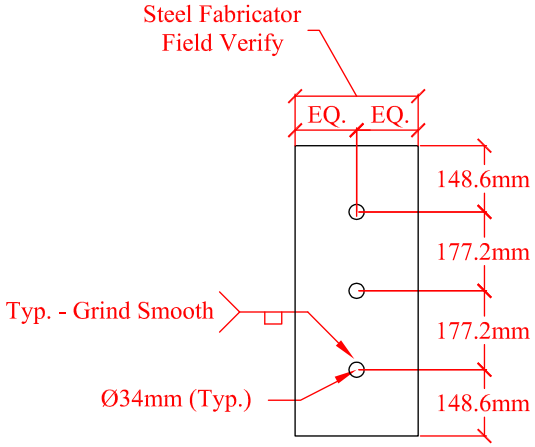

VBE Web Dblr at W18x158

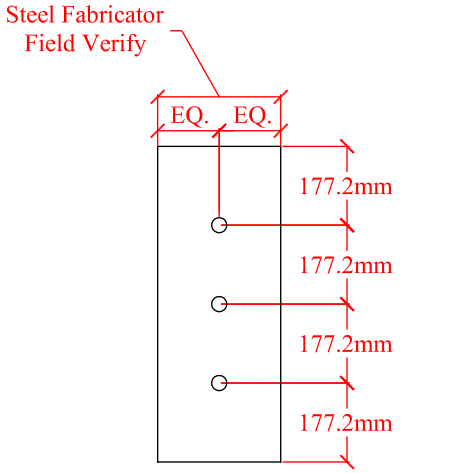

VBE Web Dblr at W21x147 (Both Ends)

100% COORD. DRAWINGS

University at Buffalo / University of Washington			DRWG:
PROJECT: NCREE Testing SC-SPSW	CONTENT: Flange Rocking Joint Detail		2b Alt/FR
BY: Patricia M. Clayton	REVISON:	DATE: 5/11/2012	SCALE: 1" = 1'-0"

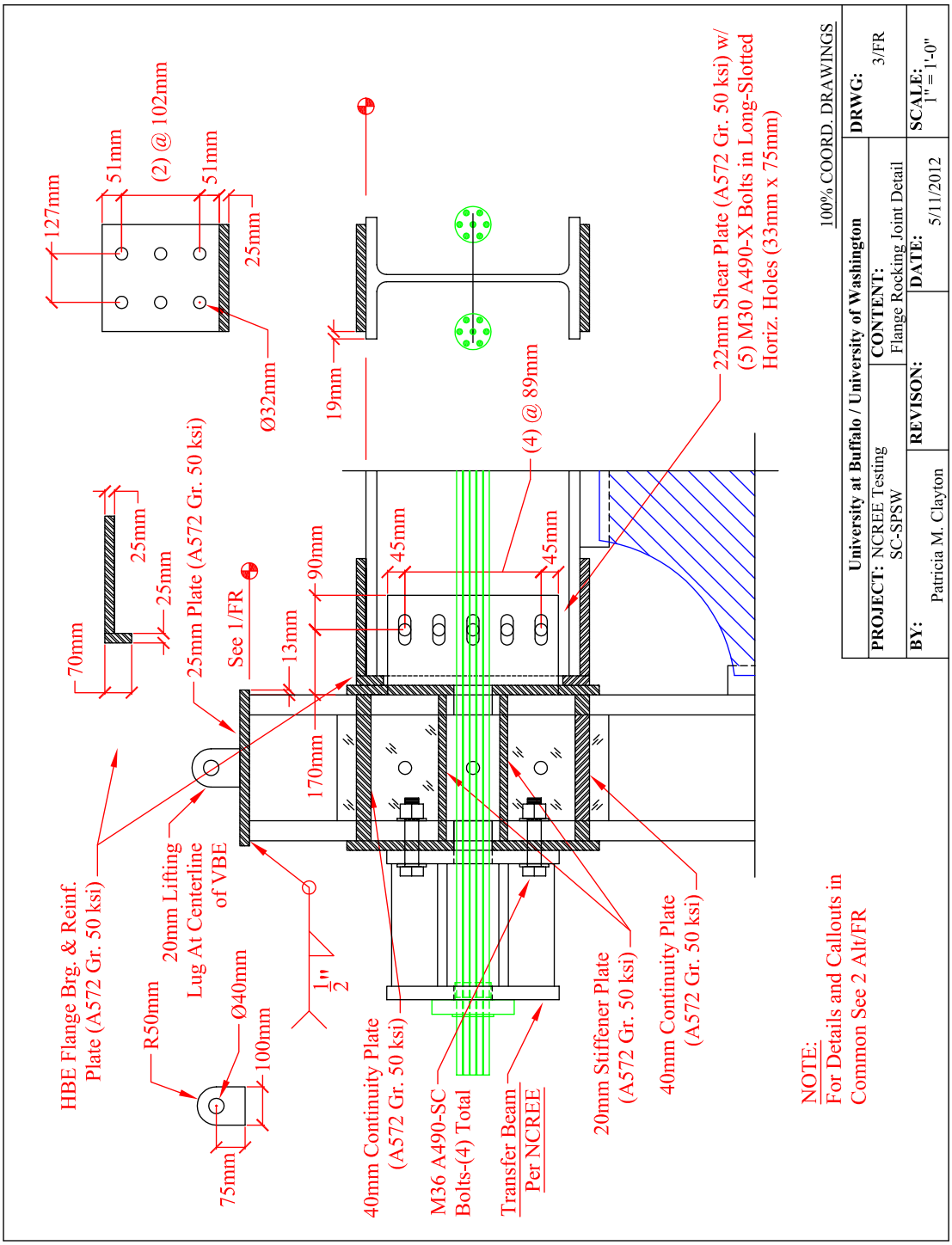
127mm
51mm
(2) @ 102mm
51mm
25mm
Ø32mm
19mm
(4) @ 89mm
22mm Shear Plate (A572 Gr. 50 ksi) w/
(5) M30 A490-X Bolts in Long-Slotted
Horiz. Holes (33mm x 75mm)
70mm
25mm
25mm
25mm Plate (A572 Gr. 50 ksi)
See 1/FR
13mm
90mm
45mm
45mm
170mm
HBE Flange Brg. & Reinf.
Plate (A572 Gr. 50 ksi)
20mm Lifting
Lug At Centerline
of VBE
R50mm
Ø40mm
100mm
75mm
1/2"
40mm Continuity Plate
(A572 Gr. 50 ksi)
M36 A490-SC
Bolts-(4) Total
Transfer Beam
Per NCREE
20mm Stiffener Plate
(A572 Gr. 50 ksi)
40mm Continuity Plate
(A572 Gr. 50 ksi)
NOTE:
For Details and Callouts in
Common See 2 Alt/FR
100% COORD. DRAWINGS
University at Buffalo / University of Washington
DRWG: 3/FR
PROJECT: NCREE Testing
SC-SPSW
CONTENT:
Flange Rocking Joint Detail
BY:
Patricia M. Clayton
REVISON:
DATE:
5/11/2012
SCALE:
1" = 1'-0"

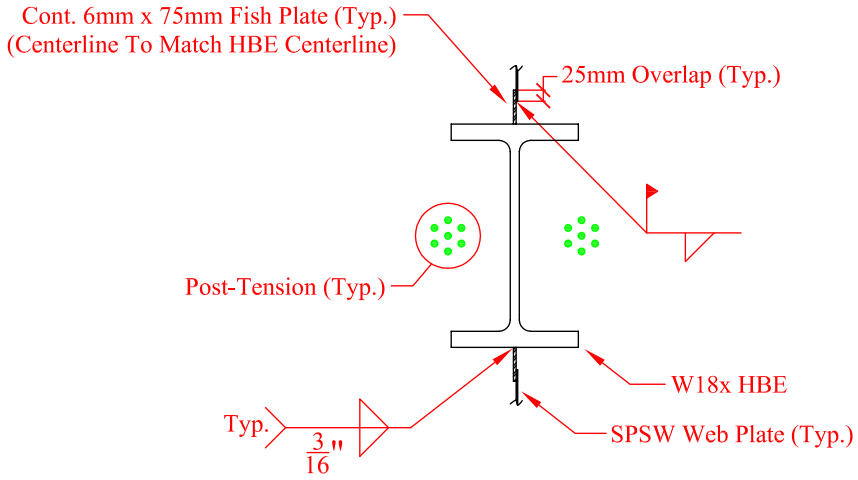

100% COORD. DRAWINGS

University at Buffalo / University of Washington			DRWG:
PROJECT: NCREE Testing SC-SPSW	CONTENT: HBE Section Detail		4/FR
BY: Patricia M. Clayton	REVISON:	DATE: 5/11/2012	SCALE: 1" = 1'-0"

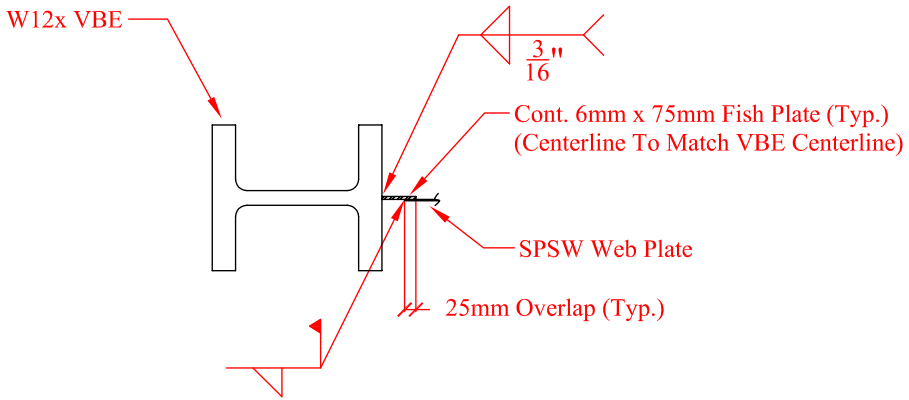

100% COORD. DRAWINGS

University at Buffalo / University of Washington			DRWG:
PROJECT: NCREE Testing SC-SPSW	CONTENT: VBE Plan Section		5/FR
BY: Patricia M. Clayton	REVISON:	DATE: 5/11/2012	SCALE: 1½" = 1'-0"

Detail 6 does not exist for the FR specimen

100% COORD. DRAWINGS

University at Buffalo / University of Washington			DRWG:
PROJECT: NCREE Testing SC-SPSW	CONTENT: Typ. PT Anchorage Detail		6/FR
BY: Patricia M. Clayton	REVISON:	DATE: 5/12/2012	SCALE: 1" = 1'-0"

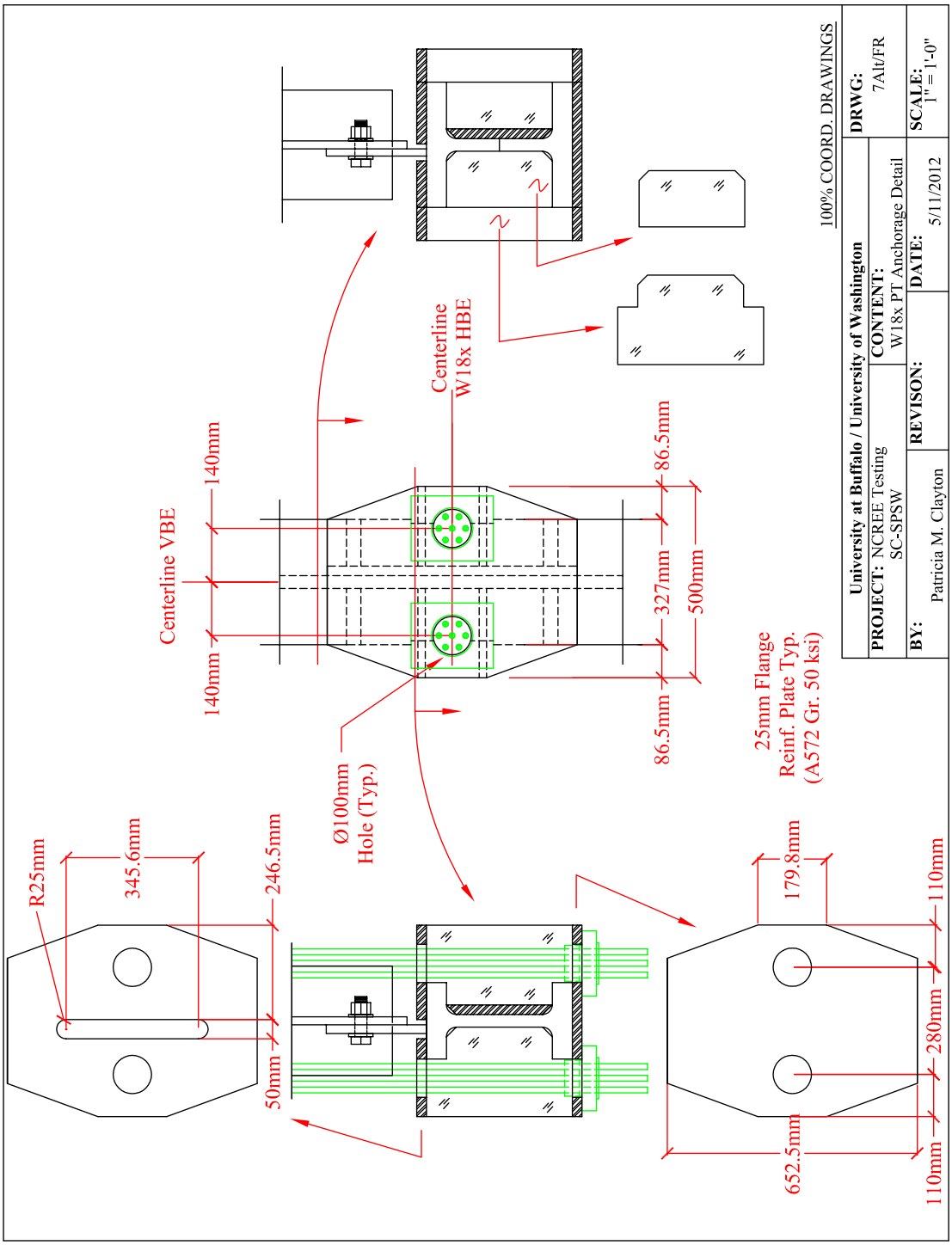
100% COORD. DRAWINGS
University at Buffalo / University of Washington
DRWG: 7Alt/FR
PROJECT: NCREE Testing SC-SPSW
CONTENT: W18x PT Anchorage Detail
BY: Patricia M. Clayton
REVISON:
DATE: 5/11/2012
SCALE: 1" = 1'-0"
Centerline VBE
140mm
140mm
Centerline W18x HBE
86.5mm
327mm
500mm
86.5mm
Ø100mm Hole (Typ.)
25mm Flange Reinf. Plate Typ. (A572 Gr. 50 ksi)
R25mm
345.6mm
246.5mm
50mm
179.8mm
110mm
652.5mm
280mm
110mm

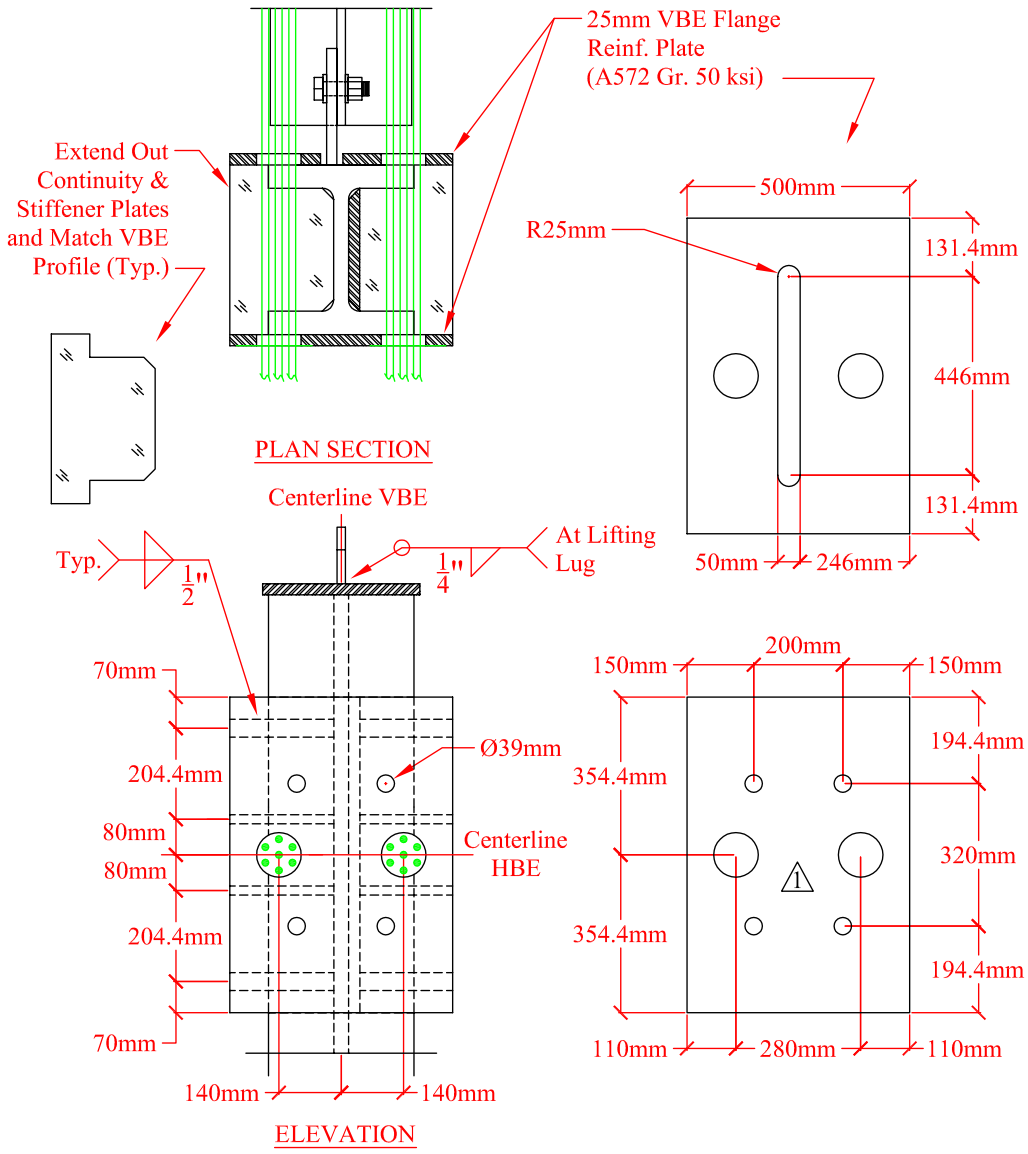

NOTE:
For VBE Panel Zone
Welds See 2a Alt/NZ

100% COORD. DRAWINGS

University at Buffalo / University of Washington			DRWG:
PROJECT: NCREE Testing SC-SPSW	CONTENT: Actuator Conn. To VBE		8/FR
BY: Patricia M. Clayton	REVISON: 1	DATE: 5/11/2012	SCALE: 1" = 1'-0"

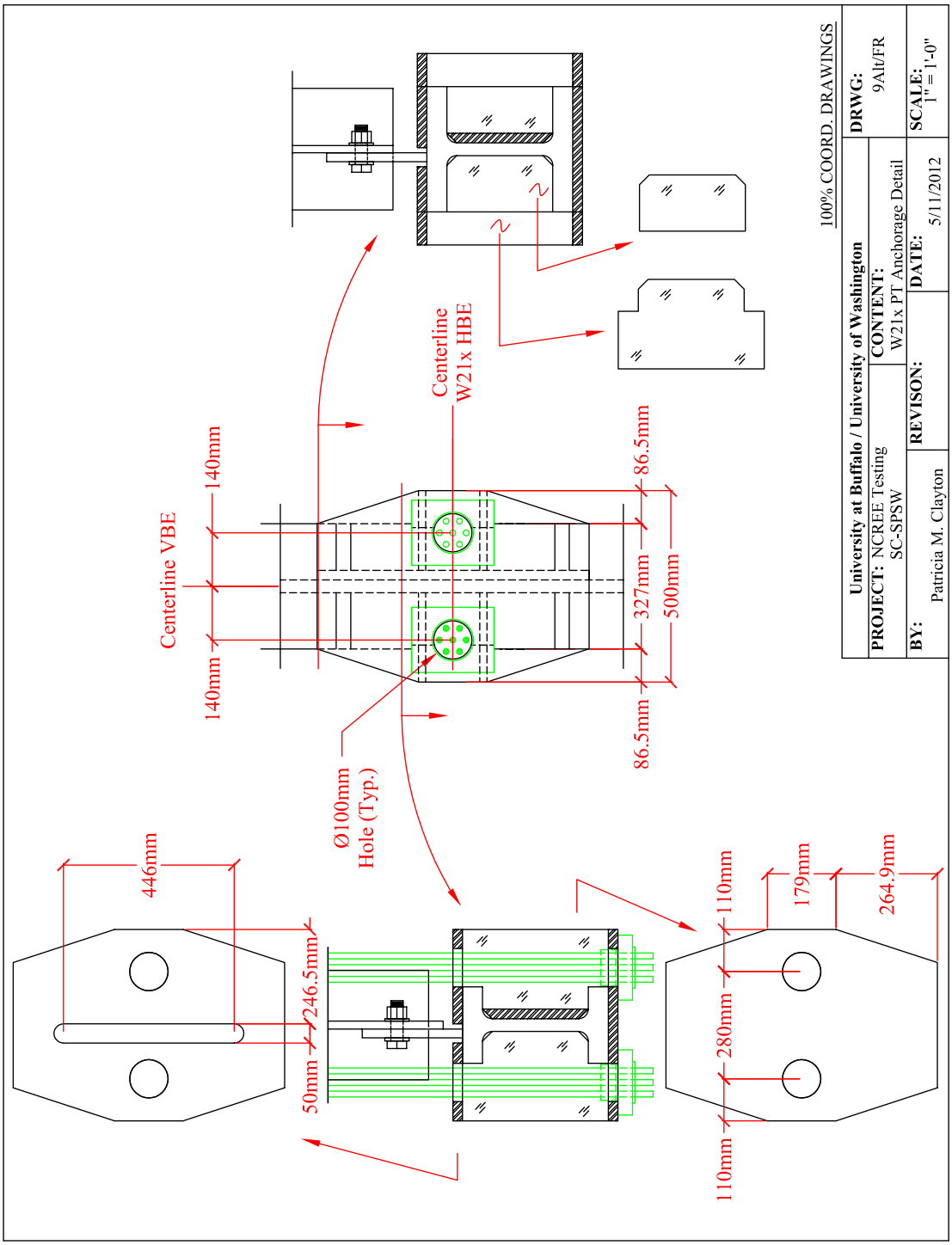
100% COORD. DRAWINGS
University at Buffalo / University of Washington
DRWG: 9Alt/FR
PROJECT: NCREE Testing SC-SPSW
CONTENT: W21x PT Anchorage Detail
BY: Patricia M. Clayton
REVISON:
DATE: 5/11/2012
SCALE: 1" = 1'-0"
Centerline W21x HBE
Centerline VBE
140mm
140mm
86.5mm
327mm
500mm
86.5mm
Ø100mm Hole (Typ.)
446mm
50mm
246.5mm
110mm
179mm
264.9mm
280mm
110mm

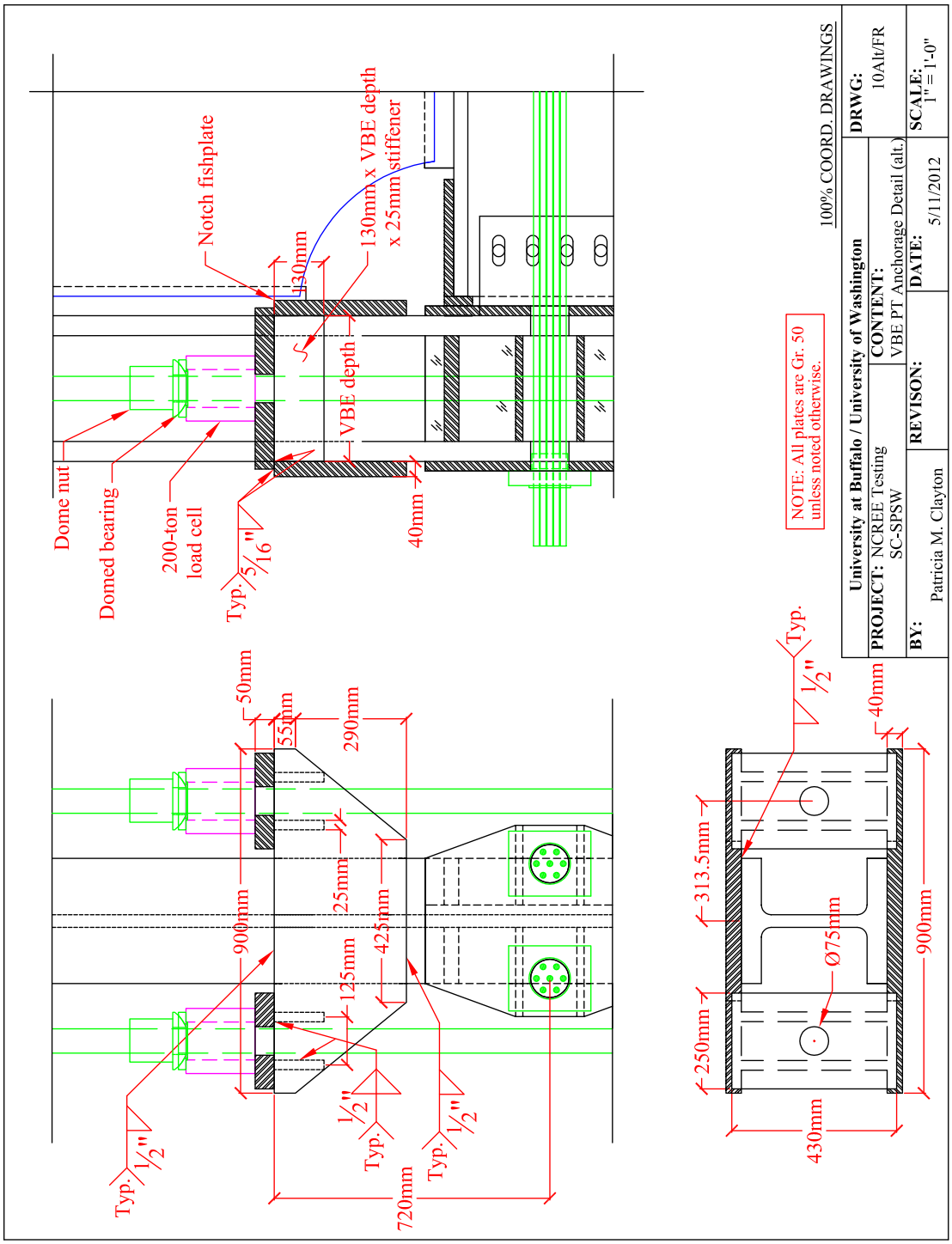
Dome nut
Domed bearing
200-ton load cell
Typ. 5/16"
VBE depth
40mm
Notch fishplate
130mm
130mm x VBE depth x 25mm stiffener
50mm
55mm
290mm
900mm
25mm
425mm
125mm
Typ. 1/2"
Typ. 1/2"
Typ. 1/2"
720mm
Typ. 1/2"
40mm
313.5mm
250mm
Ø75mm
900mm
430mm
100% COORD. DRAWINGS
NOTE: All plates are Gr. 50 unless noted otherwise.
University at Buffalo / University of Washington
DRWG: 10Alt/FR
PROJECT: NCREE Testing SC-SPSW
CONTENT: VBE PT Anchorage Detail (alt.)
BY: Patricia M. Clayton
REVISON:
DATE: 5/11/2012
SCALE: 1" = 1'-0"

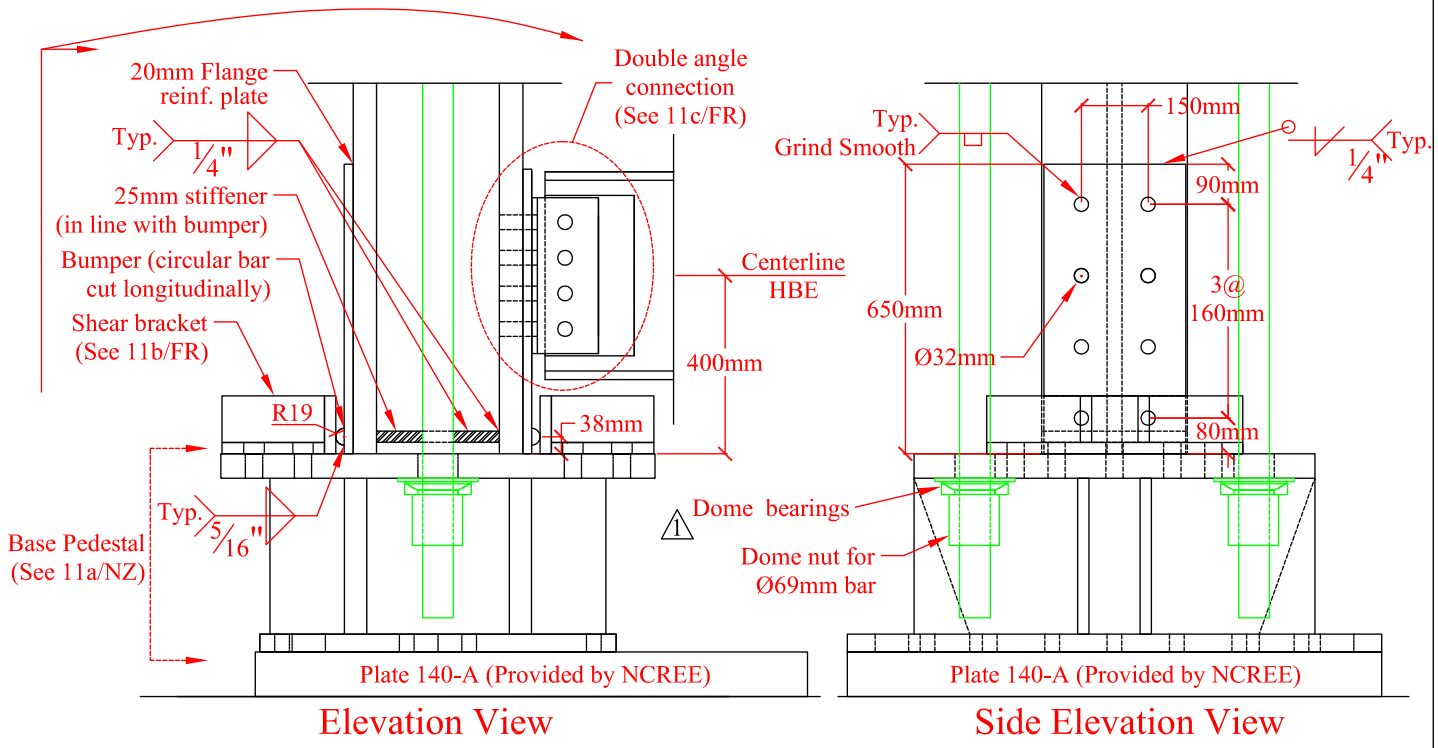

NOTE: All plates are Gr. 50 unless noted otherwise.

100% COORD. DRAWINGS

University at Buffalo / University of Washington			DRWG:
PROJECT: NCREE Testing SC-SPSW	CONTENT: VBE Base Detail		11/FR
BY: Patricia M. Clayton	REVISON: 1	DATE: 5/11/2012	SCALE: 1" = 1'-0"

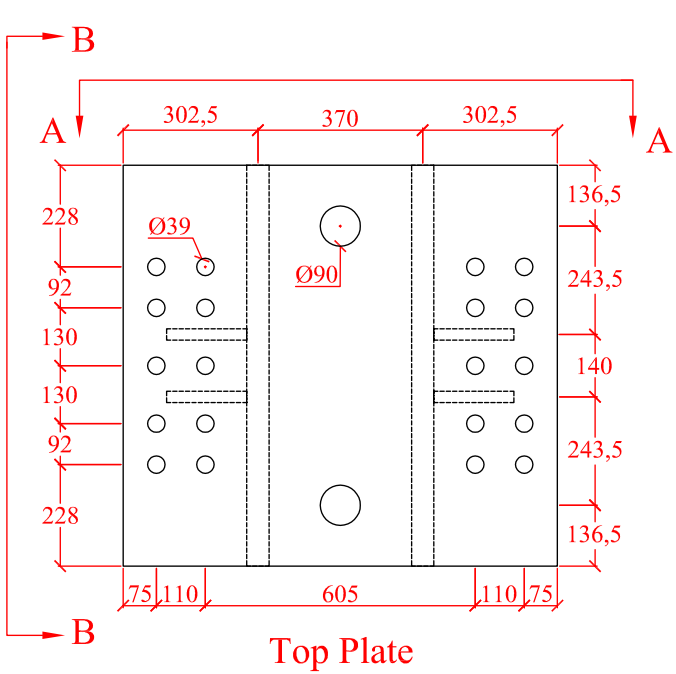

Top Plate

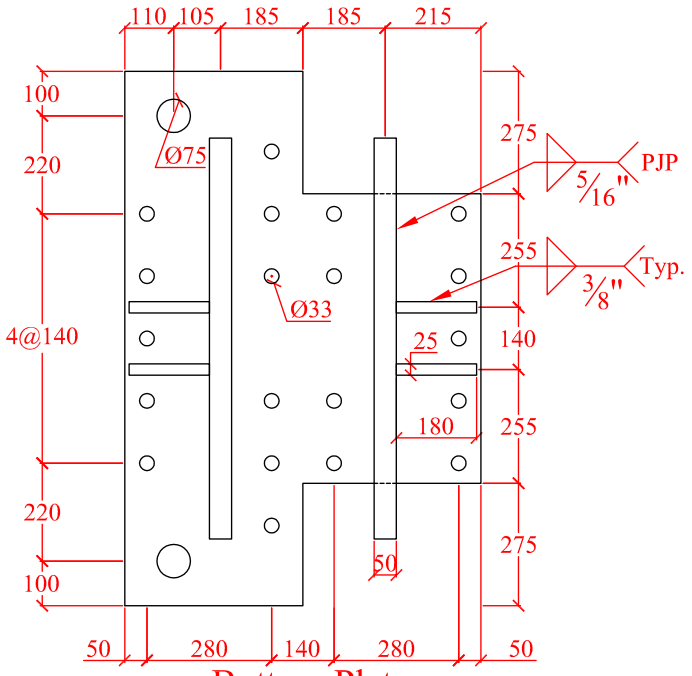

Bottom Plate

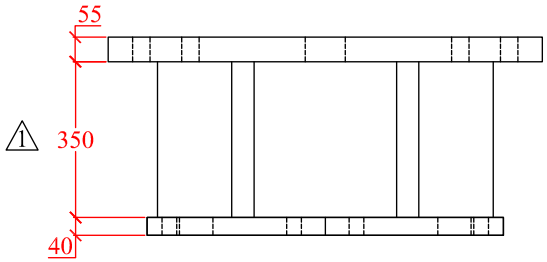

Section A-A

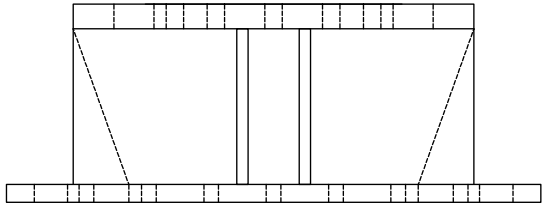

Section B-B

100% COORD. DRAWINGS

NOTE: All plates are Gr. 50 unless noted otherwise.

University at Buffalo / University of Washington			DRWG:
PROJECT: NCREE Testing SC-SPSW	CONTENT: VBE Base Detail (cont.)		11a/FR
BY: Patricia M. Clayton	REVISON: 1	DATE: 5/11/2012	SCALE: 1" = 1'-0"

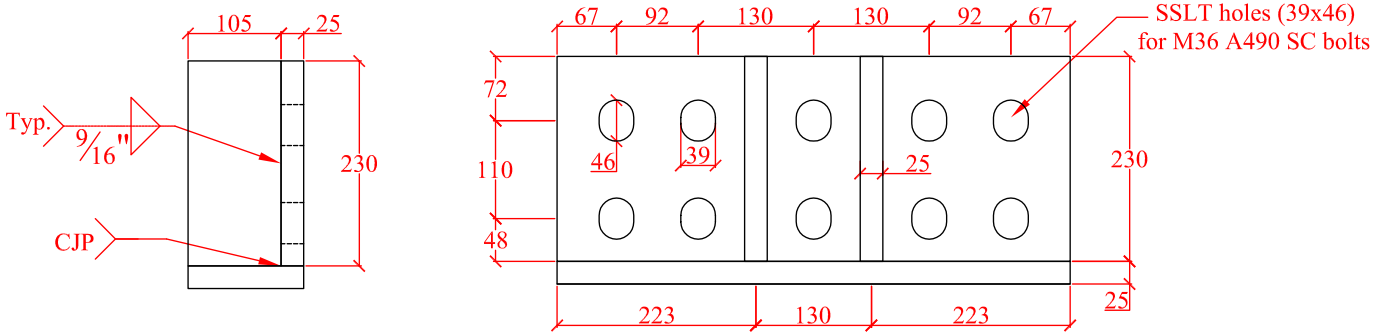

Shear Bracket

NOTE: All plates are Gr. 50 unless noted otherwise.

100% COORD. DRAWINGS

University at Buffalo / University of Washington			DRWG:
PROJECT: NCREE Testing SC-SPSW	CONTENT: VBE Base Detail (cont.)		11b/FR
BY: Patricia M. Clayton	REVISON:	DATE: 5/11/2012	SCALE: 2" = 1'-0"

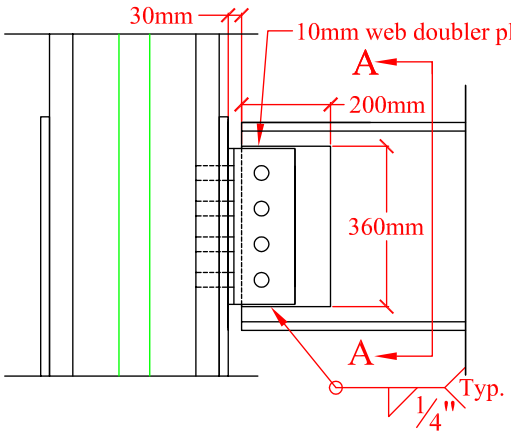

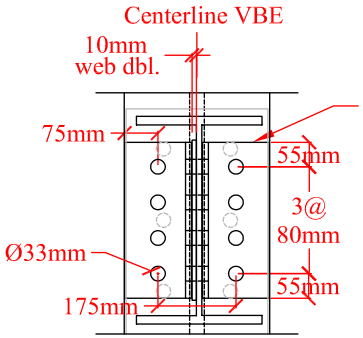

Bolted-bolted double angle
2L150mmx150mmx13mm
(A36) w/ (4) M30 A490-X bolts

(Bolt holes are sim.
on both angle legs)

Section A-A

NOTE: 20mm VBE flange reinf. plate and plug welds shown in lighter color (See 11/FR)

NOTE: All plates are Gr. 50 unless noted otherwise.

100% COORD. DRAWINGS

University at Buffalo / University of Washington			DRWG:
PROJECT: NCREE Testing SC-SPSW	CONTENT: VBE Base Detail (cont.)		11c/FR
BY: Patricia M. Clayton	REVISON:	DATE: 5/11/2012	SCALE: 1" = 1'-0"

A.2 Strain Gage Layout

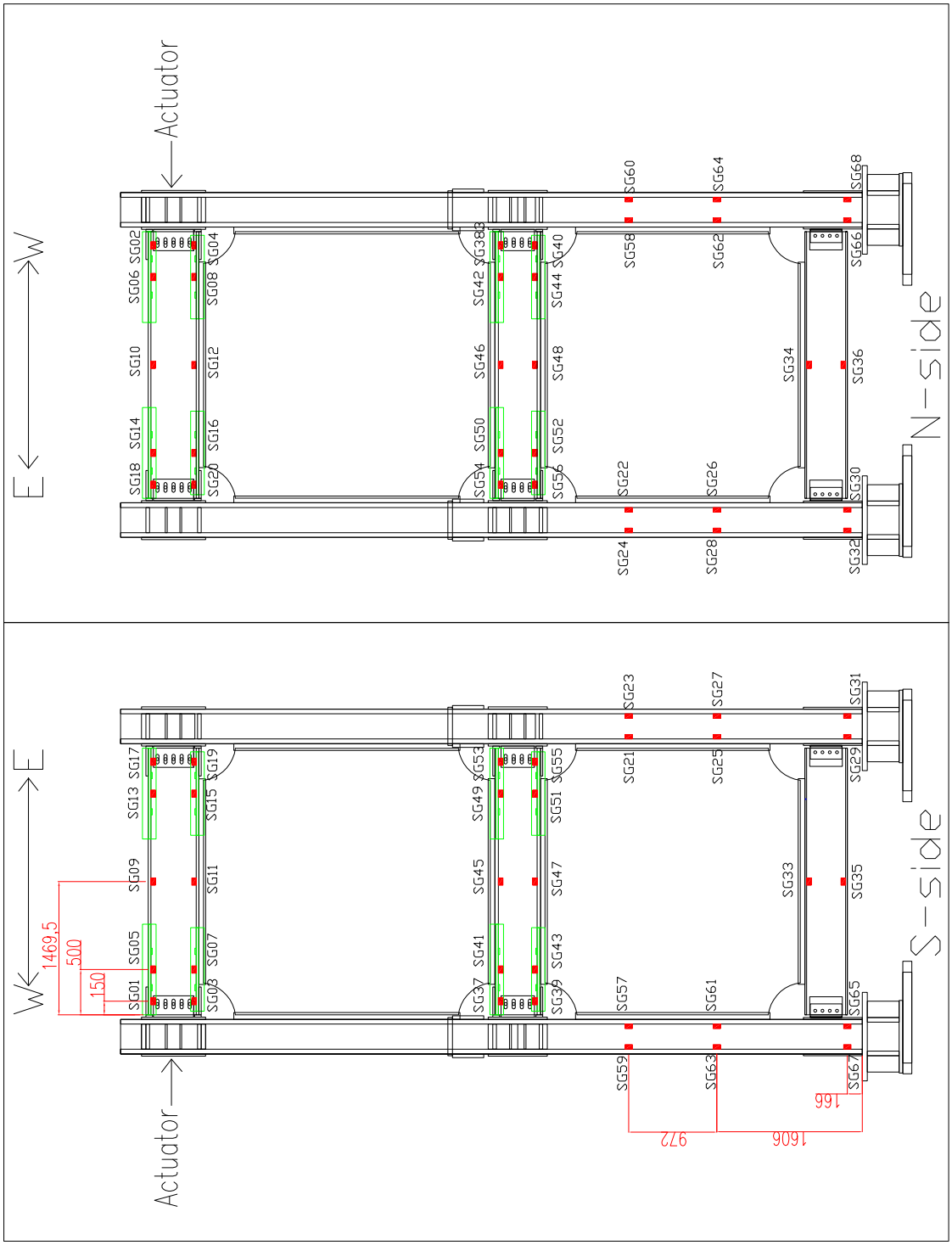

Figure A.1: Strain gage layout with naming

Appendix B

ADDITIONAL FIGURES FOR EXPERIMENTAL DATA ANALYSIS OF SUBASSEMBLY TESTS

B.1 Gap Rotation and PT forces

Below are the gap rotation, θ_r vs. drift and total PT force vs. gap rotation in the middle HBE for each specimen. The gap rotations are shown for both the north and south ends of the HBE. Notes will be made for faulty potentiometer data used to calculate gap rotations. Also note that at very large drifts, some potentiometers measuring gap opening may have reached their stroke limit. For this reason, the resulting θ_r calculation may appear to show no change in gap opening with changes in drift at large drift values; this does not represent actual behavior as the gap opening continues to increase at a steady rate after connection decompression. All PT force values have been corrected for any faulty PT load cell readings as indicated in Sec. 4.4.

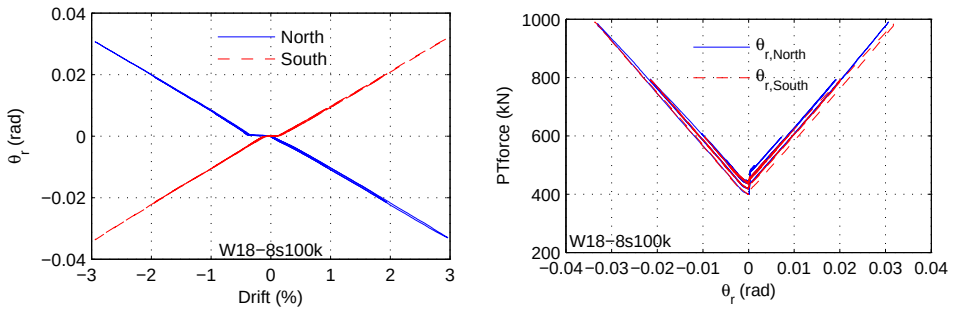

(a) (b)

Figure B.1: W18-8s100k: PT connection gap opening and PT force response

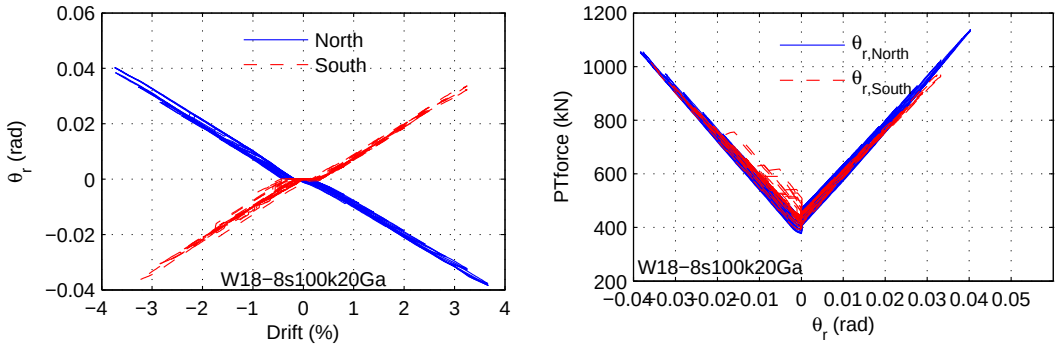

(a) (b)

Figure B.2: W18-8s100k20Ga: PT connection gap opening and PT force response (Note: potentiometer pgs2t (south end of HBE) was sticking due to a sticky substance on the shaft of the moving plunger. The problem was most evident at small drifts less than 2% drift.)

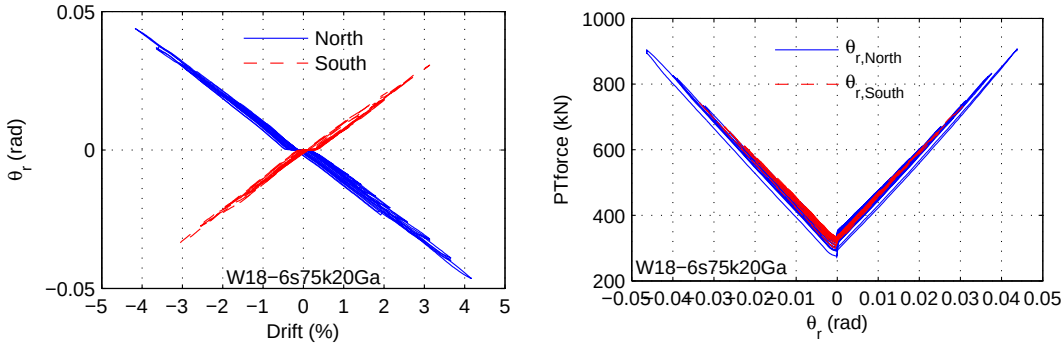

(a) (b)

Figure B.3: W18-6s75k20Ga: PT connection gap opening and PT force response

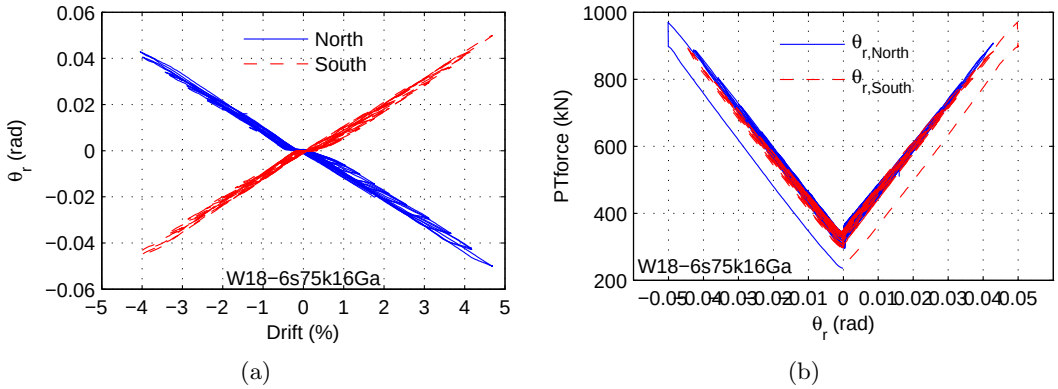

(a) (b)

Figure B.4: W18-6s75k16Ga: PT connection gap opening and PT force response

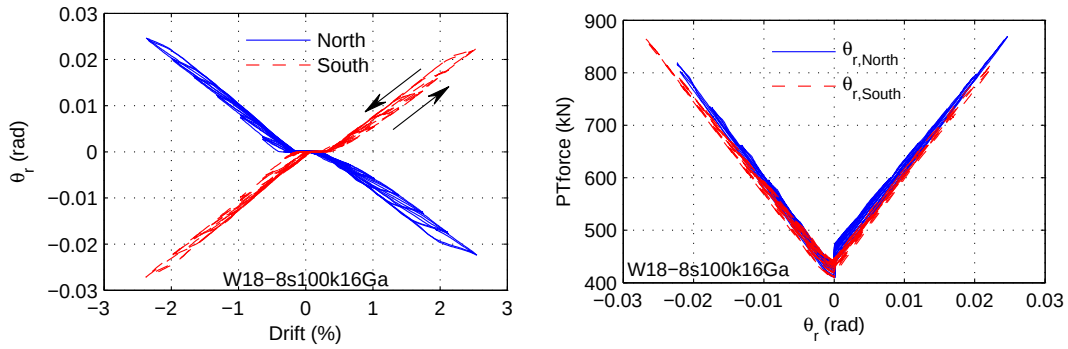

(a) (b)

Figure B.5: W18-8s100k16Ga: PT connection gap opening and PT force response

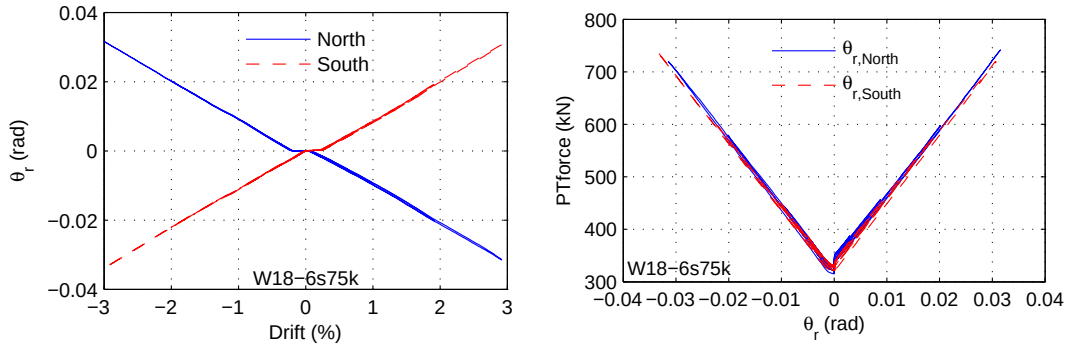

(a) (b)

Figure B.6: W18-6s75k: PT connection gap opening and PT force response

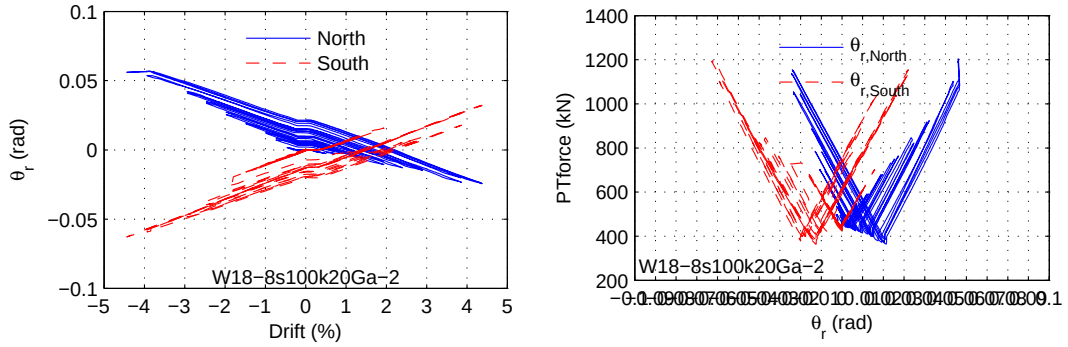

(a) (b)

Figure B.7: W18-8s100k20Ga-2: PT connection gap opening and PT force response

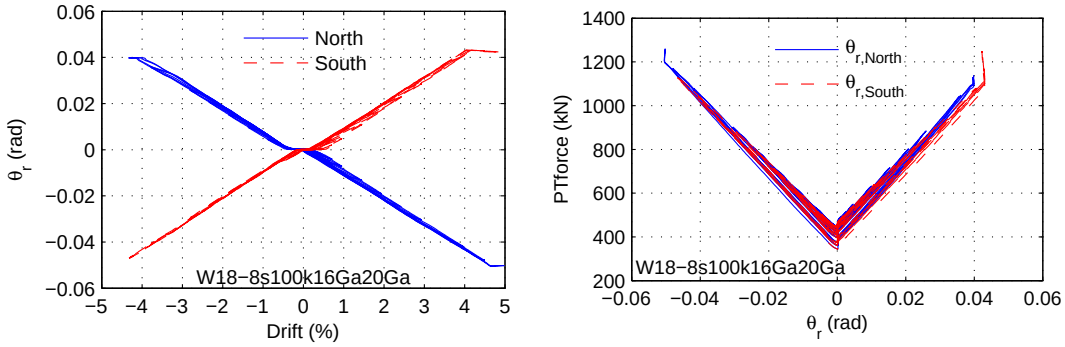

(a) (b)

Figure B.8: W18-8s100k16Ga20Ga: PT connection gap opening and PT force response

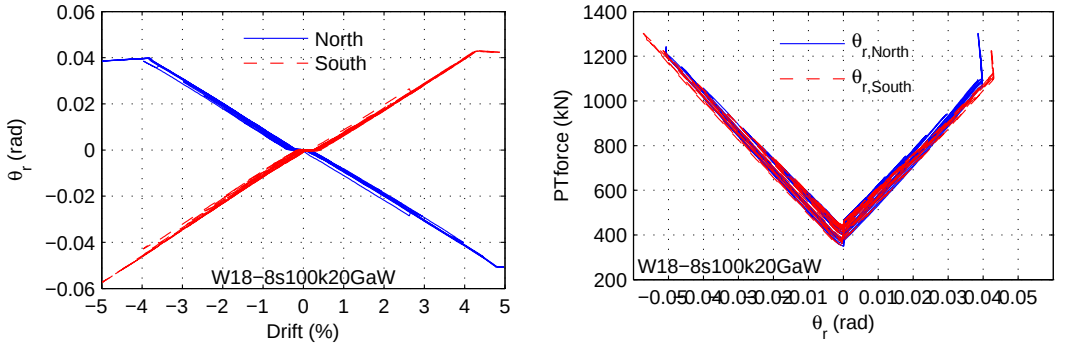

(a) (b)

Figure B.9: W18-8s100k20GaW: PT connection gap opening and PT force response (Note: potentiometers pgs2t and pgn2b (south and north ends of HBE) were not adequately secured to the specimen. The adhesive used to connect these potentiometers to the specimen slipped throughout the entire test resulting in faulty θ_r measurements.)

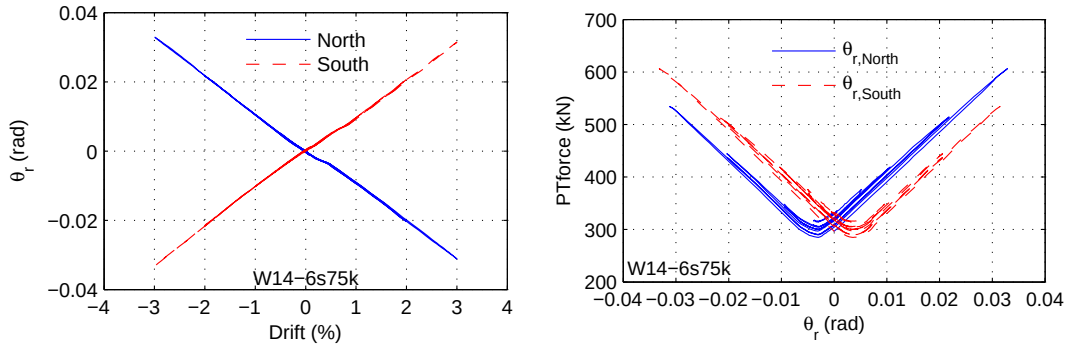

(a) (b)

Figure B.10: W14-6s75k: PT connection gap opening and PT force response

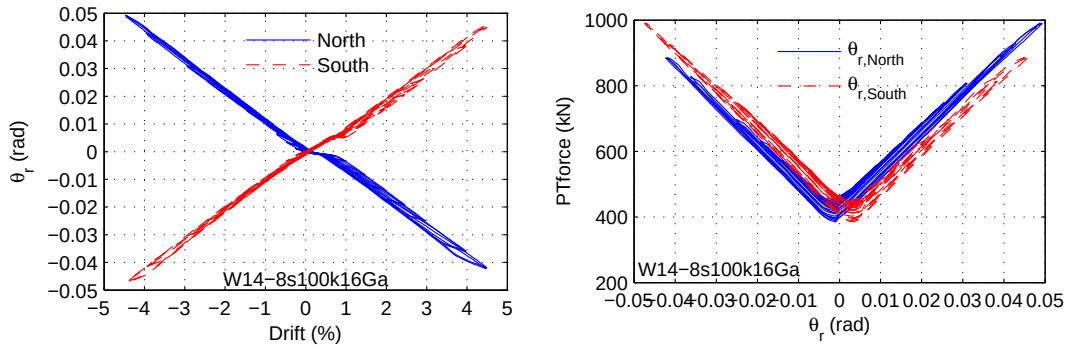

(a) (b)

Figure B.11: W14-8s100k16Ga: PT connection gap opening and PT force response

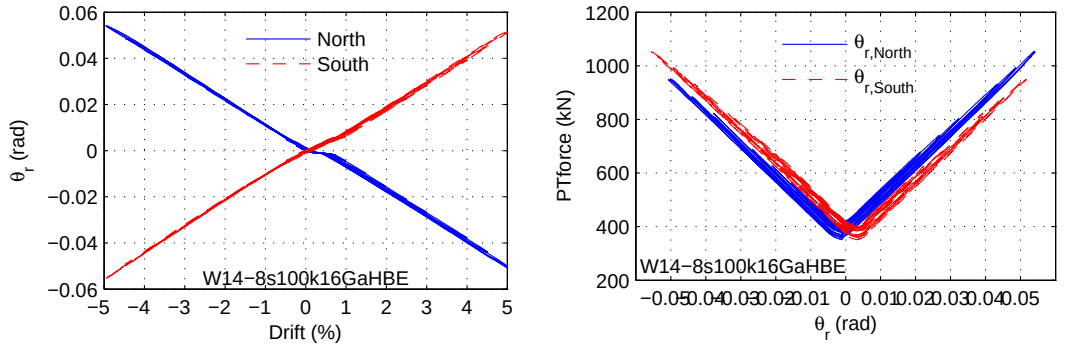

(a) (b)

Figure B.12: W14-8s100k16GaHBE: PT connection gap opening and PT force response

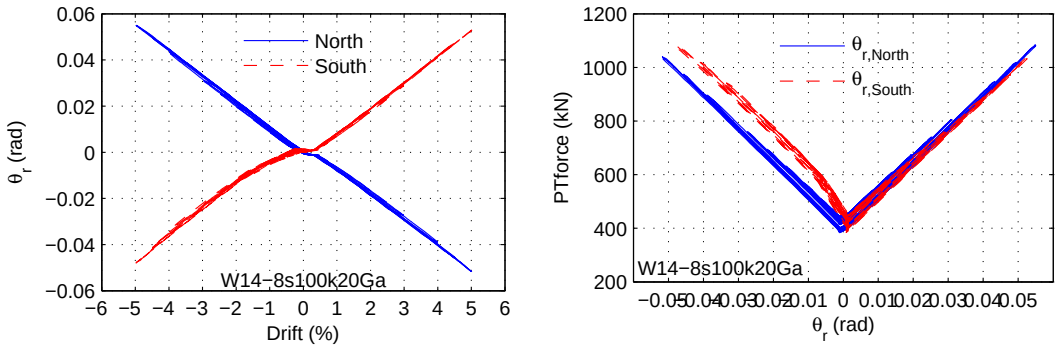

(a) (b)

Figure B.13: W14-8s100k20Ga: PT connection gap opening and PT force response

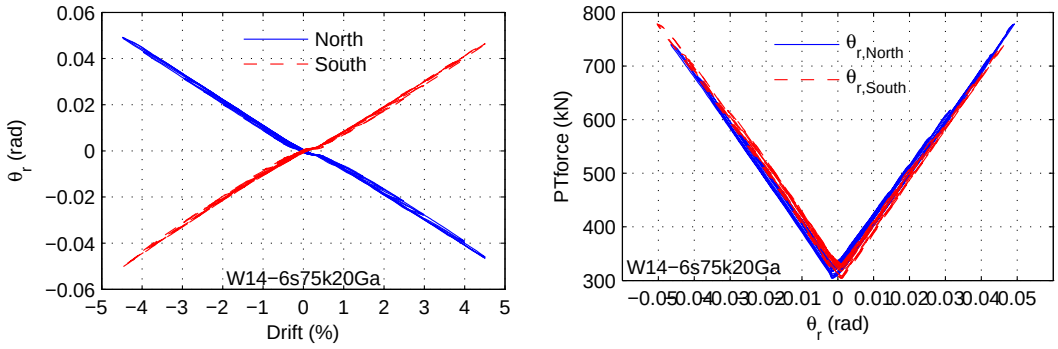

(a) (b)

Figure B.14: W14-6s75k20Ga: PT connection gap opening and PT force response

B.2 Axial and Moment Demands

Below are the axial force and moment demands calculated at each strain gage section for each specimen plotted vs. drift. When calculating demands for these figures, data from faulty strain gages was removed.

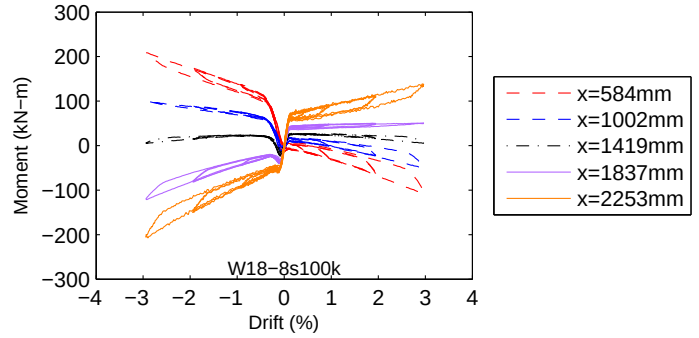

(a)

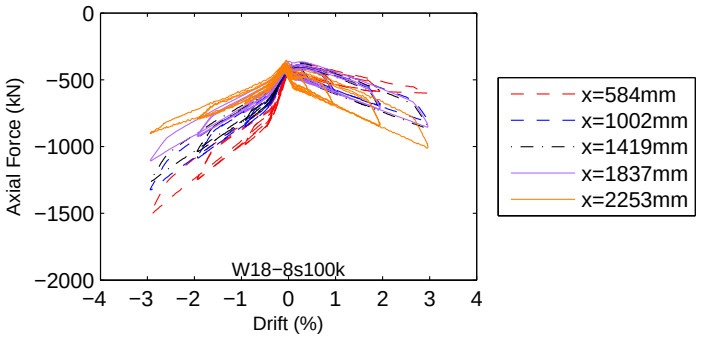

(b)

Figure B.15: W18-8s100k: Bottom HBE

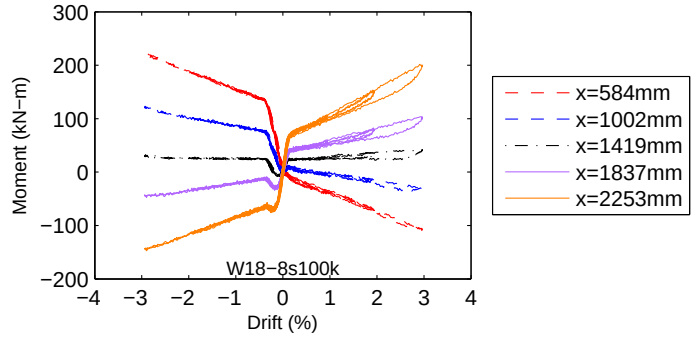

(a)

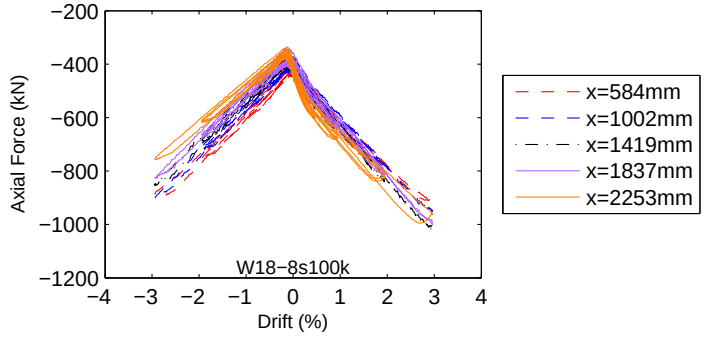

(b)

Figure B.16: W18-8s100k: Middle HBE

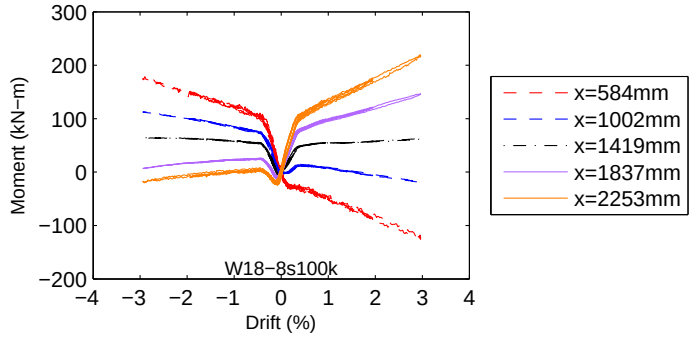

(a)

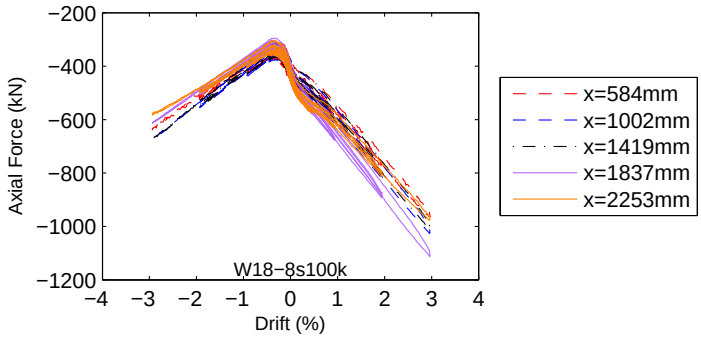

(b)

Figure B.17: W18-8s100k: Top HBE

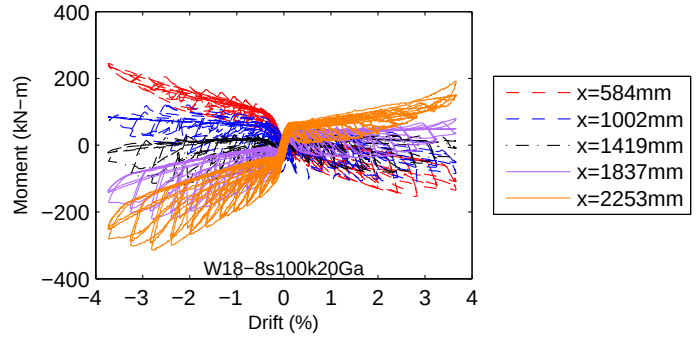

(a)

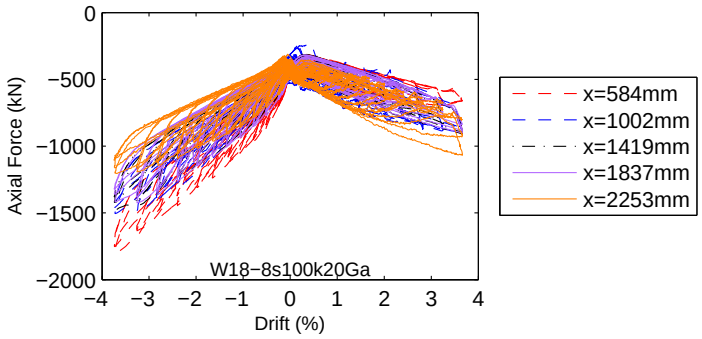

(b)

Figure B.18: W18-8s100k20Ga: Bottom HBE

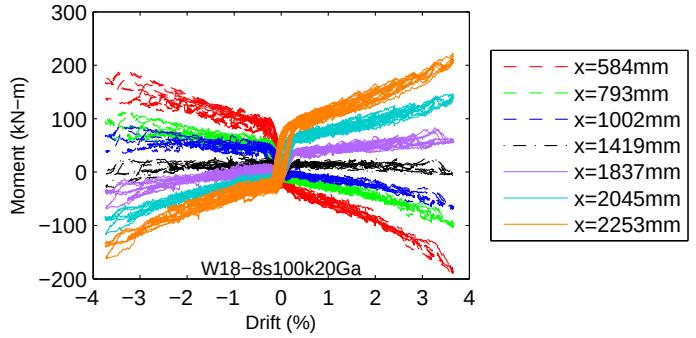

(a)

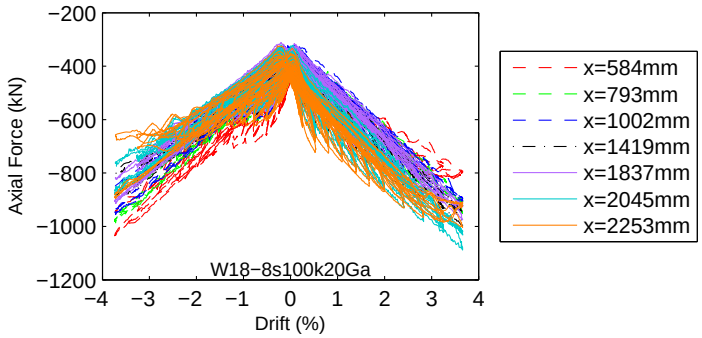

(b)

Figure B.19: W18-8s100k20Ga: Middle HBE

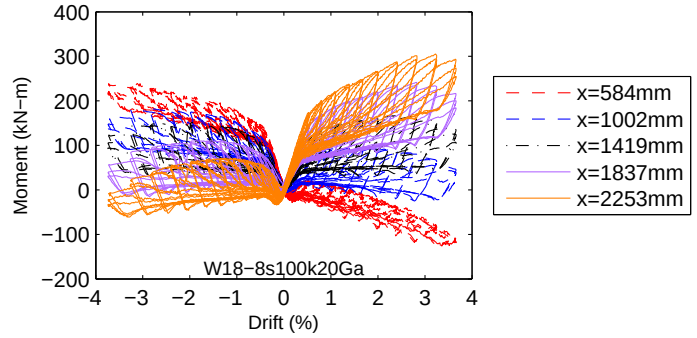

(a)

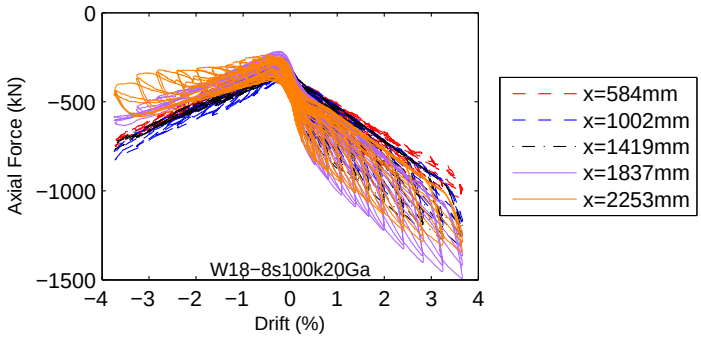

(b)

Figure B.20: W18-8s100k20Ga: Top HBE

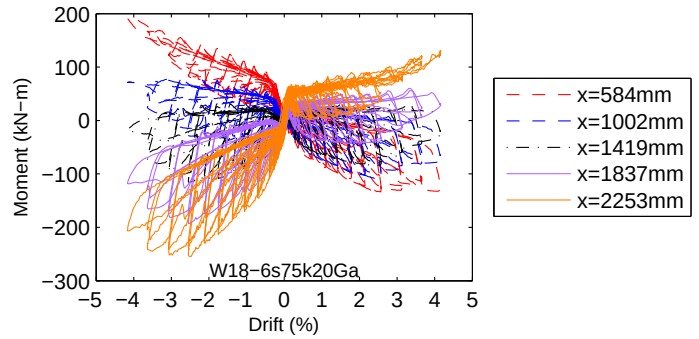

(a)

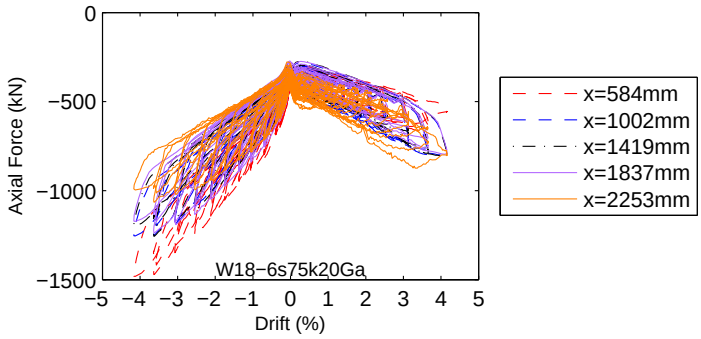

(b)

Figure B.21: W18-6s75k20Ga: Bottom HBE

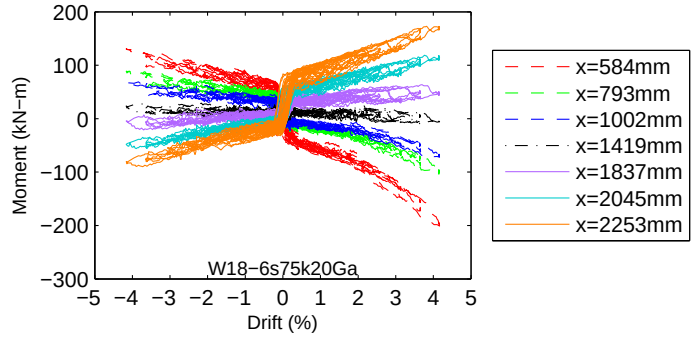

(a)

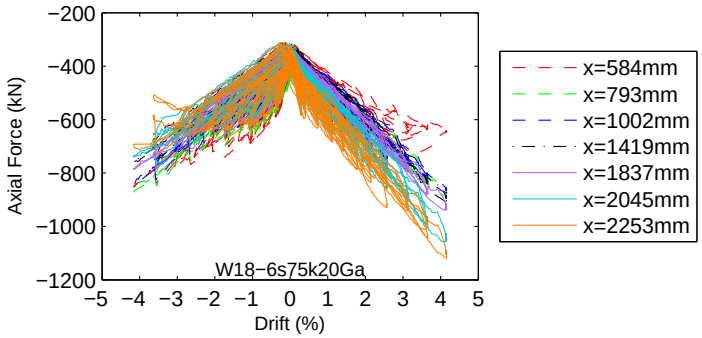

(b)

Figure B.22: W18-6s75k20Ga: Middle HBE

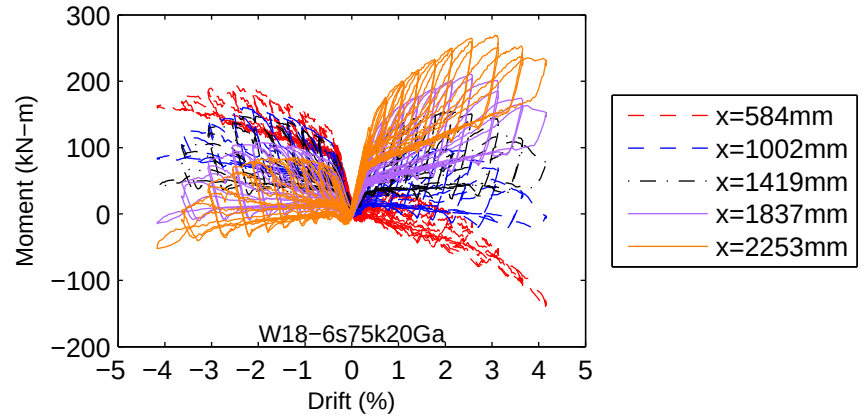

(a)

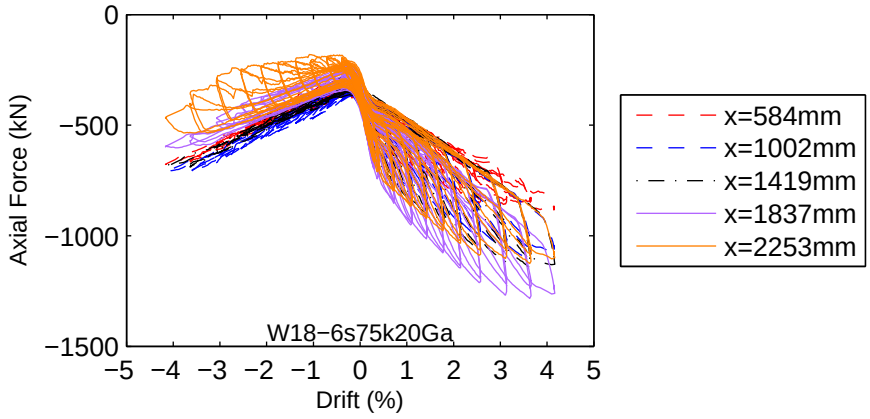

(b)

Figure B.23: W18-6s75k20Ga: Top HBE

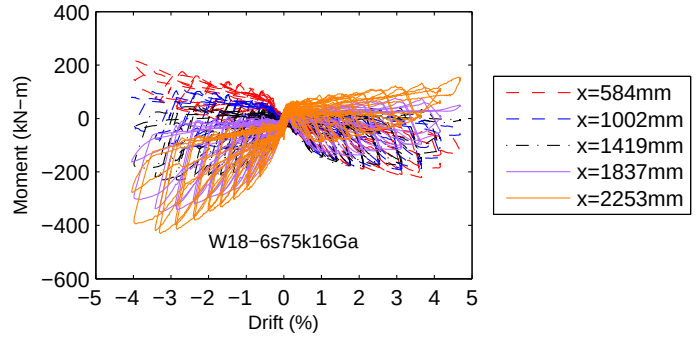

(a)

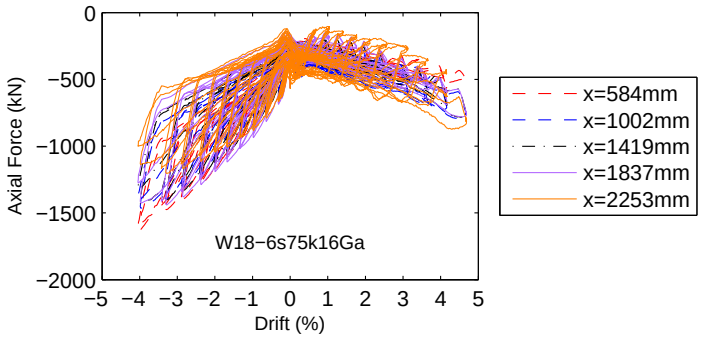

(b)

Figure B.24: W18-6s75k16Ga: Bottom HBE

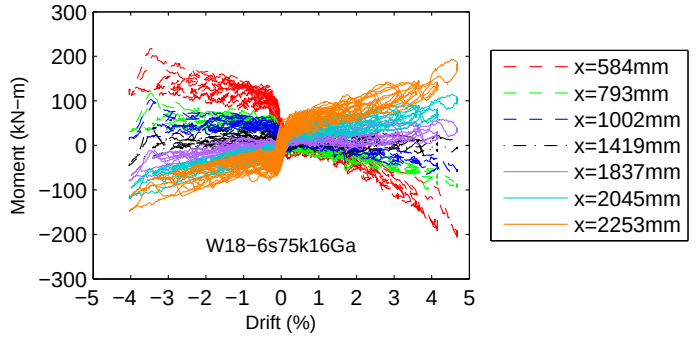

(a)

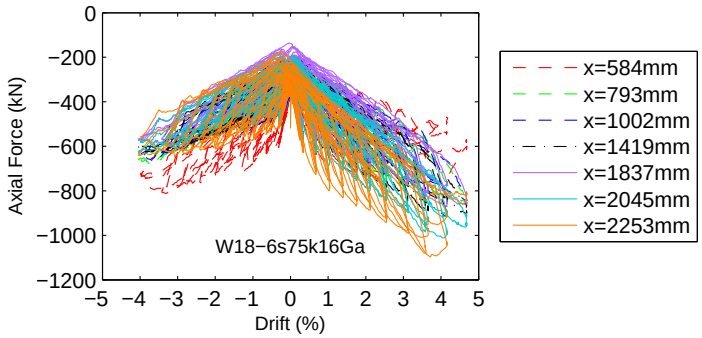

(b)

Figure B.25: W18-6s75k16Ga: Middle HBE

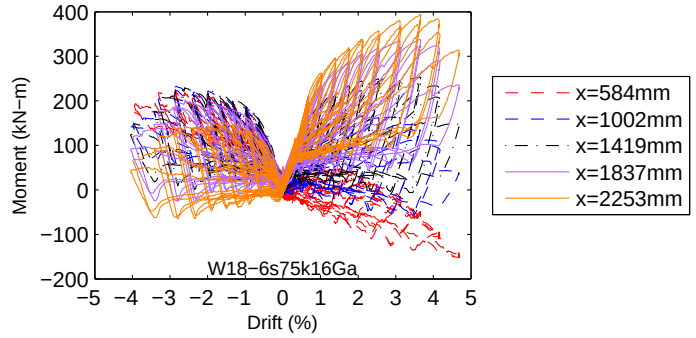

(a)

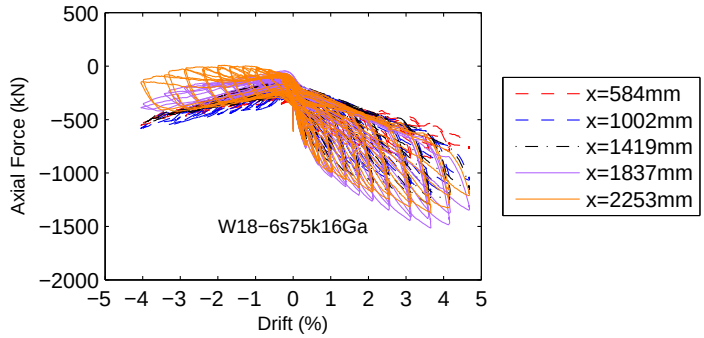

(b)

Figure B.26: W18-6s75k16Ga: Top HBE

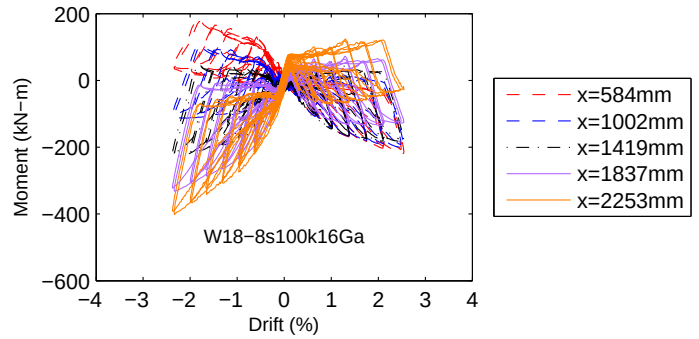

(a)

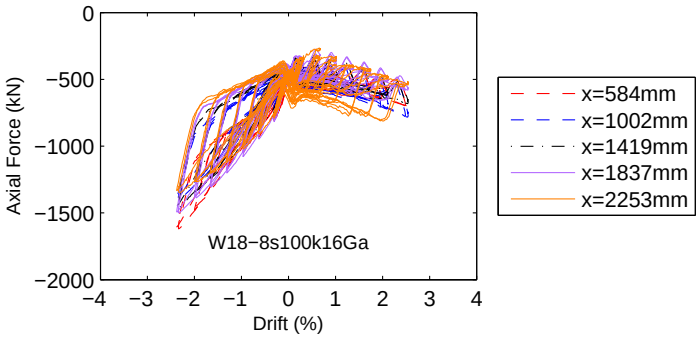

(b)

Figure B.27: W18-8s100k16Ga: Bottom HBE

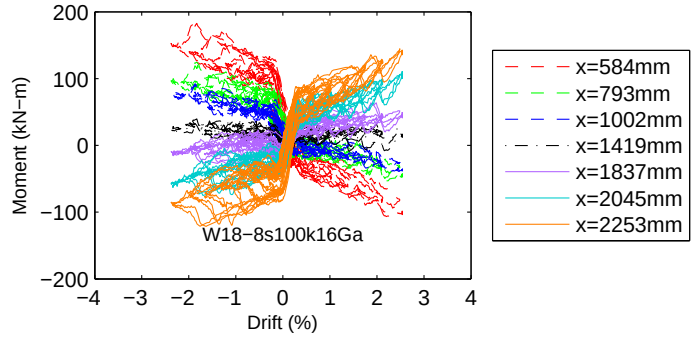

(a)

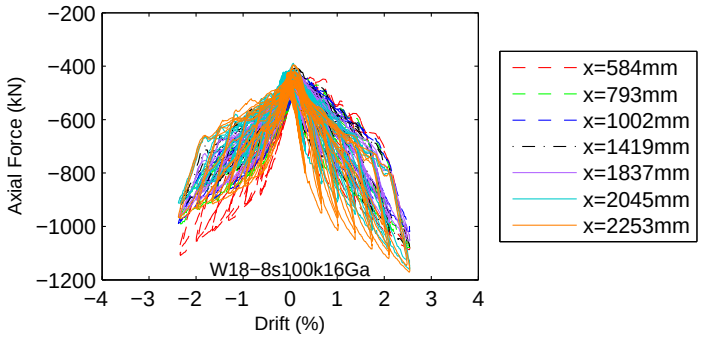

(b)

Figure B.28: W18-8s100k16Ga: Middle HBE

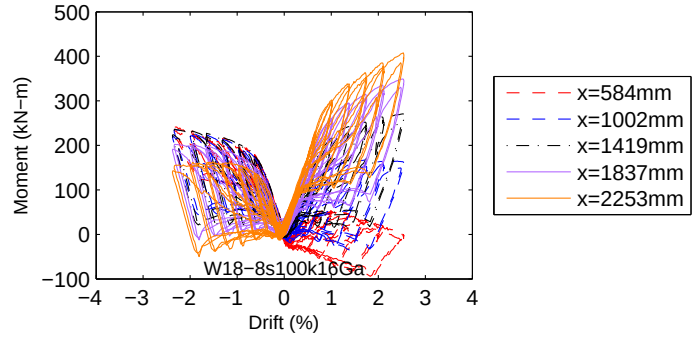

(a)

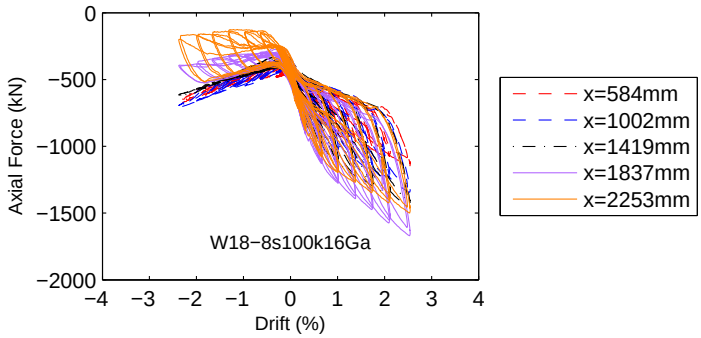

(b)

Figure B.29: W18-8s100k16Ga: Top HBE

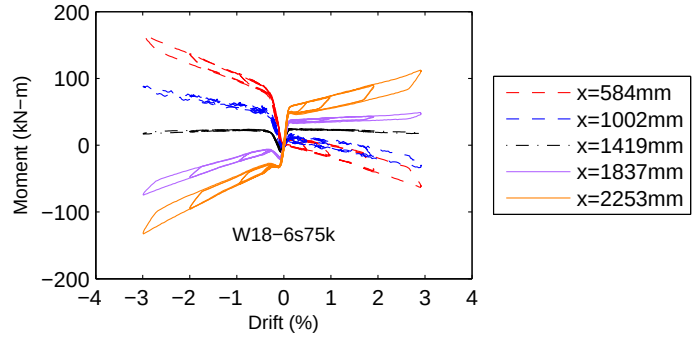

(a)

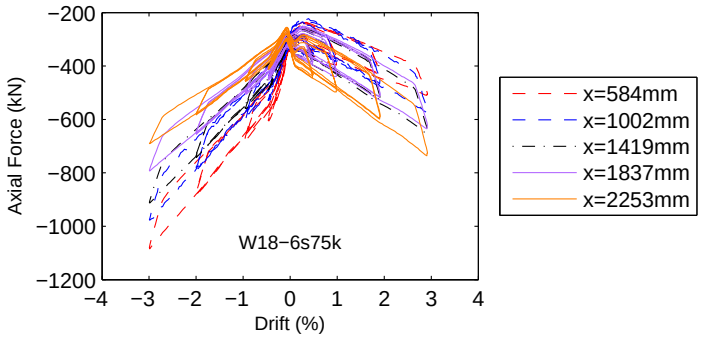

(b)

Figure B.30: W18-6s75k: Bottom HBE

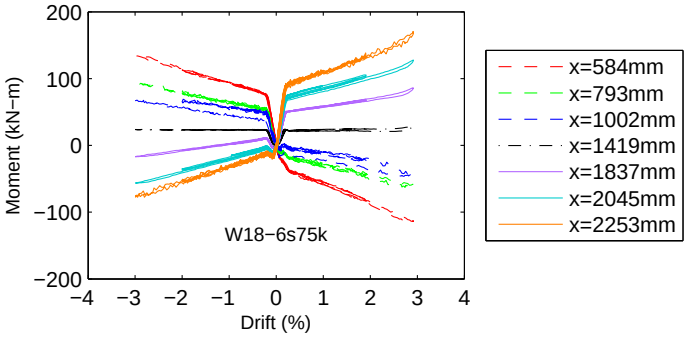

(a)

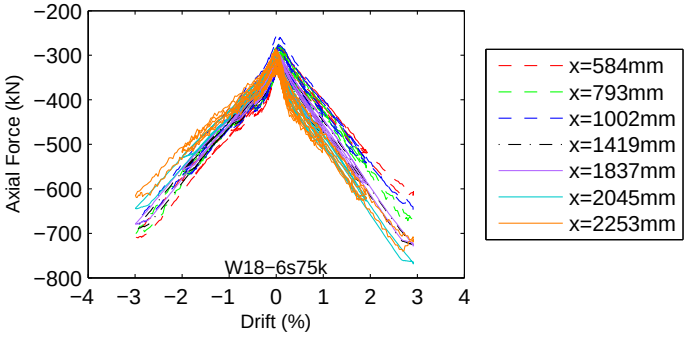

(b)

Figure B.31: W18-6s75k: Middle HBE

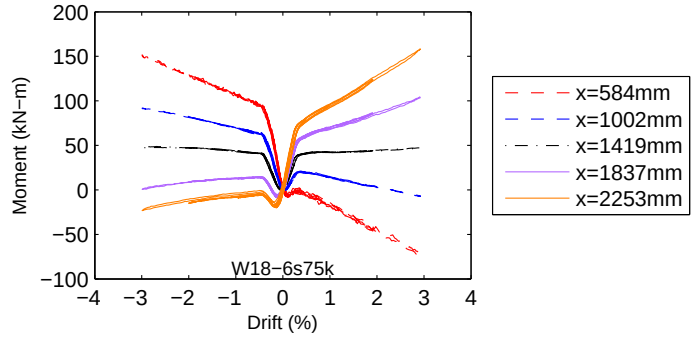

(a)

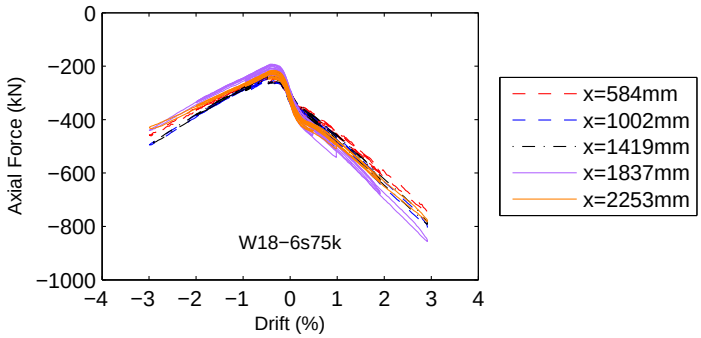

(b)

Figure B.32: W18-6s75k: Top HBE

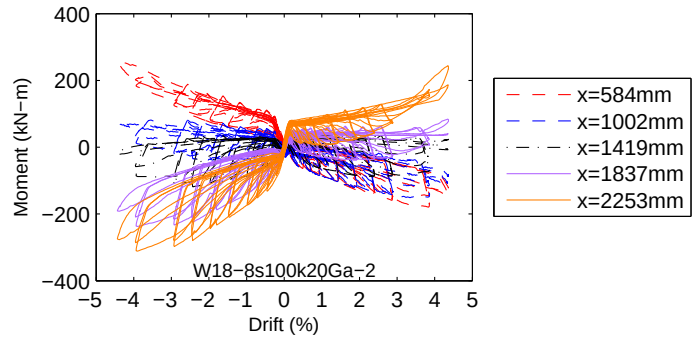

(a)

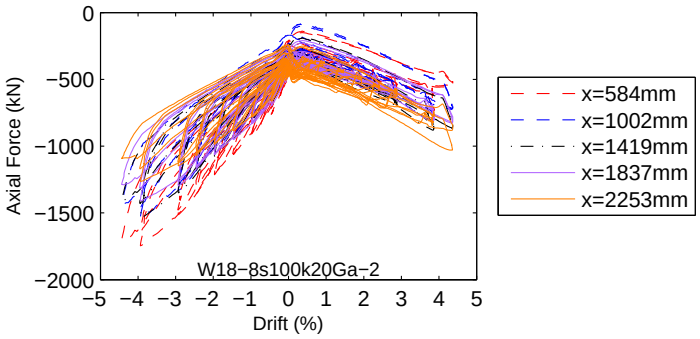

(b)

Figure B.33: W18-8s100k20Ga-2: Bottom HBE

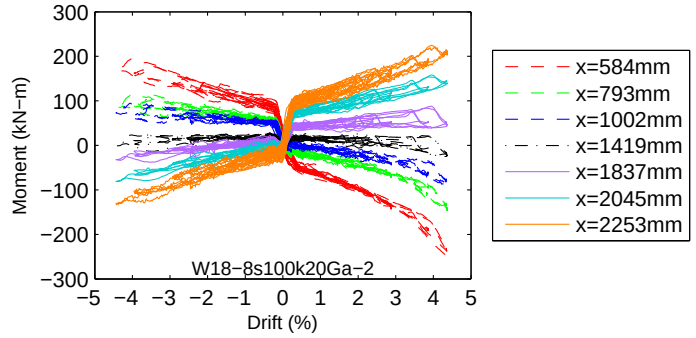

(a)

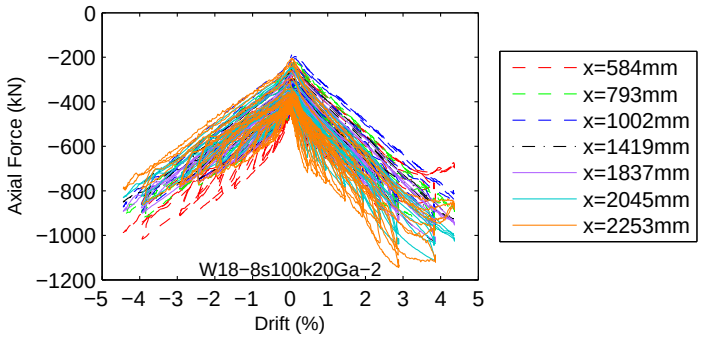

(b)

Figure B.34: W18-8s100k20Ga-2: Middle HBE

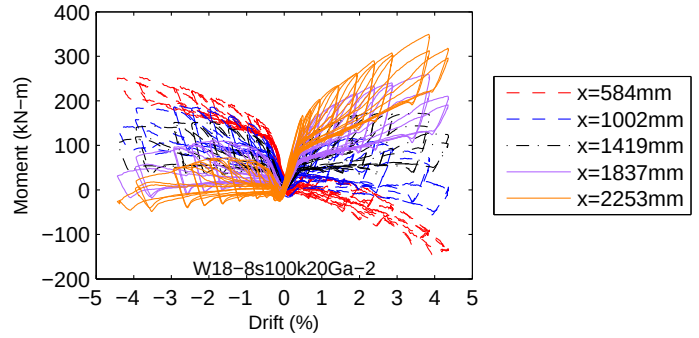

(a)

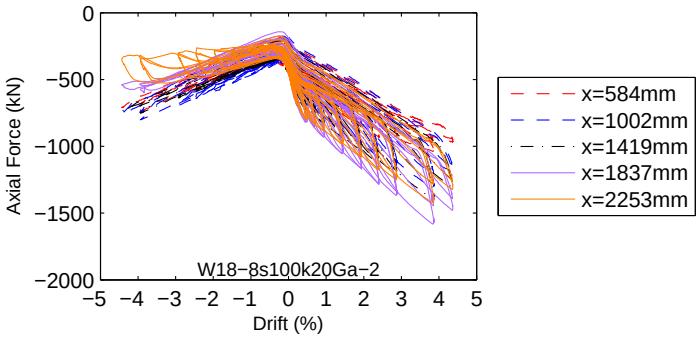

(b)

Figure B.35: W18-8s100k20Ga-2: Top HBE

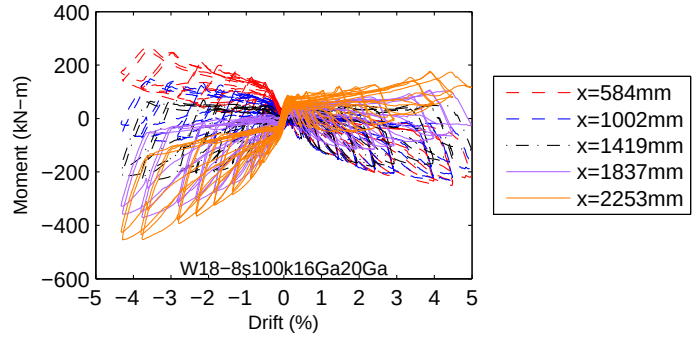

(a)

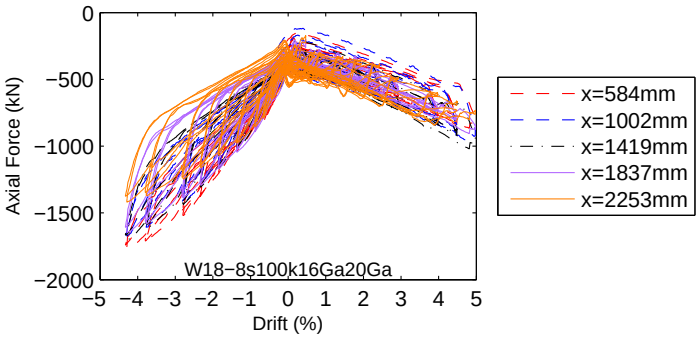

(b)

Figure B.36: W18-8s100k16Ga20Ga: Bottom HBE

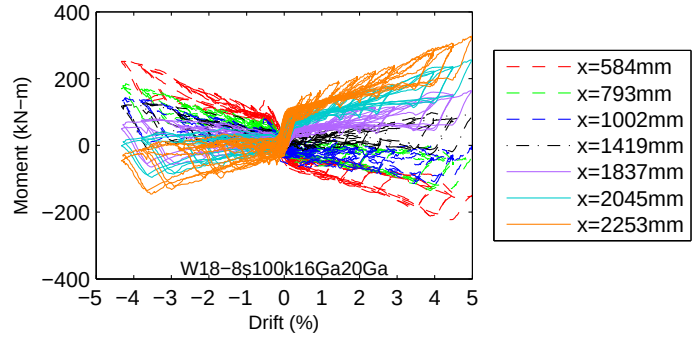

(a)

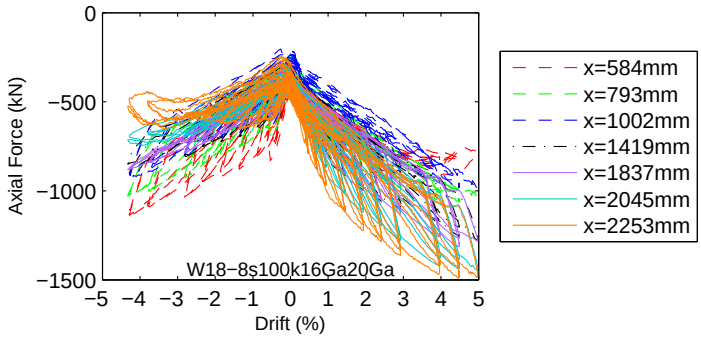

(b)

Figure B.37: W18-8s100k16Ga20Ga: Middle HBE

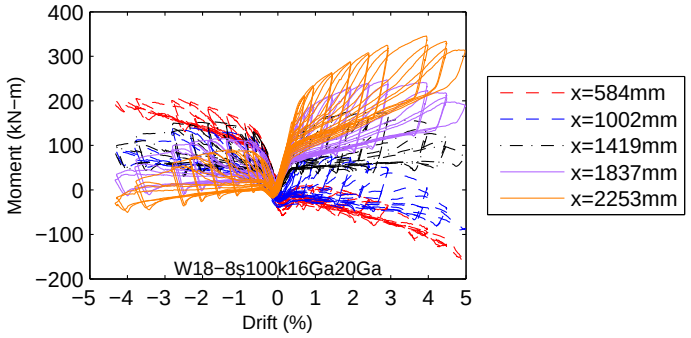

(a)

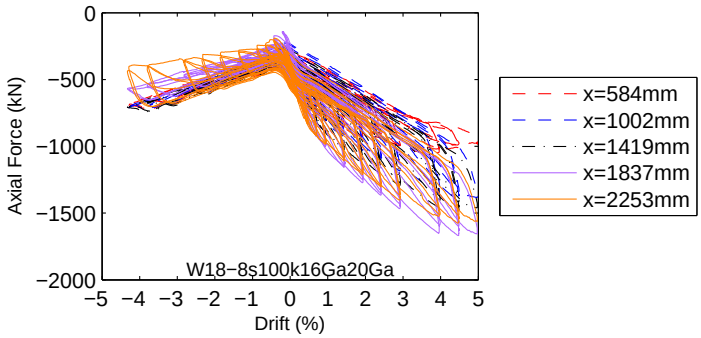

(b)

Figure B.38: W18-8s100k16Ga20Ga: Top HBE

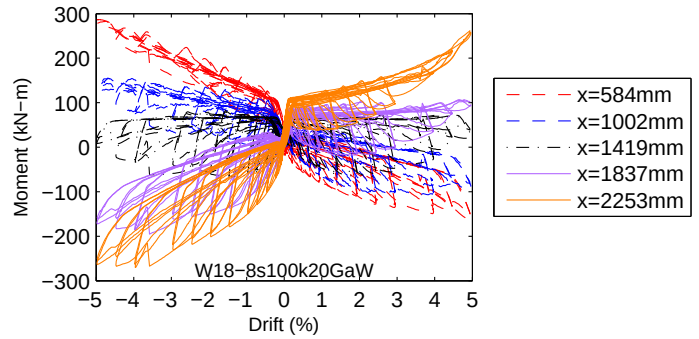

(a)

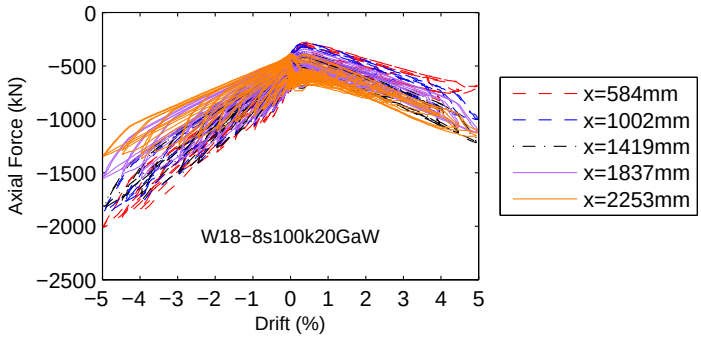

(b)

Figure B.39: W18-8s100k20GaW: Bottom HBE

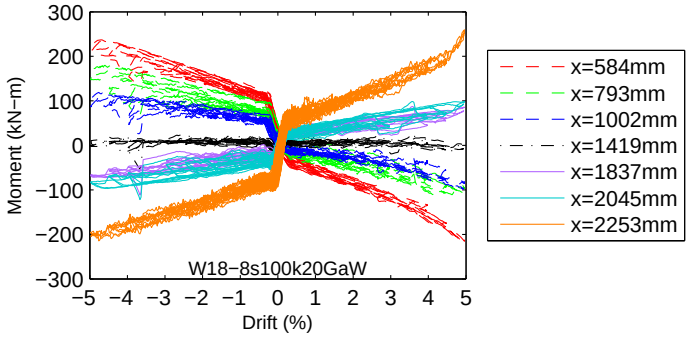

(a)

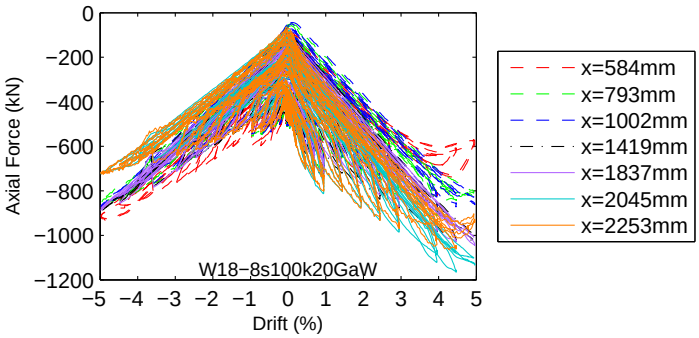

(b)

Figure B.40: W18-8s100k20GaW: Middle HBE

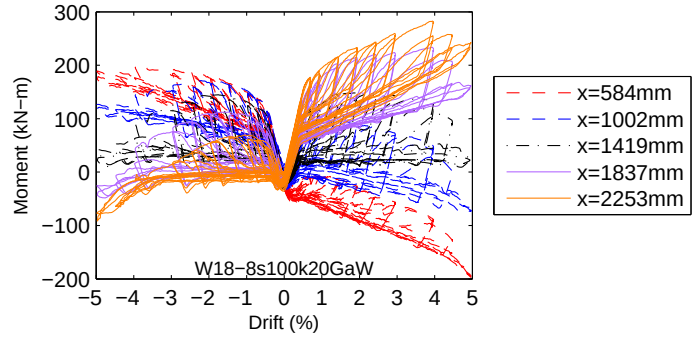

(a)

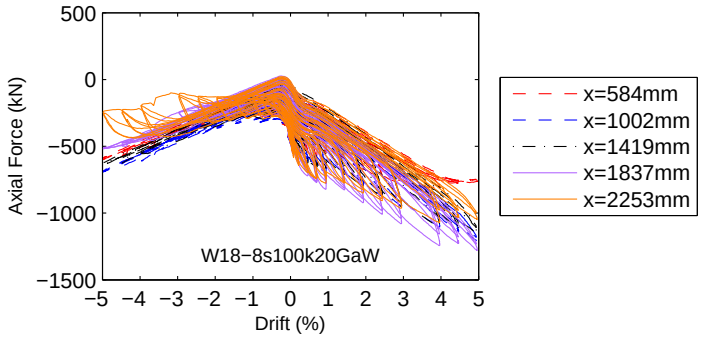

(b)

Figure B.41: W18-8s100k20GaW: Top HBE

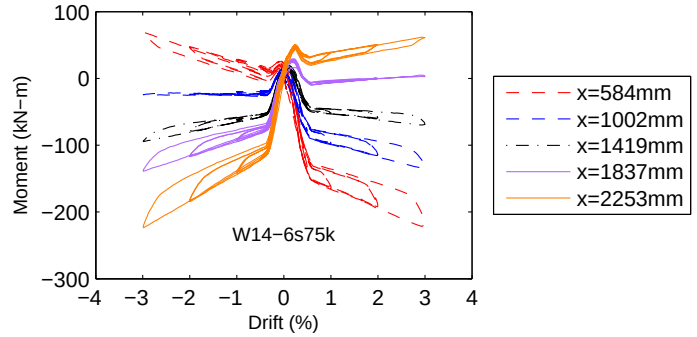

(a)

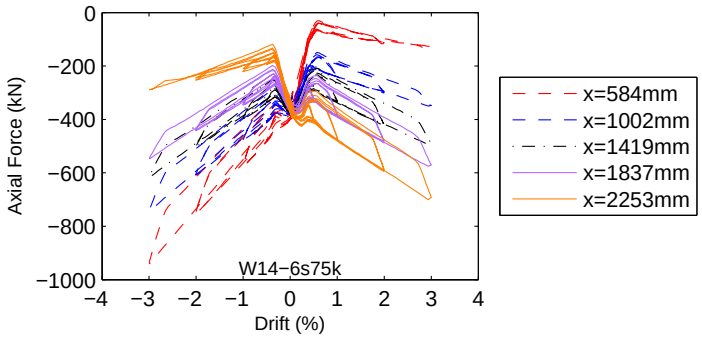

(b)

Figure B.42: W14-6s75k: Bottom HBE

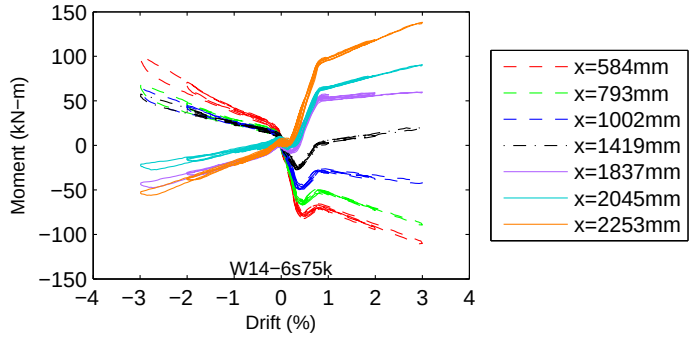

(a)

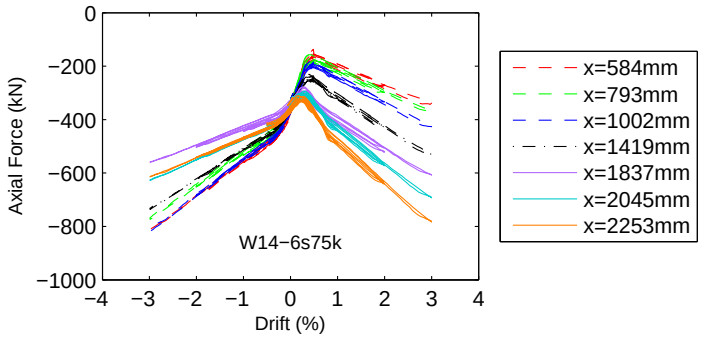

(b)

Figure B.43: W14-6s75k: Middle HBE

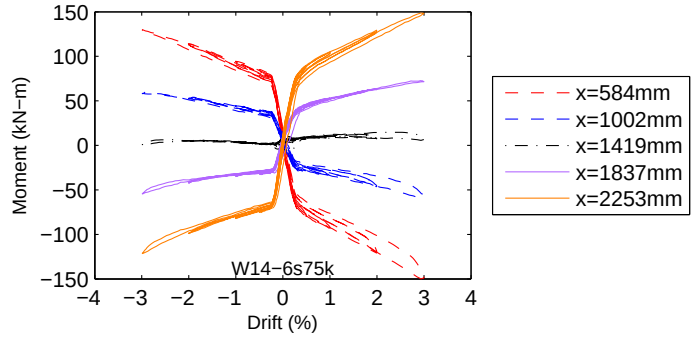

(a)

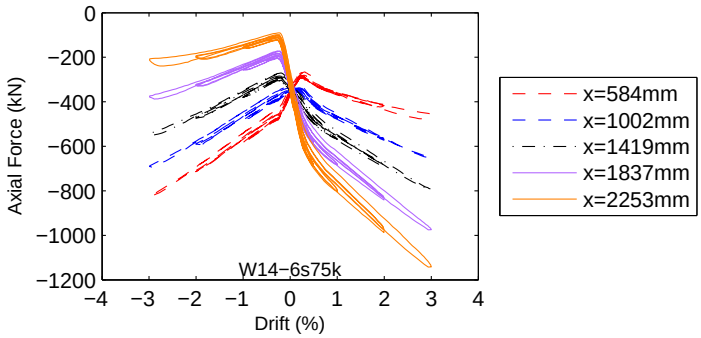

(b)

Figure B.44: W14-6s75k: Top HBE

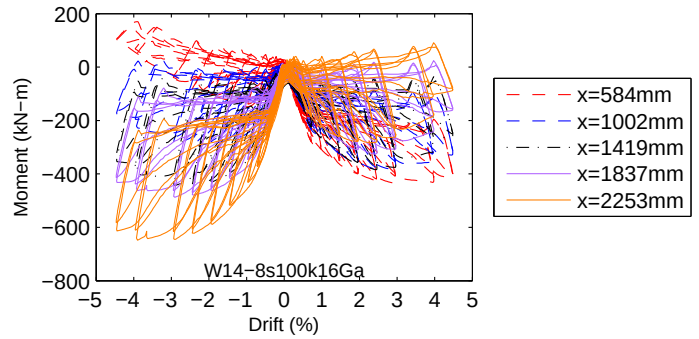

(a)

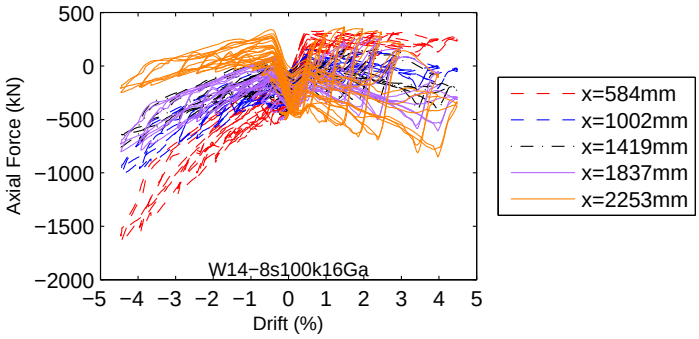

(b)

Figure B.45: W14-8s100k16Ga: Bottom HBE

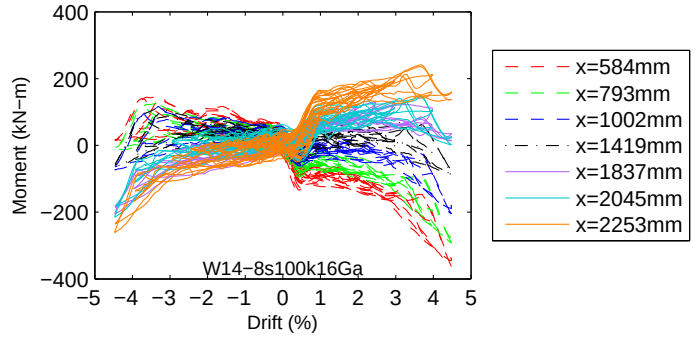

(a)

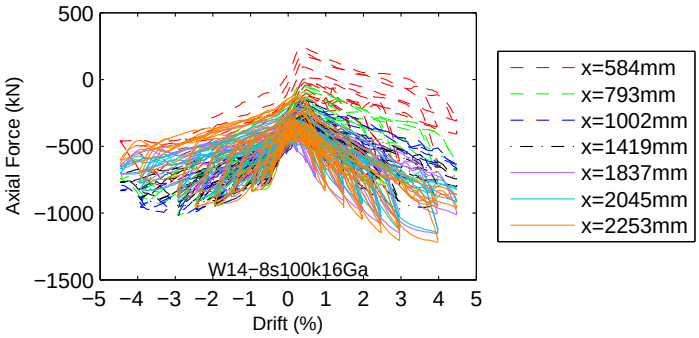

(b)

Figure B.46: W14-8s100k16Ga: Middle HBE

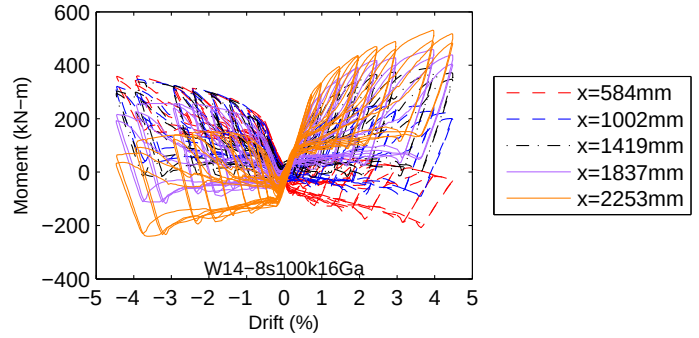

(a)

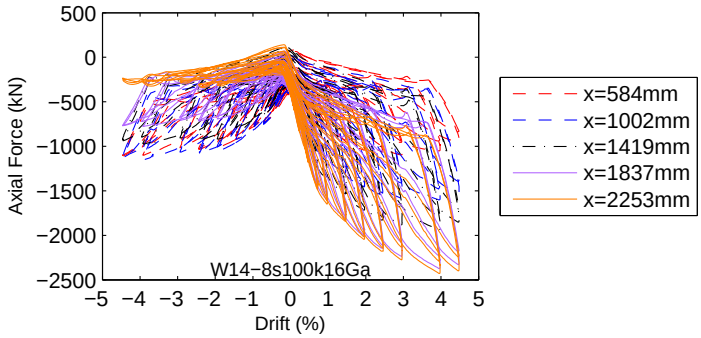

(b)

Figure B.47: W14-8s100k16Ga: Top HBE

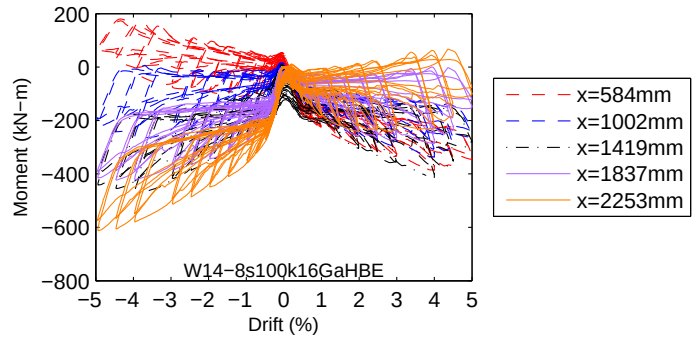

(a)

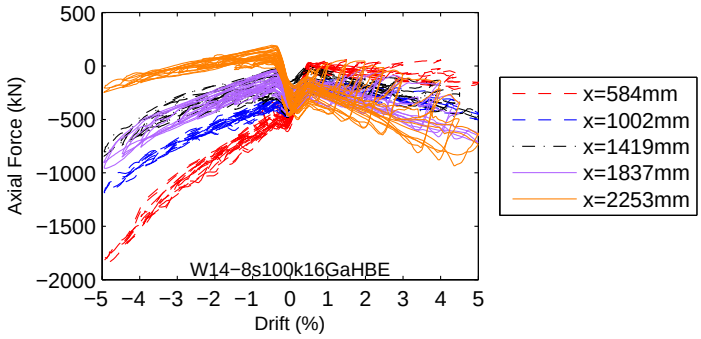

(b)

Figure B.48: W14-8s100k16GaHBE: Bottom HBE

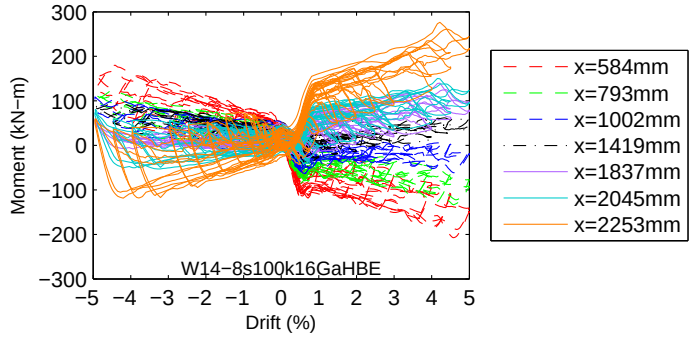

(a)

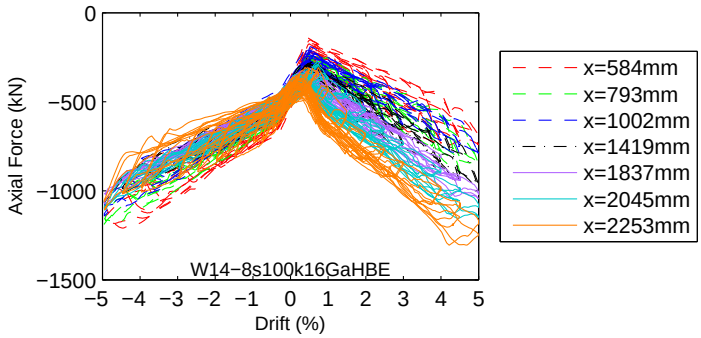

(b)

Figure B.49: W14-8s100k16GaHBE: Middle HBE

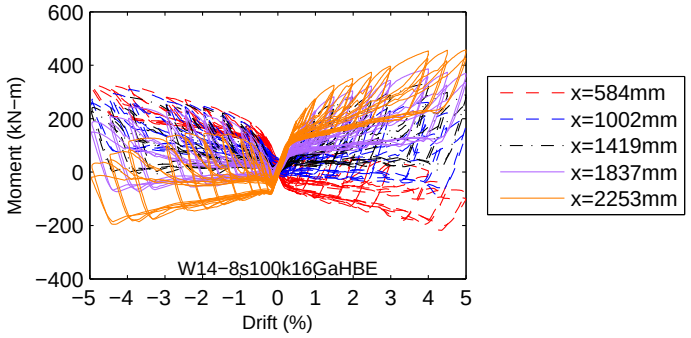

(a)

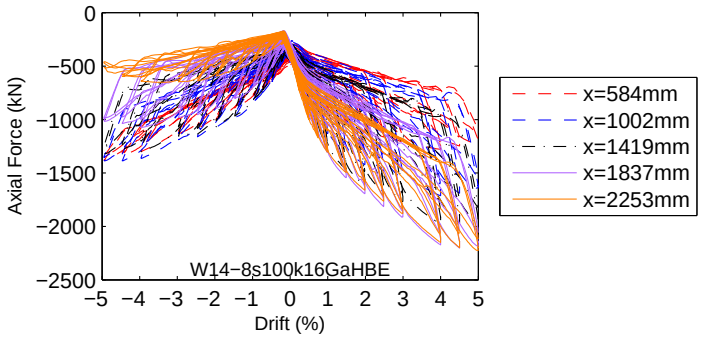

(b)

Figure B.50: W14-8s100k16GaHBE: Top HBE

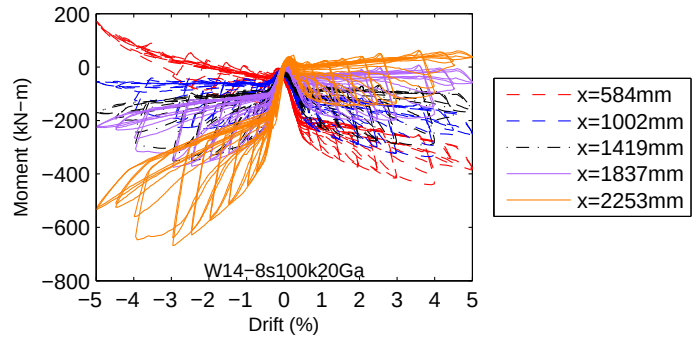

(a)

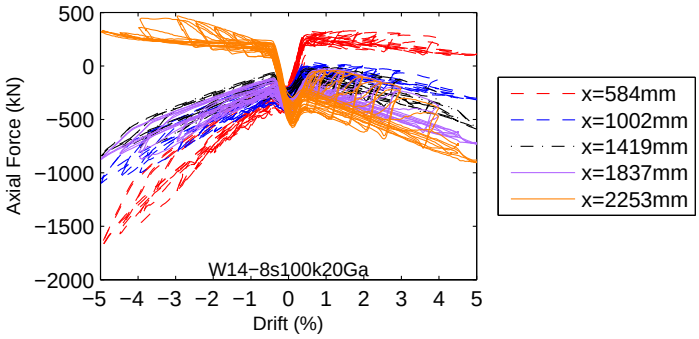

(b)

Figure B.51: W14-8s100k20Ga: Bottom HBE

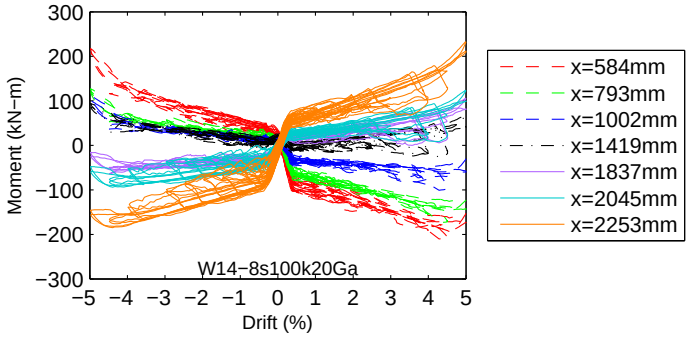

(a)

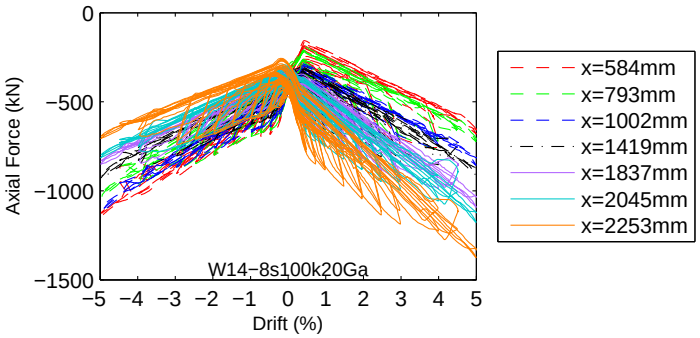

(b)

Figure B.52: W14-8s100k20Ga: Middle HBE

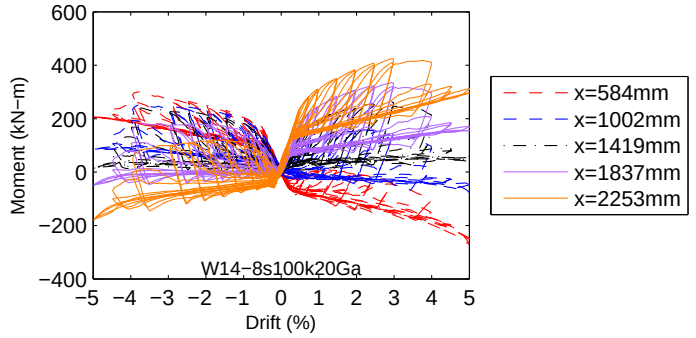

(a)

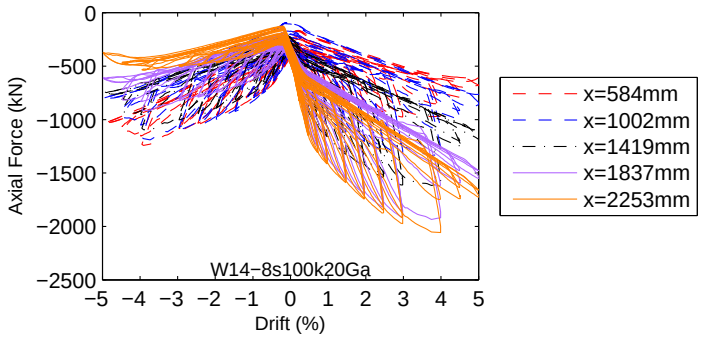

(b)

Figure B.53: W14-8s100k20Ga: Top HBE

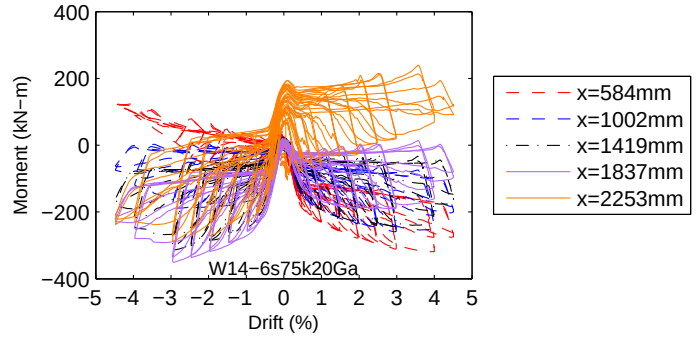

(a)

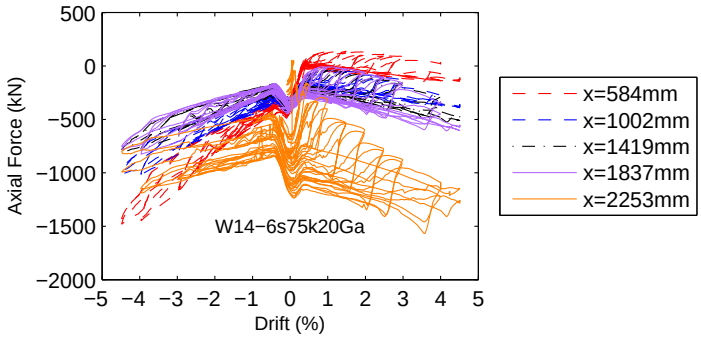

(b)

Figure B.54: W14-6s75k20Ga: Bottom HBE

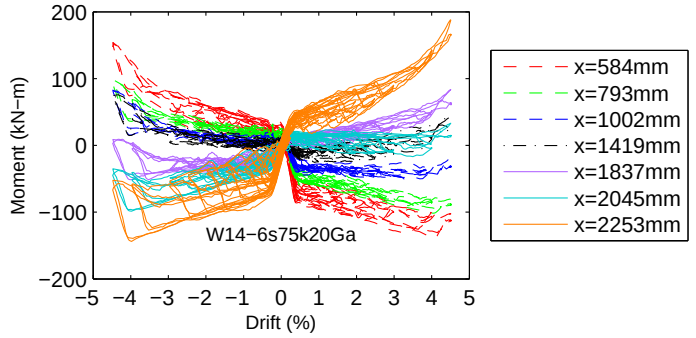

(a)

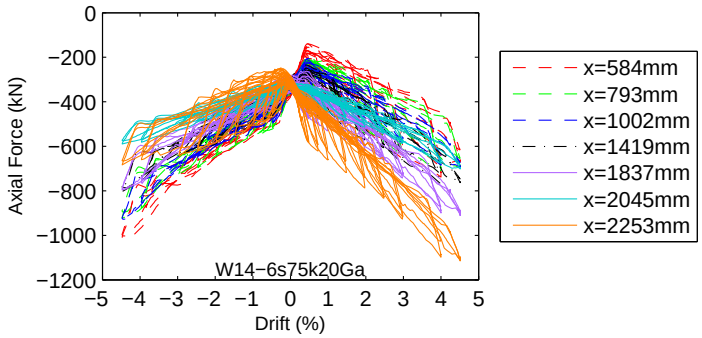

(b)

Figure B.55: W14-6s75k20Ga: Middle HBE

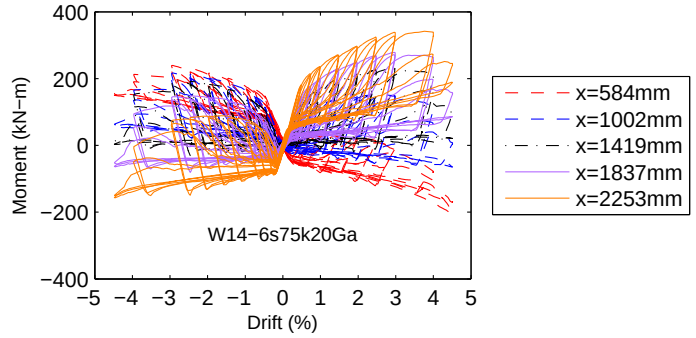

(a)

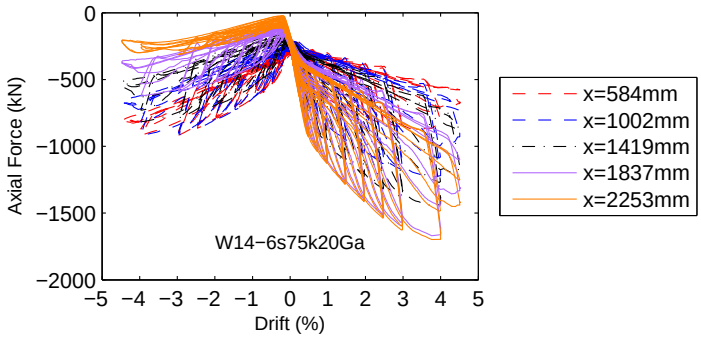

(b)

Figure B.56: W14-6s75k20Ga: Top HBE

B.3 PT losses

The PT loss vs. peak drift per cycle are plotted for each HBE (Bottom, Middle, and Top) for each specimen below. PT loss was calculated as the minimum PT force per cycle minus the minimum PT force in the first cycle of loading in each HBE.

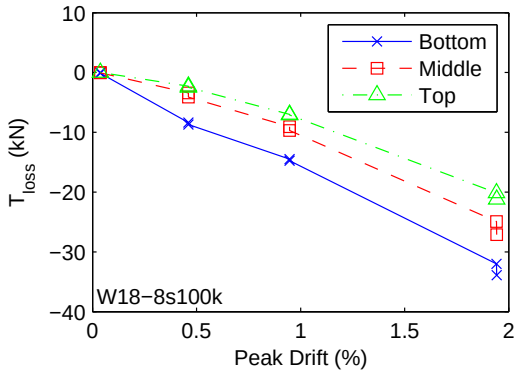

Figure B.57: W18-8s100k: PT losses

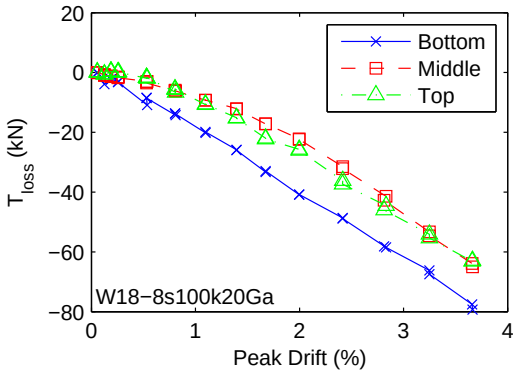

Figure B.58: W18-8s100k20Ga: PT losses

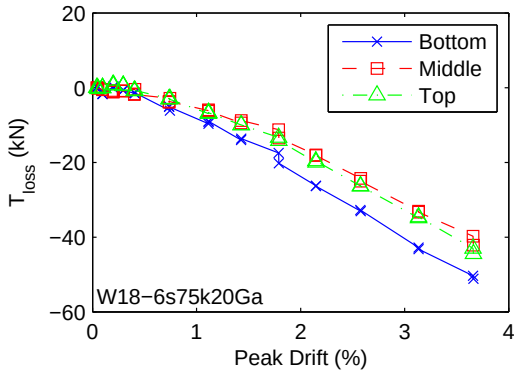

Figure B.59: W18-6s75k20Ga: PT losses

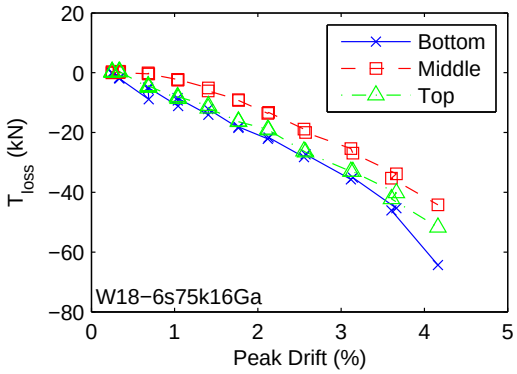

Figure B.60: W18-6s75k16Ga: PT losses

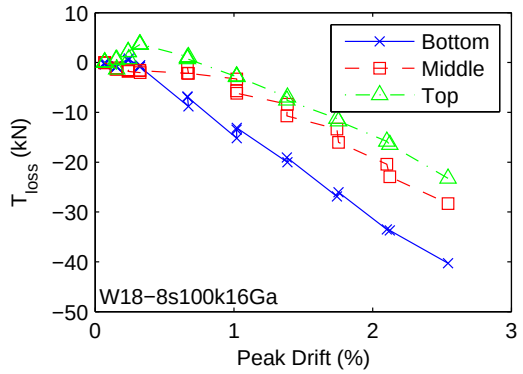

Figure B.61: W18-8s100k16Ga: PT losses

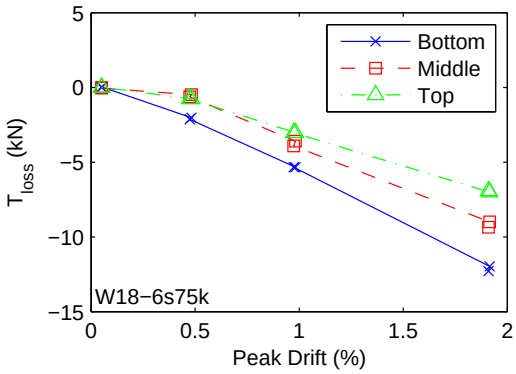

Figure B.62: W18-6s75k: PT losses

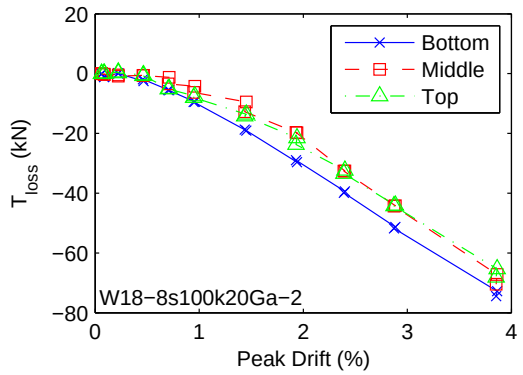

Figure B.63: W18-8s100k20Ga-2: PT losses

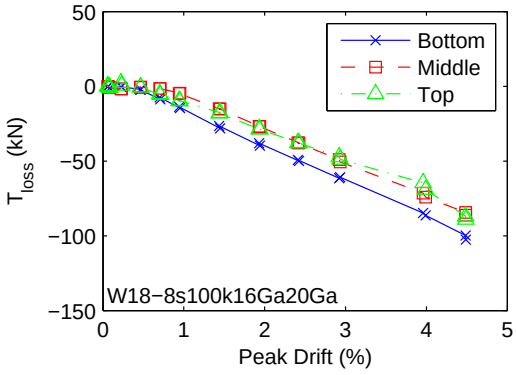

Figure B.64: W18-8s100k16Ga20Ga: PT losses

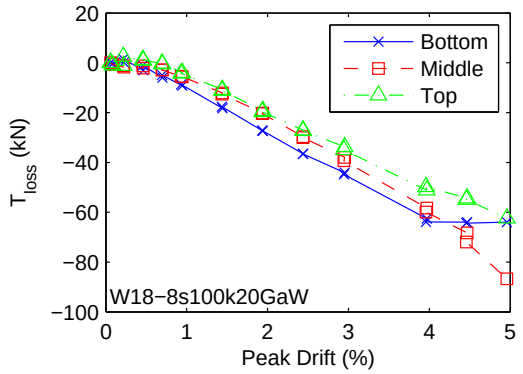

Figure B.65: W18-8s100k20GaW: PT losses

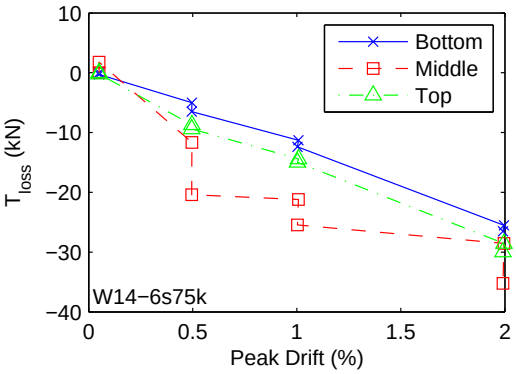

Figure B.66: W14-6s75k: PT losses

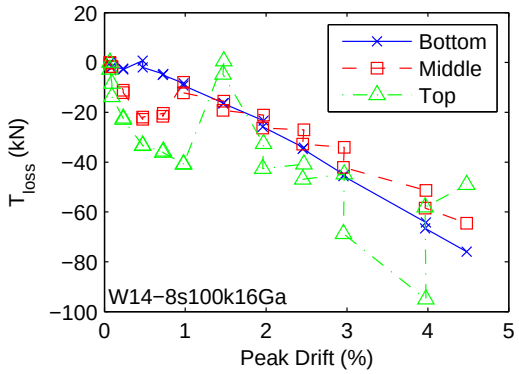

Figure B.67: W14-8s100k16Ga: PT losses

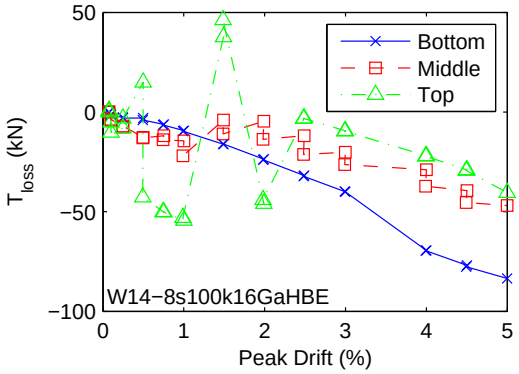

Figure B.68: W14-8s100k16GaHBE: PT losses

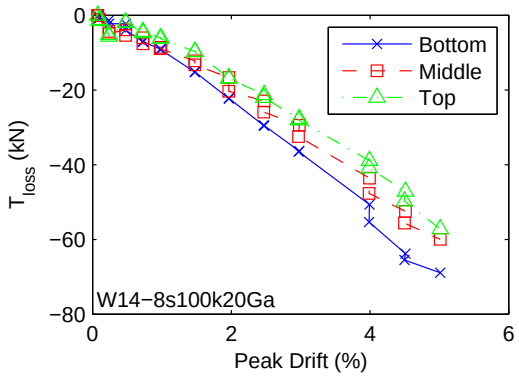

Figure B.69: W14-8s100k20Ga: PT losses

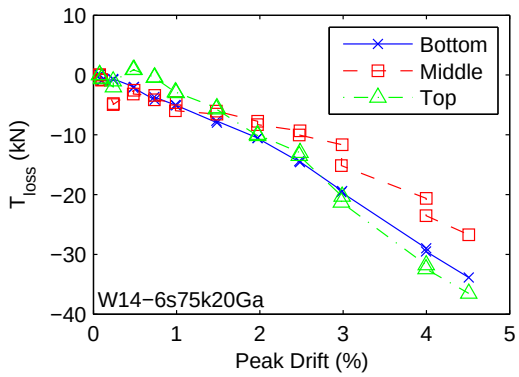

Figure B.70: W14-6s75k20Ga: PT losses

B.4 Web plate strains

Below are the web plate strains as measured from the uniaxial strain gages in specimens W18-8s100k20Ga-2, W18-8s100k16Ga20Ga, and W18-8s100k20GaW as shown in Fig. 4.7. The section number and angle correspond to the strain gage naming scheme (e.g. sgp1se2045 represents the first story web plate, section 2, oriented at 45◦ from horizontal). The cutout sections also correspond to the strain gage naming scheme (e.g. sgp1c40 represents the cutout in the first story at section 4, or south side of the middle HBE). Note that the strain gages for these specimens were only placed on one side of the web plate, and therefore include strains due to plate flexure[1]. Also note that the section numbers increase from the north side of the plate to the south (e.g. Sec. 2 is to the south, or right, of Sec. 1).

[1]Some of the strain gage data signals saturated at readings between 0.02 and 0.03, as indicated by the flat line in the reading.

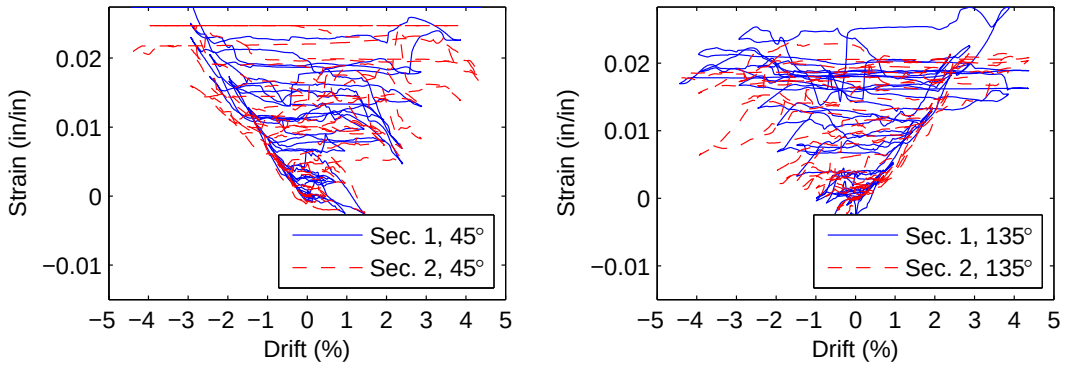

(a) 1st story along Middle HBE, 45°

(b) 1st story along Middle HBE, 135°

(c) 1st story middle of plate

(d) 1st story cutouts nearest Middle HBE

Figure B.71: W18-8s100k20Ga-2: web plate strains

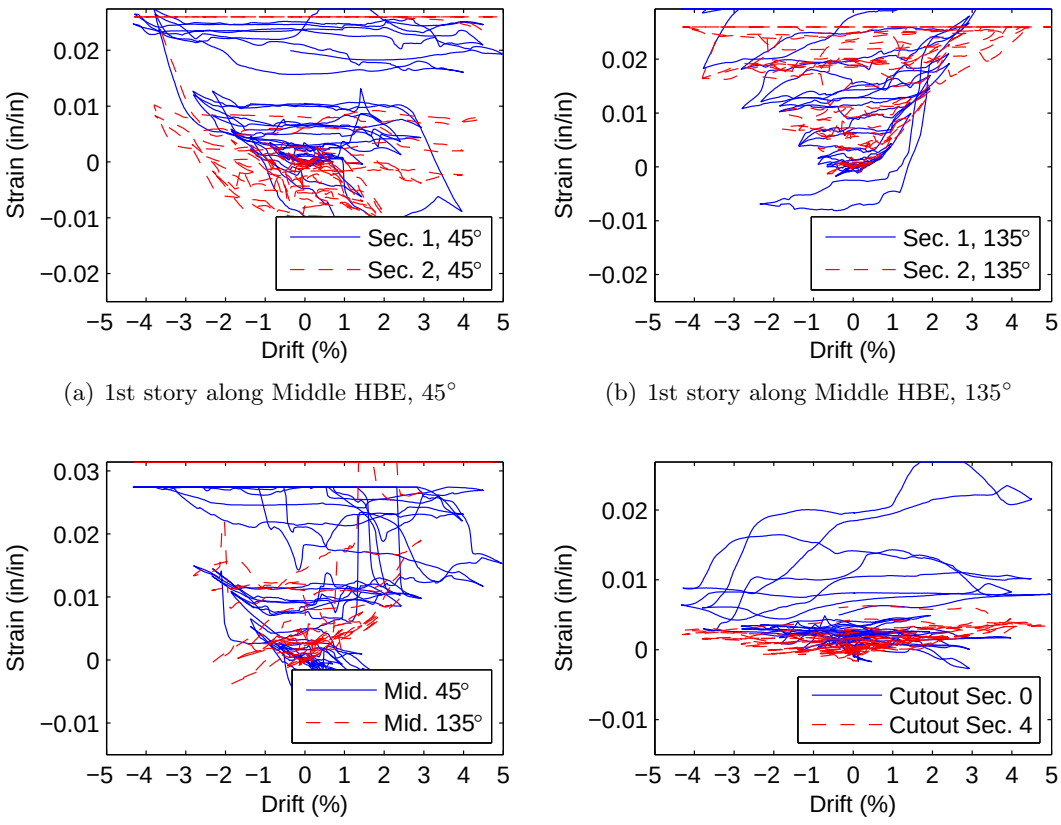

(a) 1st story along Middle HBE, 45°

(b) 1st story along Middle HBE, 135°

(c) 1st story middle of plate

(d) 1st story cutouts nearest Middle HBE

Figure B.72: W18-8s100k16Ga20Ga: web plate strains

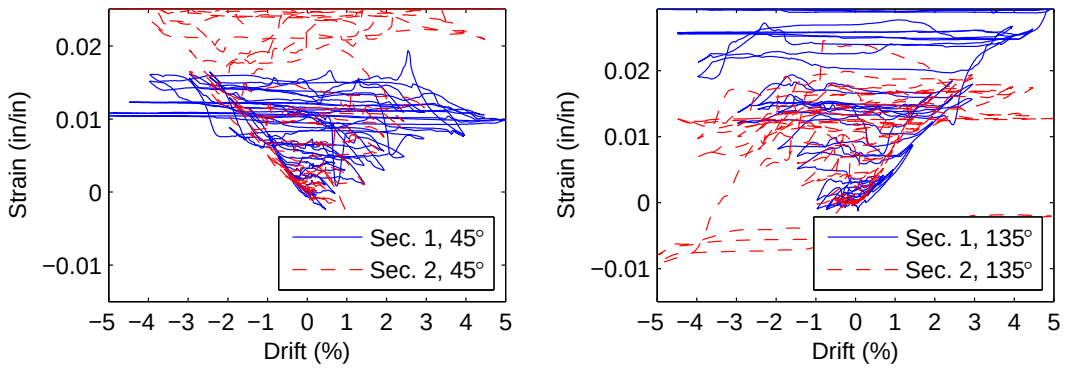

(a) 1st story along Middle HBE, 45°

(b) 1st story along Middle HBE, 135°

(c) 1st story middle of plate

(d) 1st story cutouts nearest Middle HBE

Figure B.73: W18-8s100k20GaW: web plate strains

Specimens W14-8s100k20Ga and W14-6s75k20Ga had strain gage rosettes or uniaxial gages that were placed on both sides of the web plate at the same location. The average of the gages at the same location but on opposite sides of the plate were taken as an approximation of the mid-thickness strain. The results plotted below represent the mid-thickness strain approximations. The rosettes were used to calculate principal strains (ϵ_1 and ϵ_2) and direction (α_{exp} is taken as the angle from vertical, or parallel to the VBEs). The principal strains and directions at peak positive and negative drift values are shown int he figures below. Again the section numbers are increasing from north to south.

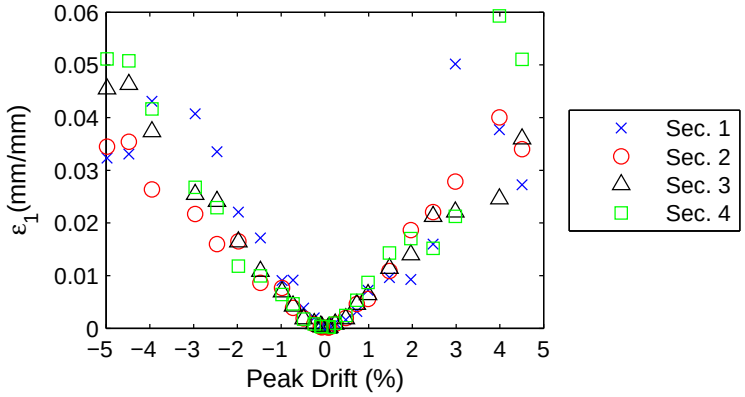

(a)

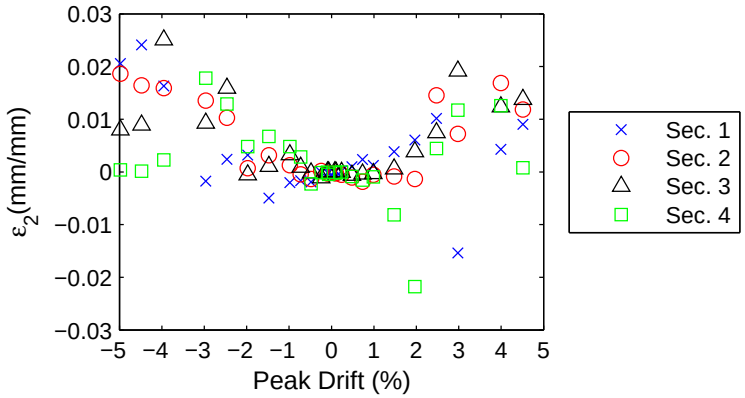

(b)

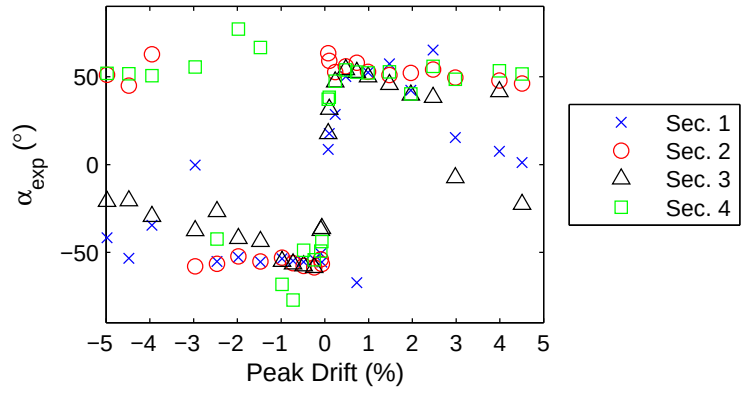

(c)

Figure B.74: W14-8s100k20Ga: 1st story along middle HBE, principal strains and directions

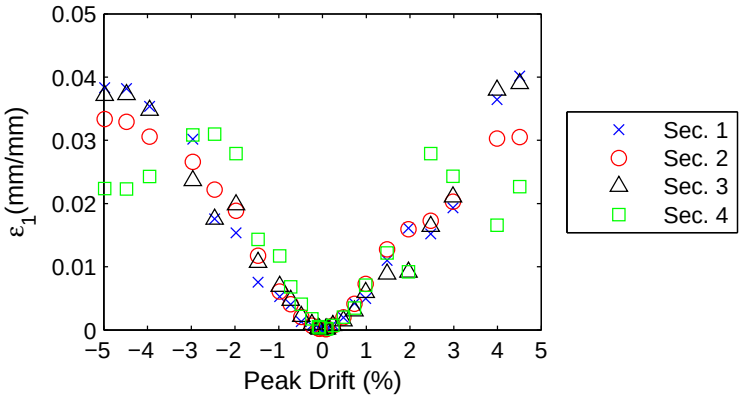

(a)

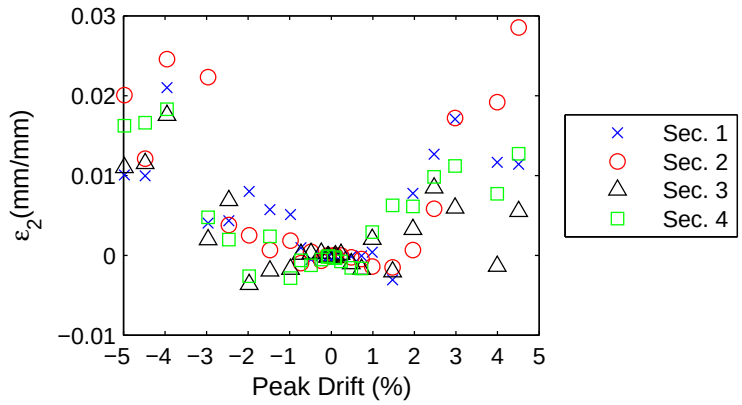

(b)

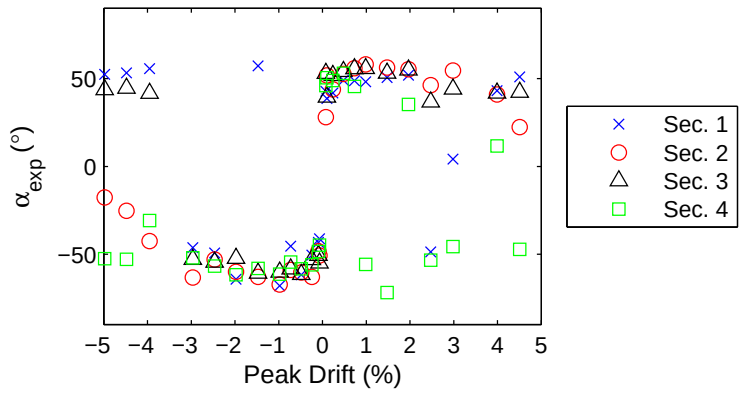

(c)

Figure B.75: W14-8s100k20Ga: 2nd story along middle HBE, principal strains and directions

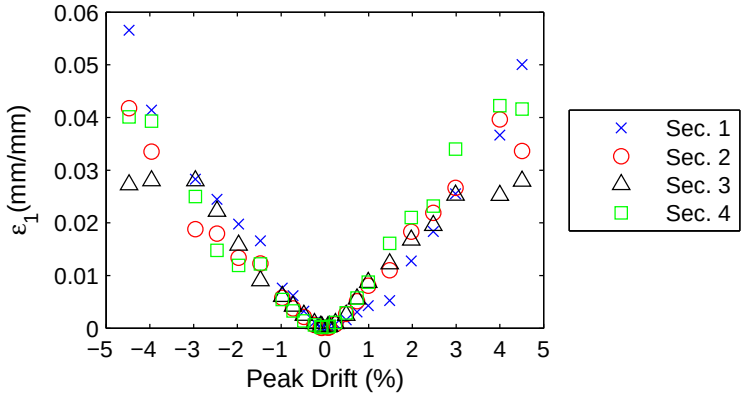

(a)

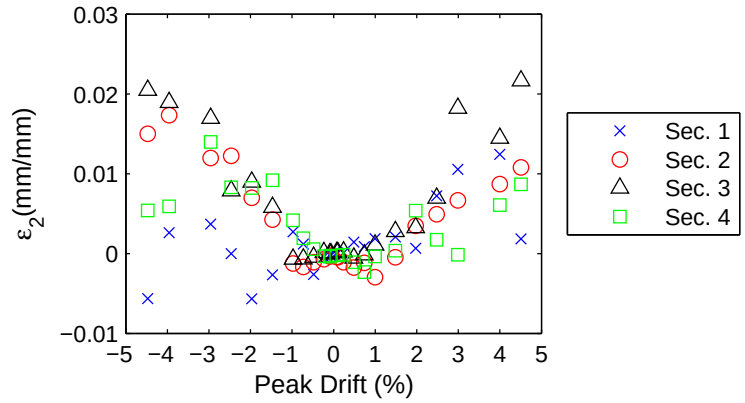

(b)

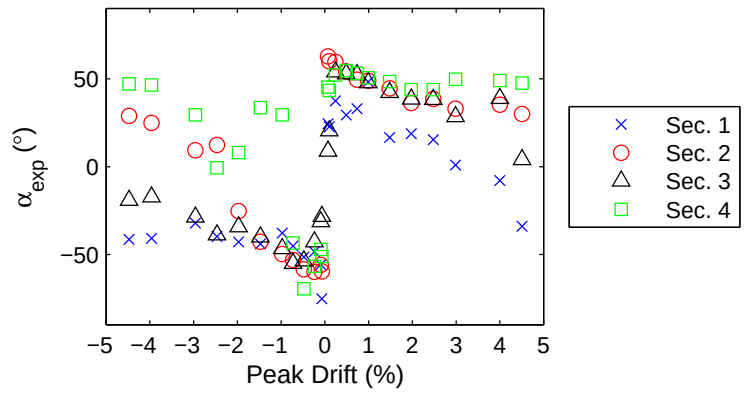

(c)

Figure B.76: W14-6s75k20Ga: 1st story along middle HBE, principal strains and directions

Appendix C

ADDITIONAL FIGURES FOR OPENSEES MODELS OF SUBASSEMBLY TESTS

The following figures show comparisons between the SC-SPSW subassembly test experimental and OpenSees numerical model global and component responses. These figures are provided as supplements to the explanations and model descriptions provided in Sec. 7.2.3. In some cases where certain data was faulty (e.g. due to a potentiometer malfunction or faulty strain gage data) the figure is either removed (it the data is unavailable) or an explanatory note describing the unexpected observed behavior is provided in the caption.

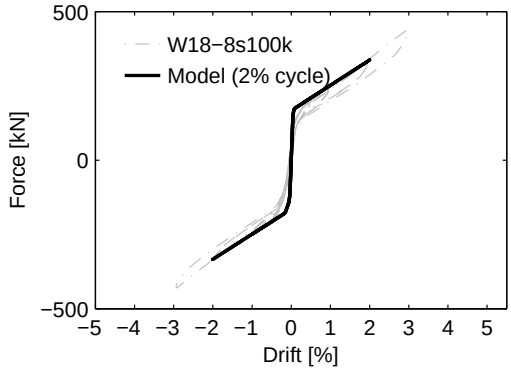

(a) W18-8s100k: PT frame model

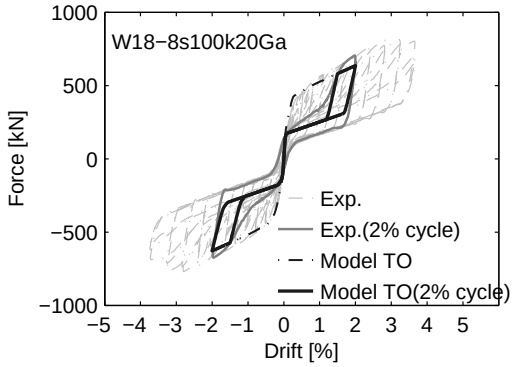

(b) W18-8s100k20Ga: Tension-only strip model

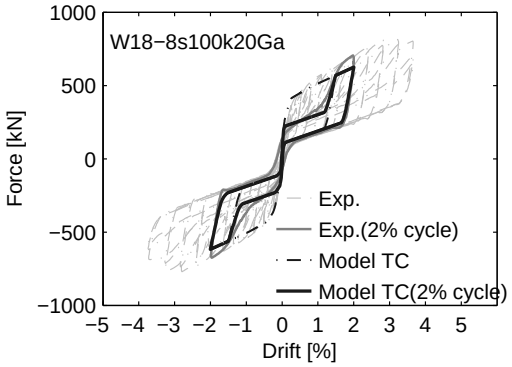

(c) W18-8s100k20Ga: Tension-compression strip model

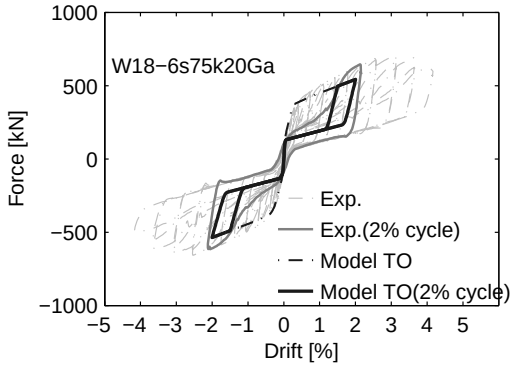

(d) W18-6s75k20Ga: Tension-only strip model

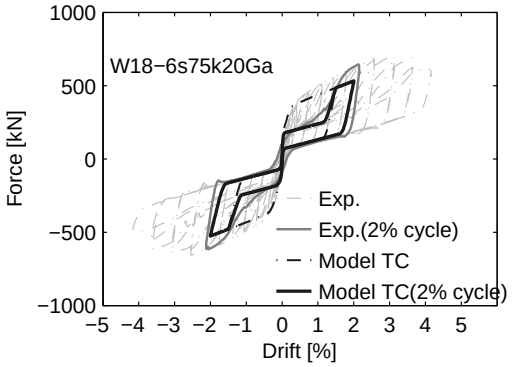

(e) W18-6s75k20Ga: Tension-compression strip model

Figure C.1: Comparison of OpenSees model and experimental global force vs. drift responses

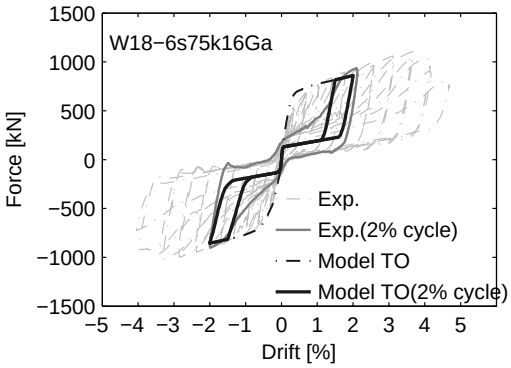

(f) W18-6s75k16Ga: Tension-only strip model

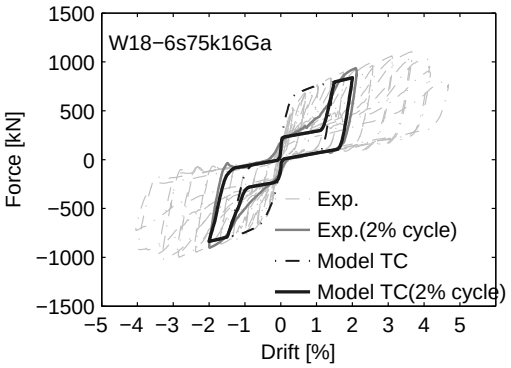

(g) W18-6s75k16Ga: Tension-compression strip model

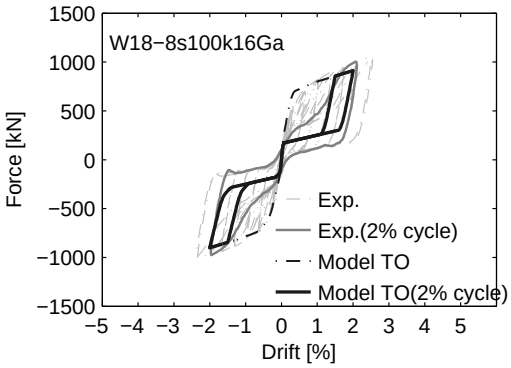

(h) W18-8s100k16Ga: Tension-only strip model

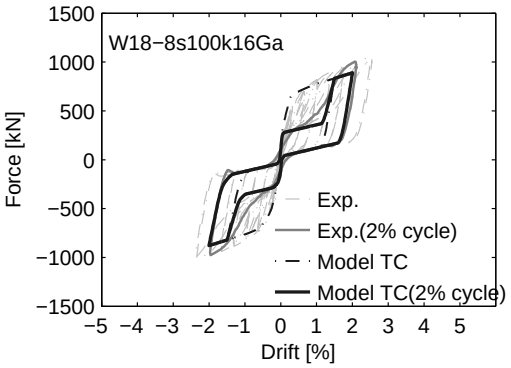

(i) W18-8s100k16Ga: Tension-compression strip model

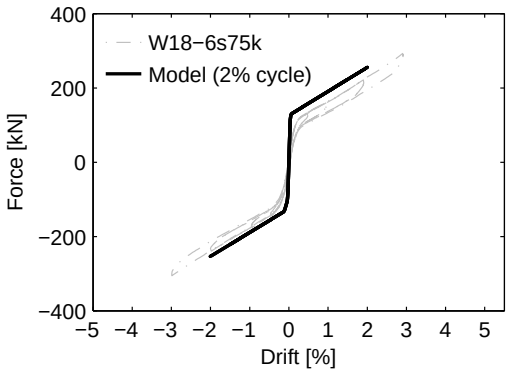

(j) W18-6s75k: PT frame model

Figure C.1: Comparison of OpenSees model and experimental global force vs. drift responses (cont.)

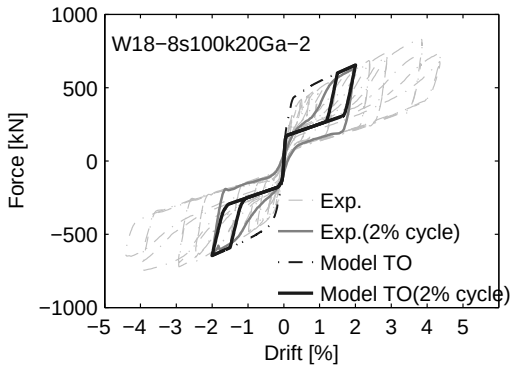

(k) W18-8s100k20Ga-2: Tension-only strip model

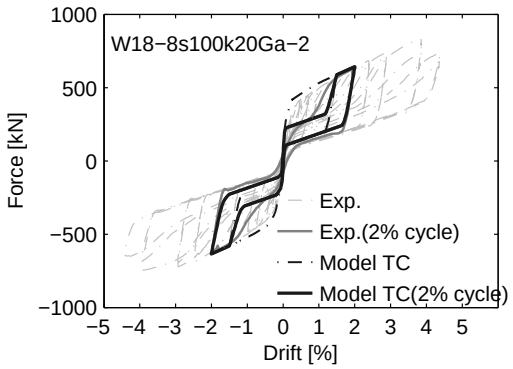

(l) W18-8s100k20Ga-2: Tension-compression strip model

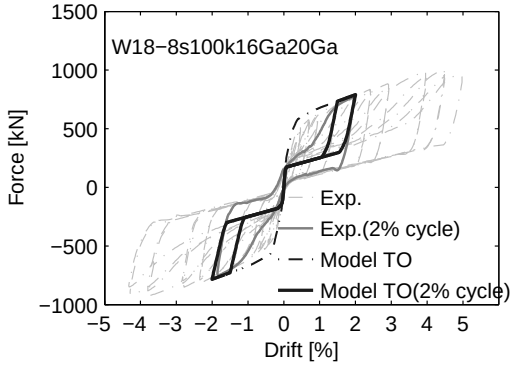

(m) W18-8s100k16Ga20Ga: Tension-only strip model

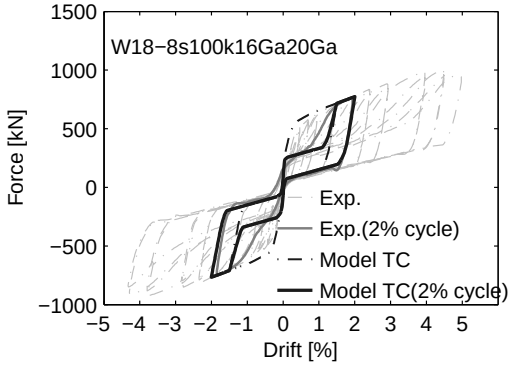

(n) W18-8s100k16Ga20Ga: Tension-compression strip model

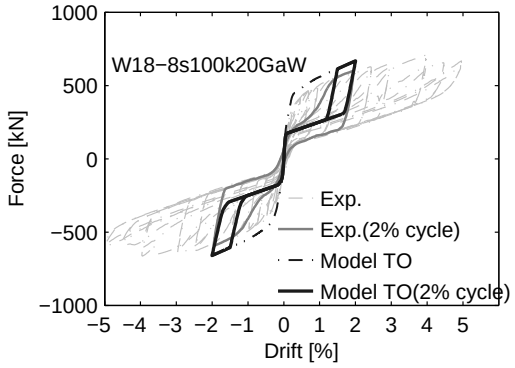

(o) W18-8s100k20GaW: Tension-only strip model

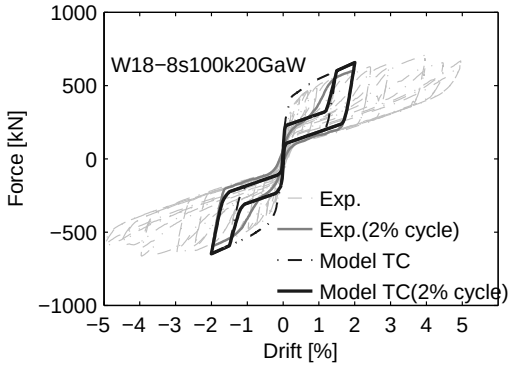

(p) W18-8s100k20GaW: Tension-compression strip model

Figure C.1: Comparison of OpenSees model and experimental global force vs. drift responses (cont.)

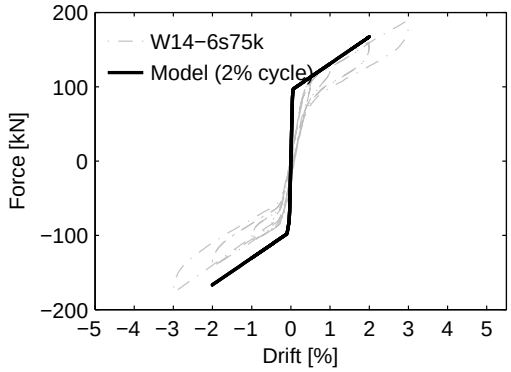

(q) W14-6s75k: PT frame model

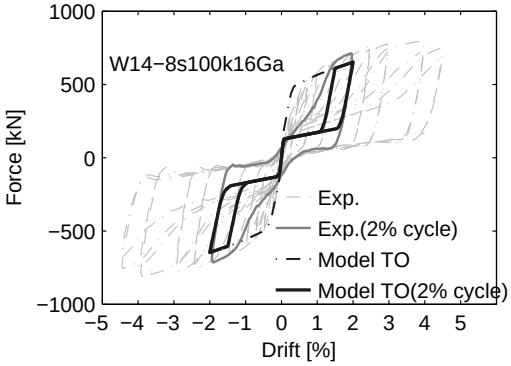

(r) W14-8s100k16Ga: Tension-only strip model

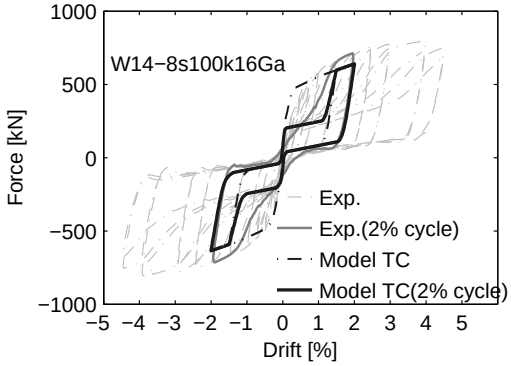

(s) W14-8s100k16Ga: Tension-compression strip model

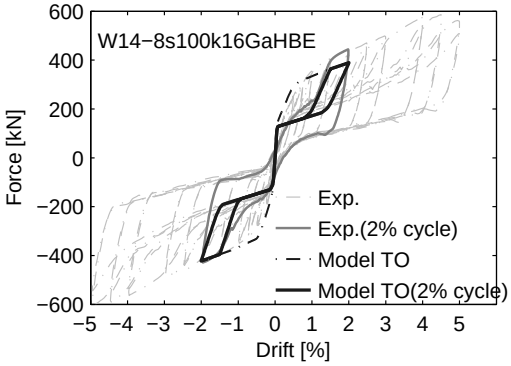

(t) W14-8s100k16GaHBE: Tension-only strip model

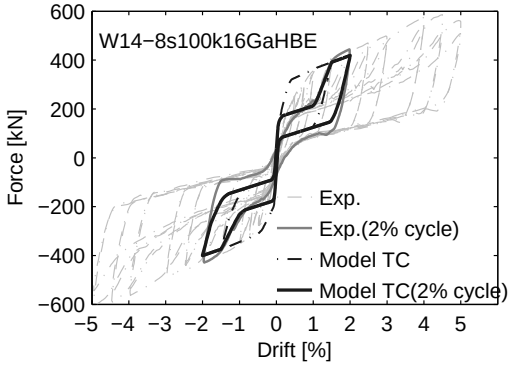

(u) W14-8s100k16GaHBE: Tension-compression strip model

Figure C.1: Comparison of OpenSees model and experimental global force vs. drift responses (cont.)

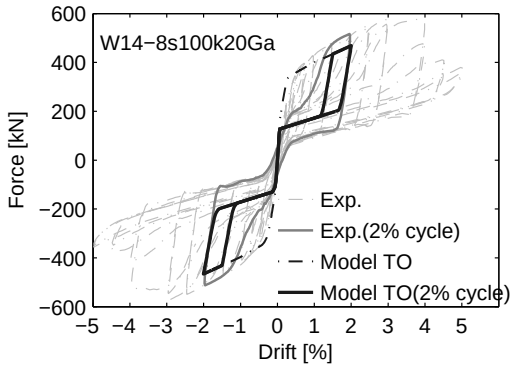

(v) W14-8s100k20Ga: Tension-only strip model

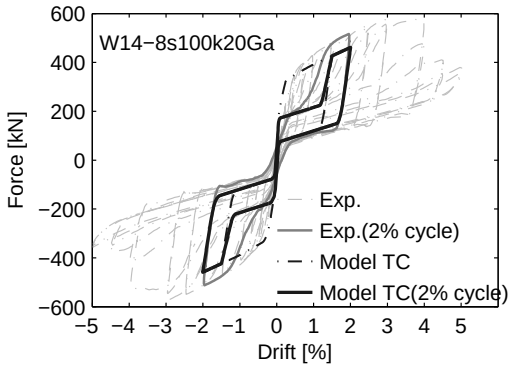

(w) W14-8s100k20Ga: Tension-compression strip model

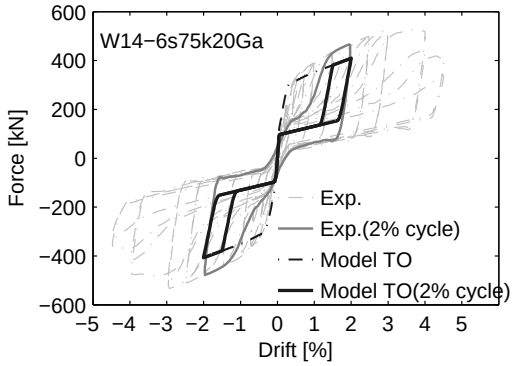

(x) W14-6s75k20Ga: Tension-only strip model

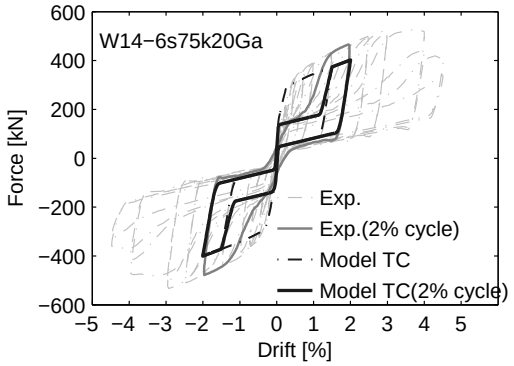

(y) W14-6s75k20Ga: Tension-compression strip model

Figure C.1: Comparison of OpenSees model and experimental global force vs. drift responses (cont.)

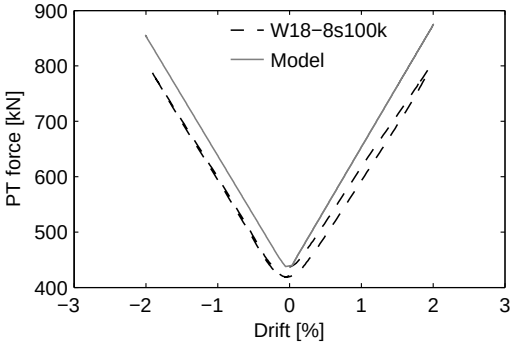

(a) Middle HBE PT force vs. drift response

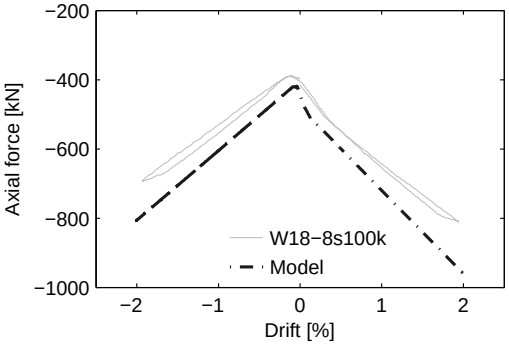

(b) Middle HBE average axial force vs. drift response

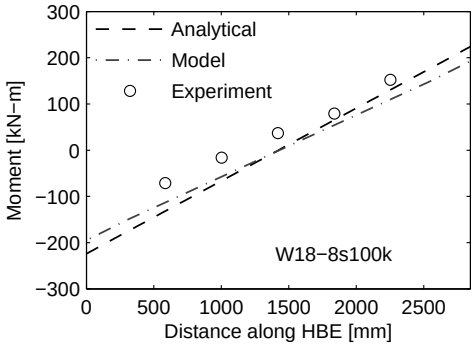

(c) Middle HBE moment distribution: approx. +2% drift

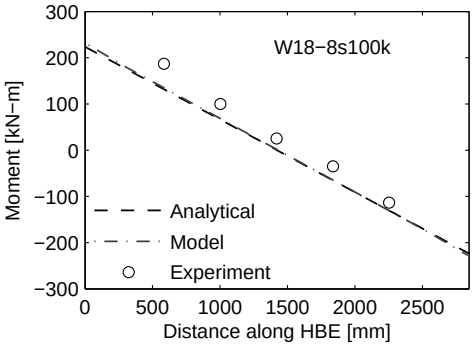

(d) Middle HBE moment distribution: approx. -2% drift

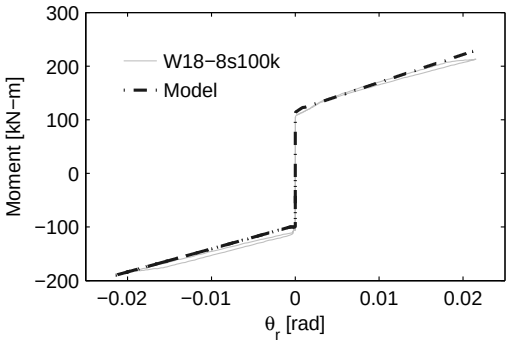

(e) Middle HBE connection moment: North end

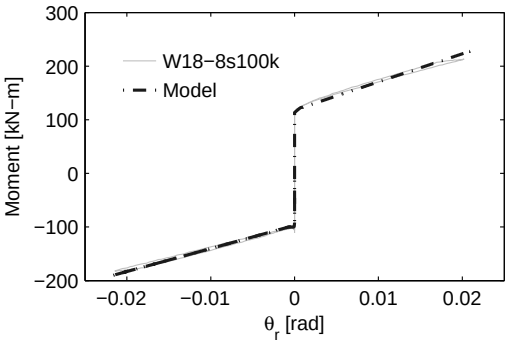

(f) Middle HBE connection moment: South end

Figure C.2: W18-8s100k: Comparison of OpenSees model and experimental component responses during 2% cycle

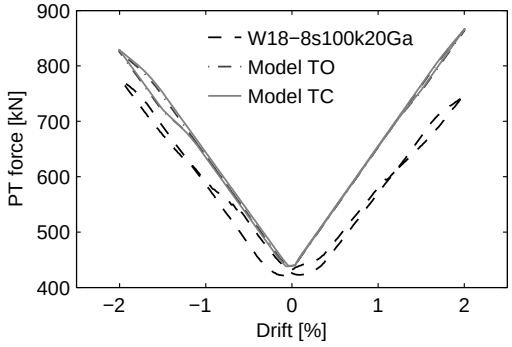

(a) Middle HBE PT force vs. drift response

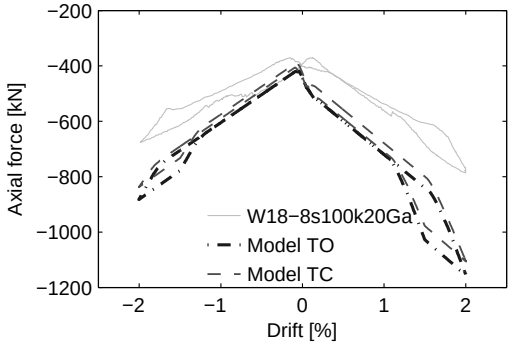

(b) Middle HBE average axial force vs. drift response

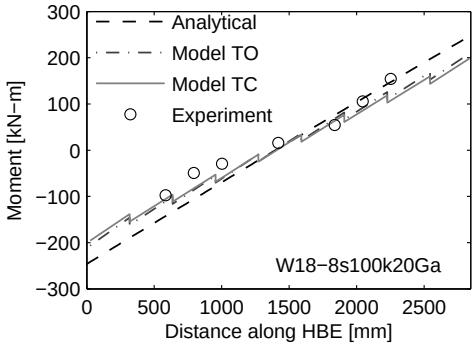

(c) Middle HBE moment distribution: approx. +2% drift

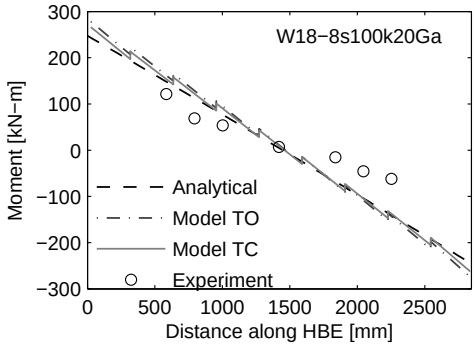

(d) Middle HBE moment distribution: approx. -2% drift

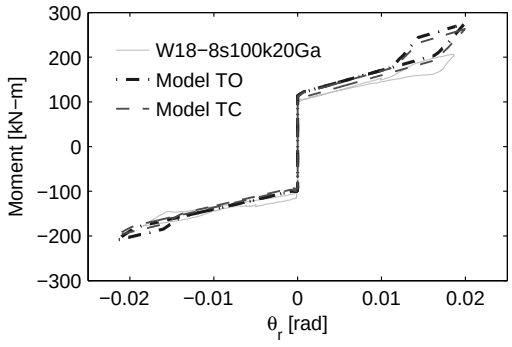

(e) Middle HBE connection moment: North end

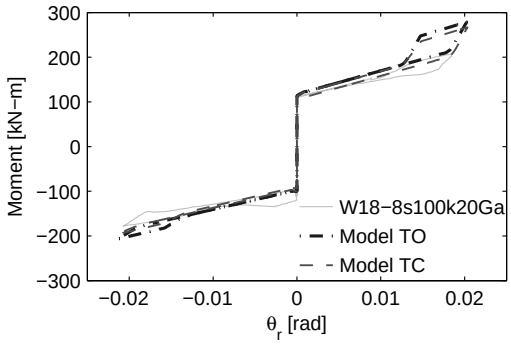

(f) Middle HBE connection moment: South end

Figure C.3: W18-8s100k20Ga: Comparison of OpenSees model and experimental component responses during 2% cycle

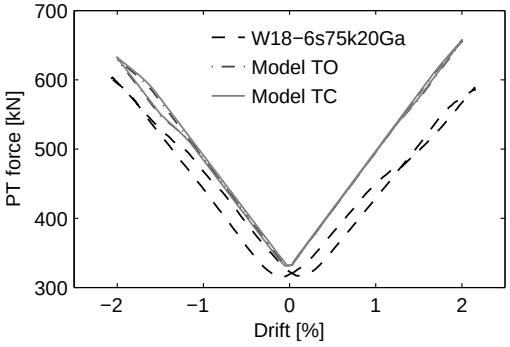

(a) Middle HBE PT force vs. drift response

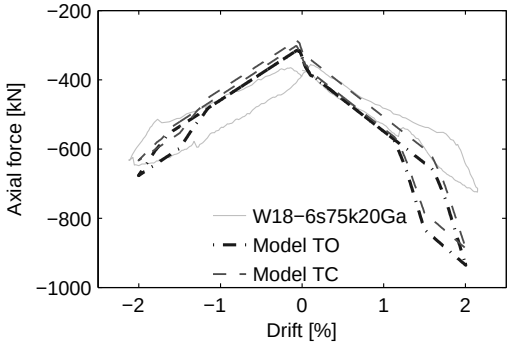

(b) Middle HBE average axial force vs. drift response

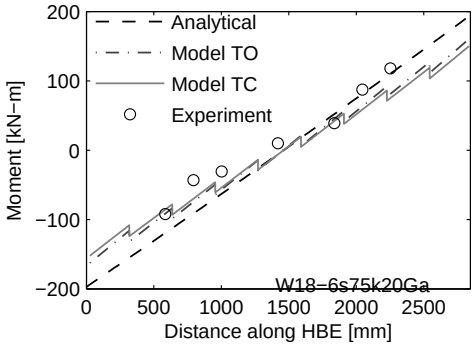

(c) Middle HBE moment distribution: approx. +2% drift

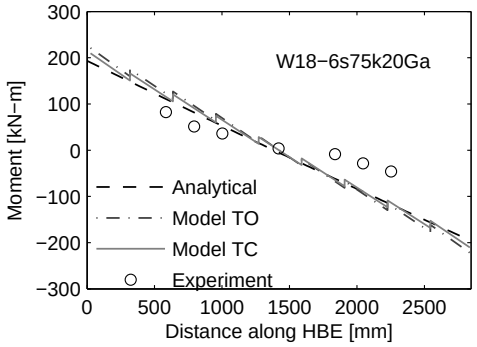

(d) Middle HBE moment distribution: approx. -2% drift

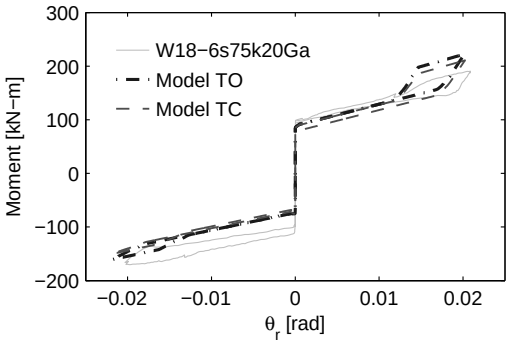

(e) Middle HBE connection moment: North end

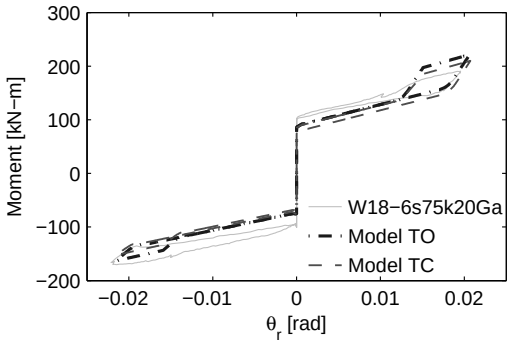

(f) Middle HBE connection moment: South end

Figure C.4: W18-6s75k20Ga: Comparison of OpenSees model and experimental component responses during 2% cycle

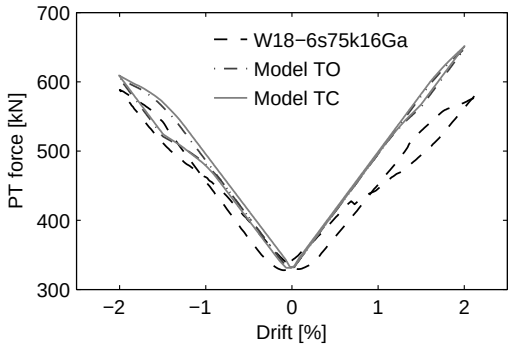

(a) Middle HBE PT force vs. drift response

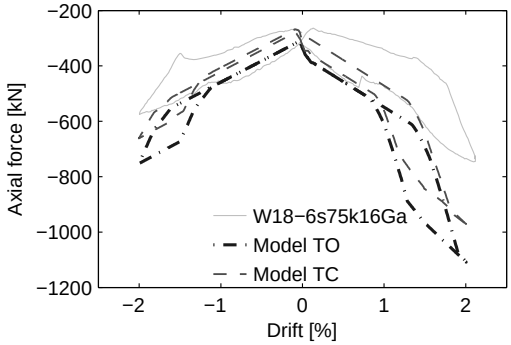

(b) Middle HBE average axial force vs. drift response

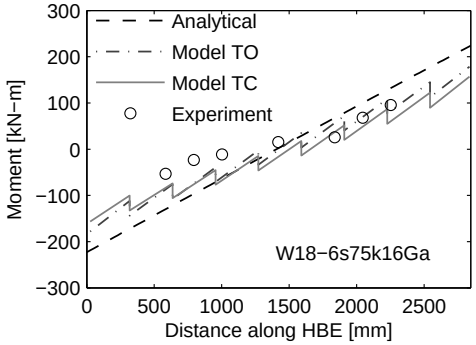

(c) Middle HBE moment distribution: approx. +2% drift

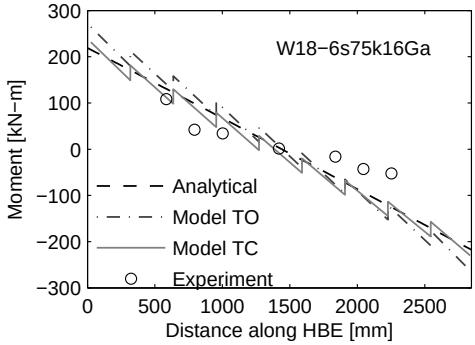

(d) Middle HBE moment distribution: approx. -2% drift

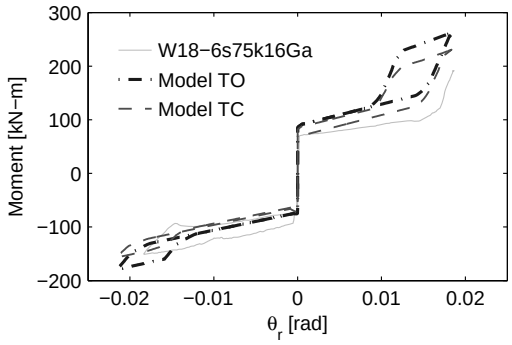

(e) Middle HBE connection moment: North end

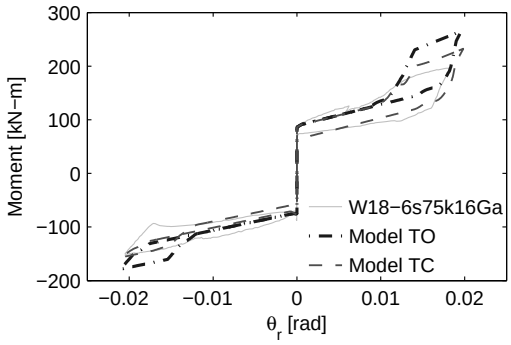

(f) Middle HBE connection moment: South end

Figure C.5: W18-6s75k16Ga: Comparison of OpenSees model and experimental component responses during 2% cycle

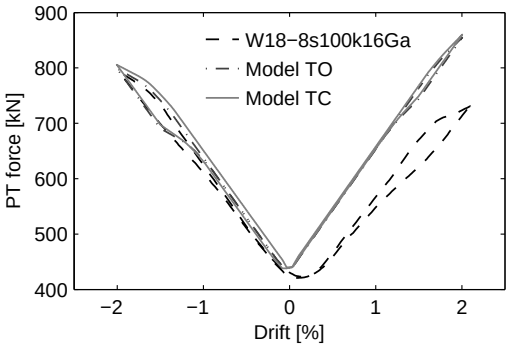

(a) Middle HBE PT force vs. drift response

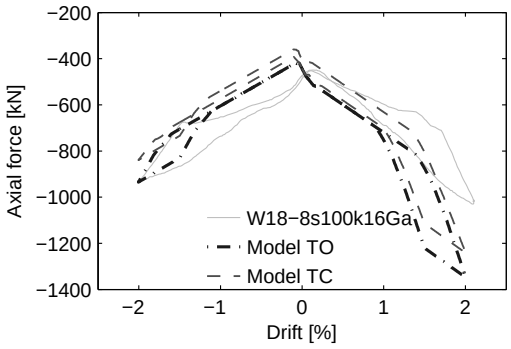

(b) Middle HBE average axial force vs. drift response

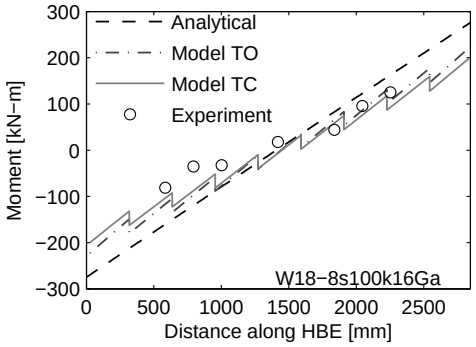

(c) Middle HBE moment distribution: approx. +2% drift

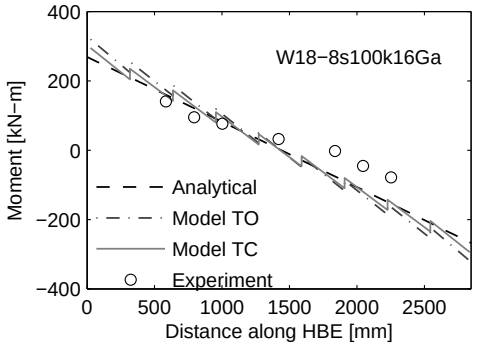

(d) Middle HBE moment distribution: approx. -2% drift

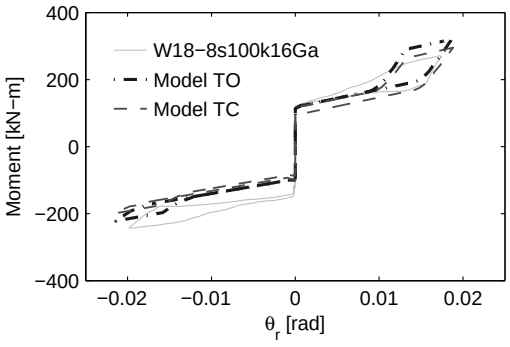

(e) Middle HBE connection moment: North end

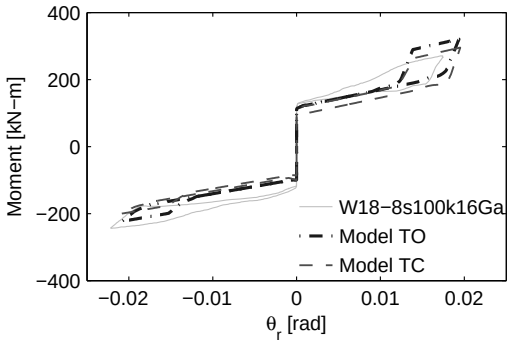

(f) Middle HBE connection moment: South end

Figure C.6: W18-8s100k16Ga: Comparison of OpenSees model and experimental component responses during 2% cycle

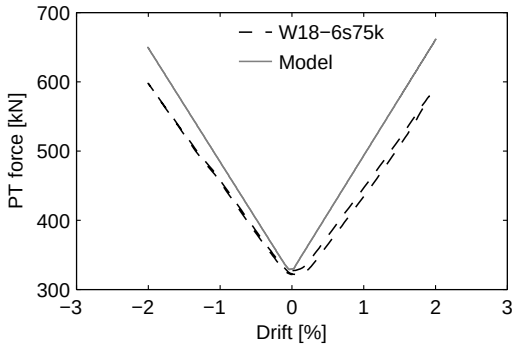

(a) Middle HBE PT force vs. drift response

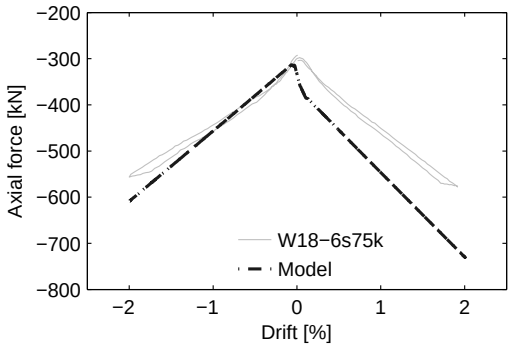

(b) Middle HBE average axial force vs. drift response

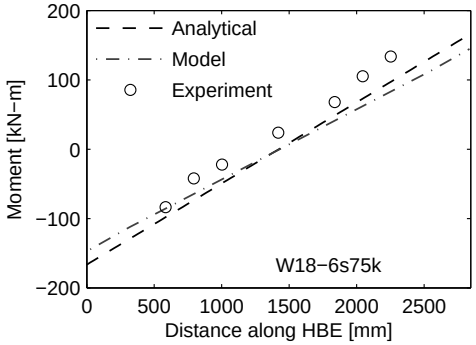

(c) Middle HBE moment distribution: approx. +2% drift

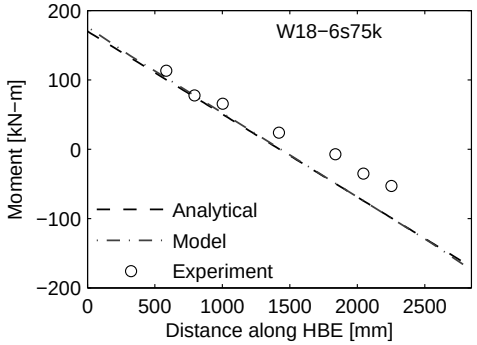

(d) Middle HBE moment distribution: approx. -2% drift

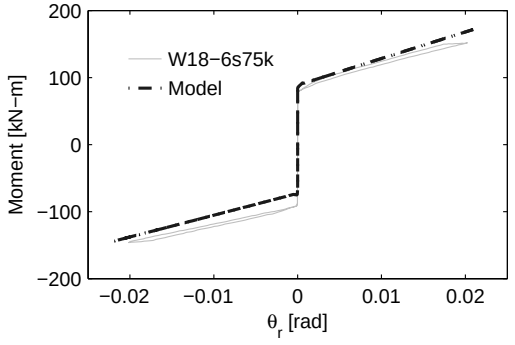

(e) Middle HBE connection moment: North end

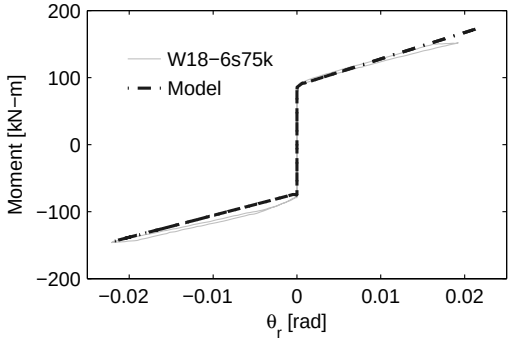

(f) Middle HBE connection moment: South end

Figure C.7: W18-6s75k: Comparison of OpenSees model and experimental component responses during 2% cycle

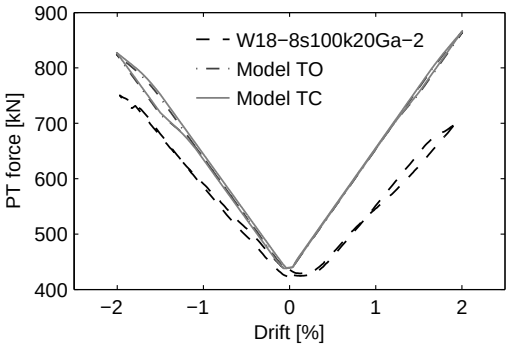

(a) Middle HBE PT force vs. drift response

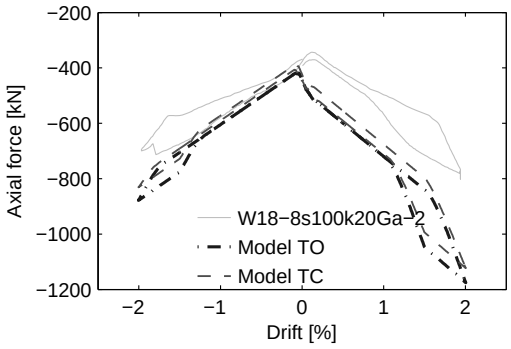

(b) Middle HBE average axial force vs. drift response

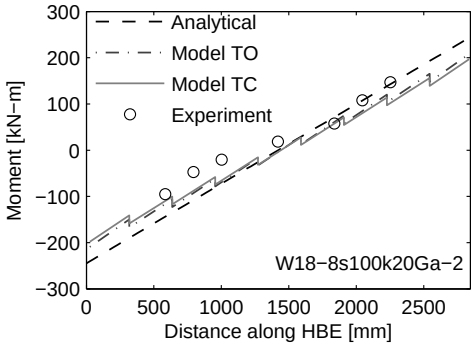

(c) Middle HBE moment distribution: approx. +2% drift

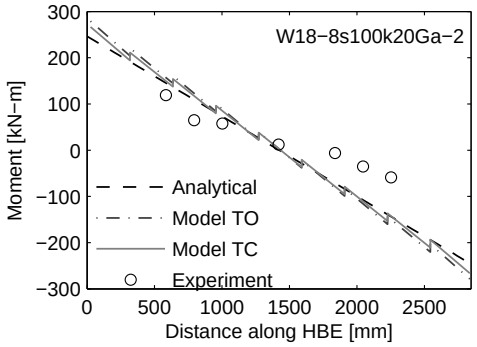

(d) Middle HBE moment distribution: approx. -2% drift

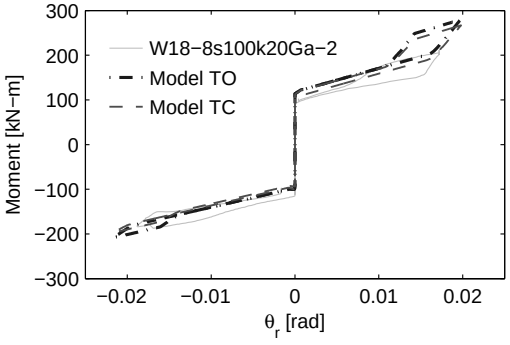

(e) Middle HBE connection moment: North end

Figure C.8: W18-8s100k20Ga-2: Comparison of OpenSees model and experimental component responses during 2% cycle

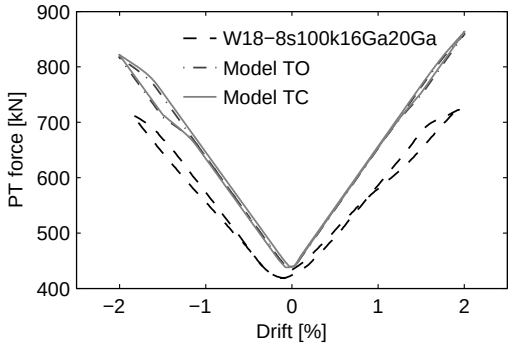

(a) Middle HBE PT force vs. drift response

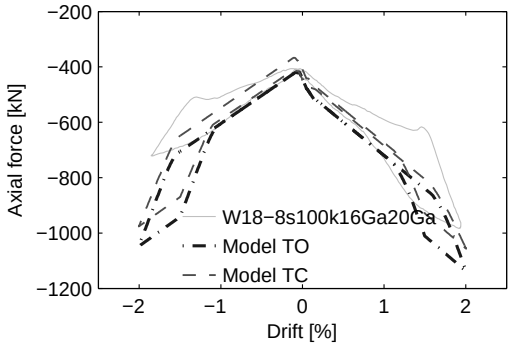

(b) Middle HBE average axial force vs. drift response

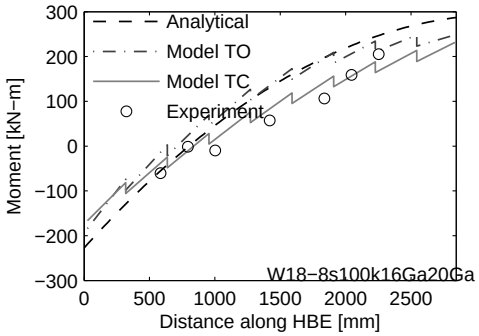

(c) Middle HBE moment distribution: approx. +2% drift

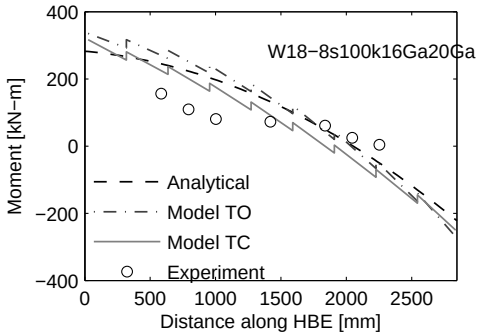

(d) Middle HBE moment distribution: approx. -2% drift

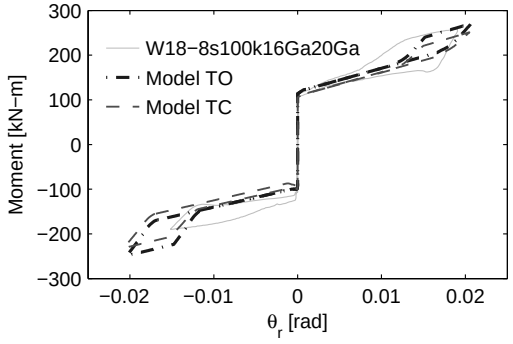

(e) Middle HBE connection moment: North end

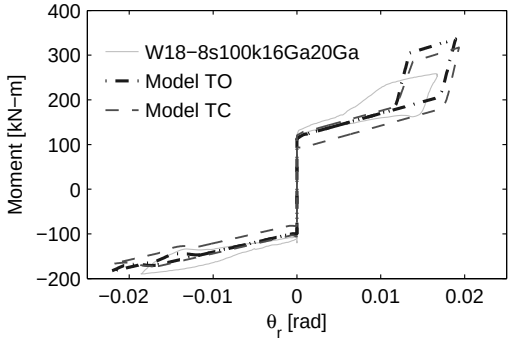

(f) Middle HBE connection moment: South end

Figure C.9: W18-8s100k16Ga20Ga: Comparison of OpenSees model and experimental component responses during 2% cycle (Note: The Calculated moment distribution for different web plate thicknesses above and below the HBE assumes an applied story shear force at that HBE (equal to $P_{HBE(web)}$), which is not present in the experimental specimen or the numerical model; therefore, the parabolic shape of the claculated moment distribution is more pronounced)

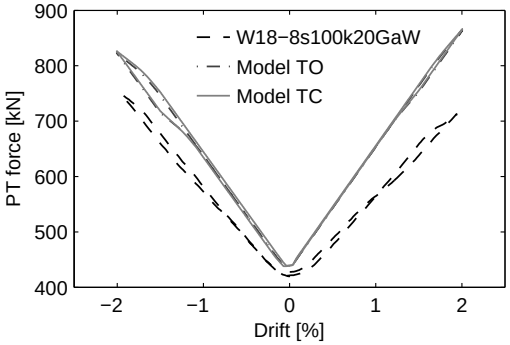

(a) Middle HBE PT force vs. drift response

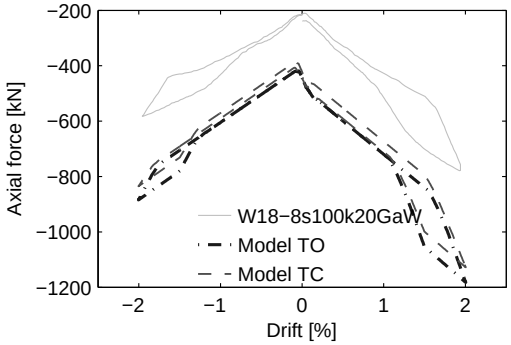

(b) Middle HBE average axial force vs. drift response

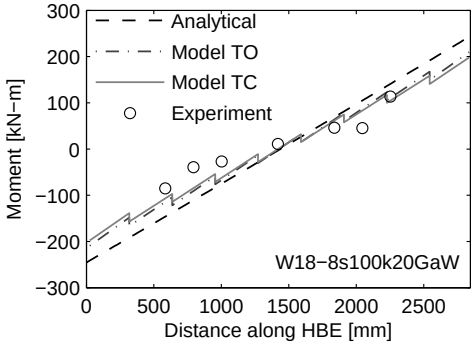

(c) Middle HBE moment distribution: approx. +2% drift

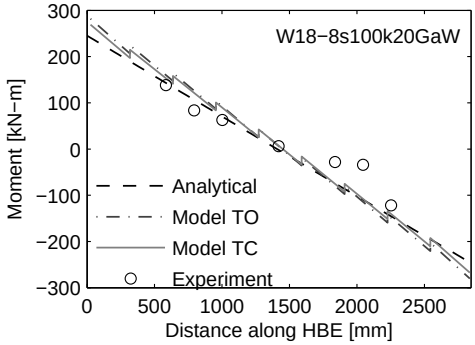

(d) Middle HBE moment distribution: approx. -2% drift

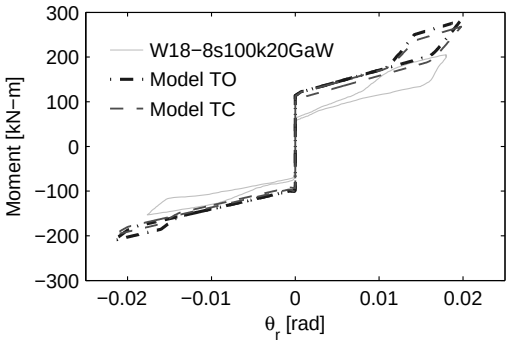

(e) Middle HBE connection moment: North end

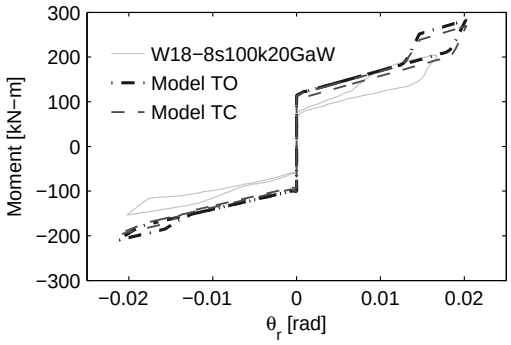

(f) Middle HBE connection moment: South end

Figure C.10: W18-8s100k20GaW: Comparison of OpenSees model and experimental component responses during 2% cycle (Note: The experimental axial force measurements derived from strain gage readings in middle HBE were drifting to lower magnitudes over the course of the test (Fig. B.40); however, PT forces did not have a similar reduction throughout the test (Fig. B.9(b)). This reduction in experimental axial force magnitude (also used to extimate connection moments) is beleived to be an artificial result of faulty strain gage readings; however, similar trends in response can be observed.)

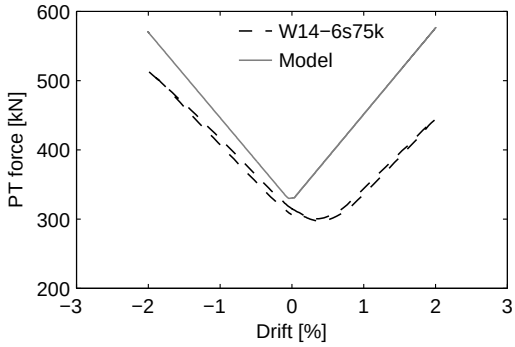

(a) Middle HBE PT force vs. drift response

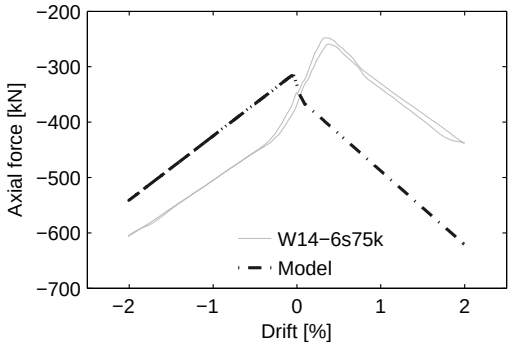

(b) Middle HBE average axial force vs. drift response

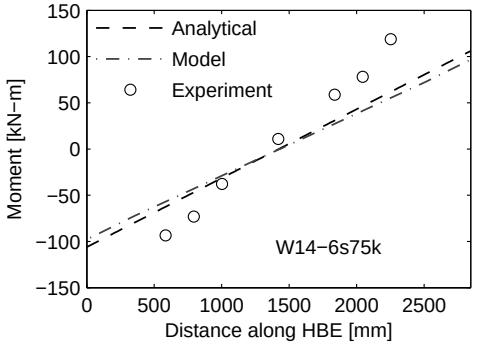

(c) Middle HBE moment distribution: approx. +2% drift

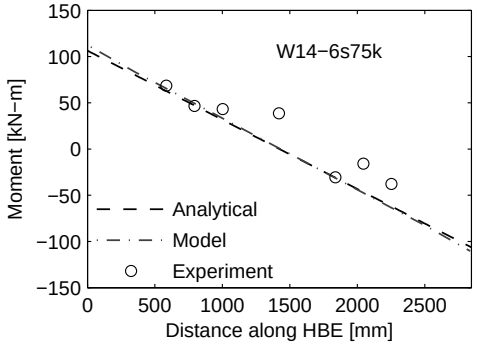

(d) Middle HBE moment distribution: approx. -2% drift

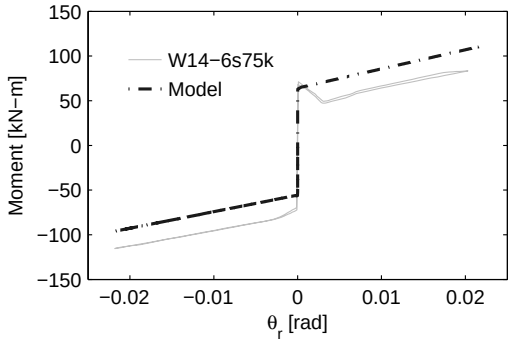

(e) Middle HBE connection moment: North end

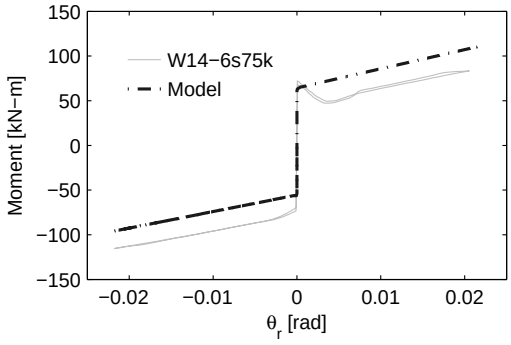

(f) Middle HBE connection moment: South end

Figure C.11: W14-6s75k: Comparison of OpenSees model and experimental component responses during 2% cycle (Note: In this test, the initial gap at the top flange of the south end of the middle HBE results in the reduction of experimental PT force (and thus HBE axial force) upon initial loading in the poitive direction. After the initial gap at the top flange closes, the gap opens at the bottom flange, and the PT forces increase as expected. This results in atypical behavior as small positive drift demands that are not observed in the model; however, trends in the post-decompression response at larger drifts (e.g. stiffnesses, etc.) can be compared to those of the model response. Results are typical for the following W14 subassembly tests.)

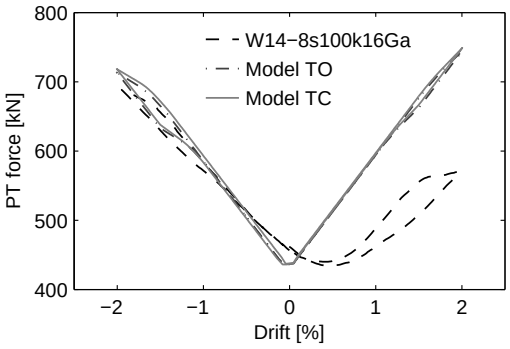

(a) Middle HBE PT force vs. drift response

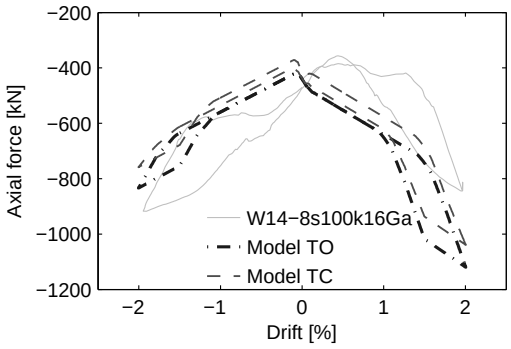

(b) Middle HBE average axial force vs. drift response

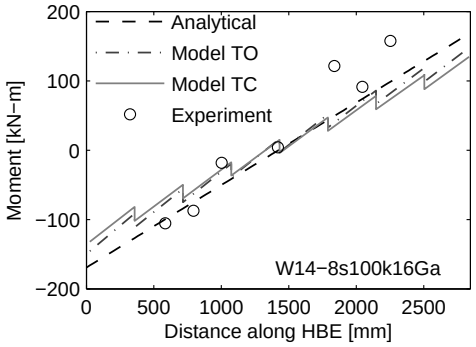

(c) Middle HBE moment distribution: approx. +2% drift

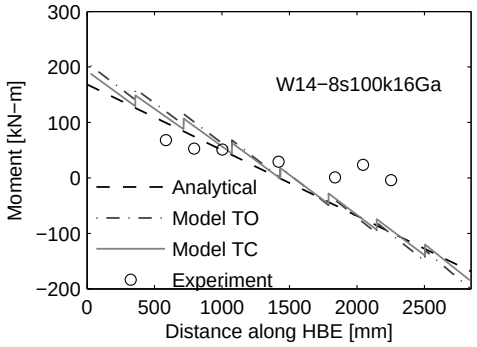

(d) Middle HBE moment distribution: approx. -2% drift

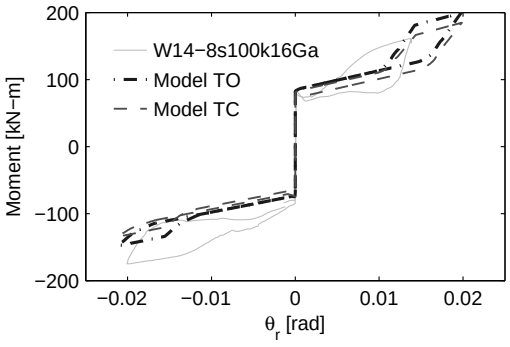

(e) Middle HBE connection moment: North end

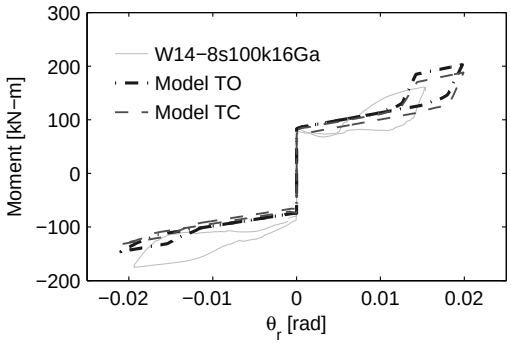

(f) Middle HBE connection moment: South end

Figure C.12: W14-8s100k16Ga: Comparison of OpenSees model and experimental component responses during 2% cycle

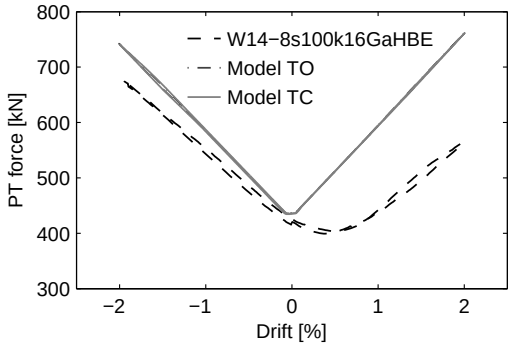

(a) Middle HBE PT force vs. drift response

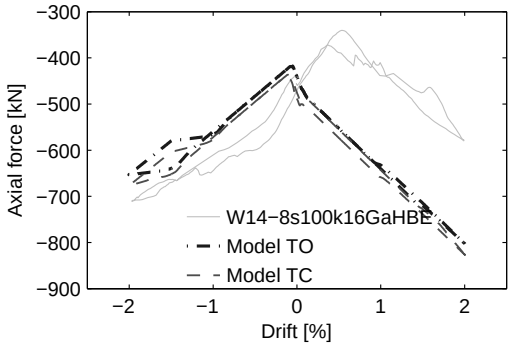

(b) Middle HBE average axial force vs. drift response

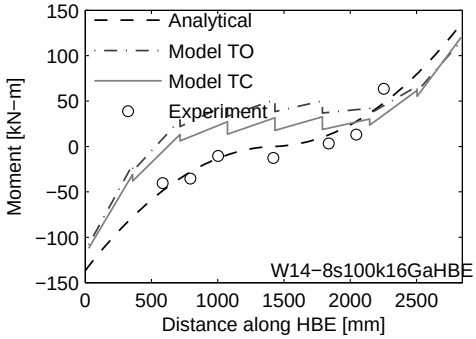

(c) Middle HBE moment distribution: approx. +2% drift

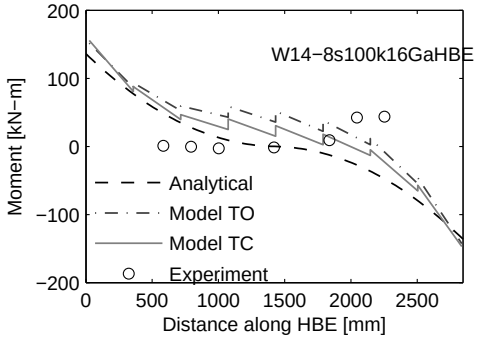

(d) Middle HBE moment distribution: approx. -2% drift

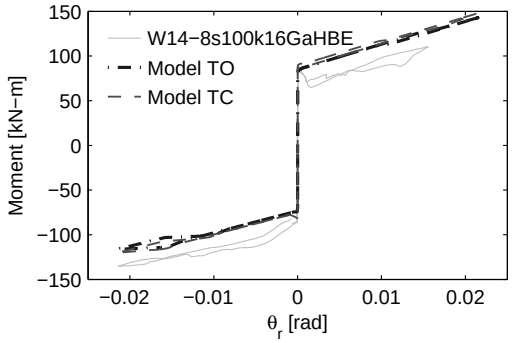

(e) Middle HBE connection moment: North end

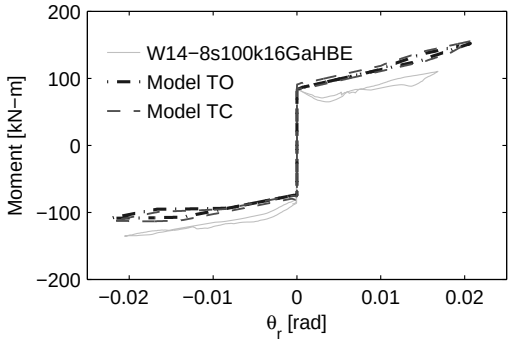

(f) Middle HBE connection moment: South end

Figure C.13: W14-8s100k16GaHBE: Comparison of OpenSees model and experimental component responses during 2% cycle (Note: The "calculated" moment distribution is an approximation (for purposed on comparison) based on the following assumptions: (i) the partial tension field extends over one-half of the web plate length, (ii) the angle of inclination is 30° as described in Sec. 7.2, and (iii) the length of the corner cutouts were ignored.)

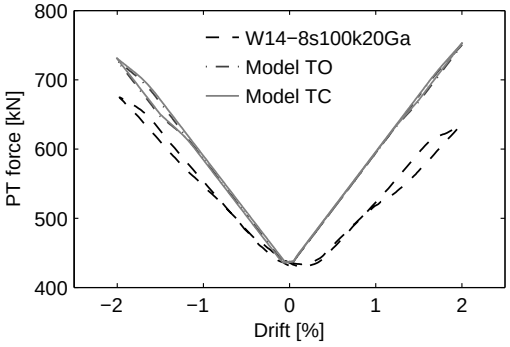

(a) Middle HBE PT force vs. drift response

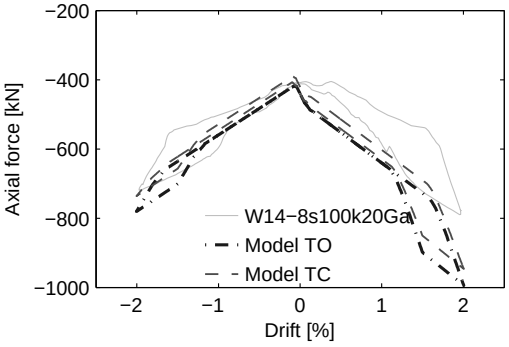

(b) Middle HBE average axial force vs. drift response

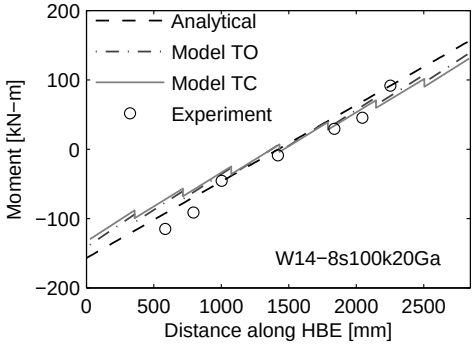

(c) Middle HBE moment distribution: approx. +2% drift

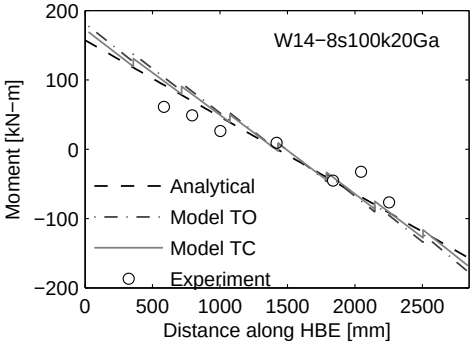

(d) Middle HBE moment distribution: approx. -2% drift

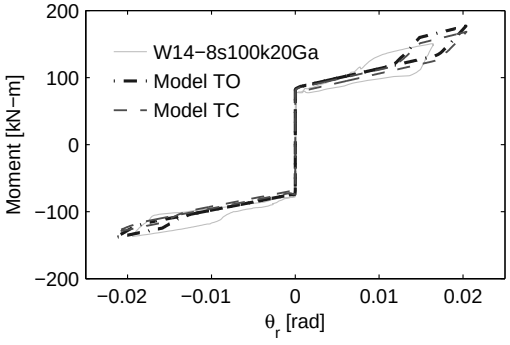

(e) Middle HBE connection moment: North end

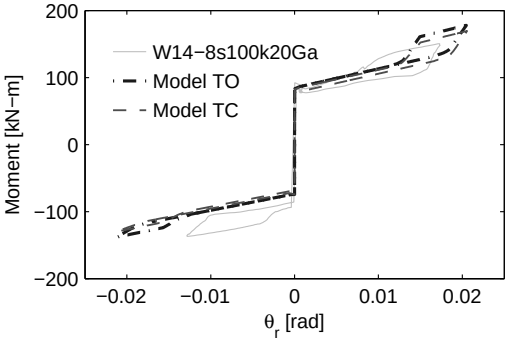

(f) Middle HBE connection moment: South end

Figure C.14: W14-8s100k20Ga: Comparison of OpenSees model and experimental component responses during 2% cycle

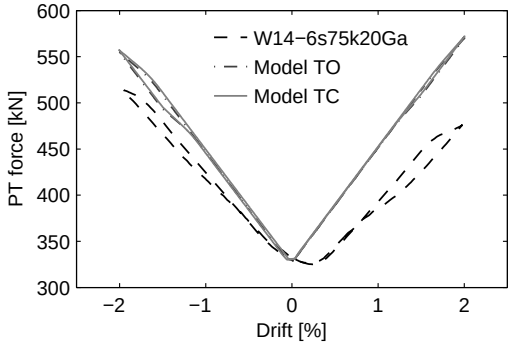

(a) Middle HBE PT force vs. drift response

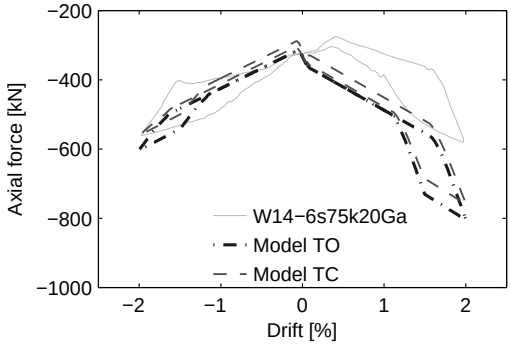

(b) Middle HBE average axial force vs. drift response

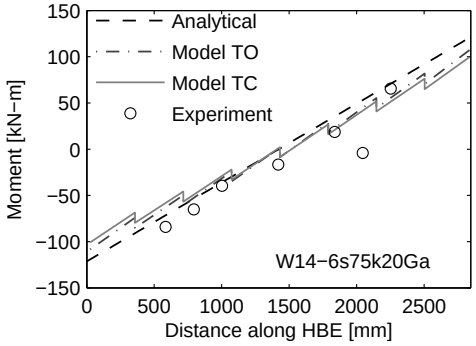

(c) Middle HBE moment distribution: approx. +2% drift

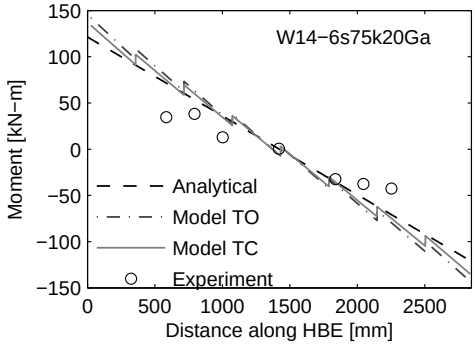

(d) Middle HBE moment distribution: approx. -2% drift

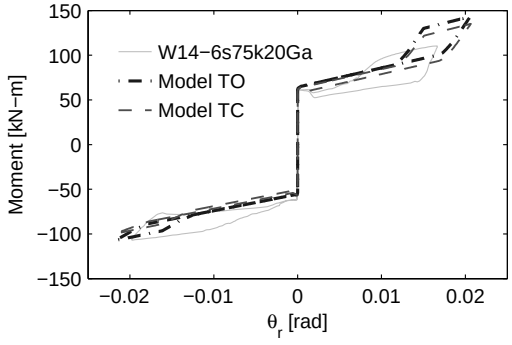

(e) Middle HBE connection moment: North end

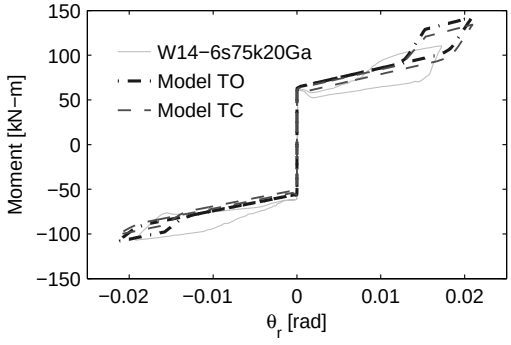

(f) Middle HBE connection moment: South end

Figure C.15: W14-6s75k20Ga: Comparison of OpenSees model and experimental component responses during 2% cycle

Appendix D

ADDITIONAL FIGURES FOR OPENSEES MODELS OF FULL-SCALE TEST

The component demand response plots for the full-scale specimen OpenSees tension-only (TO) model are shown here. These can be compared to the Model TO component demands shown in Chapter 7.

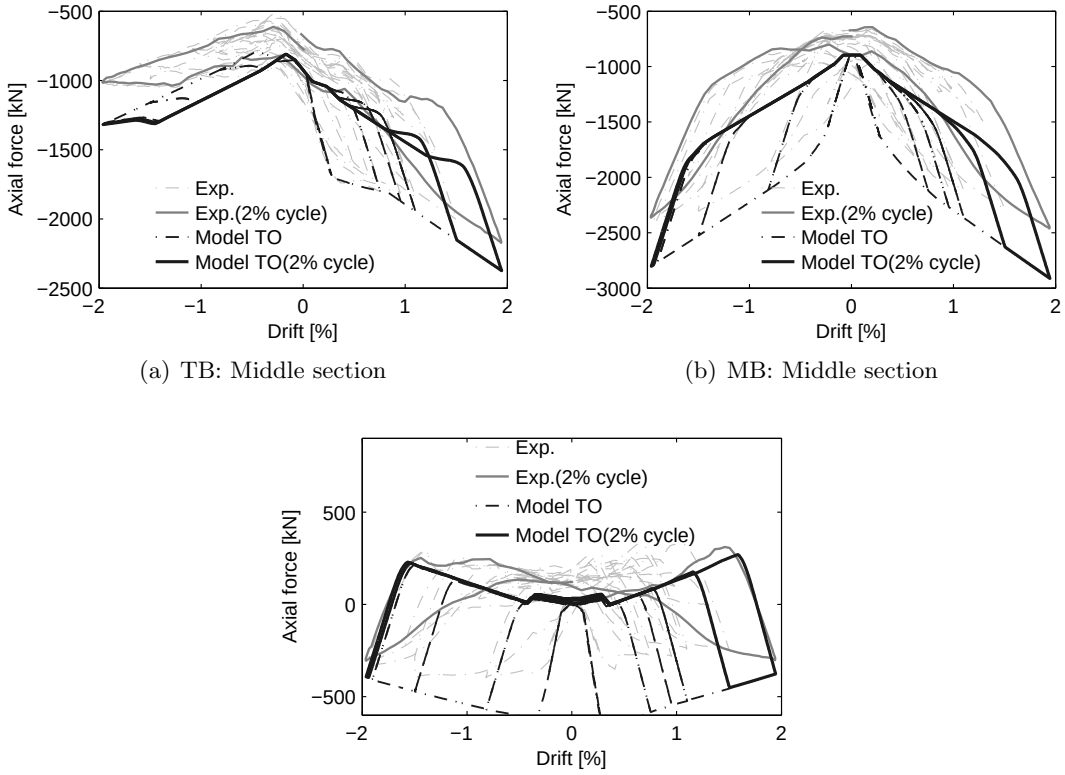

(a) TB: Middle section

(b) MB: Middle section

(c) BB: Middle section

Figure D.1: Comparison of experimental (10/50) and numerical (Model TO) axial force vs. drift demands for certain locations in full-scale specimen beams

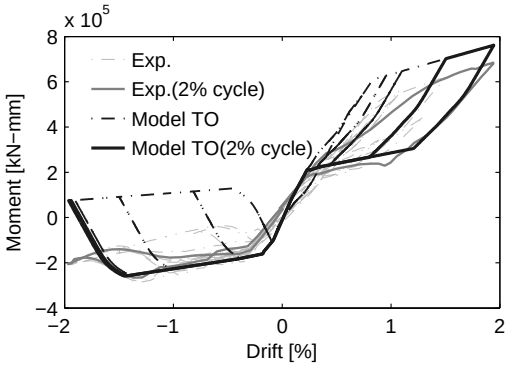

(a) TB: West section

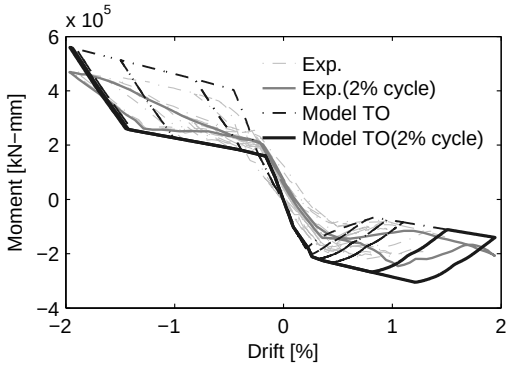

(b) TB: East section

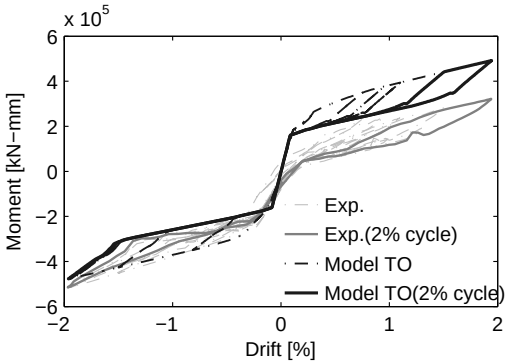

(c) MB: West section

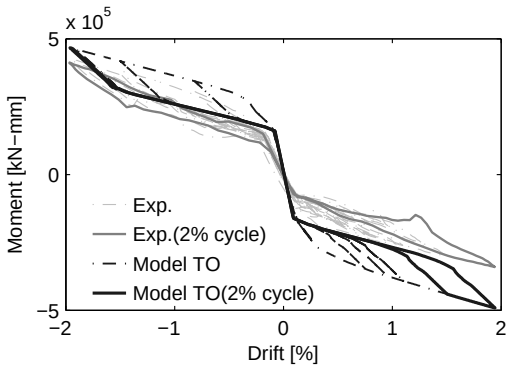

(d) MB: East section

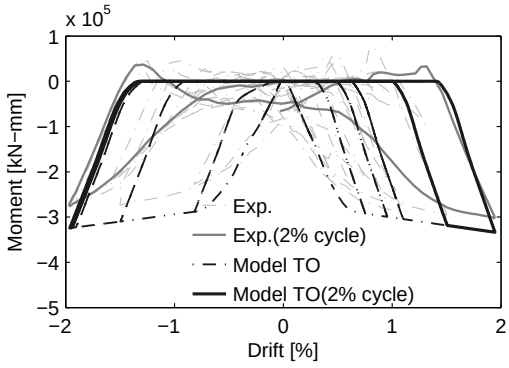

(e) BB: Middle section

Figure D.2: Comparison of experimental (10/50) and numerical (Model TO) moment vs. drift demands for certain locations in full-scale specimen beams

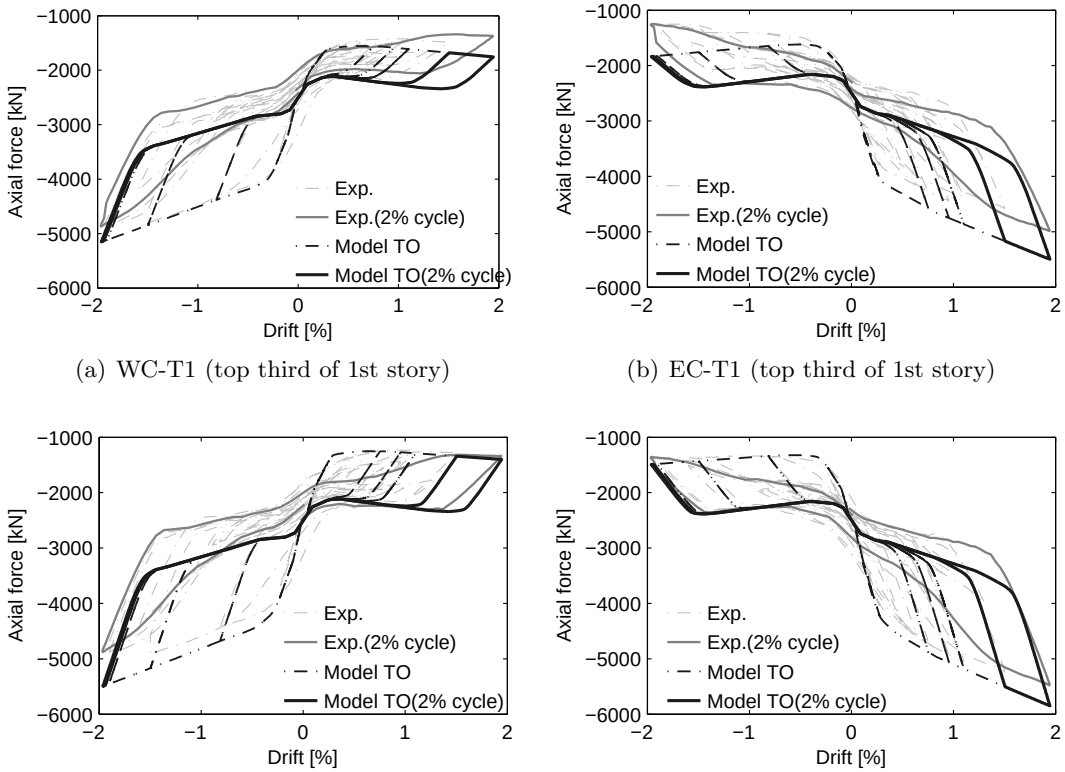

(a) WC-T1 (top third of 1st story)

(b) EC-T1 (top third of 1st story)

(c) WC-B1 (bottom third of 1st story)

(d) EC-B1 (bottom third of 1st story)

Figure D.3: Comparison of experimental (10/50) and numerical (Model TO) axial force vs. drift demands for certain locations in full-scale specimen columns

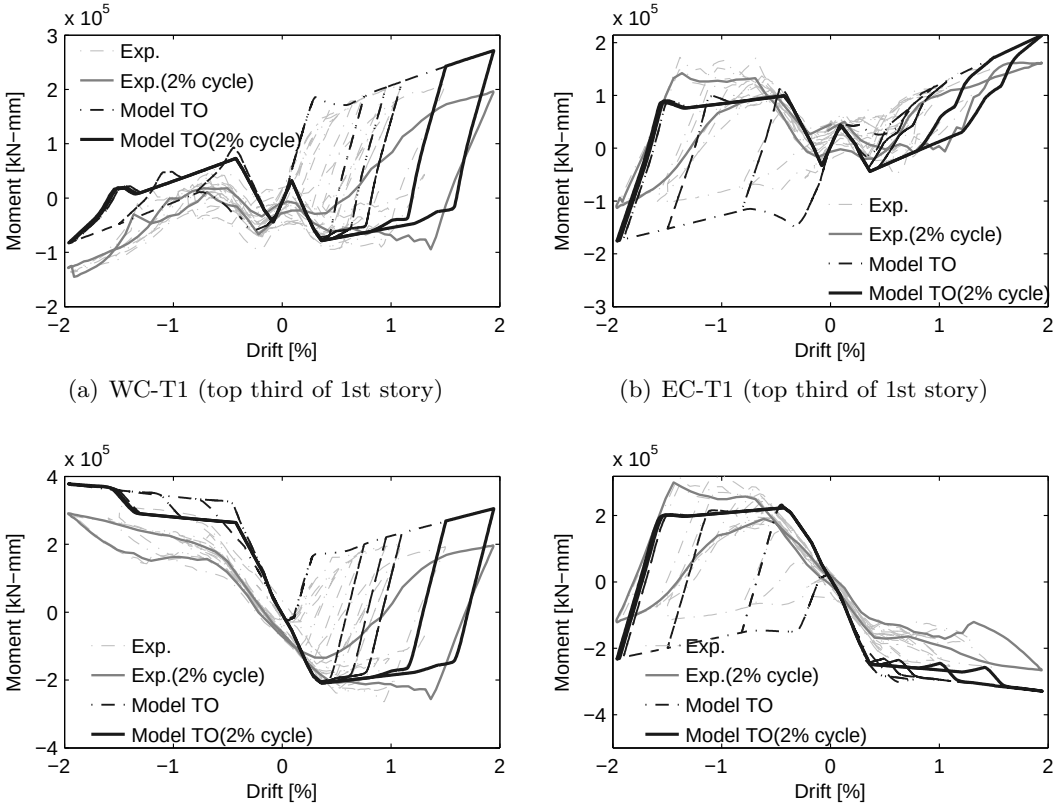

(a) WC-T1 (top third of 1st story)

(b) EC-T1 (top third of 1st story)

(c) WC-B1 (bottom third of 1st story)

(d) EC-B1 (bottom third of 1st story)

Figure D.4: Comparison of experimental (10/50) and numerical (Model TO) moment vs. drift demands for certain locations in full-scale specimen columns

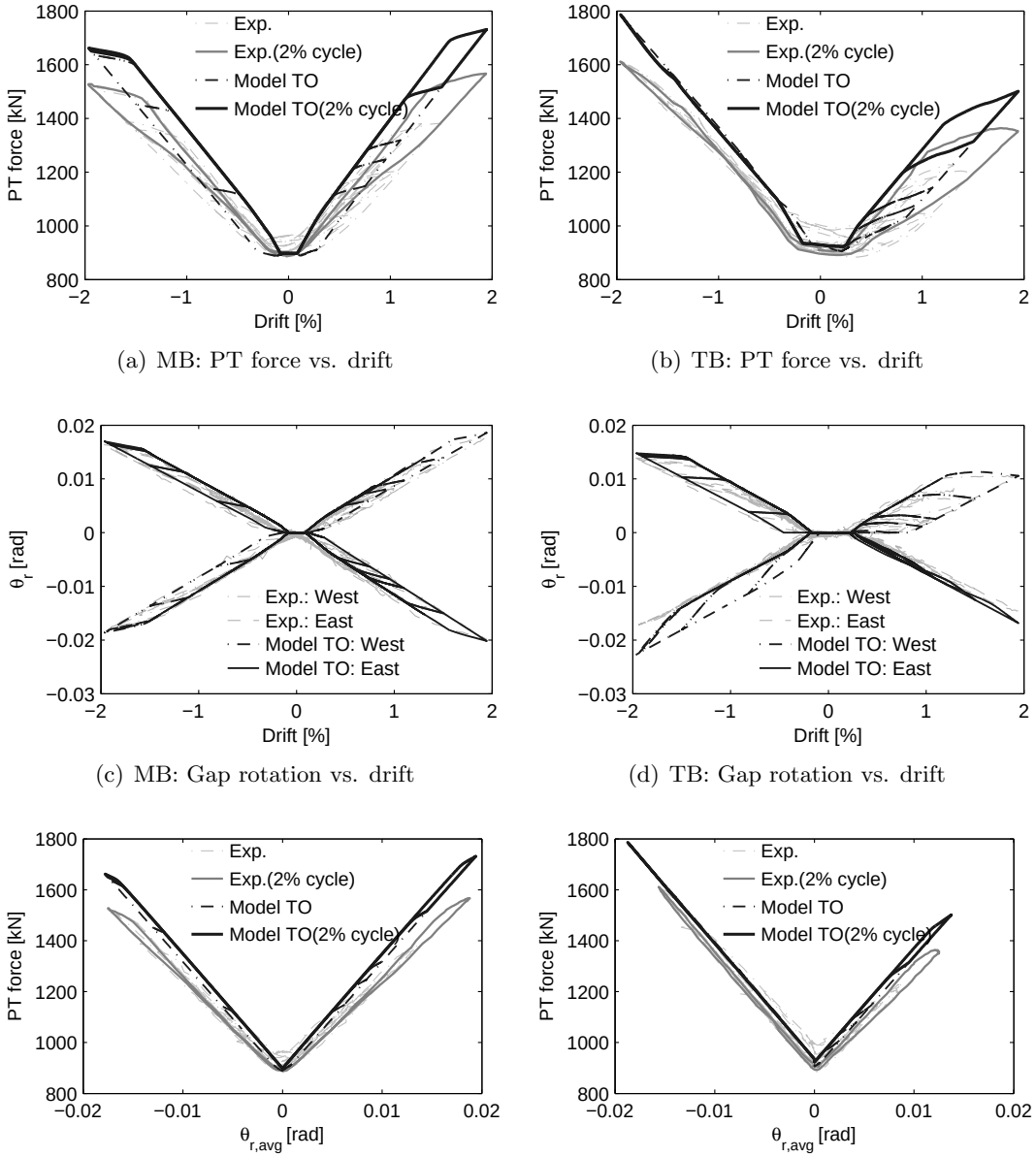

(a) MB: PT force vs. drift

(b) TB: PT force vs. drift

(c) MB: Gap rotation vs. drift

(d) TB: Gap rotation vs. drift

(e) MB: PT force vs. gap rotation

(f) TB: PT force vs. gap rotation

Figure D.5: Comparison of numerical (Model TO) and experimental (10/50 test) responses of beam PT connections for full-scale specimen

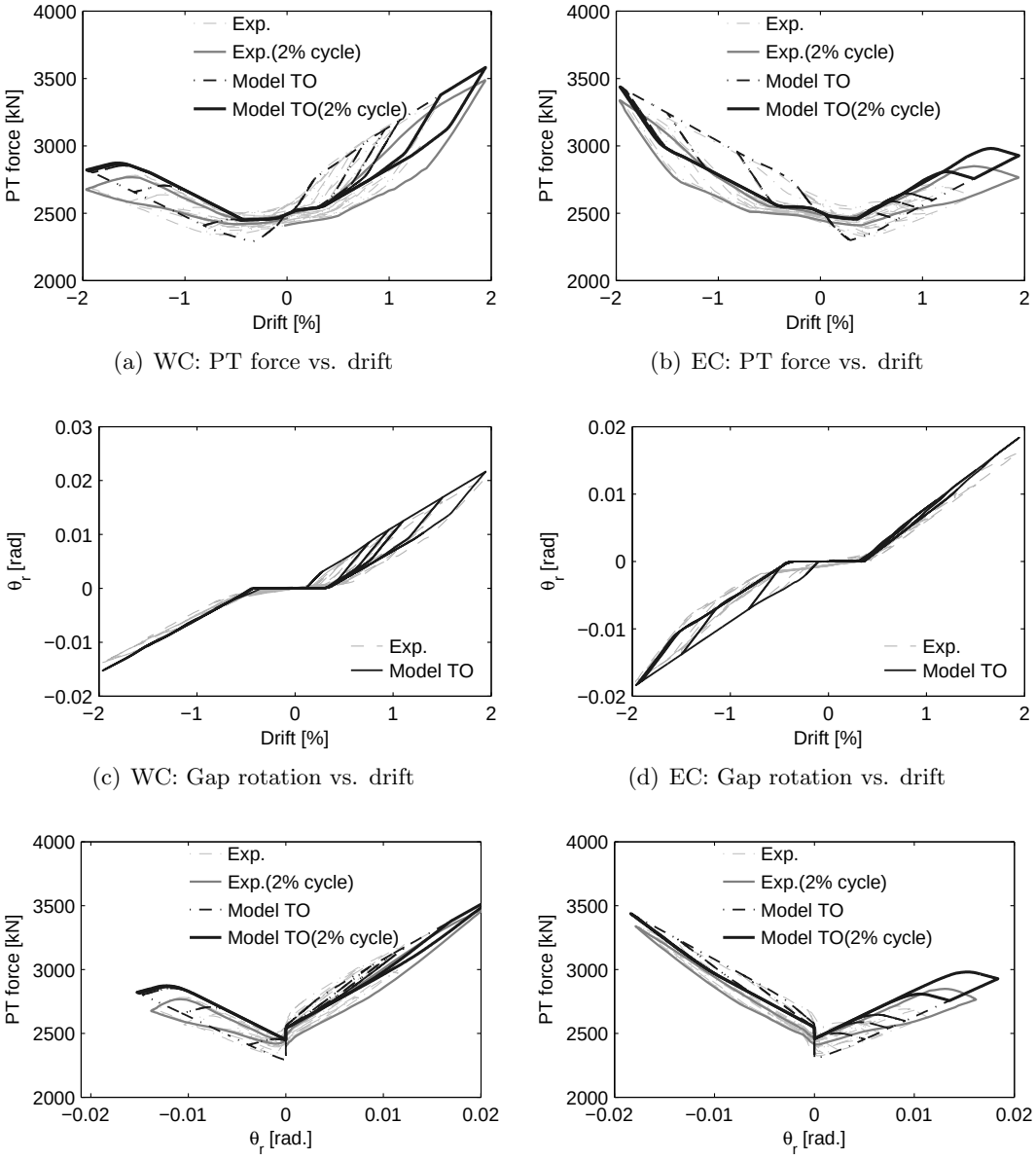

(a) WC: PT force vs. drift

(b) EC: PT force vs. drift

(c) WC: Gap rotation vs. drift

(d) EC: Gap rotation vs. drift

(e) WC: PT force vs. gap rotation

(f) EC: PT force vs. gap rotation

Figure D.6: Comparison of numerical (Model TO) and experimental (10/50 test) responses of column base PT connections for full-scale specimen

Appendix E

ADDITIONAL FIGURES FOR ABAQUS MODELS OF SUBASSEMBLY TESTS

The following figures show comparisons between the SC-SPSW subassembly test experimental and ABAQUS numerical model global and component responses. These figures are provided as supplements to the explanations and model descriptions provided in Sec. 7.3.2. In some cases where certain data was faulty (e.g. due to a potentiometer malfunction or faulty strain gage data) the figure is either removed (it the data is unavailable) or an explanatory note describing the unexpected observed behavior is provided in the caption.

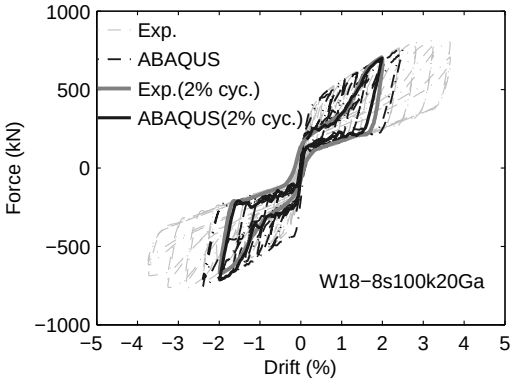

(a) W18-8s100k20Ga

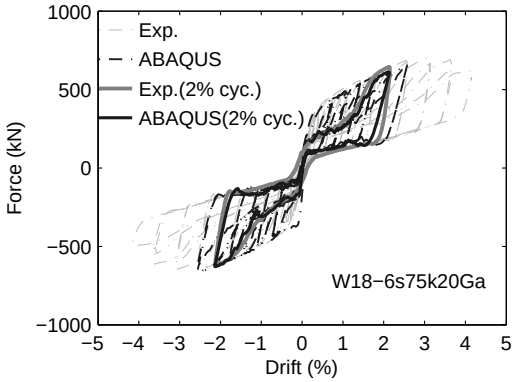

(b) W18-6s75k20Ga

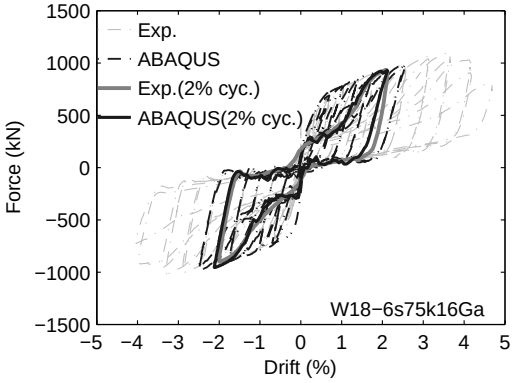

(c) W18-6s75k16Ga

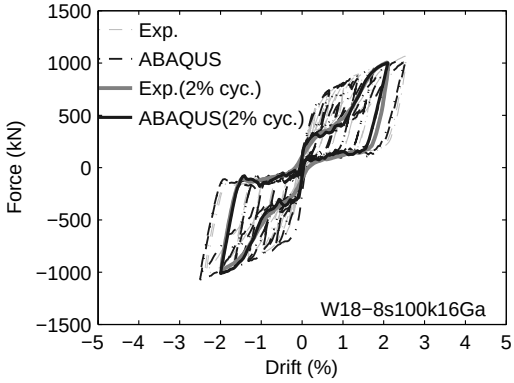

(d) W18-8s100k16Ga

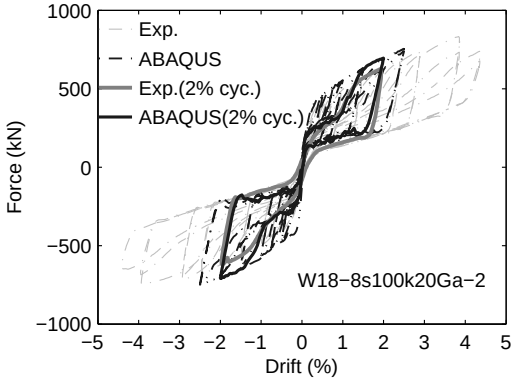

(e) W18-8s100k20Ga-2

Figure E.1: Comparison of ABAQUS model and experimental global force vs. drift responses (cont.)

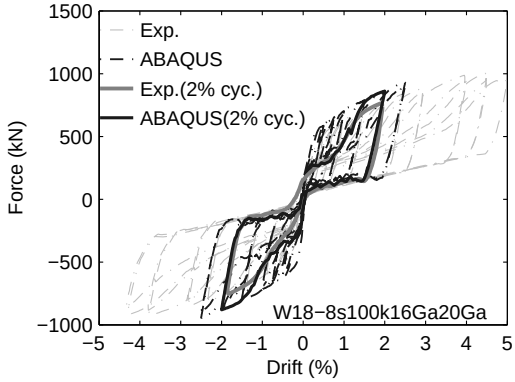

(f) W18-8s100k16Ga20Ga

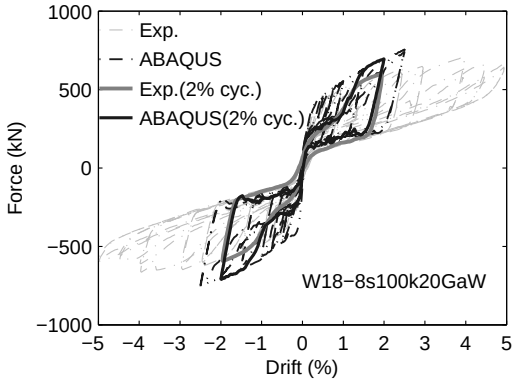

(g) W18-8s100k20GaW

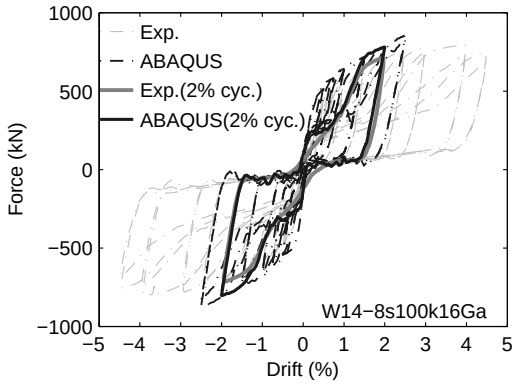

(h) W14-8s100k16Ga

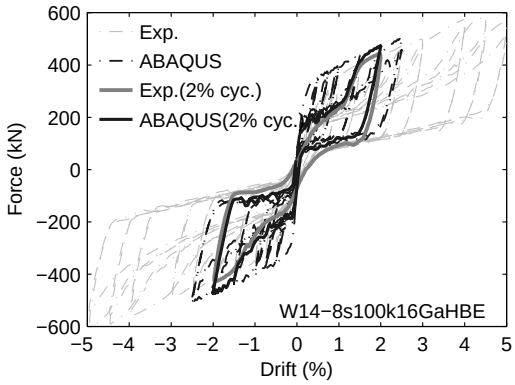

(i) W14-8s100k16GaHBE

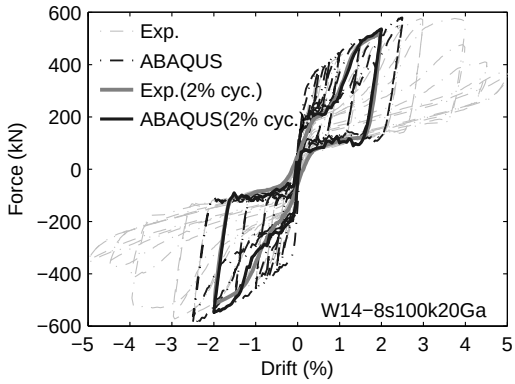

(j) W14-8s100k20Ga

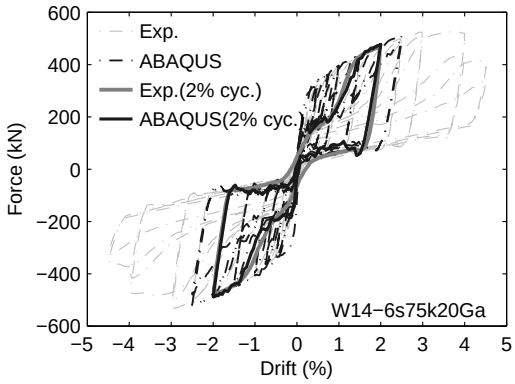

(k) W14-6s75k20Ga

Figure E.1: Comparison of OpenSees model and experimental global force vs. drift responses (cont.)

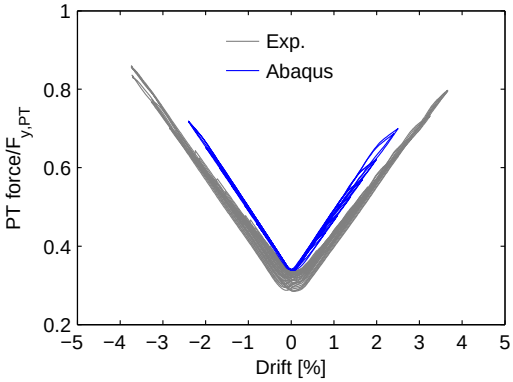

(a) Middle HBE PT force vs. drift response

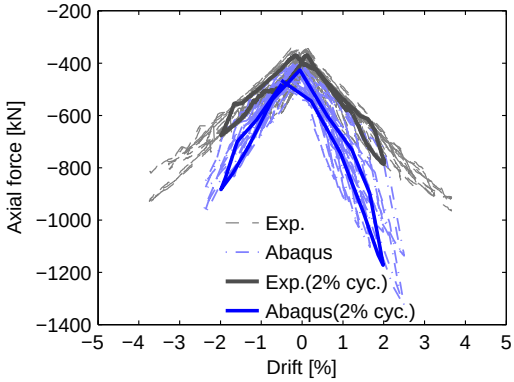

(b) Middle HBE average axial force vs. drift response

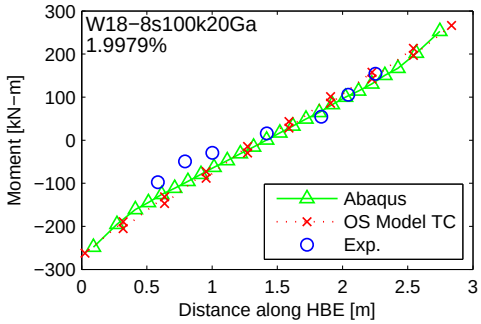

(c) Middle HBE moment distribution: approx. +2% drift

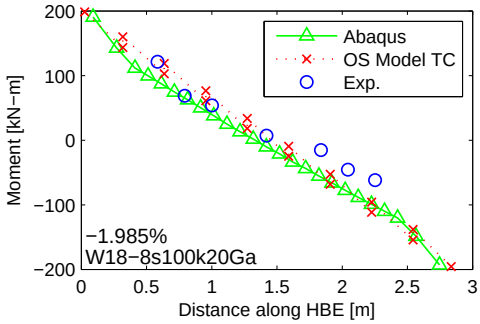

(d) Middle HBE moment distribution: approx. -2% drift

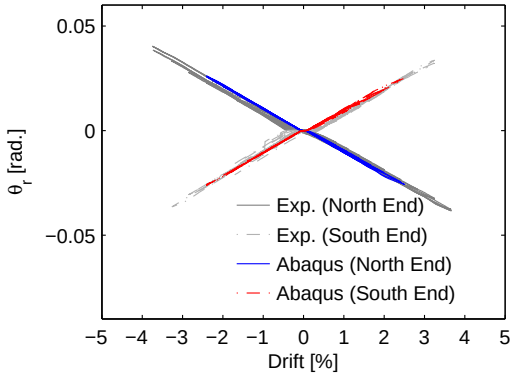

(e) Middle HBE connection rotation

Figure E.2: W18-8s100k20Ga: Comparison of ABAQUS model and experimental component responses during 2% cycle

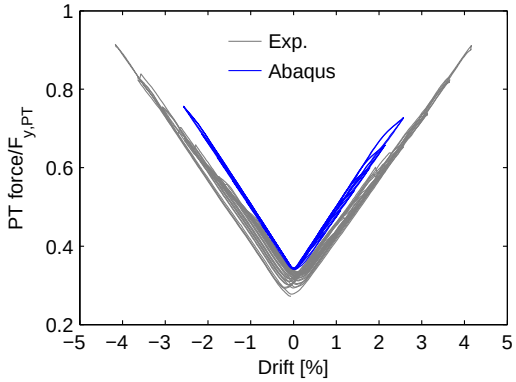

(a) Middle HBE PT force vs. drift response

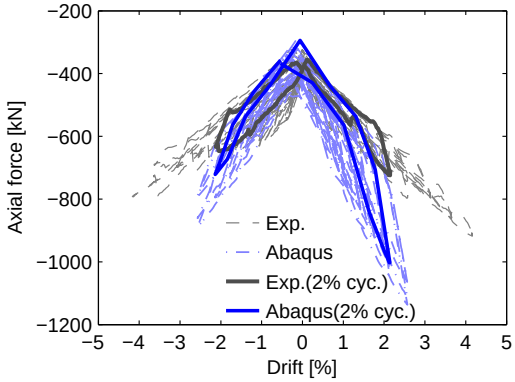

(b) Middle HBE average axial force vs. drift response

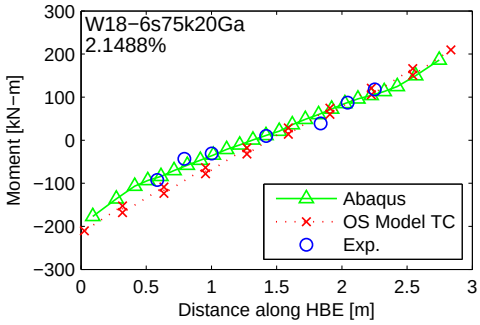

(c) Middle HBE moment distribution: approx. +2% drift

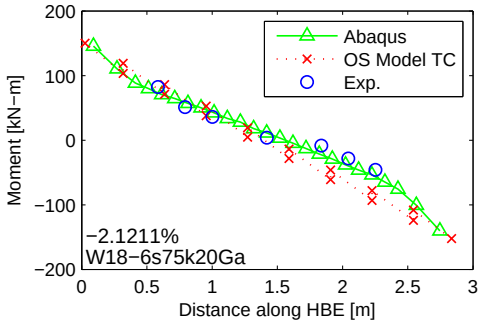

(d) Middle HBE moment distribution: approx. -2% drift

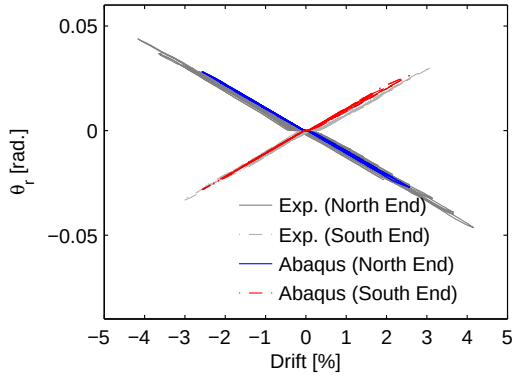

(e) Middle HBE connection rotation

Figure E.3: W18-6s75k20Ga: Comparison of ABAQUS model and experimental component responses during 2% cycle

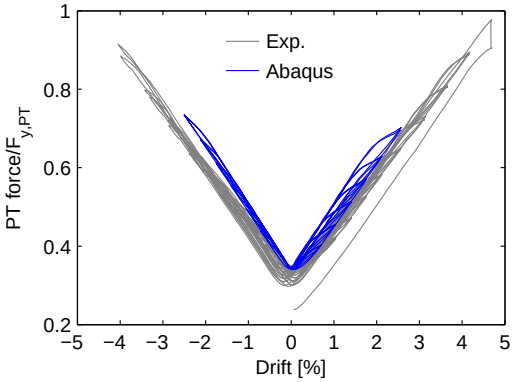

(a) Middle HBE PT force vs. drift response

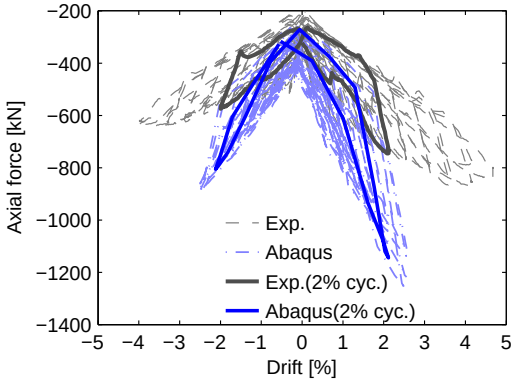

(b) Middle HBE average axial force vs. drift response

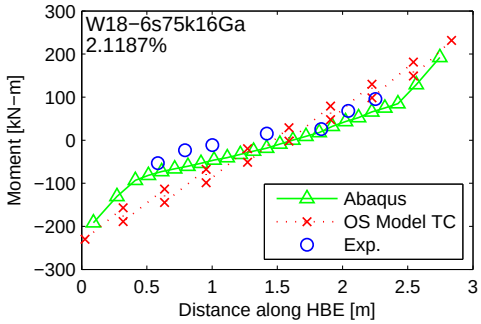

(c) Middle HBE moment distribution: approx. +2% drift

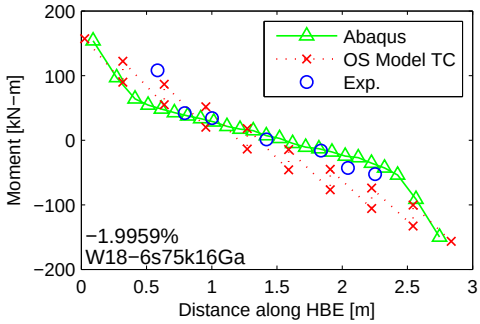

(d) Middle HBE moment distribution: approx. -2% drift

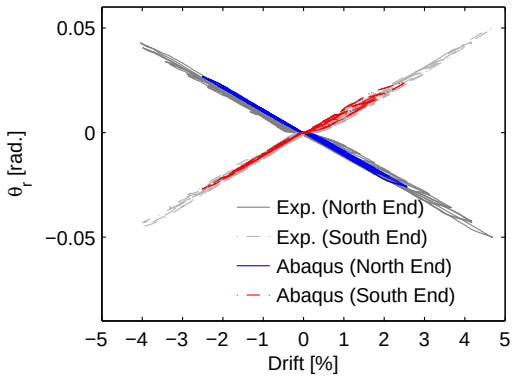

(e) Middle HBE connection rotation

Figure E.4: W18-6s75k16Ga: Comparison of ABAQUS model and experimental component responses during 2% cycle

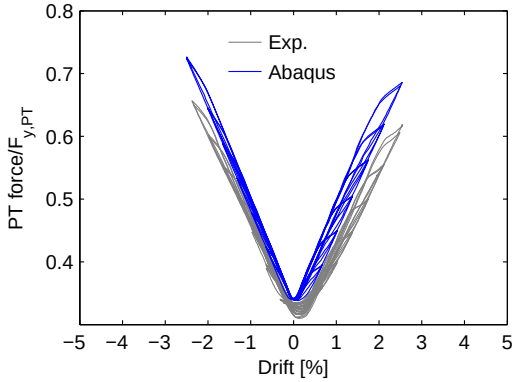

(a) Middle HBE PT force vs. drift response

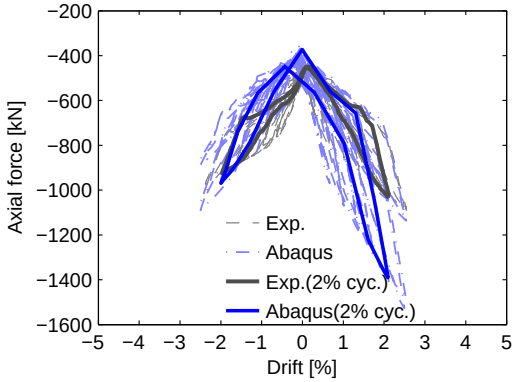

(b) Middle HBE average axial force vs. drift response

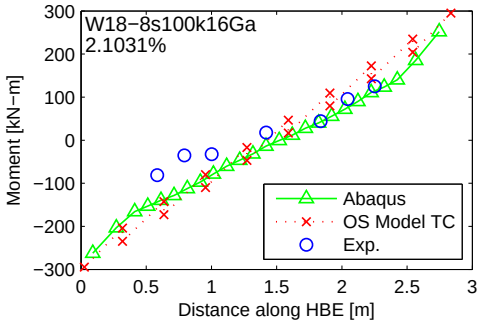

(c) Middle HBE moment distribution: approx. +2% drift

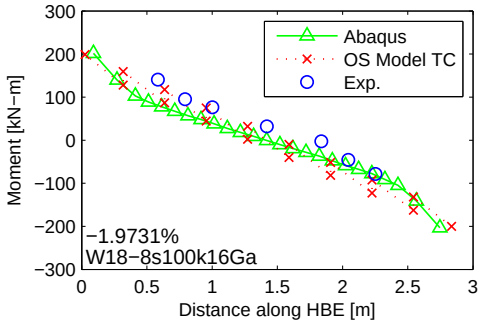

(d) Middle HBE moment distribution: approx. -2% drift

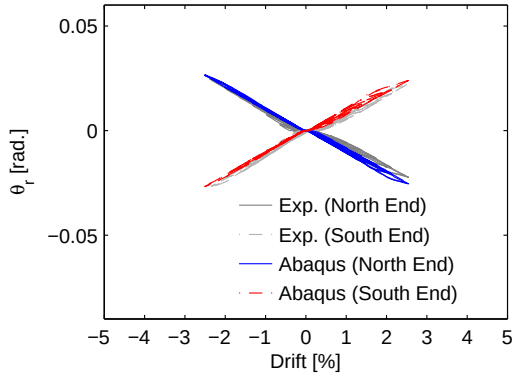

(e) Middle HBE connection rotation

Figure E.5: W18-8s100k16Ga: Comparison of ABAQUS model and experimental component responses during 2% cycle

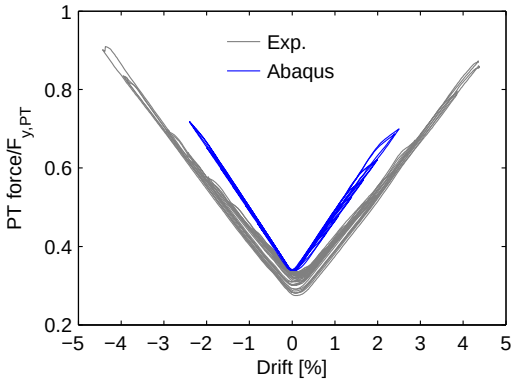

(a) Middle HBE PT force vs. drift response

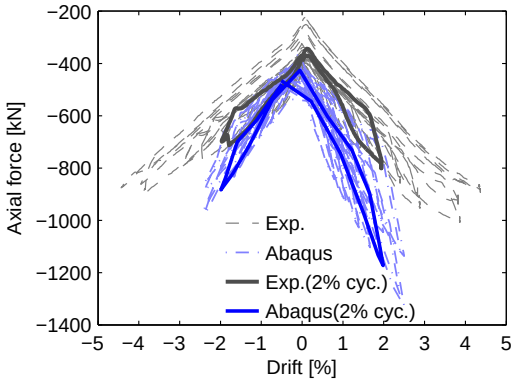

(b) Middle HBE average axial force vs. drift response

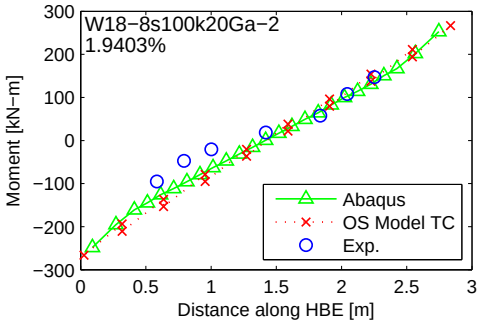

(c) Middle HBE moment distribution: approx. +2% drift

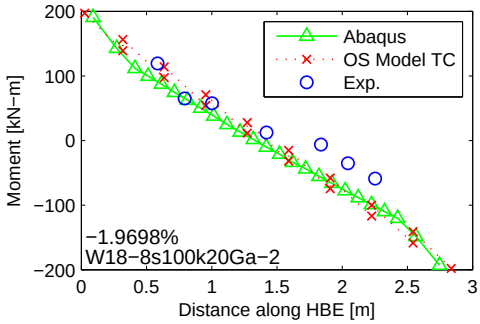

(d) Middle HBE moment distribution: approx. -2% drift

Figure E.6: W18-8s100k20Ga-2: Comparison of ABAQUS model and experimental component responses during 2% cycle

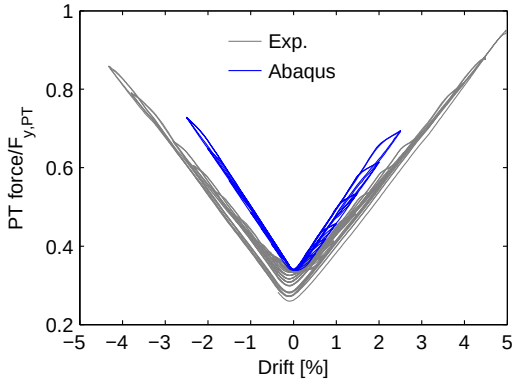

(a) Middle HBE PT force vs. drift response

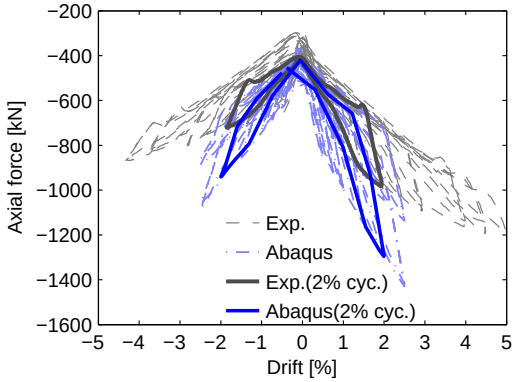

(b) Middle HBE average axial force vs. drift response

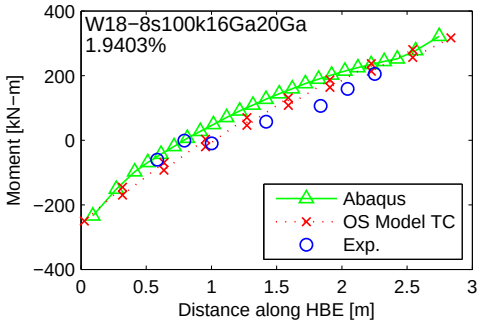

(c) Middle HBE moment distribution: approx. +2% drift

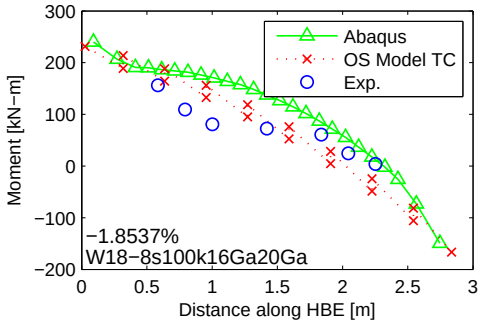

(d) Middle HBE moment distribution: approx. -2% drift

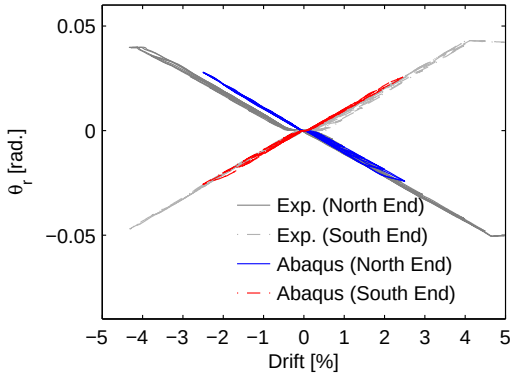

(e) Middle HBE connection rotation

Figure E.7: W18-8s100k16Ga20Ga: Comparison of ABAQUS model and experimental component responses during 2% cycle

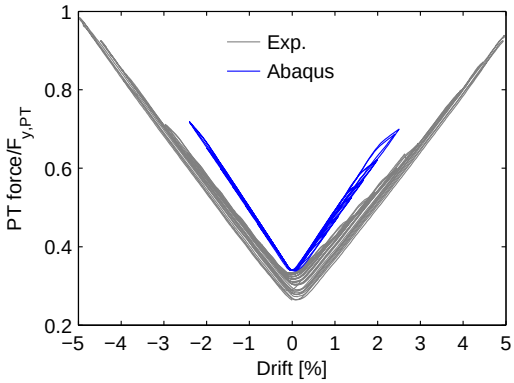

(a) Middle HBE PT force vs. drift response

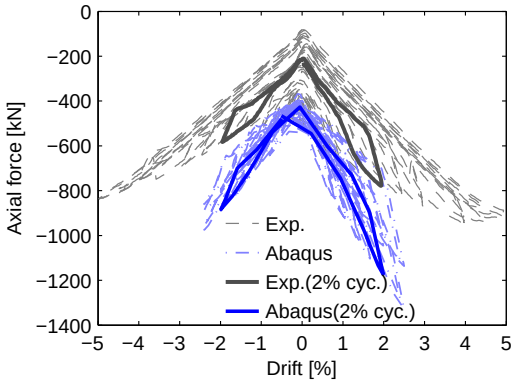

(b) Middle HBE average axial force vs. drift response

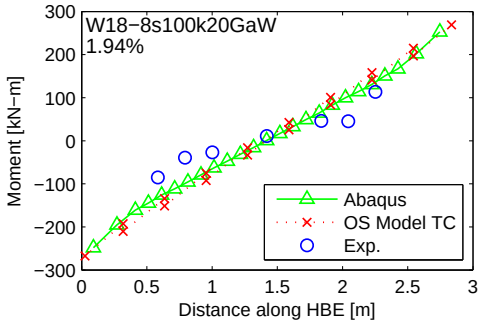

(c) Middle HBE moment distribution: approx. +2% drift

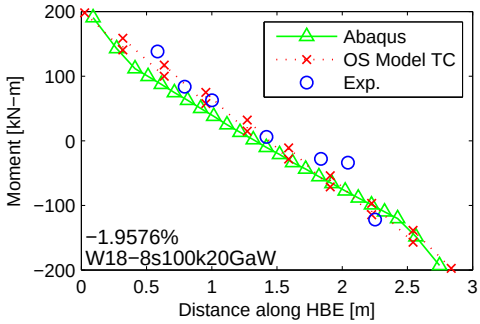

(d) Middle HBE moment distribution: approx. -2% drift

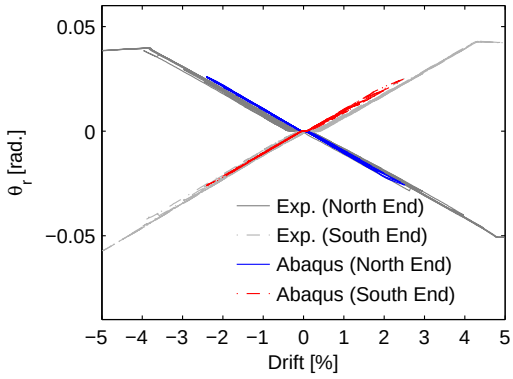

(e) Middle HBE connection rotation

Figure E.8: W18-8s100k20GaW: Comparison of ABAQUS model and experimental component responses during 2% cycle (Note: The experimental axial force measurements derived from strain gage readings in middle HBE were drifting to lower magnitudes over the course of the test (Fig. B.40); however, PT forces did not have a similar reduction throughout the test (Fig. B.9(b)). This reduction in experimental axial force magnitude (also used to extimate connection moments) is beleived to be an artificial result of faulty strain gage readings; however, similar trends in response can be observed.)

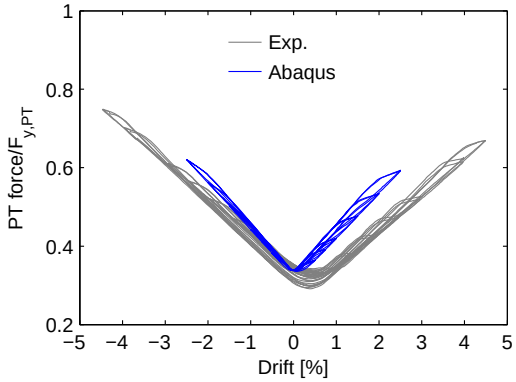

(a) Middle HBE PT force vs. drift response

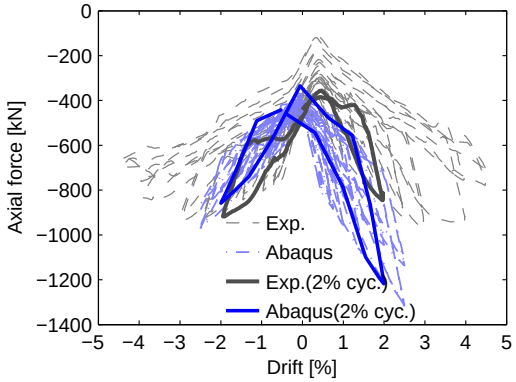

(b) Middle HBE average axial force vs. drift response

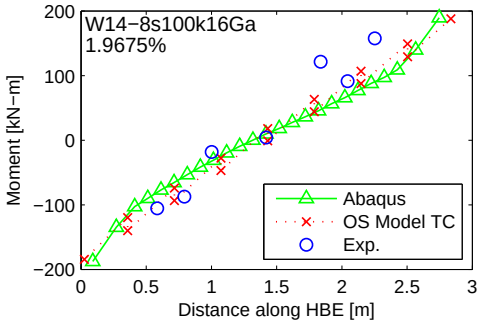

(c) Middle HBE moment distribution: approx. +2% drift

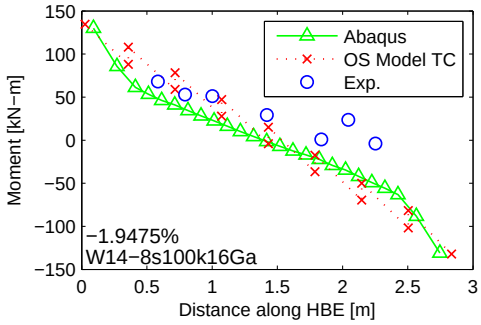

(d) Middle HBE moment distribution: approx. -2% drift

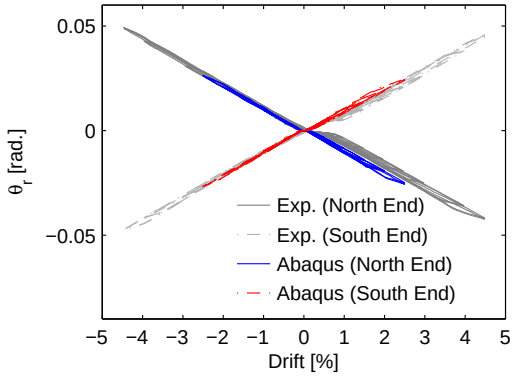

(e) Middle HBE connection rotation

Figure E.9: W14-8s100k16Ga: Comparison of ABAQUS model and experimental component responses during 2% cycle

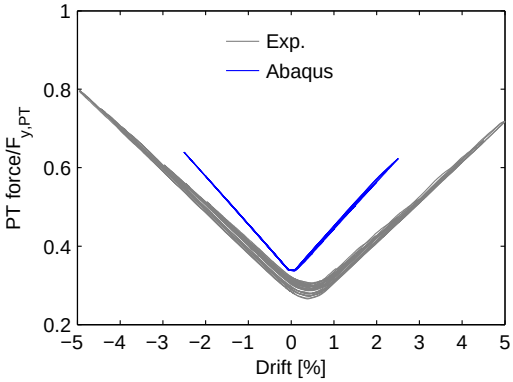

(a) Middle HBE PT force vs. drift response

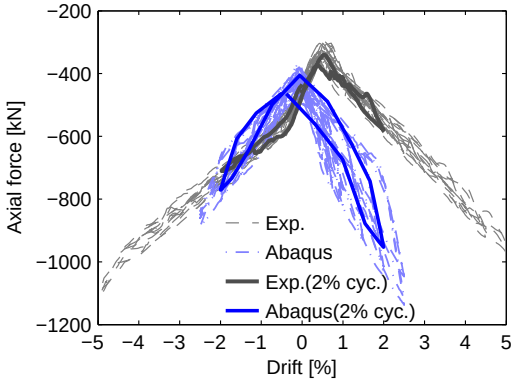

(b) Middle HBE average axial force vs. drift response

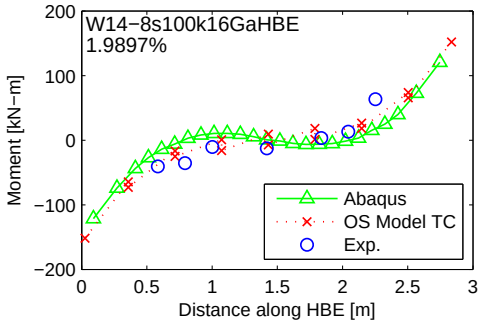

(c) Middle HBE moment distribution: approx. +2% drift

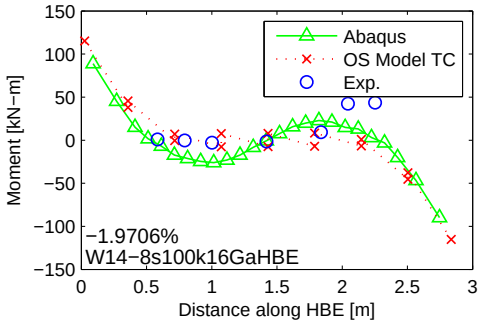

(d) Middle HBE moment distribution: approx. -2% drift

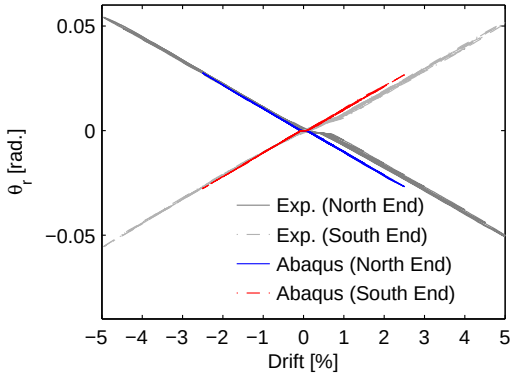

(e) Middle HBE connection rotation

Figure E.10: W14-8s100k16GaHBE: Comparison of ABAQUS model and experimental component responses during 2% cycle

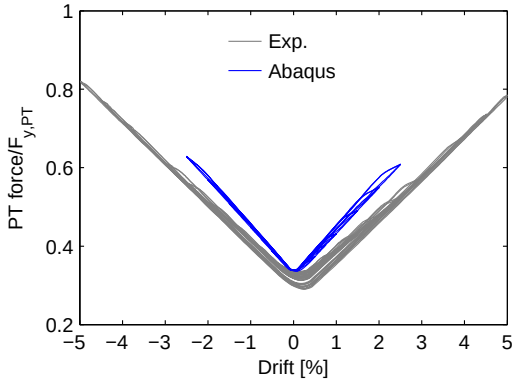

(a) Middle HBE PT force vs. drift response

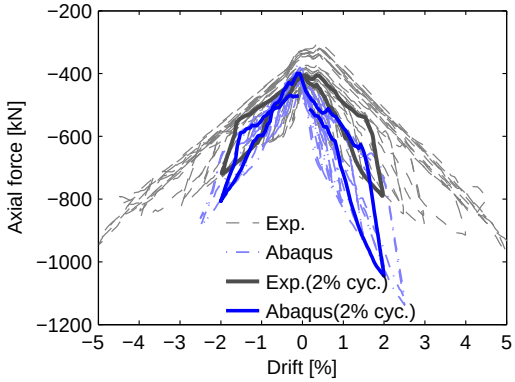

(b) Middle HBE average axial force vs. drift response

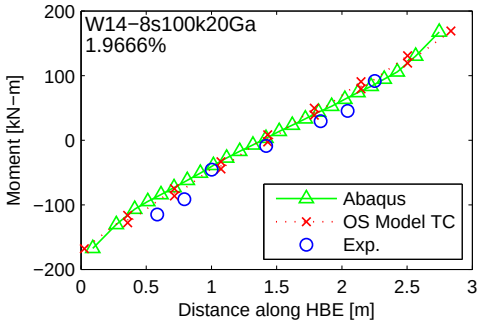

(c) Middle HBE moment distribution: approx. +2% drift

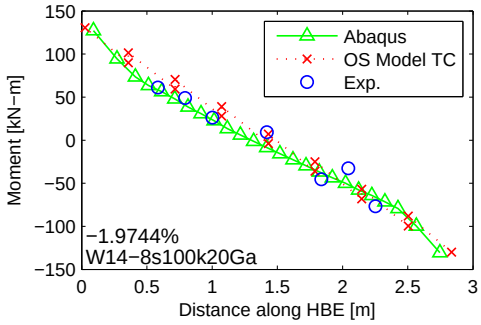

(d) Middle HBE moment distribution: approx. -2% drift

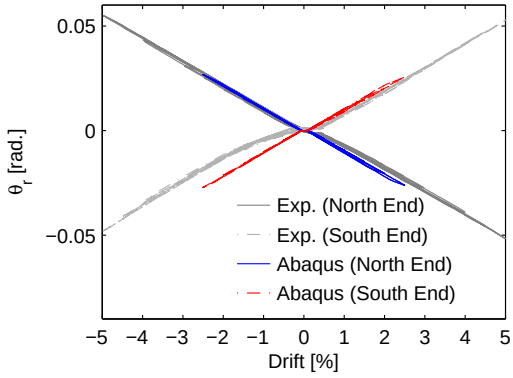

(e) Middle HBE connection rotation

Figure E.11: W14-8s100k20Ga: Comparison of ABAQUS model and experimental component responses during 2% cycle

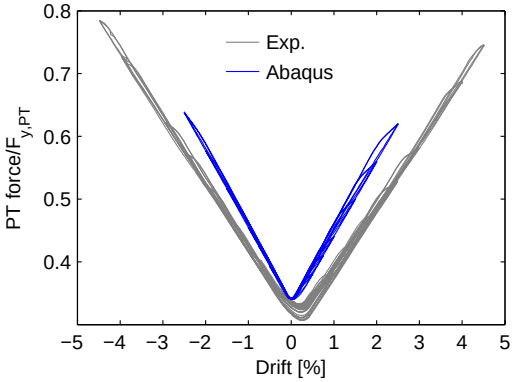

(a) Middle HBE PT force vs. drift response

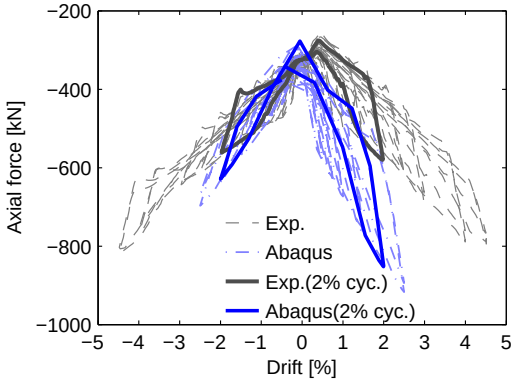

(b) Middle HBE average axial force vs. drift response

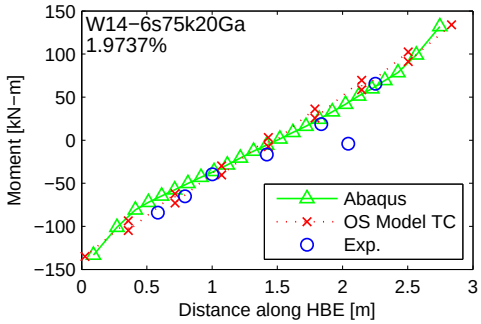

(c) Middle HBE moment distribution: approx. +2% drift

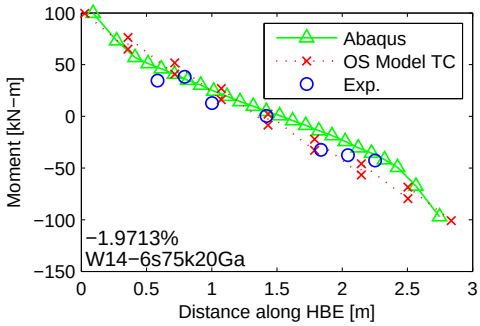

(d) Middle HBE moment distribution: approx. -2% drift

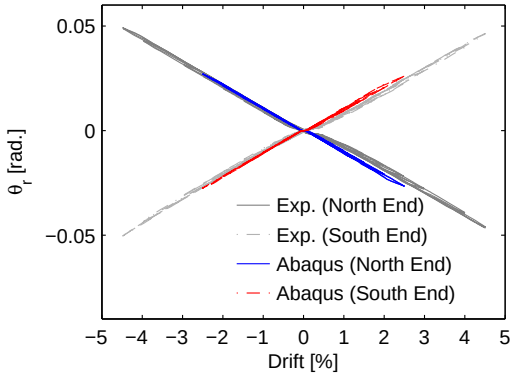

(e) Middle HBE connection rotation

Figure E.12: W14-6s75k20Ga: Comparison of ABAQUS model and experimental component responses during 2% cycle

Appendix F

RESPONSE PARAMETERS FROM TENSION-ONLY SC-SPSW BUILDING NUMERICAL STUDY

Below are the results of the nonlinear response history analyses of the three- and nine-story SC-SPSWs from Clayton [2010]. These SC-SPSW models employed the tension-only (TO) web plate strip model. In Chapter 8, the results of these simulations are compared to those of comparable SC-SPSWs modeled using the tension-compression (TC) strip model and those designed with web plates connected to the beams only.

Table F.1: Summarized response parameters from nonlinear analyses [Clayton, 2010]

Model	Response Parameter	50% in 50 yr		10% in 50 yr		2% in 50 yr	
		$\mu_{1/2}$	84th %	$\mu_{1/2}$	84th %	$\mu_{1/2}$	84th %
3-5050-6-TO	$\theta_{s,max}$ (%)	0.40	0.61	0.54	0.84	1.16	1.86
	$\theta_{resid,max}$ (%)	0.002	0.002	0.002	0.002	0.002	0.002
	D_{HBE}	0.52	0.63	0.59	0.71	0.74	0.84
	D_{VBE}	0.37	0.53	0.43	0.56	0.66	0.74
3-1050-4-TO	$\theta_{s,max}$ (%)	0.80	1.24	2.04	3.65	5.46	7.82
	$\theta_{resid,max}$ (%)	0.003	0.004	0.007	0.028	0.355	4.61
	D_{HBE}	0.49	0.53	0.66	0.82	1.00	1.15
	D_{VBE}	0.47	0.62	0.79	0.97	1.06	1.16
3-1050-6-TO	$\theta_{s,max}$ (%)	0.70	1.13	1.72	3.17	4.52	7.34
	$\theta_{resid,max}$ (%)	0.004	0.004	0.004	0.005	0.074	0.38
	D_{HBE}	0.42	0.56	0.59	0.72	0.94	1.09
	D_{VBE}	0.39	0.47	0.56	0.83	0.97	1.10
9-5050-10-TO	$\theta_{s,max}$ (%)	0.20	0.33	0.49	0.67	1.26	2.47
	$\theta_{resid,max}$ (%)	0.004	0.007	0.004	0.007	0.004	0.023
	D_{HBE}	0.28	0.51	0.55	0.60	0.68	0.83
	D_{VBE}	0.34	0.53	0.59	0.71	0.79	0.93
9-1050-6-TO	$\theta_{s,max}$ (%)	0.40	0.67	0.91	1.51	2.66	3.84
	$\theta_{resid,max}$ (%)	0.003	0.028	0.017	0.102	0.151	0.713
	D_{HBE}	0.47	0.54	0.65	0.80	0.97	1.10
	D_{VBE}	0.58	0.76	0.84	0.97	1.10	1.23
9-1050-8-TO	$\theta_{s,max}$ (%)	0.42	0.85	1.30	1.92	3.20	5.40
	$\theta_{resid,max}$ (%)	0.009	0.012	0.005	0.126	0.117	1.31
	D_{HBE}	0.45	0.51	0.52	0.57	0.70	1.00
	D_{VBE}	0.55	0.67	0.70	0.76	0.86	1.14
9-1050-10-TO	$\theta_{s,max}$ (%)	0.47	0.88	1.08	1.89	3.02	4.49
	$\theta_{resid,max}$ (%)	0.005	0.033	0.004	0.039	0.114	0.830
	D_{HBE}	0.34	0.48	0.52	0.64	0.82	1.07
	D_{VBE}	0.45	0.49	0.54	0.59	0.74	0.98

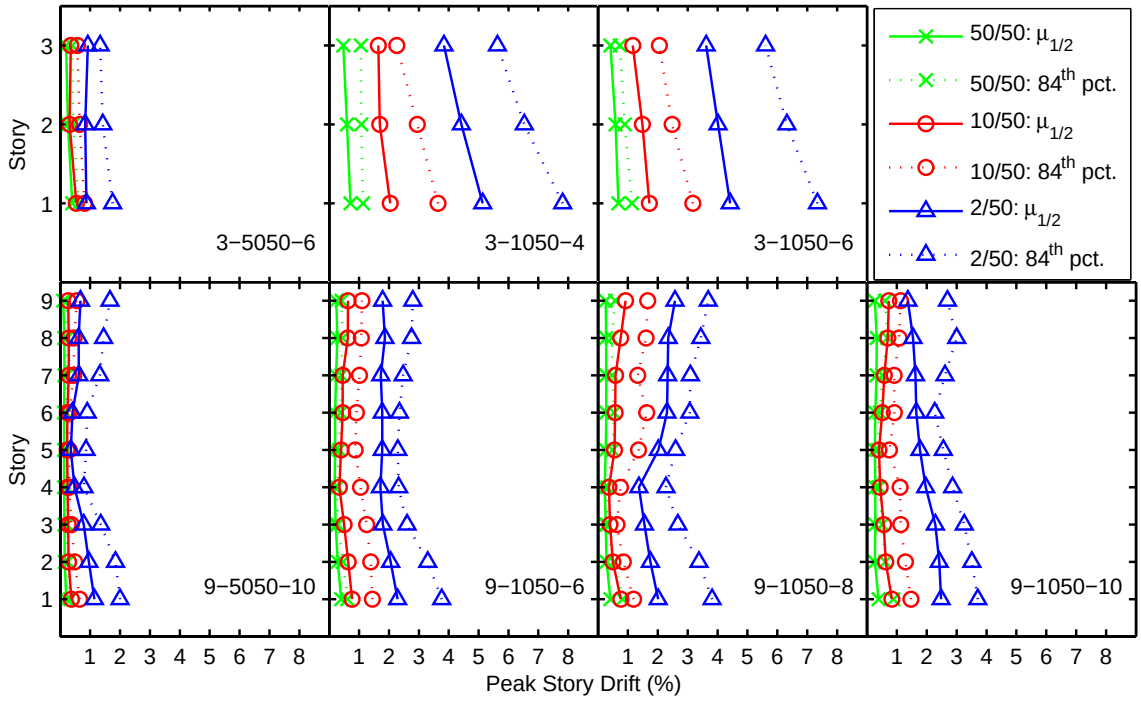

Figure F.1: Peak story drift median ($\mu_{1/2}$) and 84th percentile response [Clayton, 2010]

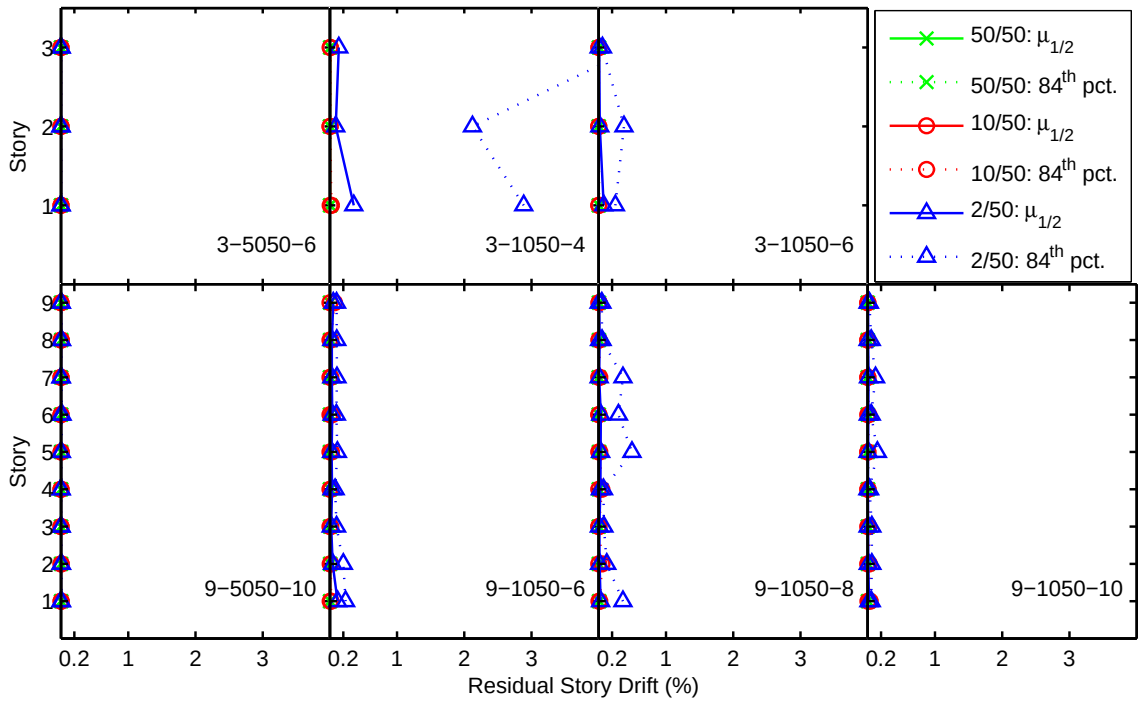

Figure F.2: Residual story drift median ($\mu_{1/2}$) and 84th percentile response [Clayton, 2010]

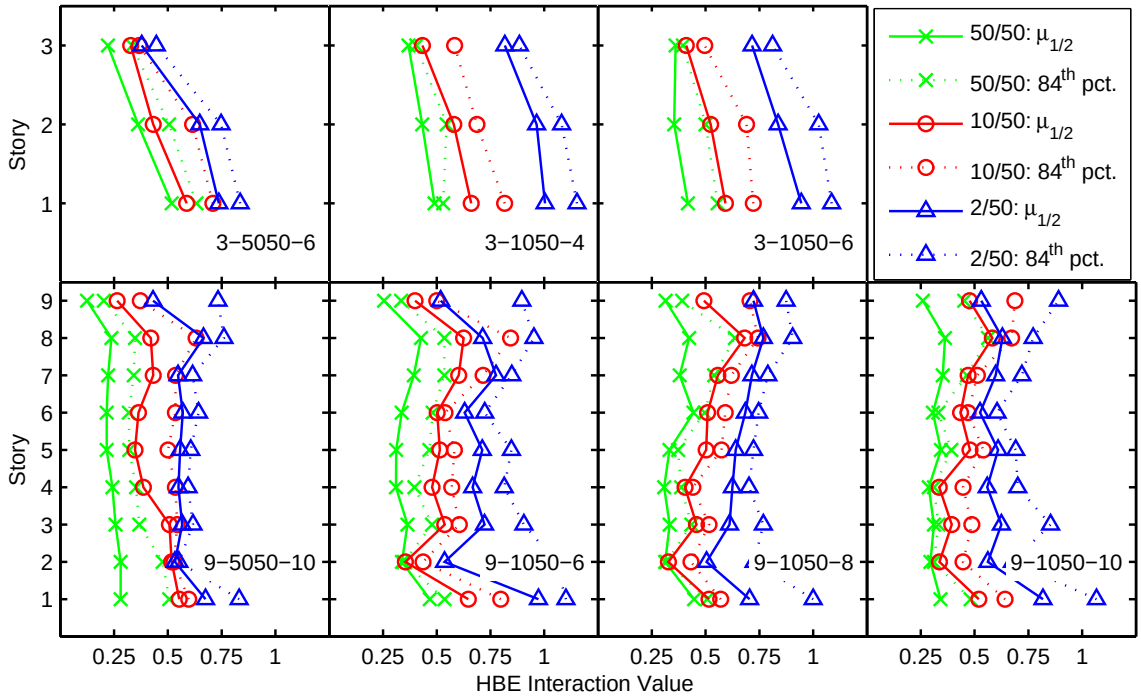

Figure F.3: HBE damage value median ($\mu_{1/2}$) and 84th percentile response [Clayton, 2010]

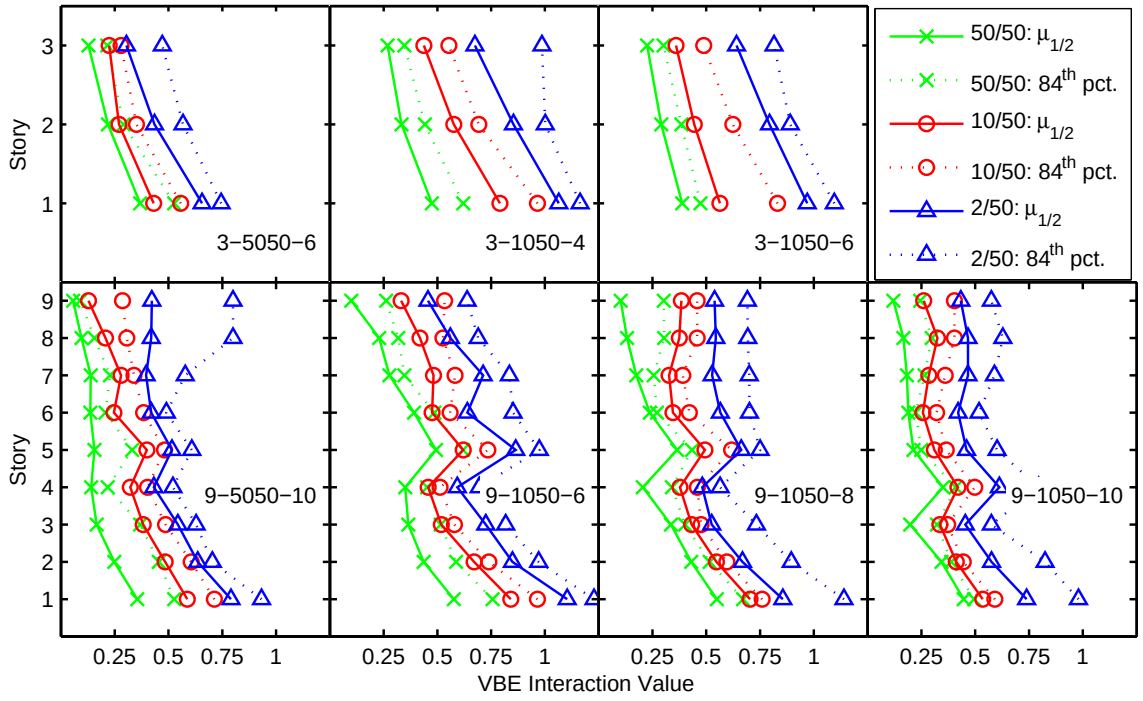

Figure F.4: VBE damage value median ($\mu_{1/2}$) and 84th percentile response [Clayton, 2010]